HAL
open science

Simulating the dynamics of harmonically trapped Weyl particles with cold atoms

Daniel Léo Suchet

To cite this version:

Daniel Léo Suchet. Simulating the dynamics of harmonically trapped Weyl particles with cold atoms. Quantum Physics [quant-ph]. Université Pierre et Marie Curie - Paris VI, 2016. English. NNT : 2016PA066262 . tel-01390499v2

HAL Id: tel-01390499

https://theses.hal.science/tel-01390499v2

Submitted on 8 Sep 2017

HAL is a multi-disciplinary open access archive for the deposit and dissemination of scientific research documents, whether they are published or not. The documents may come from teaching and research institutions in France or abroad, or from public or private research centers.

L'archive ouverte pluridisciplinaire **HAL**, est destinée au dépôt et à la diffusion de documents scientifiques de niveau recherche, publiés ou non, émanant des établissements d'enseignement et de recherche français ou étrangers, des laboratoires publics ou privés.

Département de Physique
École normale supérieure

Laboratoire Kastler Brossel
Physique quantique et applications

UPMC
SORBONNE UNIVERSITÉS

THÈSE DE DOCTORAT
DE L'UNIVERSITÉ PARIS VI

Spécialité : Physique Quantique

École doctorale : Physique en Île-de-France

réalisée

au Laboratoire Kastler Brossel

présentée par

Daniel Léo Suchet

pour obtenir le grade de :

Docteur de l'Université Pierre-et-Marie Curie (Paris VI)

Sujet de la thèse :

Simulating the dynamics of harmonically trapped Weyl particles with cold atoms

soutenue le 8 Juillet 2016

devant le jury composé de :

M.	Frédéric Chevy	Co-directeur de thèse
M.	Leonardo Fallani	Rapporteur
M.	Jean-Noël Fuchs	Examinateur
M.	Jean-Claude Garreau	Rapporteur
M.	Philippe Grangier	Examinateur
M.	Christophe Salomon	Directeur de thèse

-Ckarovala Myšička...
A ma famille.

Aknowledgements

Don't be dismayed at good-byes. A farewell is necessary before you can meet again.
And meeting again, after moments or lifetimes, is certain for those who are friends.
Richard Bach, [Bach 1977].

THey say that when you write your PhD, you should keep the hardest part for the end. And they say that you should write the acknowledgments last. I guess that is because there are so many people involved in the four-year long adventure that constitutes a PhD that it's hard to know even where to start.

I am honored that Leonardo Fallani, Jean-Noël Fuchs, Jean-Claude Garreau and Philippe Grangier accepted to be part of my jury. I was very impressed to ask researchers who taught me Physics, directly during lectures or indirectly through talks and papers, to evaluate my work and I am very grateful for the indulgence of their responses.

I am also extremely grateful to my advisors for welcoming me in the team since my Masters internship and for their supervision over the last four (and a half !) years. Their support and trust also allowed me to gain more autonomy in my project management. Frédéric Chevy has probably the broadest knowledge of Physics I know. His insatiable curiosity and uncompromising exigence for precision made our discussions extremely insightful for me and brought new ideas to move forward more than often. It was at the same time a great pleasure to share a common interest for speculative fiction - Fred is undoubtedly the geekiest member of our group (besides me?). Christophe Salomon has an incredible familiarity with cold atom experiments - with all of them, it seems. He knows the principles and applicability of every method, the order of magnitudes of every signal and of every noise, every Story and every Legend of the field. Together with his persistent enthusiasm for our work and for Physics in general, his knowledge and vision were a force driving the group forward. Tarik and I seem to be strongly anti-correlated: he had just defended when I joined the lab, and I just started writing when he came back with a permanent position. I am confident that he will bring with him a renewed energy for FERMIX and that his experience and involvement will significantly accelerate the development of the experiment.

Jean Dalibard is probably the reason why I decided to join the cold atom community, and I keep a vivid memory of his lectures on Quantum Mechanics, both at Polytechnique and at College de France. He also introduced me to Fred and Christophe. I was lucky enough that he also accepted to mentor my PhD, and we had several appointments which helped me to put into perspective the work we were performing in the lab.

I had the opportunity to work with Carlos Lobo and Johnathan Lau (University of Southampton, UK) and Olga Goulko (University of Massachusetts, USA) on Weyl fermions as well as Georg Bruun and Zhigang Wu (Aarhus University, Denmark) on mixed dimensions, and I want to thank all of them for our collaboration. It was not only a stimulating and fruitful exchange of ideas, but also a chance to promote international teamwork - even though science production rate seems sometimes limited by Skype connectivity !

I am particularly grateful to my fellow PhD students, with whom I shared the pain and pleasures of experimental physics. Diogo Fernandes was not only my friend, but also my teacher. I owe him most of the experimental techniques I learnt during my first years of PhD. He was a driving engine for the team and I envy his ability to seize a scientific project, study it and bring it to a realization. I often think of the fun we had in the lab, injecting lasers while competing to find the worst possible music (and I'm flattered to say that, if Diogo is a worthy opponent on the matter, Japanese and Korean music gave me a significant advantage). Norman Kretzschmar will always be remembered as the God of the experiment, and we seriously considered dedicating to him a small altar we believe would help increasing the overall efficiency. It took me several months to realize that his unmentioned interventions on the apparatus early in the morning were responsible for the stability of the experiment. I still admire his calm and unwavering way to address any technical issue. Franz Sievers showed me the importance of having a clear lab and a clear investigation methodology. His perseverance resulted in solid results to which we often refer today.

The new generation is now composed of Mihail Rabinovic, Thomas Reimann and Cedric Enesa. Mihail has an impressive level of expectation for the experiment, as for himself. The quality of the analyses he performs makes his work a solid stone on which the experiment can be built to last. While our first encounters were not easy, I am proud of the way we learnt to work together and happy to count him today as a friend. Thomas came in the lab as a new PhD with the knowledge of a veteran. His cheerful encouragement on every matter, both professional and personal, made him a precious support to overcome the torments of the small daily frustrations as well as the deeper wounds. His proofreading of this manuscript was a God-given help for both scientific and English corrections - all remaining mistakes are obviously entirely my fault! I also swore to him that I would thank Scottie: Scottie, thank you, section 4.3 would not have been the same without your sacrifice. I should also mention Bouygues Construction, who had a major influence on my work. I had little time to work with Cedric, who joined the team soon before the renovation works shut down the lab, but I could still enjoy his enthusiasm and broad interest for Physics, which extend way beyond the lab and already pushed him to stay long after midnight. I have no doubt that he will not only be dedicated to his own research, but will also be a fantastic mentor for future newcomers. Guys, I wish you all the best with FERMIX !

I also want to thank the Lithium team for the technical talks, lunches and drinks we shared. Over the years, the composition of the team changed, but the spirit remained: Benno Rem,

Igor Ferrier-Barbut, Andrew Grier, Sébastien Laurent, Matthieu Pierce, Shuwei Jin and Marion Delehaye. Marion and I have been working together since our Master degree, sharing our students desks before we shared our office. I was very impressed by the way she managed to deal with the "agrégation" exam while succeeding brilliantly in her PhD. Good luck with your teachings to come, may the odds be ever in your favor !

École Normale Supérieure and Laboratoire Kastler Brossel are fantastic institutions to work in, and I want to thank the directors of the LKB, Paul Indelicato and Antoine Heidmann, for welcoming me in the lab. Besides the permanent intellectual stimulation and the impressive feeling of permanently bumping into the authors of the books from which I learnt everything I know about quantum mechanics, their technical services provide a valued comfort for research. I want to express my gratitude to the mechanical, electronical and electrical workshops. A special award should be given to Didier Courtiade, Catherine Gripe and Célia Ruschinzik for protecting our apparatus (literally with *walls*) and sustaining the whole building against all odds. I also deeply enjoyed working with Florence Thibout on several side projects, taking advantage of our chance to have a permanent glass-blower attached to the lab. Thanks to her, I now know that glass is not a fragile material. On the administrative side, Nora Aissous, Delphine Charbonneau, Dominique Giaferri, Audrey Gohlke and Thierry Tardieu are doing an amazing job dealing with all the paperwork and we are all eternally thankful for that. Delphine has dozens of ideas to dynamize the institute. She offered me to join the newly created communication cell, in which I had the opportunity to see how press releases are published and understand better the relationships between our administrative controls. This collaboration was not only an occasion to know the lab better, but also a precious introduction to the politics of science.

In addition to my research activities presented in this manuscript, I had the opportunity to take part in additional scientific projects which contributed a lot to what I learnt over the last four years.

A large part of my side activities were dedicated to science mediation. When I was just an undergraduate student, Master Roland Lehoucq took me as Padawan and trained me to become his stunt. I started presenting his conference "Science in Star Wars" and progressively transformed it into my own talk. I cannot say enough how grateful I am for his confidence, which got my foot on the ladder of mediation, and for the jedi-knighting he gave me after years of collaboration.

My first experience of mediation was soon seriously improved by a first doctoral mission at the science museum Palais de la Découverte, where Kamil Fadel and Hassan Khlifi welcomed me in the Physics department. Performing physics talks in front of large audiences is a very instructive training, not only for debating skills. For instance, I realized that despite my many years of prestigious university curriculum, I could not explain satisfyingly why water was boiling without resorting to equations to hide my lack of understanding of the underlying phenomena. I learnt a lot by looking at and listening to Julien Babel, Alain de Botton, Marilyne

Certain, Atossa Jaubert, Jacques Petitpré, Emmanuel Sidot, Guillaume Trap, Marielle Verges and Sigfrido Zayas, not to mention my fellow junior mediators, and I want to thank all of them. It was a pleasure to share all kind of discussions with everyone from the Physics department, both inside and outside the Palais, and I was very happy we continued our partnership even long after I was gone. Manu is not only an excellent mediator, but also a sparring partner and a dear friend. We already had the occasions to develop together three wonderful projects and I am confident that we will find plenty of new ideas in the future !

I was very lucky that so many people put trust in me and invited me to give talks, a very stressful but extremely insightful training. Antoine Heidmann offered me twice to give a general presentation on quantum mechanics at the internal seminar of the lab. I have also been invited to present this talk at the newcomers seminar (JEPHY 2015) organized by the CNRS. Together with my friend David Elghozi, I answered a call for projects issued by the Diagonale Paris-Saclay on how fiction can be employed as a means to address science[1], and presented our work in a dozen high schools and on two science festivals. I especially want to thank Elisabeth Bouchaud, the White Queen, who made me the honor of inviting me twice to take the floor in her theater for a "Scène de Science" and the French Physical Society who accepted to promote this conference. I believe that this original approach of popular science is an interesting way to talk not only about Physics, but mostly about the scientific method.

During a round table at ICAP 2012 Claude Cohen-Tannoudji said, referring to his famous course on quantum mechanics, that the best way to learn something is probably to teach it. Thanks to Manuel Joffre and Christoph Kopper, presidents of the Physics departement at Ecole polytechnique, I was lucky enough to be accepted as teaching assistant and could experience directly what Claude was talking about during two peculiar teaching missions.

First, I joined Arnd Specka's team and took part in the preparatory semester for the new foreign students accepted at Polytechnique. It was an extraordinary opportunity not only to meet students from various cultural backgrounds, but also to think about language and methodology at least as much as about Physics. Arnd is always eager to improve his own work and promoted a very motivating ambiance in the group. Thanks to the constant support of Jean Souphanplixa and Linda Guevel, we also had very comfortable working conditions and could focus entirely on the teaching part of the job. Jean has always been the best to provide me with all sorts of technical and logistical solutions !

Second, Manuel and Christoph offered to me the opportunity to develop the International Physicists' Tournament (IPT[2]) in France, which was an amazing experience. The IPT is a worldwide competition targeting undergraduate students. Teams of six prepare 17 open Physics problems given a year in advance: what is the curvature of a curly ribbon scored with a blade ? What is the maximal range of a smoke vortex ring ? How different is the color of a stone once it is wet ? During the tournament, teams meet 3 by 3: the Reporter presents his or her solution

[1]The text of the manifesto published after this work is available here: www.penangol.fr/TGCM
[2]Official website: www.iptnet.info

to a problem in 10′, the Opponent criticizes the presentation and the Reviewer moderates the ensuing discussion. The IPT demands physics and debating skills as well as team work; it encourages students to go and talk to researchers and offers them a first chance to see how the same problem can be tackled very differently by students from different backgrounds. Polytechnique was the first French university ever invited to join the Tournament and Manuel and Christoph decided to take up the challenge. Together with Christophe Clanet, Guilhem Gallot and Roland Lehoucq, we trained four teams of students, three of which made their way to the podium. I also want to call attention to the perfect (and thus discrete) logistical backup of Sylvie Pottier and Patricia Vovard, thanks to whom the whole organization was effortless. Supervising a student research project is by itself a fruitful training, but the specifics of the IPT require an additional step back. I was very impressed by the ability of Christophe, Christoph, Guilhem, Manuel and Roland to seize any problem, come quickly to a qualitative analysis and suggest several ways to investigate quantitatively the phenomenon at stake. Watching them and coaching students, both in preparation and during the competition, actually changed my own perception of Physics. I also want to thank the whole International Organizing Committee, and especially Vivien Bonvin, Vladimir Vanovsky, Dave Farmer, James Sharp, Andreas Isacsson and Ulrich Groenbjerg for the work we have done together. It was awesome to meet year after year, not knowing whether the tournament would be held the following year, but satisfied to see our students enjoying and learning so much.

It is often difficult to carry a project by oneself, and I had several opportunities to experience that the French Physical Society (SFP) knows how to incubate initiatives and turn them into a collective effort, teaching young physicists about project management in the mean time. I am particularly grateful to Samuel Guibal, president of the Paris-centre section, Alain Fontaine and Michel Spiro, successive presidents of the SFP, who trusted me with the crazy project of the Tournament and endorsed its responsibility while giving me more than enough elbow room. They also accepted to let me pass the torch to Maxime Harazi, who decided to organize the 8th edition of the IPT in Paris. Maxime is a real workaholic and brought the Tournament to a new level of professionalism - I marvel at his unbelievable efficiency and dedication. I really had a good time working with him and the LOC-team (Erwan Allys, Nathanël Cottet, Cyrille Doux, Charlie Duclut, Marguerite Jossic, Guillaume d'Hardemare and Arnaud Raoux), and I believe that we have done an amazing job. I hope we have proven that a bunch of PhD students could be trustworthy to handle a budget over 100 k€ ! I was particularly glad that Arnaud accepted to ruin his own PhD to join the gang -not only for his now well-established treasury skills. Since our Masters degree, we had a lot of fun carrying out several projects together, and I have the feeling it is only the beginning.

A PhD is definitely not a solitary task, and in addition to all the professional supports mentioned above, and to all of those I could not cite, I want to write a few words about some of the people who raised and accompanied me throughout the last four years.

I had the privilege to meet extraordinary scientists who inspired and trained me, during lectures, collaborations and scientific debates. Damien Jurine proved to me the power of orders of magnitudes and I can still clearly picture his impersonation of a humming-bird evaluating the energetic content of a flower nectar in terms of pasta plates. Dominique Chardon gave me a rock-solid training in classical physics and instilled in me the taste for wave optics. Damien and Dominique also offered me my first teaching experience when they accepted me as TA for their oral examinations. Jean Souchay welcomed me in his group at the Paris Observatory when I was just finished with high-school. Our collaboration on quasars gave me the taste for research and continues to produce new projects. With the same generosity, Frédéric Fleuret kindly accepted to work with me when I arrived at École polytechnique, introducing me to particles physics. I keep fond memories of the dream-team of Frédéric, Olivier Drapier and Michel Gonin, with whom I learnt everything I know about data analysis. I still regret the coffee machine of the LLR... Ater we first met during a lab visit organized through the association "Boson de HixX", Yves Bréchet regularly took the time to invite me for a drink or a diner, where we talked about science, literature and conspiracy theory. He put in my hands the book [MacKay 2009] that had so far the biggest influence on my life, changing my perspectives on the environment, inspiring me to dedicate my post doc to the Physics of Energy and bringing me to a Climate March where I eventually met Aline. I owe Sebastien Balibar my first scientific encounter with climate, environment and energy, since he trusted me to proofread his book on the matter [Balibar 2015]. Thanks to Michèle Leduc and Joachim Nassar, I met Jean-François Guillemoles and Davide Boschetto, with whom I will have the chance to work in the following years, adapting conceptual tools from atomic physics to the field of solar energy.

I cannot say how much support I had from my friends during these years, nor can I thank each and every one of them as much as I would like to. I still want to mention the communicating enthusiasm of Anne Papillault and Jean-François Dars (everybody is eager to attend their suppers!), the diggings undertook with Alexandre Peyre, the countless lunch recreations offered by David Elghozi and the unfailing friendship of my brother in arms, my Pal Mathieu Hemery.

I thought of many people when it came to dedicating this thesis to someone. I then realized that all of them were actually part of my family, my unsinkable backing through the turmoil of life and catalyst of its joys. I want to thank especially my mother Anne Rosenberg for her force of will and of life and Jean-Louis for his demanding interest for all fields of knowledge, as well as his steady concern for the well being of my "little atoms". My father Gérard Suchet has always been an inspiration to imagine and carry out all kind of adventures and I owe Valérie Laboue battery-recharging stays at Saint-Ambroix, which I recommend for the mental sanity of any PhD student. My caring sister Myriam Suchet encourages me to rethink the imaginary borders separating cultures, knowledges and languages ; I am happy and proud of the intellectual playground we created together, linear combination of Physics and Literature. I would have also liked to share the pleasure of bringing this thesis to an end with Mami Luis,

Sif Rosenberg-Reiner and Josef Goldstein. I recognize their influence in many of the choices I made.

Finally, I want to thank my companion, Aline Aurias, for her unconditional love and benevolence, and for her heart-warming confidence when I felt lost in the icing maze of cold atoms. I admire the courage and honesty with which she makes life-changing decisions. I know we will keep the magic of that 21st of September going.

Contents

Acknowledgments x

Table of content xiv

1 Introduction 1

1.1 What are ultracold quantum gases ? 2

1.1.1 How cold is ultracold ? 2

1.1.2 A brief history of cold atoms 3

1.2 Why are cold atoms cool ? 9

1.2.1 Quantum simulation 9

1.2.2 Metrology and applications 13

1.3 Ultracold fermionic mixtures 13

1.3.1 Fermi-Fermi mixtures over the world 14

1.3.2 The FERMIX experiment: a mixture of fermions in mixed dimensions 15

1.4 Outline of this thesis 15

2 The FERMIX experiment 17

2.1 Vacuum chambers 19

2.2 Optical system 21

2.3 Atomic sources 25

2.3.1 Lithium Zeeman slower 26

2.3.2 Potassium 2D-MOT 27

2.4 MOT and CMOT 29

2.5 Λ enhanced D_1 gray molasses 31

2.5.1 Working principle 32

2.5.2 Experimental implementation 34

2.6 Spin polarisation 35

2.7 Magnetic system 36

2.7.1 Magnetic quadrupole trap 36

2.7.2 Magnetic transport 37

2.7.3 Magnetic bias 39

2.8 Security system 40

2.9 Radio Frequency / Microwave system 41

2.10 High power lasers **41**
2.10.1 532 nm laser 43
2.10.2 1064 nm laser 44
2.11 Imaging system **46**
2.11.1 Absorption imaging 46
2.11.2 Time-of-flight expansion of non-interacting particles 47
2.11.3 Experimental setup 49
2.12 Computer control **50**
2.13 Conclusions **51**

3 Quasi-thermalization of fermions in a quadrupole potential **53**
3.1 Equilibrium properties of neutral atoms in a quadrupole trap **55**
3.1.1 Quadrupole traps 55
3.1.2 Initial Boltzmann distribution and typical orders of magnitude 56
3.1.3 Loss mechanisms 57
3.1.4 Density of states and adiabatic compression 60
3.2 Experimental investigations **61**
3.2.1 Initial observations: anisotropic effective temperatures 61
3.2.2 Further measurements 62
3.2.3 Preliminary conclusions 66
3.3 Numerical simulations **66**
3.3.1 Numerical methods 67
3.3.2 Comparison with the experiment 69
3.4 A simple model for the effective heating **71**
3.4.1 General predictions 73
3.4.2 In the experiment: direct kick of the cloud 74
3.4.3 Another excitation: adiabatic displacement 79
3.5 Quasi thermalization in an isotropic trap **80**
3.5.1 Isotropic 2D potential 80
3.5.2 Isotropic 3D potential 82
3.6 Influence of the trap anisotropy **87**
3.6.1 Anisotropy of the steady state 87
3.6.2 Quasi-thermalization time 88
3.7 Conclusions **89**

4 Analog simulation of Weyl particles in a harmonic trap **91**
4.1 Weyl particles: from high energy Physics to cold atoms **92**
4.1.1 A paradigm in high energy physics 92
4.1.2 Emergent low energy excitations 93
4.1.3 Weyl particles in a trapping potential: the Klein paradox 98

4.2 Analogue simulation of Weyl particles **99**
4.2.1 Canonical mapping 100
4.2.2 Majorana losses and Klein paradox 100
4.2.3 Quasi-thermalization in a harmonic trap 101
4.3 Geometric potentials **104**
4.3.1 Berry phase, scalar and vector potential 104
4.3.2 Effect of the geometric potentials 107
4.4 Conclusions and outlooks **109**

5 Evaporative cooling to quantum degeneracy **111**
5.1 Diagnostic tools in the science cell **112**
5.1.1 Spin selective measurements 112
5.1.2 Spin manipulation 117
5.1.3 Calibration of the apparatus 119
5.2 Principle of evaporative cooling **123**
5.3 Evaporative cooling of Potassium **127**
5.3.1 Magnetic RF-evaporation 127
5.3.2 Loading of the optical trap 128
5.3.3 Optical evaporation 129
5.4 Double evaporative cooling of ^{6}Li and ^{40}K **132**
5.4.1 ^{6}Li-^{40}K interactions 132
5.4.2 Magnetic RF-evaporation 133
5.4.3 Optical evaporation 134
5.5 Conclusions **136**

6 Effective long-range interactions in mixed dimensions **139**
6.1 Scattering in mixed dimensions **141**
6.2 Mediated long-range interactions **145**
6.2.1 Mathematical framework 145
6.2.2 Effective interaction: general expression 147
6.2.3 Effective interaction for $\kappa_{\mathrm{CoM}} = 0$ 149
6.3 Proposal for an experimental realization **151**
6.3.1 Implementation of an optical lattice 151
6.3.2 Effective interaction between two layers 152
6.3.3 Coupled oscillations between two layers 154
6.4 Conclusions **157**

Conclusion **159**

Appendix A Appendix **163**
A.1 Alkaline atoms in magnetic fields **164**

A.1.1 Wigner-Eckart theorem and Lande factor . . . 164
A.1.2 Zeeman hamiltonian . . . 165
A.1.3 Asymptotic behaviors . . . 166
A.1.4 Breit-Rabi formula . . . 168
A.1.5 Remark on notations . . . 169
A.2 About Boltzmann equation . . . 170
A.2.1 Collisionless Boltzmann equation . . . 170
A.2.2 H theorem . . . 171
A.3 Kohn, virial and Bertrand theorems . . . 175
A.3.1 Kohn theorem . . . 175
A.3.2 Virial theorem . . . 176
A.3.3 Bertrand's theorem . . . 177
A.4 Elements of collision theory . . . 181
A.4.1 Mathematical framework . . . 182
A.4.2 Scattering eigenstates . . . 183
A.4.3 Scattering matrices, amplitude and cross section . . . 183
A.4.4 Low energy limit . . . 185
A.4.5 Feshbach resonances . . . 187
A.4.6 Getting familiar with a Feshbach resonance . . . 189
A.5 Technical references . . . 191
A.5.1 AOMs and EOMs . . . 191
A.5.2 Power supplies . . . 192
A.5.3 Optical sources . . . 192
A.5.4 RF system . . . 193
A.6 Electrical schemes . . . 193

Appendix B Publications 201
Simultaneous sub-Doppler laser cooling of fermionic... . . . 201
Analog Simulation of Weyl Particles with Cold Atoms . . . 213
La quête des températures ultrabasses . . . 220

Bibliography 233

Chapter 1 Introduction

Contents

1.1 What are ultracold quantum gases ? **2**
1.1.1 How cold is ultracold ? 2
1.1.2 A brief history of cold atoms 3
1.2 Why are cold atoms cool ? **9**
1.2.1 Quantum simulation 9
1.2.2 Metrology and applications 13
1.3 Ultracold fermionic mixtures **13**
1.3.1 Fermi-Fermi mixtures over the world 14
1.3.2 The FERMIX experiment: a mixture of fermions in mixed dimensions 15
1.4 Outline of this thesis **15**

> If the Earth was suddenly transported into the very cold regions of the solar system, the water of our rivers and oceans would be changed into solid mountains. The air, or at least some of its constituents, would cease to remain an invisible gas and would turn into a liquid state. A transformation of this kind would thus produce new liquids of which we as yet have no idea.
>
> *Antoine Laurent de Lavoisier*, [de Lavoisier 1789].

THe elegance of Physics holds perhaps to its universality: few signs combined in an equation can describe a vast range of seemingly independent phenomena, like Maxwell equations can reach from light propagation to fridge magnets. Ultracold atoms gases epitomize this universality, not only because they allow for the study of fundamental quantum properties, but also because their behavior can be largely tailored so as to mimic and help the understanding of many quantum complex systems.

This thesis is dedicated to the FERMIX experiment, which focuses on this idea of *quantum simulation*. We aim at cooling to ultra-low temperatures two atomic species in order to investigate fundamental problems from quantum and condensed matter physics. In this introduction, we first present the main properties and orders of magnitude that characterize cold atoms, before addressing two of the motivations that drove an increasing interest to the field over the last decades. We briefly review state of the art of Fermi-Fermi mixtures apparatus and introduce the FERMIX experiment, which provided the data presented in this manuscript.

1.1 What are ultracold quantum gases ?

Low temperatures alter the surrounding world: as imagined by Lavoisier, Earth would be very different if it was to be brought to an average temperature below 0°C. What Lavoisier could not envision was that cold does not only produce new liquids, but also new states of matter, where quantum mechanics prevails.

1.1.1 How cold is ultracold ?

At least two typical length scales are required to describe an ensemble of particles (see Fig. 1.1). The average interparticle distance d is a classical quantity, related to the spatial density n. The thermal de-Broglie wavelength λ_{dB} accounts for the coherent length of the wave-packet corresponding to each particle in a quantum description. It can be expressed as a function of the particle mass m and the temperature T of the ensemble:

$$d = n^{-1/3} \qquad \lambda_{\mathrm{dB}} = \sqrt{\frac{2\pi\hbar^2}{mk_BT}} \quad , \tag{1.1}$$

where $\hbar$ is the reduced Planck constant and k_B is the Boltzmann constant.

The relevant quantity to distinguish between classical and quantum regime is the dimensionless phase-space density (PSD), which accounts for the balance between interparticle distance and thermal de-Broglie wavelength:

$$\mathrm{PSD} = \lambda_{\mathrm{dB}}^3/d^3 \tag{1.2}$$

As long as the temperature is high enough for λ_{dB} to be negligible compared to d (PSD $\ll 1$), wavepackets remain well separated from one another and a classical modeling of the ensemble through a Maxwell-Boltzmann distribution provides an accurate description of the system. On the other hand, if the temperature is decreased so low that λ_{dB} becomes comparable or larger than d (PSD $\gtrsim 1$), the wavepackets interfere with one another and the quantum nature of the system becomes crucial.

Integer spin particles, *bosons*, interfere constructively. At low temperature, a bosonic ensemble undergoes a phase transition as a macroscopic amount of particles accumulate in the same microscopic level, forming a Bose-Einstein condensate. Remarkably, this transition is purely statistical and does not rely on interactions. Half-integer spin particles are called *fermions*. Since the bosonic or fermionic nature of a system only depends on the spin of its particles, it varies from one atomic isotope to the other: for instance ^{39}K and ^{41}K are bosons while ^{40}K is a fermion. By constrast with bosons, fermions interfere destructively, forbidding the simultaneous presence of two particles in the same state. At low temperature, this exclusion principle forces the ensemble to form a Fermi sea, in which all accessible states are populated by one

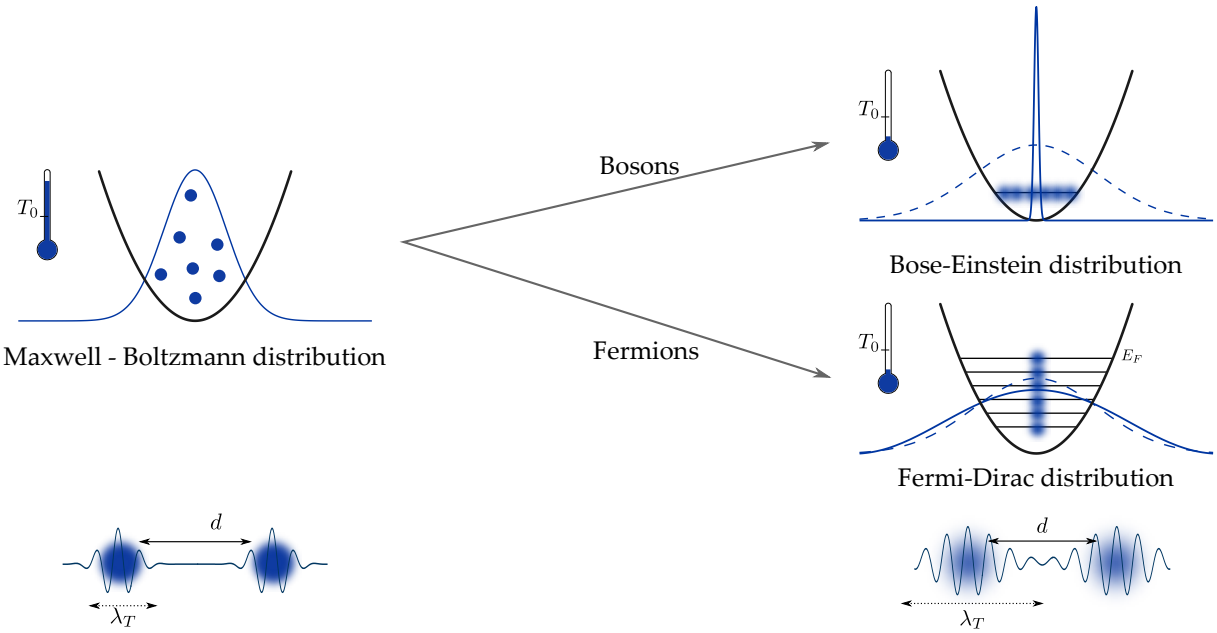

Figure 1.1: Distribution in a harmonic trap. T_0 denotes the quantum degeneracy temperature. **Left**: At high temperature, the de Broglie wavelength is small compared to the inter-particle distance. The ensemble follows a classical Maxwell-Boltzmann distribution, corresponding to a Gaussian profile. **Right**: At low temperature, the wave-packets interfere and the behavior of the system (solid line) becomes quantitatively different from the classical prediction (dashed line): bosons accumulate in the trap ground state and a form a Bose-Einstein condensate (downscaled by a factor 10), while fermions are distributed among increasing energy levels up to the *Fermi energy* E_F according to Pauli exclusion principle.

single particle, up to the Fermi energy E_F. This fermionic transition from classical regime to quantum degeneracy occurs gradually and, unlike for bosons, does not give rise to a phase transition.

The temperature below which the system becomes ultracold, usually called condensation temperature T_C for bosons and Fermi temperature T_F for fermions, depends on the particles mass and the ensemble average density. With a light mass and high density, electrons in a metal present a Fermi temperature around 30 000 K and are governed by quantum statistics at room temperature. Atoms are much heavier and show consequently a much lower quantum degeneracy temperature. In liquid phase, the critical temperature is reduced to few Kelvins, as exemplified by Helium. As for quantum gases, the thin density further decreases the border of the quantum domain and temperatures below 10^{-6} K must be reached to observe non classical behaviors (see Fig. 1.2).

1.1.2 A brief history of cold atoms

The first manifestation of a macroscopic quantum behavior took place in 1911 with the discovery of superconductivity by Kamerlingh-Onnes: as soon as mercury is cooled below 4.2 K, its electrical conductivity vanishes with a steepness typical of phase transitions. Two decades

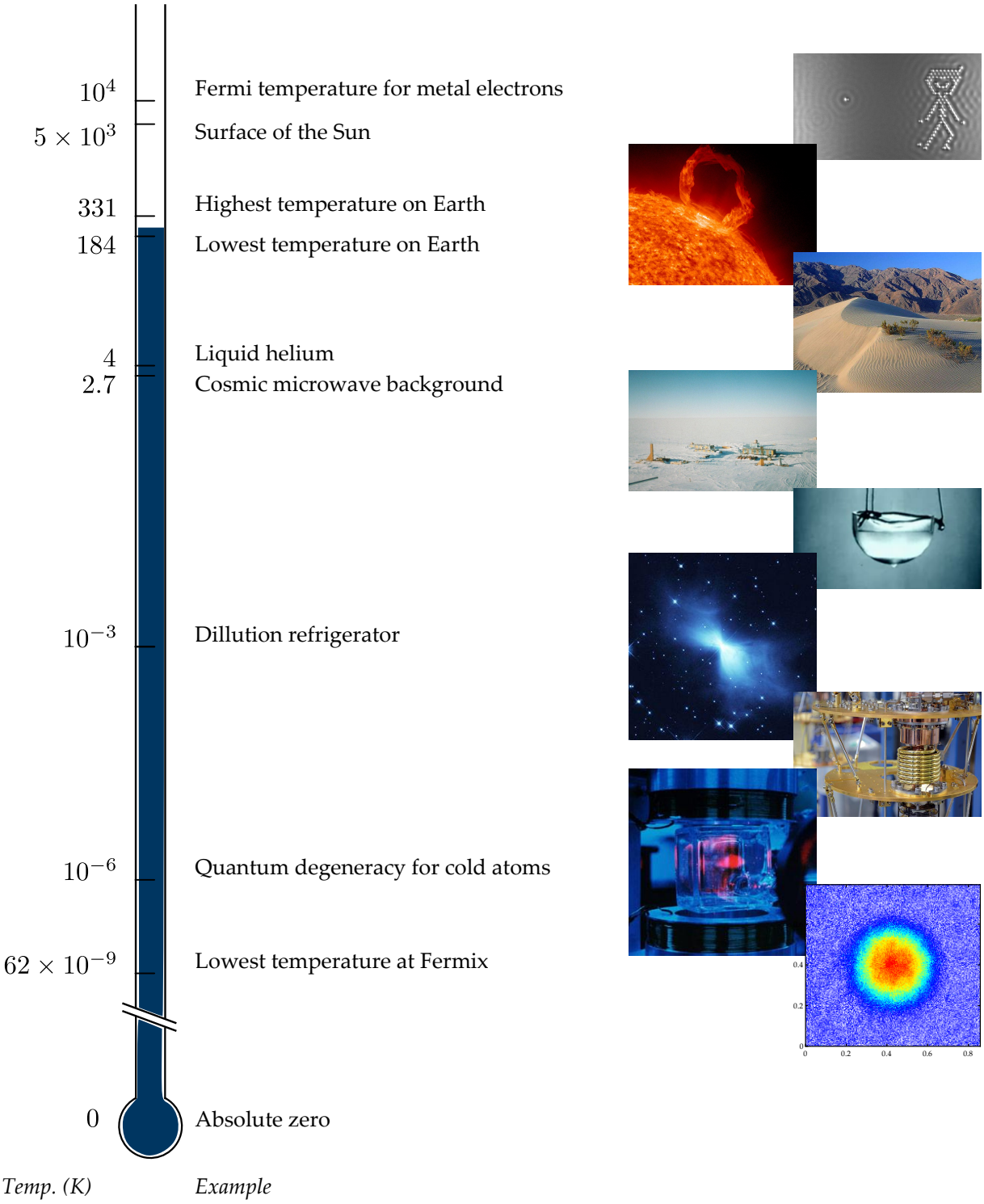

Figure 1.2: Orders of magnitude: temperature (in Kelvin) of some reference systems in log scale. Illustrations from top to bottom: "A boy and his atom" (electronic density image from a atomic pixel-art movie), surface of the sun, Mojave Desert (hottest place on Earth), Vostok station (coldest place on Earth), liquid Helium 4, Boomerang Nebula (coldest place in the Universe), dilution refrigerator, cold Rubidum atoms, degenerate ^{40}K cloud obtained in FERMIX. All pictures except the last one are under Creative Commons license.

later,Kapitza[1] and Allen and Misener[2] found that below 2.17 K, liquid Helium 4 becomes *superfluid* as its viscosity suddenly disappears, bringing an additional demonstration of the surprising properties that can arise at very low temperature.

Ultra cold bosons

In parallel to those experimental discoveries, following an earlier work by Bose[3] on black body radiation, Einstein[4] derived the conditions for the Bose-Einstein condensation introduced in the previous section. While Einstein doubted that this theory would have any practical applications ("*It is a nice theory, but does it contain any truth ?*", he wrote to Paul Ehrenfest before leaving this field of research[5]), it was found by London[6] and Tisza[7] to be an explanation for Helium 4 superfluidity.

Nevertheless, Einstein's seminal work did not include interparticles interactions which play a crucial role in Helium 4 superfluidity, notably by limiting the condensed fraction to 10% whereas an ideal gas is supposed to reach full condensation. Over the following decades, neutral atoms in gaseous phase appeared to be a promising system for the realization of weakly interacting BECs and first attempts focused polarized hydrogen, believed to be an ideal candidate thanks to its light mass. The cooling strategy relied on evaporative cooling of magnetically trapped atoms to reduce temperature below few milliKelvins (see chapter 5), but quantum degeneracy remained hindered by dipolar losses and a small atom scattering cross section which forbid efficient evaporation.

In the mid '70s, the emergence of adjustable laser light provided the field with powerful tools to manipulate atoms. The optical pumping imagined by Kastler provides a valuable way to accumulate atoms in a selected internal state[8]. Lasers also allow to control the outer degrees of freedom of atoms by acting on their internal degrees of freedom. Taking into account not only energy exchange but also momentum exchange between light and matter, Einstein had shown indeed that two radiative forces apply on an illuminated atom[9]: cycles of absorption / spontaneous emission result in a dissipative radiation pressure, pushing the atom along the direction of the beam, while cycles of absorption / stimulated emission give rise to a conservative dipole potential, proportional to the light intensity.

Those effects allow for a very efficient cooling of atoms[10] and ions[11], as soon illustrated by the iconic Magneto-Optical Trap (MOT)[12]. Together with forced evaporative cooling, they gave rise in 1995 to the first Bose-Einstein condensation of Rubidium 87[13] and Sodium 23[14]. Since then, fifteen bosonic isotopes have been cooled down to degeneracy: hydrogen[15], all

[1] [Kapitza 1938]
[2] [Allen and Misener 1938]
[3] [Bose 1924]
[4] [Einstein 1924]
[5] [Pais 2005]
[6] [London 1938]
[7] [Tisza 1938, Tisza 1947]
[8] [Kastler 1950]
[9] [Einstein 1917]
[10] [Hänsch and Schawlow 1975]
[11] [Wineland and Dehmelt 1975]
[12] [Raab *et al.* 1987]
[13] [Anderson *et al.* 1995]
[14] [Davis *et al.* 1995a]
[15] [Fried *et al.* 1998]

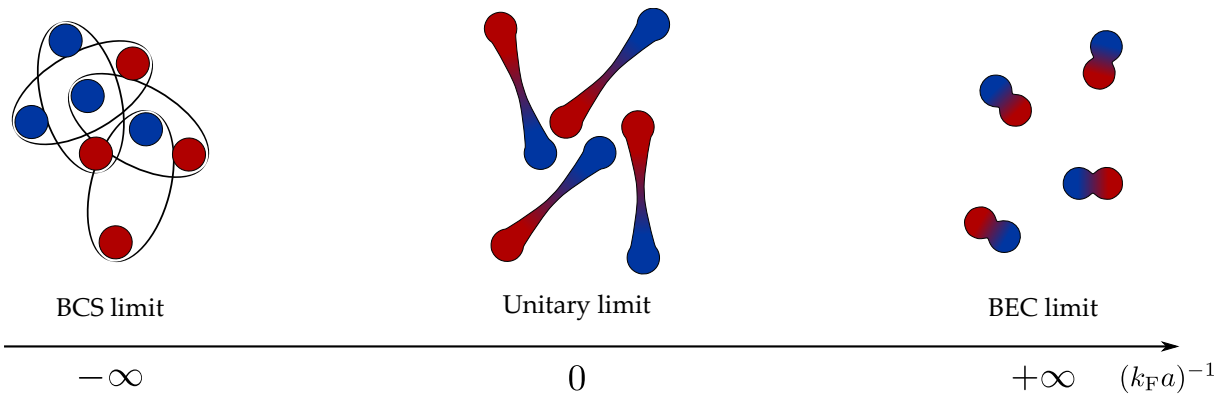

Figure 1.3: BCS-BEC crossover. As the scattering length a describing the interaction between two fermionic species (red and blue) is varied from $-\infty$ to $+\infty$, the system evolves through the *BCS-BEC crossover*, forming successively a non interacting Fermi gas ($1/k_F a \to -\infty$, where k_F is the Fermi wavevector of the gas), a correlated superfluid of pairs (BCS limit), a strongly interacting ensemble (unitary limit) and a non interacting Bose-Einstein condensate of molecules ($1/k_F a \to +\infty$).

alkali metal but Francium, two earth alkali (Calcium, Strontium), a noble gas (metastable He), a transition metal (Chromium) and three Lanthanides (Ytterbium, Erbium, Dysprosium). BEC of quasi-particles such as magnons[16] and polaritons[17] have also been reported.

In addition to the quantum phase transition, many spectacular effects related to phase coherence were observed in BEC (for a review, see for instance [Ketterle *et al.* 1999]). Owing to their wave nature, two BECs can interfere with one anther, resulting in the formation of matter wave interferences[18]. The superfluid behavior, induced by inter-particle interactions, has remarkable manifestations, such as the appearance of vortices caused by the quantization of circulation[19] or the existence of critical velocities, below which an impurity moving at constant speed can not dissipate energy but rather experience a frictionless environment[20]. All these effects have been observed experimentally.

Ultra cold fermions

Using the same cooling techniques, several groups tried to bring to degeneracy fermionic isotopes[21], the cooling of which is all the more challenging as Pauli principle forbids collisions between indistinguishable particles and prevents evaporation to low temperatures of spin-polarized ensembles. This difficulty could be overcome either by sympathetic cooling, where a bosonic cloud is actively evaporated and thermalises the fermionic sample to low temperatures[22] or by the simultaneous cooling of two distinct spin-states of the same species[23], and the first degenerate gas of fermionic ^{40}K was obtained four years after the first BEC[24]. Since

[16][Nikuni *et al.* 2000, Demokritov *et al.* 2006]
[17][Amo *et al.* 2009, Balili *et al.* 2007]
[18][Ketterle 2002]
[19][Matthews *et al.* 1999], [Madison *et al.* 2000], [Abo-Shaeer *et al.* 2001]
[20][Raman *et al.* 1999, Onofrio *et al.* 2000, Fedichev and Shlyapnikov 2001]
[21][Cataliotti *et al.* 1998]
[22][Schreck *et al.* 2001]
[23][Demarco and Jin 1998]
[24][DeMarco and Jin 1999]

then, fermionic quantum degeneracy has also been reached for Lithium 6, metastable Helium 3, three Lanthanides (Dysprosium 161, Erbium 167, Ytterbium 173) and the alkaline earth element Strontium 87.

Since atoms are neutral, most of the interparticle interactions are short-ranged. Interactions between fermions display a remarkable *universal* behavior. At low energy, elastic collisions between two particles can be essentially described by a single scalar parameter, the *scattering length*, usually noted a. For fermions, this two body quantity is sufficient to account for the whole interacting many-body problem. By contrast, additional parameters need to be considered to treat an interacting bosonic system beyond mean-field approaches. The universality of fermions appears clearly in the *unitary* regime, where the scattering length diverges and saturates the strength of the interaction. At zero temperature, the chemical potential μ and all corresponding thermodynamical properties[25] are then related to the only available scale set by the Fermi energy E_F and the strongly interacting ensemble scales like an ideal gas:

$$\mu_\infty = \xi \times E_F, \tag{1.3}$$

where $\xi \simeq 0.37$ is a universal parameter called the *Bertsch parameter*, named after Georges Bretsch, professor of the Institute of Nuclear Theory, University of Washington, who offered 600$ reward for the determination of the sign of ξ[26].

The discovery of Feshbach resonances and their adaptation to cold atoms was a turning point for the field in general and Fermions in particular. Feshbach resonances provide an experimental way to tune the strength of interactions at will, simply by raising a magnetic bias: the scattering length diverges at resonant values of the field, and can thus be adjusted to arbitrary values (see section A.4.5). Initially observed on bosonic systems[27], Feshbach resonance gave rise to fast losses due to the concomitant enhancement of inelastic collisions. Fortunately, fermions are protected from such three-body losses by the Pauli exclusion principle[28].

In addition to enabling the manifestation of the mentioned above universality, Feshbach resonances opened the way to the study of fermionic superfluidity through the so-called *BCS-BEC crossover*[29] (see Fig. 1.3). While a non-interacting Fermi gas forms a Fermi sea as described before, a small attraction between particles gives rise to weakly coupled pairs with superfluid behavior, as described by the Bardeen-Cooper-Schrieffer theory[30]. When the coupling strength increases, pairs become more tightly bounded, with maximal correlation as the scattering length diverges in the unitary limit[31]. In this regime of strong interactions, a superfluid behavior appears as soon as the temperature decreases below ∼17% of the Fermi temperature[32], giving rise to vortices[33] and critical velocity[34] as in the case of bosons. If the coupling strength is fur-

[25] [Chevy and Salomon 2012]
[26] [Baker 1999]
[27] [Inouye *et al.* 1998]
[28] [Loftus *et al.* 2002, Petrov *et al.* 2004]
[29] [Zwerger 2012]
[30] [Bardeen *et al.* 1957]
[31] [Zwierlein *et al.* 2004, Zwierlein *et al.* 2005b]
[32] [Ku *et al.* 2012]
[33] [Zwierlein *et al.* 2005a, Zwierlein *et al.* 2006]
[34] [Miller *et al.* 2007], [Delehaye *et al.* 2015]

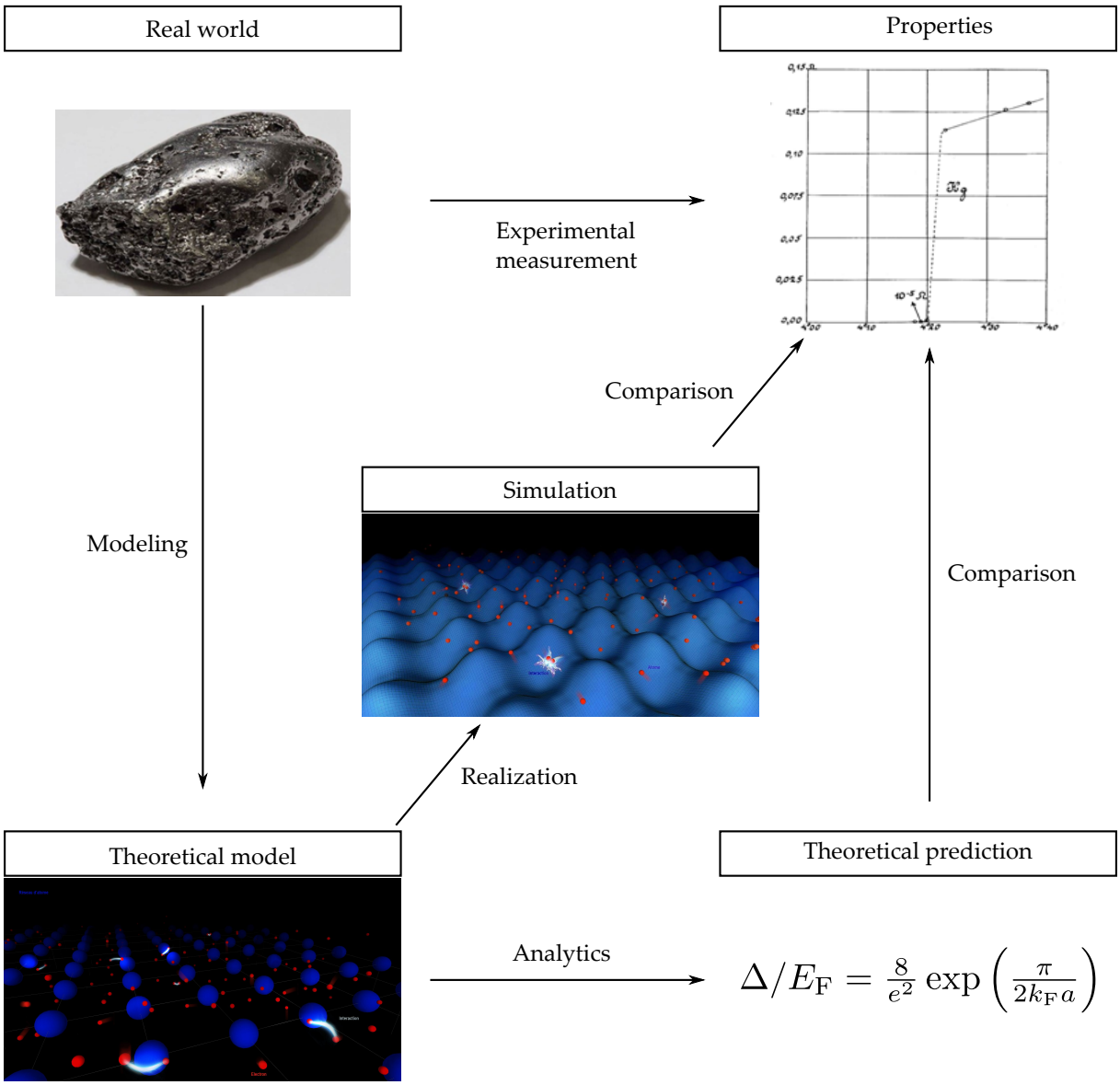

Figure 1.4: Quantum simulation. The two pictures were realized by Germain Morisseau.
A complex real system (metallic mercury) presents measurable properties (vanishing resistivity at finite temperature). In physics, the system is described by a simplified theoretical model, which can be expressed in mathematical form (interacting electrons (in red) in a perfect atomic lattice (in blue)). The reliability of the model is evaluated by comparing its predictions to the properties actually measured during experiments. It might be mathematically impossible to reach analytical predictions, and a complementary route is to simulate the model, i.e. to realize a synthetic system that follows precisely the rules of the model and to compare its properties to that of the real system. If both systems do not exhibit the same behavior, the model does not contain the elements required to describe the system of study.
Quantum simulation suggests to engineer a physical system to perform this verification, and cold atoms provide unprecedented tools to do so. In our example, fermionic atoms (in red) mimic the behavior of the electrons, the atomic lattice is replaced by an optical lattice (in blue) and the interaction between atoms is tuned so as to match that of electrons.

ther increased, fermions pair in bosonic molecules that have decreasing interactions with one another and condense if the temperature is low enough[35].

1.2 Why are cold atoms cool ?

> The program that Fredkin is always pushing, about trying to find a computer simulation of physics, seem to me to be an excellent program to follow out. [...] And I'm not happy with all the analyses that go with just the classical theory, because nature isn't classical, dammit, and if you want to make a simulation of nature, you'd better make it quantum mechanical, and by golly it's a wonderful problem, because it doesn't look so easy.
>
> *Richard Feynman*, [Feynman 1982].

Cold atoms constitute default-free and tailorable systems that can address a vast class of problems. At the same time, if cold atoms experiments require a broad range of technologies from ultra-high vacuum to laser optics (and sometimes plumbing), they remain at manageable size and allow for an extensive knowledge of the apparatus. This unique balance between accuracy and handling makes cold atoms a privileged platform for many applications.

1.2.1 Quantum simulation

If solving theoretical equations describing a many body system can be extremely challenging, performing a quantum numerical simulation on a classical computer is quickly impossible. A fully quantum treatment of a simple 10x10x10 array of spin 1/2 particles requires the simultaneous manipulation of 2^{1000} coefficients, the storage of which necessitates more bits than the number of atoms in the Universe. As suggested by Feynman, one way to circumvent this issue is to rely on *physical simulation*: a tailorable system adjusted so as to mimic the behavior of a complex problem, allowing its study (see Fig. 1.4). To simulate quantum dynamics, the statistics of the particles and the shape of the Hamiltonian of the system under scrutiny have to be reproduced. Owing to their large degree of adaptability, cold atoms have proven to be able to address a broad variety of situations[36], offering tools to tackle complex problems from condensed matter systems to particle physics, or even black holes physics[37]!

Tunable interactions

As mentioned before, Feshbach resonances give access to the experimental tuning of interactions between two particles. In the weakly attracting limit, cold fermions form a superfluid

[35][Greiner *et al.* 2003, Regal *et al.* 2003, Zwierlein *et al.* 2003]

[36][Jaksch and Zoller 2005, Bloch *et al.* 2012]

[37][Garay *et al.* 2000, Lahav *et al.* 2010]

of correlated pairs analogous to superconducting electrons in a metal. At unitarity, they allow for the study of strongly interacting degenerate systems, such as neutron stars[38], where nucleons are in a deep degenerate regime $T = 10^{-3} \times T_F$ despite a temperature around ten million Kelvin. It is also possible to preclude collisions by setting the scattering length to zero, thus realizing an ideal gas without interactions.

Adjustable population imbalance

With optical pumping and selective spin removal (see section 5.1.2), cold atoms experiments can adjust the population ratio between spin states within the atomic sample. This feature allowed the study of the Clogston-Chandrasekhar limit[39], which states that BCS-pairing in a Fermi-Fermi mixture is destroyed by the mismatch of chemical potentials[40]. Such population imbalance can also give rise to specific superfluid states, such as the so called Fulde-Ferrell-Larkin-Ovchinnikov (FFLO) phase[41].

Designable trapping potential

The potential landscape in which the atoms evolve can also be designed: as the conservative optical dipole force is proportional to the light intensity, any interference pattern shone on the ensemble will translate in a corresponding energy shift.

Inspired by the periodicity of crystalline structures, optical lattices allowed for the direct study of the Hubbard model, where interacting atoms can hop from one site to its nearest neighbors. First works focused on bosons[42]: as the ratio between interaction and tunneling is increased, particles tend to localize to minimize their energy and the passage from a delocalized superfluid to such a Mott insulator state corresponds to a phase transition. There works were soon followed by the study of Fermi-Hubbard[43] and Bose-Fermi Hubbard models[44]. The Lorentz covariance of the Bose-Hubbard Lagrangian at integer filling even allowed for the observation of a massive Higgs[45] mode, amusingly released very few weeks before the CERN announcement. In parallel, the improvement of data acquisition techniques lead to the emergence of dynamical single site imaging, equivalent to the direct observation of single electrons in a condensed matter system[46]. Such techniques allow for instance for the measurement of all correlation functions, providing access to full counting statistics[47].

[38] [Gezerlis and Carlson 2008]
[39] [Clogston 1962, Chandrasekhar 1962]
[40] [Ozawa *et al.* 2014]
[41] [Fulde and Ferrell 1964, Larkin and Ovchinnikov 1965]
[42] [Greiner *et al.* 2002]
[43] [Köhl *et al.* 2005, Strohmaier *et al.* 2007, Jordens *et al.* 2008, Schneider *et al.* 2008]
[44] [Gunter *et al.* 2006, Ospelkaus *et al.* 2006]
[45] [Endres *et al.* 2012]
[46] [Bakr *et al.* 2009, Sherson *et al.* 2010, Haller *et al.* 2015, Parsons *et al.* 2015, Cheuk *et al.* 2015]
[47] [Levitov *et al.* 1996]

Controllable disorder

While optical lattices form perfectly periodic crystalline structures (eventually limited by phase noise), cold atoms also provide a way to study the effect of disorder[48]. Notably, the inability of a wave to propagate in certain disordered potentials (Anderson localization[49]) was observed in a quasi random lattice generated by the overlap of two beams with incommensurate wavelengths[50] or by a speckle pattern[51], as well as in the kicked-rotor equivalent system[52].

Dimensionality

As will be seen in chapter 6, dimensionality plays a crucial role in many physical phenomena. For instance, the above mentioned Anderson localization presents a very different behavior in 1D (fixed localization length set by the particle's mean free path), 2D (exponential dependence of the localization edge with the particle's momentum) and in 3D (existence of a mobility edge above which localization vanishes). Using strong confinements, cold atoms experiments allow for the realization of systems in reduced dimensions and the simulation of corresponding situations.

Combining the previous control knobs, cold atoms have been used to investigate the equation of states of thermodynamics ensembles in various conditions. The equation-of-state of a system is a relation between density (or pressure) and chemical potential, temperature and internal energy. It constitutes a fundamental statistical tool, completely characterizing the equilibrium properties of the equivalent class of systems, regardless of their nature. The equation of state has been measured for dilute bosons as a function of temperature in three dimensions[53], in two dimensions[54] and in one dimension[55]. The study of ultracold gases in more than three dimensions is now considered[56], considering internal degrees of freedom of the atoms as a discrete extra dimension.

For fermions in three dimensions, the equation of state has been obtained as a function of temperature at unitarity[57], as a function of interaction strength at zero temperature[58] and as a function of spin imbalance[59]. The equation of state of the 2D Fermi gas through the BEC-BCS crossover was also recently reported[60].

[48][Fallani *et al.* 2008], [Gurarie *et al.* 2009]
[49][Anderson 1958]
[50][Casati *et al.* 1989], [Roati *et al.* 2008], [Schreiber *et al.* 2015]
[51][Billy *et al.* 2008], [Kondov *et al.* 2011]
[52][Grempel *et al.* 1984, Chabé *et al.* 2008, Manai *et al.* 2015]
[53][Ensher *et al.* 1996, Gerbier *et al.* 2003, Gerbier *et al.* 2004]
[54][Hung *et al.* 2011, Rath *et al.* 2010, Yefsah *et al.* 2011]
[55][Van Amerongen *et al.* 2008, Armijo *et al.* 2011]
[56][Boada *et al.* 2012, Celi *et al.* 2014, Zeng *et al.* 2015, Price *et al.* 2015]
[57][Thomas *et al.* 2005, Stewart *et al.* 2006, Luo *et al.* 2007, Nascimbene *et al.* 2010, Horikoshi *et al.* 2010]
[58][Shin *et al.* 2008, Bulgac and Forbes 2007, Navon *et al.* 2010]
[59][Bausmerth *et al.* 2009, Chevy 2006, Lobo *et al.* 2006, Zwierlein *et al.* 2006, Navon *et al.* 2010]
[60][Boettcher *et al.* 2016, Fenech *et al.* 2016]

Taking advantage of the different optical response of different atomic species, it is also possible to engineer a species-dependent confinement so as to realize a mixed dimensional system, where one sub part explores more dimensions than the other. This enables for instance the study of the Kondo effect, where localized (0D) impurities are immersed in a 3D mixture of two spin states[61], mimicking the interaction of itinerant fermions with magnetic impurities. More examples are detailed in the last chapter of this manuscript, which is dedicated to the study of 2D-3D systems.

Long range interaction

In addition to contact interactions, cold atoms also offer several opportunities to study the influence of long-range potentials by engineering inter-particle dipolar forces[62]. While weak dipolar gases can simply be obtain as spinor BECs with small scattering length[63], stronger interactions can be reached by using highly magnetic atoms such as Chromium, Erbium or Dysprosium[64], polar hetero molecules[65] or Rydberg states[66].

The existence of such long-range forces changes drastically the behavior of the gas, inducing specific dynamics and instabilities[67]. Those gases also allow for the simulation of a wider range of problems inspired by condensed matter systems, such as the ferrofluid-like Rosensweig instability[68], where horn-shaped crystal droplets self-organize in triangular structures.

Artificial gauge fields

Since atoms are neutral, they do not experience a Lorentz force when immersed in a magnetic field. Several experimental techniques have been found to mimic the behavior of charged particles such as electrons[69]. One way to do so is to exploit the similarity between the Lorentz and the Coriolis forces, both proportional and orthogonal to the particle velocity, which can be done by stirring the sample[70]. Another way is to imprint on the particle the same (Berry) phase as the one that would have been accumulated over the trajectory through the field (see section 4.3). This can be done by laser assisted transitions, as demonstrated both in bulk phase[71] and in optical lattices[72]. Notably, these methods allowed for the study of quantum Hall physics[73] and opened the way to the realization of the Hofstadter butterfly[74], a fractal organization of the electronic energy levels as a function of the magnetic flux per plaquette. The equivalent magnetic field reached in these experiments exceeds the values obtainable on real systems, which would require a field of $\sim 10^5$ T in a metallic lattice.

[61] [Kondo 1964, Bauer *et al.* 2013]
[62] [Santos 2010]
[63] [Stamper-Kurn and Ueda 2013]
[64] [Griesmaier 2007]
[65] [Ni *et al.* 2008]
[66] [Weimer *et al.* 2008, Pohl *et al.* 2010b, Schauß *et al.* 2012]
[67] [Lahaye *et al.* 2009]
[68] [Saito *et al.* 2009, Kadau *et al.* 2016]
[69] [Dalibard *et al.* 2011]
[70] [Madison *et al.* 2000]
[71] [Lin *et al.* 2009a]
[72] [Aidelsburger *et al.* 2011, Struck *et al.* 2013]
[73] [Mancini *et al.* 2015]
[74] [Hofstadter 1976, Aidelsburger *et al.* 2013, Miyake *et al.* 2013]

The same techniques can be applied to generate non-Abelian gauge fields[75], extending the $U(1)$ symmetry group corresponding to a magnetic field to a $SU(2)$ or $SU(3)$ symmetry. Such perspectives open the way to the quantum simulation of spin-orbit coupling[76], or even of the standard model of particle physics[77].

1.2.2 Metrology and applications

Within 25 years of existence, the field of cold atoms has given rise to some of the most precise measurements ever performed. Taking advantage of the very narrow line-width of atomic transitions, several groups realized atomic clocks with unprecedented accuracy[78], down to 10^{-18}, paving the way to a new definition of the time unit[79]. Atomic clocks are already widely used as time standards, and the launching of project PHARAO will soon provide a direct worldwide synchronization, besides allowing the fundamental study of quantum mechanics and general relativity[80]. Cold atoms are also used for precision measurements of fundamental constants, such as the fine structure constant[81], Cavendish constant[82] or the proton radius[83].

The maturity of the field also appears through the emergence of cold atom technologies out of the lab, as epitomized by the *Quantum Manifesto*, a call upon Member States and the European Commission to launch a €1 billion initiative in quantum technology [84]. Several start-ups[85] already commercialize plug-and-play sensor systems based on cold atoms to detect weak magnetic fields, probe local gravity or serve as gyroscopes.

1.3 Ultracold fermionic mixtures

Our experiment is dedicated to the study of fermionic mixtures. The simultaneous manipulation of two different species is challenging, but allows for the realization of situations that cannot be addressed by a simple spin mixture. For instance, atoms can be species-selectively confined[86] or assembled in polar molecules. The mass imbalance also results in a mismatch between Fermi surfaces, giving rise to a richer low-temperature phase diagram as mentioned in the previous section.

We work with two fermionic alkali, ^{6}Li and ^{40}K. Because of their single electron-like structure, alkali atoms are easier to address with laser light than most other atoms and constitute a privileged choice for cold atoms experiments. Among all alkali, ^{6}Li and ^{40}K are the only two stable fermionic isotopes; besides, both atoms show particularly interesting properties: ^{6}Li exhibits a very broad Feshbach resonance around 800 G and a large background scattering

[75] [Osterloh *et al.* 2005, Jacob *et al.* 2007]
[76] [Stanescu *et al.* 2007, Wang *et al.* 2012, Cheuk *et al.* 2012]
[77] [Ashery 2012]
[78] [Bloom *et al.* 2014, Nicholson *et al.* 2015]
[79] [Riehle 2015]
[80] [Laurent *et al.* 2015]
[81] [Bouchendira *et al.* 2011]
[82] [Rosi *et al.* 2014]
[83] [Pohl *et al.* 2010a]
[84] [QuantumManifesto 2016]
[85] Muquans, ColdQuanta, iXBlue
[86] [Onofrio and Presilla 2004]

length, while ^{40}K presents an inverted hyperfine structure which makes most of its trappable spin-state stable against collisions. As of today, there are five (soon six) fermion-fermion experiments in the world and all of them rely on those two species, with different cooling strategies.

1.3.1 Fermi-Fermi mixtures over the world

Pioneer works were performed in the group of Kai Dickmann, first in Munich (Germany) and later in Singapore. A triple MOT of ^{6}Li, ^{40}K and ^{87}Rb is loaded[87] and transported to a Ioffe-Pritchard trap, where fermions are sympathetically cooled by the forced RF-evaporation of Ribudium[88]. The system has been used to produce bosonic molecules in rovibrational ground state[89] and to investigate ^{6}Li-^{40}K Feshbach resonances[90].

In Amsterdam (Netherlands), the group of Jook Walraven built an apparatus with two 2D-MOT[91], one for ^{6}Li and one for ^{40}K. Potassium atoms were evaporatively cooled to degeneracy, first in a magnetic trap, then in an optical trap. The system allowed the thorough study of Feshbach resonances[92], but was closed in before Lithium degeneracy could be attained.

In Boston (USA), the group of Martin Zwierlein implemented two Zeeman slowers to capture simultaneously ^{6}Li and two Potassium isotopes, ^{40}K and ^{41}K. The forced evaporation of the bosonic ^{41}K in a magnetic trap cools all three species to degeneracy[93]. The experiment is now dedicated to the production of Na-K molecules in rovibrational ground state to study dipolar effect[94].

In Innsbruck (Austria), the group of Rudi Grimm and Florian Schreck uses a single Zeeman slower to address simultaneously ^{6}Li, ^{40}K and ^{88}Sr. Two species of the three species can be selectively captured in a MOT and loaded in an optical dipole trap. Double degeneracy was reached by performing a forced evaporative cooling on Lithium at Feshbach resonance[95]. The resulting gas presents a strong population imbalance in favor of Lithium, and was used to study the collisional stability of the mixture[96]. Focusing on the strongly interacting limit, the group observed the hydrodynamic expansion of the gas[97] and the appearance of repulsive polarons, Potassium impurities dressed by surrounding Lithium atoms[98]. In this regime, they also reported the measurement of the predicted strong atom (^{40}K)-dimer (^{6}Li-^{40}K) attraction[99].

In Shanghai (China), the group Yuao Chen is currently building a new apparatus with a design similar to ours (see below) and addresses ^{6}Li,^{40}K and ^{41}K. Bose-Einstein condensation was reached for ^{41}K and the system has been proven to be able to address fermionic isotope as well.

[87] [Taglieber *et al.* 2006]
[88] [Taglieber *et al.* 2008]
[89] [Voigt *et al.* 2009]
[90] [Costa *et al.* 2010]
[91] [Tiecke *et al.* 2009]
[92] [Tiecke *et al.* 2010a, Tiecke *et al.* 2010b]
[93] [Wu *et al.* 2011]
[94] [Park *et al.* 2012, Park *et al.* 2015]
[95] [Spiegelhalder *et al.* 2010]
[96] [Spiegelhalder *et al.* 2009]
[97] [Trenkwalder *et al.* 2011]
[98] [Kohstall *et al.* 2012]
[99] [Levinsen and Petrov 2011, Jag *et al.* 2014]

1.3.2 The FERMIX experiment: a mixture of fermions in mixed dimensions

In Paris, our group, today led by Tarik Yefsah, Frédéric Chevy and Christophe Salomon, has started a new ^{6}Li-^{40}K machine in 2008. We use a Potassium 2D-MOT and a Lithium Zeeman slower to load a double species MOT[100]. The atoms are magnetically transported to a science cell, where forced evaporation is performed first magnetically, then optically, and we reached quantum degeneracy for ^{40}K for the first time in France in July 2014. In the past, the apparatus was notably used to study the formation of heteronuclear molecules[101]. In the future, one of the main objective of the experiment is to realize mixed dimensions by confining selectively one species while leaving the other one essentially free. To that end, Lithium and Potassium are particularly well-suited, as their strong mass imbalance helps the selective confinement.

1.4 Outline of this thesis

The thesis presents the work performed during my PhD, from September 2012 to December 2015. Our main achievements are twofold: we produced a deeply quantum degenerate Potassium sample, notably by developing a new cooling scheme[102] based on optical gray molasses, and we simulated the dynamics of harmonically confined non-interacting Weyl particles with Lithium atoms in a quadrupole trap[103].

Chapter 2 : The FERMIX experiment.

The design, construction and maintenance of the apparatus constitute an important part of the work accomplished on a daily basis.

In this chapter, we present the FERMIX experiment, its typical performance and accessible knobs so as to give the reader an overview of the possibilities offered by the system and to serve as reference for future developments. We focus on recent improvements of the apparatus and notably the implementation of the so-called Λ-enhanced gray molasses, a new sub-Doppler cooling scheme which allowed us to reach a phase space density of 10^{-4} for both species within the MOT chamber.

Chapter 3 : Quasi-thermalization of fermions in a quadrupole trap.

At low temperature, spin-polarized ^{6}Li atoms behave like an ideal gas, without any interaction. Yet we observe that, in a linear potential such as a quadrupole trap, the sample relaxes towards a steady state as the energy imparted on its center-of-mass is transferred to the inner degrees of freedom of the cloud. This energy redistribution relies on the non-separability of the confining potential but the momentum distribution in the stationary state is nevertheless strongly anisotropic, with inhomogenous effective temperatures which illustrates the non-Boltzmann nature of the distribution.

[100] [Ridinger *et al.* 2011a]
[101] [Ridinger *et al.* 2011b]
[102] [Fernandes *et al.* 2012, Sievers *et al.* 2015]
[103] [Suchet *et al.* 2016]

This chapter is dedicated to the experimental, numerical and theoretical study of this phenomenon.

Chapter 4 : Analog simulation of Weyl particles in a harmonic trap

Weyl fermions are massless particles which appear as theoretical elementary particles as well as low-lying excitations in condensed matter systems. By means of a canonical mapping, we show that the behavior of such non interacting Weyl particles in a harmonic trap is equivalent to that of cold fermions in a quadrupole potential, which we studied before. We translate our previous results into predictions for the dynamics of a Weyl distribution: unlike massive particles, Weyl particles do not oscillate endlessly in a harmonic trap but relax towards a non-Boltzmann distribution. Analytical results are derived and predict anisotropic effective temperature even in an isotropic confinement. We also translate in the language of cold atoms specific properties of relativistic particles, such as the Klein paradox, equivalent to Majorana losses.

Chapter 5 : Evaporative cooling to quantum degeneracy

Going back to cooling to ultralow temperatures, we present the forced evaporation which allows us to reach deep quantum degeneracy for 3×10^5 Potassium atoms in two spin states at 62 nK, corresponding to 17% of Fermi temperature. Preliminary results concerning the loading of Lithium atoms in the optical trap and numerical simulations for the simultaneous evaporation of both species are also presented. We also review standard techniques required to manipulate and monitor a sample of cold atoms and to use it to calibrate the experimental apparatus.

Chapter 6 : Effective long range interactions in mixed dimensions

Taking advantage of the presence of two species, the FERMIX experiment should be able to address systems in mixed dimensions, where Potassium atoms are confined in 2D planes while Lithium atoms remain essentially free. We study theoretically such a situation and show how the presence of a 3D gas gives rise to effective long range interactions, mediated from one plane to the other. We suggest an experimental verification of this effect by measuring the beat-note of coupled oscillations of 2D-layers confined in neighboring sites of an optical lattice.

Chapter 2 The FERMIX experiment

Contents

2.1 Vacuum chambers **19**
2.2 Optical system **21**
2.3 Atomic sources **25**
2.3.1 Lithium Zeeman slower 26
2.3.2 Potassium 2D-MOT 27
2.4 MOT and CMOT **29**
2.5 Λ enhanced D_1 gray molasses **31**
2.5.1 Working principle 32
2.5.2 Experimental implementation 34
2.6 Spin polarisation **35**
2.7 Magnetic system **36**
2.7.1 Magnetic quadrupole trap 36
2.7.2 Magnetic transport 37
2.7.3 Magnetic bias 39
2.8 Security system **40**
2.9 Radio Frequency / Microwave system **41**
2.10 High power lasers **41**
2.10.1 532 nm laser 43
2.10.2 1064 nm laser 44
2.11 Imaging system **46**
2.11.1 Absorption imaging 46
2.11.2 Time-of-flight expansion of non-interacting particles 47
2.11.3 Experimental setup 49
2.12 Computer control **50**
2.13 Conclusions **51**

THe construction and maintenance of the experimental apparatus represents an important part of the work carried out over the last four years. As I started my Ph.D., the magnetic transport had just been implemented in its current version but showed a disappointing efficiency due to the high initial temperature of the atomic cloud. I contributed to the conception and development of a new cooling scheme, the so called D_1 gray molasses, which significantly improved this efficiency and eventually allowed the realization of a degenerate ^{40}K cloud. I also took part in the construction of the radio-frequency (RF) system for evaporation and population transfer, installed the high power lasers setup, implemented the high field power supply and worked on the construction of the security system.

The objective of this chapter is to give a general overview of the system, to describe the main steps of the experimental sequence and to show explicitly which knobs are easily accessible and tunable[1]. The last steps of cooling, allowing the realization of a quantum degenerate gas of Potassium, are described in chapter 5 together with our calibration methods.

As a convention in the figures, analog controls over the experiment are indicated in bold font and digital channels are shown in italic font. For the sake of clarity, most of the technical references are presented in annex A.5. The standard values of the main parameters are also recorded to present typical orders of magnitudes that are dealt with and to serve a reference for future developments of the experiment.

The FERMIX experiment in installed two levels below the ground, limiting all perturbations from the outside. It is composed of three separate tables, isolated by opaque panels and connected only through optical fibers, in order to avoid any stray light. Two tables are dedicated to the laser system, to generate the required laser beams, while the third one hosts the vacuum chambers (see Fig. 2.1).

A typical sequence lasts about 60 seconds. A double species magneto optical trap (3D-MOT) is loaded during 18 s, accumulating few 10^9 Lithium 6 and Potassium 40 atoms coming from a Zeeman slower and a two dimensional magneto optical trap (2D-MOT) respectively. After the atomic sources are turned off, the 3D-MOT is magnetically compressed to increase the spatial density. A brief phase of optical molasses allows for an important cooling, leading to a significant increase of the phase space density. The atoms are optically pumped to low-field seeking states in order to be transferred into a magnetic trap. An ensemble of coils allow for an adiabatic displacement of the confining potential, transporting the atoms from the MOT chamber to a science cell, 65 cm away. While a blue detuned optical plug reduces Majorana losses, an RF evaporation is performed until the cloud is cold enough to be loaded into an optical trap. An optical evaporation cools the sample further down to deep degeneracy, producing a cloud of 3×10^5 Potassium atoms in two spin states as cold as 62 nK, at 17% of the Fermi temperature. Eventually, a resonant beam is sent on the cloud and the image of its shadow is projected on a CCD camera, recording the spatial distribution of the atoms.

[1] A more detailed description of the construction of the apparatus can be found in the previous thesis of the group [Ridinger 2011, Salez 2011].

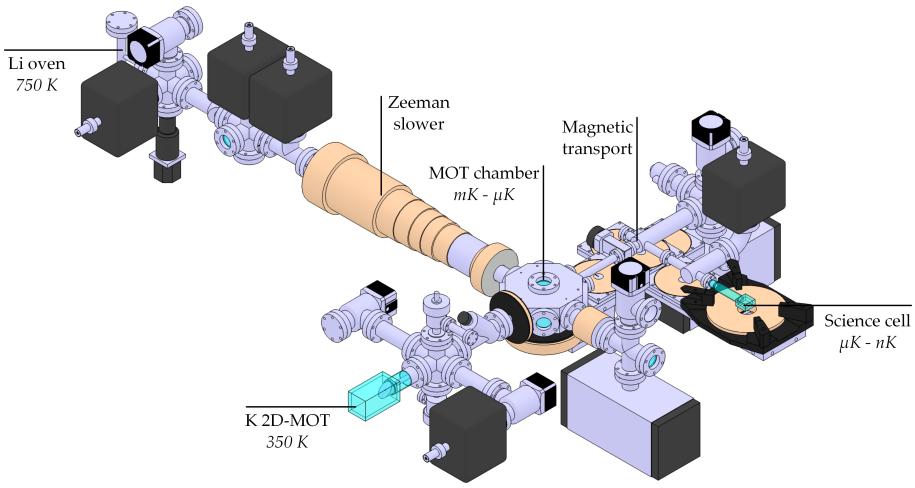

Figure 2.1: Overall picture of the vacuum chambers. The main parts are : the atomic sources (Li Zeeman slower and K 2D-MOT), the MOT chamber, the magnetic transport and the science cell.

2.1 Vacuum chambers

As the atoms are trapped and cooled down, they form an extremely sensitive system. Any background impurity colliding with the cloud would lead to losses as the atoms would be kicked out of the trapping potential, whose typical depth is between hundreds of mK for a MOT and few μK at the end of evaporation [Van Dongen *et al.* 2011]. An ultra-high vacuum (UHV), below 10^{-9} mbar and typically around 10^{-12} mbar is therefore required, as the background pressure will ultimately limit the lifetime of the ensemble. Since evaporative cooling can extend to several dozens of seconds, it is crucial that the surrounding environment generates as little perturbation as possible.

Some parts of the system are more sensitive than others and several differential pumping stages are used to improve the vacuum quality in the most critical regions. By limiting the ballistic flow of particles coming from higher pressure regions, important pressure gradients can be obtained.

The atomic sources (Lithium Zeeman slower and Potassium 2D-MOT) are obvious sources of pollution, all the more so as they require a moderate ($\sim 100°C$) to strong ($\sim 500°C$) heating on regular operation to generate satisfying fluxes. Three 20 L/s Varian ions pumps are located close to the lithium oven and one is dedicated to the potassium 2D-MOT. All-metal UHV valves can isolate atomic sources from the rest of the experiment, especially when a stronger heating is needed to regenerate the sources.

The MOT chamber is an octagonal chamber with optical windows on each face, top and bottom. The pumping is achieved by a 40 L/s Varian ion pump and a St707 non evaporable getter to adsorb H_2, H_2O, CO, and CO_2. The lifetime measured in the MOT is about 5 seconds.

The magnetic transport is an L-shaped elbow, which turning point is 30.95 cm away from

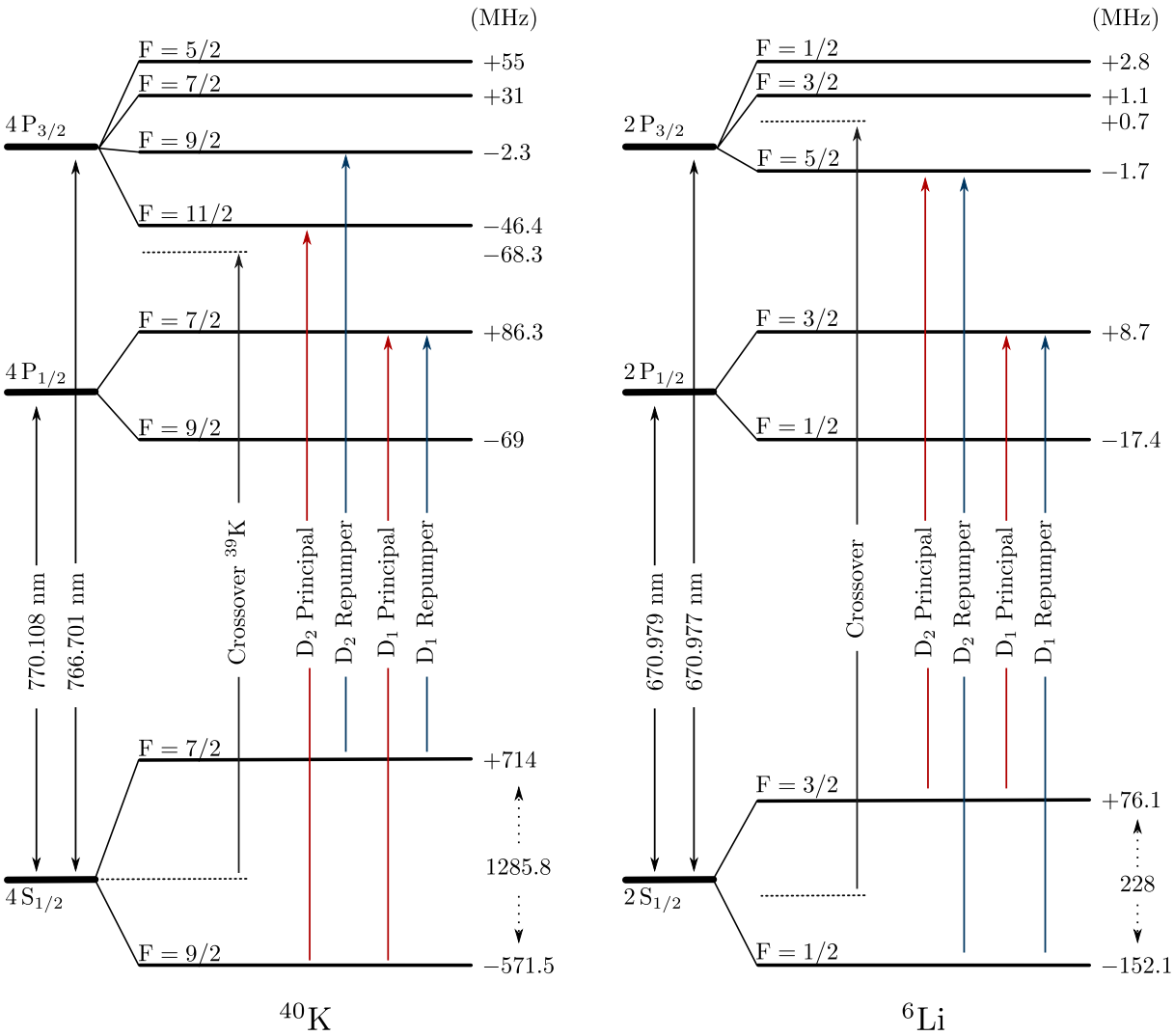

Figure 2.2: Energy levels of lithium and potassium. Note that ^{40}K has an inverted hyperfine, rendering its magnetic trappping easier. Values are taken from [Gehm 2003] and [Tiecke 2010].

Lithium ^{6}Li	δ	Transition	δ	Potassium ^{40}K
^{6}Li crossover	+ 116MHZ	D_2 Prcp	-593 MHz	^{39}K crossover
Zeeman Prcp	-76 Γ	D_2 Prcp	-3 Γ	2D MOT Prcp
Zeeman Rep	-76 Γ	D_2 Rep	-2 Γ	2D MOT Rep
3D MOT Prcp	-4.5 Γ	D_2 Prcp	-2.9 Γ	3D MOT Prcp
3D MOT Rep	-2.6 Γ	D_2 Rep	-5.2 Γ	3D MOT Rep
Imaging	0	D_2 Prcp	0	Imaging
D_1 Prcp	+4 Γ	D_1 Prcp	+2.3 Γ	D_1 Prcp
D_1 Repump	+4 Γ	D_1 Rep	+2.3 Γ	D_1 Repump

Table 2.1: Optical transitions of ^{6}Li and ^{40}K. The Potassium master laser is locked on ^{39}K crossover because this isotope is predominant in the spectroscopy cell, since its natural abundance of is over 90%.

the MOT center and 33.75 cm away from the science cell center. As the atomic sources, it can be isolated from the MOT chamber with an all-metal valve. The transport is connected to two ion pumps with flows of 20 L/s and 40 L/s and coated with Titanium-Zirconium-Vanadium alloy, a getter technology developed at CERN. Two additional strips of St707 getter are also installed.

The science cell is a glass parallelepiped of 23 mm x 23 mm x 10 mm designed for the requirements of the experiment and manufactured by Hellma GmbH. The glass walls, 4 mm thick, are made of uncoated Vycor, a fused silicon dioxide. It allows a much better optical access than the MOT chamber and benefits from the L-shape of the transport to reduce the ballistic trajectories of background particles. The ultra-low vacuum allows for lifetimes up to 100 seconds. To avoid magnetic disturbance, the closest ion pump is shielded in a mu-metal box manufactured by Atelier Soudupin.

2.2 Optical system

Laser light has proven to be an extremely versatile tool, allowing for the trapping, cooling and imaging of atoms. Cycles of absorption / spontaneous emission result in a radiative pressure exerted on the atoms while and cycles of absorption / stimulated emission lead to a conservative dipole force. Laser light also allows for the manipulation of the inner degrees of freedom by optical pumping. To address atomic transitions, it is essential to generate laser beams with adequate frequency, power and polarization; and half of the system is dedicated to this task. Most beam can be injected in a Fabry-Perot cavity (ThorLabs SA-200-5B, FSR : 1.5 GHz) simply by flipping a mirror, allowing for an easy monitoring which has proven to be extremely useful to diagnose some issues[2].

The technical details are presented in annex A.5. Logical schemes of both Lithium and Potassium optical tables are depicted in Fig 2.3 to summarize beam paths and computer controls.

Lithium and Potassium are both alkali atoms and as such they display the same simple atomic structure (see Fig. 2.1 and the main parameters summarized in table 2.2). Since the $S_{1/2}$ ground state displays two hyperfine levels, almost every beam has to be doubled by a repumping light, to avoid the accumulation of the atoms in an un-addressed state. All in all, ten beams are shaped for each atomic species.

The D_2 transition, from the ground $S_{1/2}$ level to the excited $P_{3/2}$ level, is the most commonly used. Its bandwidth $\Gamma/2\pi \sim 6\,\mathrm{MHz}$ is almost the same for both atoms and the saturation intensity, I_{sat}, on the order of milliwatts per centimeter squared, only differs by the optical wavelengths. The strategy for generating laser beams addressing the D_2 line is the same for both

[2]For instance, an important instability was found as a back reflection from one beam was accidentally injected in the TA amplifying another beam, resulting in strong fluctuations of the power ratio between both beams despite an almost constant total power. As the power of each beam was stable as long as the other beam was turned off, the problem was diagnosed by analyzing the light in a Fabry-Perot cavity and solved by dis-injecting the back reflection.

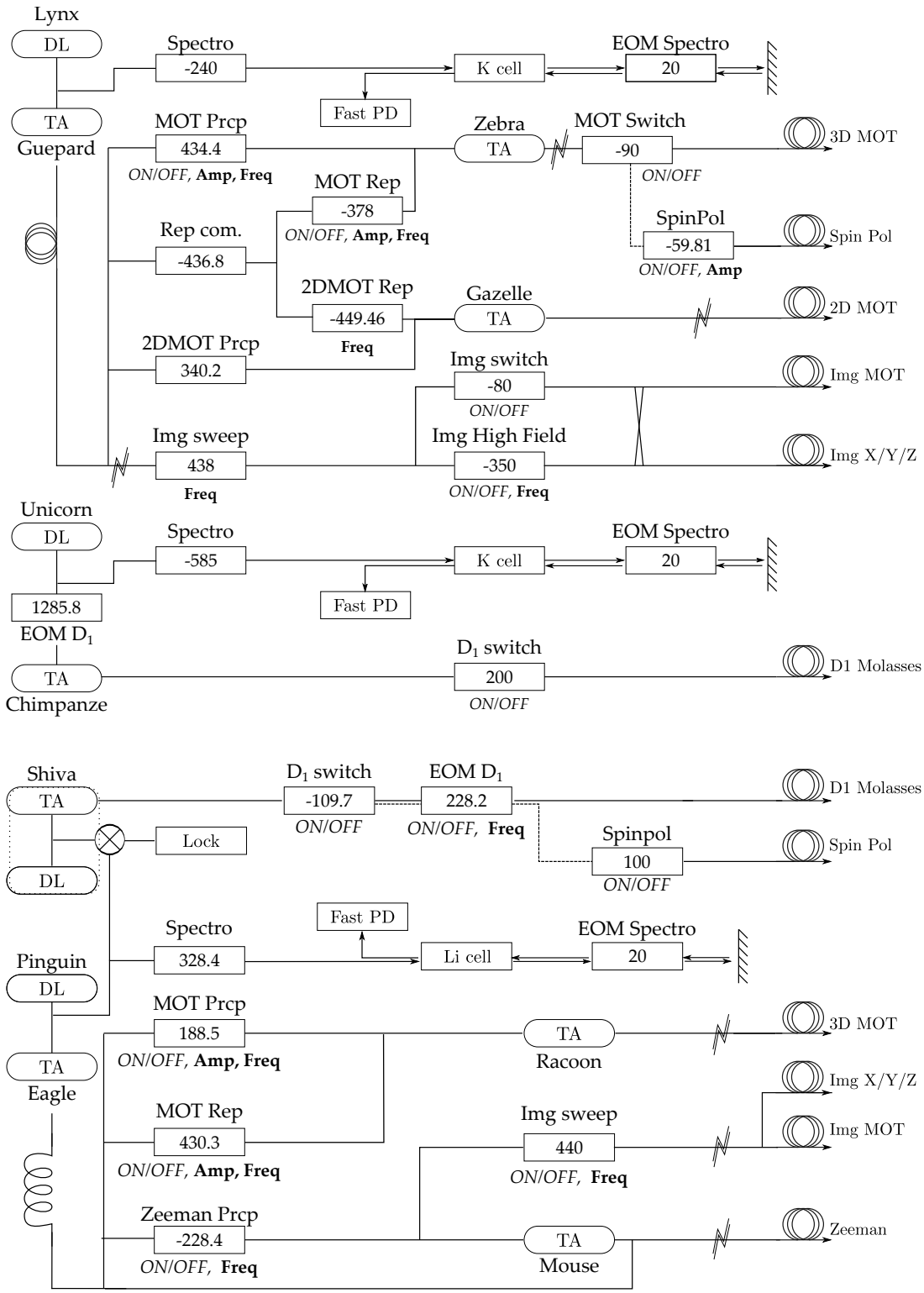

Figure 2.3: Logical scheme of the ^{40}K (top) and ^{6}Li (bottom) optical tables. Analog (digital) controls over the system are written in bold (italic) font. Optical sources are pictured with rounded box and AOM - EOM are represented with rectangular boxes and the corresponding frequency modulation is indicated in MHz. When relevant, the 0th order of an AOM is picture in dashed line. See annex A.5 for technical details. Zig-zag lines represent mechanical shutters.

	Units	^{40}K	^{6}Li
m	u	40	6
$\Gamma/2\pi$	[MHz]	6.03	5.87
$I_{\text{sat}} == \pi hc\Gamma/3\lambda^3$	[mW/cm^2]	1.75	2.54
λ_{D_2}	[nm]	766.7	670.977
λ_{D_1}	[nm]	770.1	670.992
$T_{\text{rec}} = \hbar^2 k_{D_2}^2/2mk_B$	[µK]	0.4	3.5
$T_{\text{Dop}} = h\Gamma/2k_B$	[µK]	145	141

Table 2.2: Properties of ^{40}K and ^{6}Li. We note $k_{D_i} = 2\pi/\lambda_{D_i}$ the wave vector. Values are taken from [Tiecke 2010] and [Gehm 2003] respectively.

species. A master diode is frequency locked on a saturated absorption error signal. Its light is amplified by a tapered amplifier (TA) from few mW to several hundreds of mW and injected in a single mode optical fiber for spatial filtering. The light is further divided by polarizing beam splitters, each new beam being frequency shifted by acousto-optical modulator (AOM) to reach a controlled detuning with respect to the atomic transition. An additional step of amplification is required to reach sufficient power. With the exception of the Li-Zeeman beams, principal and repumping lights are injected together in TAs with negligible power losses. This strategy enables a perfect superposition of both beams, before the light is fiber-coupled to the main table. The frequency of each beam can be adjusted over dozens of MHz by tuning the radio-frequency (RF) driving the AOMs, while their amplitudes can be controlled by attenuating the RF power. It is also crucial to be able to switch off quickly and completely the beams in order to avoid shining stray light onto the atoms, especially during evaporative cooling. AOMs allow for an attenuation of 10^{-4} within few tens of nanoseconds; a complete extinction is insured by mechanical shutters, cutting the beam in few hundreds of microseconds.

Optical sources are temperature-stabilized by Peltier elements (Roithner Lasertechnik, ref. TEC1-12705T125) that transfer the heat to the optical table through a thick aluminum plate, allowing an economical air cooling. The current supplies are protected against abrupt power failures (which happened quite often during the works in the building) by uninterruptible power supplies (Vision UPS Pro Blue 1000 VA).

An independent optical system has been implemented to address the D_1 transition, from the ground $S_{1/2}$ level to the excited $P_{1/2}$ level, and allows for optical gray molasses. For ^{40}K, the transition is 3nm away from the D_2 line, too far to be reached by the same master laser. The D_1 system follows the exact same structure as the D_2 system, with an independent master laser. The only difference between both setups is that the D_1 repumping beam is obtained not with an AOM, but as a side band generated by an electro-optical modulator (EOM) tuned at the hyperfine splitting frequency.

While the system is dedicated to ^{40}K, we could adapt it for the bosonic ^{41}K atoms with minor modifications (see Fig. 2.4). Since the atomic source contains even more ^{41}K than ^{40}K (see section 2.3.2), it is enough to change the light frequencies to address the new species.

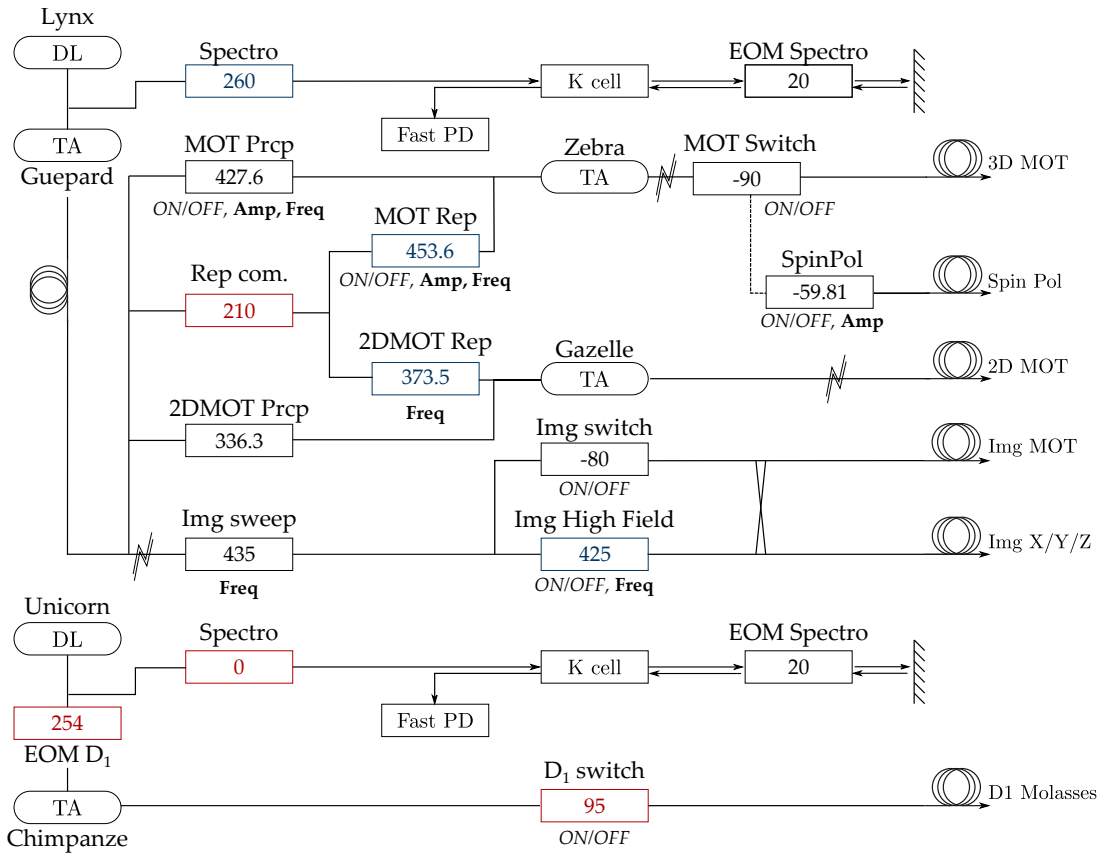

Figure 2.4: Adaptation of the potassium optical table ^{41}K. For most AOM, it is sufficient to change the driving frequency. For some AOM (in blue), the order must be changed with respect to ^{40}K setup. Some AOM (in red) must be removed or changed for a model with resonant frequency close to 100 MHz (rempumper commun and D_1 setup).

Starting with a working system for ^{40}K, it took about a month to reach ultracold temperatures with ^{41}K with the same techniques. In particular, the D_1 gray molasses described in section 2.5 could be readily applied to the bosonic isotope. Eventually, we managed to trap 2×10^5 atoms at 55 nK in an optical dipole trap described by $\omega_\perp/2\pi = 73$ Hz and $\omega_\parallel/2\pi = 4.8$ Hz. Despite a temperature close to the critical value $T_c = 72$ nK we did not observe the formation of a Bose Einstein condensate, a limitation we attribute to the too small waist of the laser beam, increasing the three-body losses.

By locking the secondary master laser (Unicorn) on the D_2 line rather than the D_1 line, it is even possible to manipulate ^{40}K, ^{41}K and ^{6}Li at the same time. However, this configuration does not permit to drive D_1 transition, limiting the sequence to a triple species MOT in absence of efficient molasses cooling.

For ^{6}Li, the two transitions are only 10 GHz apart, close enough for an alternative locking strategy instead of using an additional spectroscopy cell[3]. While the repumping beam is generated by an EOM just like on the ^{40}K system, the frequency of the principal beam is con-

[3]For a more technical description of the system, see [Fernandes 2014].

	Units	^{6}Li Zeeman slower
P	[mW]	50
I_{slow}/I_{rep}	-	8
δ_{slow}	[Γ]	-75
δ_{rep}	[Γ]	-75
Δ B	[G]	790

	Units	^{40}K 2D-MOT
P	[mW]	350
δ_{cool}	[Γ]	-3.5
δ_{rep}	[Γ]	-2.5
I_{cool}/I_{rep}	-	2
I_+/I_-	-	2.4
P_{Push}	[mW]	10
$\partial_{x,y}B$	[G/cm]	11

Table 2.3: Optimised values for the Lithium Zeeman slower and Potassium 2D-MOT.

trolled by an offset lock. This technique is adapted from [Ritt *et al.* 2004] and relies on the beat note between the locked D_2 beam and the D_1 master laser to be locked. The beating signal is recorded by a fast photo-diode (ref. Newport 1580-A)[4] and mixed with a tunable frequency reference around 9.78 GHz delivered by a dielectric resonator oscillator. The resulting signal is split between two arms, one being fed into a high pass filter while the other one provides a fixed attenuation. The comparison between both arms results in a dispersive error signal with a steep slope centered on the cut frequency of the filter. A PID circuit locks the error signal by controlling both the current of the D_1 master laser (for high frequency corrections) and the position of the optical grating in the laser cavity (for the low frequency corrections). This technique enables an accurate frequency locking (a Lorentzian fit of the mixed down signal spectrum has a full width at maximum height of 0.39 MHz for a cut frequency of 82 MHz) with a very broad locking range.

2.3 Atomic sources

As the vacuum system is completely sealed, atomic sources have to be included in the vacuum chamber to provide a ballistic flux towards the MOT chamber. As long as light induced interactions can be neglected, a simple accounting shows that the stationary amount of atoms gathered in the MOT is proportional to the incoming flux and inversely proportional to the lifetime of the trapped atoms. A high flux is therefore required to reach a sufficient atom number, a critical parameter to perform an efficient evaporation. Experimentally, we reach in the MOT chamber loading rates of 1.7×10^8 ^{6}Li/sec and 2×10^8 ^{40}K/sec. Those values are roughly five times smaller than those presented in previous works of the group and it appears that maintaining an optimal capture rate over long periods of time is very challenging. However, the current values are sufficient to reach quantum degeneracy.

[4]This photo-diode model is know to be easily damaged in the standard operation and constitutes a weak point of the setup.

2.3.1 Lithium Zeeman slower

^{6}Li atoms are coming from a Zeeman slower, a standard technique widely used in the cold atom community [Metcalf and van der Straten 1999]. Our design is an improved version of a previous experiment of the group [Schreck 2002]; the main parameters are summarized in table 2.3 (for a complete description of our system, see [Salez 2011]). Zeeman slowing has proven to be a robust technique, particularly well suited for Lithium sources. Indeed, Lithium presents a very low vapor pressure at room temperature [Nesmeyanov and Margrave 1964] and temperatures above 600 K are required to reach a sufficient ambient pressure, around 10^{-8} mbar. It might therefore be challenging to reach a compromise between significant heating and satisfying optical access, rendering difficult the direct loading from of a vapor cell.

The lithium sample, 3g of nearly pure ^{6}Li provided by Cambridge Isotope Laboratory, is heated to $\sim 500\,^\circ C$ in a cylindrical tube (the "oven") surrounded by Thermocoax cables. A thermal stream escapes from a 6 mm hole pinched on the oven and a collimation tube reduces the divergence of the outgoing atomic beam, directed to the MOT chamber. The oven temperature plays a critical role on the atomic flux and is regulated by a PID circuit.

Two superimposed laser beams are sent against the atomic stream: the *principal* beam addresses the D_2 transition $|F = 3/2\rangle \rightarrow |F = 5/2\rangle$ and the *repumping* beam drives the D_2 transition $|F = 1/2\rangle \rightarrow |F = 3/2\rangle$. The slowing strategy relies on the radiative pressure exerted on the atoms by a counter-propagating laser beam. The strength of the interaction depends on the detuning of the light with respect to the atomic frequencies, which can be affected by both the Doppler and Zeeman effects. The atoms initially have a high velocity ($v_{\text{thermal}} \sim 1000\text{m/s}$); they thus experience a strong Doppler shift, which decreases as they slow down. In order to maintain a constant detuning through the cooling process, a spatially variable magnetic field generates a Zeeman shift. As the atoms move forward, both shifts decrease so as to compensate each other. Within less than 2m, the atom velocity can be reduced below the capture velocity of the MOT: $v_{\text{final}} < v_{\text{capture}} \simeq 50\text{m/s}$. The cooling mechanism can only address atoms within a velocity range given by the difference in Zeeman shift between oven and MOT regions; faster atoms are not sensitive to the laser beams and will follow a ballistic flight unaddressed by the cooling mechanism.

To avoid sending resonant light through the MOT region, we use the so-called "spin-flip" configuration, in which the magnetic bias crosses zero and changes orientation through the slower. The final bias is non-zero and the optimal detuning for the Zeeman beams prevents them from perturbing the atoms in the MOT. This configuration also reaches a strong magnetic field difference between the two extremities of the slower, measured to 790 G, while maintaining reasonable current through the coils.

Only a small fraction of atoms actually escape from the oven and a vast majority hit its walls and tubes. As they cool down, those atoms can solidify and clog the output of the oven, resulting in a dramatically reduced flux. Luckily, the surface tension of lithium decreases with

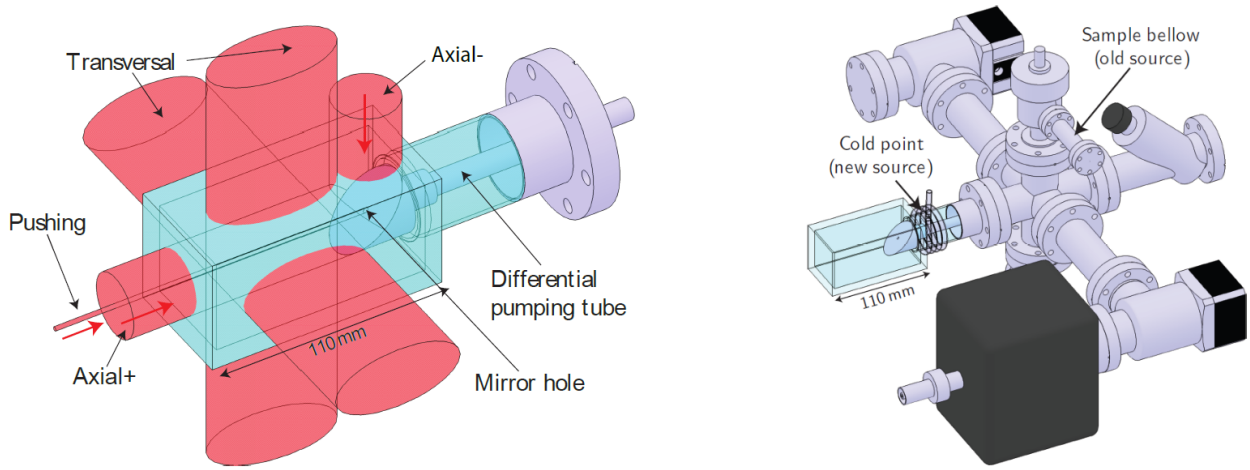

Figure 2.5: Schematics of the 2D-MOT

temperature [Yakimovich and Mozgovoi 2000] and the capillary forces drag liquid lithium back to the hotter regions, i.e. the oven. To increase this effect, the walls of the collimation tube are covered with stainless steel mesh, resulting in a larger contact surface. These precautions are not always sufficient to completely prevent the clogging and it is sometimes necessary to heat the whole area in order to liquefy solid lithium and facilitate the evacuation of the blockage. To do so, additional Thermocoax are installed along the output of the oven and the temperature is slowly increased while maintaining a gradient towards the oven ($\sim$ 25 K/cm). To avoid spreading too much Lithium out of the oven, its temperature remains below 600 °C. During the procedure, which usually lasts overnight, the lithium oven is isolated from the rest of the vacuum system to prevent its integrity.

2.3.2 Potassium 2D-MOT

Unlike ^{6}Li, a ^{40}K source needs to be optimized under economical constraints. The natural abundance of this isotope is below 0.01% and a strong enrichment is necessary. We bought from Technical Glass Inc, Aurora, USA a 100 mg sample containing 4mg of ^{40}K, 89.5mg of ^{39}K and 6.5mg of ^{41}K, for 4000$. The closure of the company makes it quite challenging to find satisfying samples on the market nowadays.

In order to avoid wasting all the atoms with an incorrect velocity range, the cooling strategy relies on a two dimensional magneto-optical trap (2D-MOT). Two pairs of counter-propagating transverse beams generate an optical molasses that slows down the atoms (see Fig. 2.5). If an atom moves in one direction, a Doppler shift brings the red-detuned facing laser closer to resonance, so that the atom experiences a force opposed to its velocity. In addition, racetrack coils induce a 2D quadrupole magnetic field with a cylindrical geometry, such that the beams, in $\sigma^+ - \sigma^-$ configuration, also generate an elastic restoring force that drags the atoms towards a 0 field line centered in the cell. If an atom is away from the magnetic center, a Zeeman

shift brings the laser pushing it towards the center closer to resonance. In one dimension, the resulting radiative pressure, taking into account both Doppler and Zeeman shifts, can be written to the lowest order under the form:

$$F(x, v_x) = -Kx - m\alpha v_x. \tag{2.1}$$

It can be shown [Dalibard 2015] that coefficients K and α depend on the light intensity and detuning, the transition linewidth and the magnetic field gradient, providing as many knobs to tune the capture and cooling efficiency.

A pair of axial beams increases the molasses effect. One of those beams (axial -) hits a 45° mirror with a hole and a part of its power is not therefore reflected. The atoms facing the shadow of the hole are only addressed by the other beam (axial +), which results in a net force pushing the atoms through the hole and towards the MOT, 55 cm away. A supplementary pushing beam, targeting the mirror hole, allows for a decoupling of powers and has proven to increase the outgoing flux by a factor 2. The main parameters of the 2D-MOT are summarized in table 2.3.

The atoms supplying the 2D-MOT are trapped from an ambient potassium pressure of $\sim 10^{-7}$ mbar. This pressure can be estimated and monitored by measuring the absorption signal in the 2D-MOT cell. The light is set at the cooling frequency and attenuated below the saturation intensity to avoid power broadening and send on a photo diode after it traveled 10.5 cm through the cell. By modulating the frequency of the light, it is possible to determine the maximal absorption of the gas, which can be related to the atomic density faced by the beam. In standard operating condition, absorption is around 40%.

It is necessary to heat the sample to generate sufficient vapor pressure. However, this procedure has proven to be tricky, as an overheating has led to a macroscopic migration of the sample towards uncontrolled low temperature regions. Three windings of a water-cooled PVC tube have been installed close to the glass-to-metal connection (see Fig. 2.5) in order to control the deposit of potassium crystals. If the source seems to migrate elsewhere, the rest of the surrounding cell is heated up to $\sim 180\,°C$ so that the atoms are brought back to the cold point where they crystallize. During this procedure, the 2D-MOT is isolated from the rest of the apparatus to protect the vacuum quality. The cold point is also set to low temperature ($12\,°C$) overnight. During normal operation, the temperature of this cold point is raised to $40\,°C$ by a water chiller Termotek[5], reaching a stationary regime within 30 minutes and allowing for a satisfying vapor pressure.

[5]The control module of this chiller model is easily damaged and had to exchange it twice in two years. Equivalent models from other companies, such as Thermotek P1020, have shown a better robustness but do not reach a satisfying temperature.

	Units	^{6}Li-MOT	^{40}K-MOT
P	[mW]	110	220
δ_{prcp}	[Γ]	-5	-3
δ_{rep}	[Γ]	-3	-5
I_{prcp}	[I_{sat}]	4	12
$I_{\text{prcp}}/I_{\text{rep}}$	-	5	20
∂B	[G/cm]	$8 \rightarrow 45$	
T	[mK]	$1 \rightarrow 0.8$	$0.24 \rightarrow 2$
N_{atoms}	[10^9]	$2.1 \rightarrow 1.9$	$3.2 \rightarrow 3$
n	[10^{11} cm^{-3}]	$0.26 \rightarrow 1.8$	$0.7 \rightarrow 3.7$
PSD	[10^{-5}]	$0.03 \rightarrow 0.3$	$0.02 \rightarrow 0.06$

Table 2.4: Optimised values for the 3D-MOT and the ensuing CMOT. The phase space density is estimated as PSD$= n\lambda_T^3$ and does not take into account the existence of different internal states.

2.4 MOT and CMOT

A magneto-optical trap (MOT) is the starting point of almost all cold atom experiments [Dalibard 2015]. Like in a 2D-MOT, a bichromatic optical molasses is combined with a magnetic gradient to cool and trap the atoms at the same time. A complete description of our system can be found in [Ridinger 2011] and the main parameters are presented in table 2.4.

Within 18 seconds, we trap 2.1×10^9 ^{6}Li-atoms at 1 mK and 3.2×10^9 ^{40}K-atoms at 240 µK. The losses due to interspecies light-induced collisions were reduced to $\sim$ 10% by using low magnetic field gradient and low repumping power. The fluorescence of trapped atoms are recorded on photodiodes and allow for a real time monitoring of the population of each species.

In a simplified Doppler model, the temperature in the MOT is ultimately limited at low laser intensity by the line-width of the optical transition. The behavior of the atoms can be described by a random walk as they absorb and re-emit photons [Gordon and Ashkin 1980], leading to a diffusion in momentum space. In steady-state, the final temperature results from the balance between the diffusion rate and the damping force and can be shown to be

$$k_B T = \frac{\hbar}{2}\frac{\delta^2 + \Gamma^2/4}{|\delta|} \geq \frac{\hbar\Gamma}{2}. \tag{2.2}$$

For both ^{6}Li and ^{40}K, this Doppler limit corresponds to $\sim$ 150 µK. Even though additional Sisyphus effects decrease the limit set by this toy model [Drewsen *et al.* 1994], the Doppler temperature gives a relevant order of magnitude for most experiments.

After the MOT is loaded, the lasers responsible for the atomic flux are turned off. It was found optimal to increase the spatial density of the cloud before the following molasses phase (see below). To do so, the magnetic field gradient is increased while the light intensities are reduced and turned closer to resonance. Densities are multiplied by a factor 5, which also leads to a higher loss rate. This compressed-MOT (CMOT) phase is therefore limited to less

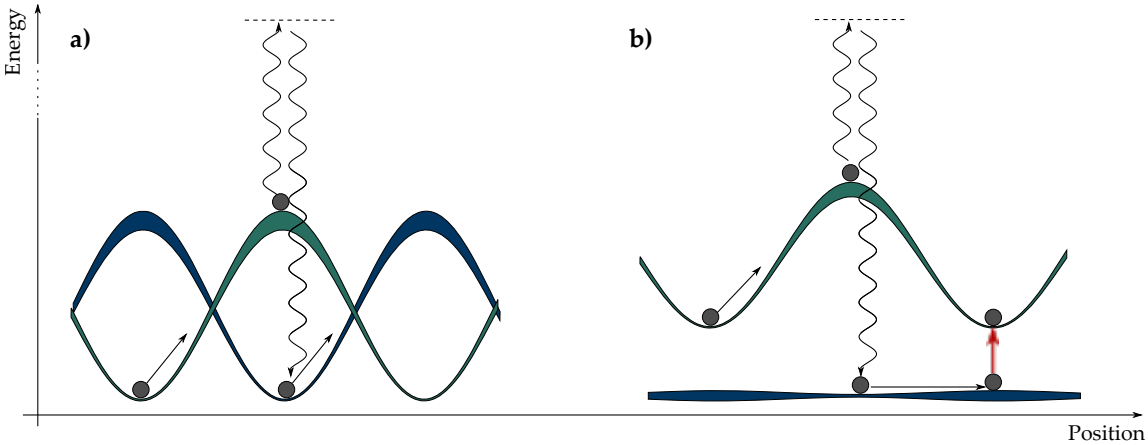

Figure 2.6: Sisyphus cooling in a bright molasses (a) and a gray molasses (b). In both cases, the spatial modulation of the energy levels is correlated with the departure rate (pictured as the width of the line), so that the atoms climb up more potential hills than they fall down. In a gray molasses, the optical pumping brings the atom to a dark state, uncoupled to the light (no light shift). The non adiabatic passage to a bright state (pictured as a red arrow) is mostly due to motional coupling.

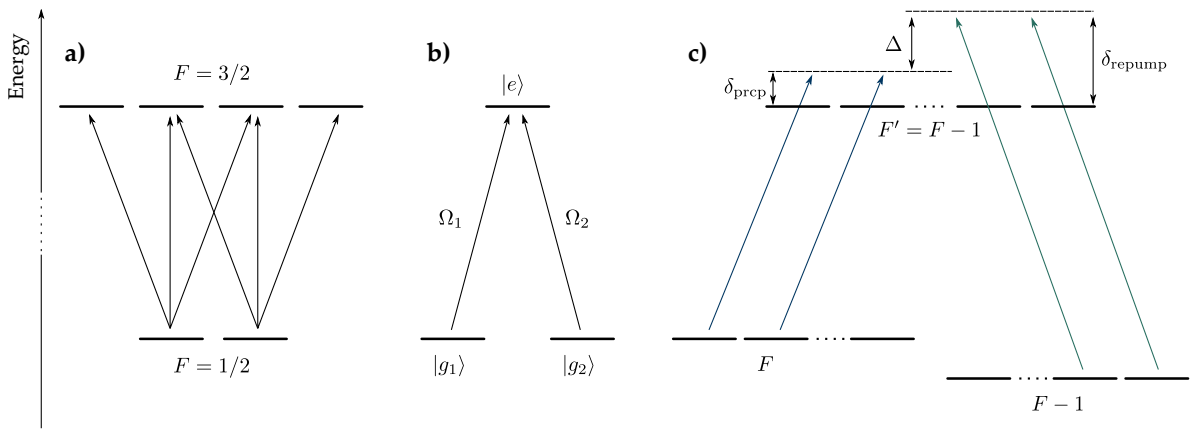

Figure 2.7: The energy levels and transitions resulting in the light shifts presented in Fig. 2.6. The standard bright Sisyphus effect is described with structure (a) while the simple Λ system (b) gives rise to a gray molasses. For ^{40}K and ^{6}Li, both intra- and inter-hyperfine transitions must be taken into account (c). The Raman detuning Δ plays an important role in the cooling efficiency, as shown in figure 2.8.

	Units	^{6}Li molasses	^{40}K molasses
P	[mW]	300	230
δ_{prcp}	[Γ]	+ 4	+ 2.3
δ_{rep}	[Γ]	+ 4	+ 2.3
I_{prcp}	[I_{sat}]	14 → 1	14→ 2.5
$I_{\text{prcp}}/I_{\text{rep}}$	-	20	8
Capture phase	[ms]	2	
Cooling phase	[ms]	3	
T	[μK]	48	11
N	[10^9]	1.2	3.2
n	[10^{11} cm^{-3}]	0.7	3
PSD	[10^{-5}]	8	10

Table 2.5: Optimised values for the D_1 molasses. To ensure a satisfying capture efficiency, we use relatively high initial intensities. Their values are decreased during a *cooling phase* to optimize the final temperature.

than 5 ms, a duration found to be short enough to avoid significant losses.

2.5 Λ enhanced D_1 gray molasses

After the MOT phase, the atomic cloud is still too hot to perform an efficient magnetic transport or to consider an evaporative cooling. Several ways exist to reduce further down the temperature of the cloud. For instance, to decrease the Doppler limit, a transition narrower than the D_2 line can be addressed, such as the $n = 2 \rightarrow n = 3$ transition for ^{6}Li [Duarte *et al.* 2011] or the $n = 4 \rightarrow n = 5$ transition for ^{40}K [McKay *et al.* 2011]. However, the corresponding light is in the near-UV domain and its implementation on the experiment is challenging because of the limited power delivered by commercially available sources.

Sisyphus cooling provides another way to reach lower temperatures [Lett *et al.* 1989] by taking advantage of the degenerate structure of the atomic ground state. Two counter propagating red detuned beams are sent on the atoms and generate a periodic modulation of the light polarization. In this configuration, both the energies of the Zeeman sub-levels and their optical pumping rates are spatially modulated (see Fig. 2.6). A positive correlation between those quantities means that atoms in one Zeeman state are most likely to be transferred to the other state when they reach a maximal energy shift. On average, atoms climb potential hills, on the top of which they are optically pumped to the bottom of the hill after they absorbed and spontaneously re-emitted a photon. As a result, they climb up more hills than they roll down, explaining the name of the mechanism and leading to a net energy loss. Considering the same random-walk description as before, the steady-state temperature is given by [Metcalf and van der Straten 1999]:

$$k_B T = \frac{\hbar \Gamma^2}{16\delta} \times \frac{I}{I_{\text{sat}}}, \tag{2.3}$$

where δ is the detuning of the beam. This can be understood as the value set by the height of the potential created by the light shift: if the atoms are too cold and slow to climb up a hill, they stop the Sisyphus cycling. For vanishing intensities, a more detailed approach gives a lower bound characterized by the recoil temperature $k_B T_{\text{rec}} = h^2/2\lambda^2 m$ ($\simeq 3.5\,\mu$K for ^{6}Li and $\simeq 0.4\,\mu$K ^{40}K).

Unfortunately, the D_2 transition of ^{6}Li and ^{40}K feature a too narrow excited $P_{3/2}$ state to allow an efficient Sisyphus cooling, since non resonant coupling are still strong enough to disrupt the required correlations between light shift and optical pumping. For ^{40}K, it is possible to reach sub-Doppler temperatures as low as 15 μK but with significant atom losses, limiting the cloud to $\sim 10^7$ atoms [Modugno *et al.* 1999, Gokhroo *et al.* 2011]. For ^{6}Li, the excited state is even narrower, forbidding the use of standard Sisyphus cooling.

We took advantage of the wider hyperfine splitting of the $P_{1/2}$ state to implement a novel cooling scheme, based on the same ideas but addressing the blue detuned D_1 transition [Fernandes *et al.* 2012, Sievers *et al.* 2015]. Two main ingredients result in a strong cooling together with a good capture efficiency : the existence of dark states among each $S_{1/2}$ hyperfine levels and of coherences between them.

The results presented in the section were published in

F. Sievers, N. Kretzschmar, D. R. Fernandes, D. Suchet, M. Rabinovic, S. Wu, C. V. Parker, L. Khaykovich, C. Salomon and F. Chevy. 'Simultaneous sub-Doppler laser cooling of fermionic ^{6}Li and ^{40}K on the D_1 line: Thoery and experiment', *Physical Review A*, **vol. 91**, no. 2, p. 023426 (2015)

2.5.1 Working principle

In a grey molasses, like in the previously described Sisyphus cooling, counter propagating beams give rise to spatial modulation of the light shift and departure rate. However, when the standard description of the Sisyphus effect relies on a $F \to F' = F + 1$ transition [Dalibard and Cohen-Tannoudji 1989], the D_1 line corresponds to the $F \to F' = F$ and $F \to F' = F - 1$ transitions (see Fig. 2.7). As a result, some linear combination of Zeeman sublevels form *dark states*, which remain uncoupled to the light and whose energy is not modulated. This is well known in the text-book Λ system, where two grounds states $|g_{1,2}\rangle$ are coupled to an excited state $|e\rangle$ by a potential V described by driving frequencies $\Omega_{1,2}$. A linear combination $|\psi_D\rangle = \frac{1}{\sqrt{\Omega_1^2+\Omega_2^2}}\left(\Omega_1 |g_1\rangle - \Omega_2 |g_2\rangle\right)$ is disconnected from the excited state : $\langle e| V |\psi_D\rangle = 0$. The generalization to 3D is not straightforward, but the existence of dark states can still be proven [Ol'shaniî and Minogin 1992].

The presence of dark states leads to two differences with the previous picture. First, once an atom is pumped from the top of a potential hill to a dark state $|\psi_D\rangle$, it remains there until a motional coupling brings it back to a bright state $|\psi_B\rangle$ (red arrow in Fig. 2.7). The probability

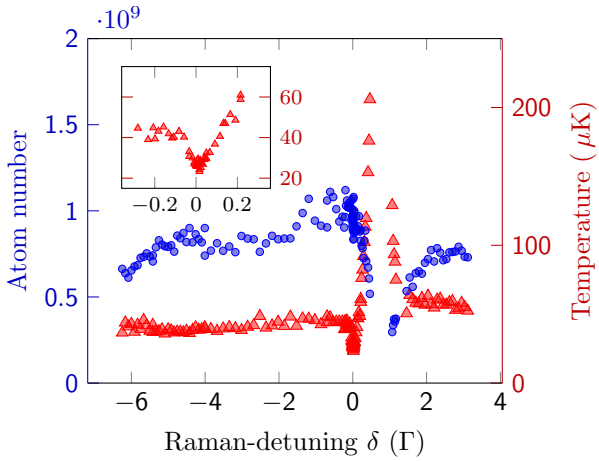

Figure 2.8: Atom number and final temperature of the ^{40}K cloud as a function of the Raman detuning Δ, as measured after 5 ms of D_1 molasses. Note the narrow cooling zone near the Raman-condition lowering the temperature (red triangles) to 20 μK and a flat cooling region below $-0.1\,\Gamma$ and above $2\,\Gamma$ resulting from gray molasses cooling without hyperfine coherence effects. The strong heating peak at small and positive Raman detuning can be described by a Fano profile. Picture from [Sievers *et al.* 2015]

for this non-adiabatic passage can be written perturbatively as [Weidemuller *et al.* 1994] :

$$P = \left| \frac{1}{2m} \frac{\langle \psi_D | \, p^2 \, | \psi_B \rangle}{E_B - E_D} \right|^2 \tag{2.4}$$

The faster the atom, the more likely it is to quit the dark state and resume Sisyphus cycles, provided that its velocity remains smaller than a capture velocity discussed below. On the contrary, cold and slow atoms accumulate in dark states, uncoupled to the light, hence the name *gray molasses*. This effective velocity-selective coherent population trapping reduces the fluorescence emitted by the atoms and allows theoretically for final temperatures lower than the recoil-limit [Aspect *et al.* 1988]. The second difference is that the light should be blue-detuned to result in a cooling effect. Equation 2.4 shows indeed that the transition is all the more probable as the energy difference between dark and bright state is small. The bright state should therefore be up-shifted for the atoms to climb up-hill, and not fall down-hill.

Since atoms accumulate in uncoupled states, gray molasses could theoretically cool the ensemble even below the recoil temperature. However, except for a $F = 1 \rightarrow F' = 1$ transition, the recoil momentum results in a slight energy mismatch between the atomic states, giving rise to off-resonant light-matter interactions which transfer atoms from dark states back to bright states and ultimately limit the lowest achievable temperatures.

The principle of gray molasses was presented in the '90s [Shahriar *et al.* 1993, Weidemuller *et al.* 1994] and implemented on the D_2 line of Cesium atoms in 1D [Valentin *et al.* 1992] and 3D [Boiron *et al.* 1995]. However, unlike the D_2 transition, the D_1 line does not provide closed transitions. In such a situation, *cooling* and *repuming* designations are not relevant since both transitions play equal roles. We will call *principal* the beam with the highest intensity,

addressing the hyperfine levels with the greatest angular momentum F, and keep the *repumper* designation for the weakest beam.

In addition to the gray Sisyphus effect induced within each hyperfine manifold by one beam, the presence of another beam gives rise to coherences between the two hyperfine levels. This feature clearly appears close to the Raman condition (see Fig. 2.8), when both beams have the same detuning with respect to the excited state ($\Delta = \delta_{\text{prcp}} - \delta_{\text{repump}} = 0$ in Fig. 2.7). The coherent driving from one hyperfine level to the other allows new dark states, resulting in a final temperature 2 to 4 times lower than out of this condition and justifying the name of the technique. On the other hand, a small red detuning from the Raman condition results in a strong heating, which can be interpreted in terms of Fano-profile [Lounis and Cohen-Tannoudji 1992]: the interference between a broad and a sharp scattering processes (namely scattering from the repumper and principal states) can strongly increase off-resonant transitions.

The theoretical description and numerical simulation of the Λ enhanced D_1 gray molasses cooling have been performed by our group with the collaboration of Saijun Wu [Sievers *et al.* 2015, Grier *et al.* 2013], and several experiments tested the main points of the theory.

2.5.2 Experimental implementation

For ^{40}K, the inverted hyperfine structure allows a double gray molasses : the principal $|F = 9/2\rangle \rightarrow |F' = 7/2\rangle$ and repumping $|F = 7/2\rangle \rightarrow |F' = 7/2\rangle$ transitions both exhibit dark states. The situation is slightly different for ^{6}Li: while the principal transition $|F = 3/2\rangle \rightarrow |F' = 3/2\rangle$ is described by the aforementioned model, the repumping transition $|F = 1/2\rangle \rightarrow |F' = 3/2\rangle$ corresponds to the standard Sisyphus cooling presented as introduction to this section. Nevertheless, the D_1 transition still allows an optical molasses forbidden by the narrow structure of the D_2 line and the hyperfine coherences at Raman resonance do improve significantly the achievable temperatures. Moreover, we observed that the robustness of the mechanism allows for the simultaneous cooling of both species without significant deterioration of the conditions with respect to the single species cooling.

We implemented the D_1 cooling with minimal modifications of the existing setup. The optical system is described in section 2.2. The light is fiber coupled to the main optical table and superimposed with the MOT beams by a D-shaped mirror[6]. The overlap takes place far from the MOT chamber, so that both beams are almost parallel as they address the atoms. This way, D_1 beams have the correct polarization, position and angle with respect to the atoms trapped in the MOT.

Experimentally, the cooling strategy must strike a balance in terms of light intensity. On the one hand, as long as the temperature is well above the recoil limit, it scales as $T \propto I/\delta$ and a lower intensity leads to a lower temperature. On the other hand, the capture velocity, estimated

[6]This D-shaped mirror constitutes a weak point for the stability of the system and requires minor realignment every other month.

	Units	^{6}Li molasses	^{40}K molasses
δ_{prcp}	[Γ]	+3	+2
δ_{rep}	[Γ]	+0.3	+0.3
I_{prcp}	[I_{sat}]	0.1	1
$I_{\text{prcp}}/I_{\text{rep}}$	-	1/ 12	1/24
Duration	[µs]	70	50
T	[μK]	$\sim$ 300	$\sim$ 200
N	[10^9]	1	3
PSD	[10^{-5}]	0.4	3

Table 2.6: Optimised values of the spin-polarisation step for the loading of the magnetic quadrupole trap. The temperatures are measured in single species operation and atom numbers are measured in the magnetic trap.

as the maximal velocity still allowing an efficient Sisyphus cycling, scales as $v_c \propto I/\delta^2$ and a lower intensity results in a poor capture efficiency. A balance was found by changing the light power through the cooling step: a high initial intensity permits the capture of most of the atoms and a slow ramp down reduces the final temperature. The main parameter values of the molasses are summarized in table 2.5.

The existence of dark states relies on the degeneracy between dressed states. If this condition can be reached between hyperfine levels by tuning the Raman detuning, it must also be preserved between Zeeman sub-levels by avoiding any kind of magnetic fields. We installed three large coils, far from the MOT chamber, to generate a homogeneous compensation bias and cancel stray field that could occur due to external conditions.

Since the implementation of the D_1 gray molasses on our experiment, it has also been used in other groups [Burchianti *et al.* 2014] and proven to work on ^{39}K [Nath *et al.* 2013, Salomon *et al.* 2013], ^{23}Na [Colzi *et al.* 2016] and ^{7}Li [Grier *et al.* 2013]. We also realized an unpublished work on ^{41}K, as mentioned in section 2.2.

2.6 Spin polarisation

After the optical molasses, the spin population of the atoms is completely unpolarized: atoms are distributed among all Zeeman sublevels of both hyperfine ground states. Before applying any kind of magnetic trapping, it is therefore useful to pump the atoms into low-field seeking states (see section 2.7.1).

A small magnetic bias ($\sim$ 1G) is applied within 400 µs, so as to select a symmetry axis. A collinear σ^+ light is applied during 70 µs for ^{40}K and 50 µs for ^{6}Li to pump the atoms into increasing m_F states. The duration of this step is kept as short as possible: as the atoms are untrapped, they expand freely, decreasing their density. Furthermore, the size of the cloud also impacts the loading efficiency of the ensuing magnetic trap and a wide distribution results in a

poor mode matching.

Since every absorption / emission cycle increases the temperature of the distribution (see table 2.2 for recoil temperatures), it is essential to minimize the number of cycles performed by the atoms. To do so, it is useful to accumulate atoms into dark states, which cannot be addressed by the light. For ^{40}K, the σ^+ light drives the $|F = 9/2\rangle \rightarrow |F' = 9/2\rangle$ transition (with an additional repuming light addressing the other hyperfine level $|F = 7/2\rangle \rightarrow |F' = 9/2\rangle$) on the D_2 line. Because of the narrow structure of the D_2 line of ^{6}Li, we drive the $|F = 3/2\rangle \rightarrow |F' = 3/2\rangle$ transition on the D_1 line instead (with a repuming light addressing the $|F = 1/2\rangle \rightarrow |F' = 3/2\rangle$). In both cases, atoms accumulate in stretch states ($|F = 9/2, m_F = 9/2\rangle$ and $|F = 3/2, m_F = 3/2\rangle$ respectively), where they can not absorb σ^+ photons for the driving transition. Despite this precaution, the final states are not completely decoupled from the light: the polarization of the beam is never perfectly σ^+ and for ^{40}K, off-resonant coupling to the $F' = F + 1$ level, enhanced by power broadening, should be taken into account. Those reasons also explain why it is important to perform the spin polarization as quickly as possible. Experimentally, we measure a temperature increase of $\sim$ 45µK for ^{40}K and $\sim$ 170µK for ^{6}Li, together with a very good pumping efficiency as almost 100% of Potassium atoms and 90% of Lithium atoms are eventually loaded in the magnetic trap.

2.7 Magnetic system

Together with light, magnetic fields provide some of the most useful ways to manipulate cold atoms by taking advantage of the energy shift resulting from the Zeeman effect. A complete derivation of the behavior of alkali atoms in a magnetic field is presented in annex A.1.

On the FERMIX apparatus, eleven independent power supplies are used to engineer the required fields. The value of the output current can be set directly (CC mode) or by controlling the delivered voltage (CV mode). While the first mode ensures a constant current, independent of the load fluctuations (due to Joule heating, for instance), the second mode permits a faster response and is used when fields must be varied quickly. Both low intensities (MOSFET) and high intensities (IGBT) transistors are used as switches to interrupt and dispatch the current through the system, as depicted in figure 2.9.

2.7.1 Magnetic quadrupole trap

As detailed in the following chapter, magnetic trapping requires the existence of a local minimum of the magnetic field modulus. The easiest way to produce such a field is certainly the anti-Helmholtz configuration, as proposed by Pauli. Two parallel coils of radius R and distant of D carry opposite currents I. Considering an origin between the two coils, the resulting field

can be expanded close to the symmetry center [Meyrath 2004]:

$$\mathbf{B} = b \begin{pmatrix} x \\ y \\ -2z \end{pmatrix} = \frac{3}{2}\mu \frac{DR^2}{(D^2+R^2)^{5/2}} I \begin{pmatrix} x \\ y \\ -2z \end{pmatrix} + O(r^3), \tag{2.5}$$

where $\mathbf{z}$ is the direction of the coils[7]. In a proper anti-Helmholtz configuration, $D = R$ and $b = \frac{48}{25\sqrt{5}}\frac{\mu I}{R^2}$. As long as the field is smaller than few Gauss, the resulting energy shift for an atom in a Zeeman sub-level m_F is the so called *quadrupole potential* :

$$\Delta E = \mu_B g_F m_F b \sqrt{x^2 + y^2 + 4z^2}, \tag{2.6}$$

where μ_B is the Bohr magneton and g_F is the Landé factor. For low field seeking states, $m_F > 0$, the potential leads to a restoring force towards the magnetic center, confining the ensemble within a volume of typical dimension $r_0 = k_B T / \mu_B b$.

After the optical pumping, atoms populate low-field seeking states and can be loaded in the magnetic gradient. However, the loading requires good mode matching between the free cloud and the confined distribution. Furthermore, as long as the trapping gradient is not settled, the gas keeps expanding and the field should thus be ramped as fast as possible to a value such that r_0 matches the initial size of the cloud.

Experimentally, the temperature of the cloud after the optical molasses is around 20µK and its size is $\sim$ 1.5 mm. We increase the current in the MOT coils as fast as possible until r_0 reaches this value. It should be noted that the ramp-up speed is limited by eddy currents induced in the metallic structures and it is likely that the field is cannot be reached in less than $\sim$ 1 ms. Almost 100% of ^{40}K atoms and 90% of ^{6}Li atoms are captured during this step. During the following 450 ms, the field is slowly raised to 80 G/cm to compress adiabatically the ensemble (see section 3.1.4), ensuring a strong confinement for the ensuing magnetic transport.

2.7.2 Magnetic transport

In many experiments, in order to perform an evaporative cooling in optimal conditions, atoms must be transported from the MOT-chamber to a science cell with better optical access and vacuum. Optical transport relies on deformable [Léonard *et al.* 2014] or movable [Gustavson *et al.* 2002] lenses to trap atoms around the focal point of a laser and displace it from one cell to the other. Magnetic transport consists in displacing the center of a magnetic gradient instead. This can be done by installing a pair of coils on a translation stage [Lewandowski 2002], a simple solution that is nevertheless challenging in terms of mechanical stability and might impact the optical access to the science cell. Another option is to switch successively

[7] Note that we define the gradient along the weak directions $\mathbf{x}$ and $\mathbf{y}$. Another convention is to define b as the gradient along the strong axis $\mathbf{z}$.

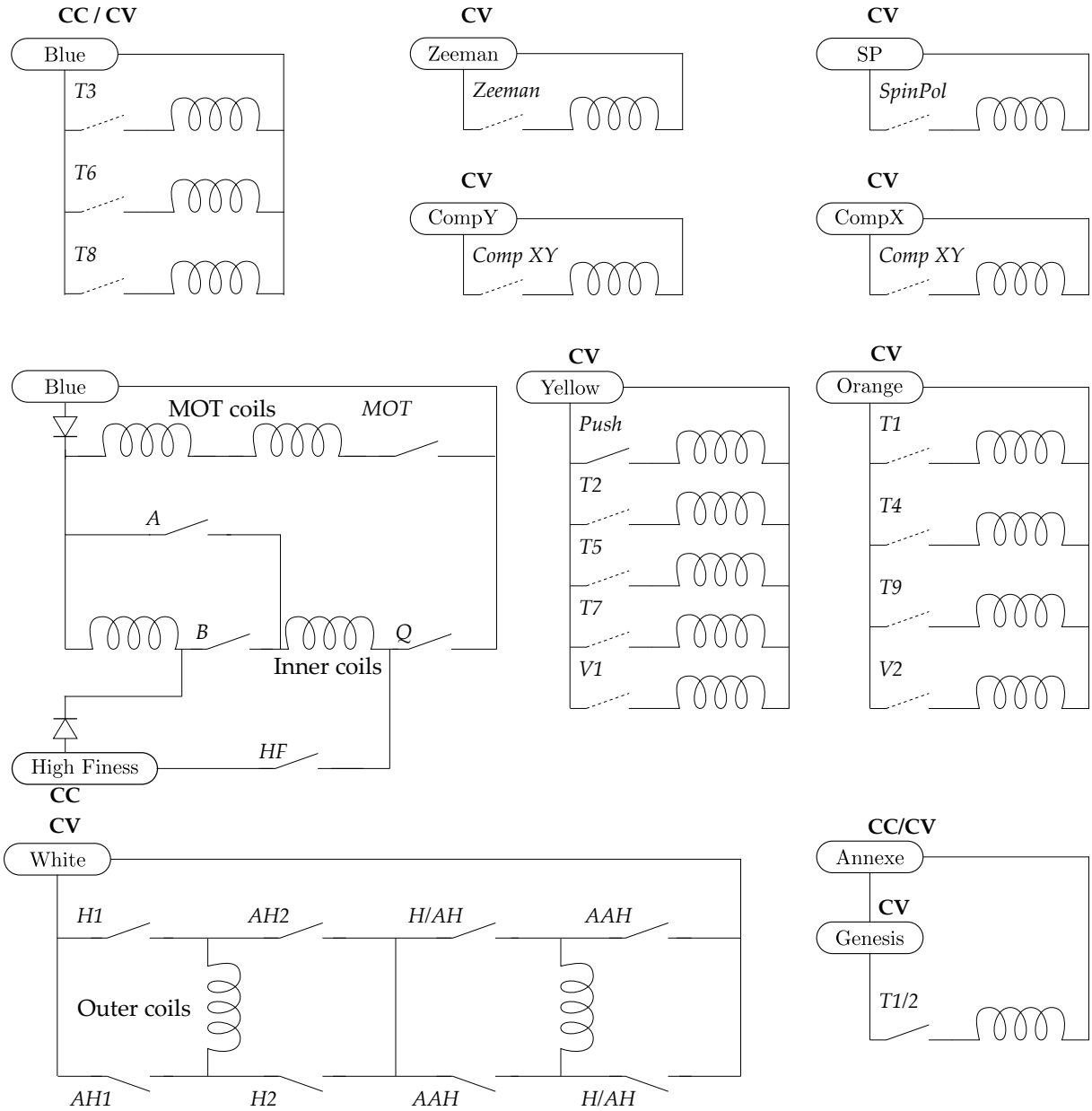

Coils	Axial field
MOT	0.91 G/A/cm
SpinPol	4.8 G/A
Push	0.16 G/A - 0.073 G/A/cm
Inner (H)	8.00 G/A + 0.61 G/A/cm^2
Inner (AH)	2.5 G/A/cm
Outter (H)	2.089 G/A - 0.29 G/A/cm^2
Outter (AH)	0.24 G/A/cm
V_1	2.8 G/A/cm
V_2	-2.8 G/A/cm

Coils	Axial field
$T_{1/2}$	0.37 G/cm - 0.29 G/cm
T_1	3.3 G/A/cm
T_2	5.5 G/A/cm
T_3	3.7 G/A/cm
T_4	5.5 G/A/cm
T_5	-3.7 G/A/cm
T_6	-2.6 G/A/cm
T_7	2.6 G/A/cm
T_8	3.7 G/A/cm
T_9	2.6 G/A/cm

Figure 2.9: Electrical system of the experiment. IGBT are pictured as solid switches, MOSFET as dashed switches. References for the power supplies are given in annex A.5. The utility of the different coils is given in the main text. Gradient are given along the strong axis. A description of the IGBT setting for MOT, inner and outer coils in Helmoltz (H) or Anti-Helmoltz (AH) configuration is given in table 2.7.

IGBT	Helm.	Anti Helm.	Inv. Helm.	Inv. Anti Helm.
H	1	0	0	1
AH	0	1	1	0
H/AH	1	1	0	0
AAH	0	0	1	1

IGBT	MOT	Helm.	Anti Helm.
MOT	1	0	0
HF	0	1	1
A	0	0	1
B	0	1	0
Q	0	1	0

Table 2.7: IGBT configuration for a versatile control of the magnetic field around the science cell. The electrical system is presented in figure 2.9.

overlapping pairs of coils, so as to deform smoothly and continuously the magnetic field.

The latter option has be implemented on the experiment and used to transport the atoms in 6 seconds 64 cm away from the MOT, through a a 90° elbow. The transport requires 14 pairs of coils (pairs $T_{1/2}$ to T_9, V_1, V_2 as well as the inner and outer pairs of coils of the science cell) and an additional push coil, as shown in figure 2.9. The ensemble holds on a metallic cooling plate, the temperature of which is water regulated (Termotek P1020) in order to avoid thermal dilatation.

Even though it represented a major time investment during its conception and realization, the magnetic transport allows for stable and reproducible experiments. For a detailed description of the transport, see [Fernandes 2014] and [Sievers 2014]. We estimate that $\sim$ 80% of the ^{40}K atoms and 70% of the ^{6}Liatoms are successfully transported to the science cell, with a temperature increase of 130 µK for both species. Those values are considerably improved by the D_1 molasses, which reduces the spread of the cloud and prevents it from clipping on the differential pumping tube at the entrance of the transport. Without the preceding CMOT and molasses steps, the transport efficiency is limited to $\sim$ 50% and the heating is increased to 400 µK.

2.7.3 Magnetic bias

Once the atoms are trapped in the science cell, it can be necessary to raise an homogeneous magnetic bias to reach Feschbach resonances or perform spin selective imaging. Bias fields are also used to compensate ambient magnetic fields during the molasses step or to select a symmetry axis during the spin polarization step.

When two coils carry the same current, the induced field close to the symmetry center takes the form:

$$\mathbf{B} = \mu \frac{R^2}{(D^2+R^2)^{3/2}} I \begin{pmatrix} 0 \\ 0 \\ 1 \end{pmatrix} + \frac{3}{2}\mu \frac{R^2\left(4D^2-R^2\right)}{(D^2+R^2)^{5/2}} I \begin{pmatrix} -zx \\ -zy \\ z^2-(x^2+y^2)/2 \end{pmatrix} + O(r^5). \tag{2.7}$$

In the Helmholtz configuration, $D = R$ and the curvature described by the last term vanishes, leaving a pure bias up to the fourth order.

	Without coils	With coils
MOT	0.6	0.3
Science cell	2.2	1.1
Zeeman	2.6	2.2
IGBT	1.5	1.5
HighFiness	1.1	1
Transport	6	2

Table 2.8: Water flux (L/min) cooling most of the coils of the experiment as well as a plate supporting high current IGBTs. Transport coils are supported by a water-cooled plate while the other coils have hollow wires allowing a direct cooling.

To allow for a versatile magnetic configuration, two pairs of coils (inner and outer) surround the science cell (see table 2.7). The inner coils can be powered either in anti-Helmholtz or Helmholtz configuration by flipping IGBT switches, while the current direction can be set independently through each of the outer coils, allowing any of the four possible configurations (anti-Helmholtz, Helmholtz or inverted configurations) and thus providing control over the magnetic field curvature.

The inner coils are also dedicated to the tuning of the Feschbach resonances. Notably, the resonance between ^{6}Li and ^{40}K is quite narrow ($\Delta B = 1\,\mathrm{G}$ around $B_0 = 100\,\mathrm{G}$) and a stable field is required to avoid accidental sweeps across the resonance. A High Finess power supply, with a current stability below 10^{-5} was purchased for this purpose[8].

2.8 Security system

As described above, the experimental setup deals with important electrical currents that might result in a strong heating of the coils, leading to a damage or a melting of the insulating plastic coating. All coils supporting high currents, as well as the magnetic transport and a metallic plate supporting IGBTs, are water-cooled to prevent such dramatic accident (see table 2.8). An additional security system was installed to monitor each water flux through flow-meters (Gems Sensors RFS and Flow Switch FS-926). In addition, several thermistors are glued on several coils to measure their temperatures. A supplementary module, dedicated to humidity measurement, is not currently used. If any of measured values passes a fixed threshold, the security systems switches off all the power supplies through their Remote Shut-Down (RSD) channel.

All technical drawings of the security system are presented in annex A.6.

[8]This model presented repeated failures, as an instrumentation amplifier (INA128P) of the command circuit was easily damaged and had to be exchanged every other day. The problem was solved by installing an analog optocoupler between the computer control channel and the input port of the power supply.

2.9 Radio Frequency / Microwave system

While lasers allow the manipulation of optical transitions, radio-frequency (∼MHz) and microwave (∼GHz) sources are required to drive transitions both between and within hyperfine Zeeman states.

Experimentally, we need to reach three distinct frequency domains. In order to perform an evaporative cooling in a magnetic trap, atoms must be selectively transferred from low-field seeking states to untrapped high-field seeking states. For ^{40}K, we drive hyperfine $|S_{1/2}, F = 9/2\rangle \rightarrow |S_{1/2}, F = 7/2\rangle$ transitions, with frequencies between 1.1 GHz and 1.28 GHz. For ^{6}Li, we address hyperfine $|S_{1/2}, F = 3/2\rangle \rightarrow |S_{1/2}, F = 1/2\rangle$ transitions, with frequencies between 228 MHz and 400 MHz. Finally, in order to manipulate the spin population of the sample, it is useful to drive transitions between Zeeman sublevels. A magnetic bias is applied to lift the degeneracy and an RF signal allows for adiabatic transfer or Rabi oscillations between the states, transferring the atoms from one state to another (as in section 5.1.2). The required frequencies depend on the amplitude of the magnetic bias, but typical values stand between 3 MHz (at few Gauss) and 50 MHz (around 200 G).

The strategy used to emit the RF/MW radiations is the same for all three domains (see Fig. 2.10). An electrical signal with a selected frequency is amplified and sent to an antenna that radiates it into electromagnetic waves. Antennae are simple windings of a thin metallic cable, with a size optimized for the emission of the dedicated radiation, placed few centimeters away from the science-cell. The resonant frequency and impedance matching of the antenna are further tuned by adapting its electrical properties with an RLC circuit and its geometry with a sizable BNC cable (see [DeMarco 2001]).

2.10 High power lasers

The final stages of the experimental sequence take place in an optical trap. Cycles of absorption / stimulated emission give rise to an energy shift called *light shift*, proportional to the light intensity I and depending on its detuning with respect to the atomic transition [Grimm *et al.* 2000] :

$$U(\mathbf{r}) = -\frac{3\pi c^2}{2\omega^2}\left(\frac{\Gamma}{\omega_0 - \omega} + \frac{\Gamma}{\omega_0 + \omega}\right) I(\mathbf{r}), \tag{2.8}$$

where ω is the light frequency, ω_0 the atomic frequency and $\Gamma \simeq 2\pi \times 6$ MHz the associated linewidth. The light intensity profile of Gaussian beam propagating along $\mathbf{z}$ takes the form:

$$I(\mathbf{r}) = \frac{2P}{\pi w^2}\frac{1}{\sqrt{1 + z^2/z_R^2}} \exp\left(-\frac{x^2 + y^2}{w^2(1 + z^2/z_R^2)}\right), \tag{2.9}$$

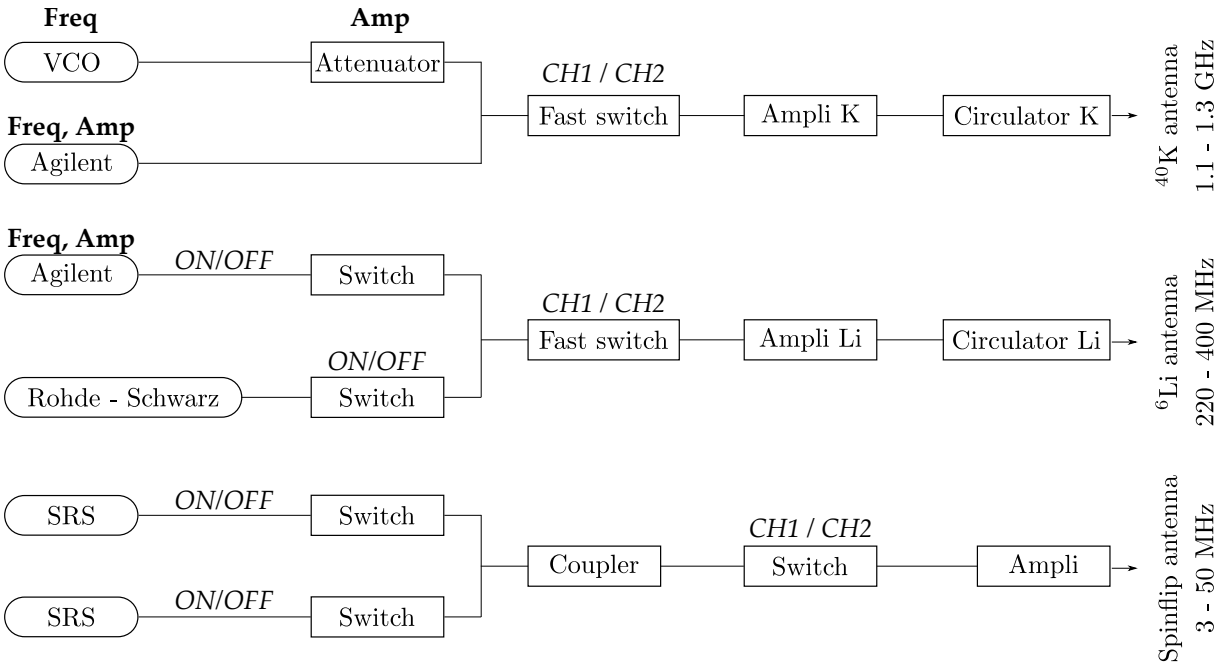

Figure 2.10: Radio-frequency and micro-wave components. The construction allows a fast switching between input channels (CH1/CH2) sources. Two Agilent sources are controlled by LAN cable and used for evaporative cooling, while the Rohde-Scwhartz and SRS sources are pre-programmed and triggered during the sequence. Technical references are given in annex A.7.

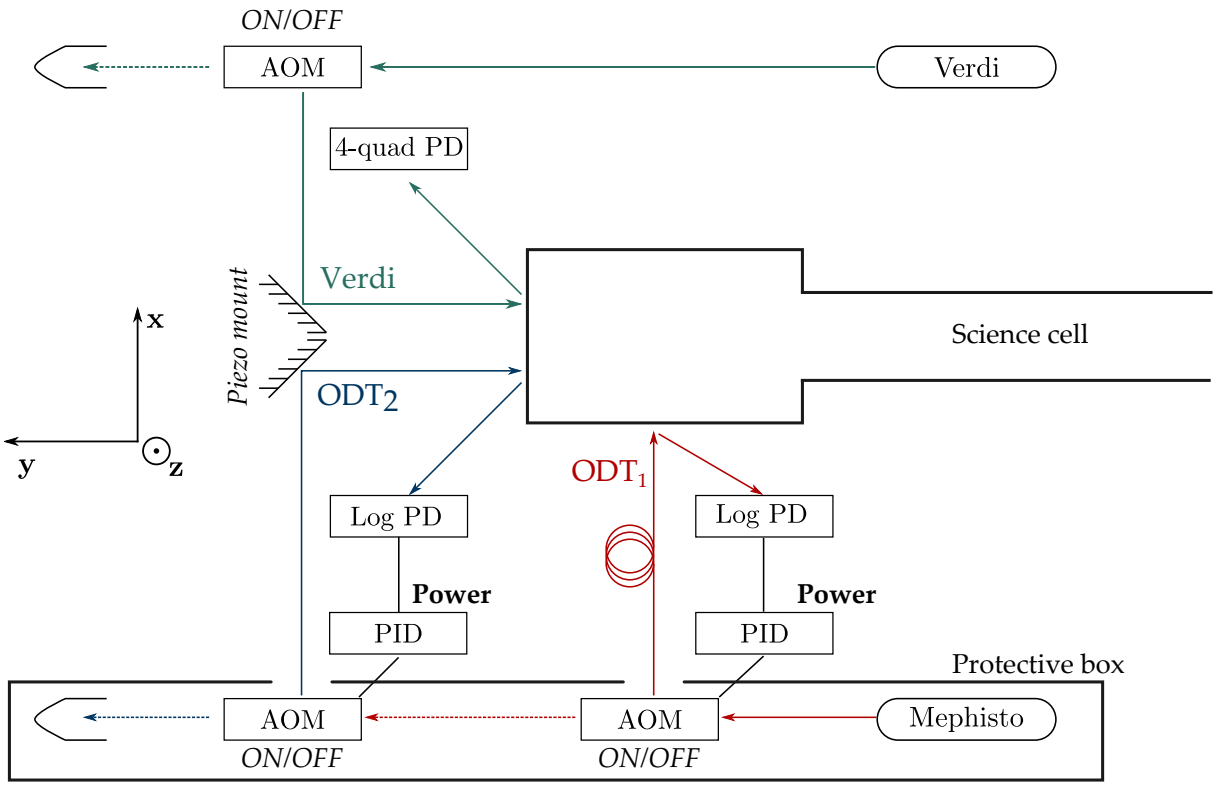

Figure 2.11: High power lasers close to the science cell. The setup is described in the main text and performances are detailed in table 2.9. We introduce directions **x** (along ODT_1 beam), **y** (along transport) and **z** (opposed to gravity).

		Verdi		ODT_1		ODT_2	
	Units	^{6}Li	^{40}K	^{6}Li	^{40}K	^{6}Li	^{40}K
λ	nm	532		1064		1064	
P	W	7		10		5	
w	µm	20		42		340	
z_R	mm	2.3		4.3		300	
U_0	µK	780	800	220	410	1.6	3.5
$\omega_\perp/2\pi$	kHz	$i\,16.6$	$i\,6.5$	4.2	2.2	0.044	0.025
$\omega_\parallel/2\pi$	Hz	$i\,100$	$i\,39$	29	12.6	-	-

Table 2.9: Main parameters of the high power lasers described in figure 2.11.Frequencies are given in the harmonic approximation (2.10) ; $\omega_\parallel$ is the axial frequency along the propagation of the beam and $\omega_\perp$ orthogonal to it. For the Verdi, the potential is repulsive and its steepness is given by the imaginary frequencies.

where w is the beam waist and $z_R = \pi w^2/\lambda$ is the corresponding Rayleigh length. Consequently, a tightly focused laser can generate a strong repulsive potential for blue detuning or attractive potential for red detuning, which can be expressed close to the focal point as:

$$U(\mathbf{r}) = \pm\left(\frac{1}{2}m\omega_\perp^2(x^2+y^2) + \frac{1}{2}m\omega_\parallel^2 z^2\right), \tag{2.10}$$

with a height (or depth) $U_0 \simeq \frac{\hbar\Gamma^2}{4|\delta|}\frac{I}{2I_{\text{sat}}}$ (typically between few μK and 1 mK) and frequencies $\omega_\perp = \sqrt{\frac{4U_0}{mw^2}}$ perpendicular to the beam propagation (typically between $\sim$ 100 Hz and $\sim$ 1 kHz) and $\omega_\parallel = \sqrt{\frac{2U_0}{mz_R^2}}$ along it (typically one hundred times smaller than $\omega_\perp$). Both repulsive and attractive potentials are used in the experiment (see Fig. 2.11 for the implementation and table 2.9 for the performances.).

2.10.1 532 nm laser

When evaporated in a magnetic quadrupole, atoms can escape the trap as they move through the center of the potential, where a vanishing bias prevents them from following the field orientation. Those *Majorana losses*, described in section 3.1.3, can be attenuated by focusing a blue-detuned laser on the central region to prevent atoms from reaching it. A Coherent Verdi single mode laser is used for this purpose, as its wavelength (532 nm) makes it repulsive for both ^{6}Li and ^{40}K. 7 watts of power are focused into a waist $w \sim 20\,\mu$m at the center of the magnetic trap, resulting in an optical plug of $\sim$ 800 µK (see Fig. 2.12).

The beam can be switched off within microseconds by means of an acousto-optical modulator. The pointing of the laser is monitored by imaging the focus of the beam on a 4-quadrant photodiode (Newport Model 2901), delivering a voltage proportional to the distance of the spot to the center of the diode. The position of the focus can be fine tuned by piezo mirrors (Newport AG-M100N) and a LabView script has been developed to bring automatically the spot on the 4-quadrant diode to a reference position. The root mean squared displacement averaged

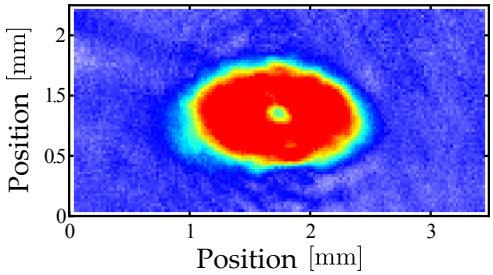

Figure 2.12: *In situ* picture of a ^{40}K cloud in a plugged quadrupole trap. Notice the depletion of atoms in the center of the distribution. The RF evaporation has been pushed to $T_{\text{cut}} = 100\,\mu K$, further than in a normal operating sequence, to reduce the size of the beam and help with the plug alignment.

over 3 minutes is around 1 µm, well smaller than the waist, showing a satisfying stability. To further reduce the sensitivity of the system, the laser beam is directed towards the transport direction (see Fig. 2.11), so that small displacements due to thermal dilatation of the transport support should be compared to the Rayleigh length of the beam $z_R \simeq 2$ mm rather than to its waist.

2.10.2 1064 nm laser

Optical traps provide comfortable conditions to perform evaporative cooling to ultralow temperatures. The trapping volume is small, and the strong confinement allows a high collision rate. Besides, unlike in a magnetic quadrupole trap, the confining potential does not depend on the spin state of the atoms and the spin composition of the cloud can thus be freely adjusted, allowing the use of Feschbach resonances.

We first implemented a Verdi Coherent single mode laser at 1064 nm. Unfortunately, this prototype was quite experimental and failed after few months. The production of this model was stopped by the constructor and we advantageously replaced it with a Mephisto Innolight module, delivering $\sim$ 18 W of power. The beam can be switched off within 0.5 µs by an AOM and is injected through a fiber for pointing stability (NKT Photonics LMA-PM-10, with a SMA 905 APC connector at the input (7°) and a SMA 906 PC connector at the output). This part of the setup is installed in a closed box over-pressurized with filtered air (Walker Filtration) to prevent dust from accumulating close to the optics, where due to high light intensities it might burn and damage the coatings.

The efficiency of the fiber coupling falls from $\sim$ 85% at low intensity to $\sim$ 60% at high powers, limiting the output power to 11 W. The light is sent along the $\mathbf{x}$ direction (see Fig. 2.11) on the science cell with a 10° angle to avoid optical interference with retro-reflected light, and focused in a $w = 42\,\mu$m waist (the corresponding Rayleigh length is $z_R = 4.3$ mm). The outgoing light is fed into an optical beam dump.

Initially, the potential must be deeper than 200 µK to capture atoms from the magnetic quadrupole trap. To perform an evaporation, the potential depth is lowered progressively

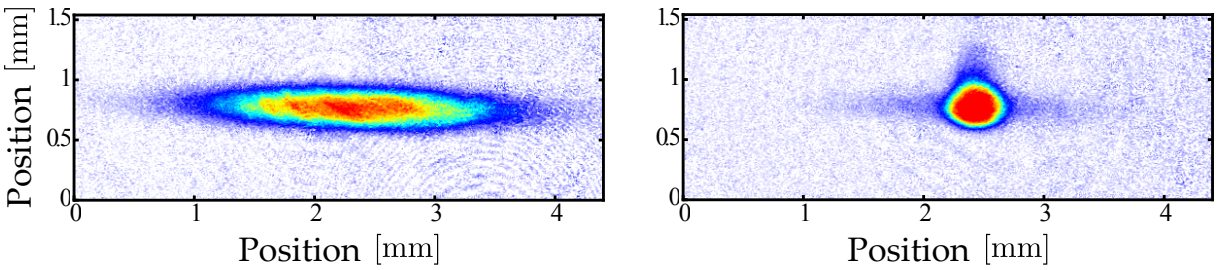

Figure 2.13: ^{40}K in the optical dipole traps. (**Left**): 7×10^6 atoms at 2 μK after 5 ms time-of-flight from the single arm ODT. (**Right**): 4×10^6 atoms at 1.2 μK after 5 ms time-of-flight the crossed ODT.

to $\sim$ 1 µK and the light intensity is accordingly varied over 4 orders of magnitude. To maintain the control and stability of the optical power through the whole range, we monitor the power of a back reflection on the science cell (Thorlabs SM05PD4A mounted InGaAs-Photodiode (FGA10)) and feed the signal in a logarithmic amplifier (Analog Devices AD8304). A PID controller (Stanford Research Systems SIM960) compares the measured value to a reference set by computer and adjust the RF power that feeds the aforementioned AOM to tune the optical power. This setup allows a retro-control and a dynamical setting of the light intensity and thus of the potential depth. In addition, taking advantage of the logarithmic amplifier, a linear ramp of the control voltage results in an exponential decrease of the optical power.

As the trapping frequency along the beam propagation axis is set by the Rayleigh length, it is much smaller than the transverse frequencies (see Fig. 2.13). In order to increase the steepness of the axial trapping at low powers, the 0th order of the AOM is recycled and sent perpendicularly to the previous beam (ODT$_2$ beam). The same power monitoring is installed to allow for an independent control of both intensities. The crossed beam position can be controlled by piezo mirrors to fine tune its overlap with the optical dipole trap.

In the quantum degenerate regime, the trapped atomic cloud is cooled around 100 nK and the pointing and power stability of the beams are crucial to avoid parasitic heating. Ultimately, the residual heating will be given by spontaneous emissions breaking the cycles of absorption and stimulated emission. The corresponding rate Γ_{sc} can be estimated to:

$$\hbar\Gamma_{sc}(\mathbf{r}) = \frac{\Gamma}{|\delta|} U_{ODT}(\mathbf{r}), \tag{2.11}$$

underlying the importance of a strong detuning to reduce the scattering rate. Each scattering event provides a recoil energy to the atoms and the resulting heating power can be estimated to

$$P_{heat} = 2E_{rec}\overline{\Gamma_{sc}} \tag{2.12}$$

where $\overline{\Gamma_{sc}}$ is the scattering rate averaged over the trap, E_{rec} is the recoil energy of the atom, and the factor 2 comes from the contribution of both longitudinal and transverse directions. Relating the energy of the cloud to its temperature through the virial theorm, we estimate the

heating effect for ^{40}K to $\dot{T} = 0.96\,\mu$K/s in the trap at full power and $\dot{T} = 10$ nK/s in the trap at the end of evaporation, a value small enough to be allow holding times of few seconds.

2.11 Imaging system

The standard data acquisition consists in sending a resonant light pulse on the atomic cloud, whose image is recorded on a charge coupled device (CCD) camera.

2.11.1 Absorption imaging

The light intensity reaching a pixel of the camera is attenuated by the optical density of the cloud integrated on the line of sight. Quantitatively, the intensity I captured at position (x, y) on the pixel matrix can be expressed thanks to the Beer-Lambert law as

$$I(x,y) = I_0(x,y)\,\exp\left(-m\sigma_{\text{abs}} \int\limits_{\text{line of sight}} dz'\, n(x',y',z')\right), \tag{2.13}$$

where $I_0(x,y)$ is the incoming intensity, σ_{abs} is the absorption cross section, m is the magnification of the imaging system and $n(x',y',z')$ is the atomic density at the position imaged on the camera.

For a frequency close to resonance, the absorption cross section can be written as [Cohen-Tannoudji *et al.* 2001]:

$$\sigma_{\text{abs}}(\omega) = \frac{3\lambda^2}{2\pi}\frac{C^2}{1+4(1+2\frac{I}{I_{\text{sat}}})\left(\frac{\delta}{\Gamma}\right)^2}, \tag{2.14}$$

where $\delta = \omega - \omega_0$ is the detuning between the light and the atomic frequencies. When scanning this detuning around the resonance, the cross section displays a Lorentzian behaviour, with width given by the natural linewidth Γ and a power-broadening factor. In most cases, the intensity is low enough for this factor to be negligible.

In this formula, C is the Clebsch-Gordan coefficient corresponding to the optical transition. If an external magnetic field gives a quantization direction, it is possible to address a closed imaging transition and $C^2 = 1$. However, in the some cases, the atomic magnetic moment is randomly distributed and we use a value averaged over all possible transition : $C^2 = 0.4$ for ^{40}K and $C^2 = 0.5$ for ^{6}Li.

It is thus possible to estimate the integrated density $n_{2D}(x,y) = \int\limits_{\text{l.o.s.}} dz\, n(x,y,z)$ from the ratio between the measured and incoming intensities. From this quantity, it is straightforward to obtain the total number of atoms, $N = \int dxdy\, n_{2D}(x,y)$. Another relevant measurement is the size $\sigma_{x,y}$ of the 1D distribution along each direction $n^x_{1D} = \int dy\, n_{2D}(x,y)$ and $n^y_{1D} =$

$\int dx\, n_{2D}(x,y)$, which can be related to the population, temperature and trapping frequencies of the cloud, as shown in the following paragraph.

2.11.2 Time-of-flight expansion of non-interacting particles

An *in-situ* image of the cloud can be taken to access directly to its density distribution. However, several non-trivial effects, such as non uniform frequency shifts due to the confining potential or remaining magnetic bias, can make the data analysis challenging. What's more, the small size of the sample may result in a too strong optical density and require an extremely good optical resolution.

An alternative way to acquire image is to perform a *time-of-flight* experiment: the trapping potential V_0 is abruptly switched off and the released atoms expand in all directions for duration τ without further interactions. Since this method was used to acquire most data in this thesis, we present it here with some details in order to derive expressions required to analyze a distribution of fermions at any temperature.

Free ballistic expansion

If fermions move freely, without interactions or outer potential, the momentum of each particle is conserved during their ballistic flight and the size of the cloud can give a direct insight on the temperature of the distribution:

$$n(\mathbf{r},\tau) = \int d\mathbf{r}_0 d\mathbf{p}_0\, f_{\mathrm{FD}}(\mathbf{r}_0,\mathbf{p}_0)\delta\left(\mathbf{r}-\mathbf{r}_0-\mathbf{p}_0 t/m\right) \tag{2.15}$$

$$= \frac{1}{(2\pi\hbar)^3}\int d\mathbf{p}_0 \frac{1}{\exp\left(\beta\frac{p_0^2}{2m}+\beta V_0\left(\mathbf{r}-\frac{\mathbf{p}_0}{m}t\right)-\beta\mu\right)+1}, \tag{2.16}$$

where f_{FD} is the Fermi-Dirac distribution, $\beta = (k_B T)^{-1}$ and we introduced the chemical potential μ.

For a harmonic trap $V_0(\mathbf{r}) = \sum_i m\omega_i^2 x_i^2/2$, the density can be analytical derived using polylogarithm function [9] :

[9] Polylogarithm function are defined as $\mathrm{Li}_n(z) = \frac{1}{\Gamma(n)}\int_0^{+\infty} dq\, \frac{q^{n-1}}{\frac{1}{z}e^q-1} \underset{z\ll 1}{\rightarrow} z$. As useful relation is $\int_{-\infty}^{+\infty} dx\, \mathrm{Li}_n(ze^{-x^2}) = \sqrt{\pi}\mathrm{Li}_{n+1/2}(z)$

$$
\begin{aligned}
n(\mathbf{r},\tau) &= -\frac{1}{\lambda_{\mathrm{dB}}^3}\left(\prod_i \frac{1}{\sqrt{1+\omega_i^2\tau^2}}\right)\mathrm{Li}_{3/2}\left[-Z\exp\left(-\frac{m}{2k_BT}\sum_i \frac{1}{2}\frac{\omega_i^2 x_i^2}{1+\omega_i^2\tau^2}\right)\right] \\
n_{2D}(x,y,\tau) &= -\frac{m\,(k_BT)^2}{2\pi\hbar^3\omega_z}\frac{1}{\sqrt{1+\omega_x^2\tau^2}\sqrt{1+\omega_y^2\tau^2}}\mathrm{Li}_2\left[-Z\exp\left(-\frac{m}{2k_BT}\left(\frac{\omega_x^2x^2}{1+\omega_x^2\tau^2}+\frac{\omega_y^2y^2}{1+\omega_y^2\tau^2}\right)\right)\right] \\
n_{1D}^x(x,\tau) &= -\sqrt{\frac{m}{2\pi}}\frac{(k_BT)^{5/2}}{\hbar^3\omega_z\omega_y}\frac{1}{\sqrt{1+\omega_x^2\tau^2}}\mathrm{Li}_{5/2}\left[-Z\exp\left(-\frac{m\omega_x^2}{2k_BT}\frac{x^2}{1+\omega_x^2\tau^2}\right)\right]
\end{aligned}
\tag{2.17}
$$

where we introduced the fugacity $Z = e^{\beta\mu}$.

In the classical limit, the temperature is large compared to chemical potential. In this regime, the integrated 1D densities (2.17) display a Gaussian distribution, whose width given by:

$$
\sigma_x^2(\tau) = \sigma_0^2 + \frac{k_BT}{m}t^2, \tag{2.18}
$$

where $\sigma_0^2 = \frac{k_BT}{m\omega_x^2}$ is the width of the initial Boltzmann distribution. By performing successive time-of-flight with increasing durations, it is therefore possible to measure the temperature T as the slope of width squared over time, without any knowledge of the trapping potential.

In the degenerate regime, the complete formula (2.17) is required to fit the non-Boltzmann distribution of the cloud. Note that the amplitude and width of the distribution are related, reducing to two the fitting parameters if the trapping frequencies are known. This allows for a simultaneous determination of the atom number and cloud temperature.

In both cases, it is remarkable that at long TOF, the isotropy of the initial momentum distribution is transferred to the position distribution, regardless of the initial trap geometry. This situation can be drastically different when particles are interacting.

Expansion in a surrounding potential

When a time-of-flight is performed at high magnetic bias, a residual curvature may still be present and give rise to a weak harmonic potential $V_{\mathrm{ext}} = \frac{1}{2}m\left(\omega_{\mathrm{ext},x}^2x^2 + \omega_{\mathrm{ext},y}^2y^2 + \omega_{\mathrm{ext},z}^2z^2\right)$, where $\omega_{\mathrm{ext},i}$ is real for a confining potential and imaginary for a repulsive potential (see section 5.1.3).

This additional effect can be taken into account in the previous expression by changing $\sqrt{1+\omega_i^2\tau^2}$ to $\sqrt{\cos^2(\omega_{\mathrm{ext},i}\tau) + \frac{\omega_i^2}{\omega_{\mathrm{ext},i}^2}\sin^2(\omega_{\mathrm{ext},i}\tau)}$, considering $\cos(i\theta) = \cosh(\theta)$.

In the classical regime, the substitution leads to

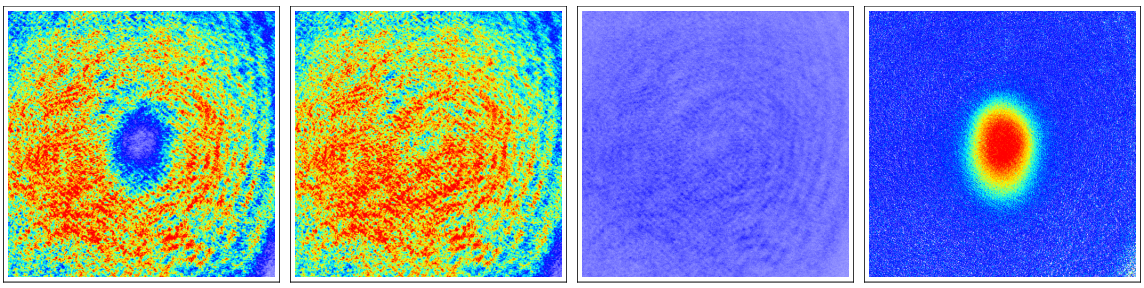

Absorption Reference Dark noise n_{2D}

Figure 2.14: Raw and treated data from absorption imaging after 5 ms TOF. On the picture, $\sim 10^7$ ^{40}K atoms after the optical molasses.

$$\sigma_x^2(\tau) \underset{\text{trap}}{=} \frac{k_B T}{m}\left(\frac{1}{\omega_i^2}\cos^2(\omega_{\text{ext},i}\tau) + \frac{1}{\omega_{\text{ext},i}^2}\sin^2(\omega_{\text{ext},i}\tau)\right) \tag{2.19}$$

$$\underset{\text{anti}}{=} \frac{k_B T}{m}\left(\frac{1}{\omega_i^2}\cosh^2(\omega_{\text{ext},i}\tau) + \frac{1}{\omega_{\text{ext},i}^2}\sinh^2(\omega_{\text{ext},i}\tau)\right) \tag{2.20}$$

Those formulas were used to characterize the curvature of the inner and outer coils close to the science cell, as shown in table 2.9.

2.11.3 Experimental setup

As presented in section 2.2, the laser system provides tunable light for imaging ^{40}K and ^{6}Li both at low magnetic bias and at high field, as the Zeeman shift induces significant changes on the resonance frequency.

A first *imaging* picture is taken with a 100 µs light pulse. The measurement is destructive, as atoms are pushed away by the probe beam. During the following 50 *ms*, the atoms are let to expand at high temperature until they collide with the surrounding chamber. A second *reference* picture is taken in the absence of atoms. Two additional *background* pictures are taken in the same conditions but in the absence of light, in order to measure the dark noise of the CCD camera. The integrated density at each point is then computed as

$$n_{2D}(x,y) = \frac{1}{m\sigma_{\text{abs}}}\log\left(\frac{I_{\text{img}} - I_{\text{img,bg}}}{I_{\text{ref}} - I_{\text{ref,bg}}}\right) \tag{2.21}$$

Four independent CCD cameras are installed on the experiment to acquire images from the MOT chamber and along three directions around the science cell. We use Pixelfly QE 270XD cameras, with a pixel matrix of 1392 px $\times$ 1024 px, a pixel size of 6.45 µm and a quantum efficiency of 25% for potassium light and 43% for lithium light. The magnification and numerical aperture of each imaging system are summarized in table 2.10.

System	w [mm]	m	NA
MOT Chamber	13.8	0.4	0.12
Science cell x	4	1.6	0.039
Science cell y	6	0.6	0.056
Science cell z	2.7	2.55	0.17

Table 2.10: Imaging system of the MOT chamber and science cell. w is the waist of the imaging beam, m the measured magnification and NA the numerical aperture calculated taking the imaging lenses as limiting aperture. The calibration procedure is explained in section 5.1.3.

2.12 Computer control

Three computers are dedicated to the control and monitoring of the experiment (see Fig. 2.15).

The main computer runs the user interface of the experiment. We use Cicero Word Generator[10], an open source software developed by Aviv Keshet at MIT for cold atom experiments. The suite is composed of two applications with a client / server architecture. The client *Cicero* is a user-friendly interface, where sequences are designed as a succession of steps with variable durations. During each step, the value of each digital and analog channel can be controlled. The server *Atticus* translates those sequences into output buffers that are downloaded to the output hardware. The software is mostly adapted for National Instrument cards and Norman Kretschmar extended the source code to integrate LAN connection (notably to address Agilent RF generators).

We currently use six analog (NI PXI-6713) and three digital output cards (NI PXI-6533 and NI PXI-6536). Each of the analog cards has 8 BNC outputs delivering 0 to 10 Volts and up to 250mA. The digital cards have 24 channels, outputting either 0V or 5V (only 3.3V for NI PXI-6536). When a digital channel is used to flip an IGBT, the fast switching of high intensities may induce high voltage in the control channel, destroying the output. To prevent this situation, most digital channels are opto-coupled to isolate them from the experiment (the electrical design of the optocoupler box is given in annex). Note also that while the digital channels provide a fixed voltage, some of the devices they control are current-controlled. It is in particular the case for most of the RF "ZAS" switches, that are notably used to turn on and off optical beams. An additional 50 Ω was installed at the input of those devices to avoid short-cutting the output card, which would result in a voltage drop of the whole control system.

Sequence steps might have very different durations: while the loading of the MOT or an evaporation can last several seconds, it takes only $\sim 100\,\mu s$ to take an image of the atoms. To avoid long redundant buffers, we synchronize the output cards with a variable frequency clock (Opal Kelly, ref. XEM 3001). This FPGA card generates pulses only when an output needs to be updated, and this variable timebase is used by output cards as sample clock. This reduces considerably the buffer size, allowing a faster loading of the sequence and a time resolution

[10] http://akeshet.github.io/Cicero-Word-Generator/

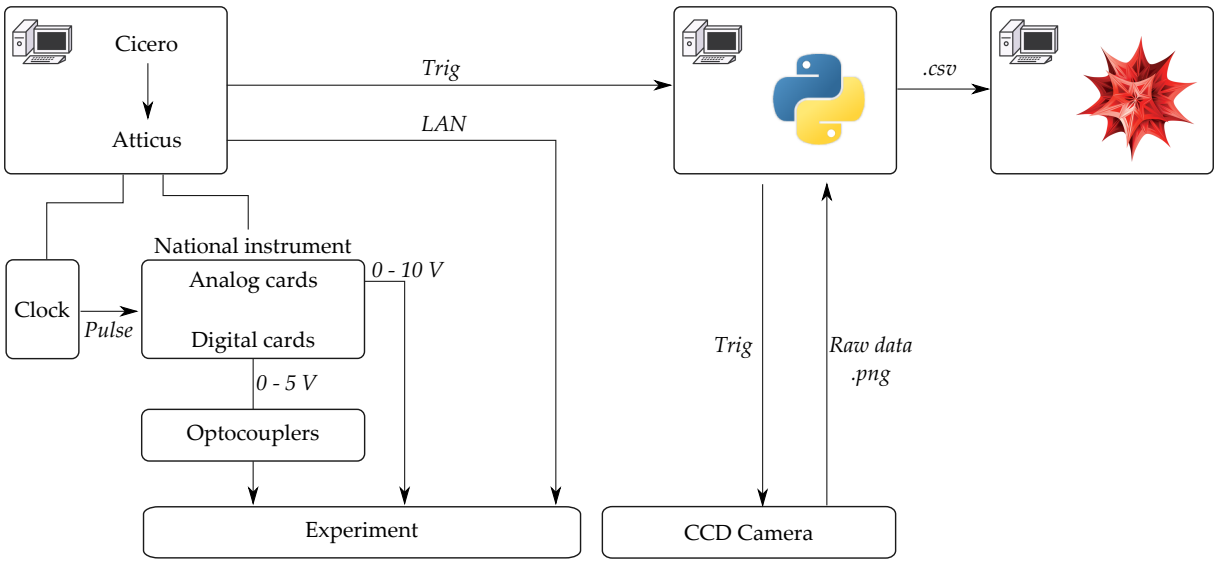

Figure 2.15: Computer control of the experiment. The type of information exchanged between the elements is written in italic font. The electronic boards for the optocoupler box are presented in annex A.6.

of $\sim 0.2\,\mu$s. A better resolution, allowing for instance smoother ramps, can be achieved by pre-setting the device and using the computer signal as a simple trigger.

A second computer controls the cameras installed on the experiment through a Python software originally coded by Martin Teichmann and further developed by successive generations of PhD students. It communicates with Atticus, triggers the camera and download the four series of raw data (see section 2.11.3). A third computer is used to treat the data, mostly using *Mathematica* scripts.

Altogether, the computer system allows for an adjustment of most experimental knobs, limiting to a minimum the physical tuning of the apparatus. Together with a good stability of the machine, the automation of data acquisition and treatment permits to run repeated sequences over long periods of time, providing a large amount of results.

2.13 Conclusions

In this chapter, we presented the main parts of the experimental apparatus and the knobs to control them. At the moment of writing, the system is reopening after almost a year of shutdown due to major works in the institute. The previous developments allowed an efficient cooling of $\sim 3 \times 10^5$ Potassium atoms to quantum degeneracy ($T = 0.17\,T_F$) within one minute. Lithium has been successfully transported to the science-cell and loaded to the optical dipole trap, but its evaporation is still challenging.

The FERMIX experiment is a powerful and demanding machine; its construction and main-

tenance are by themselves an important part of the work performed on a daily basis. It is also extremely versatile and can be tuned to address a broad variety of situations, some of which will be described in the following chapters.

Chapter 3

Quasi-thermalization of fermions in a quadrupole potential

Contents

3.1 Equilibrium properties of neutral atoms in a quadrupole trap **55**
3.1.1 Quadrupole traps 55
3.1.2 Initial Boltzmann distribution and typical orders of magnitude 56
3.1.3 Loss mechanisms 57
3.1.4 Density of states and adiabatic compression 60
3.2 Experimental investigations **61**
3.2.1 Initial observations: anisotropic effective temperatures 61
3.2.2 Further measurements 62
3.2.3 Preliminary conclusions 66
3.3 Numerical simulations **66**
3.3.1 Numerical methods 67
3.3.2 Comparison with the experiment 69
3.4 A simple model for the effective heating **71**
3.4.1 General predictions 73
3.4.2 In the experiment: direct kick of the cloud 74
3.4.3 Another excitation: adiabatic displacement 79
3.5 Quasi thermalization in an isotropic trap **80**
3.5.1 Isotropic 2D potential 80
3.5.2 Isotropic 3D potential 82
3.6 Influence of the trap anisotropy **87**
3.6.1 Anisotropy of the steady state 87
3.6.2 Quasi-thermalization time 88
3.7 Conclusions **89**

How does an excited system relax, and towards what steady state does it relax ? This question has been a bone of contention at the core of statistical physics since the emergence of Boltzmann's kinetic theory [Vilani 2010]. While the H theorem states that the thermodynamic potential of the ensemble can only decrease during its spontaneous evolution (see annex A.2),

this constraint is not strong enough to fully dictate the system's behavior (see annex A.2.2). In most cases, collisions between particles redistribute the energy in such a chaotic way that the ensemble eventually reaches a thermal distribution, completely characterized by one single scalar parameter, its temperature. However, some systems simply don't relax, such as massive particles in a harmonic trap which oscillate endlessly according to Kohn theorem [Kohn 1961]. In some systems, such as hard-core bosons in a one-dimensional lattice [Kinoshita *et al.* 2006], the existence of non trivial integrals of motion restricts the exploration of phase-space in a way that the relaxation of the initial excitation gives rise to a non-thermal distribution. It has been proposed that these systems could be described using Generalized Gibbs Ensembles [Chomaz *et al.* 2005, Rigol *et al.* 2007] that were recently observed experimentally [Langen *et al.* 2015].

Ensembles of non-interacting particles provide another example of generalized Gibbs ensembles. Indeed, the energies of each particle are independently conserved and provide as many constants of motion. This can result in a surprising behavior, despite the apparent simplicity of the system. For instance, Landau has shown that in a plasma where collisions between the charged particles are negligibly rare, collective mode of oscillations are damped, restoring an arrow of time in an isentropic evolution [Landau 1946, Ryutov 1999].

This chapter focuses on the relaxation following the excitation of collisionless Lithium atoms in a magnetic quadrupole trap which, despite many years of usage in the community, still exhibits non-intuitive behaviors. Although the absence of collisions precludes thermalization towards a proper Boltzman distribution, as reported qualitatively in [Davis *et al.* 1995a], we show that the ensemble reaches a state of quasi-equilibrium that we characterize by *effective temperatures* corresponding to the width of the momentum distribution. Surprisingly, although the potential is non-separable and should couple the different directions of motion, the dynamics along the symmetry axis of the trap appears to be only weakly coupled to the motion in the transverse plane. By contrast, effect temperatures equilibrate within this plane, corresponding to a *quasi-thermalisation*.

We first present the Boltzmann equilibrium of an atomic ensemble confined in a magnetic quadrupole potential, before we introduce our initial experimental study of the phenomenon. Numerical simulations performed to support the experimental findings are presented in the following section and a simple and robust model, relying on energy conservation and virial theorem, is presented and tested against several excitation method. We first consider a simplified excitation scheme to highlight the main features of the phenomena and then propose a more sophisticated description to account for the experimental results. Finally, we derive analytical predictions for the case of isotropic linear confinement and investigate the impact of the geometry and dimensionality of the trap.

Most of the experimental results presented in this chapter are to be published in Europhysics Letters

Daniel Suchet, Mihail Rabinovic, Thomas Reimann, Norman Kretzschmar, Franz Sievers, Christophe Salomon, Johnathan Lau, Olga Goulko, Carlos Lobo, and Frederic Chevy, "Analog simulation of Weyl particles in a harmonic trap with cold atoms", published in *Europhysics Letters*, **vol. 114**, page 26005 (2016).

A second publication, dedicated to the theoretical analysis, is currently under preparation.

3.1 Equilibrium properties of neutral atoms in a quadrupole trap

As an introduction to this chapter, we recall important results required to describe magnetically trapped atoms and estimate the related orders of magnitude relevant in the experiment.

3.1.1 Quadrupole traps

Magnetic fields provide a powerful way to trap and manipulate neutral particles. Because of their angular momentum, atoms present a magnetic moment μ which can be coupled to an applied external magnetic field $\mathbf{B_0}(\mathbf{r})$, resulting in a Zeeman shift of the energy levels. For magnetic field smaller than few Gauss, the corresponding Hamiltonian takes the form:

$$H_0\left(\mathbf{r},\mathbf{p}\right) = \frac{p^2}{2m} - \mu\,\sigma.\mathbf{B_0}(\mathbf{r}), \tag{3.1}$$

where σ is the atomic spin. As long as the spin follows adiabatically the direction of the field, the energy of a m_F Zeeman sub-level can be expressed perturbatively as

$$H_0\left(m_F,\mathbf{r},\mathbf{p}\right) = \frac{p^2}{2m} - \mu_B g_F m_F \left|\mathbf{B}(\mathbf{r})\right|, \tag{3.2}$$

where g_F is the Landé factor of the hyperfine state and $\mu_B = 1.4 \times h\,[\mathrm{MHz/G}]$ (see annex A.1 for a complete derivation). An inhomogeneous field thus modulates spatially the energy of the particles, giving rise to a restoring force towards the local minima and expelling particles from local maxima. Since Wing's theorem [Wing 1984] states that no static maximum of $|\mathbf{B}|$ can be found in vacuum, a trapping potential can be obtained only for *low-field seeking* states, which spins remain anti-parallel to local direction of the field and will be confined close to the field minima[1].

The idea of magnetic trapping was introduced as early as 1960 [Heer 1963] and several field configuration have been proposed over the following years to engineer traps relying on the same principle. Magnetic trapping quickly became one of the main techniques in the toolbox of the cold-atom community, allowing the first electromagnetical trapping of neutral atoms

[1] The same kind of situation arises for charged particles in an electrostatic field as Earnshaw's theorem states the absence of local maximum for a static potential in the vacuum. The absence of low field seeking states forbids the existence of electrostatic traps.

[Migdall *et al.* 1985] and the first realization of a quantum degenerate gas [Anderson *et al.* 1995].

A simple way to implement a magnetic trap certainly consists in two parallel coils in anti-Helmholtz configuration, as detailed in section 2.7.1. Close to their symmetry center, the field can be expressed up to the fourth order as:

$$\mathbf{B}(\mathbf{r}) = b \begin{pmatrix} x \\ y \\ -2z \end{pmatrix} + O(r^5), \tag{3.3}$$

where b is the magnetic field gradient, proportional to the electrical current. For low-field seeking particles with magnetic moment μ, the Zeeman shift results in a confining quadrupole potential:

$$V_0(\mathbf{r}) = \mu b \sqrt{x^2 + y^2 + 4z^2}, \tag{3.4}$$

displaying a strong trapping axis $\mathbf{z}$ and a weak trapping symmetry plane $(\mathbf{x}, \mathbf{y})$.

Even though more sophisticated schemes have been developed, the robustness of quadrupole trap makes them one of the most commonly used technique. In the FERMIX machine, they are used to gather atoms after the optical molasses phase, to transport atoms to the science cell and confine them during the first steps of evaporation. Nevertheless, despite many years of usage, quadrupole traps still exhibit poorly explored behaviors, as will be shown in this chapter.

3.1.2 Initial Boltzmann distribution and typical orders of magnitude

Let us consider a cloud of atoms in the potential (3.4), which corresponds to the experimental situation where Potassium and Lithium atoms (typically $\sim 10^9$) are optically pumped and loaded in the magnetic trap with typical gradients $b \simeq 80\,\mathrm{G/cm}$.

Because of collisions between the two species and among Potassium atoms, the equilibrium distribution of the ensemble can be described by a Boltzmann distribution characterized by a temperature T:

$$f_0(\mathbf{r}, \mathbf{p}) = \frac{N}{(2\pi\hbar)^3} \frac{\lambda_{dB}^3}{V_e} \exp\left(-\frac{1}{k_B T}\left(\frac{p^2}{2m} + V_0(\mathbf{r})\right)\right), \tag{3.5}$$

where $V_e = 4\pi r_0^3$ is the effective volume of the trap [Walraven 2010] and $\lambda_{dB} = \sqrt{2\pi\hbar^2/mk_BT}$ is the thermal de-Broglie wavelength. We introduced a typical length scale r_0 that describes the spread of the distribution in the potential:

$$r_0 = \frac{k_B T}{\mu_B b} \simeq 0.55\,\mathrm{mm}, \tag{3.6}$$

where the numerical value is estimated for $T \sim 300\,\mu\mathrm{K}$, corresponding to the experimental

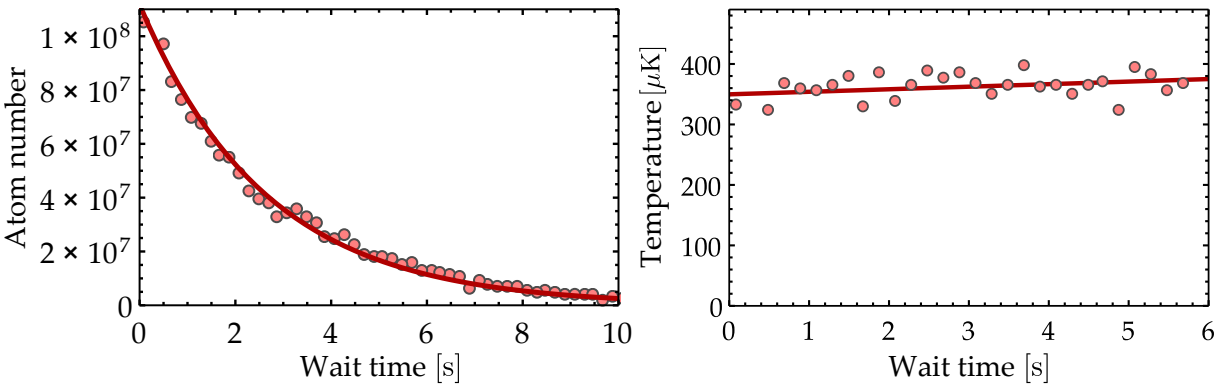

Figure 3.1: Time evolution of a Lithium cloud trapped in the quadrupole trap.**Left**: the atom number decays exponentially, with a lifetime ~ 2.8 s limited by the background pressure. **Right**: simultaneously, the temperature T slowly increases, with a heating rate estimated by a linear regression to 5.1 ± 2.1 μK/s. Here, we plot $m\sigma^2/k_B t_{TOF}^2 \propto T$, where σ is the measured width of the distribution after time-of-flight t_{TOF}.

situation.

Gravitational energy can also be taken into account, resulting in a tilt of the potential along the vertical direction. This leads a modification of the effective volume to $V_e = \frac{4\pi r_0^3}{(1-\gamma^2)^2}$, where $\gamma = \frac{mg}{2\mu_B b}$. However, in this chapter, we only consider strong magnetic trapping ($\gamma_{\mathrm{K}} \simeq 0.04$, $\gamma_{\mathrm{Li}} \simeq 0.006$) such that $\gamma \ll 1$ and we will neglect this effect.

It will also be useful to introduce a typical velocity v_0 and a time scale t_0 defined as

$$v_0 = \sqrt{\frac{k_B T}{m}} \simeq 0.6\,\mathrm{m/s}, \qquad t_0 = \frac{r_0}{v_0} \simeq 0.9\,\mathrm{ms}, \tag{3.7}$$

where the values are calculated for Lithium atoms. These scales will be used to express most results in dimensionless units by setting $k_B T = m = \mu_B b = 1$.

3.1.3 Loss mechanisms

Several mechanisms can lead to a departure of atoms from the quadrupole potential, resulting in a finite lifetime and heating rate of the remaining ensemble. Experimentally we measured in the magnetic trap a lifetime of ~ 3 s and a heating rate below $7\,\mu$K/s (see figure 3.1).

The most obvious source of losses are collisions with residual background particles, the rate of which depends on the quality of the ambient vacuum. In the MOT region, $\Gamma_{\mathrm{vac}} \sim 5$ s compatible with the measured lifetime.

It should be noted that low-field seeking trappable states are *not* the states with the lowest energy. High-field seeking states, expelled from the magnetic potential, have indeed a lower energy and any mechanism resulting in a spin flip of the atoms will lead to an expulsion from

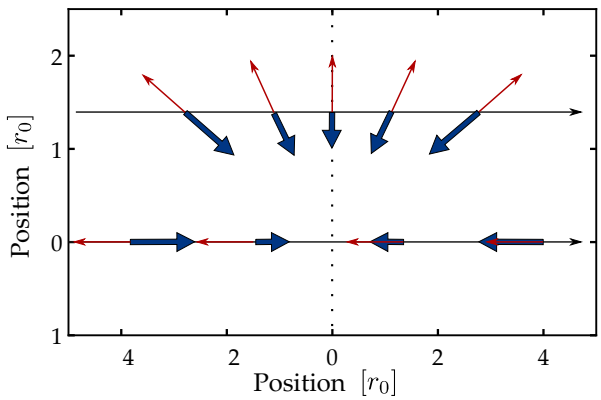

Figure 3.2: A simple picture of Majorana losses. Bold blue arrows represent the local direction of the magnetic field while thin red arrows picture the orientation of the atomic angular momentum over a trajectory from left to right. For trapped particles, the spin must remain anti-parallel with the field. In the uppercase, the direction of the magnetic field varies slowly enough for the spin to follow it adiabatically. In the lower case, as the particle moves through region where the field vanishes, the spin cannot follow its orientation and might become parallel to it, leading to the expulsion of the particle.

the trap. It is therefore essential to avoid light leaks that could not only heat the ensemble but also drive optical pumping. Two additional mechanisms can induce such spin-flips.

Majorana losses

Zeeman sublevels are defined according to the orientation of the local magnetic field. As an atom moves through the trap, it remains in the same state only if its spin follows adiabatically the direction of the field. Otherwise, the atom undergoes a non-adiabatic passage towards another Zeeman sublevel that might be expelled from the potential (see Fig. 3.2), resulting in a so-called *Majorana loss* [Majorana 1932].

The ability of a spin to follow the field direction depends on the Larmor frequency $\omega_L = \mu_B B/\hbar$. In a quadrupole potential, close to the trap center, the field vanishes and the atom is more likely to change its orientation. Majorana losses therefore appear as a leak at the bottom of the potential well: the colder the atoms, the more likely they are to pass close to the center and the more prevalent Majorana losses become. A simple estimate can provide insightful orders of magnitude [Petrich *et al.* 1995] (for a quantum description, see for instance [Bergeman *et al.* 1989]).

Let us consider an atom in a stretched state $g_F m_F = 1$, with velocity v and passing the center at a distance d. The typical magnetic field experienced by the atom is given by $B \sim db$ and varies over a typical time $\sim d/v$. If the corresponding rate is larger than the Larmor frequency, the adiabatic following breaks down; Majorana losses therefore occur if the atom

crosses a so-called *death radius*:

$$d \sim \sqrt{\frac{v\hbar}{\mu_B b}} \quad , \tag{3.8}$$

and the loss rate can be estimated as the flux through the corresponding shell

$$\frac{\dot{N}}{N} = -\Gamma_M \simeq \frac{\hbar}{m}\left(\frac{\mu_B b}{k_B T_0}\right)^2 . \tag{3.9}$$

In addition to the depletion of atoms, Majorana losses also induce a specific amount of heating, as the coldest atoms of the distribution are most likely to leave the trap. If collisions allow for a quasi-thermal equilibrium, the anti-evaporation due to Majorana losses results in a heating rate [Chicireanu *et al.* 2007]:

$$\frac{\dot{T}}{T} = +\frac{4}{9}\Gamma_M, \tag{3.10}$$

and the temperature increases over time as

$$T(t) = T_0\sqrt{1 + \frac{8}{9}\Gamma_M(T_0)t}. \tag{3.11}$$

This behavior was used by two groups to estimate the value of the Majorana rate Γ_M, found to be in reasonable agreement with the expression (3.9) up to a geometrical factor $C \sim 0.040$ for both Rubidium 87 [Dubessy *et al.* 2012] and ^{23}Na [Heo *et al.* 2010]. In the conditions of this chapter, because of the relatively high temperatures, the corresponding time scale is about one minute, much longer than the duration of the experiments.

Inelastic collisions

The internal state of an atom can change after a collision, in which case the collision is said to be *inelastic*. Since the trappability of an atom depends on its internal state, inelastic collisions can induce losses in the sample and heat significantly the remaining atoms. A careful choice of trapped states is therefore necessary.

For ^{6}Li, the only state simultaneously trappable at high temperatures in a magnetic trap *and* collisionally stable is $|F = 3/2,\, m_F = 3/2\rangle$. The linear trapping regime for the $|1/2,\, -1/2\rangle$ state extends only up to 27 G, corresponding to a temperature of 0.2 mK, too low to trap a significant amount of the initial distribution. The other low-field seeking state, $|3/2,\, 1/2\rangle$, can lead to spin-exchange collisions $|3/2,\, 1/2\rangle + |3/2,\, 1/2\rangle \rightarrow |3/2,\, 3/2\rangle + |1/2,\, -1/2\rangle$. The resulting heating, corresponding to the hyperfine splitting of the $S_{1/2}$ level, is strong enough to expel the atoms out of the trap.

For ^{40}K the situation is less tragic. Thanks to the inverted hyperfine structure, the lower manifold corresponds to higher momentum and displays several trappable states. Among them, $|F = 9/2,\, m_F = 9/2\rangle$, $|9/2,\, 7/2\rangle$ and $|9/2,\, 5/2\rangle$ are collisionally stable, as the inelastic

collision rate of the allowed transitions is very low. For instance, [DeMarco 2001] determined a two body loss rate $L_2 = 10^{-14}\,\mathrm{cm}^{-3}/\mathrm{s}$ as an upper bound for the $|7/2\rangle + |5/2\rangle \rightarrow |9/2\rangle + |3/2\rangle$ process within the F=9/2 manifold, whereas for Lithium, the inelastic spin exchange collision rate is typically around $L_2 \simeq 10^{-9}\,\mathrm{cm}^{-3}/\mathrm{s}$ for [Houbiers *et al.* 1998].

The case of inter-species spin exchange collisions will be addressed in section 5.4.

3.1.4 Density of states and adiabatic compression

As long as the trapping gradient is increased or decreased slowly enough for the ensemble to follow its evolution adiabatically, phase-space density is conserved. For instance, in a more confined trap, the spatial density is higher and the temperature increases so as to keep $n\lambda_{dB}^3$ constant. To express this conservation, we first need to find the density of state $\rho(E)$, which can be calculated as the integral over phase-space of the quantity $\delta\left(E - \frac{p^2}{2m} - U(r)\right)$:

$$\rho(E) \propto \begin{cases} \frac{E^{7/2}}{|b_x b_y b_z|} & \text{for } U(r) = \mu_\mathrm{B}\sqrt{b_x^2 x^2 + b_y^2 y^2 + b_z^2 z^2} \\ \frac{E^2}{|\omega_x \omega_y \omega_z|} & \text{for } U(r) = \frac{1}{2}m\left(\omega_x^2 x^2 + \omega_y^2 y^2 + \omega_z^2 z^2\right) \end{cases} \tag{3.12}$$

We consider a smooth compression of the trapping potential, as one of the trap parameters is ramped from an initial to a final value. As long as the process is adiabatic, the entropy is conserved through the evolution. In the canonical ensemble, the entropy can be expressed as

$$S = k_\mathrm{B}\frac{\partial\left(T\log Z\right)}{\partial T}, \tag{3.13}$$

where $Z = \int dE\,\rho(E)\exp\left(-\frac{E}{K_B T}\right)$ is the partition function. In a quadrupole trap, the previous expression of the density of states, with $b_x = b_y = b_z/2$, leads to

$$T_f = T_i\left(\frac{b_f}{b_i}\right)^{2/3}. \tag{3.14}$$

The same tools can be used to describe the adiabatic compression of a harmonic trap, which will be useful in following chapters to describe the evaporation in an optical dipole trap. If only one trapping frequency is changed, the same calculation leads to

$$T_f = T_i\left(\frac{\omega_f}{\omega_i}\right)^{1/3}. \tag{3.15}$$

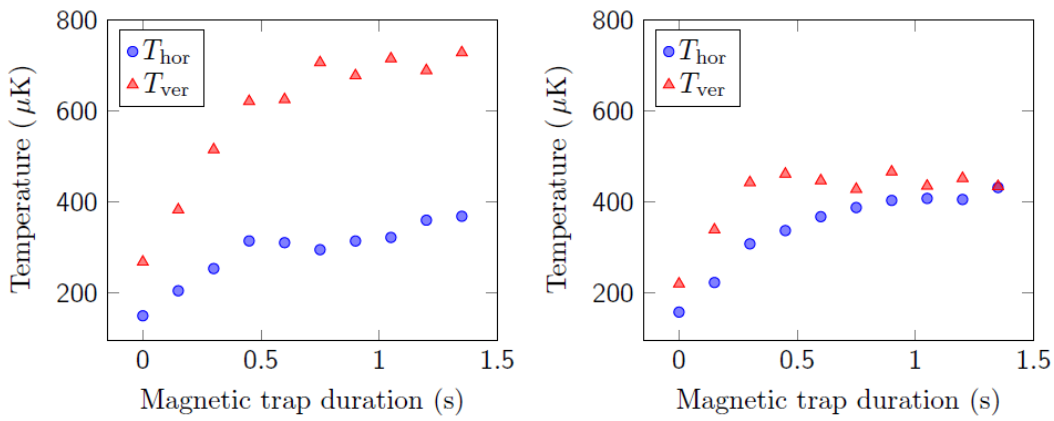

(a) ^{6}Li alone (b) ^{6}Li with ^{40}K

Figure 3.3: Thermalization experiment. Temperature of the ^{6}Li atoms as a function of the magnetic trap duration. The magnetic gradient b linearly increases from 20 G/cm to its final value of 80 G/cm in 450 ms, resulting in an adiabatic compression and heating of the cloud. Red triangles represent the vertical temperature, blue circles the temperature in horizontal direction. (a) Spin polarized, fermionic ^{6}Li in the quadrupole magnetic trap. Intra-species collisions are suppressed and the vertical and horizontal temperatures can not thermalize. (b) ^{6}Li is trapped together with ^{40}K. Inter-species collisions enable thermalization of the vertical and horizontal temperatures. Picture from [Sievers 2014].

3.2 Experimental investigations

In this section, we report our experimental observations concerning the behavior of cold ^{6}Li atoms in a quadrupole potential and we show that, despite the absence of collisions, the system relaxes towards a steady state, though non describable by a Boltzmann distribution. We start by presenting the conditions in which the phenomenon was first observed and introduce a more systematic way to study it.

3.2.1 Initial observations: anisotropic effective temperatures

After the gray optical molasses, atoms are optically pumped into low-field seeking states and a magnetic gradient is raised up to create the quadrupole potential. Once the atoms are trapped, their temperature can be measured by a time-of-flight experiment, as described in section 2.11.2: we release the atoms from the trap and record the 2D density of the cloud, as we integrate along the line of sight **y**. We then measure the width of the distribution along **x** and **z** after various waiting time and deduce the temperature from the expansion speed of the cloud; we define this way two temperatures T_x and T_z.

The initial temperatures of the Lithium cloud measured just after loading are significantly different as $T_x \simeq 150\,\mu$K and $T_z \simeq 250\,\mu$K (see Fig. 3.3). This discrepancy is attributed to the spin polarization beam, which is sent on the atoms bottom-up.

As long as both ^{40}K and ^{6}Li are loaded into the potential, the two temperatures eventually equilibrate after few hundreds of milliseconds (see figure 3.3 b): because of collisions, both distributions relax towards a Boltzmann distribution (3.5) with a temperature $T_0 \simeq 400\,\mu$K. The temperature increase between 0 and 500 ms is mostly due to the adiabatic compression of the cloud which results in the heating described by eq. (3.14). It should be noted that the preceding simultaneous D_1 cooling for both species is necessary to observe this thermalization. Before the molasses was implemented on ^{6}Li, the temperature difference between ^{40}K and ^{6}Li was so large that the overlap of their respective volumes was too small to allow for a sufficient collision rate and ^{6}Li essentially behaved as if no ^{40}K atoms were present in the trap.

The situation is drastically different when ^{6}Li is alone in the trap, as pictured in figure 3.3 a. In this case, the temperatures measured along the two directions do not reach the same value; even after 1.5 s, $T_x \simeq 315\,\mu$K and $T_z \simeq 620\,\mu$K. This implies that the equilibrium distribution must be non-Boltzmanian and as such, the notion of temperature should be dealt with more carefully. A thermal distribution, as for instance eq.(3.5), can be fully described by a well-defined uniform temperature, which is sufficient to calculate all its moments. By contrast, a more general distribution has no reasons to be characterized by a single scalar value. The quantities measured through the time-of-flight experiment should thus be treated as *effective* temperatures which represent the width of the momentum distribution:

$$T_i = \frac{\langle p_i^2 \rangle}{2m}. \tag{3.16}$$

For a thermal cloud, (3.16) obviously corresponds to the real temperature of the distribution.

3.2.2 Further measurements

In the previous experiment, the temperature discrepancy between T_x and T_z results from the kick delivered by the spin-polarizing beam propagating along $\mathbf{z}$. In order to study more quantitatively the relaxation of the system, we performed further measurements with controllable excitations.

We use interspecies interactions to prepare an initial Lithium sample in a thermal equilibrium. Experimentally, we load 10^7 Lithium 6 atoms and 10^9 Potassium atoms in the quadrupole and wait 500 ms. The reduced amount of Lithium facilitates its thermalization with Potassium at $T_0 \sim 300\,\mu$K; ^{40}K atoms are then removed from the trap by shining in resonant light, which leaves ^{6}Li unaffected.

We deliver[2] a momentum kick to the cloud by quickly turning on a magnetic bias field $\mathbf{B_0}$

[2]We first attempted to excite the cloud as previously by shining the spin-polarizing beam, with variable duration and / or intensity. However, the resulting optical pumping leads to additional losses and the starting conditions of the ensuing thermalization were excitation-dependent.

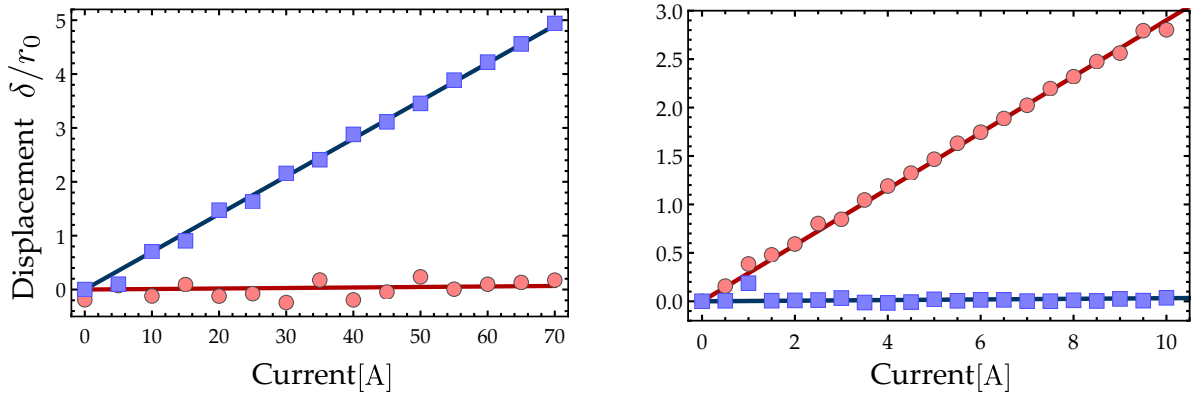

Figure 3.4: Displacement δ of the magnetic center along $\mathbf{x}$ (blue squares) and $\mathbf{z}$ (red circles) in dimensionless units as a function of the current used to generate the bias. (**Left**): the *push* coil creates a bias along $\mathbf{x}$, with $\delta_x/r_0 = 0.07\,I$. (**Right**): Along $\mathbf{z}$, the *Spinpol* coils create a bais along $\mathbf{z}$, with $\delta_z/r_0 = 0.3\,I$. In both cases, the displacement along the transverse direction is less than 1% of the displacement along the excited direction. For technical details concerning the coils, see section 2.7.

that displaces the center of the trapping potential by a distance δ:

$$\delta = \left(\frac{B_{0,x}}{b}, \frac{B_{0,y}}{b}, \frac{B_{0,z}}{2b}\right) \tag{3.17}$$

The existing set-up allowed independent displacement along $\mathbf{x}$ and $\mathbf{z}$. We calibrated the displacement by loading a small sample and raising up slowly the bias, so that the cloud can follow adiabatically the magnetic center. An *in situ* image at resonance points out the center of the potential (see Fig. 3.4). We could achieve displacements up to $\delta_x \sim 7\,r_0$ and $\delta_z \sim 4\,r_0$.

We let the cloud evolve in the displaced potential for a short time τ. The kick duration is typically a few ms and is limited by the eddy currents in the steel chamber surrounding the cloud. During the kick, the ensemble acquires an overall momentum of magnitude $q \sim \mu_B b\tau$, similar to free fall in gravity. If the kick is short enough, the displacement of the center-of-mass $d \sim \mu_B b\tau^2/2$ can be neglected.

After the duration τ, the bias is abruptly switched off, restoring the trap to its initial configuration, and we let the cloud evolve during a variable duration t before switching off all fields to perform a time of flight measurement. The resulting time evolution of the center-of-mass position is shown in figure 3.5. As expected from the previous observations, the oscillations are damped and the distribution reaches a quasi-steady state within a few milliseconds. In the mean time, we observe an increase of the momentum distribution width, which we take to represent an effective heating ΔT.

The heating ΔT results from the redistribution of the energy ΔE gathered during the kick, but this quantity is not directly accessible through the experiment. Instead, we measure center of mass momentum $\mathbf{q}$ induced by the excitation. The value of the heating ΔT as a function of the kick strength is shown in figure 3.6 and discussed below.

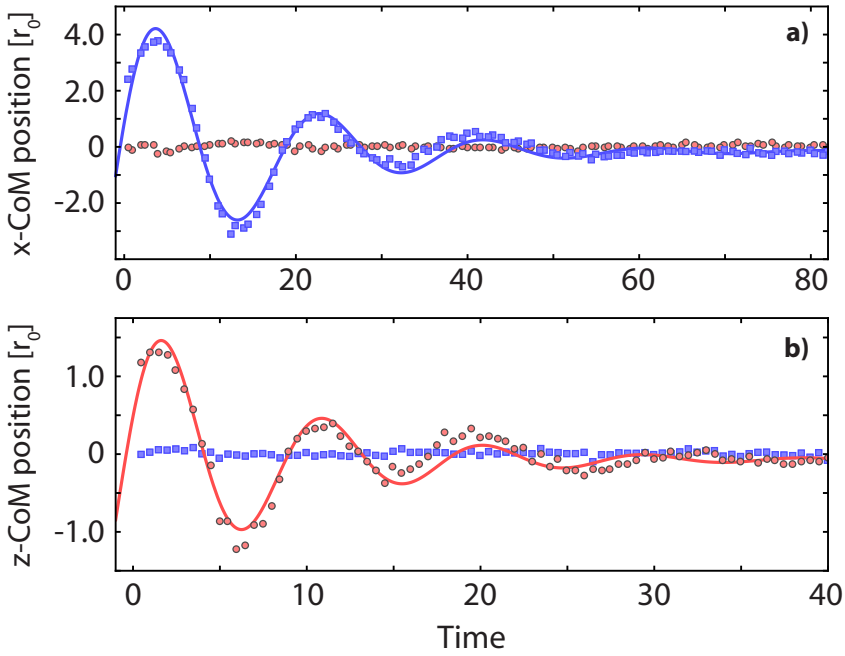

Figure 3.5: Center-of-mass oscillations of the Lithium cloud after a kick along **z** (a) and **x** (b). Blue squares (resp. red circles) are experimental data along **x** (resp. **z**). Solid lines are exponentially damped sinusoidal oscillations. Damping results solely from dephasing of single particle trajectories. Here, $r_0 = k_B T/\mu_B b \sim 0.6$ mm and $t_0 = \sqrt{m k_B T}/\mu_B b \sim 1$ ms.

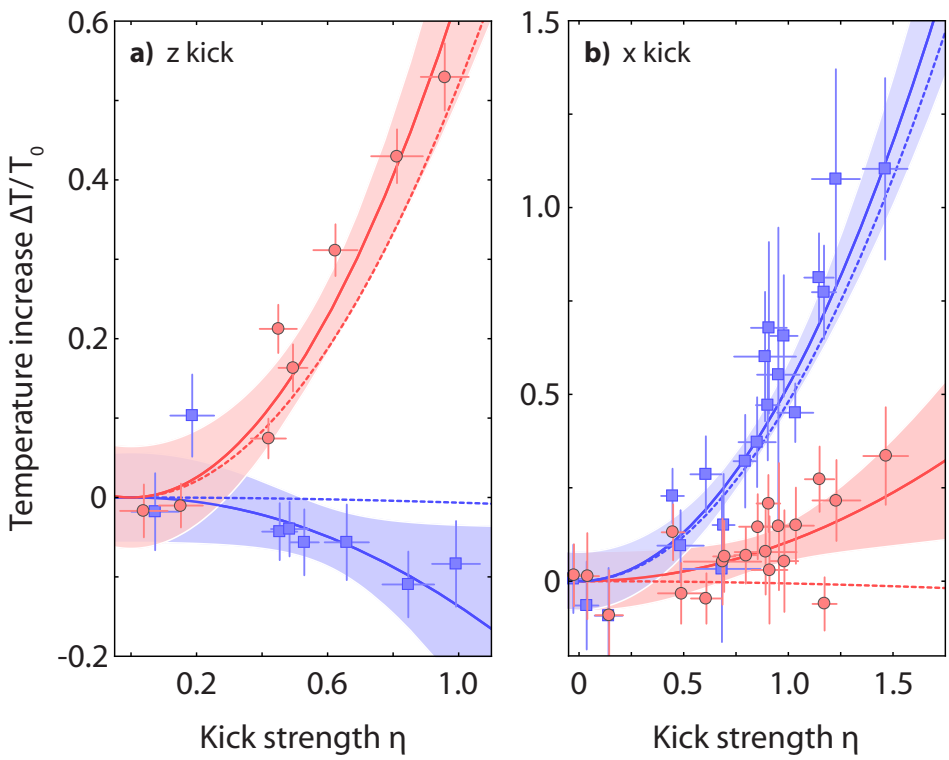

Figure 3.6: Temperature increase $\Delta T/T_0 = (T - T_0)T_0$ along **x** (blue squares) and **z** (red circles) as a function of the normalized CoM momentum η acquired during the kick. **a)** **z** momentum kick at $b = 70\,\mathrm{G/cm}$. **b)** **x** momentum kick at $b = 55\,\mathrm{G/cm}$. Solid lines are quadratic fits to the experimental data with coefficients given in the text. Error bars represent the temperature statistical uncertainty and shaded zones give the 95% confidence level of the fits. Dashed lines are results of numerical simulations presented in Fig. 3.11

A limitation for the accurate estimation of $\mathbf{q}$ originates from eddy currents, which appear when abruptly switching off the quadrupole magnetic trap (gradients are of the order of $80 - 150$ G/cm) and last several ms. The transient magnetic field creates inhomogeneous transitory Zeeman shifts which deform the atomic cloud profile at short TOF duration. Time-of-flights long enough for the eddy current to vanish show a very poor detectivity because of the relatively high temperature of the cloud and of the small mass of Lithium atoms. Cooling the sample further down leads to higher Majorana losses during the 500ms of thermalization, resulting in an additional heating of the cloud. To overcome this obstacle, we used a highly saturated probe beam with a saturation parameter s = 24, in order to power broaden the absorption resonance to a width $\Gamma' = \Gamma\sqrt{1+s}$, where $\Gamma = 6$ MHz is the natural width of the D_2 transition. Measurements were made by averaging 10 images for 6 different TOF between 1.5 and 3ms. The fit errors are given by the error bars in figure 3.6 and account for our statistical errors of typically $0.05/mk_{\mathrm{B}}$. Performing the experiment with 4 different magnetic gradients, we estimate a systematic uncertainty of $0.2/mk_{\mathrm{B}}$ for the fitted amplitude of the parabolic dependence of the heating on the momentum kick.

In addition, eddy currents can result in a potential error in the measurement of the center of mass momentum, with or without kick. For instance, in the absence of a kick, we observe a small parasitic velocity $\mathbf{v_0}$ which is proportional to the magnetic gradient b and reaches 30 cm/s at $b = 85$ G/cm. The velocity of the center of mass of the cloud after an excitation is thus given by:

$$\mathbf{v}_{\mathrm{tot}} = \mathbf{v_0} + \mathbf{q}/m, \tag{3.18a}$$

$$\mathbf{v_0} = \int_0^{+\infty} dt\, \mathbf{F}(t, x(t)), \tag{3.18b}$$

where $\mathbf{F}$ is the force due to the eddy currents. If this force varies only slowly with the position of the cloud, $\mathbf{v_0}$ does not depend on $\mathbf{q}$. We estimate $\mathbf{v_0}$ by measuring $\mathbf{v}_{\mathrm{tot}}$ in absence of kick ($q = 0$). To infer the actual momentum $\mathbf{q}$ delivered to the cloud solely by a kick, we then subtract $\mathbf{v_0}$ from the velocity $\mathbf{v}_{\mathrm{tot}}$ measured right after the kick.

The results presented in figure 3.6 show a very strong anisotropy, as the temperature increases much more in the direction of the kick than in the transverse directions. A kick in the $\mathbf{z}$ direction produces strong heating along $\mathbf{z}$, but has very little effect along $\mathbf{x}$. Conversely, a kick in the $(\mathbf{x}, \mathbf{y})$ plane results only in small heating in the $\mathbf{z}$ direction. Defining the strength of the kick through the dimensionless parameter η as per

$$\eta = \frac{\langle q \rangle}{\sqrt{mk_B T_0}}, \tag{3.19}$$

we find that for kicks along $\mathbf{x}$ the best quadratic fits are given by $\Delta T_{\mathrm{x}}/T_0 = 0.52(5)_{\mathrm{stat}}\ (20)_{\mathrm{syst}} \times \eta^2$ and $\Delta T_{\mathrm{z}}/T_0 = 0.10(4)_{\mathrm{stat}}\ (5)_{\mathrm{syst}} \times \eta^2$. For kicks along the strong axis $\mathbf{z}$, $\Delta T_{\mathrm{z}}/T_0 = 0.63(7)_{\mathrm{stat}}$

$(20)_{\text{syst}} \times \eta^2$ and $\Delta T_x/T_0 = -0.14(5)_{\text{stat}}\ (8)_{\text{syst}} \times \eta^2$.

3.2.3 Preliminary conclusions

Four main features of the experiment presented above should be emphasized:

(i) A pure ^{6}Li cloud is an ideal gas with no interactions, as proven by the anisotropy of the effective temperatures at long times. Indeed, while ^{6}Li-^{40}K interactions allow the Lithium ensemble to relax towards a thermal equilibrium within few collisions [Snoke and Wolfe 1989], ^{6}Li alone can not reach a Boltzmann distribution. The absence of collisions between ^{6}Li atoms results from the Pauli exclusion principle: as all particles are in the only trappable spin state $|F = 3/2, m_F = +3/2\rangle$, they are indistinguishable and s-wave collisions are forbidden by symmetry[3]. At the first finite order, p-wave collisions exhibit a thermal threshold, estimated to 6 mK for Lithium [Ketterle and Zwierlein 2008], which is well above the temperatures at stake. Note that for ^{40}K, the p-wave threshold is much lower, around 200 μK [DeMarco *et al.* 1999]. In addition to the simultaneous presence of several spin-states, this prevents Potassium from exhibiting the same behavior as Lithium.

(ii) Despite the absence of collisions, the ensemble does relax towards a steady state after the excitation. The relaxation can be attributed to the dephasing of the single particle trajectories as they oscillate in the potential. This behavior illustrates that collision-induced relaxation towards a thermal Boltzmann distribution is not the only way for a system to reach a stationary distribution.

(iii) The energy acquired by the atoms during the kick is redistributed within the cloud even though collisions are absent, as shown by the damping of the oscillations. The energy increase results in a spread of the momentum distribution, which appears as an effective heating.

(iv) This redistribution is strongly anisotropic, as the effective temperature increases much more along the kick direction than in the transverse direction, even though the trapping potential is non separable. The **x** and **z** axes appear to be effectively decoupled. We will show that this property, inherited from the trap geometry and dimensionality, is non trivial.

3.3 Numerical simulations

In order to account for those results, we performed numerical simulations on an ensemble of 10^5 particles. Using those simulations, we can understand the observed anisotropy and effective heating, but also study the behavior of quantities that are not accessible in the experiment for technical reasons (such as the distribution along the imaging axis **y**) or fundamental reasons

[3] S-wave and p-wave collisions are presented in annex A.4.4.

(such as a direct measurement of the imparted energy ΔE).

Several ways to excite the initial distribution can be considered. As in the experiment, a kick can be applied by displacing the trap center by an amount δ for a duration τ before bringing it back to its initial position. A simpler excitation consists of an *ideal momentum kick*, where a momentum $\mathbf{q}$ is added to each of the particles, resulting in a shift of the center-of-mass by the amount $\mathbf{q}$ in momentum space. In the same way, an *ideal position kick* consists in dragging the center-of-mass away from the trap center by an distance δ without initial velocity.

3.3.1 Numerical methods

Since the particles do not interact with each other, the trajectory of each single particle can be integrated independently from all the others and average values are obtained by summing all contribution.

Step one Generate initial conditions

The initial position (x, y, z) and momentum (p_x, p_y, p_z) of the particle are drawn at random from a Boltzmann distribution function $f(\mathbf{r}, \mathbf{p})$. Gaussian random generators are implemented in most programming languages and it is straightforward to generate the initial momentum. However, the position does not follow a usual statistics and a dedicated procedure must be applied.

We define a rescaled position $\mathbf{r}' = (x, y, 2z)$ such that the distribution function $f'(\mathbf{r}') = f(\mathbf{r})$ is isotropic. The rescaled position can be generated with two angles φ (uniform between 0 and 2π) and θ (such that $\cos\theta$ is uniform between -1 and 1), as well as a modulus $r' = |\mathbf{r}'|$, which should be drawn at random from the distribution:

$$f'(r') = \frac{1}{2}\int d^3\mathbf{p}\, d\varphi\, d\theta\, r'^2 \cos\theta\, f(\mathbf{r}, \mathbf{p}) \tag{3.20a}$$

$$= \frac{1}{2}\left(\frac{\mu_B b}{k_B T}\right)^3 r'^2 \exp\left(-\frac{\mu_B b}{k_B T} r'\right) \tag{3.20b}$$

where the $1/2$ factor comes from the Jacobian of the transformation $\mathbf{r} \to \mathbf{r}'$. It is easier for a computer to generate a random number Y between 0 and 1 with a uniform probability than to generate a radius r' from f'. From a realization y of such a random variable, it is thus straightforward to generate φ and θ, but a numerical integration is required to estimate r' [Press *et al.* 2007].

To do so, we consider $r' = g(y)$, such that the probability $f'(r')dr'$ for the corrected radius to be around r' at dr' is the probability for Y to be around y at dy. Since Y is uniformly distributed, this relation leads to $f'(r')dr' = dy$, which can be integrated as $y = \int_0^{r'} f'(x)dx$.

Noting F' the primitive function of f' with $F'(0) = 0$

$$F'(r') = 1 - \exp\left(-\frac{\mu_B b}{k_B T} r'\right)\left(1 + \frac{\mu_B b}{k_B T} r' + \frac{1}{2}\left(\frac{\mu_B b}{k_B T} r'\right)^2\right), \tag{3.21}$$

the corrected radius can be expressed as the solution of $F'(r') = y$.

In summary, three random variables $Y_{1,2,3}$ are generated between 0 and 1. The initial rescaled position is defined by $\varphi = 2\pi y_1$, $\cos\theta = 2y_2 - 1$ and r' such that $F'(r') - y_3 = 0$. From there, the real initial position is calculated as $x = r'\sqrt{1-\cos^2\theta}\cos\varphi$, $y = r'\sqrt{1-\cos^2\theta}\sin\varphi$ and $z = \frac{1}{2}r'\cos\theta$.

The same reasoning can be applied for a 2D distribution, where the corrected radius follows the distribution $f'_{2D}(r') = \left(\frac{\mu_B b}{k_B T}\right)^2 r'^2 \exp\left(-\frac{\mu_B b}{k_B T} r'\right)$. In such a case, the primitive function to be inverted is

$$F'_{2D}(r') = 1 - \exp\left(-\frac{\mu_B b}{k_B T} r'\right)\left(1 + \frac{\mu_B b}{k_B T} r'\right). \tag{3.22}$$

Step two Integrate the equations of motion

Starting from the aforementioned initial conditions, the equation of motion can be easily integrated numerically with an applied force $\mathbf{F} = -\frac{\mu_B b}{k_B T}\boldsymbol{\nabla} r'$. We used the Python numerical solver odeint from the integrate module of the scipy library and record the position and velocity of the particle at each time step.

Step three Update the mean value and the mean squared value of the distribution

In order to avoid filling the memory of the computer, we do not keep all the values for each of the$\sim 10^5$ particles of the six coordinates at each of the $\sim 10^3$ time-steps until the end of the simulation. Instead, to estimate the average and the standard deviation of the distribution, we update the mean value and the mean squared value of the distribution at each time-step after each single particle simulation:

$$\overline{x_n}(t) = \frac{1}{n}\left(x_n(t) + (n-1)\,\overline{x_{n-1}}(t)\right) \tag{3.23}$$

$$\overline{x_n^2}(t) = \frac{1}{n}\left(x_n^2(t) + (n-1)\,\overline{x_{n-1}^2}(t)\right), \tag{3.24}$$

where $x_n(t)$ is the value taken by the coordinate x at time t for the particle that has just been simulated, while $\overline{x_{n-1}}(t)$ is the average value of this coordinate at time t over the previous $(n-1)$ particles. We reduce that way the number of stored variables to the number of time steps.

Step four Calculate the standard deviation of the distribution

Once all trajectories have been simulated, we compute the standard deviation of each

coordinate at each time using the stored data:

$$\sigma^2(t) = \frac{N}{N-1}\left(\bar{x_N^2}(t) - \bar{x_N}^2(t)\right) \tag{3.25}$$

3.3.2 Comparison with the experiment

We now present the results obtained with the numerical methods presented above.

For simplicity, we first consider the behavior after an ideal momentum kick $\mathbf{q} = q_0(1,0,0)$, as presented in figure 3.7. The oscillations of the center of mass are completely damped out after $\sim 30\,t_0$, as in the experiment. This confirms that the experimentally observed damping is not due to unaccounted interactions. The simulation predicts a relaxation of the effective temperatures towards a steady state after $\sim 100\,t_0$ and an effective decoupling between the $\mathbf{z}$ and $\mathbf{x}$ direction. The $\mathbf{y}$ direction also appears to be decoupled from the strong axis $\mathbf{z}$, but reaches the same final effective temperature as the other weak axis $\mathbf{x}$. Complementary simulations of kicks along $\mathbf{y}$ or $\mathbf{z}$ confirm this behavior regardless of the kick orientation. The dynamics thus features a quasi-thermalization within the symmetry plane of the distribution.

Numerics also provide access to the time evolution of higher moments of the momentum distribution. For instance, figure 3.8 show that the first eight moments converge towards a steady value in about the same time after the same ideal momentum kick. The ensemble does seem to reach a stationary distribution, in which all measurable quantities are constant over time.

In the experiment, the momentum kick is not ideal and the shape of the excitation ramp must be taken into account in the numerics. Because of the eddy currents, the rising time of the magnetic field bias shifting the trap center is actually much longer than the current duration controlled by computer. Increasing the control duration actually results in increasing the *amplitude* of the displacement δ. The extinction of the bias is also governed by eddy currents, which set its decay time. To account for these effects, we consider excitations of constant duration τ and increasing displacement δ (see Fig. 3.9).

After an excitation characterized by a displacement δ and a duration τ, the relation between the imparted center-of-mass momentum and the effective heating in the steady state can be approximated by a quadratic fit $\Delta T_i/T = \alpha_i \eta^2$ (see Fig. 3.11). The α coefficients depend *a priori* on δ and τ; however, for short excitation times, their dependence over τ almost vanishes. Their remaining dependence on δ is depicted in figure 3.10 and is explained in the following section.

For kicks along $\mathbf{z}$, α_z does not vary significantly with the trap displacement for the experimentally relevant settings $\delta \gtrsim 1$, in which case $\alpha_z \simeq \alpha_0 = 0.5$. The value of τ essentially sets the strongest achievable kick η and we take $\tau = 0.6\,t_0$ in the simulation to cover the experimentally accessible range of excitations. The heating coefficient $\alpha_0 = 0.5$ is within error bars in

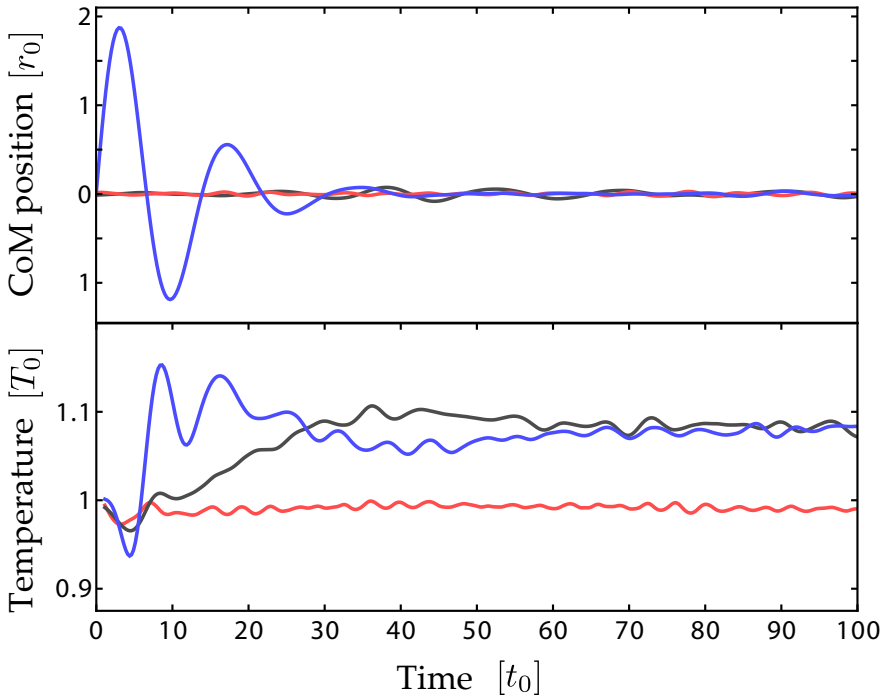

Figure 3.7: Time evolution the center-of-mass position (**above**) and of the distribution effective temperature (**below**) after a momentum kick $\mathbf{q} = q_0\,(1,0,0)$. Results from numerical simulation over 10^4 particles. Blue, grey and red lines correspond to the **x**, **y** and **z** directions respectively.
The motion is only along the kick direction **x**, but the spread of the momentum distribution affects both **x** and **y** directions. The strong axis **z** is almost unaffected by the initial excitation, showing at the end of the simulation a very slight cooling with respect to the initial distribution.

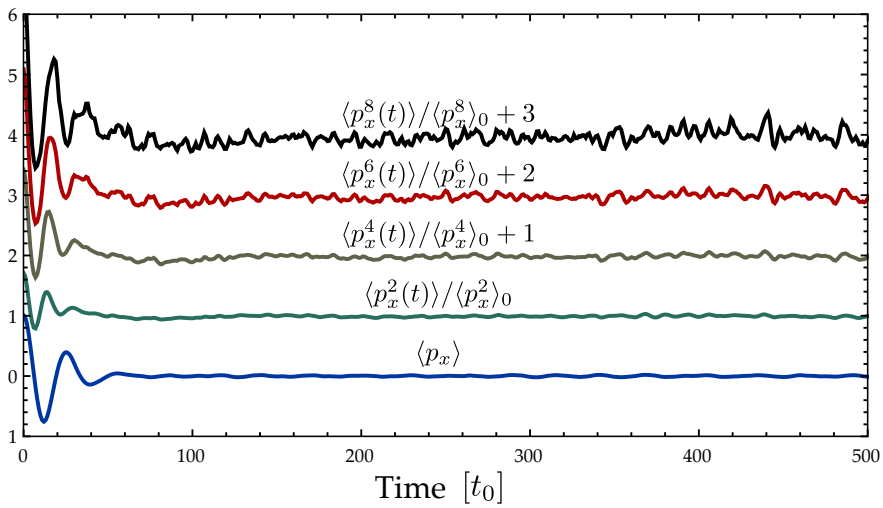

Figure 3.8: Relaxation of successive moments of the momentum distribution along **x** after an ideal kick $\mathbf{q} = q_0\,(1,0,0)$. 1st order (blue), 2nd (green), 4th order (grey), 6th order (red), 8th order (black). For clarity, results are renormalized by their stationary values ($\langle p_x^2\rangle_0 = 1.18$, $\langle p_x^4\rangle_0 = 4.17$, $\langle p_x^6\rangle_0 = 24.33$ and $\langle p_x^8\rangle_0 = 196.05$) and by the indicated offset.
All calculated moments converge to a steady value within a few hundred time units. Data points are calculated from the numerical simulation of 10^4 particles.

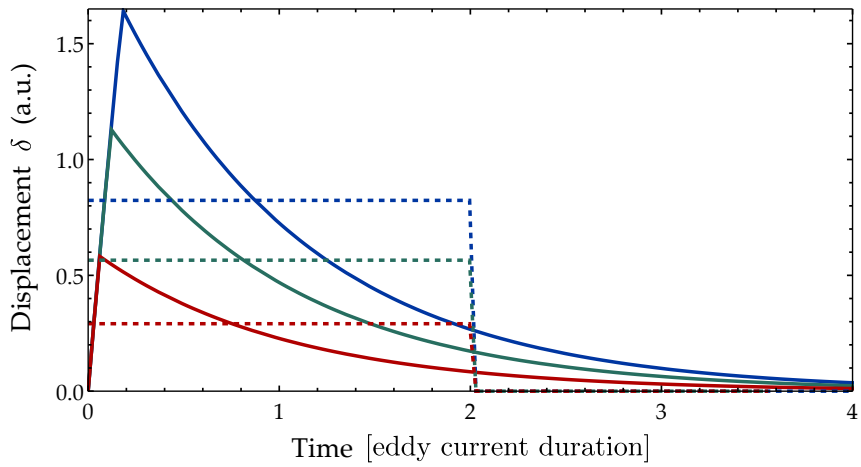

Figure 3.9: Excitation ramp. Solid lines show the time evolution of the displacement δ induced by the magnetic bias, the rise and fall duration of which is set by eddy currents. Increasing the control duration (from black to blue) actually increase the amplitude reached by the displacement δ. We approximate those kicks by step functions of constant duration τ and increasing amplitude, shown in dashed lines.

agreement with the experimental result $\alpha_z = 0.63(7)_{\text{stat}}(20)_{\text{syst}}$. The decoupling of the **x** direction appears more pronounced in the simulation $\Delta T_x/T_0 = -0.006\,\eta^2$ than in the experiment $\Delta T_x/T_0 = -0.14(5)_{\text{stat}}(8)_{\text{syst}} \times \eta^2$, a difference we attribute to imperfections of the magnetic excitation procedure.

For kicks along **x**, α_x strongly varies with the kick amplitude δ (blue points in Fig. 3.10) and therefore a quantitative comparison with the experiment requires a detailed knowledge of the shape of the transient excitation currents. This would require a complete modeling of all metallic parts in and around the experiment. Nevertheless, fitting the duration $\tau = 3t_0$ leads to $\Delta T_x/T_0 = 0.48 \times \eta^2$ (to be compared to $\Delta T_x/T_0 = 0.52(5)_{\text{stat}}(20)_{\text{syst}} \times \eta^2$) and $\Delta T_z/T_0 = -0.006 \times \eta^2$ (to be compared to $\Delta T_z/T_0 = 0.10(4)_{\text{stat}}(5)_{\text{syst}} \times \eta^2$). The chosen duration of $3\,t_0$ is consistent with the decay time of the eddy currents in our chamber (~ 3 ms).

3.4 A simple model for the effective heating

In this section, we present simple and robust arguments to account for the observed non-thermal distribution. Using energy conservation and virial theorem and two additional assumptions motivated by the previous observations, we calculate how the energy initially imparted onto the cloud is redistributed and converts into an effective heating. Within this model, we calculate analytically the expected relation between the kick strength η and the effective heating for different modes of excitation, first for the ideal kick, then for more realistic excitations.

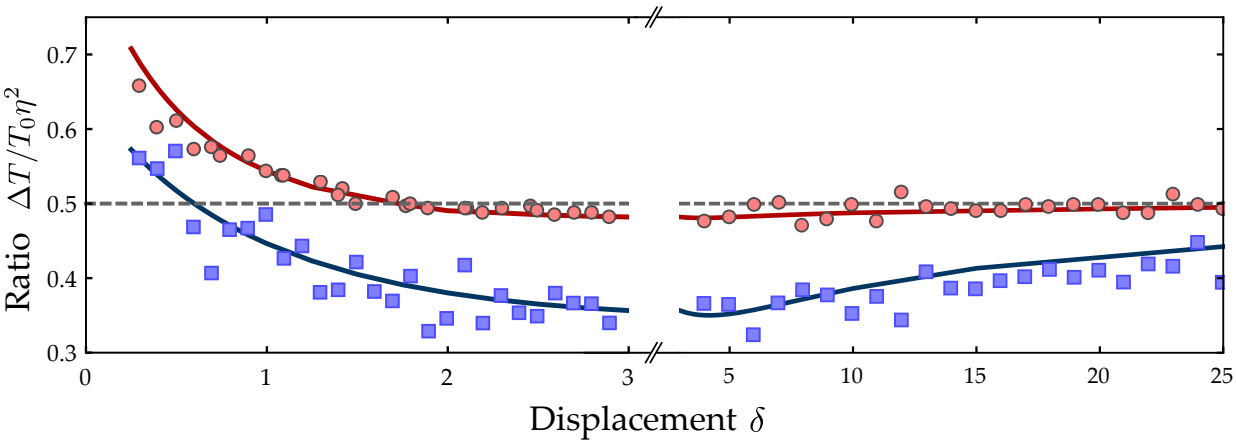

Figure 3.10: Heating coefficient α along the kick direction versus trap center displacement δ for kicks along **x** (blue) and **z** (red). α is defined as $\alpha = \Delta T/(T_0\eta^2)$, relating excess temperature to kick strength η (see text). For kicks along **z**, $\alpha_z \sim 0.5$ and is almost constant. On the contrary, for kicks along **x**, α_x shows a strong dependence on displacement δ. Solid lines are derived from equations (3.31)-(3.38) and (3.27a)-(3.27b). Filled symbols are results from numerical simulations.

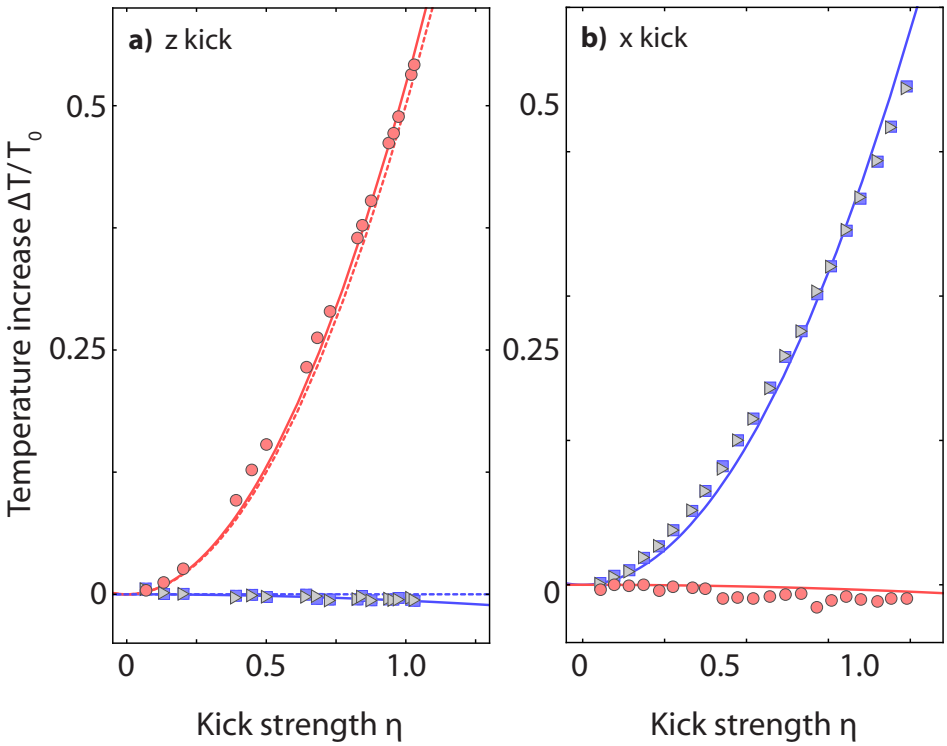

Figure 3.11: Numerical simulation of the temperature increase as a function of the normalized CoM momentum kick η. Data points are obtained by solving the classical equations of motion along **x** (blue squares), **y** (gray triangles) and **z** (red circles). In the simulation, kick duration is kept constant at $\tau = 0.6\,t_0$ for **z** and $\tau = 3\,t_0$ for **x**, with increasing values of displacement δ. The effective temperatures along **x** and **y** are equal and almost totally decoupled from **z**. Solid lines are the best quadratic fits to the data: $\Delta T_x/T_0 = \Delta T_y/T_0 = 0.48 \times \eta^2$ and $\Delta T_z/T_0 = -0.006 \times \eta^2$ for a kick along **x** and $\Delta T_x/T_0 = \Delta T_y/T_0 = -0.006\,\eta^2$, $\Delta T/T_0 = 0.52\,\eta^2$ for a kick along **z**. The dashed line in (a) is given by equation (3.41), assuming zero cross-thermalization between **z** and **x**.

3.4.1 General predictions

In our experiment, the energy transfer from the center-of-mass to the internal degrees of freedom of the atomic cloud does not rely on interactions between particles. The absence of collisions is also responsible for the non-thermal nature of the final distribution. Indeed, according to Thermodynamics' Second Law, Boltzmann's distribution maximizes the entropy of the system for a given energy. In our experiment, we start with a thermal cloud characterized by a total energy E and equilibrium entropy $S(E)$. The excitation delivers an additional energy ΔE per particle, but does so without increasing the system's entropy. The latter is also conserved throughout the ensuing evolution because the ensemble remains collisionless (see annex A.2). The final steady state thus exhibits a larger energy $E + \Delta E$ for the same entropy S, in contradiction to the usual growth of the entropy expected for a collisional system. The lack of full thermalization is then embodied by the anisotropic temperatures measured in the long time limit.

The energy transfer relies on the complexity of the single particle trajectories in phase-space, which originates from the non-harmonicity and non-separability of the underlying Hamiltonian (3.2). The same kind of behavior was reported in a Ioffe-Pritchard trap and leads to a decoupling between directions [Surkov *et al.* 1994]. A generalization of this result can be applied in our situation to describe the effective decoupling between the weak trapping plane (**x**, **y**) and the strong trapping axis **z**.

Even though the potential (3.4) has a simple form, the classical motion of confined particles is complex and quickly gives rise to chaotic behavior. For instance, by considering Poincaré sections of single particle trajectories, it was shown for instance that islands of stability appear for low energy excitations, and eventually vanish at higher energies [Bergeman *et al.* 1989]. The accurate dynamical description of the evolution towards a steady state is beyond the scope of this study.

It is nevertheless possible to reach predictive results by taking advantage of energy conservation and virial theorem[4], which states that in a steady distribution, the kinetic and potential energies are related by

$$2\langle T\rangle = \langle V\rangle\,, \tag{3.26}$$

where $\langle T\rangle = \langle p^2/2m\rangle$ is the kinetic energy stored in the distribution and $\langle V\rangle$ is its potential energy. These two conditions are nevertheless not sufficient to predict the final thermodynamic properties of the system. To calculate the final effective temperature of the cloud, we make two additional assumptions motivated by the result of the experiment and simulations:

(i) The symmetry axis **z** is almost completely decoupled from the symmetry plane (**x**, **y**).

(ii) Whatever the kick's orientation may be, the final temperatures along the **x**- and **y**-directions are equal by symmetry.

[4] A derivation of virial theorem is presented in annex A.3.2.

Under these conditions one finds for the final temperatures,

$$z-\text{kick}: \quad \Delta T_{\text{x}} = \Delta T_{\text{y}} \ll \Delta T_z \qquad \& \quad \Delta T_{\text{z}} \simeq \frac{2}{3k_B}\Delta E, \tag{3.27a}$$

$$x-\text{kick}: \quad \Delta T_{\text{x}} = \Delta T_{\text{y}} \simeq \tfrac{1}{3k_B}\Delta E \qquad \& \quad \Delta T_z \ll \Delta T_{x,y}, \tag{3.27b}$$

where ΔE is the total energy transferred to the cloud through the excitation.

These relations are confirmed by all of our numerical simulations. But, as mentioned before, it is not possible to measure ΔE directly to test the model against the experiment. It is thus necessary to relate the imparted energy to accessible parameters, such as the kick strength η. For an ideal kick, the additional energy $\Delta E = \eta^2 q_0^2/2m$ is straightforward to estimate and provides together with eq. (3.27) an accurate prediction in agreement with the numerical simulations.

3.4.2 In the experiment: direct kick of the cloud

In a more realistic situation, the relation between ΔE and η is more complicated to estimate. In this subsection, we calculate the energy and momentum gained by the atomic ensemble as the trap is shifted by a distance δ for a duration τ.

Kick strength The momentum gathered by the center-of-mass of the cloud during the excitation takes the form

$$\mathbf{q} = \int d\mathbf{r}d\mathbf{p}\, f(\mathbf{r},\mathbf{p};\,\tau)\,\mathbf{p} \tag{3.28a}$$

$$= \int d\mathbf{r}_0 d\mathbf{p}_0\, f_0(\mathbf{r}_0,\mathbf{p}_0)\,\mathbf{p}(\mathbf{r}_0,\mathbf{p}_0,\tau) \tag{3.28b}$$

Here, we used the Liouville theorem to express the conservation of volume in phase-space, $d\mathbf{r}d\mathbf{p}\, f(\mathbf{r},\mathbf{p};\,\tau) = d\mathbf{r}_0 d\mathbf{p}_0\, f_0(\mathbf{r}_0,\mathbf{p}_0)$, where $\mathbf{r}_0$ and $\mathbf{p}_0$ were the initial position and momentum of the particle at position $\mathbf{r}$ with momentum $\mathbf{p}$ at time τ and the initial distribution f_0 is given by eq. (3.5).

The momentum $\mathbf{p}(\tau)$ can be related to $\mathbf{p}_0$ using Newton's law in the displaced trap. We consider a series expansion up to the second order, which will be useful to estimate the imparted energy as well:

$$\mathbf{p}(\tau) = \mathbf{p}_0 + \tau\partial_t\mathbf{p} + \frac{1}{2}\tau^2\partial_t^2\mathbf{p} \tag{3.29}$$

$$= \mathbf{p}_0 + \tau\mathbf{F}_\delta + \frac{1}{2}\tau^2\left(\mathbf{p}_0.\boldsymbol{\nabla}_\mathbf{r}\right)\mathbf{F}_\delta \tag{3.30}$$

As the integration of the first term cancels by symmetry, the kick strength $\mathbf{q}$ can be written up to first order in τ:

$$\mathbf{q} = \tau\int d\mathbf{r}_0 d\mathbf{p}_0\, f_0(\mathbf{r}_0,\mathbf{p}_0)\,\mathbf{F}_\delta \tag{3.31}$$

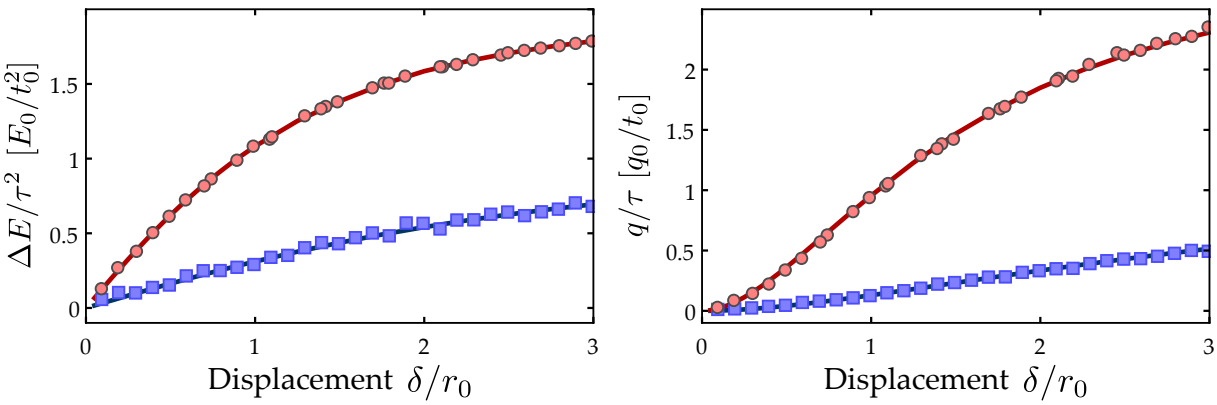

Figure 3.12: Energy increase ΔE (**left**) and momentum q (**right**) gained by the cloud after duration τ in a potential displaced by δ along the $\mathbf{x}$ direction (blue) or $\mathbf{z}$ direction (red). Axes are scaled in dimensionless units. Data points are coming from numerical simulations with 10^5 particles, solid lines are given by eq (3.38) and eq (3.31) respectively, without free parameter.

The numerical value of the integral (3.31) is plotted in figure 3.12 and shows very good agreement with the behavior observed in the simulations fort short excitation times τ.

Imparted energy During the excitation, the cloud acquires not only kinetic energy $\langle T \rangle$ as the center-of-mass falls towards the displaced trap center, but also potential energy $\langle V \rangle$, as the trap displacement reduces the cloud's confinement, enabling it to expand. To estimate the total energy given to the cloud, it is necessary to include both contributions.

Using the same strategy as before, the kinetic energy stored in the cloud at time τ can be expressed as

$$\langle T \rangle = \int d\mathbf{r}_0 d\mathbf{p}_0 \, f_0(\mathbf{r}_0, \mathbf{p}_0) \, \frac{p(\tau)^2}{2m}, \tag{3.32}$$

where the expression of $\mathbf{p}(\tau)$ is given by (3.30). Up to second order, the kinetic energy of the cloud takes the form

$$\langle T \rangle = E^0_{\text{kin}} + \frac{\tau^2}{2m} \int f_0 \, \left(F_\delta^2 + (\mathbf{p}_0.\boldsymbol{\nabla}_\mathbf{r}) \, (\mathbf{p}_0.\mathbf{F}_\delta) \right), \tag{3.33}$$

where the infinitesimal volume $d\mathbf{r}_0 d\mathbf{p}_0$ was omitted for clarity. To further simply this expression, we define $\mathcal{L}_0 = \mathbf{p}_0.\boldsymbol{\nabla}_\mathbf{r} + \mathbf{F}_0.\boldsymbol{\nabla}_\mathbf{p}$ that gives the evolution of the ensemble in the unperturbed trap and use the properties of the Liouville operator, $\int f_0 \, \mathcal{L}_0 \, [G] = 0$, obtaining:

$$\langle T \rangle = \langle T \rangle_0 + \frac{\tau^2}{2m} \int f_0 \, \mathbf{F}_\delta \, (\mathbf{F}_\delta - \mathbf{F}_0) \tag{3.34}$$

The potential energy of the cloud as the trap is brought back to its initial position can be calculated in the same way,

$$\langle V \rangle = \int d\mathbf{r}_0 d\mathbf{p}_0 \, f_0(\mathbf{r}_0, \mathbf{p}_0) \, f(\mathbf{r}, \mathbf{p}; \, \tau) \, V_0 \, (\mathbf{r}(t)) \, . \tag{3.35}$$

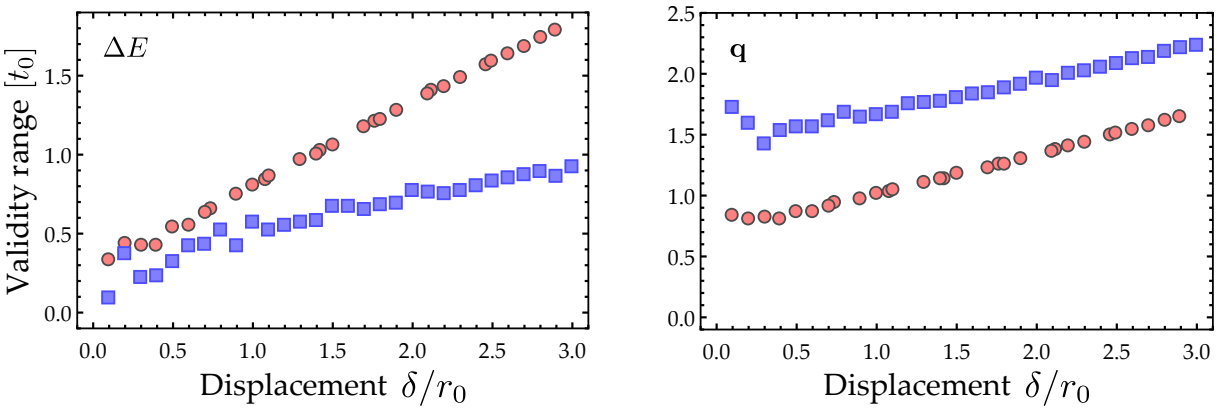

Figure 3.13: Validity range of the Taylor expansions in τ for ΔE (**left**) as given by (3.38) and q (**right**) as given by eq (3.31), as a function of the displacement δ along $\mathbf{x}$ (blue) or $\mathbf{z}$ (red). The validity range is estimated as the time after which the discrepancy between the Taylor expansion and the value estimated numerically over 10^5 particles exceeds 20%, as arbitrary threshold.

Expanding up to second order in τ

$$V_0\left(\mathbf{r}(t)\right) = V_0\left(\mathbf{r}_0 + \tau\frac{\mathbf{p}_0}{m} + \frac{1}{2m}\tau^2\mathbf{F}\right) \tag{3.36a}$$

$$= V_0\left(\mathbf{r}_0\right) + \frac{\tau}{m}\left(\mathbf{p}_0.\boldsymbol{\nabla}_\mathbf{r}\right)V_0 + \frac{1}{2m}\tau^2\left(\left(\mathbf{F}.\boldsymbol{\nabla}_\mathbf{r}\right) + \left(\mathbf{p}_0.\boldsymbol{\nabla}_\mathbf{r}\right)\left(\mathbf{p}_0.\boldsymbol{\nabla}_\mathbf{r}\right)\right)V_0 \tag{3.36b}$$

Employing the same techniques as before to take advantage of the symmetry of the integrals and the properties of the Liouville operator, we finally find:

$$\langle V\rangle = \langle V\rangle_0 + \frac{\tau^2}{2m}\int f_0\,\mathbf{F}_0\left(\mathbf{F}_0 - \mathbf{F}_\delta\right). \tag{3.37}$$

The total energy increase can therefore be written as

$$\Delta E = \frac{\tau^2}{2m}\int f_0\,\left(\mathbf{F}_0 - \mathbf{F}_\delta\right)^2. \tag{3.38}$$

The numerical value of the integral 3.38 is plotted in figure 3.12 and a very good agreements is found with the behavior observed in the simulations.

The ratio between the measured momentum (squared) and the energy increase that we want to estimate depends on the displacement δ. The numerical results has already been presented in figure 3.10 and are reproduced by eq.(3.38) and (3.31) without free parameters. For zero displacement, $\mathbf{F}_\delta = \mathbf{F}$ and, as expected, no energy is given to the cloud. For strong displacement

$\delta \gg r_0$, we can Taylor-expand the expression and obtain

$$z - \text{kick} : \Delta E = \frac{3}{2} q^2 = \frac{3}{2} E_0 \eta^2 \tag{3.39}$$

$$x - y - \text{kick} : \Delta E = \frac{3}{4} q^2 = \frac{3}{4} E_0 \eta^2 \tag{3.40}$$

As mentioned in the introduction of this section, the energy gain is in fact larger than the value $q^2/2$, because the cloud also expands during the excitation whereby it gains additional potential energy.

Inserting these asymptotic expressions in eq. (3.27), we finally obtain the relative temperature increase along the excitation direction

$$\frac{\Delta T}{T_0} = \frac{\eta^2}{2} = \alpha_0 \times \eta^2 \tag{3.41}$$

Remarkably, although the decoupling between degrees of freedom enhances the temperature increase along **z** for a given energy (eq. (3.27a), the stronger confinement reduces the amount of potential energy acquired during the kick in such way that all three directions show the same relation between temperature increase and momentum kick. The value $\alpha_0 = 0.5$ is in good agreement with the measurement performed experimentally.

The validity range of the previous Taylor expansions (3.31) and (3.38) with respect to τ depends on the value of the displacement δ and the direction of the kick. Figure 3.13 shows this validity range, estimated as the duration after which the discrepancy between the prediction of Taylor expansions and the value obtained in the simulation exceeds 20%.

Along **x**, the limiting factor is the validity of the Taylor expansion of ΔE, which appears to be an acceptable estimate only for duration τ shorter than t_0. For such shorts kick, the momentum acquired by the center of mass does not exceed q_0. As the momentum measured in the experiment can go up to $1.2\, q_0$, the Taylor expansions (3.31) and (3.38) do not apply to our results. The good agreement between the prediction (3.41) and our experimental findings shows that the validity range of the Taylor approximation is actually extended for the $\Delta E/\eta$ ratio.

Along **z**, the validity range of the approximation is limited to $\tau \sim t_0$ for most values of δ but this duration is long enough to allow kicks up to $q \sim 2q_0$, well above the values measured in the experiment. Consequently, the Taylor expansion can be relevant within experimentally accessible parameters and the prediction (3.41) can be applied, in good agreement with the measured value.

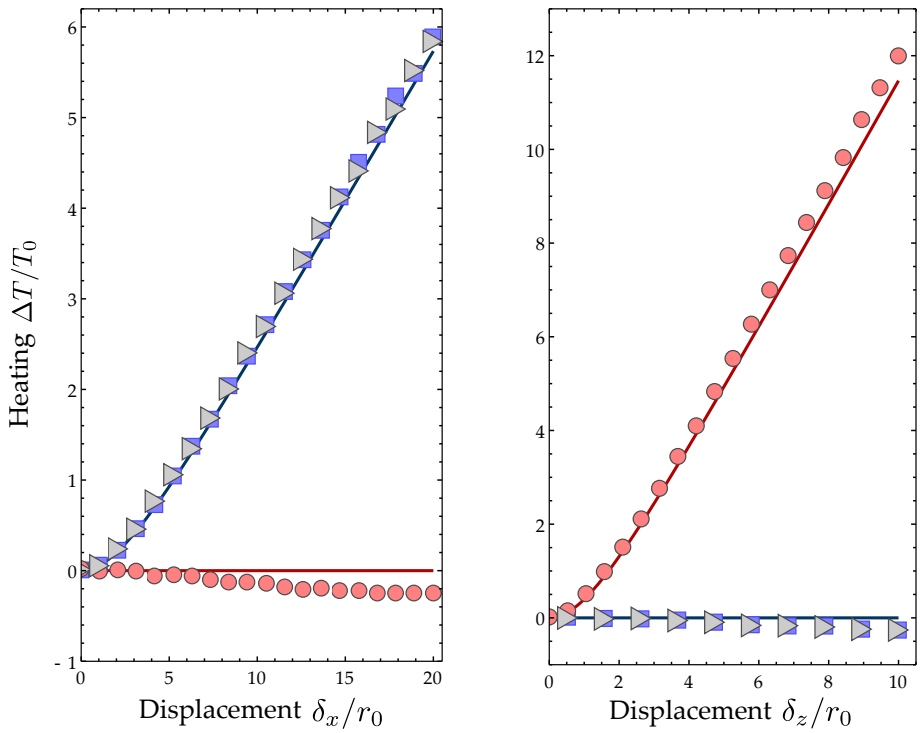

Figure 3.14: Heating after adiabatic displacement along x (left) and z (right). Results from numerical simulations over 10^4 particles. Solid lines are given by (3.44-3.43) and the energy redistribution (3.27), without any free parameter.

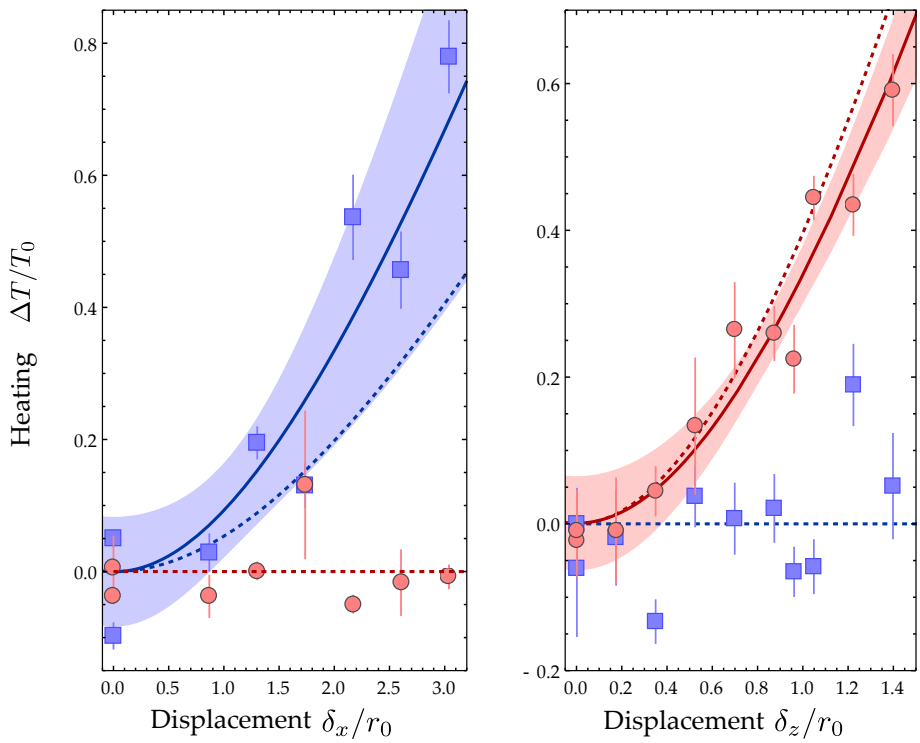

Figure 3.15: Heating along **x** (blue squares) and **z** (red circles) after adiabatic displacement along **x** (left) and **z** (right). Experimental results obtained in a trap of gradient $b = 80\,\mathrm{G/cm}$. The temperature is estimated by a time-of-flight measurement with 6 different durations. Each measurement is performed 10 times and the errors bars indicated the standard error of the fit procedure. The solid lines are fits by equations (3.44) and (3.43) respectively assuming the energy redistribution (3.27), with T_0 and b as free parameter. Dashed lines are obtained without free parameters. Shaded areas give the 95% confidence level of the fits.

3.4.3 Another excitation: adiabatic displacement

Another way to provide energy to the distribution is to displace the trap center by slowly raising up a magnetic field bias, so that the cloud can follow adiabatically the field zero. Once the trap has been displaced by a distance δ, the bias is abruptly switched off and the cloud is suddenly exposed to the initial potential. If the extinction is fast enough, no kinetic energy is given to the cloud during this process and it is possible to calculate analytically the potential energy of the ensemble:

$$\langle V \rangle = \int d\mathbf{r} d\mathbf{p}\, f_0(\mathbf{r}, \mathbf{p})\, V_0(\mathbf{r} - \delta) \tag{3.42}$$

The energy increase in then the simply the gain in potential energy:

$$z - \text{kick} : \Delta E = k_B T_0 \left(\frac{4 + (2\delta/r_0)^2 - e^{-(2\delta/r_0)}(4 + (2\delta/r_0))}{(2\delta/r_0)} - 1 \right) \tag{3.43}$$

$$x - y - \text{kick} : \Delta E = k_B T_0 \left(\frac{4 + (\delta/r_0)^2 - e^{-(\delta/r_0)}(4 + (\delta/r_0))}{(\delta/r_0)} - 1 \right) \tag{3.44}$$

Inserting (3.44) and (3.43) into (3.27), we can express the expected heating as a function of the displacement δ. The comparison with numerical simulations is shown in figure 3.14. Along $\mathbf{z}$, a slight unpredicted decrease of the effective temperature is observed in the numerics, but does not hinder the almost complete decoupling. Within the ($\mathbf{x}$,$\mathbf{y}$) plane, the analytical predictions are accurately verified by the numerical data.

Experimentally, this method has the advantage that the kick strength, simply given by the displacement δ, is easier to estimate. We keep a ^{40}K sample during the excitation, wait 200 ms, and remove it selectively just before releasing the offset bias, so the ^{6}Li ensemble starts from a thermal distribution. Measurements are performed in a magnetic gradient set to $b = 80\,\mathrm{G/cm}$.

Results are presented in figure 3.15; a fit was performed taking the initial temperature T_0 and the gradient b as free parameters. As expected, the heating along the unexcited direction is negligible compared to the heating of the excited direction. Along $\mathbf{x}$, the best fit is obtained for $T_0 = 367\,\mu\mathrm{K}$ and $b = 109\,\mathrm{G/cm}$. Along $\mathbf{z}$, with a gradient set to to the same value, the best fit is obtained for $T_0 = 340\,\mu\mathrm{K}$ and $b = 62\,\mathrm{G/cm}$. In both cases, the theoretical prediction without any free parameter is within the 95% confidence level of the fit.

This additional validation shows that the energy redistribution (3.27), which assume a quasi-thermalization within the weak trapping plane ($\mathbf{x}$,$\mathbf{y}$) and a complete decoupling with the strong axis $\mathbf{z}$ does not depend on the way the system is excited. A perfect momentum kick, a perfect position kick or the intermediate experimental regime are all compatible with the same redistribution of the imparted energy.

3.5 Quasi thermalization in an isotropic trap

The previous results (3.27) were obtained for an anisotropic trap $V_0 = \mu_B b\sqrt{x^2+y^2+4z^2}$, constrained by Maxwell equations. The effective decoupling between directions could be inherent to this specific geometry.

In this section, we study theoretically the quasi-thermalisation of non-interacting particles in an isotropic potential $V = \mu_B b\sqrt{x^2+y^2+z^2}$. We show that in such a 3D trap, the effective heating remains anisotropic as the kick orientation breaks the equivalence between all directions. Considering ideal kicks, we calculate analytically the expected heating to $\Delta T_\parallel = 7\Delta E/15$ along the kick direction, while the two transverse directions are heated by an amount $\Delta T_\perp = \Delta E/10$. Surprisingly, the result is different in a 2D isotropic potential, where the heating $\Delta T_{2\mathrm{D}} = \Delta E/3k_\mathrm{B}$ is isotropic.

3.5.1 Isotropic 2D potential

We first show that for non interacting massive particles in a two dimensional trap $V_{2\mathrm{D}} = \mu_B b\sqrt{x^2+z^2}$, the heating resulting from a momentum kick $\mathbf{q}$ is isotropic and converges towards the value $k_\mathrm{B}\Delta T_{2\mathrm{D}} = q^2/6m$ for both directions. To do so, we show that any trajectory in this 2D potential is fully characterized by two quantities, its energy E and angular momentum L_z. As a consequence, the distribution function must be isotropic. This result strongly relies on Bertrand's theorem (demonstrated in A.3.3), which states almost all but circular orbits are open. The isotropy of the heating, along with energy conservation, leads to the result.

Step 1 *Two trajectories with the same energy E and angular momentum L_z are arbitrarily close in phase-space, for almost all values of E and L_z.*

Consider two initial positions $(r_0, \theta_0, p_{r0}, L_z)$ and $(r'_0, \theta'_0, p'_{r0}, L_z)$ with the same momentum L_z and energy $E = p_r^2/2m + V(r) + L_z^2/2mr^2$. We want to show that the two trajectories starting from those two points will come arbitrarily close to one another.

Since L_z and E are constants of motion, $p_r(t)$ is immediately given by $r(t)$. We denote θ_1 the value at which the system, starting from $(r_0, \theta_0, p_{r0}, L_z)$, reaches its perihelion r_1 for the first time.

Starting from $(r'_0, \theta'_0, p'_{r0}, L_z)$, since $E' = E$, the trajectory will reach the same perihelion $r' = r_1$ with $p'_r = 0$. From one perihelion to the next one, the systems gathers a constant apside angle θ_A, which can be expressed in terms of L_z and E:

$$L_z = mr^2 d\theta/dt \tag{3.45a}$$

$$\Rightarrow \theta_A = 2\int_{\text{aphelion}}^{\text{perihelion}} \frac{L_z}{\sqrt{2m\left(H_0 - V(r') - \frac{L_z^2}{2mr'^2}\right)}r'^2}dr \tag{3.45b}$$

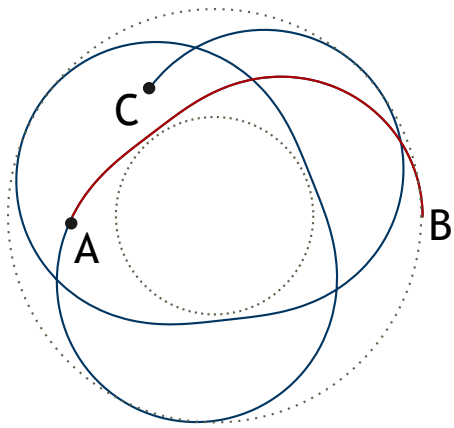

Figure 3.16: Trajectories in a linear potential. We first consider a trajectory starting at point $A = (r_0, \theta_0, p_{r0}, L_z)$. The first perihelion of this trajectory is B. We now consider a second trajectory, starting at point $C = (r'_0, \theta'_0, p'_{r0}, L_z)$ with the same energy and orbital momentum. We show that this second trajectory will come arbitrarily close to point B, meaning that the two trajectories are one and the same.

According to Bertrand's theorem, the only central potential where the apside angle is always commensurate with π are the Coulomb potential and the harmonic potential. For the linear potential considered here, the apside angle is therefore incommensurate with π, except for an ensemble of trajectories of measure zero. For all other trajectories, Poincaré's section for $\theta'[2\pi]$ is thus dense in $[0, 2\pi[$ and θ' will come to a value arbitrarily close to θ_1.

We have therefore proven that there is only one trajectory with a given (E, L_z).

Step 2 *The stationary distribution function $f(\mathbf{r}, \mathbf{p})$ only depends on the energy E and the angular momentum L_z.*

Consider a trajectory $(\mathbf{r}(t), \mathbf{p}(t))$ with $\dot{\mathbf{r}} = -\partial_{\mathbf{p}} H$ et $\dot{\mathbf{p}} = \partial_{\mathbf{r}} H$. According to Liouville's equation,

$$\frac{d}{dt} f(\mathbf{r}, \mathbf{p}) = \dot{\mathbf{r}} \partial_{\mathbf{r}} f + \dot{\mathbf{p}} \partial_{\mathbf{p}} f = -\partial_{\mathbf{p}} H . \partial_{\mathbf{r}} f + \partial_{\mathbf{r}} H . \partial_{\mathbf{p}} f = 0 \tag{3.46}$$

Therefore, for any two points $(\mathbf{r}_1, \mathbf{p}_1)$ and $(\mathbf{r}_2, \mathbf{p}_2)$ belonging to the same physical trajectory, $f(\mathbf{r}_1, \mathbf{p}_1) = f(\mathbf{r}_2, \mathbf{p}_2)$ holds.

According to the previous step, two points with the same energy and momentum have almost the same trajectory; by continuity, the distribution function can be expressed as a function of the energy and momentum only:

$$f(\mathbf{r}, \mathbf{p}) = g(E(\mathbf{r}, \mathbf{p}), L_z(\mathbf{r}, \mathbf{p})). \tag{3.47}$$

Step 3 *The heating is isotropic.*

After the kick, we assume that the system evolves towards a distribution f. As proven before, this distribution depends only on the energy and the angular momentum. In

polar coordinates (r, θ, p, φ), we can express the energy as per $E = \frac{p^2}{2m} + V(r)$ and angular momentum as $L_z = pr \sin(\theta - \varphi)$.

The momentum distribution is therefore given by:

$$n(p, \varphi) = \int d^2\mathbf{r}\, f(\mathbf{r}, \mathbf{p}) \tag{3.48a}$$

$$= \int r dr d\theta\, g\left(\frac{p^2}{2m} + V(r),\ pr \sin(\theta - \varphi)\right) \tag{3.48b}$$

$$= \int r dr d\theta'\, g\left(\frac{p^2}{2m} + V(r),\ pr \sin(\theta')\right) \tag{3.48c}$$

$n(\mathbf{p})$ is independent of the angle φ and therefore isotropic. The kinetic temperature, expressed as the standard deviation of $n(\mathbf{p})$, does not depend on the direction.

Step 4 *The energy redistribution leads to* $k_B \Delta T_{2D} = \Delta E/3$.

Using Virial theorem, we can relate the initial and final energies to the kinetic energies,

$$E = 3\langle T \rangle = 3\left(\langle T \rangle_x + \langle T \rangle_z\right). \tag{3.49}$$

We relate the kinetic energy to our definition of the effective temperature: $\langle T \rangle_x = k_B T_x/2$. Considering the isotropy of heating and energy conservation, we obtain the result

$$\Delta E = 3 k_B \Delta T_{2D}. \tag{3.50}$$

Equation (3.50) is tested against numerical simulation (see Fig. 3.18), showing very good agreement with an R-squared value above 0.997 without any free parameter.

3.5.2 Isotropic 3D potential

We show that, even in a fully isotropic 3D potential $V = \mu_B b \sqrt{x^2 + y^2 + z^2}$, the heating is anisotropic as the excited direction reaches a higher steady state temperature $k_B \Delta T_{\parallel} = 7\Delta E/15$ as the other two. Those two transverse directions receive a fraction of the input energy and reach the same final temperatures $k_B \Delta T_{\perp} = \Delta E/10$, thus showing a quasi-thermalization.

To calculate analytically the heating in an isotropic 3D linear trap, we use the property that, in a central potential, all trajectories remain planar. Within each plane, the 2D analysis of the previous paragraph can be applied. The global behavior is then obtained as the sum over all planes. The calculation presented below was performed by Jonathan Lau and Carlos Lobo.

Step 0 *Coordinate system.*

In order to take advantage of the planar nature of the trajectories, we first introduce an adequate coordinate system (see Fig. 3.17). Directions **u** and **v** are defined such that the

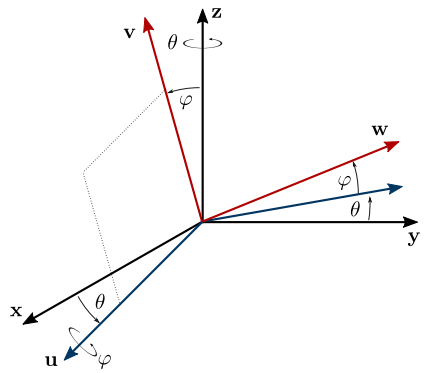

Figure 3.17: Introducing the coordinate system. We introduce the basis $(\mathbf{u}, \mathbf{v}, \mathbf{w})$, derived from the Cartesian coordinates with two rotations θ and φ such that the motion of the particle remains in the $(\mathbf{u}, \mathbf{v})$ plane.

plane they generate contains the relevant trajectory. Starting from the Cartesian coordinates $(\mathbf{x}, \mathbf{y}, \mathbf{z})$, we consider a rotation θ around the $\mathbf{x}$ direction, followed by a rotation φ around the $\mathbf{u}$ direction.

Within the $(\mathbf{u}, \mathbf{v})$ plane, we consider polar coordinates (r, α_r) for the position and (p, α_p) for the momentum. We can therefore express Cartesian coordinates as

$$x = r\cos\alpha_r \sin\varphi + r\sin\alpha_r \sin\theta\cos\varphi \tag{3.51a}$$

$$y = -r\cos\alpha_r \cos\varphi + r\sin\alpha_r \sin\theta\cos\varphi \tag{3.51b}$$

$$z = r\sin\alpha_r \cos\theta \tag{3.51c}$$

and resp. for $r \to p$ and $\alpha_r \to \alpha_p$.

The Jacobian of this transformation is therefore given by $|J| = r^2 p^2 \left|\sin\left(\alpha_r - \alpha_p\right)\cos\theta\right|$

Step 1 *Estimation of the energy contained in a plane (θ, φ) after a small kick q_z along z up to the second order.*

The initial distribution of the cloud is given by a Maxwell-Boltzmann distribution:

$$f\left(\mathbf{r}, \mathbf{p}, t = 0^-\right) = A\exp\left(-\frac{1}{k_\mathrm{B}T}\left(\frac{p^2}{2m} + \mu_B b r\right)\right). \tag{3.52}$$

where the constant A normalizes the distribution.

At $t = 0$, we perturb the ensemble by applying a sudden momentum kick q_z:

$$f\left(\mathbf{r}, \mathbf{p}, t = 0^+\right) = f\left(\mathbf{r},\ \mathbf{p} - q_z\mathbf{u_z},\ t = 0^-\right) \tag{3.53}$$

We calculate the kinetic and potential energies for the particles orbiting in a plane (θ, φ) right after the excitation. Using the aforementioned coordinates, we can express the dis-

tribution function as

$$f = A \exp\left(-\frac{q_z^2}{2mk_\mathrm{B}T} - \frac{\mu_B br}{k_B T} - \frac{p^2 - 2pq_z \cos\theta \sin\alpha_p}{2mk_B T}\right). \tag{3.54}$$

The potential and kinetic energies are given by

$$\langle V\rangle_{\text{plane}} = \int d\alpha_r d\alpha_p dp dr\, |J|\, \mu_B br\, f\left(r, \alpha_r, p, \alpha_p\right), \tag{3.55}$$

$$\langle T\rangle_{\text{plane}} = \int d\alpha_r d\alpha_p dp dr\, |J|\, \frac{p^2}{2m} f\left(r, \alpha_r, p, \alpha_p\right). \tag{3.56}$$

and their analytical forms can be expressed using the modified Bessel functions.

Even though the kinetic and potential energies evolve during the relaxation of the cloud, the total amount of energy imparted onto the plane, $\langle E\rangle_{\text{plane}} = \langle T\rangle_{\text{plane}} + \langle V\rangle_{\text{plane}}$, is conserved and can be calculated with the initial values obtained above.

For small enough kicks (ie $q_z \ll \sqrt{mk_\mathrm{B}T}$), we expand the expression initial energies $\langle T\rangle^0_{\text{plane}} + \langle V\rangle^0_{\text{plane}}$ up to the second order in q_z:

$$\langle E\rangle_{\text{plane}} = \frac{9|\cos\theta|}{4\pi} k_\mathrm{B}T + \frac{3|\cos\theta|}{32m\pi}\left(16\cos^2\theta + 3\cos(2\theta) - 9\right) q_z^2 + O(q_z^3). \tag{3.57}$$

Step 2 *Expression of the effective temperature within the orbital plane as a function the imparted energy.*

In the steady state, we can relate the energy of the plane to the spread of the momentum distribution using the virial theorem:

$$\langle T\rangle^\infty_{\text{plane}} = 2\langle V\rangle^\infty_{\text{plane}} \Rightarrow \langle E\rangle_{\text{plane}} = 3\langle T\rangle^\infty_{\text{plane}} = \frac{3}{2m}\left(\langle p_u^2\rangle + \langle p_v^2\rangle\right). \tag{3.58}$$

Step 3 *Expression of the effective temperature along each direction as a function of the energy imparted onto each orbital plane.*

We can relate the distributions along $(\mathbf{x}, \mathbf{y}, \mathbf{z})$ to their expressions along each plane:

$$\langle p_x^2\rangle = \langle p_u^2 \sin^2\varphi\rangle + \langle p_v^2 \sin^2\theta\cos^2\varphi\rangle + 2\langle p_u p_v \sin\theta\cos\varphi\sin\varphi\rangle \tag{3.59a}$$

$$\left\langle p_y^2\right\rangle = \langle p_u^2 \cos^2\varphi\rangle + \langle p_v^2 \sin^2\theta\sin^2\varphi\rangle - 2\langle p_u p_v \sin\theta\cos\varphi\sin\varphi\rangle \tag{3.59b}$$

$$\langle p_z^2\rangle = \langle p_v^2 \cos^2\theta\rangle \tag{3.59c}$$

Since the system is invariant under a rotation around the kick direction, the distribution is independant of φ and the cross terms vanish. Furthermore, as proven in the previous paragraph, the equilibrium momentum distribution is isotropic within a 2D isotropic plane and $\langle p_u^2\rangle = \langle p_v^2\rangle$. We can therefore define a non ambiguous temperature for the

	1D	2D isotropic	2D anisotropic	3D isotropic	3D exp. trap (**x**,**y**)	3D exp. trap (**z**)
$k_B\Delta T_x$	$2\Delta E/3$	$\Delta E/3$	$2\Delta E/3$	$7\Delta E/15$	$\Delta E/3$	0
$k_B\Delta T_z$	-	$\Delta E/3$	0	$\Delta E/10$	0	$2\Delta E/3$
$k_B\Delta T_y$	-	-	-	$\Delta E/10$	$\Delta E/3$	0

Table 3.1: Heating along each direction for different trap geometries. Results for the 1D, 2D and 3D isotropic traps are analytical calculations verified with numerical simulations (the 1D case can not be realized experimentally due to Majorana losses). Results for the 2D and 3D anisotropic traps assume complete decoupling between **x**, **y** and **z**.

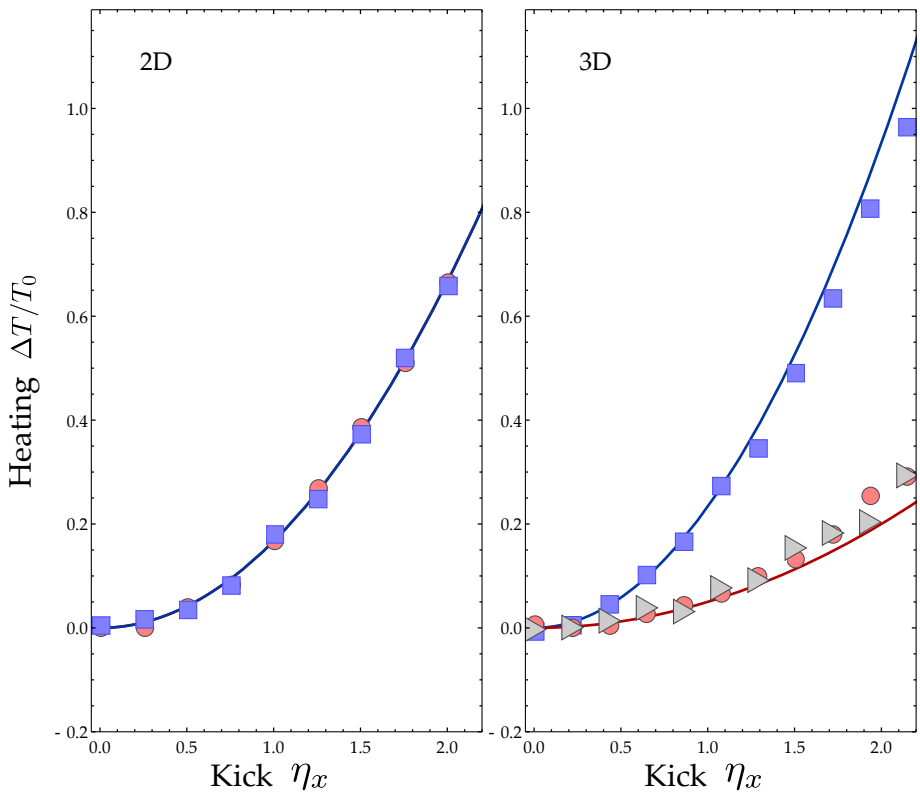

Figure 3.18: Heating as a function of the kick strength after an excitation along **x** in an isotropic 2D trap (left) and 3D trap (right). Temperatures are given along **x** (blue squares), **y** (gray triangles) and **z** (red circles). Points are obtain by numerical simulation over 10 000 particles. Solid lines are given by equations (3.50) and (3.62a-3.62b) with $\Delta E = q^2/2m$ without any free parameter.

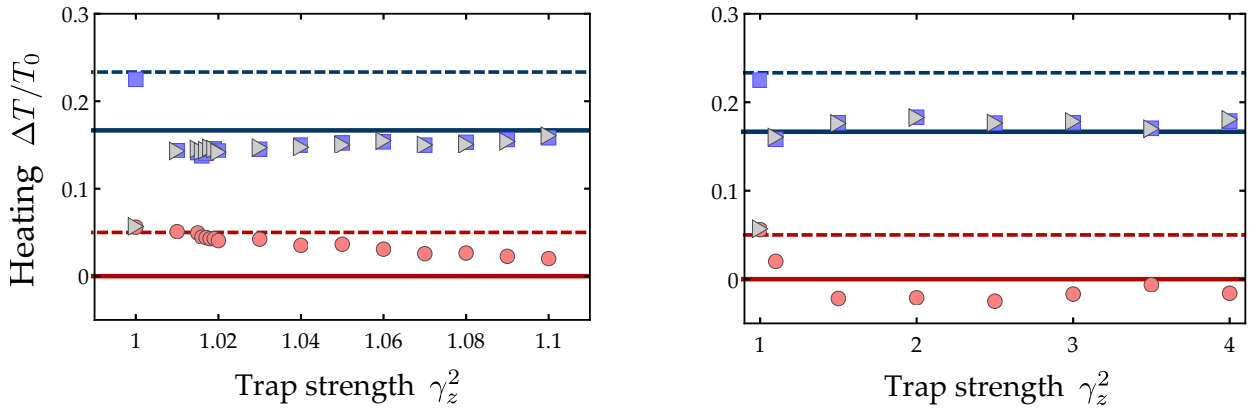

Figure 3.19: Heating after an excitation of amplitude ΔE along **x** in an anisotropic potential $V = \mu_B b\sqrt{x^2+y^2+\gamma_z^2 z^2}$, as a function of the anisotropy factor γ_z^2. Temperatures are given along **x** (blue squares), **y** (gray triangles) and **z** (red circles). Points are obtained by numerical simulation over 100 000 particles. Dashed lines show the prediction for an isotropic trap as derived in eq. (3.62). Solid lines are given by the previous model, assuming a complete decoupling between **z** and the other two directions. Note that the heating along **y** brutally jumps from its value in an isotropic trap $\Delta T_y/T_0 = \Delta E/10$ to a value close to a strongly anisotropic situation $\Delta T_y/T_0 = \Delta E/3$ as soon as $\gamma_z^2 \neq 1$.

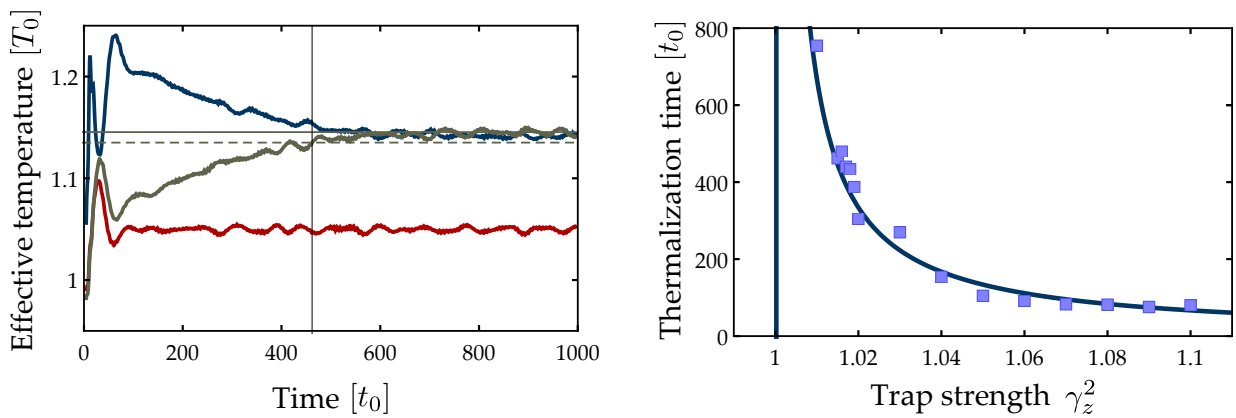

Figure 3.20: **Left**: the thermalization time is estimated as the duration after which the unexcited direction **y** reaches its final value $T_y = T_x$. **Right**: Thermalization time as a function of the anisotropy factor γ_z^2. The solid line given by the best hyperbolic fit $t = \frac{6.67}{\gamma_z^2-1}t_0$.

plane,

$$\frac{1}{m}\left\langle p^2\right\rangle_{\text{plane}} = \frac{1}{3}\left\langle E\right\rangle_{\text{plane}}. \tag{3.60}$$

The above expressions (3.59) can be therefore further simplified to:

$$k_{\text{B}}T_y = k_{\text{B}}T_x = \left\langle p_x^2\right\rangle = \frac{m\pi}{6}\int_0^{\pi} d\theta\ \left\langle E\right\rangle_{\text{plane}}\left(1+\sin^2\theta\right), \tag{3.61a}$$

$$k_{\text{B}}T_z = \left\langle p_z^2\right\rangle = \frac{m\pi}{3}\int_0^{\pi} d\theta\ \left\langle E\right\rangle_{\text{plane}}\cos^2\theta. \tag{3.61b}$$

Step 4 *Expression of the effective heating.* The expression of $\langle E\rangle_{\text{plane}}$ obtained before can be readily integrated to relate the heating in each direction to the kick initially applied to the atoms. Considering that the energy transferred to the cloud is $\Delta E = q_z^2/2m$, we can express the heating as a function of the kick's energy:

$$k_{\text{B}}T_y = k_{\text{B}}T_x = \Delta E/10, \tag{3.62a}$$

$$k_{\text{B}}T_z = 7\Delta E/15. \tag{3.62b}$$

Equations (3.62a-3.62b) are in very good agreement with numerical simulations, reaching R-squared values above 0.9 without any free parameter, as shown in figure 3.18.

Results obtained in this section are summarized in table 3.1. Remarkably, it appears that the expected heating remains *anisotropic* even in a 3D isotropic trap, but that this results strongly depends on the system dimensionality.

3.6 Influence of the trap anisotropy

We have shown that the energy redistribution for non-interacting particles in a strongly anisotropic trap $V = \mu_B b\sqrt{x^2+y^2+4z^2}$ is qualitatively different from the one in a isotropic trap $V = \mu_B b\sqrt{x^2+y^2+z^2}$. In the first case, the anisotropy is set by the trap while in the second, the symmetry breaking is induced by the excitation. In this section, we investigate numerically the intermediate regime as we vary the trap geometry by playing with a factor $\gamma_z > 1$:

$$V = \mu_B b\sqrt{x^2+y^2+\gamma_z^2 z^2}. \tag{3.63}$$

3.6.1 Anisotropy of the steady state

We first estimate the effective heating resulting from an initial excitation along $\mathbf{x}$ as a function of the trap geometry γ_z^2. Results are presented in figure 3.19 and show a very flat behavior: as soon as the trap shows the slightest anisotropy $\gamma_z^2 > 1$, the heating along $\mathbf{x}$ and $\mathbf{y}$ suddenly jump

from their isotropic value (3.62) to their fully decoupled value (3.27). Along **z**, the effective heating becomes continuously smaller as the confining potential becomes more anisotropic, reaching an almost complete decoupling as soon as $\gamma_z^2 > 1.1$

The energy redistribution thus weakly depends on the confinement geometry: in all anisotropic configurations, the symmetry plane is almost decoupled from the symmetry axis and presents a homogeneous heating. The situation observed in the previous chapter is thus not due to a peculiar geometry but illustrates a broadest kind of behavior.

3.6.2 Quasi-thermalization time

In an isotropic trap, if the steady-state towards which the distribution relaxes scarcely depends on the confinement geometry, the time it takes for the system to relax does.

We estimate the quasi-thermalization time τ as the time it takes for the unexcited direction **y** to reach 99% of its final value. Results are resented in figure 3.20. The more symmetric the trap, the longer the relaxation time, which diverges as the confinement becomes isotropic. A rational fit estimates the scaling law to $\tau \propto (\gamma_z^2 - 1)^{-1}$, with an R-squared value of 0.99.

The scaling can be interpreted in terms of precession period. It is well known that in a Newtonian field such as gravity, an anisotropy of the source distribution leads to precession of the orbital plane. Jonathan Lau extended the result to a quadrupole potential and showed that, in the $(\gamma_z^2 - 1) \ll 1$ limit, the precession rate of a single particle trajectory can be expressed as:

$$\dot{\phi} = -\frac{E\,L_z}{3L^3}(\gamma_z^2 - 1), \tag{3.64}$$

where **L** is the angular momentum of the particle. This scaling suggests that the equipartition of energy within the (**x**,**y**) plane is due to this precession mechanism. This qualitative picture explains the abrupt change in behavior for the **y** heating as well as the progressive evolution of the **z** heating for increasing values of γ_z. The slower the precession rate, the longer it takes for the dephasing to redistribute the energy along the two directions of the symmetry plane. For a small anisotropy, the energy redistribution is first dictated by the isotropic behavior, before the precession of orbital planes equilibrate temperatures along **x** and **y**. The heating along **z** thus remains close to its isotropic value, while the heating along **x** and **y** reach the average value between both directions. As γ_z increases, the dynamics changes qualitatively as the precession dispatches the energy faster and faster. For a large anisotropy, the imparted energy is first redistributed between within the symmetry plane, before other repartitions could take place.

3.7 Conclusions

In this chapter, we have shown that, even in the absence of interactions, a spin-polarized Lithium cloud in a quadrupole potential can relax towards steady state. We characterize this non-Boltzmann equilibrium by effective temperatures corresponding to the spread of the momentum distribution, an experimentally accessible parameter. If the cloud is perturbed by an initial excitation, the imparted energy is redistributed owing to the dephasing of single particle trajectories and results in an effective heating. The non-thermal nature of the steady state appears clearly as the final temperatures do not equilibrate between directions, but show a decoupling between the strong axis z and the symmetry plane (x,y). Yet, within the symmetry plane, the temperatures do equilibrate regardless of the initial excitation, showing a quasithermalization.

Assuming a complete decoupling, general considerations allow for quantitative predictions of the heating resulting from an initial excitation. Numerical simulations were performed and verified those results in various situations (ideal kick, experimental excitation, adiabatic displacement). Their application to experiments requires to estimate the imparted energy from measurable parameters, such as the center of mass momentum or position. This estimation depends on the actual description of the excitation and we propose two different schemes for which analytical predictions, numerical simulations and experimental results are in satisfying agreement.

We demonstrated analytically the value of the effective heating in an isotropic trap and show that the result strongly depends on the dimensionality of the system. In 2D, the temperature increase becomes isotropic regardless of the initial excitation while in 3D, the kick's direction provides a symmetry breaking. The isotropic geometry appears as a particular case, as the ensemble evolves towards an almost decoupled steady state as soon as the confinement is slightly anisotropic, with a relaxation time all the shorter as the anisotropy increases.

In the next chapter, we will show that the exact same behavior appears on an ensemble of non-interacting relativistic Weyl particles confined in a harmonic trap.

Chapter 4 Analog simulation of Weyl particles in a harmonic trap

Contents

4.1 Weyl particles: from high energy Physics to cold atoms **92**
4.1.1 A paradigm in high energy physics 92
4.1.2 Emergent low energy excitations 93
4.1.3 Weyl particles in a trapping potential: the Klein paradox 98
4.2 Analogue simulation of Weyl particles **99**
4.2.1 Canonical mapping 100
4.2.2 Majorana losses and Klein paradox 100
4.2.3 Quasi-thermalization in a harmonic trap 101
4.3 Geometric potentials **104**
4.3.1 Berry phase, scalar and vector potential 104
4.3.2 Effect of the geometric potentials 107
4.4 Conclusions and outlooks **109**

Massless Weyl particles constitute one of the paradigms of High Energy Physics and emerge in condensed matter systems in the form of low-energy excitations. Unlike massive particles, they possess a linear dispersion relation around the so called *Weyl point*. This linearity induces the conservation of helicity, i.e. the projection of the particle's spin onto the direction of its momentum, resulting among other things in remarkable transport properties. The behavior of Weyl particles in a trap is also highly non-intuitive, as they undergo anomalous tunneling which can lead to a decrease or cancellation of the back-scattering on a potential barrier, as depicted by the *Klein paradox*.

Those properties have brought an increasing interest in Weyl particles, even more so as they have also been suggested to represent possible platforms for quantum computation and quantum information processing. Using a canonical mapping, we show that some properties of non-interacting Weyl particles confined in a harmonic trap can be simulated and studied with cold atoms in a quadrupole potential. In absence of collisions, all the results presented in the previous chapter can therefore be applied to describe the evolution of out-of-equilibrium Weyl particles following an initial excitation. We show that, unlike massive particles which would oscillate without damping, a distribution of Weyl particles in a harmonic trap relaxes

towards a steady state, even in the absence of interactions and that the energy initially imparted onto the cloud is redistributed anisotropically. This analogy also allows us to translate specific properties of ultra-relativistic particles in the language of cold atoms, interpreting for instance the Klein paradox as a manifestation of Majorana losses.

In this chapter, we first review some properties of Weyl particles and recent developments in the field. We introduce the mapping that allows the analog simulation of harmonically trapped Weyl particles with cold atoms and adapt results from the previous chapter to describe the relaxation dynamics of a Weyl ensemble dragged away from the trap center. We then derive geometric potentials associated with the Berry phase of the system and study numerically the influence of the resulting topological properties on the previous dynamics. Finally, we show that our approach of analogue simulation can be used to study a much wider variety of problems, such as massive relativistic particles or particles with 2D spin-orbit coupling.

4.1 Weyl particles: from high energy Physics to cold atoms

Recents observations of Weyl particles in condensed matter systems [Huang *et al.* 2015, Lu *et al.* 2015, Xu *et al.* 2015b] have brought them under the limelights[1]. We start this chapter by reviewing the main properties of Weyl fermions that triggered the wide interest for this field of research.

4.1.1 A paradigm in high energy physics

Weyl fermions were first introduced in 1929 as massless solutions to the Dirac equation [Weyl 1929]

$$\left(i\hbar\gamma^{\mu}\partial_{\mu} - m\right)\Psi = 0 \tag{4.1}$$

where the Dirac matrices $\gamma^{0,1,2,3}$ are defined such that the Hamiltonian $H = \gamma^0\left(\gamma^i p_i + m\right)$ is hermitian and satisfies the relativistic equation $H^2 = m^2c^4 + p^2c^2$. Together with Majorana and Dirac fermions [Pal 2010], Weyl fermions provide a description of all possible spin 1/2 matter fields.

Two properties related to the spin of a particle serve as criteria to discriminate between solutions of the Dirac equation. The *helicity* corresponds to the projection of the spin $\mathbf{S}$ of a particle onto its momentum $\mathbf{p}$

$$h = 2\frac{\mathbf{S}.\mathbf{p}}{p}. \tag{4.2}$$

For a spin 1/2 particle, the eigenvalue of such an operator are $+1$, corresponding to "right-handed" particles and -1, corresponding to "left-handed" particles. The helicity operator commutes with the Dirac Hamiltonian (4.1), meaning that helicity is a conserved quantity for free

[1] And allowed all kinds of puns, as epitomized by the viewpoint "Where the Weyl Things Are" [Vishwanath 2015] or the commentary "It's been a Weyl coming" [Bernevig 2015]. Nature Physics editorial [Editorial 2015] summarized the situation: *"Like London buses, you wait for a Weyl then a few come along at once."*

particles. As a dot product, helicity is also obviously invariant under rotations, but not under Lorentz boosts. For an observer going faster than the particle, the orientation of the momentum is inverted and the helicity changes sign.

On the other hand, the *chirality* is defined by the effect of the $\gamma^5 = i\gamma^0\gamma^1\gamma^2\gamma^3$ matrix, which anti-commutes with all Dirac matrices. Two projectors $L, R = \frac{1}{2}\left(1 \mp \gamma^5\right)$ can be defined from this operator, leading to a partition of the Hilbert space as the sum of left-chiral and right-chiral solutions of the Dirac equation

$$\Psi = \Psi_L + \Psi_R, \tag{4.3}$$

with $\Psi_L = L\Psi$, $L\Psi_L = \Psi_L$ and $R\Psi_L = 0$, and equivalent relations can be written for Ψ_R. The chirality has opposite properties with respect to helicity: it is boost invariant, but is not conserved through the evolution of free particles because γ^5 anticommutes with the mass term $\gamma^0 m$.

In absence of rest mass, the helicity and chirality of Weyl fermions can be identified and constitute a well defined quantity, independent of the observer (as the velocity of massless particles is invariant under a Lorentz boost) and conserved through the time evolution (as γ^5 anti-commutes with all terms of the Hamiltonian). Left and right handed Weyl fermions appear as irreducible representations of the Lorentz group and, remarkably, any massive fermionic field (Majorana or Dirac) can be expressed as the direct sum of two massless Weyl fields with opposite helicities.

Weyl fermions appear as building blocks of particle physics, but had never been observed directly in that field. They were suggested at first to describe neutrinos, but the observation of flavour oscillations implying a non-zero rest mass ruled out this hypothesis.

4.1.2 Emergent low energy excitations

Even though Weyl fermions have no existence of their own in high energy physics, they appear as a relevant description of low energy excitations of electrons in crystalline structures with a linear dispersion relation around a so-called Weyl point. In both low and high energy physics, the Hamiltonian takes the form

$$H_{\text{Weyl}} = \hbar \sum_{i \in \{x,y,z\}} c_{ij} k_i \sigma_j = \hbar c\, \mathbf{k}.\boldsymbol{\sigma}, \tag{4.4}$$

where $\hbar$ is the reduced Planck constant, c has dimension of velocity, $\mathbf{k}$ is the momentum of the particle (relative to the Weyl point) and σ_i are Pauli matrices (in the basis of the bands involved). The latter equality corresponds to an isotropic dispersion relation. Because of this analogy and because of the very small overlap between the valence and conduction bands, condensed matter systems displaying such a dispersion relation are called *Weyl semi metals* [Nielsen and Ninomiya 1983, Young *et al.* 2012]. The corresponding dispersion relation is pictured in figure

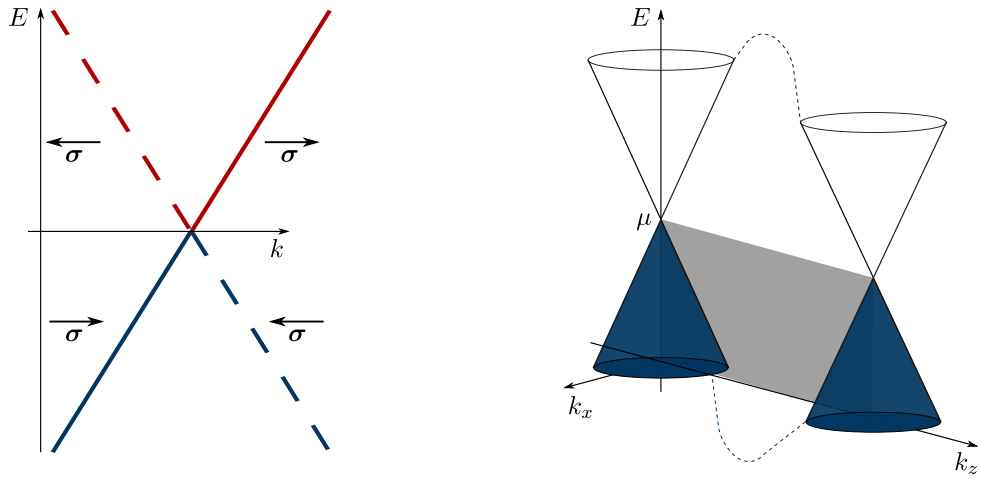

Figure 4.1: **Left**: one dimensional dispersion relation around a Weyl point described by (4.4), for spin σ oriented along $+\mathbf{x}$ (solid line) or along $-\mathbf{x}$ (dashed line). Particles with positive helicity (ie spin aligned with momentum) have positive energies (red) while particles with negative helicity have negative energies (blue). **Right**: filling of two Weyl points in momentum space. The distance between the nodes is set by the geometric properties of the material. The two bands connect far from the nodes, as indicated by the dashed lines. The grey plane represents the surface state resulting from the topological properties of the system (see main text), with energies in the gap between the nodes. Fermi arcs are the 1D Fermi surface of those states.

4.1.

Equation (4.4) reminds the low energy excitations emerging from 2D Dirac points in graphene [Geim and Novoselov 2007]. However, the difference of dimensionality leads to very distinctive properties[2]. A gap can easily be opened in a graphene Dirac cone by an orthogonal magnetic field, inducing an additional term $\mu B \sigma_z$, where μ is the magnetic moment of the particle. By contrast, all three Pauli matrices are involved in (4.4) and the Weyl cone is therefore protected against most perturbations [Turner and Vishwanath 2013].

The robustness of a Weyl point can be related to the existence of a topological quantity, the *chirality quantum number* [Hosur and Qi 2013], which is defined as

$$\chi = \mathrm{sign}[\det(c_{ij})] = \pm 1. \tag{4.5}$$

The chirality quantum number corresponds to the Chern number of the valence band: as an electron follows adiabatically the eigenstates of the band $|u_{\mathbf{k}}\rangle$, it experiences the equivalent of an effective vector potential $\mathbf{A} = i\langle u_{\mathbf{k}}|\boldsymbol{\nabla}_{\mathbf{k}}|u_{\mathbf{k}}\rangle$, corresponding to a Berry connection in momentum space [Berry 1984]. After a round-trip, the resulting accumulated phase corresponds to an

[2]Dirac points can also be extended to 3D, where they describe the touching point of four bands. Just like Dirac fermions can be expressed as the direct sum of two Weyl fermions, a Dirac point can be seen as the overlap of two Weyl points with opposite chirality. The resulting Dirac point has no topological protection as additional 4×4 matrices can open a gap, but its robustness can nevertheless be increased by the crystalline symmetries.

effective magnetic flux of

$$\iint d^2\mathbf{k}.\mathbf{A} = \oint_{FS} d\mathbf{k}\,\mathbf{F}(\mathbf{k}).d\mathbf{S}(\mathbf{k}) = 2\pi\chi, \tag{4.6}$$

where the integral can be carried over any Fermi surface enclosing the Weyl node and $\mathbf{F}(\mathbf{k}) = \boldsymbol{\nabla}_{\mathbf{k}} \times \mathbf{A}$ is analogous to a Berry curvature. Equation (4.6) corresponds to the flux that would induce a single magnetic charge, which is why Weyl points are sometimes treated as magnetic monopoles in the momentum space. We will show in section 4.3 that this properties remains true for trapped Weyl particles.

In between two separated Weyl points, each 2D slice in momentum space can be thought as a topological insulator with a gap depending on the distance to the nodes. In finite size samples, this results in the existence of edge states whose energies belong to the gap between the nodes (see Fig. 4.1). Those edge states give rise to a characteristic feature of Weyl semimetals, as their filling up to the chemical potential corresponds to a 1D Fermi surface called *Fermi arc*. Using angle resolved photo-emission spectroscopy [Behrends *et al.* 2015], such Fermi arcs were recently observed in TaAs [Xu *et al.* 2015a], Na_3Bi [Xu *et al.* 2015b] as well as in photonic crystals [Lu *et al.* 2015].

The previous discussion shows that every Weyl point has a fixed chirality and radiates a Chern flux. This topological property leads to a phenomenon specific to 3D systems: the Adler-Bell-Jackiw chiral anomaly [Adler 1969, Bell and Jackiw 1969], which corresponds to the non-conservation of electric charge. For particles with unit charge e and chirality χ described by (4.4), an electric $\mathbf{E}$ and magnetic $\mathbf{B}$ fields induce an electromagnetic current $\mathbf{j}_\chi$ such that

$$\partial_t n_\chi + \mathrm{div}(\mathbf{j}_\chi) = -\chi \frac{e^3}{32\pi^2\hbar^2}\mathbf{E}.\mathbf{B}, \tag{4.7}$$

where n_χ is the density of particles with chirality χ. The apparent paradox is solved by considering that, since the total Chern number over all bands should be zero, Weyl points necessarily exist as pairs with opposite chirality [Nielsen and Ninomiya 1981] and the total current $j_+ + j_-$ is well conserved as charges are pumped from one point to the other (see Fig. 4.2).

The chiral anomaly 4.7 also induces remarkable transport properties [Burkov 2015], such as

- Negative magneto-resistance

  One of the first signatures of the chiral anomaly was suggested in the form of a negative magneto resistance [Nielsen and Ninomiya 1983]. If the temperature and chemical potential are small enough for the positive Landau levels ($n > 0$ in Fig. 4.2) not to be populated, collisions between particles with the same chirality are suppressed due to lack of available phase-space. In absence of impurities in a clean sample, the charge imbalance can only be relaxed through collisions of particles close two different Weyl points. As Weyl points are well separated in momentum space, such processes require strong momentum

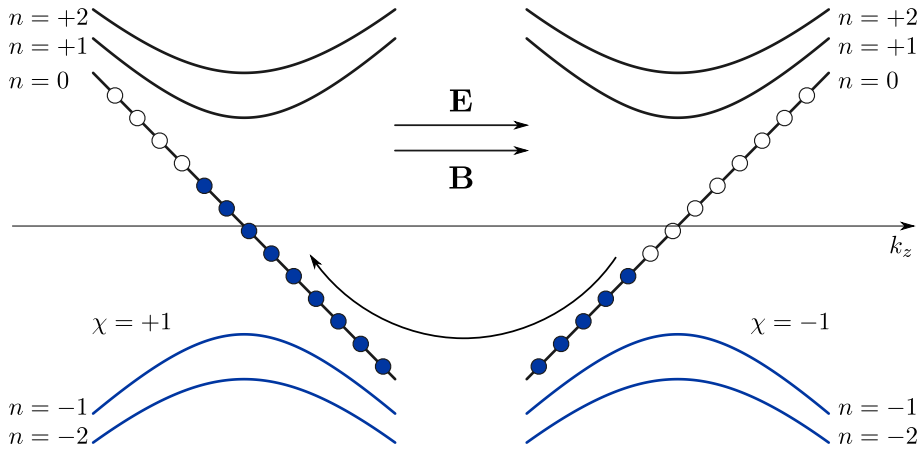

Figure 4.2: Landau levels of a Weyl particle. In an external magnetic field $B\mathbf{u}_z$, the energy spectrum of a charged particle in (4.4) is given for $n \neq 0$ by $E_n = \text{sign}(n)c\sqrt{2\hbar|n|eB + (\hbar k_z)^2}$, where k_z is the momentum from the Weyl node along the direction of the magnetic field. The zeroth Landau levels $n = 0$ are highly degenerate (with a factor $SeB/\hbar$, S being the sample area) and provide one dimensional chiral levels with different energies for right chiral nodes ($E_0 = +\hbar c k_z$) and left chiral nodes ($E_0 = -\hbar c k_z$). The occupancy of the zeroth Landau levels is pictured with filled symbols.
An intuitive picture recovers the expression (4.7) of the chiral anomaly [Hosur and Qi 2013]. In presence of a magnetic field $\mathbf{B}$, the zeroth Landau levels can be pictured as conducting wires parallel to the magnetic field. An external electric field $\mathbf{E}$ sets particles in motion through those wires. Because the zeroth Landau Level is chiral, the slope of the relation dispersion is fixed for each Weyl nodes. Particles are pumped from one node to the other, resulting in a apparent non-conservation of the charge for each node taken separately.

transfer and the corresponding relaxation time can be long, improving the conductivity of the electron gas. Furthermore, the degeneracy of the Landau levels contributing to the current is proportional to the magnetic field's strength. Those two effects lead to a decrease of the resistance in the direction of an applied magnetic field, proportional to the field strength, as opposed to the response of an ordinary metal or semiconductor that shows a weak, positive magneto-resistance independent of the external field orientation.

Observations of such negative magneto-resistance was reported, for instance in $Bi_{0.97}Sb_{0.03}$ [Kim *et al.* 2013], HgMnTe [Orlita *et al.* 2014] and TaAs [Huang *et al.* 2015]. Most of these experiments were performed in a semi-classical regime, without Landau-level quantization, where intra-node collisions dominate over other relaxation processes. In such cases, the negative magneto-resistance effect still remains but scales with the square of the magnetic field [Son and Spivak 2013].

- Anomalous Hall effect

As mentioned before (eq. (4.6)), each 2D slice between the Weyl nodes in momentum space can be thought of as topological insulators with unit Chern number. As a result, charged particles in presence of an electric field give rise to a current $\mathbf{J} = \mathbf{E} \times \mathbf{G}_h$ orthog-

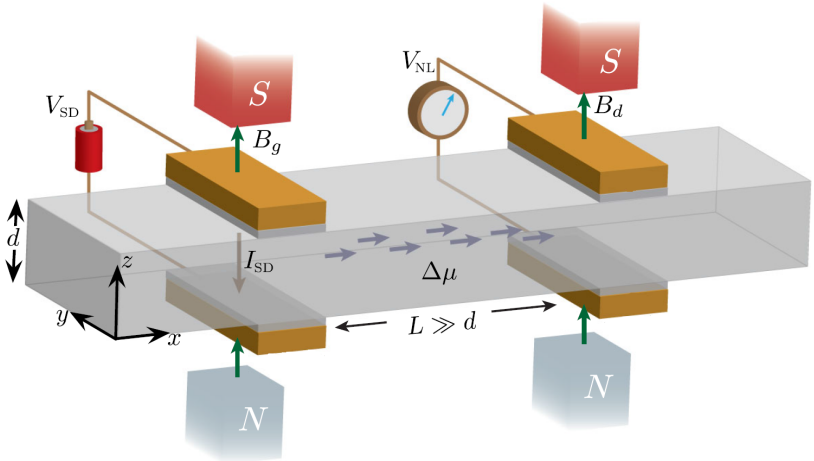

Figure 4.3: A possible setup to probe the existence of a non-local transport. A voltage V_{SD} is applied at one end of the sample. At a distance L much larger than the typical range of the induced current (set by the sample thickness d), the presence of a persistent voltage V_{NL} advertises the existence of a chiral anomaly, which prevents the relaxation of carriers' populations. Illustration from [Parameswaran *et al.* 2014], where a measurement of this non-ohmic voltage is suggested by taking advantage of an external magnetic field.

onal to the field. The Hall conductivity $\mathbf{G}_h$ can be expressed as:

$$\mathbf{G}_H = \frac{e^2}{2\pi\hbar}\sum_i \chi_i \mathbf{k}_i, \tag{4.8}$$

where the sum is taken over the Weyl points, χ_i is the chirality of the node and $\mathbf{k}_i$ its position in momentum space [Burkov 2014]. This conductivity is not proportional to an external magnetic field and does not depend on impurities, but relies only on the intrinsic properties of the material (namely the distance between Weyl nodes), hence the name intrinsic anomalous Hall effect (AHE) [Nagaosa *et al.* 2010].

- Non-local transport

  Another spectacular behavior related to the chiral anomaly takes the form of non-local transport properties, as a persistent voltage can be measured much further from the electrodes than the standard Ohmic range.

  Consider a rectangular piece of ordinary metal with four contacts attached as in figure 4.3. Two of those contacts are used as source and drain for an electric current J. The voltage applied between those points quickly drops away from the contacts, with a typical distance given by the mean free path, limited by the width d of the sample.

  In a Weyl semimetal in presence of a local magnetic field, the chiral anomaly gives rise to an imbalance between the occupation of the two Weyl nodes. As mentioned above, the relaxation of the imbalance is limited by internode scattering and the corresponding mean free path can be much larger than sample width. At distances $L \gg d$, the valley

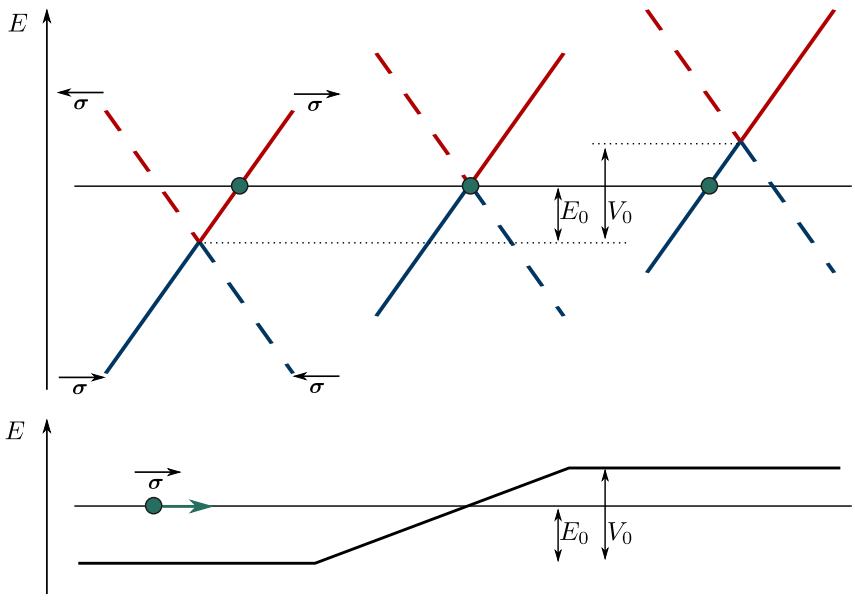

Figure 4.4: Illustration of the Klein paradox. As a Weyl particle arrives on a potential barrier, it can access the lowest branch of the dispersion relation. The spin of the particle is conserved as the potential commutes with it (the particle remains on a solid line) and the potential thus scatters a particle of positive momentum to a negative momentum state. The direction of motion, given by $\partial_{\mathbf{p}} H$, is preserved and the particle keeps moving forward, tunneling through the barrier.

imbalance remains and could be measured with a local probe magnetic field, whereas the Ohmic voltage has vanished [Parameswaran *et al.* 2014].

4.1.3 Weyl particles in a trapping potential: the Klein paradox

Around Weyl- or Dirac points, the linearity of the dispersion relation makes the local density of carrier extremely sensitive to electric fields, and opens the way to the engineering of quantum devices by applying an external confinement. For instance, quantum dots using electrostatic gates could be realized in graphene strips, despite the high density of conduction electron $n_e \simeq 4 \times 10^{15}\,\mathrm{cm}^{-2}$ [Castro Neto *et al.* 2009]. Such quantum dots in semi metal are promising candidates for the realization of quantum dots solar cells, as their reduced gap allows for efficient multiexciton generation [Delerue and Allan 2011].

However, unlike massive particles described by the Schrodinger equation, relativistic-like particles have a peculiar ability to escape through potential barrier under certain conditions, rendering the realization of localized states challenging. This effect originates from the Klein paradox[3] [Klein 1929] and is pictured in figure 4.4. As a Weyl particle arrives at a potential barrier, it can access the lowest branch of the dispersion relation, where the kinetic energy decreases with momentum. As a result, the particle tunnels through barriers much higher than its energy, with perfect transmission for an infinitely high barrier. In the strictly one dimen-

[3]Historically, Klein paradox was introduced for massive particles facing barriers exceeding twice their rest mass.

sional case, such as carbon nano-tubes, the Klein paradox leads to a suppression of the back-scattering of relativistic electrons [Ando *et al.* 1998] and forbids their trapping. In the 2D case, Klein paradox can be extended to show that the quantum tunneling of a particle through a barrier possesses resonant incident angles, at which the barrier becomes transparent [Katsnelson *et al.* 2006]. Apart from these specific cases (1D and resonant angles at 2D), it is *a priori* possible to confine relativistic-like particles despite Klein paradox, for instance by applying a harmonic electric potential on a layer of graphene [Silvestrov and Efetov 2007].

4.2 Analogue simulation of Weyl particles

Predicted decades ago, the observation of Weyl points was reported only recently. A reason might be that the pairing of Weyl points with opposite chiralities makes the experimental realization of Weyl semimetals challenging. Indeed, in most materials, Weyl points are degenerate and the resulting Dirac semimetal does not feature the topological properties mentioned above. To lift the degeneracy and separate Weyl points in momentum space, time-reversal or inversion symmetry must be broken, strongly constraining the exploitable compounds.

Owing to their high degree of control and versatility, ultra-slow cold atoms offer a complementary route for the experimental study of ultra-fast relativistic Weyl particles. For instance, the simulation of Weyl particles has recently been proposed as a 3D extension of the 2D Harper Hamiltonian where inversion symmetry breaking, required to generate Weyl points, would be ensured by a site-dependent hopping phase [Dubček *et al.* 2015]. However, such a realization requires a very fine control of the artificial magnetic flux per plaquette, all the more so as the lattice is large: flux fluctuations above 1-2% would destroy the Weyl nodes in a $160\times160\times160$ lattice [Lepori *et al.* 2015]. Ions chains have also been proven able to mimic the behavior solutions of Dirac equation [Gerritsma *et al.* 2010], including Klein paradox [Gerritsma *et al.* 2011].

In this section, we propose an alternative approach: instead of reproducing the exact Hamiltonian (4.4), we show that non-interacting Weyl particles confined in a harmonic trap can be mapped onto Lithium atoms in a quadrupole potential. This mapping enables us to apply results presented in the previous chapter to predict the relaxation of Weyl particles which were dragged away from the trap center. We can also interpret properties of Weyl particles in terms of atomic physics, highlighting for instance the parallel between the Klein paradox and Majorana losses.

4.2.1 Canonical mapping

Let us first recall the Hamiltonian of a spin 1/2 particle with magnetic moment μ in a magnetic field, as introduced at the beginning of the previous chapter:

$$H_0\left(\mathbf{r},\mathbf{p}\right) = \frac{p^2}{2m} - \mu\,\boldsymbol{\sigma}.\mathbf{B_0}(\mathbf{r}), \tag{4.9}$$

where $\boldsymbol{\sigma}$ are the Pauli matrices. In a quadrupole trap, the magnetic field takes the form $\mathbf{B}(\mathbf{r}) = b(\gamma_x x,\, \gamma_y y,\, \gamma_z z)$, where z is the symmetry axis of the coils, b denotes the magnetic field gradient and Maxwell's equations imply $\gamma_x = \gamma_y = 1$, $\gamma_z = -2$.

Starting from the above Hamiltonian (4.9), we define $\mathbf{X}$ and $\mathbf{P}$ by a canonical mapping exchanging position and momentum:

$$X_i = \frac{cp_i}{\mu b\gamma_i}, \qquad P_i = -\frac{\mu b x_i \gamma_i}{c}, \tag{4.10}$$

with c being an arbitrary velocity scale. These new coordinates verify the commutation relation $[\mathbf{X},\mathbf{P}] = i\hbar$ and can be used to rewrite the previous Hamiltonian as:

$$H = c\,\boldsymbol{\sigma}.\mathbf{P} + \frac{1}{2}k_0\sum_i \gamma_i^2 X_i^2, \tag{4.11}$$

where $k_0 = \mu^2 b^2/mc^2$ (note that k_0 has the dimension of a spring constant, not of a wave vector). The first term corresponds to the kinetic energy $c\boldsymbol{\sigma}\cdot\mathbf{P}$ of a massless Weyl particle moving at velocity c while the second one is readily identified as an anisotropic harmonic potential, characterized by spring constants $k_i = \gamma_i^2\mu^2 b^2/mc^2$ along each direction i. Massless Weyl particles in a harmonic trap are thus equivalent to massive atoms in a magnetic field gradient. In the following, Weyl particles and massive atoms will be referred to using upper- and lower-case symbols respectively.

4.2.2 Majorana losses and Klein paradox

The single-particle trajectories of the Weyl particles or Lithium atoms can be obtained using Ehrenfest's theorem, applied to the Hamiltonians (4.11) and (4.9).

$$\dot{X}_i = c\sigma_i \tag{4.12}$$
$$\dot{P}_i = -k_0\gamma_i^2 X_i \tag{4.13}$$
$$\dot{\boldsymbol{\sigma}} = 2c\boldsymbol{\sigma}\times\mathbf{P}/\hbar. \tag{4.14}$$
$$\dot{p}_i = \mu b\gamma_i\sigma_i \tag{4.15}$$
$$\dot{x}_i = p_i/m \tag{4.16}$$
$$\dot{\boldsymbol{\sigma}} = 2\mu_B\boldsymbol{\sigma}\times\mathbf{B}(\mathbf{r})/\hbar. \tag{4.17}$$

Note that Eq. (4.12) through (4.17) are fully quantum, but since we work in the classical regime, we will only consider their mean values.

Equation (4.14) describes the precession of the Weyl particle's spin around the direction of its momentum **P** just like eq. (4.17) does for the well-known atomic spin precession around the local magnetic field. Those equations motivate a re-interpretation of Klein paradox in terms of Majorana losses, described in section 3.1.3. For both systems, as long as the rate of change of the particle's energy is small enough (i.e. much smaller than $2Pc/\hbar$ for Weyl particles and $2\mu_B B/\hbar$ for atoms), the spin follows adiabatically the local orientation of the momentum for Weyl particles and of the magnetic field for atoms, and its helicity is conserved throughout the trajectory.

The breakdown of this adiabatic following leads to spin flips and an helicity inversion, corresponding to a transfer to negative energy states which are expelled from the trap. This loss process corresponds to Majorana losses for magnetically trapped and Klein paradox for Weyl particles, which thus appear as two descriptions of the same phenomenon.

Just like the death radius d describes the distance below which the magnetic field is too weak for atoms with velocity v to follow adiabatically the local orientation of the field, we can define a *death momentum* P below which Weyl particles at distance D from the trap center are most likely to undergo helicity-flips. Following the same procedure as in section 3.1.3, or simply using the canonical mapping (4.10) introduced before, we express:

$$d_{\text{death}} \sim \sqrt{\frac{v\hbar}{\mu_B b}} \quad \rightarrow \quad P_{\text{death}} \sim \sqrt{\frac{\hbar}{c} k_0 D}. \tag{4.18}$$

For a confined ensemble at temperature T, the corresponding loss rate can be estimated to:

$$\Gamma_{\text{Majorana}} \simeq \frac{\hbar}{m}\left(\frac{\mu b}{k_B T}\right)^2 \quad \rightarrow \quad \Gamma_{\text{Klein}} \simeq \hbar k_0 \left(\frac{c}{k_B T}\right)^2. \tag{4.19}$$

Just like Majorana losses prevent the existence of a true thermodynamic equilibrium in a quadrupole trap, Klein paradox prevents the stable trapping of Weyl particles in external potentials. In one dimension, particles will necessarily move through regions where the adiabatic following breaks down, rendering their trapping impossible. In higher dimensions, some trajectories can avoid the death region and, for sufficiently high temperatures, Klein-Majorana losses can be neglected. In such conditions, particles of positive and negative helicities are described by the effective Hamiltonians:

$$H_\pm = \pm cP + \frac{1}{2}\sum_i k_i X_i^2. \tag{4.20}$$

4.2.3 Quasi-thermalization in a harmonic trap

In the previously described experiment, Lithium atoms are spin-polarized in the hyperfine state $|F = 3/2, m_F = 3/2\rangle$ and, strictly speaking, are not spin 1/2 particles. However, as long

as Majorana losses can be neglected, they are described by the same Hamiltonian as positive helicity Weyl particles in absence of Klein paradox (see equation (4.20)) and will consequently exhibit similar dynamics, with a magnetic moment $\mu = \mu_B$, where μ_B is the Bohr Magneton. The results presented in the previous chapter about Lithium atoms can therefore be generalized to predict the behavior of Weyl particles in a harmonic trap. To do so, we first explicit more carefully the equivalence between the two systems:

Trapping potential In the previous chapter, we studied the relaxation of collisionless Lithium atoms in a linear trap $V = \mu_B b\sqrt{x^2 + y^2 + \gamma_z^2 z^2}$ after being excited out of equilibrium. Those results can be transposed to predict the behavior of Weyl particles in a harmonic potential:

$$V = \frac{1}{2}k_0(x^2 + y^2 + \gamma_z^2 z^2). \tag{4.21}$$

Effective temperature For ^{6}Li atoms, we considered an effective kinetic temperature $k_B T_i = \langle p_i^2 \rangle / m$. Equivalently, we define an effective potential temperature for Weyl particles corresponding to the spread of the position distribution:

$$k_B T_i = k_i \langle X_i^2 \rangle. \tag{4.22}$$

Excitation For ^{6}Li atoms, we considered an ideal momentum kick, shifting the momentum distribution by an amount q_0. Equivalently, this corresponds to an ideal position kick $R_0 = \sqrt{k_B T / k_0}$, dragging the Weyl particles away from the trap center, releasing them and letting them oscillate in the harmonic potential.

In addition, we also treated ideal position kicks, shifting the position distribution by an amount δ, and a realistic description of the experimental sequence, during which the cloud acquires a momentum $\mathbf{q}$ while it evolves in a shifted potential for a duration τ. Equivalently, we consider for Weyl particles an ideal momentum kicks, changing the position of the Weyl point in momentum space, and an intermediate regime, as the Weyl distribution moves by an amount $\langle \mathbf{R} \rangle$ while evolving for a duration τ in a shifted Weyl node.

Kick strength For ^{6}Li atoms, we defined an experimentally accessible kick strength η, which could be used to estimate the energy imparted onto the cloud during the excitation. To transpose all previous results, we extend equation (3.19) to define a kick strength for Weyl fermions:

$$\eta = \sqrt{\frac{\sum_i k_i \langle R_i \rangle^2}{k_B T_0}} \tag{4.23}$$

We can now translate the conclusions of the previous chapter into predictions for harmonically trapped Weyl particles:

(i) After an initial excitation, the center of mass of a Weyl distribution does not oscillate endlessly, but stops after oscillations. This behavior contrasts strongly with the one of massive particles in the same potential, which would oscillate forever owing to Kohn theorem (see annex A.3.1). The damping results from the dephasing of single particle trajectories.

Noting that $\langle\sigma\rangle^2 = 1$, equation (4.12) shows that even in a harmonic trap, Weyl particles move at a constant velocity c, whereas classical massive particles would move with a constant oscillation frequency. As a result, massive particles would remain in phase with each other and their center of mass would keep oscillating, while the momentum distribution of a Weyl particles cloud spreads in such a way that the center of mass eventually comes to a halt. For Lithium atoms in a quadrupole trap, the dephasing and the resulting damping are due to the linearity of the potential energy; for Weyl particles, both effects are due to the linearity of the kinetic term.

(ii) The energy ΔE acquired during the excitation is redistributed, increasing internal energy of the Weyl-cloud and leading to a spread in position space. The steady-state distribution is non-thermal and the relaxation towards it can be interpreted in terms of effective heating. A partial quasi-thermalization takes place, as some of the directions can reach the same final temperature regardless of the kick's orientation. The relation between the imparted energy ΔE and the measurable kick strength η depends on the modality of the excitation.

(iii) The spread of the distribution depends on whether the trap is anisotropic and on the dimensionality of the system.

In a 3D isotropic confinement, the kick direction provides a symmetry breaking and the kicked direction reaches a higher temperature as the other two. The situation is completely different in 2D, where both axis reach the same temperature, regardless of the kicks orientation:

$$\Delta T_{\parallel}^{3D} = \frac{7}{15k_B}\Delta E \quad \& \quad \Delta T_{\perp}^{3D} = \frac{1}{10k_B}\Delta E. \tag{4.24}$$

$$\Delta T_{\parallel}^{2D} = \Delta T_{\perp}^{2D} = \frac{2}{3k_B}\Delta E. \tag{4.25}$$

As soon as the trap presents a slight anisotropy $\gamma_z > 1$, the directions of the symmetry plane reach the same final value and are decoupled from the symmetry axis. Taking into account energy conservation, virial theorm and assuming a complete decoupling, the corresponding effective heating ΔT can be related to the imparted energy ΔE by the relations:

$$z-\text{kick}: \quad \Delta T_{\mathrm{x}} = \Delta T_{\mathrm{y}} \ll \Delta T_z \qquad \& \quad \Delta T_{\mathrm{z}} \simeq \frac{2}{3k_B}\Delta E, \tag{4.26}$$

$$x-\text{kick}: \quad \Delta T_{\mathrm{x}} = \Delta T_{\mathrm{y}} \simeq \tfrac{1}{3k_B}\Delta E \qquad \& \quad \Delta T_z \ll \Delta T_{x,y}, \tag{4.27}$$

The relaxation time τ also depends on the anisotropy, and will be shorter if the trap is more anisotropic, with a scaling law expected to be:

$$\tau \propto (\gamma_z^2 - 1)^{-1}. \tag{4.28}$$

4.3 Geometric potentials

As we wrote the expression of the Hamiltonian (4.9) experienced by ^{6}Li in a magnetic gradient, or that of Weyl particles in a harmonic trap (4.21), we assumed that the spin would follow adiabatically the local direction of the field. However, this hypothesis induces additional effects that we have not taken into account so far [Berry 1984]. When the particle travels through the field, the adiabatic evolution of its internal state leads to geometric gauge potentials and the phase accumulated during the trip can be expressed as the sum of two contributions [Aharonov and Stern 1992]: a dynamical phase due to the energy of the particle and a geometrical phase due to its path. This additional term may lead to a higher degree of mixing of the effectively decoupled directions.

Indeed, magnetic quadrupoles have already been used to generate non trivial topological properties. For instance, by slowly lowering the magnetic center into an optically trapped condensate, it is possible to realize an effective magnetic monopole as the spins of the ensemble follow the direction of the field [Ray *et al.* 2014]. Berry phases have also been displayed in a similar system, the so-called time-averaged orbiting potential trap (*TOP-trap*) [Petrich *et al.* 1995], where the field's zero describes a circular orbit at a frequency smaller than the Larmor frequency (for the atoms to follow adiabatically the direction of the field) but larger than the oscillation frequency (so that the atomic motion is mostly dictated by the average value of the potential). It was shown in [Müller *et al.* 2000, Franzosi *et al.* 2004] that the equilibrium position of an atomic cloud confined in such a trap was slightly tilted depending on the sense of rotation of the zero. In the equivalent picture, the topological properties of Weyl particles could perhaps be put forward by a periodic displacement of the Weyl point in momentum space, which would result in a finite equilibrium momentum depending on the node path.

In this section, we estimate the Berry potentials of Weyl fermions in a harmonic potential and determine numerically their influence on the previously studied quasi-thermalization.

4.3.1 Berry phase, scalar and vector potential

A standard way to derive the expression of the geometric potentials consists in assuming the adiabatic following of the internal state of the system and to estimate the time evolution of the wavefunction [Sukumar and Brink 1997]. We follow a similar approach for the Hamiltonian of Weyl particles in a harmonic trap (4.21).

To simplify the calculations, we consider a set a variable ($Z' = \gamma_Z^{-1} Z$, $P'_Z = \gamma_Z P_Z$), such that the anisotropy is transferred to the kinetic term and the Hamiltonian takes the form:

$$H = \frac{1}{2} k_0 R'^2 + \boldsymbol{\sigma}.\mathbf{P}' c. \tag{4.29}$$

In momentum space, the local eigenstates are given by the direction of the momentum $\mathbf{P}$:

$$\boldsymbol{\sigma}.\mathbf{P}' c \left|\pm\right\rangle_{\mathbf{P}'} = \epsilon_\pm \left(\mathbf{P}'\right) \left|\pm\right\rangle_{\mathbf{P}'}, \tag{4.30}$$

where the eigenenergies are $\epsilon_\pm \left(\mathbf{P}'\right) = \pm P' c$. In order to refer to a fixed quantification direction, we define a unitary operator $\mathcal{R}(\mathbf{P})$ such that

$$\left|\pm\right\rangle_{\mathbf{P}} = \mathcal{R}(\mathbf{P}) \left|\pm\right\rangle. \tag{4.31}$$

Considering the position $\hat{\mathbf{R}} = i\hbar \boldsymbol{\nabla}_{\mathbf{P}}$ as an operator, we can write its transformed expression as:

$$\mathcal{R}^\dagger(\mathbf{P}) \hat{\mathbf{R}} \mathcal{R}(\mathbf{P}) = \hat{\mathbf{R}} + \hat{\mathbf{T}}(\mathbf{P}), \tag{4.32}$$

where the Hermitian matrix operator $\hat{\mathbf{T}}(\mathbf{P})$ is defined as:

$$\hat{\mathbf{T}}(\mathbf{P}) = i\hbar \mathcal{R}^\dagger(\mathbf{P}) \left(\boldsymbol{\nabla}_{\mathbf{P}} \mathcal{R}(\mathbf{P})\right). \tag{4.33}$$

Within this rotated frame, the transformed Hamiltonian takes the form:

$$H' = \mathcal{R}^\dagger(\mathbf{P}') H \mathcal{R}(\mathbf{P}') = \frac{1}{2} k_0 \left(\hat{\mathbf{R}}' + \hat{\mathbf{T}}(\mathbf{P}')\right)^2 + c\mathcal{R}^\dagger(\mathbf{P}') \left(\boldsymbol{\sigma}.\mathbf{P}'\right) \mathcal{R}(\mathbf{P}'), \tag{4.34}$$

As long as the energy difference between eigenstates is large enough to prevent non-adiabatic passage, the system remains polarized along the rotated quantification axis:

$$\left|\psi_+ (t)\right\rangle = \int d^3\mathbf{P}' \varphi_+ \left(\mathbf{P}', t\right) \left|\mathbf{P}'\right\rangle \otimes \left|+\right\rangle_{\mathbf{P}'}. \tag{4.35}$$

Using Schrödinger equation, we express the time evolution of the amplitude φ_+:

$$i\hbar \frac{\partial}{\partial_t} \varphi_+ =_{\mathbf{P}'} \left\langle + \right| H \varphi_+ \left| + \right\rangle_{\mathbf{P}'} \tag{4.36a}$$

$$= \left\langle + \right| H' \varphi_+ \left| + \right\rangle \tag{4.36b}$$

$$= \left[\frac{k_0}{2} \left(\mathbf{R}' - \mathbf{A}(\mathbf{P}')\right)^2 + \epsilon_+ + U(\mathbf{P}')\right] \varphi_+, \tag{4.36c}$$

where we introduced the Berry connection $\mathbf{A}(\mathbf{P})$, which behaves like a vector potential:

$$\mathbf{A}(\mathbf{P}) = -\left\langle + \right| \hat{\mathbf{T}}(\mathbf{P}) \left| + \right\rangle = -i\hbar \times {}_{\mathbf{P}}\left\langle + \right| \boldsymbol{\nabla}_{\mathbf{P}} \left| + \right\rangle_{\mathbf{P}}, \tag{4.37}$$

and a geometric scalar potential $U(\mathbf{P})$ defined as:

$$U(\mathbf{P}) = \frac{k_0}{2} \times \langle + | \hat{\mathbf{T}}(\mathbf{P})^2 - \mathbf{A}(\mathbf{P})^2 | + \rangle = \frac{\hbar^2 k_0}{2} \times |_{\mathbf{P}} \langle - | \boldsymbol{\nabla}_{\mathbf{P}} | + \rangle_{\mathbf{P}} |^2 . \tag{4.38}$$

The adiabatic following thus gives rise to two additional terms which must be taken into account when calculating the time evolution of the system. To obtain the explicit expression of the geometric forces and implement them in the numerical simulations, we decompose the local eingenstates $|\pm\rangle_{\mathbf{P}}$ onto the fixed direction $\mathbf{P_z}$:

$$|+\rangle_{\mathbf{P}} = \sqrt{\frac{1+P_Z}{2}} |+\rangle_{\mathbf{P_Z}} + \sqrt{\frac{1-P_Z}{2}} \frac{P_X + iP_Y}{\sqrt{P_X^2 + P_Y^2}} |-\rangle_{\mathbf{P_Z}} \tag{4.39a}$$

$$|-\rangle_{\mathbf{P}} = \sqrt{\frac{1-P_Z}{2}} \frac{P_X - iP_Y}{\sqrt{P_X^2 + P_Y^2}} |+\rangle_{\mathbf{P_Z}} + \sqrt{\frac{1+P_Z}{2}} |-\rangle_{\mathbf{P_Z}} . \tag{4.39b}$$

With those expression, we can compute the expression of the scalar potential and of the effective magnetic field corresponding to the Berry curvature $\mathbf{B}_A = \boldsymbol{\nabla}_{\mathbf{P}'} \times \mathbf{A}(\mathbf{P}')$:

$$U(\mathbf{P}) = \frac{\hbar^2 k_0}{2} \frac{(1+\gamma_Z^2)P_X^2 + (1+\gamma_Z^2)P_Y^2 + 2\gamma_Z^2 P_Z^2}{4(P_X^2 + P_Y^2 + \gamma_Z^2 P_Z^2)^2}, \tag{4.40a}$$

$$\mathbf{B}_A(\mathbf{P}) = \hbar \frac{\gamma_Z}{2} \frac{\mathbf{P}}{(P_X^2 + P_Y^2 + \gamma_Z^2 P_Z^2)^{3/2}}. \tag{4.40b}$$

Remarkably, the effective magnetic field takes the form of an electric field radiated by a single charge; as mentioned in the introduction of this chapter, Weyl points behave like magnetic monopoles in momentum space.

In order to simulate numerically the relaxation of an ensemble in presence of those additional terms, we first introduce dimensionless variables:

$$\mathbf{X} = X_0 \tilde{\mathbf{X}}, \quad \mathbf{P} = P_0 \tilde{\mathbf{P}}, \quad t = t_0 \tilde{t}, \tag{4.41}$$

$$X_0 = \sqrt{k_B T / k_0}, \quad P_0 = k_B T / c, \quad t_0 = \sqrt{k_B T / k_0 c^2}, \tag{4.42}$$

The time evolution of the mean values is given by Ehrenfest's theorem:

$$\frac{d}{d\tilde{t}} \tilde{P'}_i = -\tilde{X}'_i, \tag{4.43a}$$

$$\frac{d}{d\tilde{t}} \tilde{X}_i = \frac{\gamma_i \tilde{P}_i}{\sqrt{\sum \gamma_j^2 \tilde{P}_j^2}} + \frac{P_0^3}{\hbar_0^2 k_0} F_{U,i} + \frac{P_0^2}{k_0 X_0 \hbar_0} F_{A,i}, \tag{4.43b}$$

where $\mathbf{F}_U = -\boldsymbol{\nabla}_{\mathbf{P}'} U$ and $\mathbf{F_A} = k_0 \mathbf{X} \times (\boldsymbol{\nabla}_{\mathbf{P}'} \times \mathbf{A}(\mathbf{P}'))$. We introduced $h_0 = \sqrt{(k_B T)^3 / k_0 c^2}$ so as

to define a dimensionless Planck's constant:

$$\tilde{\hbar} = \frac{\hbar}{\hbar_0} = 0.002 \times \frac{b\,[\mathrm{G/cm}]}{(T\,[\mu\mathrm{K}])^{3/2}}, \tag{4.44}$$

where the numerical value is given for the equivalent Lithium system. At the temperature considered before, $\tilde{\hbar} = 0.0003$.

4.3.2 Effect of the geometric potentials

Starting from the same thermal distribution as before,

$$f_0(\mathbf{R}_0, \mathbf{P}_0) \propto \exp\left(-\frac{1}{k_B T}\left(\frac{k_0}{2}R_0^2 + c\sqrt{{P_x}^2 + {P_y}^2 + \gamma_z^2 {P_z}^2}\right)\right), \tag{4.45}$$

we now consider a time evolution dictated by (4.43). Even in the absence of kick, this initial distribution is not stationary because of the additional geometric terms. However, for dimensionless Planck's constants up to $\tilde{\hbar} = 1$, their influence is small enough for the effective heating to remain below 2% of the initial temperature, even after a hold time of 1000 time units. The absence of effect was observed both for isotropic and anisotropic confinements.

The manifestation of geometric terms appears more pronounced in the dynamical behavior of the ensemble. For instance, figure 4.5 (left) shows the dependence over $\tilde{\hbar}$ of the effective heating resulting from a ideal kick $\delta = R_0(1, 0, 0)$ within the symmetry plane of an anisotropic trap. For increasing values of $\tilde{\hbar}$, an additional coupling appears between directions[4]: the two effective temperatures of the symmetry plane continue to equilibrate, but at a lower value as the third direction gains a larger part of the imparted energy.

In the experimental conditions of this chapter and the previous one, the mixing due to geometric terms can legitimately be neglected. Nevertheless, we can push forward the investigation to see if we can find a configuration that highlights a signature of the Berry terms.

The enhanced heating along the symmetry axis seems to be an promising quantity to display the effect of the geometric potentials (see Fig. 4.5, right), all the more as it starts from almost zero background. However, a higher value of $\tilde{\hbar}$ also results in a higher Klein-Majorana loss rate, which can not be neglected anymore. To take those losses into account, we remove particles as soon as their trajectory brings them too close to the death momentum, i.e.

$${\tilde{P}_x}^2 + {\tilde{P}_y}^2 + \gamma_z^2 {\tilde{P}_z}^2 < \tilde{\hbar}\sqrt{\tilde{X}^2 + \tilde{Y}^2 + \tilde{Z}^2}. \tag{4.46}$$

The number of remaining particles as a function of time is shown in figure 4.6 (left). Remarkably, the losses saturate within few dozen of time units and the number remains almost con-

[4]This enhancement of the coupling is much weaker in an isotropic confinement, where the effect appears to be limited to less than few percent for $\tilde{\hbar} \leq 1$.

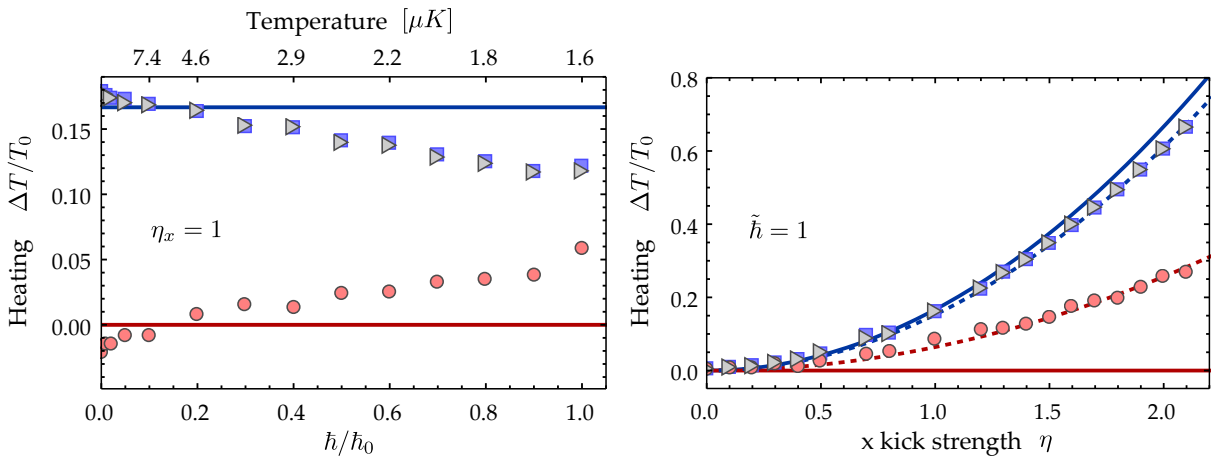

Figure 4.5: **Left**: Effective heating along **x** (blue squares), **y** (gray triangles) and **z** (red circles) as a function of $\tilde{\hbar} = \hbar/\hbar_0$. Temperatures corresponding to $\tilde{\hbar}$ for the equivalent ^{6}Li system is a magnetic quadrupole $b = 100$ G/cm are indicated above the graph. The heating is recorded at long times after an ideal kick $R_0 \times (1,0,0)$ in an anisotropic confinement ($\gamma_x^2 = \gamma_y^2 = 1$, $\gamma_z^2 = 4$). The solid lines are given by the previous predictions in absence of geometric potentials (4.26) and (4.27). The slight discrepancy for **z** close to $\tilde{\hbar} = 0$ was already observed in the previous chapter.
Right: Effective heating as a function of the kick strength η in the same trap, for $\tilde{\hbar} = 1$ (same color code). Solid lines are given by the previous predictions in absence of geometric potentials (4.26) and (4.27). Dashed lines are the best quadratic fits to the data. Within the symmetry plane (**x**,**y**), the behavior is scarcely affected ($\Delta T_x = \Delta T_y = 0.304 \times \Delta E$ instead of $\Delta E/3$) while the heating along **z** is significantly enhanced ($\Delta T_z = 0.1 \times \Delta E$ instead of ~ 0 in the absence of coupling).
Klein-Majorana losses are not taken into account here.

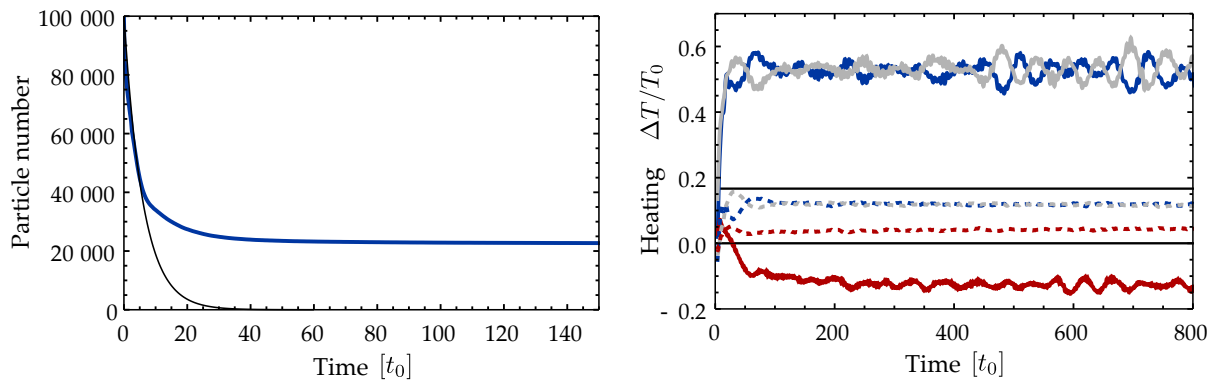

Figure 4.6: **Left**: Remaining atom number as a function of time, after a unit kick with $\tilde{\hbar} = 1$. Losses are defined by the passage through a death-circle in momentum space (4.46). The steady value is close to 22 500 particles and decreases by less than 2% between $t = 100\,t_0$ and $t = 1000\,t_0$. The initial decay, fit by an exponential (black line) corresponds to a rate of ~ 0.2 per time unit, within the order of magnitude expected by the Klein-Majorana loss rate (4.19).
Right: Effective heating as a function of time after a kick $R_0 \times (1,0,0)$ with $\tilde{\hbar} = 1$. Solid lines: taking into account Klein-Majorana losses. Dashed lines: without losses. Straight lines: previous predictions in absence of geometric potentials (4.26) and (4.27), for comparison. The effective heating resulting from the energy redistribution is overwhelmed by the modification of the distribution due to the losses.

stant up to 1000 t.u. The behavior is due to the absence of collisions: as trajectories are not redistributed, particles whose trajectories are subject to losses are quickly expelled while the other particles might never get even close to the death momentum, at least for small durations compared to a -possible- ergodicity period of the system.

The effective temperature of the remaining particles is presented in figure 4.6 (right) as a function of time. The Klein-Majorana losses have a strong impact on the effective heating, changing significantly the shape of the distribution at long times and completely overwhelming the previously mentioned signal.

The interplay between Berry phases and Klein-Majorana losses illustrates that both effects can be seen as two manifestations of the same underlying adiabatic hypothesis [Sukumar and Brink 1997]. In the basis set by the local eigenstates, the Berry potentials correspond to diagonal matrix elements of the operator (4.33), depicting the continuous following of the same state, while the Klein-Majorana losses are described by off-diagonal terms, resulting in the breakdown of the adiabatic following. While an optimal value for $\tilde{\hbar}$ can perhaps be found in our quadrupole-like configuration to observe a maximal influence of the Berry terms, this relation between topological properties and non-adiabatic following has a broader range and will be investigated in a future work.

4.4 Conclusions and outlooks

Using a canonical mapping, we showed that non-interacting Weyl particles in an anisotropic harmonic trap are equivalent to cold fermionic atoms such as ^{6}Li in a quadrupole potential. Taking benefit of this analogy, we could also interpreted the Klein paradox in terms of Majorana losses and concluded that Weyl particles could be trapped in 2D and 3D potentials at sufficiently high temperatures.

We derived the expression of the topological potentials and showed numerically that their effects were not significant at the previously considered temperatures. At lower temperatures however, they result in a coupling of the symmetry axis $\mathbf{z}$ with the symmetry plane ($\mathbf{x}$,$\mathbf{y}$), but their signal is hindered by the increased Klein-Majorana losses. The interplay between both effects highlights the underlying adiabatic hypothesis.

Extending the results obtained in the previous chapter, we showed that Weyl particles dragged away from the center of a harmonic would not oscillate like massive particles, but relax towards a non-thermal steady-state as the imparted energy leads to an anisotropic spread of the distribution. The long-time distribution remains anisotropic in a 3D isotropic trap, but becomes isotropic in 2D. However, the slightest symmetry breaking of the confinement leads to an strong decoupling between the symmetry axis and the symmetry plane.

The canonical mapping presented here is not limited to the simulation of Weyl fermions, but can address a broader range of problems, such as the dynamics of harmonically confined

massive relativistic particles. Indeed, in a Ioffe-Pritchard trap, a bias field gives rise to a non-zero magnetic field at the trap center and the overall field is of the form $B = \sqrt{B_0^2 + b^2 \sum_i \alpha_i^2 x_i^2}$. In this case, the analogue system would be described by the relativistic kinetic energy $E = \sqrt{m^2c^4 + p^2c^2}$ where the mass can be tuned as a function of B_0.

The very same mapping allows for the study of spin-orbit coupling [Koller *et al.* 2015]. In a hybrid trap consisting of the superposition of an optical dipole trap and a 2D magnetic quadrupole trap, the Hamiltonian takes the form

$$h = \frac{p^2}{2m} + \frac{m\omega^2}{2}(x^2 + y^2) + \frac{m\omega_z^2 z^2}{2} - \mu_\mathrm{B} b(\sigma_x x - \sigma_y y). \tag{4.47}$$

Applying our mapping to the variables (x, y, p_x, p_y) leads to the equivalent Hamiltonian

$$H = \frac{P^2}{2m} + \frac{m\omega^2}{2}(X^2 + Y^2) + \frac{m\omega_z^2 Z^2}{2} - \frac{\mu_\mathrm{B} b}{m\omega}(\sigma_x P_x + \sigma_y P_y), \tag{4.48}$$

which turns out to describe a 2D spin-orbit coupled particle. Finally, in the same trap, it is also possible to engineer a Rashba coupling by taking $X = p_y/m\omega$, $P_x = -m\omega y$, $Y = p_x/m\omega$, $P_y = -m\omega x$.

These results illustrate the powerful ability of Physics to take advantage of similarities between systems of very different natures to study a complicated problem with a handier experiment.

Chapter 5

Evaporative cooling to quantum degeneracy

Contents

5.1 Diagnostic tools in the science cell **112**
5.1.1 Spin selective measurements 112
5.1.2 Spin manipulation 117
5.1.3 Calibration of the apparatus 119
5.2 Principle of evaporative cooling **123**
5.3 Evaporative cooling of Potassium **127**
5.3.1 Magnetic RF-evaporation 127
5.3.2 Loading of the optical trap 128
5.3.3 Optical evaporation 129
5.4 Double evaporative cooling of ^{6}Li and ^{40}K **132**
5.4.1 ^{6}Li-^{40}K interactions 132
5.4.2 Magnetic RF-evaporation 133
5.4.3 Optical evaporation 134
5.5 Conclusions **136**

Laser cooling and sub-Doppler techniques opened the way to a significant decrease of the achievable temperatures, but most optical cooling strategies are limited to a phase-space density of $\sim 10^{-3}$, notably because of light induced collisions. An efficient way to overcome this difficulty and reach ultralow temperatures is the so called *evaporative cooling*, which was first proposed and applied to magnetically trapped hydrogen [Hess 1986, Hess *et al.* 1987], and soon successfully adapted to other alkali atoms [Petrich *et al.* 1995, Ketterle and Druten 1996].

The working principle of evaporative cooling is known to every one who tried to drink a hot beverage and cooled it by blowing on its surface. As a fraction of the particles is taken away (mostly particles with highest energies, capable of escaping the liquid phase), the distribution is out of equilibrium, but collisions soon redistribute the remaining energy and the ensemble relaxes towards a thermal state. The new equilibrium has a colder temperature than the previous one, all the more so as the thermalization required to pay the latent heat to restore a satisfying vapor pressure. In this way, the temperature can be decreased to extremely

low values as long as particles can be sacrificed, which already implies that a large initial atom number is crucial to reach quantum degeneracy.

This chapter is dedicated to the experimental realization of an ultracold gas of ^{40}K: 1.5×10^5 atoms in the $|9/2,-9/2\rangle$ state and as many in the $|9/2,-7/2\rangle$ state were cooled to $T = 62\,\mathrm{nK}$, at 17% of the Fermi temperature T_F. Lithium atoms have also been transported to the science cell and partially loaded in the dipole trap; their cooling to degeneracy is still to be achieved and will be addressed at the end of the chapter.

In the first section, we present the standard techniques which allow for the manipulation and measurement of the internal state of the atoms and show how to use the sample to calibrate the apparatus, a compulsory step to interpret correctly the experimental data. We then briefly illustrate the principles of evaporative cooling to underline the main parameters of the technique, which is performed in three steps that we detail: the cloud is first cooled in a magnetic trap, then transferred into an optical dipole trap and further evaporated to degeneracy. Eventually, we summarize the short and middle term projects that can be addressed by the FERMIX machine as soon as the system will have fully recovered from its long inactivity due to the major renovation works in the institute.

5.1 Diagnostic tools in the science cell

The realization of an cold atomic sample is at the same time an objective of the FERMIX experiment and a means to characterize the apparatus, a precise knowledge of which is required to interpret any experimental data. The objective of this section is twofold: we introduce standard techniques used to measure and manipulate spin populations and show how to use them in order to estimate and calibrate the properties of our experimental setup.

In this section, all examples will deal with ^{40}K, for which the measurements were performed in the experiment.

5.1.1 Spin selective measurements

Thermometry in the quadrupole trap

As the atomic cloud reaches the magnetic quadrupole trap of the science cell, it is too large and hot with respect to the cell size and the field of view of the imaging to allow long time-of-flight experiments. An alternative way to probe its temperature is to estimate the energy distribution of the ensemble. To do so, it is possible to rely on a so-called *radio-frequency knife*: RF-radiation of frequency ω_cut is sent on the atoms to drive a transition from a trappable $|F = 9/2\rangle$ state to a $|F = 7/2\rangle$ state which is expelled from the trap. As the Zeeman shift is inhomogeneous within the quadrupole magnetic field, only a fraction of the atoms will actually undergo a transition.

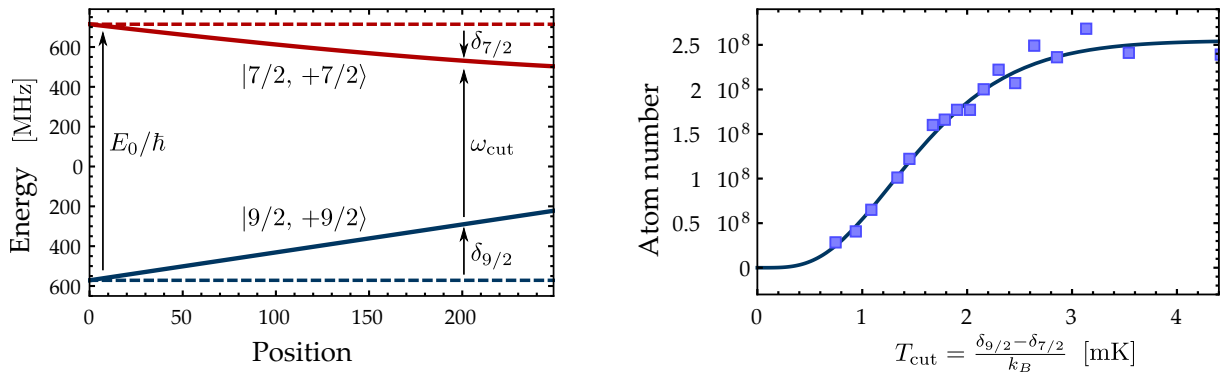

Figure 5.1: **Left**: RF knife. A radio frequency ω_{cut} selectively removes atoms with an energy higher than $\Delta E = E_0 - \hbar\omega_{\text{cut}} = \hbar(\delta_{9/2} - \delta_{7/2})$, where E_0 is the hyperfine splitting of the ground state and δ_m is the Zeeman frequency shift of the $|m\rangle$ sub-level. The choice of $\hbar\omega_{\text{cut}}$ thus sets the trap depth $\eta = (E_0 - \hbar\omega_{\text{cut}})/k_{\text{B}}T = T_{\text{cut}}/T$. **Right**: RF Thermometry: the number of atoms with an energy smaller than $k_{\text{B}}T_{\text{cut}}$ in a quadrupole trap only depends on the distribution temperature. A fit $N(T_{\text{cut}}) = N_0 \times P(9/2, T_{\text{cut}}/T)$ allows to estimate the temperature T. Here, we measure a temperature of 360±5 µK for 2.5×10^8 atoms as they arrive in the science cell.

Those atoms are located in a shell of magnetic field B_{cut} such that

$$\hbar\omega_{\text{cut}} = E_0 + \Delta E\left(B_{\text{cut}}\right), \tag{5.1}$$

where E_0 is the hyperfine splitting of the $S_{1/2}$ state and $\Delta E\left(B_{\text{cut}}\right) = \eta k_{\text{B}}T$ is the additional energy difference between the two states caused by the Zeeman effect. Assuming that collisions ensure a good redistribution of the trajectories, any atom with an energy higher than $\Delta E\left(B_{\text{cut}}\right)$ will cross the shell at some point of its oscillations and will be expelled from the trap. This picture motivates the name of the technique (see Fig. 5.1).

Strictly speaking, the height of the cut depends on the atomic spin state. However, at low temperatures (below few mK), the difference in Zeeman shifts between the $|9/2, 9/2\rangle \rightarrow |7/2, 7/2\rangle$ transition and the $|9/2, 7/2\rangle \rightarrow |7/2, 7/2\rangle$ transition is small enough to treat all trappable spin states as the same.

If the duration of RF knife is long enough for all atoms with high enough energy to reach the RF-knife, but short enough to avoid evaporation so that the ensemble's temperature remains constant, the remaining atom number N_{cut} is given by:

$$\frac{N_{\text{cut}}}{N_0} = P(9/2, T_{\text{cut}}/T), \tag{5.2}$$

where N_0 is the total atom number, P is the normalized incomplete Gamma function[1] and we

[1]We define incomplete Gamma functions as:

$$\Gamma(a, \eta) = \int_0^{\eta} du\, u^{a-1} e^{-u}.$$

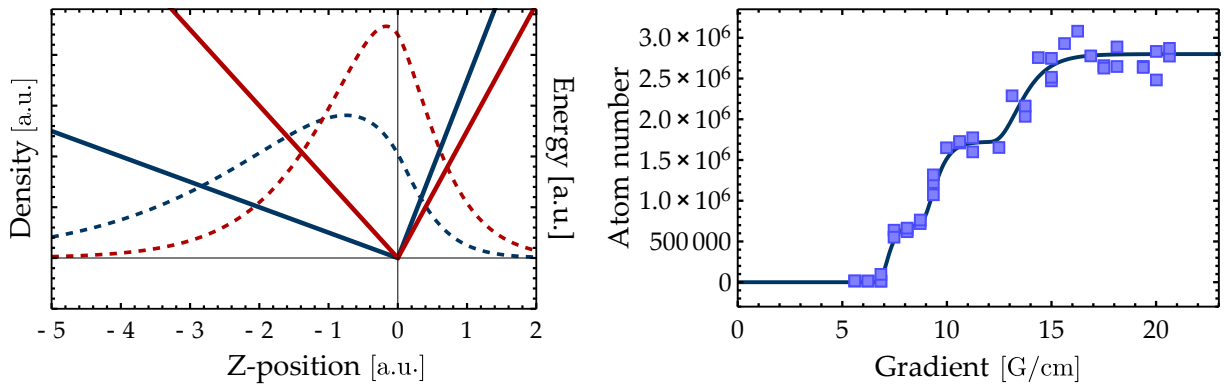

Figure 5.2: Controlled spilling experiment. **Left**: Confining potential (solid line) and spatial distribution (dashed line) for Potassium atoms in the $|9/2\rangle$ (red lines) and $|7/2\rangle$ (blue lines) spin states in the same magnetic gradient b. Gravity is oriented along **-z**. The reduced momentum of the $|7/2\rangle$ state induces a reduced confinement and thus a wider spread of the distribution. **Right**: remaining atom number as a function of the trap opening b. The fit function is given by equation (5.4) for $m_F \in \{9/2, 7/2, 5/2\}$. We take N_0, $\alpha = L/r_0 b_0^{1/3}$, $f_{9/2}$ and $f_{7/2}$ as free parameters and fit their values to $f_{9/2} = 0.25 \pm 0.02$, $f_{7/2} = 0.36 \pm 0.03$, $f_{5/2} = 1 - f_{7/2} - f_{9/2} = 0.39 \pm 0.04$

used the expression of the density of state $\rho(E) \propto E^{7/2}$ demonstrated in section 3.1.4.

By measuring N_{cut} for decreasing values of T_{cut}, we obtain a tomographic reconstruction of the cloud (see Fig. 5.1), with initial atom number and temperature as the only free parameters.

Controlled spilling from a quadrupole trap

As the RF-knife cannot resolve the difference between $|9/2, 9/2\rangle$ and $|9/2, 7/2\rangle$ states, it is not appropriate to probe the spin composition of the ensemble. A complementary approach is to use the difference of trapping stiffness experienced by different spin states. While the stretched low field seeking state experiences a linear potential with a slope $\mu_B b$, the other states evolve in a potential of slope $(m_F/F) \times \mu_B b$ and display a larger spread in the trap.

In a real experiment, the extension of the distribution is ultimately limited by the size of the coils or the proximity of obstacles such as the wall of the vacuum chamber. The distance L to the obstacle imposes a spin-selective cut on the distribution $E_{\text{cut}}(m_F) = (m_F/F) \times \mu_B L$. Furthermore, gravity results in an effective decrease of the trapping stiffness along **z** by an amount

$$b_g = m_K g/\mu_B \simeq 7\,\text{G/cm}. \tag{5.3}$$

Those functions are related to the standard Euler Gamma function through $\Gamma(a) = \Gamma(a, \infty)$ and we introduce the normalized ratio :

$$P(a, \eta) = \Gamma(a, \eta)/\Gamma(a)$$

These effects can be used to measure the spin population of the cloud by controlled spilling. Starting from a compressed quadrupole trap b_0, we decrease the magnetic gradient to b, causing the distribution to spread. If the trapping force exerted on a spin-state becomes weaker than gravity (ie $\frac{m_F}{F}\mu_B b < b_g$), atoms in this state will fall out off the trap. The total remaining number of atoms is given by:

$$\frac{N}{N_0} = \sum_{m_F>0} f_{m_F} \times P\left(\frac{9}{2}, \frac{m_F/F \times b - b_g}{b^{2/3} b_0^{1/3}} \frac{L}{r_0}\right) \theta\left(\frac{m_F}{F} b - b_g\right), \tag{5.4}$$

where N_0 is the initial atom number, $r_0 = k_B T/\mu_B b_0$ is the typical extension of the spatial distribution and f_{m_F} is the fraction of atoms in the m_F state. The denominator accounts for the cooling induced by the adiabatic decompression of the trap, as demonstrated in section 3.1.4.

An example of this measurement is presented in figure 5.1.

Stern Gerlach experiment

The Stern-Gerlach experiment is one of the most well-known methods to determine the spin composition of a sample[2]. As different spin states experience different potential slopes $(m_F/F) \times \mu_B b$, a free fall in a magnetic gradient spatially separates the populations of Zeeman sublevels.

Experimentally, we perform Stern-Gerlach measurements to probe the spin composition of a cloud in the optical dipole trap. We take advantage of the presence of two sets of coils close to the science cell to switch on simultaneously a magnetic gradient b, which will separate the spin states, and a magnetic bias, which moves the magnetic zero far from the cloud. As the atoms are released from the optical potential, they fall in a modified gravity $g(1 - 2m_F\mu_B b/Fb_g)$. For sufficiently long times of flight t_{TOF}, such that the distance between two successive states $\sim \mu_B b t_{\mathrm{TOF}}^2/2$ is larger than the spread of the cloud $\sigma(t) = \sqrt{\sigma_0^2 + k_B T/m \times t_{\mathrm{TOF}}^2}$, the population of each spin state can be resolved as shown in figure 5.3. However, the correct evaluation of the spin population may require an additional step: because of the spatial inhomogeneity of the magnetic field, all spin-states do not share the same imaging frequency. In addition, the Clebsch-Gordan coefficient depends on the addressed transition. Those parameters must be taken into account in the form of corrective factors when calculating the atom number with absorption imaging.

High field imaging

At high magnetic bias, the Zeeman shift differs enough from one spin state to the other to allow spin-specific imaging. The resonance value of the optical transition can be calculated analytically by taking into account the energy shift of both the ground state (as given by the

[2]And to support legends, as illustrated by the article "Stern and Gerlach: How a Bad Cigar Helped Reorient Atomic Physics" [Friedrich and Herschbach 2003]

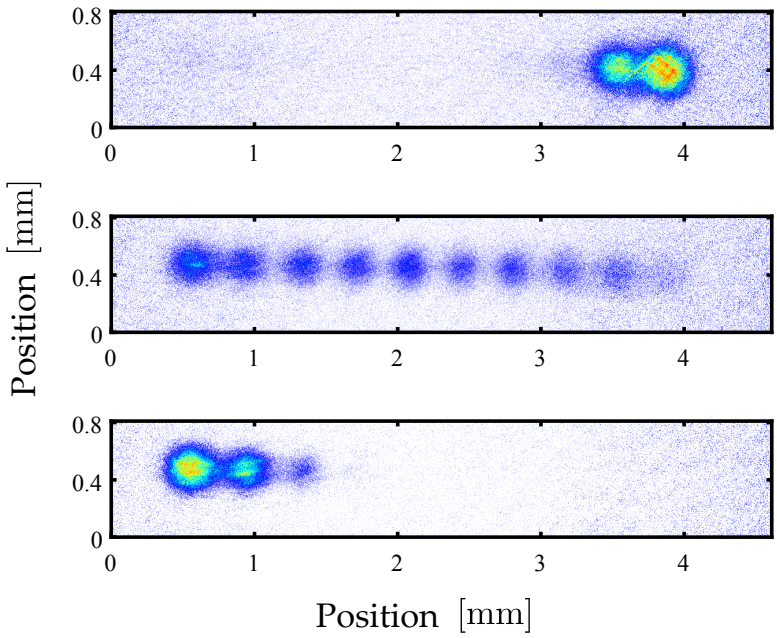

Figure 5.3: Stern-Gerlach experiment: a time-of-flight in a magnetic gradient separates spatially the populations of Zeeman sublevels. Pictures are taken after the first optical evaporation, as atoms are captured in the optical dipole trap. **Top**: atoms in the $|9/2\rangle$ and $|7/2\rangle$ states, after the evaporation. **Bottom**: after the adiabatic transfer, the atoms populate the $|-9/2\rangle$ and $|-7/2\rangle$ states. **Middle**: by ramping back and fourth the driving RF frequency, the atoms can be distributed among all 10 Zeeman sublevels. The adiabatic passage is described in section 5.1.2.

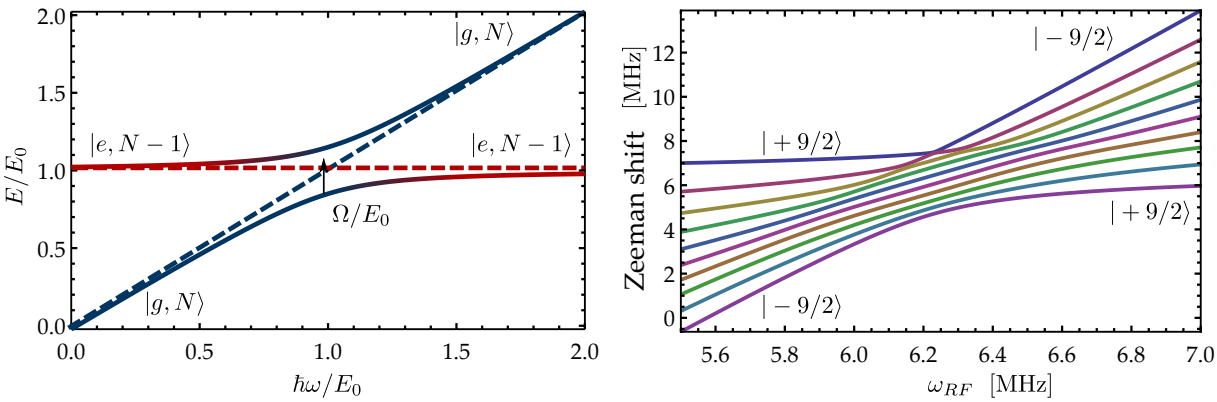

Figure 5.4: Landau Zener adiabatic sweep. **Left**: Eigenenergies of the dressed states of a simplified 2 levels system. The bare ground state $|g\rangle$ is pictured in blue and the bare excited state $|e\rangle$ in red. In dashed line, $\Omega_R = 0$ does not allow the anti-crossing of the two levels. **Right**: Eigen-energies of the 10 Zeeman sublevels of a ^{40}K atom. A magnetic bias of 20 G leads to an energy shift at zero frequency. All levels are coupled by a Rabi frequency $\Omega_R = 700$ kHz. Most notably, the low-field seeking state $|-9/2\rangle$ is transfered to the other stretch state $|+9/2\rangle$ by sweeping the RF from low to high frequency.

Breit-Rabi formula) and the excited state (as given by the Paschen-Back formula). As soon as the magnetic bias exceeds $\sim$ 100 G, the difference between resonance frequencies are much larger than the atomic linewidth and the population of each Zeeman sublevel can be imaged independently.

In the experiment, we work around the Feschbach resonance of Potassium at 200 G. The corresponding detuning is around 300 MHz with respect to the imaging frequency at zero field, too far to be reached simply by detuning the already installed acousto-optical modulator. A dedicated imaging system was thus installed to address the required transition.

5.1.2 Spin manipulation

Once the atoms are loaded into a spin independent confinement, such as a dipole trap, their spin states can be manipulated without (or with limited) losses. In this section, we present techniques dedicated to the control of the spin composition of the cloud. We will not address optical pumping, which was already described in section 2.6.

Landau-Zener adiabatic passage

The *adiabatic passage* allows for the transfer of atoms from one state to the other (for a pedagogical derivation, see [Steck 2012]). To get a simplified picture, let us consider a system with only two energy levels $\{|g\rangle, |e\rangle\}$ separated by E_0 and coupled by a Rabi frequency Ω_R resulting from an RF-radiation of frequency ω_{RF} (see figure 5.4). As the radiation frequency increases, the coupling between the two states results in the anti-crossing of the energy levels. At low

frequency, in the ground state of the {atom + radiation } system, the atomic state is essentially $|g\rangle$. At high frequency, the ground state of the total system corresponds to an atomic state essentially in the $|e\rangle$ level. By slowly sweeping the RF frequency from low to high values, the total system adiabatically follows its ground state and atoms are transferred from $|g\rangle$ to $|e\rangle$.

The Landau-Zener formula expresses the probability of successfully following one state during the transfer. We consider a linear ramp of frequency, performed over a duration T from $\omega_{\mathrm{RF}} = E_0/\hbar - \Delta/2$ to $\omega_{\mathrm{RF}} = E_0/\hbar + \Delta/2$, with $\Delta \gg \Omega_R$. The probability for an atom initially in the ground state to end up in the excited state is then given by [Landau 1932, Zener 1932, Rubbmark *et al.* 1981]:

$$P(g \to e) = 1 - \exp\left(-\frac{2\pi\Omega_R^2 T}{\Delta}\right). \tag{5.5}$$

For the transfer to be efficient, its duration T must be much longer than Ω_R^{-1}.

Experimentally, the energy difference E_0 is generated by the difference in energy shifts between Zeeman sublevels. Within the $F = 9/2$ manifold of ^{40}K, 10 sub levels must be taken into account (see Fig. 5.4) and the complete derivation is more complicated than for the two-levels system. Nevertheless, this simplified picture is still valid if the magnetic bias is strong enough to go beyond the linear Zeeman regime. In that case, the difference between successive resonant frequencies can be larger than the Rabi frequency and the complete adiabatic passage is then practically reduced to 9 independent passages $|9/2\rangle \to |7/2\rangle \to ... \to |-9/2\rangle$. For instance at 19.2 G, the resonant frequencies of the $|9/2\rangle \to |7/2\rangle$ and $|7/2\rangle \to |5/2\rangle$ transitions are $\sim 2\pi \times 6.213$ MHz and $\sim 2\pi \times 6.151$ MHz respectively, while the Rabi frequency is estimated to be $\Omega_R \simeq 10$ kHz. With those values, we could transfer more than 90% of Potassium atoms from the $|9/2\rangle$ state to the $|-9/2\rangle$ state (see Fig. 5.3).

Complementary, a fast ramp can be used to flip spins non-adiabtically from one state to the others. When ramping quickly, the driving frequency back and fourth through the resonance, spin populations of both levels tend to equilibrate in the end (see Fig. 5.3).

Spin selective removal

It is sometimes useful to prepare a fully spin-polarized sample, for instance to measure Rabi oscillations towards an empty state or to avoid interspecies interactions. One way to do so is to take advantage of the difference between energy shifts that affect the Zeeman sublevels. If an applied magnetic bias is strong enough, the separation between optical transitions ($|S_{1/2}, F = 9/2, m_F\rangle \to |P_{3/2}, F = 11/2, m'_F\rangle$) or RF transitions resonances ($|S_{1/2}, F = 9/2, m_F\rangle \to |S_{1/2}, F = 7/2, m'_F\rangle$) can be larger than the transition bandwidth and allows to address each sublevel independently. The energy acquired during the transition is large enough to expel the atom from the trapping potential and the population of a Zeeman state can thus be selectively removed with only minor influence on the remaining atoms.

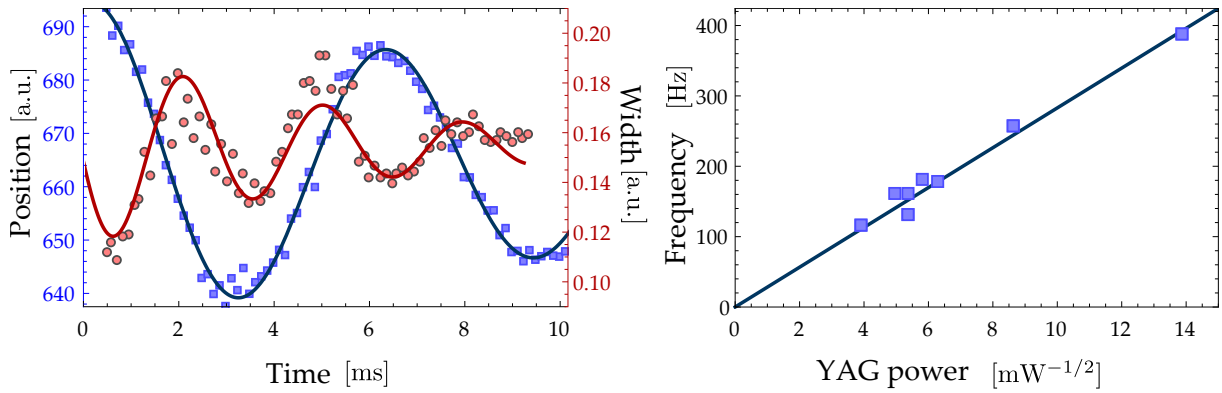

Figure 5.5: **Left**: estimation of the radial trapping frequencies by measuring the center-of-mass position (blue points) and the cloud spatial spread (red points). Solid lines are given by sinusoidal fit with exponential decay. **Right**: estimation of the beam waist. $\omega(P) = \sqrt{\frac{12c^2}{m\omega_0^2}\frac{\Gamma}{\Delta}\frac{P}{w^4}}$, where ω_0 is the frequency of the D_2 transition, Γ its bandwidth, Δ its detuning with respect to the laser frequency and m the mass of the atom. P is measured with a bolometer and the beam waist w is a free parameter. The best fit is obtained for $w = 38.6\,\mu\text{m} \pm 0.7$.

5.1.3 Calibration of the apparatus

While the previous sections were dedicated to the control and probing of the atomic sample, we show in this section how the sample can be used to calibrate the trapping frequencies of the optical trap, the Rabi frequency of the RF radiation driving the $|-9/2\rangle \leftrightarrow |-7/2\rangle$ transition, the magnetic biases and curvatures as well as the imaging magnification.

Trap frequency

A precise knowledge of the confining frequencies is required to estimate correctly the atomic density, which is involved in most physical quantities such as the collision rate or the Fermi temperature. In addition, the measurement of the oscillation frequencies of a cloud, and its comparison to the bare trap frequency, is an interesting way to put under scrutiny several effects, for instance the influence of interactions (see section 6.3.3).

Atoms provide an easy way to measure the frequency ω_0 of their confining potential. Kohn theorem, demonstrated in annex A.3.1, states that the oscillation frequency of cloud's center of mass is set by ω_0, regardless of the atomic interactions. To measure ω_0 it is sufficient to kick the center of mass, for instance by switching quickly off and on the confining potential, such that the cloud begins to fall. The ensuing oscillations give access to the trap frequency. An alternative way is to take advantage of the *breathing mode*: for a non-interacting gas, the spread of the distribution also oscillates, but at twice the trapping frequency [Guery-Odelin *et al.* 1999]. Both measurements are illustrated in figure 5.5.

By measuring the trapping frequency in an optical dipole trap for several laser powers, it is

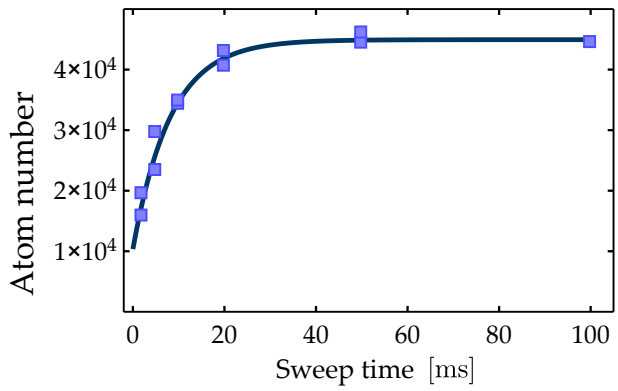

Figure 5.6: Rabi frequency measurement for $V_{pp} = 0.2$. We fit $N(t) = N_0 \left(1 - \exp(-2\pi\Omega_R^2 \frac{t\,[\mathrm{ms}]}{100\,[\mathrm{kHz}]}\right)$ and estimate $\Omega_R = 0.55$ kHz ± 0.04.

also possible to estimate the waist of the beam, given that $\omega \propto \sqrt{P}/w^2$. The power dependence picture on figure 5.5 gives for instance $w = 38.6\,\mu\mathrm{m} \pm 0.7$, in reasonable agreement with the expected value of 42 μm based on the parameters of the optical elements used in the setup.

Rabi frequency

The adiabatic passage described before provides a useful way to measure the Rabi frequency Ω_R driving the transition induced by the RF radiation. Equation (5.5) shows that the efficiency of the adiabatic transfer depends on whether the RF sweep is performed faster than the Rabi frequency. By measuring the transfer efficiency for several sweep velocities, it is therefore possible to estimate the value of Ω_R.

Experimentally, we prepare a sample in a pure $|-9/2\rangle$ state. We then perform an RF ramp of width $\Delta = 100$ kHz and variable duration T around the resonant frequency of the $|-9/2\rangle \rightarrow |-7/2\rangle$ transition at 115 G and we measure the number of atoms in the $|-7/2\rangle$ state. The result is pictured in figure 5.6 for peak-to-peak voltage of 0.2 V delivered by the RF generator. Given that the Rabi frequency scales as the square root of the RF power, ie linearly with the peak-to-peak voltage, we can estimate its value for any radiative power. At maximum power, $V_{pp} = 10$ V and the corresponding Rabi frequency can be calculated to be $\Omega_R = 27.7$ kHz.

Magnetic bias

An accurate calibration of the magnetic bias induced by a set of coils in Helmholtz configuration is required to take advantage of Feschbach resonances, all the more so as the resonances for ^{6}Li-^{40}K are less than a Gauss wide. An efficient way to perform such a calibration is to measure the Zeeman shift of the resonant frequency of a well known transition. The resolution of the measurement will be ultimately limited by the width of the transition, and it is therefore

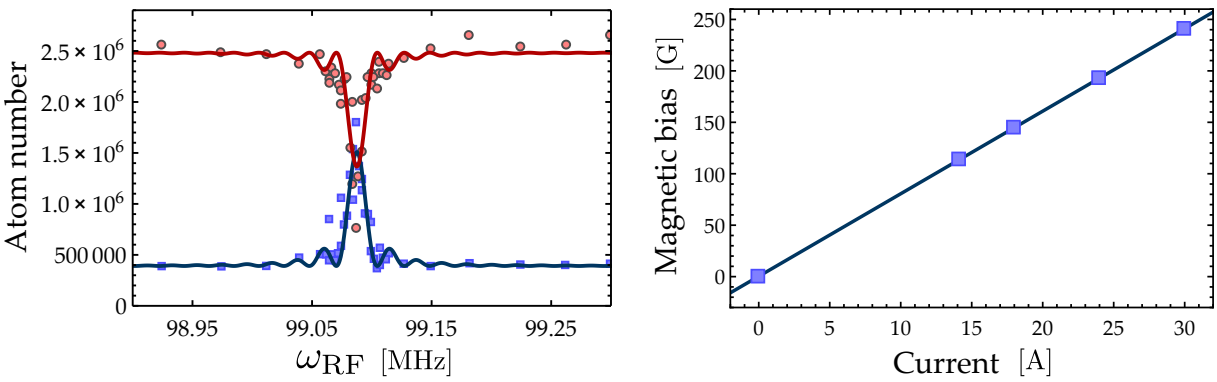

Figure 5.7: **Left**: population of the $|9/2\rangle$ (red circles) and $|7/2\rangle$ (blue squres) states after an RF pulse of $\tau = 18\,\mu$s as a function of the RF frequency. We fit simultaneously both set of data with the expression of the Rabi oscillation (5.6) and the analog formula for the population in the other state. The best fit is obtained for $\eta = 0.55$, $\Omega\tau = 0.51 \times \pi$ and $\omega_0 = 99.0874 \pm 0.0004$ MHz, corresponding to a magnetic bias $B = 202.326 \pm 0.001$ G. **Right**: Calibration of the inner coils close to the science cell. A linear fit close to high fields gives $B[G] = 8.0 \times I[A] + 0.31$

advantageous to address a hyperfine transition, with a width set by Rabi frequency Ω_R, rather than an optical transition for which $\Gamma \sim 2\pi \times 6$ MHz.

Experimentally we prepare a sample mostly in the $|9/2\rangle$ state. After setting the magnetic bias to a fixed value, we drive the $|9/2\rangle \rightarrow |7/2\rangle$ transition by sending a RF-radiation of frequency ω_{RF} for a duration τ such that $\tau\Omega_R \simeq \pi$, and we measure the atom number in both states as a function of the RF frequency. The number of atoms remaining in the $|9/2\rangle$ state after the pulse is given by

$$N_{9/2} = N^0_{9/2} + \frac{N^0_{7/2} - N^0_{9/2}}{1 + (\omega_{\mathrm{RF}} - \omega_0)^2 / \Omega_R^2} \times \sin^2\left(\sqrt{\Omega_R^2 + (\omega_{\mathrm{RF}} - \omega_0)^2}\tau/2\right), \tag{5.6}$$

where $\hbar\omega_0$ is the energy difference between both states set by the Zeeman shift and N^0_i is the initial population of the state $|i\rangle$. The population transfer is maximal when the RF frequency is exactly equal to the Zeeman shift, which can be related to the magnetic field through the Breit-Rabi formula. The result of such an experiment is shown in figure 5.7 and effectively provides a measurement of the magnetic bias with a precision up to the milliGauss regime.

Magnetic curvature

As soon as two coils are not in a perfect Helmoltz configuration, they produce not only a magnetic bias but also a magnetic curvature b'', which appears as a second order term in the spatial Taylor expansion of the field close to the symmetry center, leading to a Zeeman shift of the form

$$E(\mathbf{r}) = E_0(\mathbf{r}) - \frac{1}{2}m\omega_B^2(x^2 + y^2) + \frac{1}{2}m\left(\sqrt{2}\omega_B\right)^2 z^2, \tag{5.7}$$

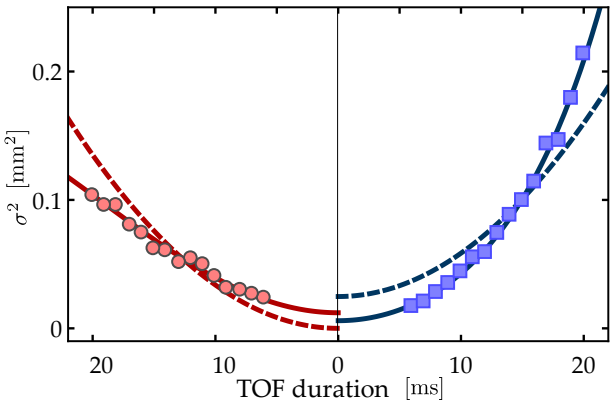

Figure 5.8: Time of flight measurement of the magnetic curvature induced by the inner coils close to the science cell at 30 A. Blue squares (red circles) show the cloud width measured along the **x** (**z**) direction as a function of time. For atoms in the $|-9/2\rangle$, the curvature leads to a trapping potential along **z** and expulse the atoms along the other two directions. Solid lines are fits given by (5.8), with $\omega_{x,y,z}$, ω_B and T as free parameters. We obtain the best fit for $\omega_B = 6.5 \pm 0.1$ Hz. Dashed lines are the best fit assuming $\omega_B = 0$, for comparison.

where E_0 denotes the shift due to the magnetic bias alone and $\omega_B = \sqrt{\mu_B g_F m_F b''/m}$. This curvature results in a slight modification of the trapping frequency, which might be difficult to measure directly. A time of flight experiment provides an alternative way to estimate b'' as the expansion of a cloud in such a surrounding potential is given by:

$$\sigma^2_{x,y}(t) = \frac{k_B T}{m}\left(\frac{1}{\omega^2_{x,y}}\cosh(\sqrt{2}\omega_B t) + \frac{1}{2\omega^2_B}\sinh(\sqrt{2}\omega_B t)\right) \tag{5.8a}$$

$$\sigma^2_z(t) = \frac{k_B T}{m}\left(\frac{1}{\omega^2_z}\cos(\omega_B t) + \frac{1}{\omega^2_B}\sin(\omega_B t)\right), \tag{5.8b}$$

where $\omega_{x,y,z}$ are the initial trapping frequencies before the cloud is released. These formulae are used to fit the expansion dynamics of the cloud as shown in figure 5.8 with ω_B as free parameter, thus allowing for the measurement of the magnetic curvature.

Imaging magnification

A time-of-flight experiment enables one not only to calibrate the magnetic curvature, but also to determine the magnification of the imaging system. We first bring the camera into focus by moving the imaging lens on a translation stage so as to minimize the size of the image of a very small cloud. A coarse estimate of the magnification of the system can be obtained by measuring the size of a calibrated stainless steel mesh of 320×320 µm placed successively close to both sides of the science cell. To perform a more accurate measurement, we release a small and cold cloud from the optical dipole trap and measure the position of its center of mass as it falls. Its real acceleration, set by gravity, is well known in absolute value. The measured acceleration

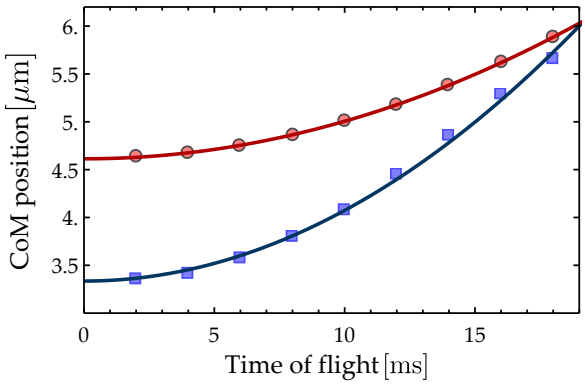

Figure 5.9: Calibration of the imaging magnification along **x** (blue) and **y** (red). We record the raw position (position in pixel × size of a pixel) as a function of time and fit a parabola $x(t) = x_0 + a_0 t^2/2$. The magnification is estimated as $m = a_0/g$. Here, we obtain $m = 1.59$ for the imaging system along **x** and $m = 0.6$ for the imaging system along **y**.

then depends on the pixel size of the CCD camera (6.45 μm) and on the magnification of the imaging system. The comparison of both values thus allows for a calibration of the optical system. However, this method assumes the absence of any remanent magnetic gradient, which would alter the effective gravity. Because of its heavier mass, ^{40}K is naturally a much better candidate for those measurements than ^{6}Li.

Now that we introduced the calibrated toolbox required to manipulate and probe the atomic samples, we turn to the description of the cooling technique that allowed us to reach quantum degeneracy for ^{40}K.

5.2 Principle of evaporative cooling

The objective of evaporative cooling is to increase above unity the phase-space density of the distribution, defined as:

$$\mathrm{PSD} = n_0 \lambda_{dB}^3 = N\,\lambda_{dB}^3/V_e, \tag{5.9}$$

where λ_{dB} is the de Broglie wavelength already introduced and n_0 is the central density. We also introduce the trap volume V_e, which corresponds to the volume that would be occupied by the gas if its density was uniformly n_0:

$$V_e = \frac{N}{n_0} = \int d^3r\, \exp(-\frac{U(\mathbf{r})}{k_\mathrm{B}T}). \tag{5.10}$$

We quantify the efficiency of the evaporation using the ratio:

$$\alpha = -\frac{d\log(\mathrm{PSD})}{d\log(N)}, \tag{5.11}$$

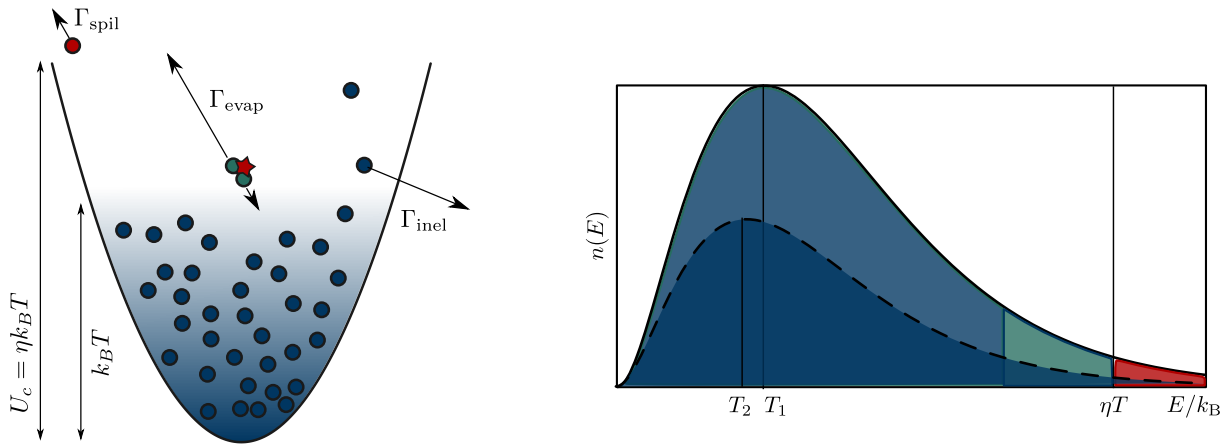

Figure 5.10: Principle of evaporative cooling. **Left**: in a trap in finite depth, collisions between particles redistribute the energy. Particles which gathered most of the energy and leave the trap ; the remaining distribution has therefore less energy and relaxes towards a colder temperature. Spilling and inelastic processes induce atom losses without evaporation. **Right**: starting from a thermal distribution at temperature T_1, we consider decrease the trap depth to $\eta k_{\text{B}} T$. Atoms with an energy higher than the cut (red) will be spilled and a fraction of the distribution will eventually get evaporated (green). The remaining atoms (blue) relax towards a thermal distribution at temperature $T_2 < T_1$.

which essentially expresses how many atoms must be sacrificed in order to gain one order of magnitude in phase-space density.

As mentioned in the introduction of this chapter, evaporative cooling consists in selectively removing a fraction of the ensemble with the highest energies. Inter-particle interactions redistribute the remaining energy within the sample, causing a relaxation towards a thermal distribution after few collisions[3] and repopulating the high energy wings of the distribution, which can again be evaporated further. This process is an out-of-equilibrium problem with time dependent parameters and a quantitative treatment can be extremely sophisticated. In this section, we present a simple qualitative model with the objective of highlighting the main parameters that are relevant for an experimental optimization of the process. This approach is mainly inspired by [Davis *et al.* 1995b] and [Cohen-Tannoudji 1996].

Let us consider a conservative trap $U \propto r^{3/\delta}$ with a finite depth U_c (see Fig. 5.10). We assume that the atomic distribution is almost thermal, so that a temperature T can be defined for the distribution. In many approaches, the ensemble is for instance described by a truncated Boltzmann distribution:

$$f(\mathbf{r}, \mathbf{p}) = n_0 \lambda_{dB}^3 \exp(-\frac{H(\mathbf{r}, \mathbf{p})}{k_{\text{B}} T}) \times \theta(U_c - H(\mathbf{r}, \mathbf{p})). \tag{5.12}$$

A key parameter is the ratio between the trap depth and the cloud temperature $\eta = U_c / k_{\text{B}} T$: the higher the trap, the more energy particles take away from the ensemble as they evaporate.

[3] $\sim$ 3 for a uniform single species gas to $\sim$ 20 for hetero-species gas in a linear trap [Walraven 2010]

A rule of thumb can be formulated by reducing the problem to a single parameter κ, which expresses the average excess of energy taken away by an evaporated atom. If η is lowered, the loss of $dN < 0$ atoms thus corresponds to an energy variation $dE = (\eta + \kappa)k_B T \times dN$. Relating the energy and temperature of the cloud through the virial theorem $E = (3/2 + \delta)Nk_B T$, the cooling resulting from this energy loss can be expressed as:

$$\frac{dT}{T} = \left((\frac{3}{2} + \delta)(\eta + \kappa) - 1 \right) \frac{dN}{N}. \tag{5.13}$$

The phase-space density decreases because of atom losses, but increases because of the cooling. These two contributions lead to the following balance:

$$\frac{d(\mathrm{PSD})}{\mathrm{PSD}} = \frac{dN}{N} - (\frac{3}{2} + \delta)\frac{dT}{T} = -\left(\eta + \kappa - (\frac{5}{2} + \delta) \right) \frac{dN}{N}. \tag{5.14}$$

If the trap remains deep enough, the gain in temperature compensates the atomic losses, and the phase-space density increases.

According to this simplified picture, it appears as if the deeper the potential, the more efficient the evaporation. However, the situation is rendered more complicated by the presence of additional inelastic and spilling losses as well as parasitic heating, which constrain the evaporation dynamics (see Fig. 5.10). If the trap is too high, very few collisions will result in particles being energetic enough to evaporate and the cooling will be extremely slow, leaving enough time for those additional losses to deplete the sample. The evaporation should therefore be *forced* by actively decreasing the trap depth to accelerate the process.

This analysis points out a second key parameter of any evaporation, namely the ratio between the rate of non-evaporative processes and the actual evaporation rate, which is essentially set by the trap depth and geometry as well as the collision rate:

$$\gamma_{\mathrm{coll}} = \frac{1}{2^{(\delta+1/2)}} n_0 \sigma \bar{v}, \tag{5.15}$$

where $\bar{v} = \sqrt{\frac{8k_B T}{\pi m}}$ is the particles' average quadratic speed and $\sigma = 4\pi a^2$ is the scattering cross section, related to the scattering length a (see annex A.4.3).

If the dynamical decrease of the trap depth is correctly performed, the collision rate can increase during the evaporation and even diverge in finite time (the so called *runaway* regime), owing to the non linearity of the process. However, this regime can only be attained if the average number of collisions per particle before leaving the trap inelastically (given by $\gamma_{\mathrm{coll}}/\Gamma_{\mathrm{inel}}$) is large enough. Numerically, in a harmonic trap, this number must exceed $\sim$ 300 for the runaway regime to be achievable [Guery Odelin 1998].

Several refinements can be introduced to improve the toy model presented above. For instance, in real evaporations, inelastic processes such as Majorana losses do not occur at a con-

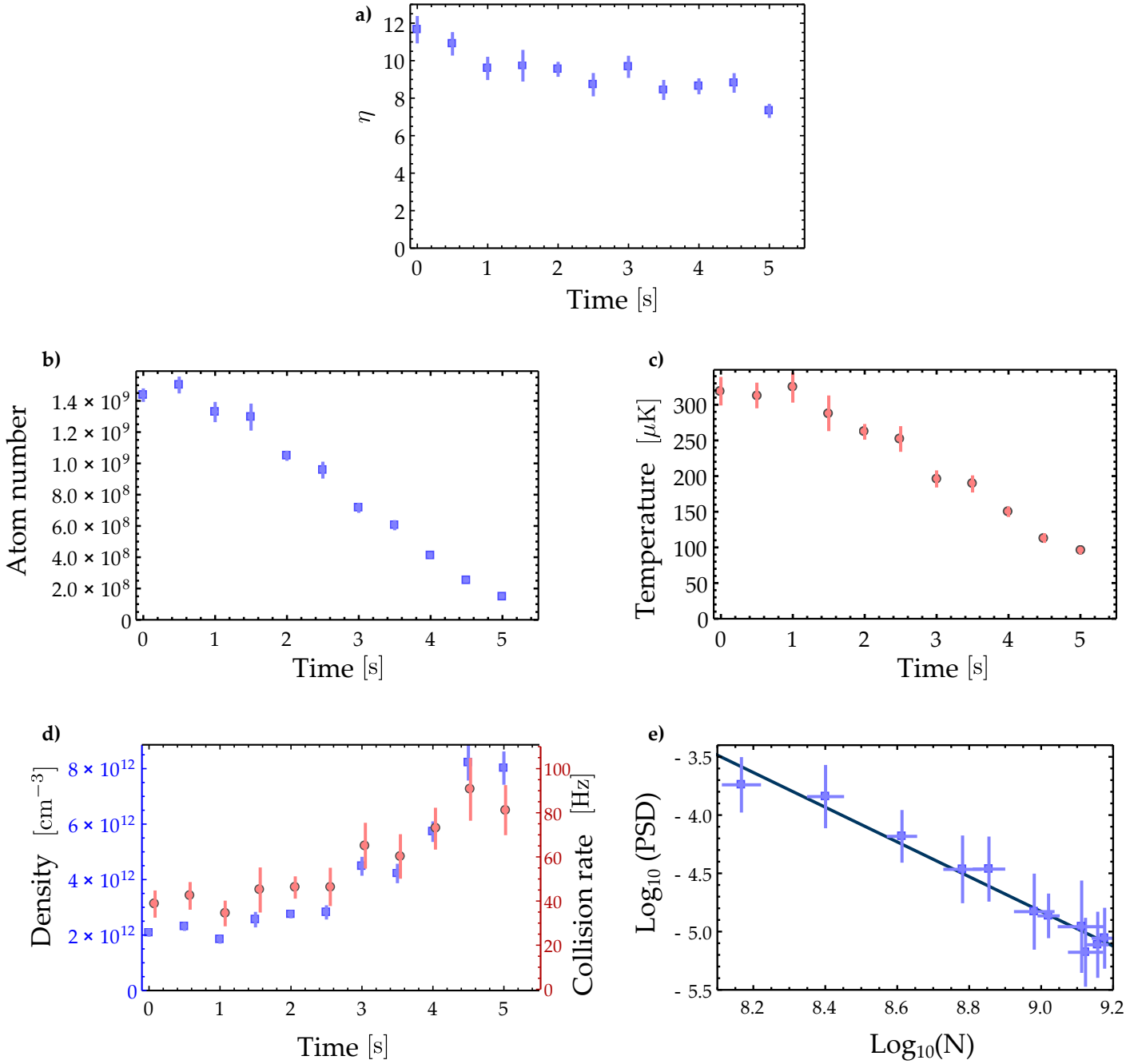

Figure 5.11: Magnetic evaporation of ^{40}K: starting from 1.5×10^9 atoms at 320 μK, we obtain 2×10^8 atoms at 90 μK after 5 seconds of evaporation. All points come from experimental data. **a)** Trap depth $\eta = T_{\text{cut}}/T$, where the cut temperature is set by the RF-knife. **b)** Atom number through the evaporation. **c)** Temperature, as measured by the RF tomography technique (see section 5.1.1) through the evaporation. **d)** Density (blue squares) and s-wave collision rate (red circles) through the evaporation. **e)** Evaporation efficiency, estimated to $\alpha \simeq 1.5$.

stant rate, but are in fact temperature dependent. A more detailed description of the scattering cross section σ can also be required, notably to take into account p-wave interactions which play a predominant role for ^{40}K above $\sim$ 20 μK [DeMarco *et al.* 1999, Fernandes 2014]. Whats more, we assumed that the trap kept the same steepness throughout the process, which will not be the case in an optical potential [Ketterle and Druten 1996]. Nevertheless, this simplified picture provides some rule-of-thumb scaling laws and identifies two key parameters as the main experimental knobs to tune the efficiency of the evaporation, namely the ratio between the trap depth and the ensemble temperature, as well as the ratio between the collision rate and the inelastic loss rate.

5.3 Evaporative cooling of Potassium

As Potassium atoms arrive in the magnetic quadrupole trap in the science cell, they form a cloud of $\sim$ 10^9 atoms at $\sim$ 320 μK, mostly in the $|9/2, 9/2\rangle$ and $|9/2, 7/2\rangle$ states. Magnetic confinement offers a large trapping volume as well as a good steepness, and direct evaporative cooling has been proven to be efficient enough to reach quantum degeneracy [DeMarco and Jin 1999]. However, in order to manipulate the spin states and to take advantage of Feschbach resonances, atoms must be loaded into an optical trap which, unlike a quadrupole trap, is spin-independent. With the perspective of achieving double degeneracy of ^{6}Li and ^{40}K, the loading of a dipole trap is therefore not optional. Yet, as the ensemble arrives in the science cell, it is too hot and too large to be efficiently loaded into an optical dipole trap of limited depth. To increase the mode matching, and hence the loading efficiency, our cooling strategy can be decomposed into three steps: the Potassium cloud is first evaporatively cooled in the magnetic trap, then transferred into the optical dipole trap and further evaporated to quantum degeneracy.

5.3.1 Magnetic RF-evaporation

The RF-knife introduced in section 5.1.1 provides a simple means to decrease arbitrarily the trap depth η of the magnetic confinement by adjusting the driving frequency. Experimentally, we start with a sample of 1.5×10^9 atoms at $\sim$ 320 μK in a quadrupole trap with a magnetic field gradient $b = 125$ G/cm, corresponding to a PSD of 7×10^{-6}. We ramp down linearly the frequency of the RF knife from $T_{\text{cut}} = 3.5$ mK to $T_{\text{cut}} = 0.7$ mK in 5 seconds. At the end of the evaporation, the sample contains 10% of the initial atoms at 95 μK, corresponding to a phase-space density of 2×10^{-4}.

The evaporation efficiency, defined as (5.11), is rather low with $\alpha \sim 1.5$, to be compared to $\alpha \sim 3$ for the RF evaporation of Rubidium. As a result, despite excellent initial conditions compared to other ^{40}K experiment, we can only obtain standard values at the end of this step. The reasons for this limitation are still to be fully understood. The efficiency should be quite robust with respect to the initial spin composition of the cloud, as both s-wave and p-wave

collisions take place [DeMarco *et al.* 1999]. Losses due to background pressure are moderate, as proven by the long lifetime of the sample in the dipole trap ($\gtrsim$ 60 s). In a quadrupole trap, special care should also be given to Majorana losses (previously described in section 3.1.3), which strongly reduce the evaporation efficiency.

Majorana losses are indeed equivalent to an anti-evaporation process, as atoms with lowest energy spend more time close to the magnetic zero and are therefore most likely to leave the trap. The temperature increases as $T_0\sqrt{1+t/T_M}$ and the corresponding heating rate, proportional to $\frac{\hbar}{m}\left(\mu_B b/k_B T\right)^2$, increases as the temperature is lowered. For ^{40}K at 75 μK, we measure $T_M \sim 9\,s$, which is comparable with the evaporation time. In order to circumvent this issue, we focus on the trap center a repulsive blue detuned 532nm laser beam so as to prevent atoms from reaching the magnetic zero [Davis *et al.* 1995a, Dubessy *et al.* 2012]. The setup was presented in section 2.10.1 and results in an optical plug of $\sim$ 0.8 mK height. Majorana losses are now strongly suppressed, as illustrated by the increased heating of $T_M \sim 70\,s$.

Despite its moderate efficiency, this sequence is quick and optimized to increase the atom number loaded in the optical trap, as described in the following section, allowing for the realization of a degenerate cloud.

5.3.2 Loading of the optical trap

During the RF evaporation, a red-detuned 1064nm laser of waist w is shone onto the atoms (see section 2.10.2 for technical references), resulting in a hybrid optical and magnetic potential[4]:

$$U_{\text{hybrid}} = \mu_B b\sqrt{x^2+y^2+4z^2} - U_0 \exp\left(-2\frac{y^2+(z-z_0)^2}{w^2}\right) + mgz + E_0, \tag{5.16}$$

where $U_0 \sim 0.5$ mK is the optical trap depth and E_0 is set such that $U_{\text{min}} = 0$, as shown on figure 5.12 [Lin *et al.* 2009b]. To avoid Majorana spinflips, the laser beam does not cross the magnetic center but rather passes at a distance $z_0 \sim -100\,\mu$m, chosen to optimize the trap loading. Along the propagation direction **x**, the optical confinement set by the Rayleigh length is negligible compared to the magnetic trapping set by $r_0 = k_B T/\mu_B b$. The resulting trapping frequency is thus set by the magnetic field gradient:

$$\omega_{\parallel} = \frac{1}{2}\sqrt{\frac{\mu_B b}{m z_0}}. \tag{5.17}$$

The partition of atoms between the magnetic and optical potentials can be pictured by estimating the occupied volume (see Fig. 5.12). At high temperatures, the volume is essentially that of a magnetic trap while, at low temperature, it is mostly that of the optical trap, meaning that the atoms are transferred from one to the other. The hybrid trap thus benefits from advan-

[4]The optical plug is not included in eq.5.16.

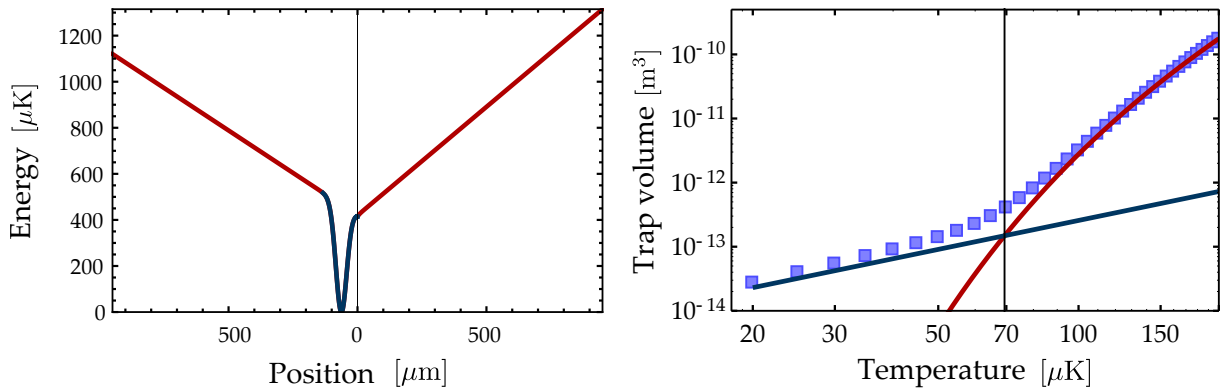

Figure 5.12: Hybrid trap. **Left**: trapping potential. In red, the magnetic contribution captures a large volume but is spin dependent. In blue, the optical contribution presents a larger depth but a smaller volume. The position of the optical dipole trap is found to be optimal $\sim 100\,\mu$m below the magnetic center. **Right**: effective volume of a distribution in (5.16) as a function of the temperature (blue squares). The solid lines are the effective volume in a purely optical (blue) and magnetic (red) potential. As the temperature goes down, the atoms accumulate in the optical potential.

tages of both trapping strategies (large volume of the magnetic quadrupole trap, broad range of evaporation and spin independence of the optical dipole trap) without their main drawbacks.

Experimentally, at the end of the RF-evaporation, we ramp down the magnetic gradient adiabatically to $\sim b_g = mg/\mu_B = 7$ G/cm within 400ms. This step loads 20% of the atoms in the optical dipole trap, mostly in the $|9/2\rangle$ and $|7/2\rangle$ states, resulting in a sample of 2.8×10^7 atoms at 45 μK. Even though the loading is adiabatic, the modification of the trap geometry does not conserve the phase-space density [Weber *et al.* 2003]. This *dimple* effect leads to an increase the PSD by a factor 15 to 3×10^{-3}.

5.3.3 Optical evaporation

Considering a simplified two-levels atom, a laser propagating along $\mathbf{x}$ will induce a trapping potential which can be written close to its focal point as [Grimm *et al.* 2000]:

$$U_{\mathrm{ODT}}(\mathbf{r}) = \frac{1}{2}m\omega_\perp^2(y^2+z^2) + \frac{1}{2}m\omega_\parallel^2 x^2, \tag{5.18}$$

where $\omega_\perp = \sqrt{\frac{4U_0}{mw^2}}$ is the strong trapping frequency and $\omega_\parallel = \sqrt{\frac{2U_0}{mz_R^2}}$ is typically one hundred times smaller. Those frequencies depend on the trap depth, which can be expressed as a function of the light intensity I and of its detuning δ with respect to the atomic transition:

$$U_0 = \frac{\hbar\Gamma^2}{4|\delta|}\frac{I}{2I_{\mathrm{sat}}}, \tag{5.19}$$

where Γ is the natural linewidth of the optical transition and I_{sat} is the saturation intensity.

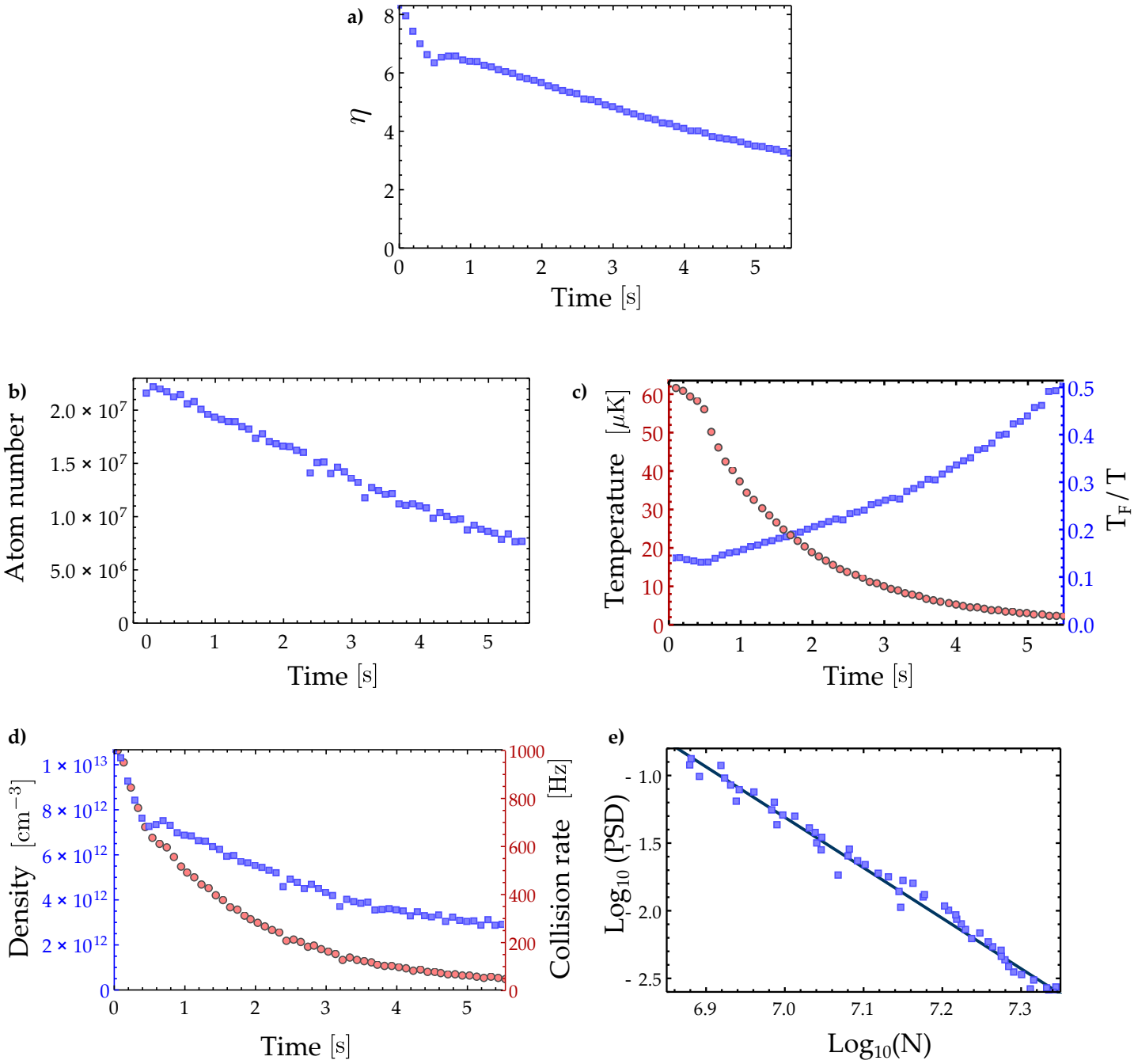

Figure 5.13: Optical evaporation of ^{40}K: starting from 2.8×10^7 atoms at 45 μK, we obtain 8×10^6 atoms at 1.5 μK after 5.5 seconds of evaporation. All points come from experimental data. **a)** Trap depth $\eta = T_{\text{cut}}/T$, where the cut temperature is set by the optical power. **b)** Atom number through the evaporation. **c)** Temperature (red circles) and ratio to the Fermi temperature T_F (blue square) through the evaporation. **d)** Density (blue squares) and s-wave collision rate (red circles) through the evaporation. **e)** Evaporation efficiency, estimated to $\alpha \simeq 3.7$.

To perform the evaporation, we decrease exponentially the optical power from 10 W to 170 mW in 5.5 seconds, thereby reducing the trap depth. At the end of this step, the sample is composed of 8×10^6 atoms at 1.5 μK and the efficiency of the evaporation can be estimated to be $\alpha \sim 3.7$ (see Fig. 5.13).

Unlike in a magnetic trap, the trapping frequencies of an optical dipole trap depend on the light intensity $\omega \propto \sqrt{I}$, and both the confinement and the collision rate decrease during the cooling [O'Hara *et al.* 2001]. At the end of the evaporation, the axial frequency is reduced to $\omega_{\parallel} \sim 2.5$ Hz, which prevents any efficient further cooling.

To increase the axial confinement, a second laser beam with a much larger waist is sent perpendicularly to the first optical dipole trap (technical details were presented in section 2.10.2). The polarization of both beams are orthogonal to prevent interference and the resulting trapping frequencies are given by the superposition of both potentials:

$$\omega_x = \omega_{\perp 2},\ \omega_y = \omega_{\perp 1},\ \omega_z = \sqrt{\omega_{\perp 1}^2 + \omega_{\perp 2}^2}, \tag{5.20}$$

where $\omega_{\perp 1,2}$ denotes the radial trapping frequencies of the first and second laser beam.

Experimentally, we ramp up the second beam with a waist $w_2 = 340\,\mu$m to 4.8W within 1.5s, leading to a potential of depth $U_0 = 3.5\,\mu$K and radial frequency $\omega_{\perp 2}/2\pi = 25$ Hz. The loading rate of the cross trap is kept slow because of the weak axial frequency but shows a good efficiency as, eventually, 4.8×10^6 atoms are trapped in the dimple. The finite depth of the potential results in an additional evaporation and despite the compression of the cloud, its temperature decreases to 1.3 μK, showing an increase of the PSD to $T/T_F = 0.7$.

To tune inter-particle interactions by taking advantage of Feschbach resonances (see appendix A.4.5), Potassium atoms must be transferred into the adequate spin states. The adiabatic passage described in section 5.1.2 is used to populate the $|-9/2\rangle$ and $|-7/2\rangle$ states with equal atom number. These states present a s-wave Feschbach resonance at $B_0 = 202$ G, with a width $\Delta B = 7$ G. However, a p-wave resonance is also located around 200 G [Gaebler *et al.* 2007], increasing the inelastic losses and rendering challenging the use of the s-wave resonance to enhance the evaporation efficiency. For the time being, we performed the final of evaporation at the background value of the scattering length, far above the resonance in order to be able to bring the interactions to zero without crossing the unitary regime.

The final step of evaporation takes place in the crossed dipole trap. The axial frequency is kept constant by the second beam while the power of the first beam is decrease from 170 mW to 57 mW in 14 seconds.

To determine the atom number and temperature, we ramp the magnetic bias to 209 G$= B_0 + \Delta B$, such that scattering length vanishes and perform a time of flight for the non-interacting ensemble. The result for a 20 ms TOF is shown in figure 5.14. We measure 1.5×10^5 atoms in the $|-9/2\rangle$ state, and roughly the same amount in the $|-7/2\rangle$ state, at a temperature of 60

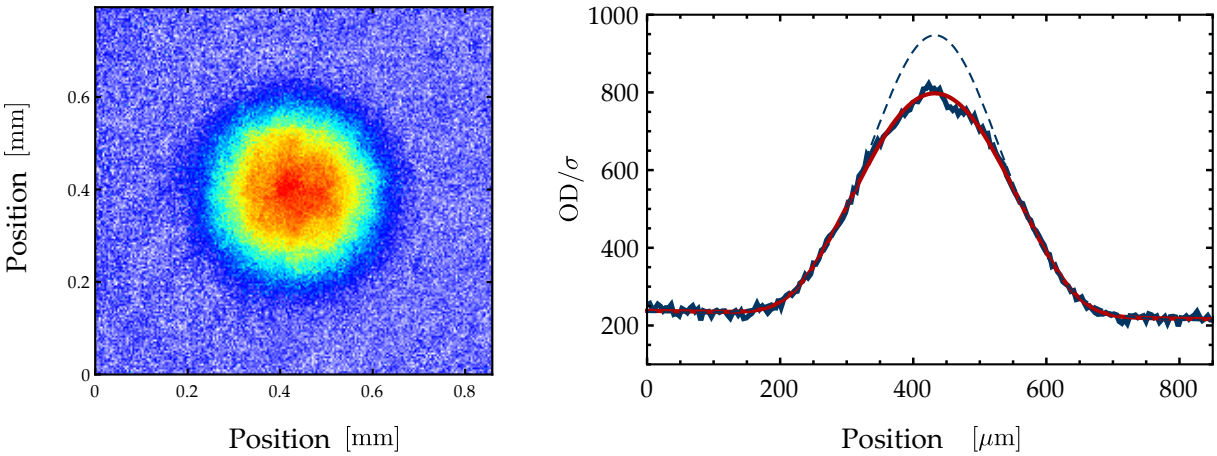

Figure 5.14: **Left**: 2D spatial density of the cloud, averaged over 5 pictures, at the end of evaporation in the $|9/2, -9/2\rangle$ state, after 20 ms TOF. **Right**: corresponding 1D integrated density (solid blue line). The best fit with a polylogarithm function (solid red line) gives an atom number of 1.5×10^5 atoms, a temperature of $T = 62$ nK and a degeneracy parameter $T/T_{\mathrm{F}} = 0.16$. The corresponding Fermi temperature, T_{F}=400 nK, is in excellent agreement with its theoretical value. For comparision, a non degenerate gaussian fit (dashed line) gives the same atom number, but a much higher temperature $T = 140$ nK. The discrepancy between both fits highlights the non-classical behavior of the sample.

nK.

The ratio to the Fermi temperature can be estimated directly by fitting the 1D-integrated density with a Polylogarithm function (see section 2.11.2), or indirectely by calculating the Fermi temperature as:

$$k_B T_F = \hbar\overline{\omega}(6N)^{1/3} \simeq 395\text{nK}, \tag{5.21}$$

where $\overline{\omega}^3 = \omega_x\omega_y\omega_z$ is the harmonic average of the trapping frequencies. Both methods are in excellent agreement and give $T/T_{\mathrm{F}} = 0.16$, implying that the sample was cooled down to the deeply degenerate regime.

5.4 Double evaporative cooling of ^{6}Li and ^{40}K

One of the objectives of the FERMIX experiment is to produce a double degenerate Fermi gas of ^{6}Li and ^{40}K. At the moment of writing this thesis, we were able to cool 2×10^6 ^{6}Li atoms down to 68 μK in the plugged magnetic trap and to load 4.5×10^5 of them at 38 μK in the optical dipole trap, in which the evaporative cooling is still to be performed. In this section, we present these preliminary results and suggest strategies for further cooling to degeneracy.

5.4.1 ^{6}Li-^{40}K interactions

The inter-species interactions constitute a key parameter of the simultaneous cooling of ^{6}Li and ^{40}K. If the overlap between the clouds of ^{6}Li and ^{40}K is large enough, collisions will

redistribute the energy between the two distributions and facilitate the thermalization of the clouds. This effect was already used in connection with the quasi-thermalization experiments (section 3.2.1) to prepare a thermal Lithium gas in a magnetic trap.

For the ^{6}Li-^{40}K system, the triplet scattering length was reported to be $a_t = 62\,a_0$ and the singlet scattering length at $a_s = 52\,a_0$, where a_0 is Bohr radius [Wille *et al.* 2008]. The positions and widths of ^{6}Li-^{40}K Feschbach resonances were thoroughly studied experimentally [Tiecke *et al.* 2010a] and theoretically [Tiecke *et al.* 2010b]. It should be noted that Feschbach resonances also increase inelastic collisions, resulting in a finite decay rate [Naik *et al.* 2011].

Far from those enhanced losses, the spin exchange collision rate between ^{6}Li and ^{40}K is reasonably small. This results from the inverted hyperfine structure of Potassium, which strongly suppresses spin relaxation if any of the two interacting atoms is in the lowest Zeeman sublevel [Simoni *et al.* 2003]. The small difference between the singlet and triplet scattering lengths further reduces the inelastic collision rate. As a consequence, it has been shown that a mixture of 10^4 ^{40}K atoms immersed in a sea of 10^7 ^{6}Li atoms was collisionally stable, with a two body loss rate for Potassium below $L_2 = 6 \times 10^{-13}\,\mathrm{cm}^{-3}/\mathrm{s}$ across the entire Lithium BEC-BCS crossover [Spiegelhalder *et al.* 2009].

5.4.2 Magnetic RF-evaporation

After the magnetic transport, we obtain 10^8 Lithium atoms in the science cell at 400 μK. Only the $|F = 3/2, m_F = 3/2\rangle$ spin state is stable against spin exchange collisions and trappable in a magnetic quadrupole. As mentioned in the previous chapters, since s-wave collisions are forbidden by the Pauli principle and p-wave collisions are present only above 6 mK, a cold pure ^{6}Li sample behaves like an ideal gas and does not thermalize by itself. To cool and evaporate a Lithium sample, it is therefore necessary to consider the sympathetic cooling technique, which consists in cooling actively one species (Potassium in our case) while relying on collisions to thermalize the other species with the coolant [Modugno *et al.* 2001].

The cooling of Lithium represents an additional thermal load for Potassium, whose evaporation must dissipate both internal energies. The presence of Lithium thus reduces the efficiency of the Potassium evaporation and starting from the same initial conditions, much less atoms reach the same final temperature. It was observed in [Tiecke 2009] that the density of Potassium was limited to $10^{12}\,\mathrm{cm}^{-3}$, two orders of magnitude below its value for a single species evaporation. In our experiment, we reduce the Lithium sample arriving in the science cell to 10^7 atoms by detuning the Zeeman slower, so as to minimize the detrimental effects for Potassium.

The load can be further reduced by removing Lithium atoms with highest energies. Taking advantage of the large difference between the ^{6}Li and ^{40}K hyperfine splittings (228 MHz and 1.2 GHz respectively), it is indeed possible to utilize two species-specific RF knifes to tune independently the trap depth for both species. We found the optimal configuration to be $T_{\mathrm{cut}}^{\mathrm{Li}} =$

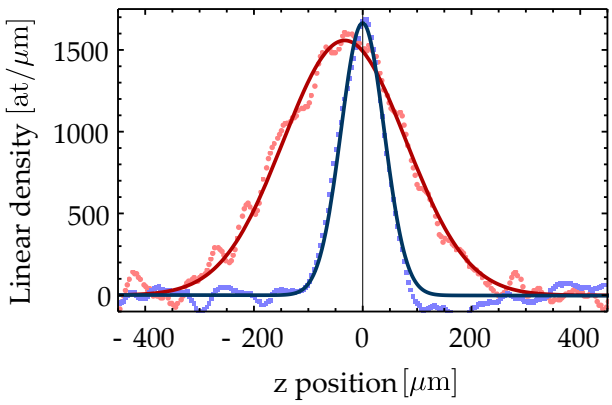

Figure 5.15: 4.5×10^5 Lithium atoms (in red) and 1.9×10^5 Potassium atoms (in blue) at ∼38 μK in the optical dipole trap at the end of the RF evaporation, after 0.5 ms TOF.

$1.5 \times T^{\mathrm{K}}_{\mathrm{cut}}$.

The optical plug plays a crucial role for the evaporation of Lithium, which is much lighter than Potassium and thus has a ~ 6 times higher Majorana loss rate. In absence of the plug, the anti-evaporation due to Majorana losses prevents any efficient cooling of the Lithium sample and also keeps Potassium at higher temperatures. With the plug, we measured a lifetime of ~ 20 s for 2×10^6 Lithium atoms at 68 μK at the end of the evaporation. After the magnetic quadrupole is switched off, we measure in the optical dipole trap 4.5×10^5 Lithium atoms and 1.9×10^5 Potassium atoms at ∼38 μK, as shown in picture 5.15.

5.4.3 Optical evaporation

The constraints for the optical evaporation are quite different from the ones present in the magnetic trap. As the trapping potential is now spin-independent, we can consider a $|1/2\rangle - |-1/2\rangle$ spin mixture of Lithium to take advantage of the large s-wave scattering length. On the other hand, the trap geometry can not be tuned independently for both species and it is about half as deep for Lithium as for Potassium. Lithium atoms will thus have much higher evaporation and spilling rates than Potassium. For instance, in a deep potential $\eta_{\mathrm{K}} = 10$, the Lithium evaporation rate is $e^{-\eta_{\mathrm{Li}}}/e^{-\eta_{\mathrm{K}}} \simeq 150$ times faster than the one of Potassium [Fernandes 2014]. Moreover, the mass imbalance between the two species is such that Lithium atoms will take most of the kinetic energy during binary collisions. The sympathetic cooling of Potassium by Lithium is therefore extremely demanding in terms of initial atom numbers, requiring a reduced Potassium sample immersed in a large Lithium cloud [Spiegelhalder *et al.* 2010].

An alternative approach is being considered in our group to allow the simultaneous cooling of two samples with approximately the same atom numbers [Fernandes 2014].

In an equilibrated mixture, the collision rate between potassium atoms (set by $a_{\mathrm{K}} = 170\, a_0$) is larger than the interspecies collision rate ($a_{\mathrm{LiK}} = 63\, a_0$) but smaller than collision rate between

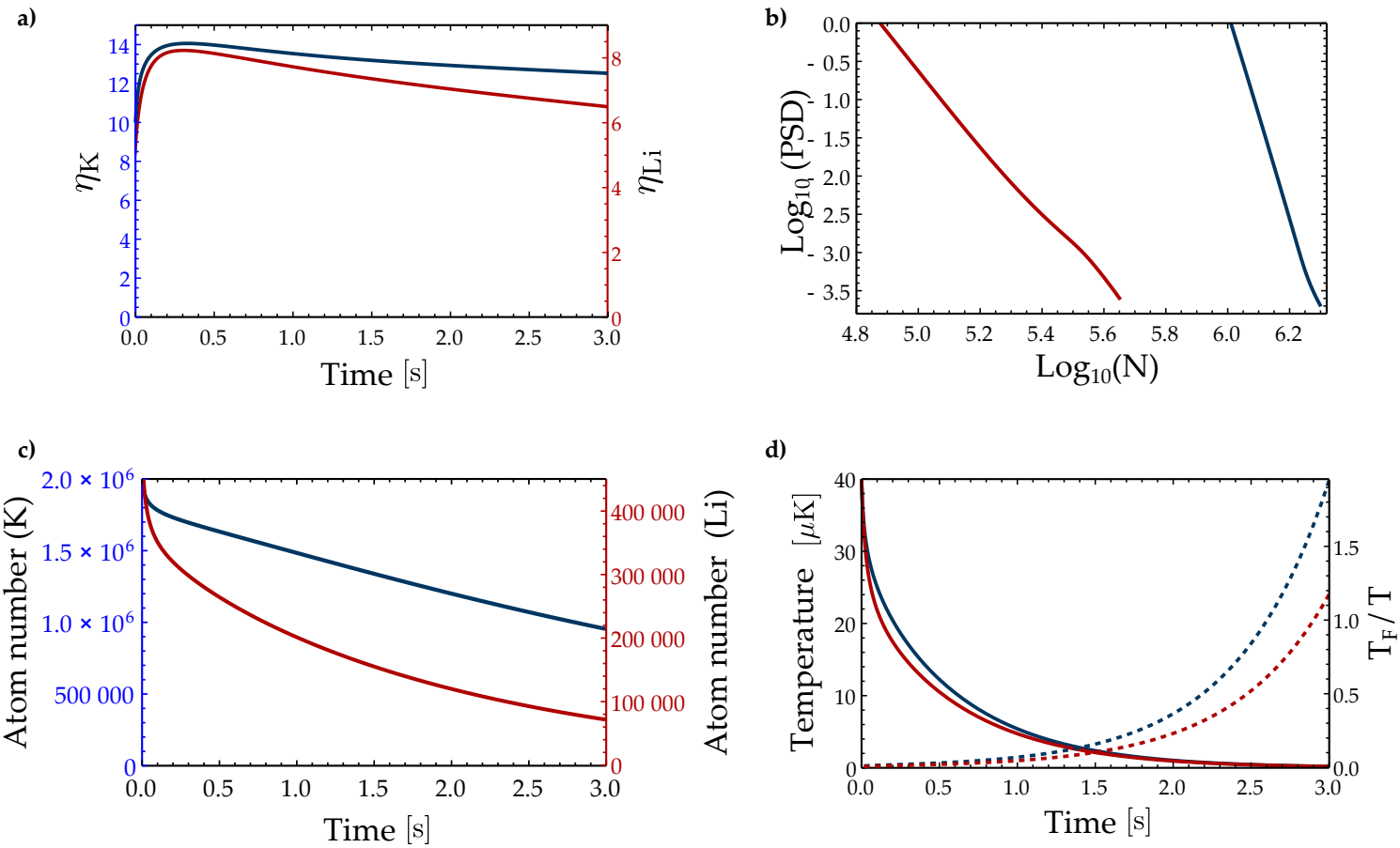

Figure 5.16: Simultaneous optical evaporation of ^{6}Li and ^{40}K: starting from 4.5×10^5 Lithium atoms at 40 μK and 2×10^6 Potassium atoms at the same temperature, we obtain 7×10^4 atoms at 190 nK and 10^6 Potassium atoms at 200 nK after 3 seconds of evaporation. The scattering lengths are : $a_K = 1000 a_0$, $a_{Li} \sim -300\, a_0$ and $a_{LiK} = 63\, a_0$. Inelastic losses are not taken into account. Numerical simulations performed by Cedric Enesa.
All data for ^{6}Li are shown in red (resp. blue for ^{40}K). **a)** Trap depth $\eta = T_{cut}/T$. The trap is about twice as deep for ^{40}K as for ^{6}Li. **c)** Atom number through the evaporation. **d)** Temperature (solid lines) and ratio to the Fermi temperature T_F (dashed lines) through the evaporation. **b)** Evaporation efficiency, estimated to $\alpha_{Li} \simeq 4.4$ and $\alpha_K \simeq 13.4$.

Lithium atoms ($a_{\mathrm{Li}} \sim -300\,a_0$). This results in the evaporation rate of Potassium being much smaller than the one of Lithium, all the more so as the trap is deeper for ^{40}K than for ^{6}Li. As a consequence, Potassium is sympathetically cooled by Lithium ; because of the mass imbalance, the resulting thermal load is too heavy for keeping a satisfying amount of ^{6}Li at the end of evaporation. One strategy to circumvent this issue is to accelerate the evaporation of Potassium by enhancing its intra-species collision rate. If the scattering lengths are such that

$$a_{\mathrm{K}} \gg a_{\mathrm{Li}} \gg a_{\mathrm{LiK}}, \tag{5.22}$$

very few interspecies collisions take place and the dual-species cooling essentially reduces to two independent single species evaporations. Both evaporations may occur at the same rate, as the higher scattering rate of Potassium compensates the difference in trap depth. In this case, Potassium remains as cold as Lithium and the thermalization of both species at the end of evaporation does not lead to a significant atom loss. Experimentally, this can be done by taking advantage of the Feschbach resonance of Potassium at 202 G. For instance, provided that the intra-species scattering length is increased to $a_{\mathrm{K}} = 1000 a_0$, the evaporation rate is almost the same for both species for a trap depth of $\eta_{\mathrm{K}} \simeq 8$.

A preliminary simulation was performed by Cedric Enesa using a classical model and neglecting inelastic losses (see Fig. 5.16) [Enesa 2015]. Starting from 4.5×10^5 Lithium atoms at 40 µK and 2×10^6 Potassium atoms at the same temperature, we obtain 7×10^4 Lithium atoms at 190 nK and 10^6 Potassium atoms at 200 nK after 3 seconds of evaporation. This model implies to a very good cooling efficiency for Lithium with $\alpha_{\mathrm{Li}} \simeq 4.4$, even in presence of Potassium. The evaporation efficiency of Potassium, $\alpha_{\mathrm{K}} \simeq 13.4$, is due to the high η_{K} cut ratio. Its value is clearly overestimated, as inelastic losses, which also increase close to the Feschbach resonance, are not taken into account. Nevertheless, these preliminary results are encouraging for the experimental realization of a double species degeneracy.

5.5 Conclusions

In this chapter, we reviewed standard techniques which were applied to monitor and manipulate the internal degrees of freedom of the Potassium cloud, and use it to calibrate our apparatus. We have shown that we could produce for the first time in France a cloud of ^{40}K with 1.5×10^5 atoms in the $|-9/2\rangle$ state and as many in the $|-7/2\rangle$ state, at a temperature of 62 nK corresponding to 17% of the Fermi temperature, in the deeply degenerate regime. We presented preliminary works concerning the simultaneous evaporative cooling of ^{6}Li and ^{40}K, resulting in the loading of $2-4 \times 10^5$ atoms at 40 µK in the optical dipole trap. Numerical simulation were performed to support an innovative cooling strategy, where both species are evaporated independently at similar rates, to avoid a too strong thermal load on the Lithium cloud.

As a longer term project, once both ^{6}Li and ^{40}K are brought to degeneracy, the FERMIX apparatus will focus on the realization of ultra-cold mixtures in mixed dimensions. Taking advantage on the difference of trapping potential experienced by the two species, it is indeed possible to engineer a species-selective trap to strongly confine one atomic cloud while keeping the other one almost free. The next and last chapter is dedicated to some perspectives opened by such systems.

Chapter 6

Effective long-range interactions in mixed dimensions

Contents

6.1 Scattering in mixed dimensions **141**
6.2 Mediated long-range interactions **145**
6.2.1 Mathematical framework 145
6.2.2 Effective interaction: general expression 147
6.2.3 Effective interaction for $\kappa_{\mathrm{CoM}} = 0$ 149
6.3 Proposal for an experimental realization **151**
6.3.1 Implementation of an optical lattice 151
6.3.2 Effective interaction between two layers 152
6.3.3 Coupled oscillations between two layers 154
6.4 Conclusions **157**

At the end of XIXth century, the English theologian Edwin Abbott imagined in a religious satire how different life would be if we were to live in a two dimensional world [Abbott 1884]. As it turned out, dimensionality plays indeed a crucial role for many physical phenomena, which have a completely different behavior in 2D or 1D as compared to the usual 3D situation. For instance, in reduced dimensions, thermal fluctuations destroy any long range order at finite temperature and prevent spontaneous symmetry breaking, as stated by the Mermin-Wagner theorem [Mermin and Wagner 1966] (see [Hadzibabic and Dalibard 2011] for a pedagogic approach). As a consequence, some phase transitions are forbidden, such as the ferro/para magnetic transition or Bose Einstein condensation. Instead, systems in reduced dimensions exhibit peculiar properties, such as the emergence of quasi-long range order through the so called Berezinskii-Kosterlitz-Thouless transition in two dimensions [Berezinskiĭ 1972, Kosterlitz and Thouless 1973, Minnhagen 1987] or the formation of specific states of matter, as epitomized in one dimension by the bosonic Tonks-Girardeau [Girardeau 1960] gase and the ferminionc Luttinger-Tonomaga liquid [Giamarchi 2004]. Moreover, we have shown in the previous chapters that the anisotropy of Weyl particles quasi-thermalization was also dimension dependent.

As mentionned in the introduction, cold atoms provide powerful tools for the experimental study of systems in reduced dimensions, allowing the realization of the previously mentioned

problems[1]. Furthermore, atomic systems allow for additional methods to tune the elastic interactions. Indeed, in experimental realization, systems in reduced dimensions are obtained from confined 3D systems. They therefore always display a finite transverse length $l_\perp$, much smaller than both the inter-particle spacing and thermal wavelength (such that transverse degrees of freedom remain frozen out) but much larger than the range of the van der Waals type interactions. Consequently, two-body interactions are unaffected by the confinement at short distances and the scattering length[2] a is then set by the 3D scattering length a_{3D} and the confinement length $l_\perp$ [Petrov and Shlyapnikov 2001]. This also results in so called *confinement induced resonances* [Olshanii 1998], which occur when a_{3D} approaches $l_\perp$ and allow to tune interactions within the plane from strongly repulsive to strongly attractive [Haller *et al.* 2010].

Cold atoms could also open the door to a supplementary approach considering *mixed dimensions*, where part of the system is confined in 0-, 1- or 2D while the other part evolves with more degrees of freedom. For instance, the scattering of matter waves off fixed disordered impurities, giving rise to the Anderson localization, can be seen as a 0D-3D system[Anderson 1958]. The interaction between electrons confined in a graphene layer with freely propagating photons comes down to a 2D-3D problem [Novoselov *et al.* 2005]. In more exotic situations, gravity can be pictured as an 11 dimensional quantity restricted to our 4 dimensional world [Maartens 2004]. Some of those problems can be simulated by the FERMIX experiment, as Potassium atoms can be confined in 2D planes by an optical lattice which will leave Lithium atoms mostly unaffected.

Effective interactions in mixed dimensions have been previously addressed in the literature. For instance, [Recati *et al.* 2005, Fuchs *et al.* 2007] showed that two localized impurities immersed in a 1D quantum liquid present Casimir-like interactions by calculating the action of the system, from which the free energy is derived. Their results were extended in [Schecter and Kamenev 2014] to the case of mobile impurities. Closer to our situation, the interactions between a 2D and a 3D ideal Fermi gas is described in [Nishida and Tan 2008], and extended in[Nishida 2010] to estimate with a diagrammatic approach the behavior of two 2D layers connected by an ideal 3D Fermi gas.

In this chapter, we propose an approach developed in collaboration with Georg Bruun and Zhigang Wu. We first describe 2D-3D interactions between a free atom and a confined one. We then turn to the calculation of the effective long range interaction between two 2D-planes immersed in a 3D cloud which can carry momentum from one plane to the other. Using the standard tools of atomic physics, we recover some of the results published in the literature and extend our predictions to unaddressed situations, as the 3D cloud is brought to the BEC side of the Feshbach resonance. Finally, we consider an experimental proposal to test the predictions

[1]The realization of Tonks Girardeau gas was first reported in 2004 [Paredes *et al.* 2004] and that of Luttinger liquid in 2005 [Moritz *et al.* 2005]. The BKT transition was observed in 2006 [Hadzibabic *et al.* 2006].

[2]The definition of the scattering length requires some precautions. In particular, the scattering amplitude tends to zero for low energies in 2D, in stark contrast with the 3D behavior, where it can be used to define the scattering length [Levinsen and Parish 2015].

using Potassium layers confined in an optical lattice and immersed in a 3D Lithium cloud. If a 2D layer is dragged away from equilibrium, the mediated long-range interaction should set in motion the neighboring planes and the measurement of the beat-note frequency of the oscillations provides an experimental access to the interlayer interactions.

6.1 Scattering in mixed dimensions

In this section, we introduce a description of a 2D-3D collision, where A-atoms are confined in a 2D plane $z_A = 0$ while B-atoms are free to move in three dimensions. As a first remark, we notice that the problem is equivalent to a 3D scattering event: while the system has five degrees of freedom, the conservation of momentum along the two dimensions of the confining plane reduces the number of independent quantities to three. As in a 3D scattering situation, we will be able to consider a scattering length to account for the interaction properties.

Notations

In this chapter, we will deal simultaneously with vectors in two and three dimensions. As often as possible, 3D vectors are written with roman letters $\mathbf{r}$ and 2D vectors with bold Greek letters $\boldsymbol{\rho}$. A 3D vector $\mathbf{v} \in \mathbb{R}^3$ can be decomposed as an in-plane vector $\boldsymbol{v}_\perp \in \mathbb{R}^2$ and a transverse component v_z. Conversely, a 2D vector $\boldsymbol{v}_\perp \in \mathbb{R}^2$ and an additional component v_z can be assembled to form a 3D vector $\mathbf{v} = \lceil \boldsymbol{v}_\perp, v_z \rfloor$.

We also also introduce the standard identities to avoid any ambiguity on the choice of normalization:

In 3D:

$$\sum_{\mathbf{k}} = \left(\frac{L}{2\pi}\right)^3 \int d^3\mathbf{k}$$

$$\mathrm{I_d} = \sum_{\mathbf{k}} |\mathbf{k}\rangle \langle \mathbf{k}| = \int d^3\mathbf{r}\ |\mathbf{r}\rangle \langle \mathbf{r}|$$

$$\langle \mathbf{k}|\ \mathbf{r}\rangle = \frac{1}{\sqrt{L^3}} \exp\left(i\mathbf{k}.\mathbf{r}\right)$$

$$\psi^\dagger(\mathbf{r}) = \frac{1}{L^{3/2}} \sum_{\mathbf{k}} e^{-i\mathbf{k}.\mathbf{r}} c^\dagger_{\mathbf{k}}$$

$$c^\dagger_{\mathbf{k}} = \frac{1}{L^{3/2}} \int d^3\mathbf{r}\, e^{i\mathbf{k}.\mathbf{r}} \psi^\dagger(\mathbf{r})$$

$$\tilde{U}(\mathbf{k}) = \int d^3\mathbf{r}\, e^{i\mathbf{k}.\mathbf{r}} U(\mathbf{r})$$

$$U(\mathbf{r}) = \frac{1}{(2\pi)^3} \int d^3\mathbf{k}\, e^{-i\mathbf{k}.\mathbf{r}} \tilde{U}(\mathbf{k})$$

In 2D:

$$\sum_{\boldsymbol{\kappa}} = \left(\frac{L}{2\pi}\right)^2 \int d^2\boldsymbol{\kappa}$$

$$\mathrm{I_d} = \sum_{\boldsymbol{\kappa}} |\boldsymbol{\kappa}\rangle \langle \boldsymbol{\kappa}| = \int d^2\boldsymbol{\rho}\ |\boldsymbol{\rho}\rangle \langle \boldsymbol{\rho}|$$

$$\langle \boldsymbol{\kappa}|\ \boldsymbol{\rho}\rangle = \frac{1}{\sqrt{L^2}} \exp\left(i\boldsymbol{\rho}.\boldsymbol{\kappa}\right)$$

$$\psi^\dagger(\boldsymbol{\rho}) = \frac{1}{\sqrt{L^2}} \sum_{\boldsymbol{\kappa}} e^{-i\boldsymbol{\rho}.\boldsymbol{\kappa}} c^\dagger_{\boldsymbol{\kappa}}$$

$$c^\dagger_{\boldsymbol{\kappa}} = \frac{1}{\sqrt{L^2}} \int d^2\boldsymbol{\rho}\, e^{i\boldsymbol{\rho}.\boldsymbol{\kappa}} \psi^\dagger(\boldsymbol{\rho}$$

$$\tilde{U}(\boldsymbol{\kappa}) = \int d^2\boldsymbol{\rho}\, e^{i\boldsymbol{\kappa}.\boldsymbol{\rho}} U(\boldsymbol{\rho})$$

$$U(\boldsymbol{\rho}) = \frac{1}{4\pi^2} \int d^2\boldsymbol{\kappa}\, e^{-i\boldsymbol{\kappa}.\boldsymbol{\rho}} \tilde{U}(\boldsymbol{\kappa})$$

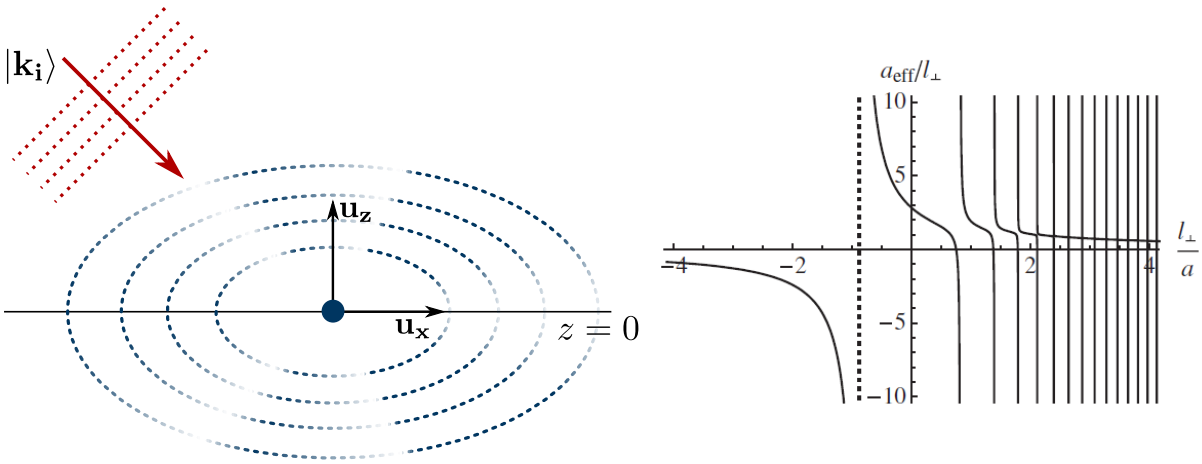

Figure 6.1: Scattering in mixed dimension. **Left**: At lowest order, the scattering eigenstates (6.9) are the superposition of a plane wave (in red) and an elliptical wave (in blue). The amplitude $f(\mathbf{k_i}, \mathbf{n})$ gives the amplitude of probability for incident particle to be scattered in direction $\mathbf{n}$ (represented by the shade of the blue dashed line). **Right**: Numerical estimation of the 2D-3D scattering length. Figure from [Nishida and Tan 2008].

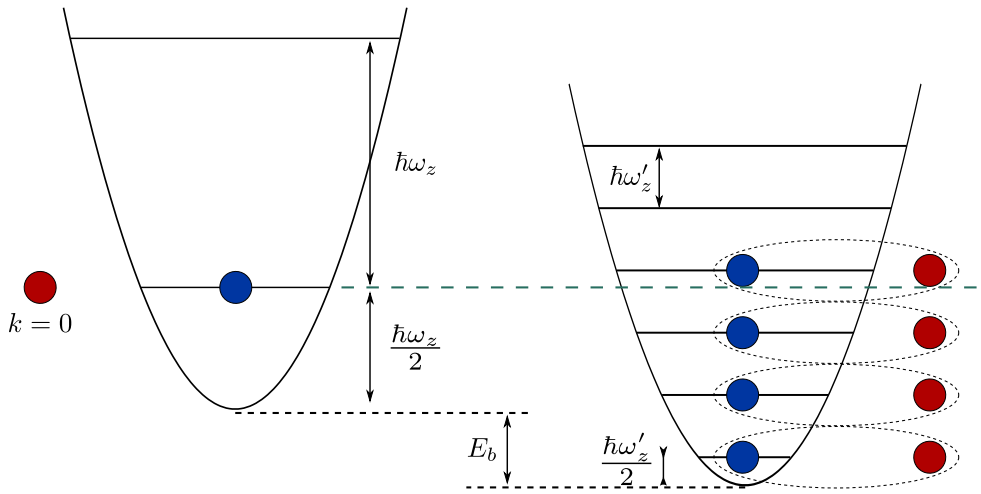

Figure 6.2: Resonance conditions for the $a_{2\text{D}-3\text{D}}$ scattering length. When the energy of the scattering state is equal to that of a bound state (see eq. (6.13), the scattering length diverges. Graphically, this corresponds to the crossing of the green dashed line with an energy level of the harmonic oscillator in the right-hand side of the picture. We denote $\omega'_z = \sqrt{m_B/\mu\omega_z}$ the trapping frequency of an 2D-3D molecule and $E_b = \frac{\hbar^2}{2\mu a^2_{\text{A}-\text{B}}}$ its binding energy.

Our approach follows the description of 3D-3D interactions presented in annex A.4.2. As a 2D and a 3D particles are interacting, the corresponding Hamiltonian takes the form:

$$H = \frac{1}{2m_B}\left(p_{B\perp}^2 + p_{Bz}^2\right) + \frac{p_{A\perp}^2}{2m_A} + V\left(\mathbf{r}_{B\perp} - \mathbf{r}_{A\perp}, z_B\right) \tag{6.1}$$

We introduce the center of mass quantities $(\mathbf{R}, \mathbf{P})$ and the relative coordinates $(\mathbf{r}, \mathbf{p})$ to rewrite the previous equation as:

$$H = \frac{P_\perp^2}{2M} + \left(\frac{p_\perp^2}{2\mu} + \frac{m_A}{m_A + m_B}\frac{p_z^2}{2\mu}\right) + V(\mathbf{r}) \tag{6.2a}$$

$$= H_{\text{CoM}}^{2D} + H_0 + V, \tag{6.2b}$$

where $M = m_A + m_B$ is the total mass and $\mu = m_A m_B/(m_A + m_B)$ is the reduced mass. The eigenstates of H_0 are 3D planes waves $|\mathbf{k}\rangle$ with anisotropic masses, such that the corresponding eigenenergies take the following form:

$$E_{\mathbf{k}}^0 = \frac{\hbar^2}{2\mu}(k_x^2 + k_y^2 + \frac{m_A}{m_A + m_B}k_z^2). \tag{6.3}$$

To each plane wave $|\mathbf{k}\rangle$ can be associated a scattering eingenstate $|\psi_{\mathbf{k}}^+\rangle$ with the same energy $E_{\mathbf{k}}^0$. These eigenstates satisfy the Lippman-Schwinger equation:

$$|\psi_{\mathbf{k}}^+\rangle = |\mathbf{k}\rangle + G_{0+}(E_{\mathbf{k}}^0)V|\psi_{\mathbf{k}}^+\rangle, \tag{6.4}$$

with $G_0(E_{\mathbf{k}}^0) = \left(E_{\mathbf{k}}^0 - H_0 + i\eta\right)^{-1}$ being the resolvent. The matrix elements of the resolvent are Green functions and can be estimated by introducing a closure relation over plane waves:

$$\langle\mathbf{r}|G_0(E_{\mathbf{k}}^0)|\mathbf{r}'\rangle \quad = \quad \frac{-\mu}{2\pi\hbar^2}\sqrt{\frac{m_A + m_B}{m_A}}\,\frac{\exp\left(i\widetilde{k}\times\hat{\rho}\right)}{\hat{\rho}}, \tag{6.5}$$

where we introduced the relative position $\boldsymbol{\rho} = \mathbf{r} - \mathbf{r}'$ and the deformed vectors

$$\tilde{\mathbf{k}} = \begin{bmatrix} k_x \\ k_y \\ \sqrt{\frac{m_A}{m_A+m_B}}k_z \end{bmatrix} \tag{6.6}$$

$$\widehat{\boldsymbol{\rho}} = \begin{bmatrix} \rho_x \\ \rho_y \\ \sqrt{\frac{m_A+m_B}{m_A}}\rho_z \end{bmatrix} \tag{6.7}$$

At distances large compared to the finite range b of the interaction potential, $\hat{\boldsymbol{\rho}} \simeq \hat{r} - \hat{\mathbf{n}}.\hat{\mathbf{r}}'$, where $\hat{\mathbf{n}} = \hat{\mathbf{r}}/\hat{r}$ is the direction of the deformed position $\hat{\mathbf{r}}$. As pictured in figure 6.1, the scattering eigenmodes appear as the superposition of a plane and an ellipsoidal wave:

$$\psi_{\mathbf{k}}^+(\mathbf{r}) = \frac{\exp(i\mathbf{k}.\mathbf{r})}{\sqrt{L^3}} + f(\mathbf{k}, \hat{\mathbf{n}})\,\frac{\exp\left(i\widetilde{k}\times\widehat{r}\right)}{\widehat{r}}, \tag{6.8}$$

where the contribution along the direction $\hat{\mathbf{n}}$ is set by the scattering amplitude f:

$$f(\mathbf{k},\hat{\mathbf{n}}) = -\frac{\mu}{2\pi\hbar^2}\sqrt{\frac{m_A+m_B}{m_A}}\int d^3\mathbf{r}'\ \exp\left(-i\widetilde{k}\times(\hat{\mathbf{n}}.\hat{\mathbf{r}}')\right)V\left(\mathbf{r}'\right)\psi^+_{\mathbf{k}}\left(\mathbf{r}'\right) \tag{6.9}$$

To simplify this expression, we restrict ourselves to the Born approximation and replace within first order of perturbation theory $\psi^+_{\mathbf{k}}(\mathbf{r}) \to \exp(i\mathbf{k}.\mathbf{r})/\sqrt{L^3}$ in the integral (6.9). At low energies, considering that the length scale set by the wave vector is much smaller than the range of the potential $k \ll b^{-1}$, the exponential factor in the integral (6.9) is close to 1 and the scattering amplitude takes the isotropic form of a 2D - 3D scattering length:

$$\lim_{k\to 0} f(k) = -\frac{a_{\text{2D-3D}}}{\sqrt{L^3}} = -\frac{1}{\sqrt{L^3}}\frac{\mu}{2\pi\hbar^2}\sqrt{\frac{m_A+m_B}{m_A}}\int d^3\mathbf{r}'\ V\left(\mathbf{r}'\right). \tag{6.10}$$

The optical theorem[3], stating the conservation of the flux during the scattering, allows us to express the scattering eigenstate as

$$\psi^+_{\mathbf{k}}(\mathbf{r}) = \frac{\exp(i\tilde{\mathbf{k}}.\hat{\mathbf{r}})}{\sqrt{L^3}} - \frac{a_{\text{2D-3D}}}{1+i\tilde{k}a_{\text{2D-3D}}}\frac{\exp\left(i\widetilde{k}\times\widehat{r}\right)}{\widehat{r}}, \tag{6.11}$$

where we used $\tilde{\mathbf{k}}.\hat{\mathbf{r}} = \mathbf{k}.\mathbf{r}$.

It is straightforward to verify that the wave functions (6.11) are also stationary solutions of Schrödinger equation when the scattering potential V is replaced by the pseudo potential:

$$U(\boldsymbol{\rho}) = g_{\text{2D-3D}} \times \delta(\boldsymbol{\rho})\frac{\partial}{\partial\hat{\rho}}(\hat{\rho}.), \tag{6.12}$$

where $g_{\text{2D-3D}} = a_{\text{2D-3D}} \times \sqrt{\frac{m_A}{m_A+m_B}}\frac{2\pi\hbar^2}{\mu}$. Together with (6.14), this expression shows that the 2D-3D coupling constant can be replaced by the 3D-3D coupling constant as long as the scattering length is small enough compared to other length scales. For regular functions, the pseudo potential (6.12) is equivalent to a Dirac potential $U(\boldsymbol{\rho}) = g_{\text{2D-3D}}\,\delta(\boldsymbol{\rho})$, which we will use in the following.

To estimate the value of the scattering length and relate it to the 3D-3D scattering length between A and B atoms, a more detailed description of the system is required [Massignan and Castin 2006]. A-atoms are not purely 2D, but rather confined to the ground state of an harmonic trap of frequency ω_z. At distances shorter than the transverse length $l_z = \sqrt{\hbar/m_A\omega_z}$, the confining potential becomes irrelevant and the interaction only depends on the standard A-B scattering length $a_{\text{A-B}}$. This short-distance condition constraints the long-distance behavior of scattering states, and the corresponding numerical integration has been reported in [Nishida and Tan 2008] (see Fig. 6.1). In particular, $a_{\text{2D-3D}}$ shows resonances when the energy of the open

[3]The optical theorem takes the form $4\pi|f|^2 = \text{Im}(f)$ (see annex A.4.3).

channel ($\hbar\omega_z/2$) coincides with the energy of a bound state in the closed channel [Lamporesi *et al.* 2010]:

$$\frac{\hbar\omega_z}{2} = \hbar\omega_z\sqrt{\frac{m_A}{m_A+m_B}}\left(n'+\frac{1}{2}\right) - \frac{\hbar^2}{2\mu a_{\mathrm{A-B}}^2}, \tag{6.13}$$

where the second term of the right-hand expression is the binding energy of the A-B Feshbach molecule (see annex A.4.5) and the first term results from the confinement of the molecule in potential $\mu\omega_z^2 r^2/2$ (see Fig. 6.2).

The width of the successive resonances decreases as l_z increases and $a_{\mathrm{2D-3D}}$ approaches the limit

$$a_{\mathrm{2D-3D}} \underset{\frac{l_z}{a_{\mathrm{A-B}}}\to\infty}{\longrightarrow} a_{\mathrm{A-B}}\sqrt{\frac{(m_A+m_B)}{m_A}}, \tag{6.14}$$

which we will use as a numerical estimate to lay down orders of magnitude.

6.2 Mediated long-range interactions

Let us consider two parallel planes of A-atoms (Potassium in our case) separated by a distance Δz. Assuming that there exist only contact interactions, the two layers can naturally not interact with one another. An intermediate 3D cloud of B-atoms (Lithium) changes this situation: excitations can now propagate through the B cloud and carry momentum from one layer to the other. In other words, the presence of a 3D cloud allows for a mediated long range interaction between the 2D planes (see figure 6.3). In this section, we calculate the effective long-range potential experienced by A-atoms in the presence of a B-cloud.

6.2.1 Mathematical framework

Neglecting many body effects within the planes, we consider two single A impurities confined in facing 2D planes and interacting with the B cloud. The Hamiltonian of the system can be written as:

$$H = H_A + H_B + V, \tag{6.15}$$

where H_A (resp. H_B) accounts for A-atoms (resp. B-atoms) and $V = V_1^{\mathrm{2D-3D}} + V_2^{\mathrm{2D-3D}}$ denotes the local interaction between each 2D plane and the 3D cloud. Each contact interaction can be described as:

$$V_\alpha^{\mathrm{2D-3D}} = \int d^3\mathbf{r}d^2\boldsymbol{\rho}\, U_\alpha\left(\mathbf{r}_\parallel - \boldsymbol{\rho}\right)\delta\left(r_\perp - z_\alpha\right)\psi_B^\dagger(\mathbf{r})\psi_{A,\alpha}^\dagger(\boldsymbol{\rho})\psi_{A,\alpha}(\boldsymbol{\rho})\psi_B(\mathbf{r}), \tag{6.16}$$

where $\psi_B^\dagger(\mathbf{r})$ ($\psi_B(\mathbf{r})$) creates (annihilates) a B-atom at position $\mathbf{r}$ and $\psi_{A,\alpha}^\dagger(\boldsymbol{\rho})$ ($\psi_{A,\alpha}(\boldsymbol{\rho})$) creates (annihilates) an A-atom at position $\boldsymbol{\rho}$ in the layer α. We consider only a weak coupling between

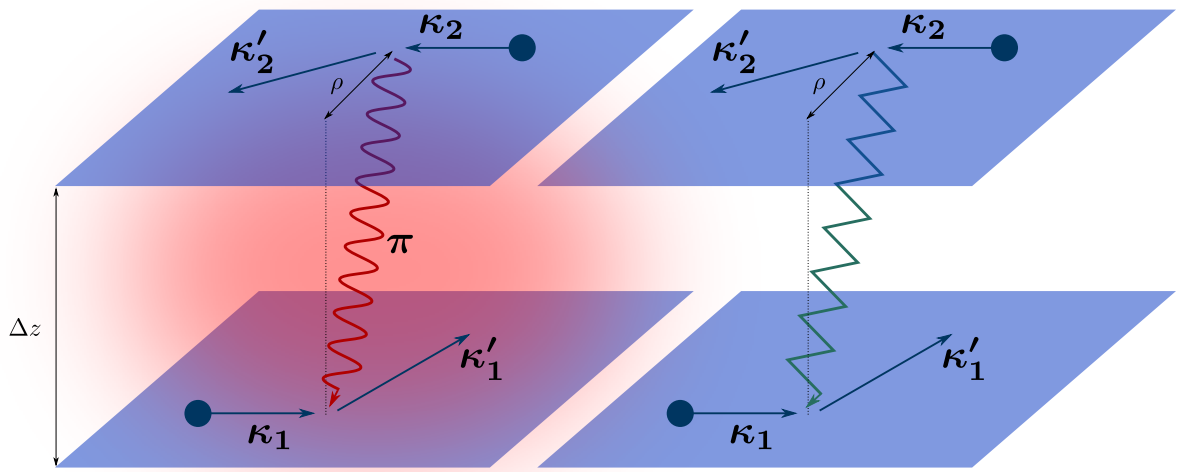

Figure 6.3: Effective long range interaction. **Left**: two 2D planes of A atoms (blue) separated by Δz can exchange momentum by creating and absorbing excitations in an intermediate 3D gas of B atoms (red). **Right**: the previous situation can be equivalent to a direct long-range interaction between the two planes (green broken line), in the absence of intermediate B-atoms.

the 2D and 3D species, which we describe using the pseudo potential $U_\alpha(\boldsymbol{\rho}) = g_{2\mathrm{D}-3\mathrm{D}}\,\delta(\boldsymbol{\rho})$ introduced before.

The situation we aim to describe corresponds to scattering events of the form:

$$|i\rangle = |\text{ground}\rangle \otimes |\boldsymbol{\kappa}_1\rangle \otimes |\boldsymbol{\kappa}_2\rangle \to |f\rangle = |\text{ground}\rangle \otimes |\boldsymbol{\kappa}_1'\rangle \otimes |\boldsymbol{\kappa}_2'\rangle\,, \tag{6.17}$$

where states are expressed in the basis

$$|\text{3D B} - \text{atoms}\rangle \otimes |\text{2D A} - \text{atoms (plane 1)}\rangle \otimes |\text{2D A} - \text{atoms (plane 2)}\rangle\,. \tag{6.18}$$

To parameterize this transition, we introduce the center of mass momentum $\boldsymbol{\kappa}_{\mathrm{CoM}} = (\boldsymbol{\kappa}_1 + \boldsymbol{\kappa}_2)/2$, conserved during the process. We note with $\boldsymbol{\pi}$ the exchanged momentum

$$\boldsymbol{\pi} = \boldsymbol{\kappa}_1' - \boldsymbol{\kappa}_1 = \boldsymbol{\kappa}_2 - \boldsymbol{\kappa}_2', \tag{6.19}$$

which is related to the energy transferred from one plane to the other:

$$\Delta E = E_{\kappa_1'} - E_{\kappa_1} = E_{\kappa_2} - E_{\kappa_2'} = \frac{\hbar^2}{2m_A}\boldsymbol{\kappa}_{\mathrm{CoM}}.\boldsymbol{\pi}. \tag{6.20}$$

Real case		Effective case
$H = H_A + H_B + V$		$H_{\text{eq}} = H_A + V_{\text{eff}}$
$\downarrow$		$\uparrow$
$T_{if} = \langle f \vert V G_0 V \vert i \rangle$	$\Longleftrightarrow$	$T_{if} = \langle f \vert V_{\text{eff}} \vert i \rangle$

Table 6.1: Definition of the effective long range interaction V_{eff}. We define the effective interaction between two A-atoms as the potential V_{eff} that leads to the same transition amplitude from the initial state $|i\rangle$ to the final state $|f\rangle$ as the first contributing order of the mixed dimensional case (i.e. second order, as shown in section 6.2.2), where the interaction is mediated by the B-cloud.

Scattering properties can be addressed using the S matrix, which expresses this transition amplitude as the overlap between the initial and final states subjected to the time evolution operator $U_I(t_1, t_2) = \exp(-iV(t_2 - t_1)/\hbar)$:

$$S_{if} = \langle f | U_I(+\infty, -\infty) | i \rangle = \delta_{f,i} - 2i\pi\delta(E_f - E_i) T_{if} \tag{6.21}$$

The T matrix can in turn be expanded through the Dyson equation

$$T = V + VG_0V + ..., \tag{6.22}$$

where the resolvent G_0 is given by

$$G_0(z) = \frac{1}{z - (H_A + H_B)}. \tag{6.23}$$

We define the effective long range interaction as the potential V_{eff} which gives rise to the same T matrix within the Born approximation as the real contact potential V up to first contributing order (see table 6.1).

6.2.2 Effective interaction: general expression

We need to estimate the leading order in the expansion of the T matrix. Since we consider scattering events in which the Lithium cloud is eventually and initially in the same state, the first order $T = V$ does not contribute and we must therefore estimate:

$$T_{if} = \langle f | VG_0(E_{\kappa_1} + E_{\kappa_2}) V | i \rangle . \tag{6.24}$$

We calculate only Hartree terms, describing to interlayer exchange interactions, and neglect Fock terms, which would correspond to intra-layer forward scattering. The second order of the

matrix element T_{if} is the sum of two contributions:

$$T_{if} = \langle f| V_1^{2D-3D} G_0 \left(E_{\kappa_1} + E_{\kappa_2}\right) V_2^{2D-3D} |i\rangle + \langle f| V_2^{2D-3D} G_0 \left(E_{\kappa_1} + E_{\kappa_2}\right) V_1^{2D-3D} |i\rangle . \tag{6.25}$$

This matrix element is related to the density-density response function of the 3D B-cloud and can be expressed through its compressibility χ_B:

$$T_{if} = \frac{1}{2\pi L^2} g_{2D-3D}^2 \times \int dk_z \, e^{-ik_z \Delta z} \, \chi_B \left(\left[\begin{array}{c} \boldsymbol{\pi} \\ k_z \end{array} \right], \frac{\hbar}{2m} \boldsymbol{\kappa}_{\mathrm{CoM}} . \boldsymbol{\pi} \right), \tag{6.26}$$

where the center of mass momentum $\boldsymbol{\kappa}_{\mathrm{CoM}}$ and the exchanged momentum $\boldsymbol{\pi}$ were already defined above. We will now briefly present the main steps of the calculation.

- Introducing closure relations, we isolate the B-cloud so as to express both terms of (6.25) as matrix elements of an operator A acting only on the 3D gas. Taking $T_{if} = T_{if}^{(1)} + T_{if}^{(2)}$, we write for instance:

$$T_{if}^{(1)} = \langle B : \mathbf{0}| M |B : \mathbf{0}\rangle \tag{6.27a}$$

$$M = \langle \boldsymbol{\kappa'}_1| V_1 |\boldsymbol{\kappa}_1\rangle G_0^{(B)} (\Delta E) \langle \boldsymbol{\kappa'}_2| V_2 |\boldsymbol{\kappa}_2\rangle \tag{6.27b}$$

  where $G_0^{(B)}(z) = \frac{1}{\Delta E - H_B}$. The objective is then to sum over all intermediate states of the mediating B-cloud.

- Matrix elements of interspecies potentials V_α can be expressed so as to explicitly sum over all transverse momentums:

$$\langle \boldsymbol{\kappa'}_1| V_1 |\boldsymbol{\kappa}_1\rangle = \frac{1}{2\pi L^2} \tilde{U}_1 \left(\boldsymbol{\kappa'}_1 - \boldsymbol{\kappa}_1\right) \int dp_z \, e^{-ip_z z_1} \left(\int d^3\mathbf{r} \, e^{i\lceil \boldsymbol{\kappa}_1 - \boldsymbol{\kappa'}_1, p_z \rfloor . \mathbf{r}} \psi_B^\dagger(\mathbf{r}) \psi_B(\mathbf{r}) \right) \tag{6.28}$$

- Because of momentum conservation, the T matrix element (6.25) can be simplified to:

$$\begin{aligned} T_{if} = & \frac{1}{2\pi L^5} \int dp_z \, e^{-ip_z(z_1 - z_2)} \tilde{U}_2(-\boldsymbol{\pi}) \tilde{U}_1(\boldsymbol{\pi}) \\ & \times \langle 0| \left(F_{-\mathbf{p}} \widehat{G_0^{(B)}} (\Delta E) F_{\mathbf{p}} + F_{\mathbf{p}} \widehat{G_0^{(B)}} (\Delta E) F_{-\mathbf{p}} \right) |0\rangle \end{aligned} \tag{6.29}$$

  where $F_{\mathbf{p}} = \int d^3\mathbf{r} \, e^{i\mathbf{p}.\mathbf{r}} \psi_B^\dagger(\mathbf{r}) \psi_B(\mathbf{r})$ with $\mathbf{p} = \lceil \boldsymbol{\pi}, p_z \rfloor$.

- The operator appearing in the previous expression can be directly related to the compressibility of the B-cloud, which we define in the following way: if a system is perturbed by

an excitation $w(\mathbf{r},t) = \mu \cos(\mathbf{k}.\mathbf{r} - \omega t)$, its density response is given by:

$$\rho_{\mathbf{k}} = \frac{1}{L^3} \int d^3\mathbf{r}\, e^{-i\mathbf{k}.\mathbf{r}} \left\langle \psi^\dagger(\mathbf{r})\psi(\mathbf{r}) \right\rangle \tag{6.30a}$$

$$= \frac{1}{2}\mu\chi(\mathbf{k},\omega)e^{-i\omega t}. \tag{6.30b}$$

Expressing the time evolution of the system initially at rest under the influence of W, we can show that $\chi(\mathbf{p}, \Delta E/\hbar) = L^{-3} \langle 0| \left(F_{-\mathbf{p}} \widehat{G_0}(\Delta E) F_{\mathbf{p}} + F_{\mathbf{p}} \widehat{G_0}(\Delta E) F_{-\mathbf{p}} \right) |0\rangle$, hence the expression (6.26).

According to our definition of the effective long range potential, the expression (6.26) corresponds to the matrix element $\langle \boldsymbol{\kappa'}_1, \boldsymbol{\kappa'}_2 | V_{\text{eff}} | \boldsymbol{\kappa}_1, \boldsymbol{\kappa}_2 \rangle$. To express the effective potential as a function of the inter-particle distance in real space, we apply a Fourier-transform to this expression:

$$V_{\text{eff}}(\boldsymbol{\kappa}_{\text{CoM}}, \boldsymbol{\rho}) = \left(\frac{L}{2\pi}\right)^2 \times \int d^2\boldsymbol{\pi}\, T_{if}\, e^{-i\boldsymbol{\pi}.\boldsymbol{\rho}} \tag{6.31a}$$

$$= \frac{1}{8\pi^3} g_{2D-3D}^2 \times \int d^3\mathbf{k}\, e^{-i(\mathbf{k}_\perp.\boldsymbol{\rho} + k_z.\Delta z)}\, \chi_B\left(\mathbf{k}, \frac{\hbar}{2m}\mathbf{k}_\perp.\boldsymbol{\kappa}_{\text{CoM}}\right) \tag{6.31b}$$

6.2.3 Effective interaction for $\kappa_{\text{CoM}} = 0$

The existence of a favored frame, in which the 3D cloud stands still, breaks the Galilean invariance of the problem. This results in the explicit dependence of the effective potential (6.31) on the center of mass momentum $\boldsymbol{\kappa}_{\text{CoM}}$ through the exchanged energy $\Delta E = \frac{\hbar^2}{2m}\mathbf{k}_\perp.\boldsymbol{\kappa}_{\text{CoM}}$, which sets the relevant frequency in the compressibility.

In order to get a simplified picture, we first consider the case where the center of mass of the two Potassium atom system is at rest $\boldsymbol{\kappa}_{\text{CoM}} = 0$. The effective potential is then given by the Fourier transformation of the compressibility at zero frequency:

$$V_{\text{eff}}(\boldsymbol{\rho}) = \frac{1}{8\pi^3} g_{2D-3D}^2 \times \int d^3\mathbf{k}\, \exp\left(-i\mathbf{k}.\begin{bmatrix} \boldsymbol{\rho} \\ \Delta z \end{bmatrix}\right) \chi_B(\mathbf{k}, 0) \tag{6.32}$$

Ideal 3D Fermi gas

If the 3D B-cloud is an ideal Fermi gas, the compressibility is well known [Giuliani and Vignale 2005] and the long range potential in real space takes the same form as in the Ruderman-Kittel-

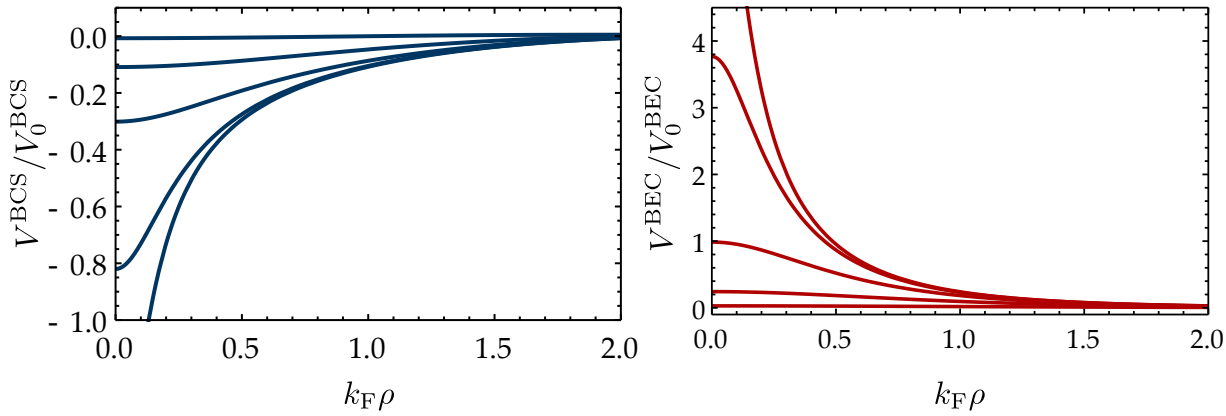

Figure 6.4: Effective long range interaction. **Left**: the 3D gas is a Bose-Einstein condensate of dimers with healing length ξ and the interaction takes the form of a Yukawa potential (6.38). We normalize the potential with $V_0^{\rm BEC} = -g_{2D-3D}^2 n_D m_D/\pi\hbar^2\xi$. **Right**: the 3D gas is an ideal Fermi gas with Fermi wave vector k_F and the interaction takes the form of a RKKY potential (6.34). We normalize the potential with $V_0^{\rm FG} = g_{2D-3D}^2 m_B k_F^4/\pi^3\hbar^2$.

Kasuya-Yosida (RKKY) interaction:

$$\chi_{\rm FG}(\mathbf{k},0) = -\frac{mk_F}{2\pi^2\hbar^2}\left(\frac{1}{2}+\frac{k^2-4k_F^2}{8k_Fk}\log\left|\frac{k-2k_F}{k+2k_F}\right|\right), \tag{6.33}$$

$$V_{\rm eff}^{\rm FG}(\boldsymbol{\rho}) = g_{2D-3D}^2\frac{m_Bk_F^4}{\pi^3\hbar^2}\times\frac{2k_FR\cos(2k_FR)-\sin(2k_FR)}{(2k_FR)^4}, \tag{6.34}$$

where $k_F = \left(6\pi^2 n_B\right)^{1/3}$ is the Fermi wave vector of the 3D B-cloud and $R = \sqrt{\rho^2+\Delta z^2}$ the distance between A-atoms. The expression is the same as the one derived in [Nishida 2010] for a weak 2D-3D coupling.

3D Bose-Einstein condensate

On the BEC side of the crossover, 3D B-fermions form a condensate of strongly bound dimers. Accordingly, the 2D-3D scattering length (6.14) should account for the interaction between A-atoms and B-dimers:

$$a_{\rm A-B} \to a_{\rm A-D} \quad \& \quad m_B \to m_D = 2m_B. \tag{6.35}$$

As long as the interspecies scattering length remains small compared to the size of the molecules[4], the atom-dimer scattering length can be approximated by the first order Born approximation [Zhang *et al.* 2014]:

$$a_{\rm A-D} = 4\frac{m_A+m_B}{m_A+2m_B}\times a_{A-B}, \tag{6.36}$$

[4] i.e. $a_{\rm 2D-3D} \ll a_{\rm B}$, where $a_{\rm B}$ is the intraspecies scattering length of B.

by estimating the interaction energy of a particle A with the cloud of dimers to $g_{\mathrm{A-D}} n_D = g_{\mathrm{A-B}} n_B$.

Using the Bogoliubov description, the compressibility of the B-gas can be expressed analytically [Pethick and Smith 2008] and the long range interaction (6.31) takes the form of a Yukawa potential:

$$\chi_{\mathrm{BEC}}(\mathbf{k}, 0) = -\frac{n_{\mathrm{D}}}{m_{\mathrm{D}} c^2} \frac{1}{1 + \frac{1}{2}\xi^2 k^2}, \tag{6.37}$$

$$V_{\mathrm{eff}}^{\mathrm{BEC}}(\boldsymbol{\rho}) = -g_{2D-3D}^2 \frac{n_D m_D}{\pi \hbar^2 \xi} \times \frac{\exp\left(-\sqrt{2}|R|/\xi\right)}{|R|/\xi}, \tag{6.38}$$

where $n_{\mathrm{D}} = n_B/2$, $m_{\mathrm{D}} = 2m_B$ are the density and mass of the molecular dimers, $c = \sqrt{g_{\mathrm{D}} n_{\mathrm{D}}/m_{\mathrm{D}}}$ is the speed of sound in the condensate and $\xi = \hbar/\sqrt{2} m_B c$ is the corresponding healing length. The dimer-dimer coupling constant g_D can be related to the atom-atom coupling constant as $g_D = 0.6\, g_B$ [Petrov *et al.* 2005].

The calculation in the unitary limit is more challenging, as the compressibility of the B-cloud is not analytical anymore. An estimate could perhaps be obtained from the Fourier transform in real space of the numerical results reported in [Kinnunen and Bruun 2015] and will be the subject of a future work.

6.3 Proposal for an experimental realization

Once a double degenerate mixture of ^{6}Li and ^{40}K is obtained, the FERMIX experiment should be able to address the study of mixed dimensional systems by confining one species in an optical lattice and keeping the other species almost free. In order to take advantage of the weaker mass of Lithium, we have chosen to trap Potassium atoms in the lattice.

In this section, we will consider the impact of the effective long-range interaction on two coupled 2D layers. We first summarize the properties of the optical setup constructed to generate the required lattice. We then extend the description of the effective potential to account for the interaction between the two layers. Finally, we present a proposal that would enable us to test the previous predictions against experimental results.

6.3.1 Implementation of an optical lattice

The optical setup described in this section has been realized and tested by Mihail Rabinovich. A preliminary signal has been obtained on the atoms, but the setup is not fully implemented yet.

		^{6}Li	^{40}K
Trap depth	U_0 [μK]	6.4	39
Transverse freq.	$\omega_\perp/2\pi$ [Hz]	440	380
Axial freq.	$\omega_\parallel/2\pi$ [kHz]	170	160
Tunneling time	τ	~6 µs	~60 s
Axial temperature	$\hbar\omega_\parallel/k_B$ [µK]	7.9	7.5
Fermi temperature	T_F [µK]	-	1.8
Heating rate	$\dot{T}$ [µK/s]	0.053	0.19

Table 6.2: Expected trapping parameters in the optical lattice, assuming a beam power of 150 mW and a waist of 80 μm. The Fermi temperature of Potassium is estimated for 5×10^3 atoms per plane. The tunneling time is estimated with expression (6.39) for ^{40}K and by the truncation of the central equation to 40 terms for ^{6}Li.

The laser source is a commercial photodiode lasing up to 150 mW at 808 nm. The diode is installed in a home-made mount with a grating in Littrow configuration, reducing its linewidth below 1 MHz. A tapered amplifier increases the optical power and an AOM allows a fast switching of the beam. At the output of a polarization maintaining fiber, this system delivers up to 500 mW of optical power. Technical details are presented in annex A.6.

To generate the optical lattice, the light will be send along the same direction as the optical dipole trap ($\mathbf{x}$ axis) and retro-reflected. The resulting potentials for ^{6}Li and ^{40}K are presented in table 6.2. In the ground state, the tunneling time is related to the hopping constant $\tau = \hbar/4J$. In the tight binding limit,

$$\frac{J}{E_r} \simeq \frac{4}{\sqrt{\pi}} \left(\frac{V_0}{E_r}\right) \exp\left(-2\sqrt{\frac{V_0}{E_r}}\right), \tag{6.39}$$

where E_r is the recoil energy and V_0 the lattice depth [Dalibard 2013]. For Potassium, the associated time scale is very large, and atoms will essentially remain in the ground state of each lattice site since $T_\parallel > T_\mathrm{F}$. By contrast, Lithium displays a short tunneling time, which means that atoms will hop from one site to the other, as an almost free gas with an effective mass $m^* = 1.22\, m_\mathrm{Li}$.

6.3.2 Effective interaction between two layers

We now consider two clouds confined in two separated layers generated by the setup described in the above section, with 2D densities $n_{1,2}(\boldsymbol{\rho})$. According to our previous calculations (6.34-6.38), the range of the potential, given by the healing length ξ on the BEC side of the cross over and by the Fermi wave vector k_F on the BCS side, is small compared to the size of the 2D plane set by the trapping frequency. We can therefore assume that the atomic density with a significant contribution to the interaction energy is almost constant over the range of the

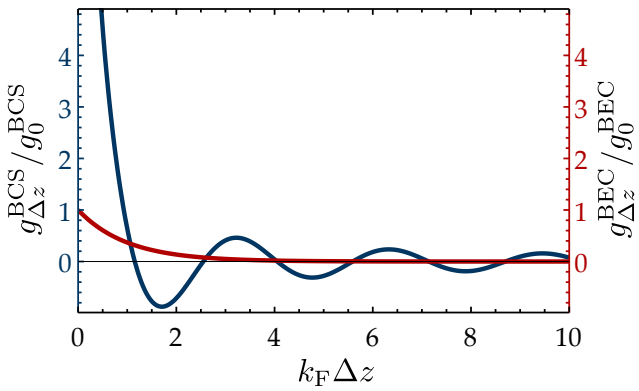

Figure 6.5: Dependence of the coupling constant $g_{\Delta z}$ characterizing the effective long range interaction as a function of the distance Δz between the two planes. We note k_F the wave-vector of the 3D mediating gas. In blue, the 3D gas in an ideal Fermi gas and we normalize the coupling constant by $g_0^{\mathrm{FG}} = g_{2D-3D}^2 \times mk_F^2/4\pi^2\hbar^2$. In red, the 3D gas is a Bose-Einstein condensate of molecules, with sound velocity c and we normalize the coupling constant by $g_0^{\mathrm{BEC}} = -g_{2D-3D}^2 n_D/\hbar c$.

potential:

$$\int d^2\boldsymbol{\rho}_1\, n_1(\boldsymbol{\rho}_1)\left(\int d^2\boldsymbol{\rho}_2\, V_{\mathrm{eff}}(\boldsymbol{\rho}_1,\boldsymbol{\rho}_2) n_2(\boldsymbol{\rho}_2)\right) \simeq \int d^2\boldsymbol{\rho}\, n_1(\boldsymbol{\rho}) n_2(\boldsymbol{\rho}) \times g_{\mathrm{eff}}. \tag{6.40}$$

In this approximation, the effective potential (6.31) can be simplified further:

$$g_{\mathrm{eff}}(\boldsymbol{\kappa}_{\mathrm{CoM}}) = \int d\boldsymbol{\rho}\, V_{\mathrm{eff}}(\boldsymbol{\kappa}_{\mathrm{CoM}}, \boldsymbol{\rho}) \tag{6.41a}$$

$$= \frac{g_{2D-3D}^2}{8\pi^3} \times \int d^3\mathbf{k}\, e^{-ik_Z\Delta z}\left(\int d^2\boldsymbol{\rho} e^{-i\mathbf{k}_\perp.\boldsymbol{\rho}}\right)\chi_B\left(\mathbf{k}, \frac{\hbar}{2m}\mathbf{k}_\perp.\boldsymbol{\kappa}_{\mathrm{CoM}}\right) \tag{6.41b}$$

$$= \frac{g_{2D-3D}^2}{2\pi} \times \int dk_z\, e^{-ik_Z\Delta z}\,\chi_B\left(k_z\mathbf{e}_z, 0\right) = g_{\Delta z} \tag{6.41c}$$

Remarkably, the coupling constant $g_{\Delta z}$ does not depend on the center of mass momentum. Its expression can be evaluated on both sides of the BEC-BCS cross over:

$$g_{\Delta z}^{\mathrm{FG}} = g_{2D-3D}^2 \frac{mk_F^2}{4\pi^2\hbar^2} \times \frac{(2k_F\Delta z)\cos(2k_F\Delta z) - \sin(2k_F\Delta z) + (2k_F\Delta z)^2\left(\mathrm{si}(2k_F\Delta z) - \pi/2\right)}{(2k_F\Delta z)^2}, \tag{6.42}$$

$$g_{\Delta z}^{\mathrm{BEC}} = -g_{2D-3D}^2 \frac{n_D}{\hbar c} \times \exp\left(-\sqrt{2}\frac{\Delta z}{\xi}\right), \tag{6.43}$$

where $\mathrm{si}(x) = \int_0^x dt\, \frac{\sin(t)}{t}$ is the sine integral function. The behavior of these two terms is depicted in figure 6.5.

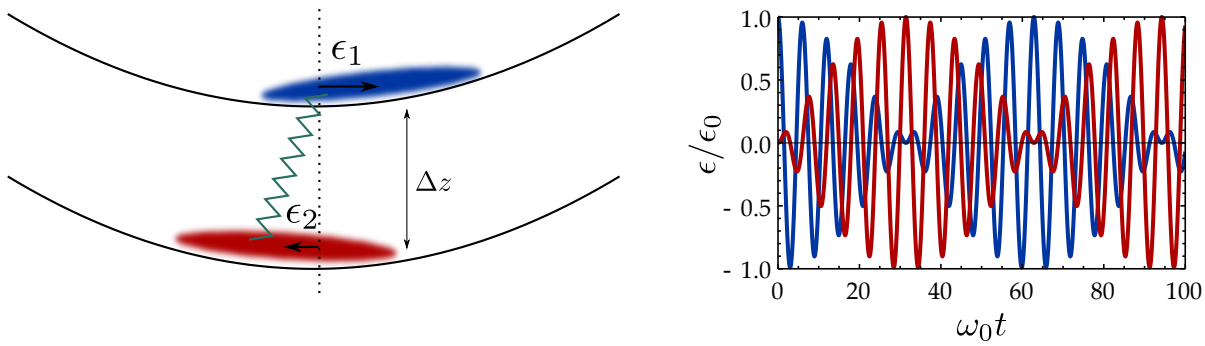

Figure 6.6: Coupled oscillations induced by the effective interaction. **Left**: The blue cloud is initially dragged to a distance ϵ_0 from the trap center and released. In absence of interactions, its center of mass would simply oscillate at the trap frequency. However, the interplane interaction transfers energy from the first plane to the second one, initially at rest. In this situation, the motion of the unexcited plane is a proof of the existence of a long range interaction and the beating period provides a measurement of the coupling strength. **Right**: time evolution of ϵ_1 (blue) and ϵ_2 (red), as given by classical equation of motion (6.48) with $\omega_A = 1.1 \times \omega_0$. Initially, $\epsilon_1 = \epsilon_0$ and $\epsilon_2 = 0$.

6.3.3 Coupled oscillations between two layers

One way to test experimentally the previous results would be to measure the in-plane oscillation frequencies of two Potassium layers[5] interacting through a 3D Lithium cloud. This method is inspired by [Matveeva *et al.* 2011] in which such a situation is considered for dipolar long range interactions, and has been proven to be very a powerful tool for measuring small couplings [Delehaye *et al.* 2015].

In the optical lattice, the 2D planes of Potassium are not only strongly confined in the axial direction **z**, but also weakly in the transverse plane. Dragged away from equilibrium, for instance by focusing a laser close to the lattice so as to deform the optical potential, a Potassium pancake will oscillate in the (**x**,**y**) plane. Because of the coupling between consecutive planes, the oscillation of one layer will transfer energy to and induce motion among its neighbors[6]. The coupled oscillations' frequency depends on the strength of the coupling and thus provides an experimental access to test of our predictions.

To estimate this frequency, we consider the situation pictured in figure 6.6 with two 2D clouds filled with N particles, separated by Δz and confined in the (**x**,**y**) plane by the potential:

$$V_{\text{trap}} = \frac{1}{2} m\omega_0^2 \left(x^2 + y^2\right). \tag{6.44}$$

We drag the system away from the trap center, for instance along **x**, and release it. We denote

[5] In this section, we restrict the analysis to two interacting layers, but it could be extended to describe the behavior of several coupled planes stacked on the 1D lattice sites. Rather than a modulation of the oscillation amplitude, the long-range coupling would then result in the propagation of transverse oscillation along the pile.

[6] In an equivalent picture, the coupling between planes lifts the degeneracy of individual oscillators, which results in a frequency shift with respect to the bare oscillations.

ϵ_i the small displacement of the center of mass of cloud i. The oscillation frequency can be deduced from the expression of the energy of the system. We first calculate the interaction energy between both clouds :

$$E_{\text{int}} = \int d^2\mathbf{r_1} d^2\mathbf{r_2} \left(V\left(\mathbf{r_1} - \mathbf{r_2}\right) n_1\left(\mathbf{r_1} - \epsilon_1 \mathbf{u_x}\right) n_2\left(\mathbf{r_2} - \epsilon_2 \mathbf{u_x}\right)\right) \tag{6.45a}$$

$$= E_{\text{int}}^{\epsilon=0} + I\epsilon_1\epsilon_2 - \frac{1}{2} I\left(\epsilon_1^2 + \epsilon_2^2\right), \tag{6.45b}$$

where we used a Taylor expansion of n_i to the second order and introduced

$$I = \int d^2\boldsymbol{\rho}_1\, d^2\boldsymbol{\rho}_2 \left(V_{\text{eff}}\left(\boldsymbol{\rho}_1 - \boldsymbol{\rho}_2\right) \frac{\partial n_1}{\partial x} \frac{\partial n_2}{\partial x} \right). \tag{6.46}$$

The previous integral can be further simplified using expression (6.41): assuming that Potassium atoms constitute an ideal Fermi gas within each plane, (6.46) simply becomes:

$$I = g_{\Delta z} N \frac{m^2\omega_0^2}{2\pi\hbar^2}. \tag{6.47}$$

The total energy of the system corresponds to the sum of the kinetic, potential and interaction energies:

$$\Delta E(\boldsymbol{\epsilon}) = E_0^{\epsilon} + I\,\epsilon_1\epsilon_2 - \frac{1}{2} I\left(\epsilon_1^2 + \epsilon_2^2\right), \tag{6.48}$$

where $\Delta E(\boldsymbol{\epsilon})$ is the increase of energy due to the initial excitation and E_0^{ϵ} is the bare energy in absence of interaction:

$$E_0^{\epsilon} = \frac{1}{2} N m \dot{\epsilon_1}^2 + \frac{1}{2} N m \dot{\epsilon_2}^2 + \frac{1}{2} N m \omega_0^2 \epsilon_1^2 + \frac{1}{2} N m \omega_0^2 \epsilon_2^2. \tag{6.49}$$

In order to further reduce the problem, we consider separately the two eigenmodes of the oscillations. The energy of the symmetric solution $\epsilon_1 = \epsilon_2$ corresponds to a harmonic oscillator with frequency ω_S independent of I, while that of the anti-symmetric solution $\epsilon_1 = -\epsilon_2$ explicitly relies on the interaction:

$$\omega_S = \omega_0 \tag{6.50}$$

$$\omega_A = \omega_0 \sqrt{1 - \frac{m g_{\Delta z}}{\pi\hbar^2}} \tag{6.51}$$

The corresponding values are summarized in table 6.3. Within experimentally realistic parameters, on the BEC side of the resonance, the symmetric and anti-symmetric modes are expected to show a frequency difference of 11 Hz, which should be accessible through measurements [Ferrier-Barbut *et al.* 2014]. By contrast, on the BCS side, the frequency difference is much smaller, rendering the measurement of the effects due to long range interactions difficult.

Besides the direct measurement of the oscillation frequencies, the coupled motion provides an easier way to test our predictions. If only one plane is initially excited, the initially imparted energy will be transferred back and forth between the two oscillators (see Fig. 6.6). The ampli-

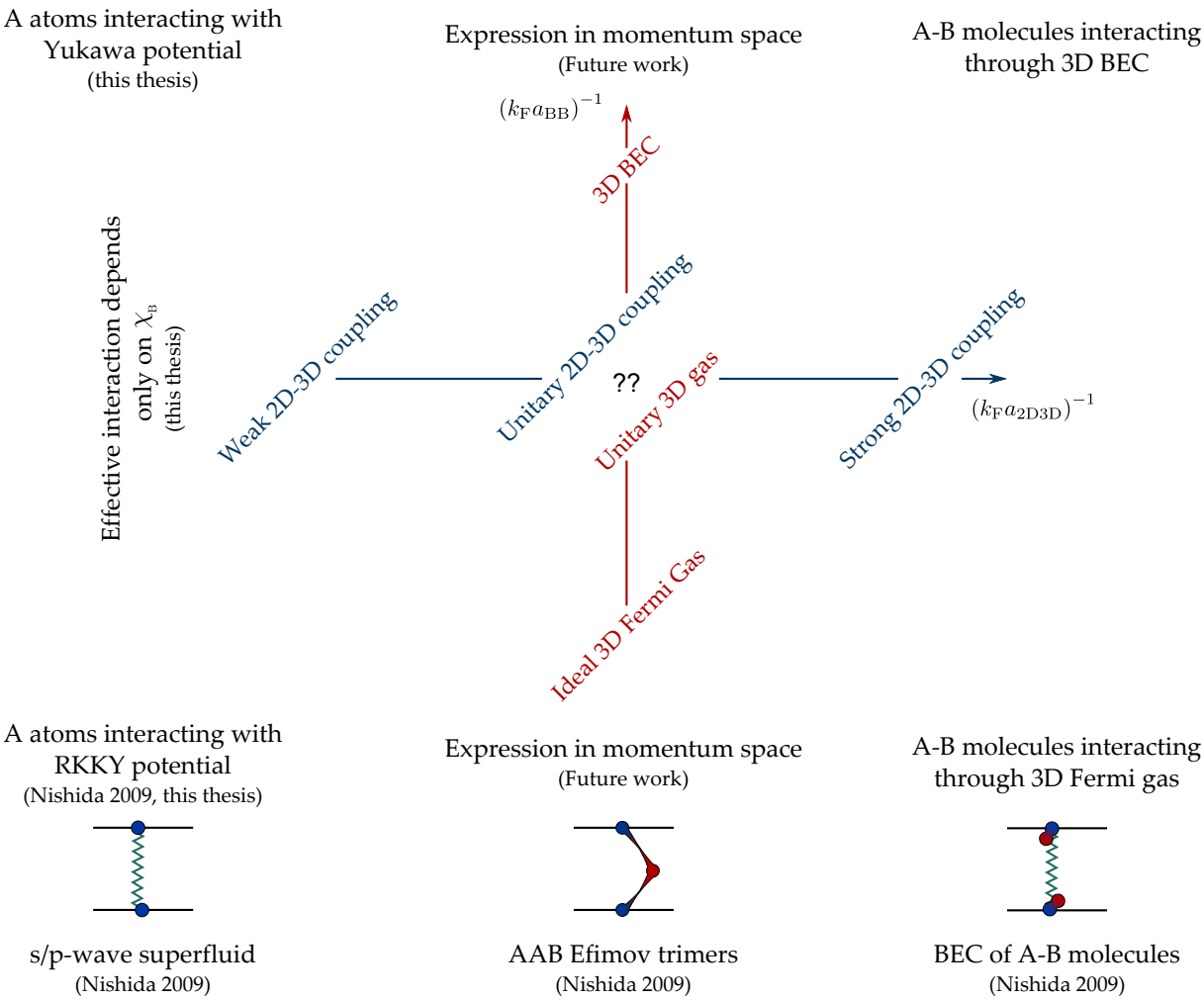

Figure 6.7: Summary of results presented and to come. The phase diagram for a ideal 3D Fermi gas as a function of the 2D-3D coupling strength was reported in [Nishida 2010]. We investigate the behavior of the system also as a function of the 3D-3D interactions. In this thesis, we focused on the $k_F a_{2D-3D} \to 0^-$ limit, allowing Born approximation. We recover the RKKY potential on the BCS side of the 3D cloud and predict a Yukawa potential on the BEC side. A more general derivation, addressing the strong 2D-3D interaction, will be the subject of a future work with Georg Bruun and Zhigang Wu. In the opposite limit $k_F a_{2D-3D} \to 0^+$, 2D and 3D particles are expected to pair in mixed dimensional molecules. The same treatment could be applied to estimate the interaction mediated from one molecule to the other by the unpaired 3D particles.

BEC		Ideal Fermi Gas	
ξ	2.7 μm	k_F^{-1}	0.32 μm
V_0^{BEC}	$0.7 \times 10^{-5}\, E_F$	V_0^{FG}	$7.2 \times 10^{-5}\, E_F$
$g_{\Delta z}^{\mathrm{BEC}}$	$6.32 \times 10^{-45}\, \mathrm{J/m^2}$	$g_{\Delta z}^{\mathrm{FG}}$	$1.62 \times 10^{-46}\, \mathrm{J/m^2}$
$\omega_A - \omega_S$	11.6 Hz	$\omega_A - \omega_S$	-0.07

Table 6.3: Orders of magnitude for the anti-symmetric mode induced by mediated long range interaction. The optical lattice parameters are presented in table 6.2. The coupling is expressed in units of the Potassium Fermi energy E_F. The 2D-3D coupling constant is estimated to $g_{2D3D} = g_{\mathrm{LiK}}\sqrt{m_K/(m_K + 1.22\, m_{Li})}$, with $a_{\mathrm{LiK}} = 63 \times a_0$.

tude of motion will thus be periodically modulated, the beat note frequency being given by the difference between the symmetric and anti-symmetric eigenmodes.

6.4 Conclusions

In this chapter, we described interactions in mixed dimensions as the superposition of an incident plane wave and a scattered ellipsoidal wave. We studied the case of effective long range interactions, where the excitations of a 3D system allow for the exchange of momentum between two separated 2D planes. We extended previous theoretical predictions to address the case where the 3D gas is ramped across over the BEC-BCS crossover. Assuming weak 2D-3D interactions, we showed that the mediated long range interaction can be related to the compressibility of the 3D gas. Within the Hartree approximation, it approaches asymptotically a Yukawa potential on BEC side and a RKKY potential on the BCS side. Those results are presented in figure 6.7.

We then proposed an experimental verification of our model. We presented the setup which will give rise to a mixed-dimensional system to lay down relevant orders of magnitudes. We suggested to probe the existence of long range interactions by measuring the coupled oscillations of two planes. The frequency of the anti-symmetric mode, which appears as a beat-note frequency, can be related to the strength of the coupling and provides a way to test our predictions.

To conclude this chapter, we recall the main limitations of the previous study:

- All calculations were done at zero temperature. Experimentally, we expect to work at temperatures around 5 to 15% of the Fermi temperature.
- The 2D-3D interaction is supposed to be weak enough to be treated within Born's approximation, and taken into account simply by the coupling constant $g_{2\mathrm{D}-3\mathrm{D}}$. This approximation is justified when $a_{2\mathrm{D}-3\mathrm{D}}$ is the smaller length scale of the problem, which can be realized by taking advantage of Feshbach resonances to tune its value.

- A-atoms are treated as single impurities ; their statistics and interactions are not taken into account, nor is their influence on the 3D cloud. Those effects can be experimentally minimized by working with dilute 2D gases, such that 3D particles are much more numerous.
- When moving through the B-cloud, A-atoms can radiate propagating excitations which would take away their energy. Following the Landau criterion, such a situation would arise if the velocity of an A particle exceeds the sound velocity in the B superfluid and this effect remains negligible as long as the A atoms' Fermi velocity is small enough [Delehaye *et al.* 2015].
- The tuning of the interspecies interactions can be experimentally challenging. The Feshbach resonances are known to be narrow and display a short lifetime due to enhanced inelastic losses. This will probably limit the reachable scattering length, but we showed that a measurable signal should be accessible at background value.

Some of these points are currently under investigation in collaboration with Zhigang Wu and Georg Bruun.

Conclusion

The main results presented in this thesis are twofold.

First, we have significantly improved the FERMIX apparatus. We notably developed and implemented a new cooling scheme, the so-called Λ enhanced gray molasses, which takes advantage of the existence of dark states among and between the hyperfine manifolds addressed by the D_1 transition. This technique could be applied simultaneously on both ^{6}Li and ^{40}K, enabling us to reach a phase-space density of 10^{-4}, the highest value reported for the laser cooling of these two species. It has since then been successfully adapted to the cooling of other isotopes (Lithium 7, Potassium 39, Potassium 41) and species (Sodium 23), proving its broad range of application.

The improvement in phase-space density allowed us to realize the first degenerate ^{40}K gas in France, with 3×10^5 atoms in two spin states at 62 nK, corresponding to 17% of the Fermi temperature. Several experiments could be performed with such a sample.

For instance, a highly degenerate fermionic cloud is expected to display dramatically altered light scattering properties, as the Pauli principle forbids the decay of an excited state to an occupied ground state and thus reduces the accessible phase-space [Görlitz *et al.* 2001]. Two temperature ratios play a crucial role in this blocking of spontaneous emission, analogous to the Purcell effect [Purcell 1946]. The degree of degeneracy of the ensemble, estimated as the ratio $\xi = T/T_F$ between the temperature of the cloud and the Fermi temperature, accounts for the occupancy of phase-space. The recoil strength, expressed as the ratio $\kappa = T_R/T_F$ between the recoil temperature and the Fermi temperature, is related to the likelihood for a fermion initially immersed in the Fermi sea to reach a state above the Fermi surface after absorbing and re-emitting a photon. The smaller these two ratios, the stronger the Pauli blocking, and significant effects above 20% of scattering suppression can be obtained as soon as $\xi < 0.2$ and $\kappa < 1$. Due to its inverted hyperfine structure, ^{40}K is a promising candidate for the observation of this effect [Shuve and Thywissen 2009], as open transitions can be closed by the Pauli blocking, resulting in an apparent increase of the measured atom number.

The long-term objective of the FERMIX experiment is the simultaneous cooling of ^{6}Li to degeneracy. A preliminary measurement showed that both species could be loaded in the optical dipole trap, but a significant improvement of the atom number is still required to maintain a satisfying efficiency during the last steps of evaporation. In order to reduce the thermal load for Lithium and keep balanced populations, we plan to take advantage of the Potassium Fesh-

bach resonance to decouple effectively both evaporations. Hopefully this cooling scheme will soon make the FERMIX experiment able to study ultra-cold Fermi-Fermi mixtures.

Once both species have been brought to ultra-low temperatures, they could be used to realize a mixed-dimensional system. We developed a theoretical analysis of such a situation, where ^{40}K is confined in 2D-planes immersed in a 3D ^{6}Li cloud. We demonstrated that an effective long range interaction can be mediated from one layer to the next one by the surrounding cloud and derived the expression of the coupling within Born's approximation on both the BEC and BCS sides of the resonance. We proposed a scheme for an experimental verification of our predictions by measuring the beat-note period of coupled oscillations between pancakes confined in neighboring sites of an optical lattice.

Besides this proposal, several problems could be studied by relying on such a mixed dimensional simulator. For example, mixed dimensions open new perspectives for Efimov physics. In the unitary limit, three particles can form Borromean-like trimers, whose binding energies form a geometric series characterized by a universal factor [Efimov 1970, Efimov 1973]. It was long believed that these Efimov trimers could only exist in three dimensions, where the short-range boundary condition enforces a non trivial interaction at unitarity. However, mixed dimensions provide additional ways to generate Efimov bound states, provided that the mass ratio of the two involved species belongs to a critical interval [Nishida and Tan 2011]. A fermionic ^{6}Li-^{40}K degenerate mixture, such as the one we aim at producing, is well suited for such realizations, as two 2D Potassium atoms can bind with and through a 3D Lithium atom. Furthermore, the existence of inter-layer configurations helps preventing three-bodies recombinations and increases the stability of Efimov trimers with respect to the 3D scenario.

Furthermore, with the appropriate optical configuration, the FERMIX apparatus could be used to engineer alternative mixed-dimensional schemes, for instance 1D-3D or 0D-3D systems. In addition to Efimov physics, these systems offer the opportunity to study specific phenomena, such as the Kondo effect mentioned in the introduction.

Second, we proved that some dynamical properties of non-interacting Weyl particles in a harmonic trap could be simulated with spin-polarized Lithium atoms in a quadrupole trap. Our method relies on a canonical mapping to translate properties of Weyl fermions into the language of atomic physics. For instance, this mapping allowed us to re-interpret the Klein paradox as Majorana spin-flip losses.

Despite their apparent simplicity, we have shown that these equivalent systems display non trivial properties. We showed that an ensemble of Weyl particles dragged away from the trap center does not oscillate continuously, but relaxes towards a strongly anisotropic steady state which cannot be described by a Boltzmann distribution. This provides an interesting example of relaxation in the absence of collisions, midway between harmonically confined massive particles, which oscillate without damping, and interacting particles in non harmonic potentials, which usually relax towards a thermal state.

As the oscillations are damped, the energy initially imparted to the center of mass of the ensemble is redistributed within the cloud. Defining effective temperatures as the second moments of the distribution, we characterized the heating following the excitation. Even though the Hamiltonian is non separable, the strongly confining axis appears to be almost decoupled from the symmetry plane. Yet, within this plane, effective temperatures equilibrate, showing a quasi-thermalization. Using general theorems, we estimated the expected heating and find a good agreement between theory and numerics without free parameters. Experimentally, these predictions have been successfully tested against two different excitation methods.

In order to study the influence of the trap geometry, we derived analytical results for the relaxation in an isotropic trap based on Bertrand's theorem. In 3D, we have shown that the effective heating remains anisotropic as the excitation breaks the initial symmetry. By contrast, the effective heating becomes isotropic in 2D. These results were validated and extended to intermediate trap geometries by numerical simulations, notably allowing an estimation of the relaxation time and suggesting an interpretation of the quasi-thermalization based on the precession of orbital planes.

We derived expressions of the involved Berry phases and showed numerically that the additional coupling they provide is negligible at the considered temperatures. The simultaneous enhancement of the influence of geometric potentials and of Klein-Majorana losses, while compromising the ability of quasi-thermalization to illustrate topological properties, illustrates that both effects originate from the same adiabatic hypothesis.

Finally, it should be noted that the very same mapping could be used to study various situations. For instance, particles in a Ioffe-Pritchard trap appear as analog to massive relativistic particles, while in a hybrid magneto-optical trap, they could be used to engineer a Rashba coupling.

The FERMIX experiment is about to reach its intended operational capacities and demonstrates an increasing ability to address fundamental problems of quantum mechanics. As shown in this work, the experiment highlights several strengths of Physics. Universality first of all, as two systems with very different natures, such as ultra-slow cold atoms and ultra-fast relativistic Weyl particles, can be found to behave in the same way. It also epitomizes the interplay between theory and experiment, as both are accessible in the lab: the setup remains on a human scale and standard concepts can be readily derived and tested against data. But mostly, it illustrates how new lines of research can sometimes emerge by serendipity: even well-known and thoroughly studied systems such as the quadrupole magnetic trap can exhibit an un-described behavior, providing new tools for the study of exotic situations and pushing forward the boundaries of understanding.

Chapter A Appendix

Contents

A.1 Alkaline atoms in magnetic fields **164**
- A.1.1 Wigner-Eckart theorem and Lande factor 164
- A.1.2 Zeeman hamiltonian 165
- A.1.3 Asymptotic behaviors 166
- A.1.4 Breit-Rabi formula 168
- A.1.5 Remark on notations 169

A.2 About Boltzmann equation **170**
- A.2.1 Collisionless Boltzmann equation 170
- A.2.2 H theorem 171

A.3 Kohn, virial and Bertrand theorems **175**
- A.3.1 Kohn theorem 175
- A.3.2 Virial theorem 176
- A.3.3 Bertrand's theorem 177

A.4 Elements of collision theory **181**
- A.4.1 Mathematical framework 182
- A.4.2 Scattering eigenstates 183
- A.4.3 Scattering matrices, amplitude and cross section 183
- A.4.4 Low energy limit 185
- A.4.5 Feshbach resonances 187
- A.4.6 Getting familiar with a Feshbach resonance 189

A.5 Technical references **191**
- A.5.1 AOMs and EOMs 191
- A.5.2 Power supplies 192
- A.5.3 Optical sources 192
- A.5.4 RF system 193

A.6 Electrical schemes **193**

THis appendix presents and demonstrates some of the fundamental results used in the main text of the manuscript. Annex A.1 is dedicated to the Zeeman effect, throughly used in the field of cold atoms. Annex A.2 introduces Boltzmann equation and illustrates some historical paradoxes of the H theorem, at the core of the kinetic theory of gases. Annex A.3 demonstrates

the Kohn, virial and Bertrand's theorem, with an original approach. Annex A.4 summarizes elements of the elastic collisions theory required to address scattering problems. Eventually, annex A.5 provides the technical references of the devices used on the apparatus.

A.1 Alkaline atoms in magnetic fields

The Zeeman effect accounts for the influence of an external magnetic field on the eigenelements of an atom. The atom is coupled to the field through its magnetic momentum $\boldsymbol{\mathcal{M}}$, which can be related to the angular momentums (orbital $\mathbf{L}$, intrinsic $\mathbf{S}$ and nuclear $\mathbf{I}$) through Wigner-Eckart theorem. As a consequence, a small field will lift the degeneracy of the so called *Zeeman sublevels* which differ only by their projected angular momentum. At a highest order, the impact on the hyperfine splitting must be taken into account. In asymptotic regimes, convenient formulae can be derived to estimate the Zeeman shifts. If the magnetic field is small enough, such that its influence is negligible compared to the hyperfine splitting, the energy shift of each Zeeman sublevel is linear with the field and proportional to its projected momentum. If the magnetic field is strong enough, such that the hyperfine splitting can be neglected, the energy shift is still proportional to the field but only depends of the electron intrinsic orientation. The calculation can be explicitly carried out for $\mathbf{L} = 0$; the resulting Breit-Rabi formula is therefore appropriate for the ground states of alkali atoms and plays an important role in our case.

This appendix reviews and summarizes the main results describing the behavior of alkali atoms such as Lithium and Potassium in a magnetic field.

A.1.1 Wigner-Eckart theorem and Lande factor

The magnetic momentum of an atom is a vectorial operator and follows as such the Wigner-Eckart theorem: The restriction of any vectorial operator $\mathbf{V}$ to an eigenspace of the angular momentum $\mathbf{F}$ is proportional to the angular momentum with a coefficient

$$\frac{\langle \mathbf{V}.\mathbf{F} \rangle_F}{F(F+1)\hbar^2}. \tag{A.1}$$

Here, a vectorial operator is defined by its commutation relations $[F_x, V_x] = 0$, $[F_x, V_y] = i\hbar V_z$ and $[F_x, V_z] = -i\hbar V_y$ (and circular permutations) while the mean value can be estimated on any state of the eigenspace.

Three angular momentum are required to describe an atomic state and the magnetic momentum can therefore be expressed as the sum of three contribution. The proportionality factor between a magnetic momentum and the related angular momentum is expressed with Bohr magneton $\mu_B = \frac{e\hbar}{2m_e} \simeq 1.4 \times h\,\mathrm{MHz/G}$ and so called *Landé factor*, usually noted g.

- The orbital momentum $\mathbf{L}$ of the electron is associated to a magnetic momentum $\boldsymbol{\mathcal{M}}_L = -\frac{\mu_B}{\hbar} g_L \mathbf{L}$ with $g_L = 1$.

δ_L	s	p	d	f
Li	0.40	0.04	0	0
K	2.19	3.59	2.46	0.02

g_J	$S_{1/2}$	$P_{1/2}$	$P_{3/2}$
Li	2	0.666	1.335
K	2	2/3	4/3

Table A.1: Landé factors (left) and quantum defects for Lithium and Potassium, as given by [Burkhardt and Leventhal 2010]

^{40}K	a_{hf}	b_{hf}
$4^2S_{1/2}$	-285.730	-
$4^2P_{1/2}$	-34.523	-
$4^2P_{3/2}$	-7.585	-3.445

^{6}Li	a_{hf}	b_{hf}
$2^2S_{1/2}$	152.136	-
$2^2P_{1/2}$	17.386	-
$2^2P_{3/2}$	-1.155	-0.10

Table A.2: Hyperfine structure of ^{6}Li and ^{40}K, as given by [Arimondo *et al.* 1977]

- The intrinsic momentum $\mathbf{S}$ of the electron (or spin) is associated to a magnetic momentum $\boldsymbol{\mathcal{M}}_S = -\frac{\mu_B}{\hbar} g_S \mathbf{S}$ with $g_s \simeq 2$. This value is predicted by Dirac equation; magnetic anomalies modify it by $\sim +0.02$.

- The nuclear momentum $\mathbf{I}$ is associated to a magnetic momentum $\boldsymbol{\mathcal{M}}_I = -\frac{\mu_B}{\hbar} g_I \mathbf{I}$. The factor g_I depends of the nuclei but is always much smaller than 1 (1.7×10^{-4} for ^{40}K and -4.5×10^{-4} for ^{6}Li).

It is often useful to consider composed angular momentum, such as $\mathbf{J} = \mathbf{L} + \mathbf{S}$ and $\mathbf{F} = \mathbf{J} + \mathbf{I}$. We can therefore introduce the corresponding Landé factors

$$g_J = \frac{g_S}{2} \frac{J(J+1) + S(S+1) - L(L+1)}{J(J+1)} + \frac{g_L}{2} \frac{J(J+1) + L(L+1) - S(S+1)}{J(J+1)}, \tag{A.2}$$

$$g_F = \frac{g_J}{2} \frac{F(F+1) + J(J+1) - I(I+1)}{F(F+1)} + \frac{g_I}{2} \frac{F(F+1) + I(I+1) - J(J+1)}{F(F+1)}. \tag{A.3}$$

The Wigner-Eckhart theorem is extremely useful as long as the vectorial operator can be correctly approximated by its restriction to a subspace of the angular momentum. This is correct as long as the variations due to the operator are small compared to the difference between two subspaces. Since S and I are intrinsic quantities, the previous results are always correct. For L (resp. J, F), they hold until the energy shift becomes comparable to the atomic structure of $\sim 100\,\text{THz}$ (resp fine structure $\sim 100\,\text{GHz}$, hyperfine structure $\sim 100\,\text{MHz}$)

A.1.2 Zeeman hamiltonian

To account for the Zeeman effect on alkali, we describe an atom with the following Hamiltonian [Cohen-Tannoudji *et al.* 1997],

$$H = H_0 + W_{\text{so}} + W_{\text{hf}} + H_Z, \tag{A.4}$$

where

- H_0 describes a spinless valence electron in the electrostatic potential of the nuclei and core electron cloud. For alkali atoms, the energy of an orbit depends not only on the principal quantum n, but also on the angular momentum $\mathbf{L}$, as the orbit can bring the valence electron to cross inner electronic layers. This effect can be simply taken into account by the so-called *quantum defect* [Hanle 1984]. The eigenenergies then take the form $E_0(n, L) = -R_y / (n - \delta_{n,L})^2$, where R_y is the Rydberg constant and $\delta_{n,L}$ is the quantum defect, mostly depending on L (see table A.1).

- W_{so} describes the coupling between the spin $\mathbf{S}$ and the orbital angular momentum $\mathbf{L}$. It can be written, as any interaction lifting the degeneracy of the $\mathbf{J} = \mathbf{S} + \mathbf{L}$ levels, under the form:

$$W_{\text{so}} \propto \mathbf{L}.\mathbf{S} \simeq a_{\text{f}} \left(J(J+1) - L(L+1) - S(S+1) \right), \tag{A.5}$$

  where a_{f} gives the fine structure splitting.

- W_{hf} accounts for the coupling to the angular momentum of the nuclei, generating the hyperfine structure of the atom:

$$W_{\text{hf}} = \frac{a_{\text{hf}}}{\hbar^2} \mathbf{I}.\mathbf{J} + \frac{b_{\text{hf}}}{\hbar^2} \frac{3(\mathbf{I}.\mathbf{J})^2 + \frac{3}{2}\hbar(\mathbf{I}.\mathbf{J}) - I^2 J^2}{2I(2I-1)J(2J-1)} \tag{A.6a}$$

$$= \frac{a_{\text{hf}}}{2} \left(F(F+1) - I(I+1) - J(J+1) \right) \text{ if } b_{\text{hf}} = 0 \tag{A.6b}$$

  where a_{hf} and b_{hf} are the magnetic dipole and electric quadrupole constants respectively.

- H_Z describes the coupling of magnetic momentums to an external magnetic field:

$$\hat{H_Z} = -\left(\hat{\boldsymbol{\mathcal{M}}}_S + \hat{\boldsymbol{\mathcal{M}}}_L + \hat{\boldsymbol{\mathcal{M}}}_I \right) .\mathbf{B} \tag{A.7}$$

A.1.3 Asymptotic behaviors

- At low field: linear Zeeman effect treatment

  If the Zeeman shift is much smaller than the hyperfine splitting, the Zeeman effect can be taken into account perturbatively. Atomic states are correctly described by their projected angular momentum m_F and their (degenerate) energies are given by:

$$E(m_F) = E_0(n, L) + a_{\text{hf}} \left(F(F+1) - I(I+1) - J(J+1) \right) / 2 \tag{A.8}$$

  Up to first order in perturbation, the Zeeman effect is given by

$$\Delta E = \langle m_F | \, H_Z \, | m_F \rangle = \frac{\mu_B}{\hbar} g_F B \, m_F \tag{A.9}$$

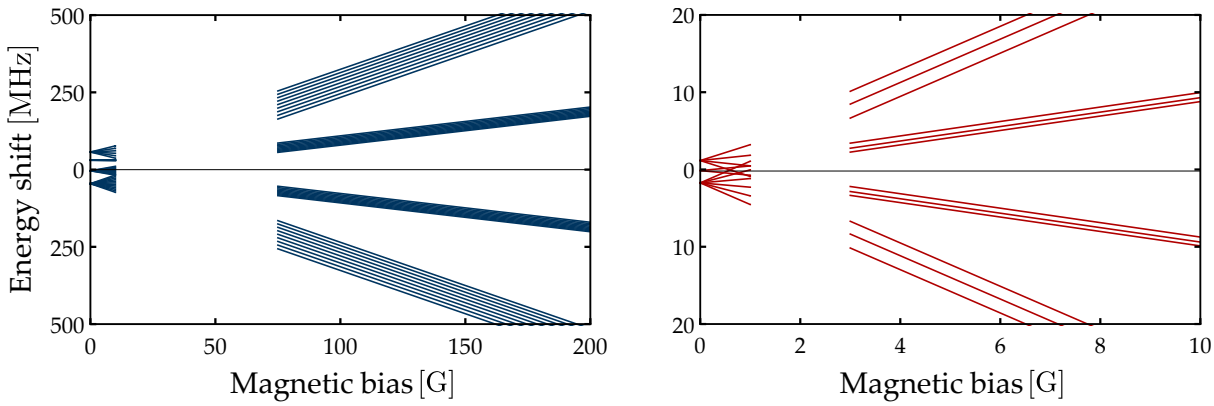

Figure A.1: Asymptotic regimes for the Zeeman shift of the $P_{3/2}$ states of ^{40}K (left) and ^{6}Li (right) as a function of the magnetic field. The low field regime is given by equation (A.9), where the coupling to the magnetic field is treated perturbatively. The high field regime is given by equation (A.11b), where the hyperfine structure is estimated as a perturbation.

For Lithium as well as Potassium, this regime is only valid as long as the magnetic field does not exceed few Gausses (see Fig. A.1).

- At high field: Paschen-Back regime

If the Zeeman shift is much larger than the hyperfine splitting, the restriction of the Hamiltonian to an eigenspace of the angular momentum $\mathbf{F}$ is not relevant anymore and the projected momentum m_F is not a good quantum number to describe the situation. The magnetic momentum $\boldsymbol{\mathcal{M}}$ cannot be expressed with $\mathbf{F}$ but must be described as the sum of $\boldsymbol{\mathcal{M}}_I$ and $\boldsymbol{\mathcal{M}}_J$, making m_I and m_J the relevant quantum numbers.

We therefore consider the eigenstates $|n, L, S, J, I, m_J, m_I\rangle$ of the Hamiltonian $H = H_0 + W_{\text{so}} + H_Z$, whose energies shift with respect to $B = 0$ are given by

$$\Delta E = \mu_B \left(g_J m_J + g_I m_I\right) B/\hbar \tag{A.10}$$

To take into account the hyperfine splitting, we calculate at lowest order

$$\delta E = \langle m_J, m_I| \, H_{\text{hf}} \, |m_J, m_I\rangle \tag{A.11a}$$

$$= a_{\text{hf}} m_I m_J + b_{\text{hf}} \frac{9m_I^2 m_J^2 - 3I(I+1)m_J^2 - 3J(J+1)m_I^2 + IJ\,(I+1)\,(J+1)}{4IJ(2I+1)(2J+1)} \tag{A.11b}$$

For Potassium, this regime is valid as soon as $B > 50\,\text{G}$ for $P_{3/2}$ states (resp. $B > 200\,\text{G}$ for $P_{1/2}$ states). For Lithium, this regime is valid as soon as $B > 3\,\text{G}$ for $P_{3/2}$ states (resp. $B > 30\,\text{G}$ for $P_{1/2}$ states). It is therefore the relevant expression to estimate the shifts at typical biases of the experiment (see A.1).

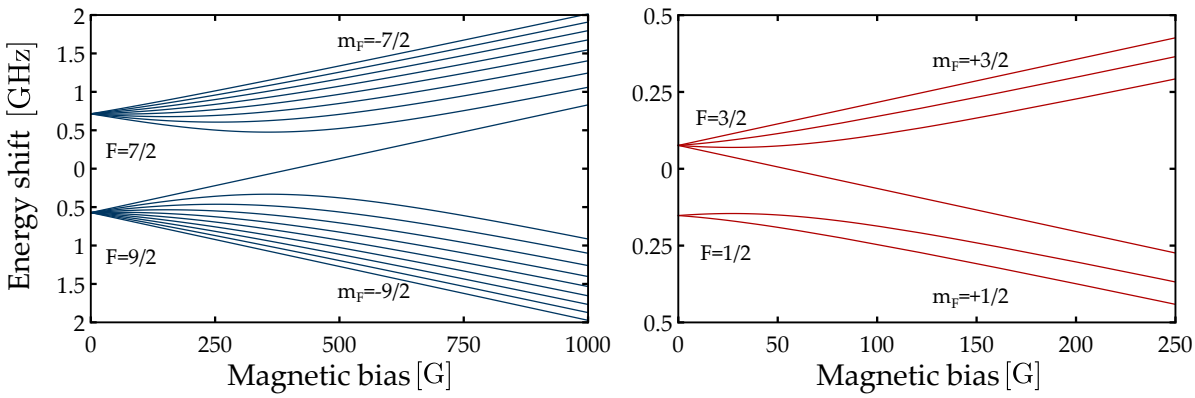

Figure A.2: Zeeman shift of the $S_{1/2}$ manifold of ^{40}K (left) and ^{6}Li (right) as a function of the magnetic field, as estimated by the Breit Rabi formula (A.15)

A.1.4 Breit-Rabi formula

For S orbitals, as the angular momentum $L = 0$, the Zeeman effect can be analytical calculated as show in [Breit and Rabi 1931]. Using standard notations, we rewrite

$$H = H_0 + a_{\text{hf}} \left(I_z J_z + \frac{1}{2} \left(I_+ J_- + I_- J_+ \right) \right) / \hbar^2 + \mu_B B \left(g_J J_z + g_I I_z \right) / \hbar \tag{A.12}$$

Since $J = 1/2$, we can expand the matrix expression of the Hamiltonian over the basis $\{|n,\, L = 0,\, S,\, J = S,\, I,\, m_J,\, m_I\rangle\} = \{|m_J, m_I\rangle\}$:

$$H - H_0 = \begin{pmatrix} E\left(m_F = -\left(I + \frac{1}{2}\right)\right) & 0 & 0 & & 0 \\ 0 & M_{11}(-I) & M_{12}(-I) & & 0 \\ 0 & M_{21}(-I) & M_{22}(-I) & & 0 \\ & & & \ddots & \\ 0 & 0 & 0 & & E\left(m_F = \left(I + \frac{1}{2}\right)\right) \end{pmatrix} \tag{A.13}$$

where the M matrices have the following form

$$M_{11}(m_I) = a_{\text{hf}} m_I / 2\hbar^2 + \mu_B B \left(\frac{g_J}{2} + m_I g_I \right) / \hbar, \tag{A.14a}$$

$$M_{22}(m_I) = -a_{\text{hf}} \left(m_I + 1 \right) / 2\hbar^2 + \mu_B B \left(-\frac{g_J}{2} + \left(m_I + 1 \right) g_I \right) / \hbar, \tag{A.14b}$$

$$M_{12}(m_I) = a_{\text{hf}} \sqrt{I(I+1) - \left(m_I + 1 \right) m_I} / 2\hbar^2 = M_{21}(m_I). \tag{A.14c}$$

This block matrix can be easily diagonalized: the stretch states $m_F = \pm\left(I + 1/2\right)$ are already eigenstates and each subspace $\{|-1/2, m_I\rangle, |+1/2, m_I - 1\rangle\}$ with a constant m_F is stable. The

corresponding eigenvalues give the Zeeman shift:

$$\Delta E = \begin{cases} \frac{a_{\mathrm{hf}}}{2\hbar^2} I \pm \frac{\mu_B}{\hbar}\left(\frac{g_J}{2} + g_I I\right) B & \text{for } m_F = \pm\left(I + \frac{1}{2}\right) \\ -\frac{a_{\mathrm{hf}}}{4\hbar^2} + g_I \mu_B m_F B \pm \frac{a_{\mathrm{hf}}\left(I+\frac{1}{2}\right)}{2}\sqrt{1 + \frac{2\mu_B(g_I - g_J)m_F}{a_{\mathrm{hf}}\left(I+\frac{1}{2}\right)^2} B + \frac{\mu_B^2(g_I-g_J)^2}{a_{\mathrm{hf}}^2\left(I+\frac{1}{2}\right)^2} B^2} & \text{for } |m_F| < \left(I + \frac{1}{2}\right) \end{cases} \tag{A.15}$$

Their values are plotted on figure A.2.

A.1.5 Remark on notations

As shown in this appendix, the hyperfine states are eigenstates of the system only at zero field. The projected angular momentum m_F is therefore not a good quantum number generally speaking, when arbitrary magnetic field are applied. Nevertheless, we will refer to those numbers to label without ambiguity the eigenstates of the Zeeman Hamiltonian. Strictly speaking, the spin-state $|m_F\rangle$ should be understood as the eigenstate adiabatically connected to $|m_F\rangle$ at zero field.

A.2 About Boltzmann equation

We review and summarize some of the properties of Boltzmann equation used in chapter 3, and present two of the historical paradoxes associated to the H-theorem to illustrate the complexity of the relaxation problem. For a more detailed presentation, see for instance [Pottier 2007].

A.2.1 Collisionless Boltzmann equation

We consider a dilute gas of N neutral atoms, which we assume to be described at time t by a distribution $f(\mathbf{r}, \mathbf{p}, t)$, not necessarily the equilibrium function. $f(\mathbf{r}, \mathbf{p}, t)\, d\mathbf{r}d\mathbf{p}$ gives the probability to find at time t a particle in volume $d\mathbf{r}$ around $\mathbf{r}$ with a momentum as close as $d\mathbf{p}$ from $\mathbf{p}$.

Liouville theorem states that the distribution function is constant along any trajectory in phase space. In absence of interactions between particles, it simply corresponds to particle conservations: the number of particles in the phase-space volume $d\mathbf{r}'d\mathbf{p}'$ around $(\mathbf{r}', \mathbf{p}')$ at time t' used to be in the phase-space volume $d\mathbf{r}d\mathbf{p}$ around $(\mathbf{r}, \mathbf{p})$ at time t, provided that

$$\partial_t \mathbf{r}(t) = \mathbf{p}(t)/m, \tag{A.16a}$$

$$\partial_t \mathbf{p}(t) = \mathbf{F}(\mathbf{r}(t)), \tag{A.16b}$$

where $\mathbf{F} = -\partial_{\mathbf{r}} U$ is the outer potential exerted on the atoms.

In terms of distribution function, Liouville theorem can be written as $f(\mathbf{r}', \mathbf{p}', t')\, d\mathbf{r}'d\mathbf{p}' = f(\mathbf{r}, \mathbf{p}, t)\, d\mathbf{r}d\mathbf{p}$, which we can express as

$$\left(\partial_t + \frac{\mathbf{p}}{m}\partial_{\mathbf{r}} + \mathbf{F}\partial_{\mathbf{p}}\right) f = 0, \tag{A.17}$$

and we introduce the Liouville operator $\mathcal{L}$ such that $\partial_t f = -\mathcal{L} f$:

$$\mathcal{L} = \frac{\mathbf{p}}{m}.\nabla_{\mathbf{r}} + \mathbf{F}.\nabla_{\mathbf{p}} \tag{A.18}$$

Equilibrium distribution

Starting from given initial conditions, it is almost impossible to predict from the previous equations the steady state that the system is going to reach. On the other hand, it is straightforward to verify that a Boltzmann distribution f_0 define as:

$$f_0(\mathbf{r}, \mathbf{p}) = \frac{N}{(2\pi\hbar)^3} \frac{\lambda_{dB}}{V_e} \exp\left(-\beta\left(\frac{p^2}{2m} + U(\mathbf{r})\right)\right), \tag{A.19}$$

where $V_e = \int d\mathbf{r} \exp\left(-\beta U(\mathbf{r})\right)$ is the effective volume occupied by the gas, is an stationary solution of the collisionless Boltzmann equation (A.17).

Considering a kinetic definition of the temperature as the standard deviation of the momentum distribution, we identify $\beta = (k_B T)^{-1}$ for the Boltzmann distribution (A.19). Remarkably, f_0 is completely defined by this single scalar parameter T, which implies that any physical quantity can be expressed as a function of the temperature. This is not the case for all solutions to the Boltzmann equation, and a steady state distribution can require more than one parameter.

The Boltzmann distribution plays a crucial role in the kinetic theory of gases and we introduce two properties of the Liouville operator that are useful to derive the results presented in this manuscript

- $\mathcal{L}[f_0] = 0$, since Boltzmann's distribution is a stationary solution of Boltzmann's equation.
- $\mathcal{L}$ is antisymmetric for the scalar product, ie $\langle \alpha | \mathcal{L}\left[\beta\right] \rangle = -\left\langle \mathcal{L}\left[\alpha\right] | \beta \right\rangle$ with

$$\langle \alpha | \beta \rangle = \int d\mathbf{r} d\mathbf{q}\, f_0 \alpha \beta \tag{A.20}$$

A.2.2 H theorem

General formulation of the Boltzmann equation

If interactions cannot be neglected between atoms, Liouville theorem still applies for the N particles distribution function. Several strategies can be considered to estimate the marginal single particle distribution. The BBGKY hierarchy treats the problem iteratively, expressing the single particle distribution as the solution of an equation involving the two-particles distribution and so on. The Vlasov equation corresponds to a mean field treatment of the second order of the BBGKY development and serves as framework for most of plasma physics.

Boltzmann approach relies on a series of simplifications:

- Only binary collisions are taken into account. This supposes that the gas is dilute enough for three-body events to be extremely rare.
- All collisions are considered as elastic and no internal degrees of freedom are changed. Most of the time, the interactions are treated as independent of the energy of the particles.
- All collisions are micro-reversible: the probability for two colliding atoms with momentum $\mathbf{p}_1$ and $\mathbf{p}_2$ to emerge from the collision with momentum $\mathbf{p}_1'$ and $\mathbf{p}_2'$ is the same as the probability of the reverse process.

- The *Stosszahlansatz*, or pre-collisional chaos, is probably the strongest hypothesis as it supposes that, before their interaction, the two particles are completely uncorrelated.

Under those conditions, the time evolution of the distribution function can be expressed as

$$\left(\partial_t + \frac{\mathbf{p}}{m}\partial_{\mathbf{r}} + \mathbf{F}\partial_{\mathbf{p}}\right) f = \left(\frac{\partial f}{\partial t}\right)_{\text{collisions}}, \tag{A.21}$$

where the collision term takes the form

$$\left(\frac{\partial f}{\partial t}\right)_{\text{collisions}} = \int d\mathbf{q} \int d\Omega\, \sigma\left(\mathbf{p}, \mathbf{q}, \Omega\right) \left|\frac{\mathbf{p}}{m} - \frac{\mathbf{q}}{m}\right| \left(f_{\mathbf{p}'} f_{\mathbf{q}'} - f_{\mathbf{p}} f_{\mathbf{q}}\right). \tag{A.22}$$

In the integral, $\mathbf{p}'$ has the same modulus as $\mathbf{p}$ but is oriented in the Ω direction and $\mathbf{q}'$ is fixed by the energy and momentum conservation. The cross-section $\sigma(\Omega)$ corresponds to the probability for particles to deviate from their initial trajectories by a solid angle Ω. The value of the cross section depends on the nature of the interactions, as detailed in annex A.4.

H theorem

It is often assumed that, in presence of collisions, the distribution function will eventually relax towards f_0 (even though particles in a harmonic potential provide a good counter example through the undamped oscillations of both the center-of-mass motion (see Kohn theorem below) and the monopole breathing mode [Lobser *et al.* 2015]). The qualitative idea relies on the H theorem, that plays a key-role in Boltzmann theory and has been a bone of contention since its formulation [Vilani 2010].

Boltzmann introduced the quantity H define as

$$H(t) = \int d\mathbf{r} d\mathbf{p}\, f\left(\mathbf{r}, \mathbf{p}, t\right) \log f((\mathbf{r}, \mathbf{p}, t) \tag{A.23}$$

which can easily be related to the more familiar entropy $S(t) = -k_B H(t)$.

The H-theorem states that this quantity can only decrease during the time evolution of the system

$$\frac{d}{dt} H(t) \leq 0 \tag{A.24}$$

or equivalently, the entropy of the isolated system can only increase.

The demonstration relies on the integration of eq.(A.21) and the inequality saturates for distributions such that the collision term vanishes. In the interacting case, the only distributions verifying this condition are the local Maxwellians defined as

$$f\left(\mathbf{r}, \mathbf{p}, t\right) = n(\mathbf{r}, t) \left(\frac{1}{2\pi m k_B T(\mathbf{r}, t)}\right)^{3/2} \exp\left(-\frac{(\mathbf{p} - m\mathbf{u}(\mathbf{r}, t))^2}{2 m k_B T(\mathbf{r}, t)}\right), \tag{A.25}$$

where the density n, temperature T and velocity $\mathbf{u}$ fields are free parameters. Note that such a distribution may not be a steady state of Boltzmann equation (ie $\mathcal{L}[f] \neq 0$). The non-interacting case, considered in chapter 3 and 4, provides an additional situation of evolution with constant entropy.

Classical paradoxes

- Loschmidt's reversibility paradox [Loschmidt 1876]

> Starting from a given initial condition, H decreases during the evolution of the system. At time t, H has reached a value $H(t) < H_0$ and we reverse the speed of all particles. Since collisions are micro-reversible, the system will resume its initial configuration in which $H = H_0$. During this evolution, H has increased, in contradiction with the H theorem.

This paradox relies on a wrong interpretation of the Stosszahlansatz: as time is reversed, the micro-reversibility implies that particles display *pre-collisional* correlations, but *post-collisional* chaos. Deriving Boltzmann equation with this modified hypothesis inverses the sign of the collision term: the entropy decreases (or the quantity H increases) during the evolution of the system. Qualitatively, the reverse evolution starts with correlated particles and every collision brings the system closer to the initial distribution, where all particles were uncorrelated; the decrease of entropy translates this loss of information. A further objection can then be formulated:

> The situation presented above shows that Boltzmann equation is not relevant to describe some systems, such as distributions with initial correlations.

The assessment is true, but does not constitute a paradox of any kind, as illustrated by spin echo experiments. However, these systems with strong initial correlations require a very delicate construction and a typical configuration, drawn at random in phase-space, is very unlikely to display such features. The story says that, as Boltzmann was confronted to Loschmidt's reversibility paradox, he answered: "Go ahead then, reverse them !".

- Poicaré-Zermelo's recurrent paradox [Zermelo 1896]

Poicaré demonstrated in 1889 the recurrence theorem [Poincaré 1890]:

> Let us consider a system which dynamics conserves the phase volume of any finite element and which evolution remains contained in a finite phase space volume. Then, after sufficiently long time (the so-called *Poincaré recurrence time*), the system will return to a state arbitrarily close to its initial state.

Owing to Liouville theorem and energy conservation, the two premesis are verified for most closed physical systems. Few years after the publication of Poincaré memoir, Zermelo formulated a paradox relying on his theorem:

> How can a system returns to its initial configuration, with the initial quantity H_0, if H can only increase during its evolution ?

Mathematically, the paradox comes from the applicability of the Poincaré theorem, which concerns finite systems of N particles. Boltzmann equation supposes an infinite number of degrees of freedom and is therefore not subject to the theorem.

Physically however, systems do contain a finite number of particles. Nevertheless, the recurrence time scales exponentially with N and for macroscopic samples, the corresponding periods are much longer than the age of the universe. What's more, Boltzmann equation remains valid only as long as the Stosszahlansatz is relevant. Long before the recurrence time is reached, the pre-collisional correlations might not be negligible and the system will exit the validity range of the H theorem.

A.3 Kohn, virial and Bertrand theorems

In this annex, we present derivations of three theorems used in the main text, namely the Kohn, virial and Bertrand's theorems. The demonstration of the latter is an original work, inspired by several proofs reported in the literature.

A.3.1 Kohn theorem

Kohn's theorem is a very strong result to study particles trapped in a harmonic potential and was first formulated to describe the cyclotron motion of particles in a static, uniform magnetic field [Kohn 1961]. It states that regardless of the inter-particles interactions, the center of mass of the distribution oscillates at the cyclotron frequencies. Its extension in [Brey *et al.* 1989] generalized this result to the case of identical particles in a harmonic trap. Later, in [Dobson 1994], the "harmonic potential theorem" demonstrates the rigid transport of the many-body wavefunction.

Proof

We describe trapped particles with the Hamiltonian

$$H = H_{\text{kin}} + H_{\text{trap}} + H_{\text{int}} = \sum_i \frac{p_i^2}{2m} + \sum_i \frac{1}{2} m\omega^2 r_i^2 + \sum_{i,j} w\left(\mathbf{r}_i - \mathbf{r}_j\right). \tag{A.26}$$

We introduce the center of mass variables $\mathbf{R} = \sum_i \mathbf{r}_i/N$ and $\mathbf{P} = \sum_i \mathbf{p}_i$, as well as the relative coordinates $\boldsymbol{\xi}_i = \mathbf{r}_i - \mathbf{R}$ and $\mathbf{q}_i = \mathbf{p}_i - \mathbf{P}/N$. With these notations, we can rewrite the Hamiltonian (A.26) as:

$$H = H_{\text{CoM}} + H_{\text{rel}}, \tag{A.27a}$$

$$H_{\text{CoM}} = \frac{P^2}{2Nm} + \frac{1}{2} Nm\omega^2 R^2, \tag{A.27b}$$

$$H_{\text{rel}} = \sum_i \frac{q_i^2}{2m} + \sum_i \frac{1}{2} m\omega^2 \xi_i^2 + \sum_{i,j} w\left(\boldsymbol{\xi}_i - \boldsymbol{\xi}_j\right). \tag{A.27c}$$

Note that relative- and center of mass- coordinates commute and $[\mathbf{R}, \mathbf{P}] = i\hbar$. We have therefore $[H_{\text{rel}}, \mathbf{R}] = [H_{\text{rel}}, \mathbf{P}] = 0$, and the center of mass follows the simple Hamiltonian of a trapped particle with mass Nm in a harmonic potential.

The same proof can be applied for particles with a charge q in an additional static or uniform magnetic field $\mathbf{B}(\mathbf{r}) = \boldsymbol{\nabla} \times \mathbf{A}$ and uniform electric field $\mathbf{E}(t)$. The center of mass Hamiltonian is then given by

$$H_{\text{CoM}} = \frac{(\mathbf{P} - Q\mathbf{A})^2}{2M} + \frac{1}{2} M\omega^2 R^2 + Q\mathbf{E}(t).\mathbf{R}, \tag{A.28}$$

with $Q = Nq$ and $M = Nm$.

The theorem can be further extended to show that the wave function of the N particles system can be expressed as the product of a center of mass wave function and an "internal" wave function. To do so, we must introduce the Jacobi coordinates $\mathbf{u}_1 = \mathbf{r}_1 - \mathbf{r}_2$, $\mathbf{u}_2 = \frac{\mathbf{r}_1+\mathbf{r}_2}{2} - \mathbf{r}_3$, ..., $\mathbf{u}_n = \frac{\mathbf{r}_1+...+\mathbf{r}_n}{n} - \mathbf{r}_{n+1}$ and the corresponding momenta. Those coordinates do verify the canonical commutation relations and we can show that they can be used to rewrite H_{rel}, hence the result.

A.3.2 Virial theorem

Virial theorem was formulated by Rudolf Clausis in 1870 [Clausius 1870] and applies to particles in a potential $V(\mathbf{r})$ such that

$$V(\lambda \mathbf{r}) = \lambda^n V(\mathbf{r}). \tag{A.29}$$

In particular, this class includes all potential with the form $V(\mathbf{r}) = \left(\alpha_x x^p + \alpha_y y^p + \alpha_z z^p\right)^q$, with $n = pq$.

The theorem can be formulated as follows: for any ensemble submitted to a potential (A.29), the kinetic energy E_{K} and the potential energy E_P in the steady states are related through the relation:

$$2E_{\text{K}} = nE_{\text{P}} \tag{A.30}$$

Virial theorem is often used in stellar physics and provides for instance a derivation of Chandrasekhar limit for the stability of white dwarf stars.

Lemma *Euler Theorem*

For any potential, if $\epsilon \ll 1$, we can write $V((1+\epsilon)\mathbf{r}) \simeq V(\mathbf{r}) + \epsilon\,(\mathbf{r}.\partial_{\mathbf{r}})\,V(\mathbf{r})$

Since $V((1+\epsilon)\mathbf{r}) = (1+\epsilon)^n V(\mathbf{r}) \simeq V(\mathbf{r}) + n\epsilon V(\mathbf{r})$, this leads to Euler theorm for homogeneous functions:

$$(\mathbf{r}.\partial_{\mathbf{r}})\,V(\mathbf{r}) = nV(\mathbf{r}) \tag{A.31}$$

Proof We describe an ensemble of particles in a potential V with the distribution function $f(\mathbf{r}, \mathbf{p}, t)$. The evolution of f is governed by Liouville equation

$$\partial f = \mathcal{L} f,$$

with the Liouville operator being $\mathcal{L} = \frac{\mathbf{p}}{m}.\partial_{\mathbf{r}} - (\partial_{\mathbf{r}} V)\,.\partial_{\mathbf{p}}$.

Let us consider the quantity $C(t) = \langle \mathbf{r}.\mathbf{p} \rangle = \int f\,\mathbf{r}.\mathbf{p}$. In steady state, $\partial_t C = 0$ and we can express

$$0 = \int \partial_t f\,\mathbf{r}.\mathbf{p} = \int \mathcal{L}\,(f)\;\mathbf{r}.\mathbf{p} = -\int f\,\mathcal{L}\,(\mathbf{r}.\mathbf{p}) \tag{A.32}$$

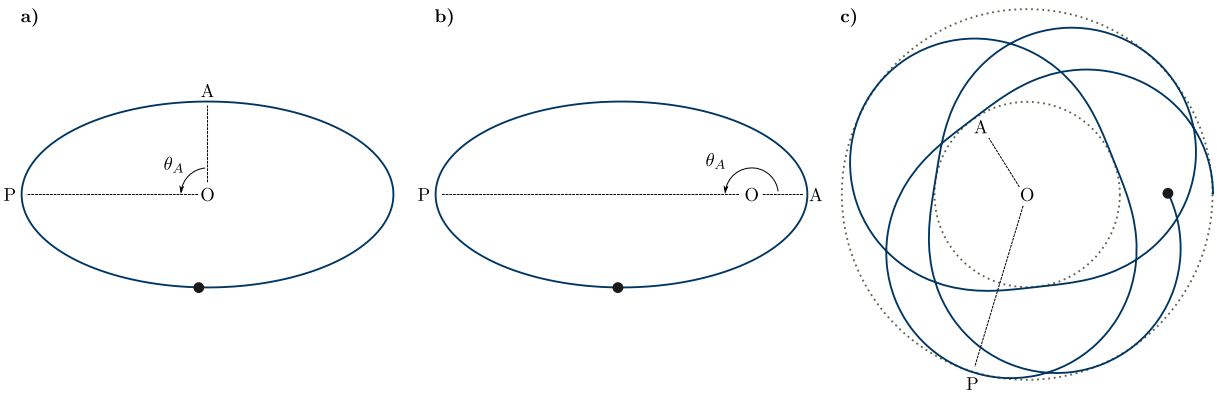

Figure A.3: Three orbits in central potentials. In a), the Hook potential results in an apside angle $\theta_A = \pi/2$. In b), the Coulomb potential gives $\theta_A = \pi$. In c), an arbitrary potential gives a rosette-like trajectory.

where we integrated by parts. Using Euler theorem, we can express $\mathcal{L}(\mathbf{r}.\mathbf{p}) = p^2/m - nV$, and the previous condition leads to

$$\int f \frac{p^2}{m} = n \int f V \tag{A.33}$$

hence the virial theorem.

A.3.3 Bertrand's theorem

Bertrand's theorem describes the behaviour of particles trapped in a central force potential $V(r)$. The theorem states that, even if any arbitrary potential admits a circular orbit, only two are such that all bound orbits are closed: the Coulomb potential $V_C(\mathbf{r}) = -\kappa/r$ and the Hook potential $V_H(\mathbf{r}) = \kappa' r^2$.

The corollary of this theorem is that any potential apart from V_C and V_C will admit rosette-like orbits, as the particle will cover densely all positions between the aphelion and the perihelion (see Fig. A.3)

The theorem was first formulated in 1873 by J. Bertrand [Bertrand 1873] (see [Santos *et al.* 2011] for an english translation) as a general analysis of bound orbits. It was proposed as a tool for the study of the three-body problem and can be used as an alternative demonstration to the shape of Newton's gravitational potential, since all trajectories observed among celestial bodies are closed.

Several proofs to Bertrand's theorem can be found nowadays. Most of them have the same structure and only differ in the last step of the demonstration. The original proof uses a global approach; a perturbative method can also be applied [Goldstein *et al.* 2001] or additionnal constant of motion can be invoked [Martinez-y Romero *et al.* 1992]. Many more rely on an

inverse transform [Grandati *et al.* 2008, Santos *et al.* 2009]. Here, we show a global approach inspired by [Arnold *et al.* 1997].

Few words of vocabulary, illustrated on figure A.3:

- The apside angle θ_A is the angle $\widehat{AOP}$ between the the aphelion A, the center O et the perihelion P.
- An orbite is closed if the trajectory followed by a particle will eventually loop. Equivalently, this condition corresponds to the apside angle being commensurate with π: $\theta_A = \frac{m}{n}\pi$.

Step 1 *If all orbits are closed, than the apside angle must be the same for all trajectories*

Let us consider a closed orbit. As mentioned above, this condition requires that the apside angle of this trajectory is commensurate with π.

If the apside angle was not the same for all orbits, but depended continuously of the energy or angular momentum of the trajectory, it would necessarily take values incommensurate with π according to the intermediate value theorem.

Therefore, if all orbits are closed, they must all have the same apside angle θ_A.

Step 2 *For almost circular orbits, the only central potentials with constant apside angles are $V(r) = \kappa \ln r/r_0$ and $V(r) = \kappa r^\alpha$ with $\alpha > -2$ and $\alpha \neq 0$. The corresponding apside angles are $\theta_A = \frac{\pi}{\sqrt{2+\alpha}}$*

We consider a point-like particle with mass m subject to the force $\mathbf{F}(r) = -\partial_r V(r)\mathbf{u}_r$ and decribe its trajectory in polar coordinates (r, θ).

The energy conservation can be expressed as

$$E = \frac{1}{2}m\dot{r}^2 + \frac{1}{2}mr^2\dot{\theta}^2 + V(r). \tag{A.34}$$

Using the conservation of angular momentum $\mathbf{L} = mr^2\dot{\theta}\mathbf{u}_z$, we can express the kinetic energy as a function of the distance r and of its angular dependance:

$$\dot{r}^2 + r^2\dot{\theta}^2 = \left(\frac{L_z}{mr^2}\frac{dr}{d\theta}\right)^2 + \frac{L_z^2}{2mr^2}. \tag{A.35}$$

We follow Binet's notation $u = r^{-1}$, so that $\frac{du}{d\theta} = -\frac{1}{r^2}\frac{dr}{d\theta}$ and we can write eq.(A.34) as

$$E = \frac{L_z^2}{2m}\left(\frac{du}{d\theta}\right)^2 + V_{\text{eff}}(u), \tag{A.36}$$

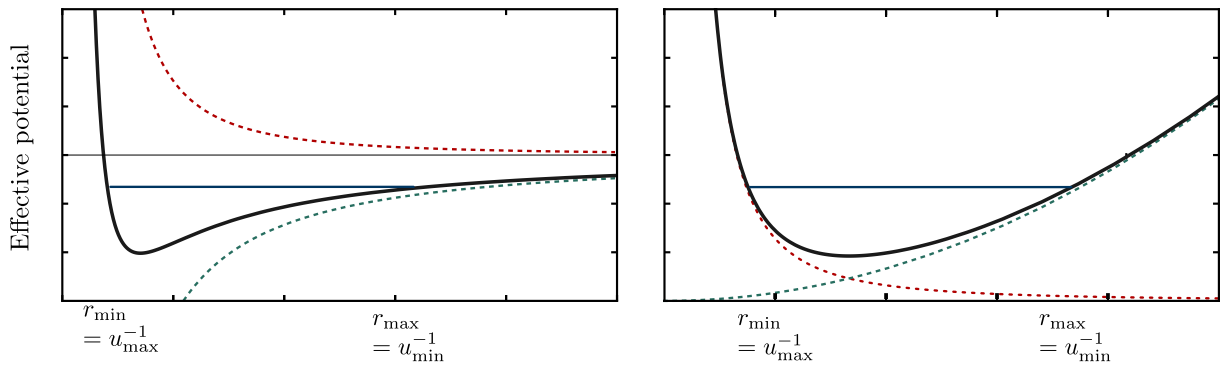

Figure A.4: Effective potentials (black line), expressed as the sum of the kinetic (red dashed line) and potential (green dashed line) energies, for $\alpha < 0$ (left) and $\alpha > 0$ (right). For a given energy (blue horizontal line), the aphelion ($r_{\min}$) and perihelion ($r_{\max}$) define the accessible position range.

where we introduced (see Fig. A.4)

$$V_{\text{eff}}(u) = \frac{L_z^2}{2m}u^2 + V(u^{-1}). \tag{A.37}$$

Let us consider a circular trajectory u_0 with energy E_0 and momentum L_z and a stable orbit close to it, such that $u = u_0 + \rho(\theta)$. Up to the second order, $V_{\text{eff}}(u) = V_{\text{eff}}(u_0) + \frac{1}{2}\rho^2 V''_{\text{eff}}(u_0)$ since $V'_{\text{eff}}(u_0) = 0$ and eq. (A.36) reads

$$E = \frac{L_z^2}{2m}\left(\frac{d\rho}{d\theta}\right)^2 + \frac{1}{2}\rho^2 V''_{\text{eff}}(u_0), \tag{A.38}$$

which describes an oscillation with the angular frequency

$$\Omega = \sqrt{\frac{mV''_{\text{eff}}(u_0)}{L_z^2}} = \sqrt{\frac{3V'(r_0) + r_0 V''(r_0)}{V'(r_0)}} > 0, \tag{A.39}$$

where we used $V'_{\text{eff}}(u_0) = 0 \Rightarrow V'(r_0) = L_z^2/mr_0^3$ and expressed the stability of the orbit.

Without any loss of generality, we can chose the origin such that $u = u_0 + A\cos\Omega\theta$. The aphelion is reached for $\theta = 0$ and the perihelion for $\theta = \theta_A = \pi/\Omega$. The condition expressed in step 1 thus leads to

$$\frac{3V'(r) + rV''(r)}{V'(r)} = 2 + \alpha, . \tag{A.40}$$

with $\alpha > -2$. For $\alpha = 0$, eq. (A.40) leads to $V(r) = \kappa \ln r/r_0$ and $\theta_A = \pi/\sqrt{2}$, and we can rule out this potential since its aspide angle is incommensurate with π. For $\alpha \neq 0$, we find $V(r) = \kappa' r^\alpha$ and

$$\theta_A = \frac{\pi}{\sqrt{2+\alpha}}. \tag{A.41}$$

Step 3 *The only possible values for the apside angle to be commensurate with π are $\alpha = 2$ and $\alpha = -1$, hence Bertrand's theorem*

For each value of α, since the apside angle is the same for all trajectories, we will restrict the study to a convenient situation and express the apside angle using eq. (A.36)

$$\theta_A = \frac{L_z u_{\max}}{\sqrt{2m}} \int_{\frac{u_{\min}}{u_{\max}}}^{1} \frac{dx}{\sqrt{E - V_{\text{eff}}(x u_{\max})}}. \tag{A.42}$$

For $\alpha > 0$, we consider an orbit with an energy $E \to +\infty$. The aphelion is approaching zero as $u_{\max} = r_{\min}^{-1} \to \infty$, while the perihelion as located at $u_{\min} = 0$ (see Fig.A.4). We can thus consider $V(1/u_{\max}) \to 0$ and therefore $E \simeq \frac{L_z^2}{2m} u_{\max}^2$. We can express the effective potential as:

$$V_{\text{eff}}(x u_{\max}) = E x^2 + \frac{L_z^\alpha}{(2m)^{\alpha/2} E^{\alpha/2}} \frac{\kappa}{x^\alpha} \underset{E \to \infty}{\simeq} E x^2 \tag{A.43}$$

Considering $\frac{u_{\min}}{u_{\max}} \to 0$, eq. (A.42) leads to

$$\theta_A \underset{E \to \infty}{\longrightarrow} \int_0^1 \frac{dx}{\sqrt{1 - x^2}} = \pi/2. \tag{A.44}$$

Comparing eq. (A.44) and (A.41), the only possible potential is the Hook potential, corresponding to a harmonic motion with $\alpha = 2$.

For $\alpha < 0$, orbits can exist only if $\kappa < 0$ and $E < 0$. With such prerequisites, we consider an orbit with an energy $E \to 0^-$. The aphelion is then given by $-\kappa u_{\max}^{-\alpha} = \frac{L_z^2}{2m} u_{\max}^2$ while the perihelion as located at $u_{\min} = 0$ (see Fig. A.4). The apside angle is thus converging towards

$$\theta_A \underset{E \to 0}{\longrightarrow} \frac{L_z u_{\max}}{\sqrt{2m}} \int_0^1 \frac{dx}{\sqrt{-\frac{L_z^2}{2m} u_{\max}^2 x^2 - \kappa x^{-\alpha} u_{\max}^{-\alpha}}} = \frac{\pi}{2 + \alpha}. \tag{A.45}$$

Comparing eq. (A.45) and (A.41), the only possible potential is the Coulomb potential, corresponding to an elliptique motion with $\alpha = -1$.

A.4 Elements of collision theory

The behavior of a many body system depends crucially on the interactions between particles, as epitomized by the BEC-BCS crossover. In the appendix, we review the main tools used to model a two-body elastic interaction.

The study of the interacting and scattering properties of a system is a wide field and can easily be the object of a dedicated work. The objective of this presentation is simply to explicit, without demonstration, most of the concepts used in the previous chapters (scattering length, Feshbach resonance...) and to introduced the tools required to describe interactions in mixed dimensions (chapter 6).

The approach follows essentially that of [Walraven 2010] and [Cohen-Tannoudji and Guery Odelin 2011] to which we refer for all demonstrations of the results stated here.

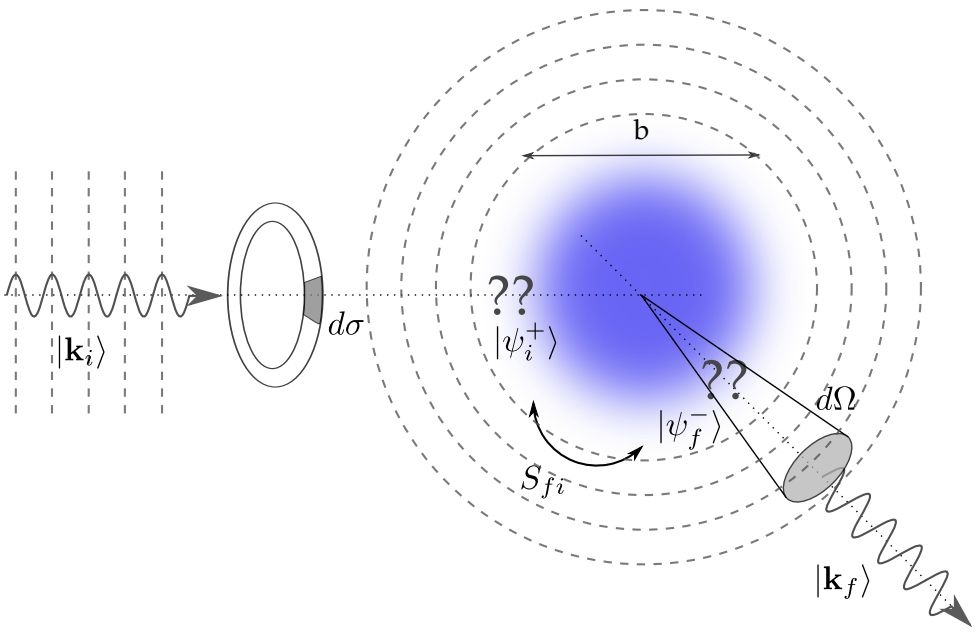

Figure A.5: Scattering on a central potential. An incoming plane wave $|\mathbf{k_i}\rangle$ propagates towards a scattering center of finite range b. Following adiabatically the potential, the initial state becomes $|\psi_i^+\rangle$ close to the center.. The interaction can project the incoming state onto the outgoing state $|\psi_f^-\rangle$, which will in turn become a plane wave $|\mathbf{k_f}\rangle$ far from the center. The probability amplitude of such a scattering is given by the S-matrix element S_{fi}, which can be estimated thanks' to the T matrix. The superposition of all outgoing waves can be described as a spherical wave with the scattering amplitude f. The cross section $d\sigma(\Omega)$ expresses the size of the effective target that leads to a deviation Ω.

A.4.1 Mathematical framework

Let us consider two particles traveling towards each other from a far distance (ie larger than the interaction range). As they move closer, the interaction disturbs their trajectories. Because of energy and momentum conservation, in absence of internal state modification, the particles will eventually separate from each other and resume their motion. The interaction dictates the deviation of the particles or, equivalently, the dephasing of the wavefunction. Those main ingredients are depicted on figure A.5.

We describe the two interacting particles by the wavefunction Ψ and the following Hamiltonian:

$$H_{\text{tot}} = \frac{p_1^2}{2m_1} + \frac{p_2^2}{2m_2} + V(\mathbf{r}_1 - \mathbf{r}_2) \tag{A.46a}$$

$$= \frac{P^2}{2(m_1 + m_2)} + \left(\frac{p^2}{2m} + V(\mathbf{r})\right), \tag{A.46b}$$

where we introduced the reduced mass $m = \frac{m_1 m_2}{m_1 + m_2}$, the center of mass momentum $\mathbf{P} = \mathbf{p}_1 + \mathbf{p}_2$, the relative momentum $\mathbf{p} = \frac{1}{m}(m_2\mathbf{p}_1 - m_1\mathbf{p}_2)$, and the relative position $\mathbf{r} = \mathbf{r}_1 - \mathbf{r}_2$. Taking advantage of the commutation of the relative- and center-of-mass quantities, we seperate Ψ as

$$\Psi(\mathbf{r}_1, \mathbf{r}_2) = \varphi(\mathbf{R})\,\psi(\mathbf{r}). \tag{A.47}$$

In the following, we will concentrate on the scattering problem described by ψ and the Hamiltonian

$$H = \frac{p^2}{2m} + V(r), \tag{A.48}$$

corresponding to the scattering of a particle on a central potential.

We set the universe in a theorist shoe box of size L, allowing the quantification of wave vectors $|\mathbf{k}\rangle$, eigenstates of $H_0 = p^2/2m$. We also consider an adiabatic switching on and off of the scattering potential overtime, following Gell-Mann and Goldberger:

$$V(\mathbf{r}, t) = V(\mathbf{r}) \exp\left(-\frac{\eta|t|}{\hbar}\right), \tag{A.49}$$

with $\eta \to 0^+$. Qualitatively, this corresponds to considering that the interaction occurs during a finite time. Long before the particle arrives close to the potential center, and long after it was scattered, the interaction is negligible. This allows us to consider quantities long before and long after the scattering:

$$f(\pm\infty) = \lim_{\eta \to 0} \pm \frac{\eta}{\hbar} \int_0^{\pm\infty} f(t) e^{\mp \eta t/\hbar} dt \tag{A.50}$$

A.4.2 Scattering eigenstates

To predict the properties of the interaction, we consider the eigenelements $(\psi_{\mathbf{k}}, E_{\mathbf{k}})$ of the Hamiltonian and review their main properties:

$$H\psi_{\mathbf{k}} = E_{\mathbf{k}}\psi_{\mathbf{k}}. \tag{A.51}$$

- Each state $|\mathbf{k}\rangle$ with energy ϵ_k of the free Hamiltonian H_0 is associated to an advanced and delayed scattering steady state $|\psi^{\pm}_{\mathbf{k}}\rangle$ such that

$$|\psi^{\pm}_{\mathbf{k}}\rangle \equiv U_I\left(0, \mp\infty\right)|\mathbf{k}\rangle \tag{A.52a}$$
$$= \left(1 + G_{\pm}(\epsilon_k)V\right)|\mathbf{k}\rangle \tag{A.52b}$$
$$H|\psi^{\pm}_{\mathbf{k}}\rangle = \epsilon_k|\psi^{\pm}_{\mathbf{k}}\rangle \tag{A.53}$$
$$G_{\pm}(E) = \frac{1}{E - H \pm i\eta} \tag{A.54}$$

  where $U_I(t,t') = \exp\left(-i\frac{t'-t}{\hbar}V\right)$ is the evolution operator in interaction representation. In other words, starting from a plane wave $|\mathbf{k}\rangle$ far from the potential, the wave function becomes $|\psi^{+}_{\mathbf{k}}\rangle$ close to the scattering center but keeps the same energy $\epsilon_{\mathbf{k}}$. Equivalently, a wavefunction $|\psi^{-}_{\mathbf{k}'}\rangle$ close to the scattering center will eventually become a plane wave $|\mathbf{k}'\rangle$ far from it.

- The resolvant $G(E)$ satisfies Dyson equation

$$G(z) = G_0(z) + G_0(z)VG(z), \tag{A.55}$$

  where $G_0(E) = \frac{1}{E-H_0\pm i\eta}$ is the *resolvent*, whose matrix elements correspond to Green functions. This self consistent equation plays a crucial role to expand perturbatively the scattering elements presented below.

- The scattering eigenstates satisfy Lippman-Schwinger equation

$$|\psi^{\pm}_{\mathbf{k}}\rangle = |\mathbf{k}\rangle + G_{0\pm}(E_k)V|\psi^{\pm}_{\mathbf{k}}\rangle \tag{A.56}$$

A.4.3 Scattering matrices, amplitude and cross section

Because of the scattering, a plane wave $|\mathbf{k}\rangle$ propagating towards the center will give rise to outgoing waves in different directions $|\mathbf{k}'\rangle$ and the properties of the scattering potential dictates the amount radiated in each direction. We introduce the main tools used to describe and predict those deviations.

S Matrix The S matrix characterizes the probability amplitude for an incident state $|\mathbf{k}\rangle$ to

emerge as an outgoing state $|\mathbf{k}'\rangle$ after the collision.

$$S_{\mathbf{k}',\mathbf{k}} = \langle \mathbf{k}' | \, U_I \left(-\infty, +\infty\right) |\mathbf{k}\rangle \tag{A.57a}$$

$$= \langle \psi^-_{\mathbf{k}'} \, | \psi^+_{\mathbf{k}} \rangle \, , \tag{A.57b}$$

ie the probability amplitude is the overlap between the initial state forward propagated to the potential and the final state retropropagated to the potential (see figure A.5).

T Matrix

The T matrix is directly related to the S matrix by the relation

$$S_{fi} = \delta_{f,i} - 2i\pi\delta\left(E_f - E_i\right) T_{fi}. \tag{A.58}$$

The point of this relation is that the T matrix can be easily expanded in terms of the interaction potential V and the resolvant G, allowing its evaluation. Using Dyson equation, the T matrix takes the following form

$$T = V + VGV = V + VG_0V + VG_0VG_0V + ... \tag{A.59}$$

Scattering amplitude

Far away from the scattering center, the scattering eigenstates are plane waves. Closer to the center, they can be expressed as the superposition of a plane wave and a spherical wave, which amplitude in the direction $\mathbf{u}$ is given by the scattering amplitude $f\left(\mathbf{k}, \mathbf{u}\right)$:

$$\psi^+_{\mathbf{k}}(r\mathbf{u}) \simeq \frac{1}{\sqrt{L^3}} e^{i\mathbf{k}.\mathbf{r}} + \frac{1}{\sqrt{L^3}} f\left(\mathbf{k}, \mathbf{u}\right) \frac{e^{ikr}}{r} \tag{A.60}$$

where

$$f\left(\mathbf{k}, \mathbf{u}\right) = -\frac{m\sqrt{L^3}}{2\pi\hbar^2} \int d^3\mathbf{r}' \, e^{-i\mathbf{k}.\mathbf{r}'} V(\mathbf{r}') \psi^+_{\mathbf{k}}(\mathbf{r}') \tag{A.61}$$

The scattering amplitude is the natural description of the cross section, presented below. It can be estimated from the T matrix through the relation

$$f\left(k, \mathbf{n}, \mathbf{u}\right) = -\frac{mL^3}{2\pi\hbar^2} \langle k\mathbf{u}|T|\mathbf{k}\rangle \tag{A.62}$$

Cross sections

The differential cross section $\frac{d\sigma}{d\Omega}$ express the likelihood for an incoming particle to be scattered in the solid angle Ω. More quantitatively, with an incoming particle flux ϕ_i, the outgoing flux ϕ_s at a distance r in the solid angle Ω with a precision $d\Omega$ is set by:

$$\phi_i d\sigma = \phi_s(r, \Omega) r^2 d\Omega. \tag{A.63}$$

Taking into account the symmetry properties of indistinguishable particles, the differential cross section corresponding to the scattering from $\mathbf{k}$ to $\mathbf{k}'$ is related to the scattering amplitude through

$$\frac{d\sigma}{d\Omega}(\mathbf{k} \to \mathbf{k}') = \begin{cases} |f(k,\theta) + f(k,\pi-\theta)|^2 & \text{for bosons} \\ |f(k,\theta) - f(k,\pi-\theta)|^2 & \text{for fermions} \\ |f(k,\theta)|^2 & \text{for distinguishable particles} \end{cases} \tag{A.64}$$

where θ is the angle between $\mathbf{k}$ and $\mathbf{k}'$. The total cross section expresses the likelyhood for a particle to be deviated in any direction. It is related to the scattering amplitude through the *optical theorem*, which expresses the flux conservation

$$\sigma_{\text{tot}}(k) = \int d\Omega \, \frac{d\sigma}{d\Omega} = \frac{4\pi}{k} \text{Im}\left(f\left(k, \theta = 0\right)\right). \tag{A.65}$$

A.4.4 Low energy limit

When considering ultracold atoms, further simplifications allow to summarize the effect of the interaction to few scalar parameters, notably the scattering amplitude, which we introduce in this section.

Assuming a spherical interaction potential, we decompose the wavefunction into spherical harmonics with increasing orbital momentum l. Because of energy and momentum conservation, the effect of the scattering is essentially described by the dephasing η_l accumulated be each partial wave during the process. We express the scattering amplitude and cross section as a sum over all spherical modes:

$$f(k,\theta) = \sum_{l=0}^{+\infty} (2l+1) f_l \mathrm{P}_l(\cos(\theta)) \tag{A.66a}$$

$$f_l = \frac{1}{2ik}\left(e^{2i\eta_l(k)} - 1\right) \tag{A.66b}$$

$$\sigma_l(k) = 4\pi \sum_l (2l+1)|f_l|^2 \tag{A.67a}$$

$$= \frac{4\pi}{k^2} \sum_l (2l+1) \sin^2 \eta_l \tag{A.67b}$$

where P_l are Legendre polynomials and $\eta_l(k)$ is the phase shift of the partial wave l.

For arbitrary potential with a finite range b, this phase can be written in the low energy limit as:

$$\tan \eta_l \underset{kr \to 0}{\simeq} -\frac{2l+1}{\left[(2l+1)!!\right]^2} (k a_l)^{2l+1}, \tag{A.68}$$

where a_l is the l-wave *scattering length*. The result can be extended for power-law potential $V \propto r^{-s}$ for partial waves $l < \frac{1}{2}(s-3)$.

Each spherical harmonic contributing to the wavefunction has a angular momentum $l(l+1)\hbar^2$. At the range of the interaction potential, this momentum results in a kinetic barrier which

can be overcome only if the kinetic energy of the colliding particle is high enough:

$$\frac{\hbar^2 k^2}{2m} > \frac{l(l+1)\hbar^2}{b^2} \Leftrightarrow \frac{2\pi b}{\lambda_{\mathrm{dB}}} > l \tag{A.69}$$

As a result, at low energy $\lambda_{\mathrm{dB}} \gg b$, only the first harmonic $l = 0$, the so-called *s-wave*, will contribute to the scattering.

S wave collisions Considering equation (A.68), we introduce the scattering length a and the effective interaction length r_e to expand the s-wave phase shift:

$$\cot(\eta_0) = -\frac{1}{ka} + \frac{1}{2}kr_e + ... \tag{A.70}$$

The scattering amplitude and the cross section for distinguishable particles thus take the form

$$f_0 = \frac{1}{k\cot(\eta_0) - ik} \simeq \frac{1}{-\frac{1}{a} + \frac{1}{2}r_e k^2 - ik} \tag{A.71a}$$

$$\sigma_0(k) = 4\pi|f_0|^2 = \frac{4\pi a^2}{\left(1 - \frac{1}{2}ar_e k^2\right) + (ka)^2} \tag{A.71b}$$

If the interaction can be reduced to the single *s-wave* contribution, it is entirely described at low energy by the scattering length, which accounts for the dephasing induced by the collision. The specificities of the potential can then be neglected and the scattering is equivalent to the one caused by a pseudo potential:

$$U(\mathbf{r}) = \frac{2\pi\hbar^2}{m} a \times \delta(\mathbf{r}) \frac{\partial}{\partial r} r. \tag{A.72}$$

Singlet and triplet scattering length To describe the interaction between two alkali atoms, the spin degree of freedom must also be taken into account. Considering only the electrons, the spin configuration can be either symmetric (triplet state) or anti-symmetric (singlet). Because of Pauli principle, the symmetry will constrain the orbital wave-function of the electron cloud and thus the interaction experienced by the atoms at a given internucleus distance r. The interatomic electrostatic potential should therefore be expressed as the superposition of a singlet and triplet potential:

$$V_{\mathrm{el}}(\mathbf{r}) = V_{\mathrm{s}}(\mathbf{r}) \left|S=0\right\rangle \left\langle S=0\right| + V_{\mathrm{t}}(\mathbf{r}) \left|S=1\right\rangle \left\langle S=1\right| \tag{A.73}$$

$$= V_D(\mathbf{r}) + J(\mathbf{r})\, \mathbf{S_1}.\mathbf{S_2}, \tag{A.74}$$

where $\mathbf{S} = \mathbf{S}_1 + \mathbf{S}_2$ is the total electronic spin, $V_{\mathrm{D}} = \frac{1}{4}\left(V_{\mathrm{s}} + 3V_{\mathrm{t}}\right)$ and $J = V_{\mathrm{t}} - V_{\mathrm{s}}$. At low temperature, the singlet and triplet potential result in scattering lengths a_s and a_t respectively. The triplet scattering length notably accounts for the collisions

	^{6}Li-^{6}Li	^{6}Li-^{40}K	^{40}K-^{40}K
a_s/a_0	39	52	104
a_t/a_0	-2200	63	169
Ref.	[Ottenstein *et al.* 2008]	[Falke *et al.* 2008]	[Wille *et al.* 2008]

Table A.3: singlet and triplet scattering length for the atoms at stake in the FERMIX experiment. The values are expressed in units of Bohr radius $a_0 = 52.92$ pm.

between stretch-states. Their values for Li and K are given in table A.3

P wave collisions For spin polarized fermions, the symmetry of the internal state forbids any symmetric external wave-function because of Pauli principle. S-wave collisions are thus ruled out and the first contributing order is given the so called *p-wave* collisions,

$$\cot(\eta_1) = -\frac{3}{k^3 a_1^3} + \frac{1}{k r_1}. \tag{A.75}$$

The scattering amplitude and the cross section for distinguishable particles take the form

$$f_1 = \frac{1}{k\cot(\eta_1) - ik} \simeq \frac{1}{-\frac{3}{k^2 a_1^3} + \frac{1}{r_1} - ik^2} \tag{A.76a}$$

$$\sigma_1(k) = 12\pi |f_1|^2 = \frac{12\pi a_1^2}{\left(\frac{a_1}{r_1} - \frac{3}{k^2 a_1}\right)^2 + a_1^2 k^2} \tag{A.76b}$$

Note that the first spherical harmonic is anti-symmetric and p-wave collisions are therefore forbidden for indistinguishable bosons.

Temperature dependence The cross section of s- and p-waves collisions at finite temperature can be estimated as

$$\sigma_{s,p}(T) = \int d^3\mathbf{k}\, n(\mathbf{k}, T)\sigma_{s,p}(\mathbf{k}) \tag{A.77}$$

where $n(\mathbf{k}, T)$ is the density of particles in momentum space at temperature T. For distinguishable particles, p-waves predominate at high temperatures but vanish at low temperature. The crossover regime is around 6 mK for Lithium. For Potassium, p waves collisions predominates over s-waves until $\sim 100\,\mu$K and remain significant until $20\,\mu$K [DeMarco *et al.* 1999].

A.4.5 Feshbach resonances

Initially introduced in nuclear physics [Feshbach 1962], Feshbach resonances are the experimental way to tune the interactions at will; they are one of those magical knobs that make

cold atoms such a versatile platform. Here, we simply introduce the main concepts behind scattering resonances. For a detailed review, see [Chin *et al.* 2010].

Because of energy and momentum conservation, two elastically interacting particles cannot form a bound state and will eventually leave as free states. Nevertheless, the existence of bound states can strongly alter the scattering properties as a virtual coupling between the open and closed channel will change phase shifts. This coupling is that much stronger as the energy of both state are equal, just like the scattering of light by a two levels system is maximal as the light has the same frequency as the atomic transition. Close to resonance, the energy difference between bound and scattering states dictates the value of the scattering length; if this difference can be adjusted, any scattering length can be achieved.

More quantitatively, considering a zero energy scattering state $|\psi_0^+\rangle$ coupled by the Hamiltonian W to a bound state $|\psi_{\text{res}}\rangle$ of energy E_{res} close to 0 (see figure A.6), the scattering length takes the form:

$$a = a_{\text{bg}} + \frac{2\pi^2 m}{\hbar^2} \frac{\left|\langle\psi_0^+| W |\psi_{\text{res}}\rangle\right|^2}{E_{\text{res}} + \Delta E}, \tag{A.78}$$

where the background value a_{bg} is the scattering length in absence of coupling and ΔE is the energy shift of the bound state induced by the coupling.

Experimentally, the most usual way to take advantage of this effect is the so-called *magnetic Feshbach resonance*, which plays on the differential Zeeman shift between the singlet and triplet states. Because they don't have the same magnetic moment, the singlet and triplet states don't experience the same energy shift in a given magnetic field. At low energy, only the lowest state is accessible and provides scattering states $|\psi_0^+\rangle$ (open channel). However, the magnetic interaction between electronic spins can couple both states and transfer colliding atoms to a bound state $|\psi_{\text{res}}\rangle$ with an energy close to the scattering state (closed channel). By tuning on the magnetic field, it is possible to adjust the energy difference between $|\psi_0^+\rangle$ and $|\psi_{\text{res}}\rangle$, leading to a divergence of the scattering length when the two energies coincides. Close to the resonance, the scattering length takes indeed the form [Moerdijk *et al.* 1995]:

$$a = a_{\text{bg}} \left(1 - \frac{\Delta B}{B - B_0}\right), \tag{A.79}$$

where B is the applied magnetic bias, B_0 is the field for which both states have the same energy (including the energy shift due to the coupling) and ΔB is the width of the resonance.

In addition to the elastic process considered in this section, inelastic collisions resulting in atom losses are also increased close to Feshbach resonances and should be taken into account in a more quantitative approach.

The idea of tuning cold atoms interaction through magnetic Feshbach resonances was proposed in the early '90s [Tiesinga *et al.* 1993] and realized soon after [Inouye *et al.* 1998]. The same strategy can be applied with other means to control the energy difference between a

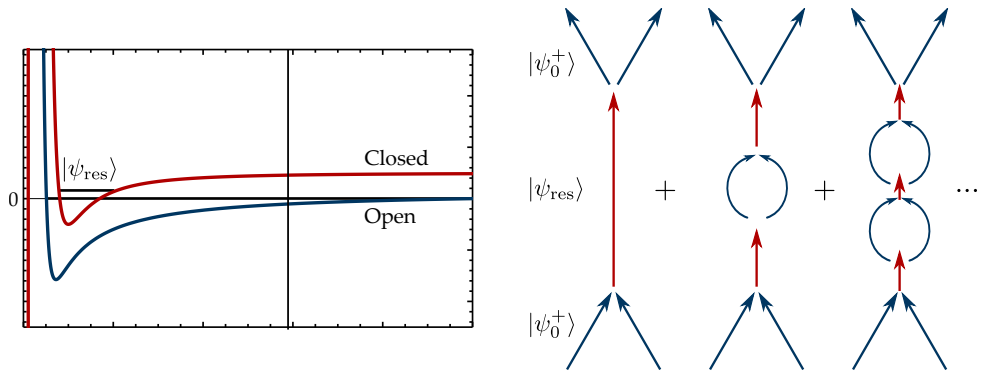

Figure A.6: Feshbach resonance. **Left**: Two channel model. At finite magnetic field, the singlet state (red) is up shifted with respect to the triplet state (blue), which is therefore the only accessible channel (open channel) for scattering states with lowest energy $|\psi_0^+\rangle$. The energy difference between the closed channel bound state $|\psi_{\rm res}\rangle$ and the scattering state $|\psi_0^+\rangle$ determine the value of the scattering length. **Right**: Resonant scattering. Just like the scattering of light by a two level system, the elastic interaction of two atoms is strongly altered when bound and scattering states have equal energy, allowing an efficient virtual coupling between both states.

bound state in the closed channel and a scattering state in the open channel, such as microwave [Papoular *et al.* 2010], RF- [Moerdijk *et al.* 1996] or optical [Theis *et al.* 2004] dressing. Those alternatives allow the simultaneous and independent control of several scattering lengths in a multicomponent gas [Zhang *et al.* 2009].

A.4.6 Getting familiar with a Feshbach resonance

As mentioned before, ^{40}K features a 7 G wide Feshbach resonance at 202 G, allowing a complete control over the scattering length between $|-9/2\rangle$ and $|-7/2\rangle$ states. So far, we did not take advantage of this resonance on the FERMIX experiment and several text-book measurements could be useful to develop a better knowledge of our system [Ketterle and Zwierlein 2008]. One easy way to observe a resonance is to measure the reduced lifetime due to the increase of the inelastic scattering rate [Courteille *et al.* 1998]. However, a more accurate study shows that the maximal three body losses enhancement is located well below the actual resonance.

A more accurate method to determine the position of a Feshbach resonance is to study the formation of Feshbach molecules. At large positive scattering length, two colliding atoms described by the two channel Hamiltonian present a bound state of energy:

$$E_b \sim \frac{\hbar^2}{2\mu a^2}, \tag{A.80}$$

where $a > 0$ is the scattering length and μ the reduced mass. Atoms can be adiabatically transfered to this *Feshbach molecule* as they follow the lowest energy state through a sweep across the Feshbach resonance, starting from a small negative scattering length [Regal *et al.* 2003].

Experimentally, this can be done by ramping the magnetic bias; the sweeping time should be slow compared to the Landau-Zener rate 0.11 G/μs/10^{13} cm^{-3} for ^{40}K, but fast enough to limit enhanced losses induced by the resonance. A transfer efficiency up to 90% can be achieved with this method.

When imaging the cloud at the atomic resonant wavelength λ, molecules are transparent if $a \lesssim \lambda/2\pi$ and the formation of molecules appears as a decrease of the atom number. On the other hand, the total atom number is restored by ramping the field back up to its initial value. At colder temperatures, molecules undergo Bose-Einstein condensation and the distribution presents a characteristic bimodal distribution [Zwierlein *et al.* 2005b].

A radio-frequency radiation with a frequency resonant with the binding energy (A.80) can dissociate the molecules, revealing their presence [Chin *et al.* 2004]. With such a RF-spectroscopy, it is possible to determine the onset of molecular dissociation and hence the value of the field for which (A.80) vanishes [Bartenstein *et al.* 2005]. While this method is particularly well suited for ^{6}Li, for which the electron and nuclear spins are decoupled as soon as the magnetic field exceeds few hundreds of Gauss, rendering the resonant frequency very insensitive to small magnetic fluctuations (1.5 kHz/G for the $|1/2, 1/2\rangle \to |1/2, -1/2\rangle$ transition at 800 G). A satisfying resolution can thus be achieved without dedicated field stabilization. By contrast, for ^{40}K, the resonant frequency of the $|9/2, -9/2\rangle \to |9/2, -7/2\rangle$ transition close to the 202 G Feshbach resonance varies by 150 kHz/G, but this increased sensitivity is still sufficient to allow for measurements with kilohertz resolution.

A.5 Technical references

In this appendix, we present most of the technical references of the elements presented in the figures of chapter 2.

A.5.1 AOMs and EOMs

Name	RF Source	Device	Ampli	Freq (MHz)
		Lithium		
Li Lock	VCO	CrystalTech 3200-115	ZHL-1-2W	94.26
Li MOT Rep	VCO	CrystalTech 3200-115	ZHL-1-2W	215.16
Li MOT Prcp	VCO	CrystalTech 3080-125	ZHL-1-2W	94.26
Li Zee Prcp	VCO	CrystalTech 3200-124	ZHL-1-2W	170.11
Li Img Sw	VCO	CrystalTech 3200-124	ZHL-1-2W	126.8
Li D1	VCO	CrystalTech 3200-124	ZHL-1-2W	-189
Li SpinPol	VCO	CrystalTech 3200-124	ZHL-1-2W	-224.73
Li EOM Spectro	VCO	CrystalTech 3080-122	ZHL-1-2W	-80
Li EOM D1	VCO	CrystalTech 3200-124	ZHL-1-2W	-175
		Potassim		
K D2 Lock	VCO	InterAction ATM 1101A2	ZHL-1-2W	-120
K 3D Prcp	VCO	CrystalTech 3200-124	ZHL-1-2W	217.2
K Rep Com	VCO	CrystalTech 3200-124	ZHL-1-2W	-218.44
K 2D Prcp	VCO	CrystalTech 3200-124	ZHL-1-2W	170.11
K Img Sweep	VCO	CrystalTech 3200-124	ZHL-1-2W	126.8
K 3D Rep	VCO	CrystalTech 3200-124	ZHL-1-2W	-189
K 2D Rep	VCO	CrystalTech 3200-124	ZHL-1-2W	-224.73
K Img switch	VCO	CrystalTech 3080-122	ZHL-1-2W	-80
K Img HF	VCO	CrystalTech 3200-124	ZHL-1-2W	-175
K 3D Switch	VCO	CrystalTech 3080-122	ZHL-1-2W	-90
K SP	VCO	CrystalTech 3080-122	ZHL-1-2W	-59.81
K D1 lock	VCO	CrystalTech 3200-124	ZHL-1-2W	-267.93
K D1 switch	VCO	CrystalTech 3200-124	ZHL-1-2W	200
K EOM Spectro	VCO	Qubig	ZHL-1-2W	20
K EOM D1	WinfreakTech SynthNV	Qubig E0-K40-3M	ZHL-5W-2G+	1285.8
		High power lasers		
YAG1	VCO	MCQ80-A2.5-L1064	ZHL-20W-13+	79.7
YAG2	VCO	MTS80-A3-1064AC	ZHL-1-2W	80.6
Verdi	VCO	MCQ110-A2-VIS	ZHL-1-2W	109

Table A.4: AOM and EOM for on the optical tables.

A.5.2 Power supplies

Power supply	Ref	Control	Use
Zeeman	Delta Electronika SM 35-45	CV	Zeeman
SpinPol	Delta Electronika SM 1540-D	CV	Bias
Blue	Delta Electronika SM 45-140	CC/CV	MOT, transport, quad trap
Yellow	Delta Electronika SM 45-70D	CV	Push, Transport
Orange	Delta Electronika SM 45-70D	CV	Transport
White	Delta Electronika SM 15-400	CC/CV	Quad trap, compensation
Annexe	Delta Electronika SM 30-200 (x2)	CV	Transport
Genesys	TDK-Lambda GEN 50-200	CV	Transport
HighFiness	High Finesse 30A/15V	CC	Bias
CompX	Delta Electronika ES 030-10	CV	Compensation
CompY	Delta Electronika ES 030-10	CV	Compensation

Table A.5: Power supplies described in figure 2.9.

A.5.3 Optical sources

Name	Reference	I(A)	T(°C)	Output (mW)
	Lithium			
Pinguin	EYP-RWE-0790-0400-0750-SOT3-0000	0.104	19.3	20
Eagle	EYP-TPA-0765-01500-3006-CMT03-0000	0.87	22	120
Racoon	EYP-TPA-0765-01500-3006-CMT03-0000	0.8	18.5	120
Mouse	EYP-TPA-0765-01500-3006-CMT03-0000	0.8	16	40
Shiva	Toptica DL pro 770nm	0.148/0.870	19.4/20	115
	Potassium			
Lynx	EYP-RWE-0790-0400-0750-SOT3-0000	0.085	20	25
Guepard	EYP-TPA-0765-01500-3006-CMT03-0000	2.4	23	260
Gazelle	EYP-TPA-0765-01500-3006-CMT03-0000	2.5	19	380
Zebra	EYP-TPA-0765-01500-3006-CMT03-0000	2.9	15.5	250
Unicorn	Toptica DL pro 770nm	0.1	21.3	24
Chimpanze	EYP-TPA-0765-01500-3006-CMT03-0000	2.3	21	180
	High power lasers			
Verdi	Coherent Verdi V12	38	24	11 W
Mephisto	Innolight Mephisto MOPA 25W	50	24	22 W
	Optical lattice			
Dog	Axcel Photonics M9-808-0150	0.061	25	150 mW
Bear	TA-EYP-TPA-0808-01000-4006-CMT04-0000	2.5	17	980 mW

Table A.6: Laser sources and tapered amplifiers. Output powers of TAs are measured at the output of a single mode optical fiber. Output powers for diodes are measured at the injection of the following TA.

A.5.4 RF system

Type	Ref	Freq. (MHz)	Power
VCO	MC -ZX95-1300	400 - 1300	+ 8 dBm
Agilent	N5161A MXG ATE	0.1 - 3000	+ 13 dBm
Rode-Schwarz	SMB 100A	0.09 - 1100	+ 18 dBm
SRS	DS 345	10^{-8} - 30	+ 20 dBm
Switch	MC ZAS-1	5 - 450	- 50 dB
Fast Switch	MC ZASW-2-50DR+	0 - 5000	- 90 dB
Ampli K	MC ZHL-30W-252+	0.7 - 2500	+ 50 dB
Ampli Li	MC LZY-1+	20 - 512	+ 40 dB
Ampli	MC LZY-22+	0.1 - 200	+ 43 dB
Coupler	MC ZSCJ-2-1+	5 -500	-
Circulator K	RADC-800-2000M-S23	800 - 2000	-
Circulator Li	RADC-225-400M-N23	225-400	-

Table A.7: RF components described in figure 2.10.

A.6 Electrical schemes

In this appendix, we present the electrical schemes of the security system and the optocoupler box which isolates the command card from the IGBTs. Those drawings were conceived and realized by the workshop of the institute.

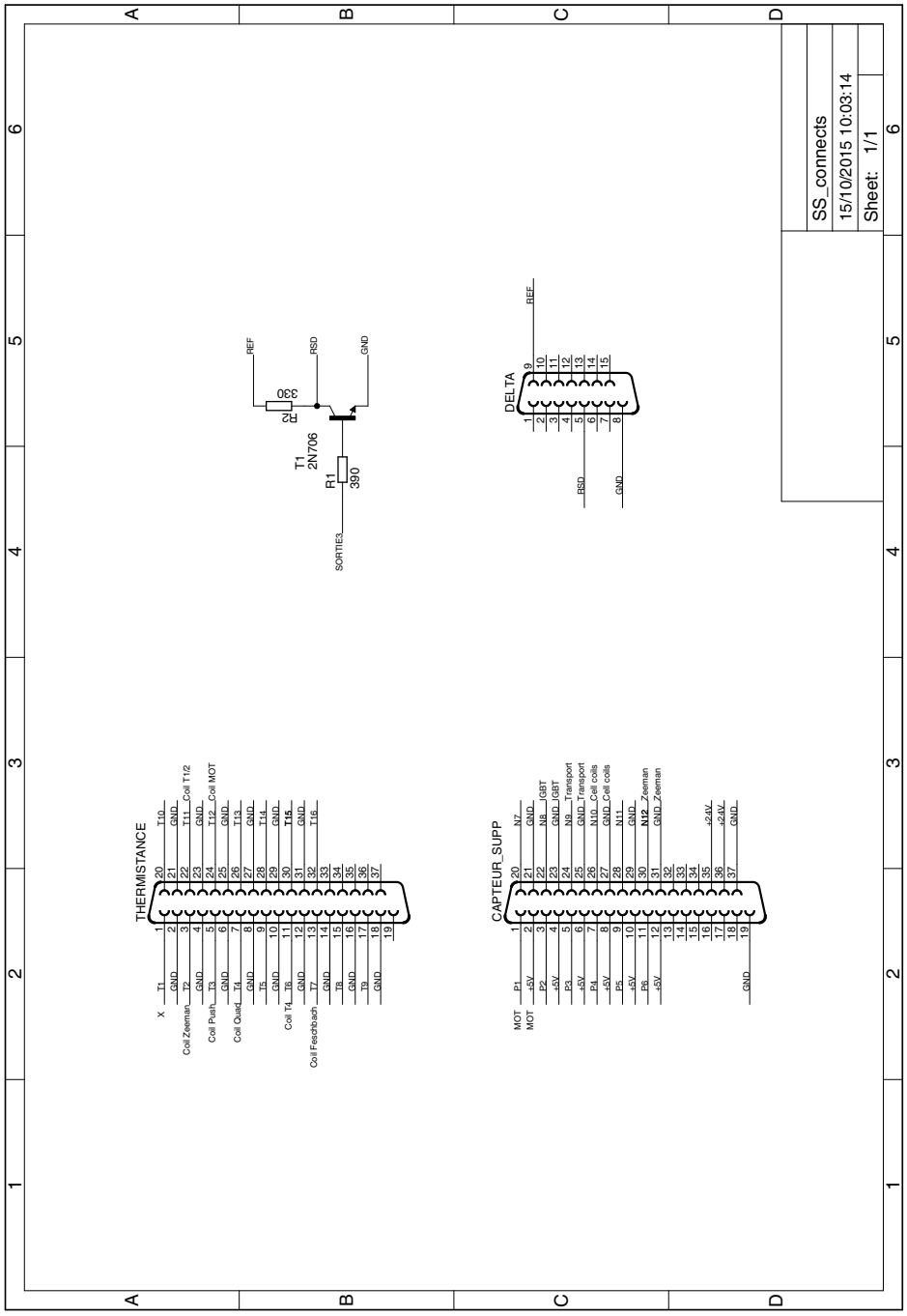

Figure A.7: Security system: connections to and from the box. The output is a 0-5V TTL signal provided to the Remote Shut Down circuit of each power supply.

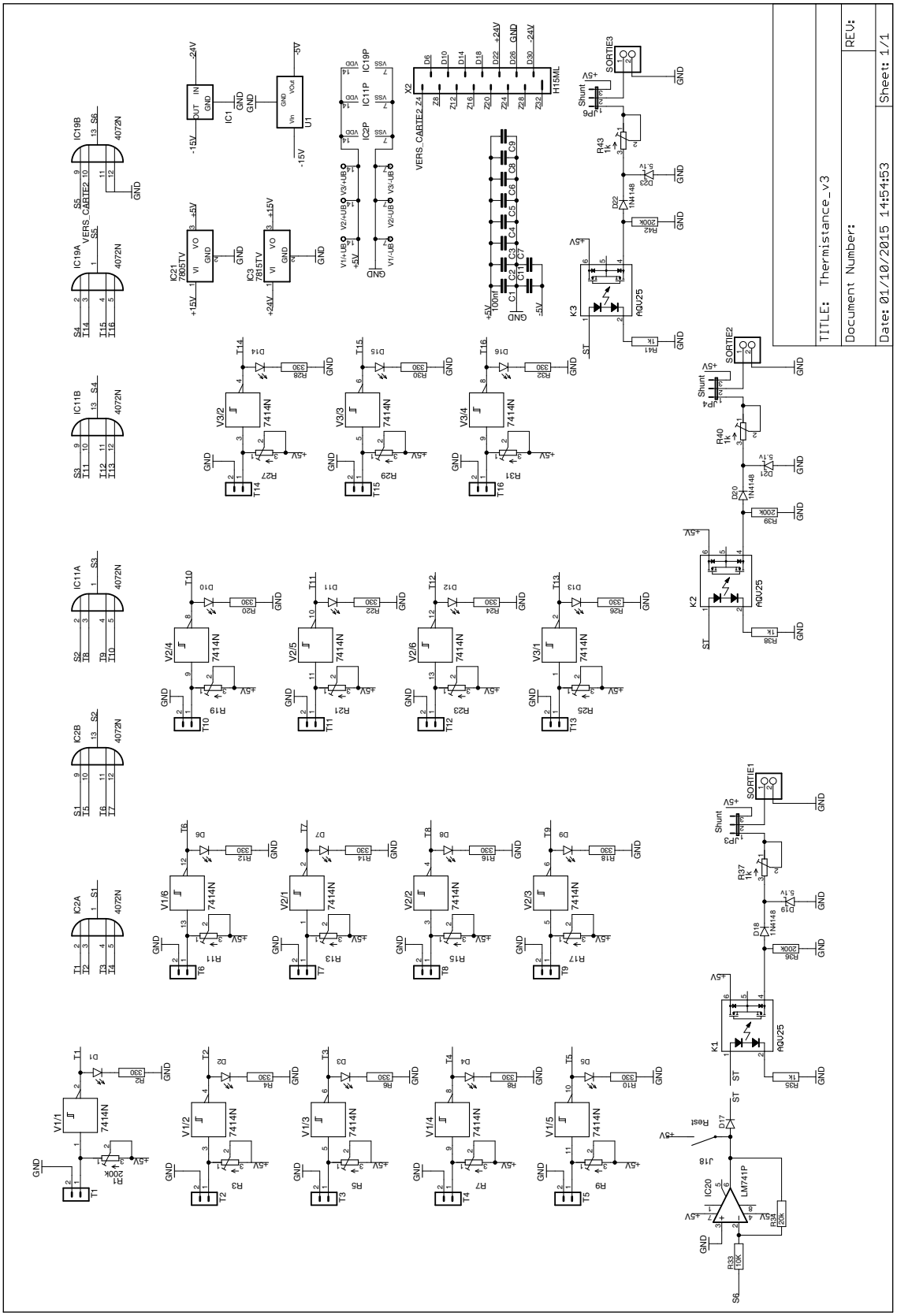

Figure A.8: Security system: thermistances monitoring and main output. The value of 8 thermistors is continuously compared to reference values set by potentiometers. If one of the monitored temperature exceeds the threshold, the output signal of the security system is switched off to 0V.

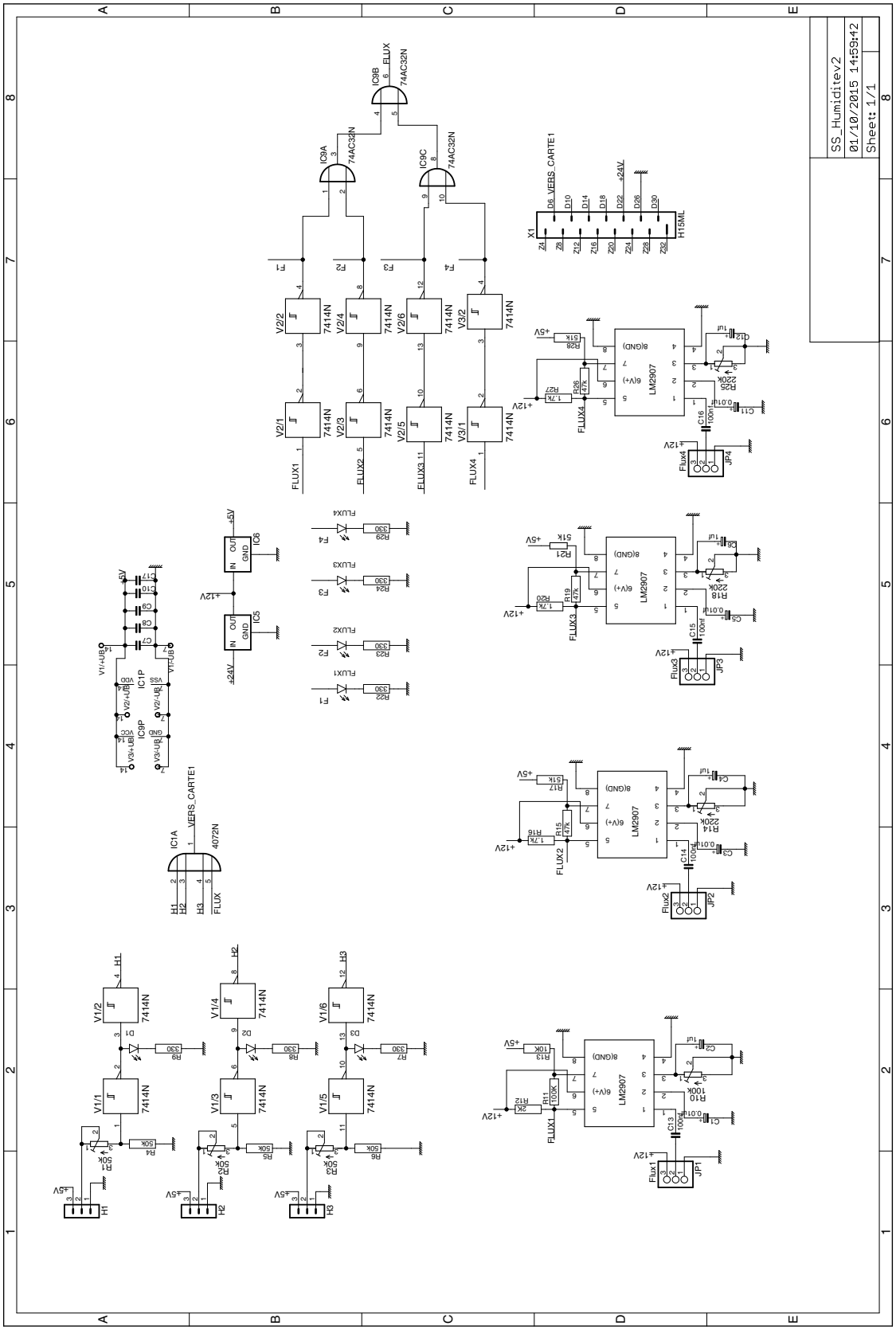

Figure A.9: Security system: humidity monitoring. This card is not currently used in our experiment.

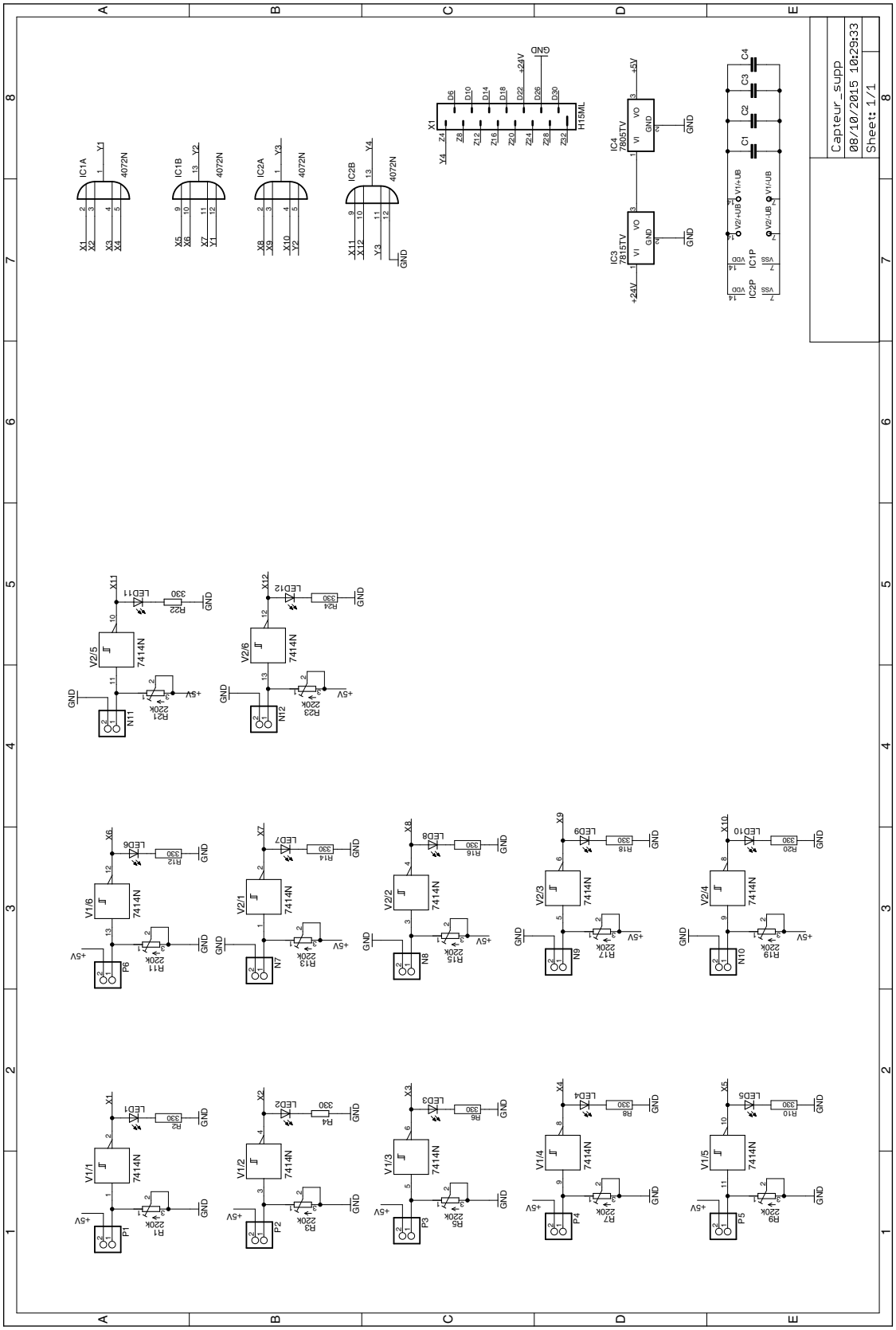

Figure A.10: Security system: flow monitoring. The water flows of 6 cooling systems are continuously monitored. If any of them is below a threshold fixed by a potentiometer incorporated on the fluxmeters, the output signal of the security system is switched off to 0V.

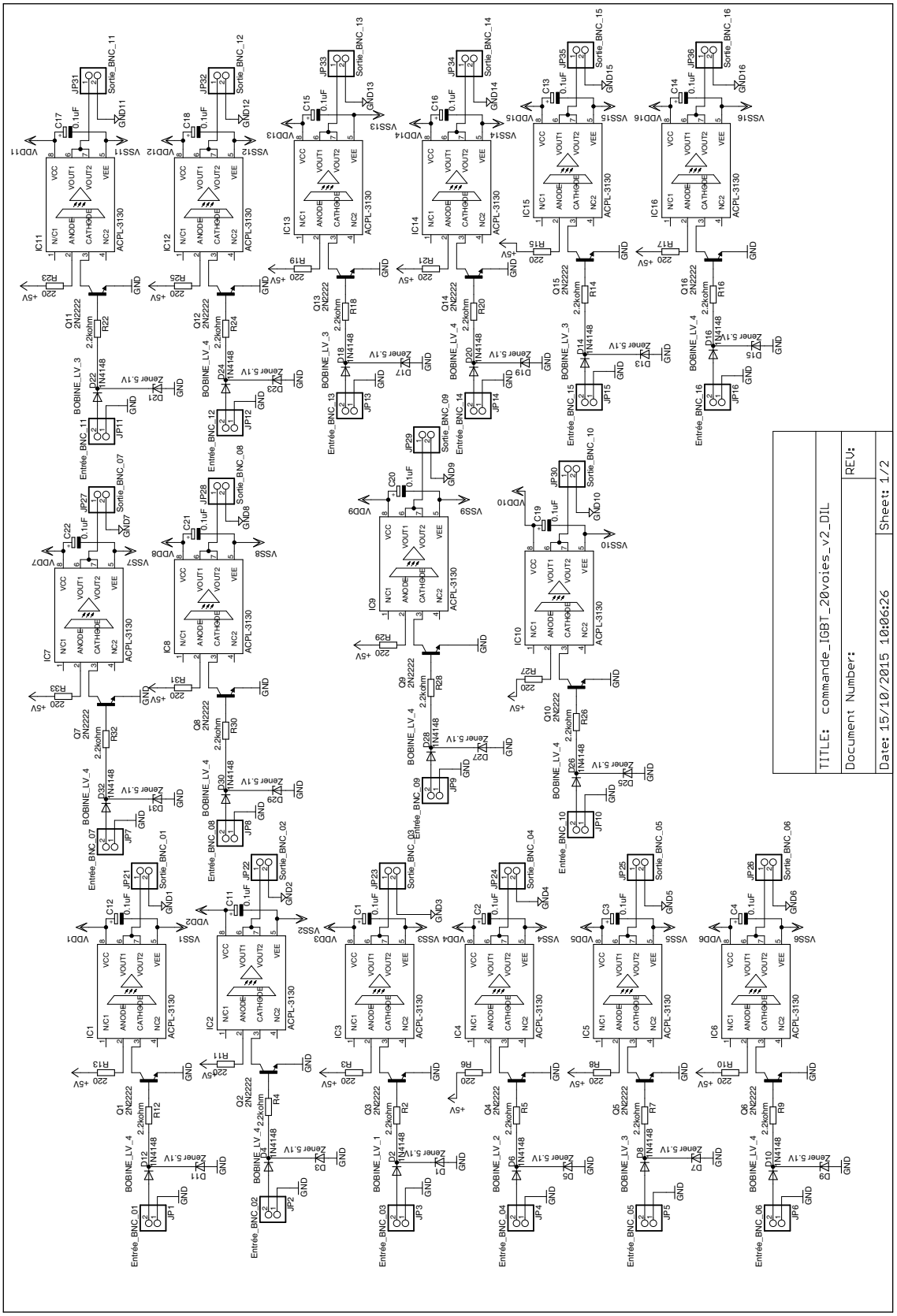

Figure A.11: Optocouplers between computer and system (1/2).

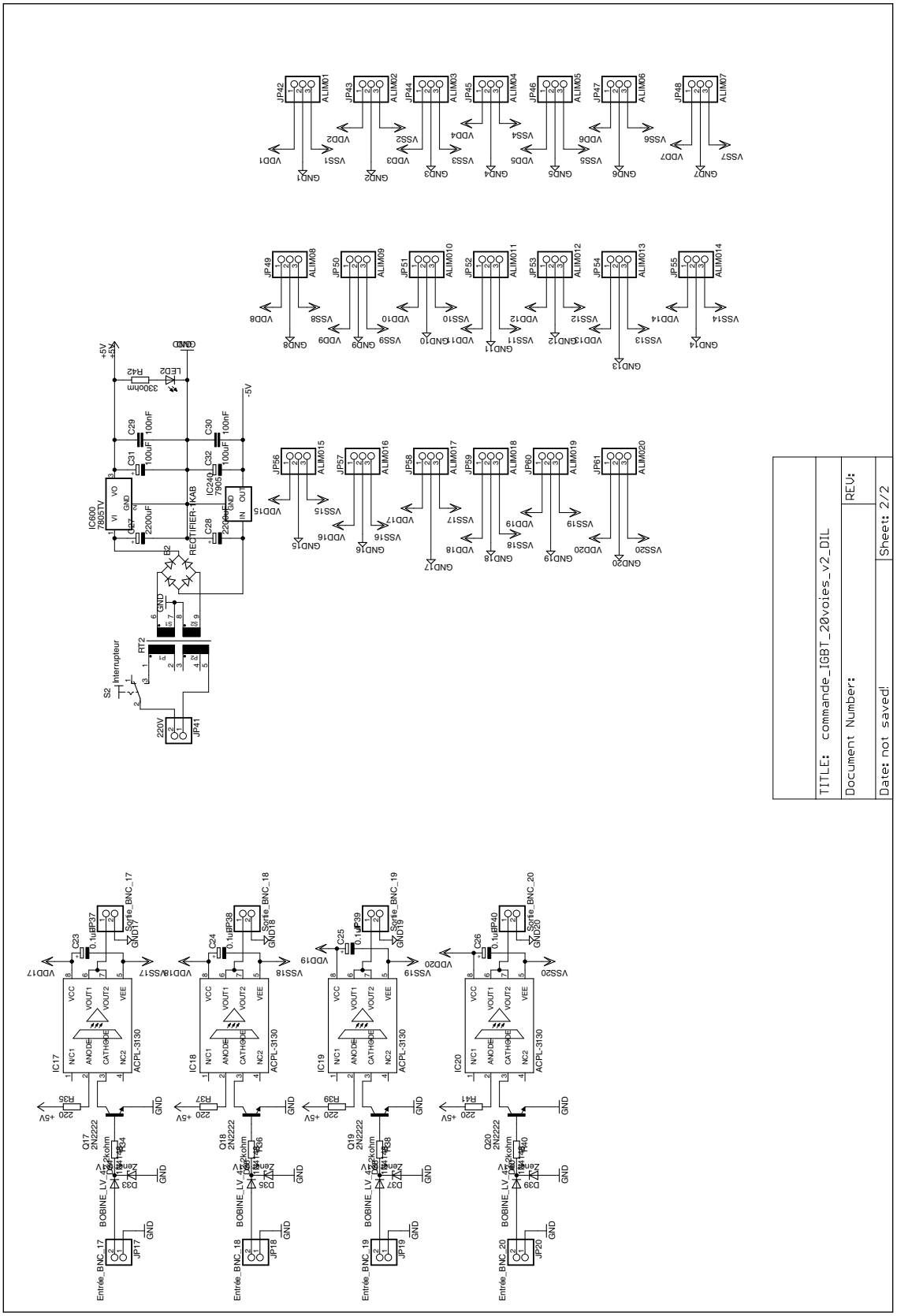

Figure A.12: Optocouplers between computer and system (2/2).

Chapter B Publications

Contents

Simultaneous sub-Doppler laser cooling of fermionic... 201
Analog Simulation of Weyl Particles with Cold Atoms 213
La quête des températures ultrabasses 220

Simultaneous sub-Doppler laser cooling of fermionic...

Franz Sievers, Norman Kretzschmar, Diogo Rio Fernandes, Daniel Suchet, Michael Rabinovic, Saijun Wu, Colin V. Parker, Lev Khaykovich, Christophe Salomon, and Frédéric Chevy, 'Simultaneous sub-Doppler laser cooling of fermionic ^{6}Li and ^{40}K on the D_1 line: Theory and experiment', *Physical Review A*, **vol. 91**, issue 2, page 023426 (2015)

Simultaneous sub-Doppler laser cooling of fermionic ^{6}Li and ^{40}K on the D_1 line: Theory and experiment

Franz Sievers,[1,*] Norman Kretzschmar,[1] Diogo Rio Fernandes,[1] Daniel Suchet,[1] Michael Rabinovic,[1] Saijun Wu,[2,†] Colin V. Parker,[3] Lev Khaykovich,[4] Christophe Salomon,[1] and Frédéric Chevy[1]

[1]*Laboratoire Kastler Brossel, École Normale Supérieure, CNRS, UPMC, 24 rue Lhomond, 75005 Paris, France*

[2]*State Key Laboratory of Surface Physics and Department of Physics, Fudan University, 200433 Shanghai, People's Republic of China*

[3]*James Franck Institute, Enrico Fermi Institute and Department of Physics, University of Chicago, Chicago, Illinois 60637, USA*

[4]*Department of Physics, Bar-Ilan University, Ramat-Gan 52900, Israel*

(Received 30 October 2014; revised manuscript received 30 January 2015; published 23 February 2015)

We report on simultaneous sub-Doppler laser cooling of fermionic ^{6}Li and ^{40}K using the D_1 optical transitions. We compare experimental results to a numerical simulation of the cooling process applying a semiclassical Monte Carlo wave-function method. The simulation takes into account the three-dimensional optical molasses setup and the dipole interaction between atoms and the bichromatic light field driving the D_1 transitions. We discuss the physical mechanisms at play, identify the important role of coherences between the ground-state hyperfine levels, and compare D_1 and D_2 sub-Doppler cooling. In 5 ms, the D_1 molasses phase greatly reduces the temperature for both ^{6}Li and ^{40}K at the same time, with final temperatures of 44 and 11 μK, respectively. For both species this leads to a phase-space density close to 10^{-4}. These conditions are well suited to direct loading of an optical or magnetic trap for efficient evaporative cooling to quantum degeneracy.

DOI: 10.1103/PhysRevA.91.023426 PACS number(s): 37.10.De, 32.80.Wr, 67.85.−d

I. INTRODUCTION

The road towards quantum degeneracy in atomic gases usually starts with a laser cooling and trapping phase. The resulting initial phase-space density of the atomic ensemble and the initial collision rate should be as high as possible for initiating efficient evaporative cooling to quantum degeneracy. Sub-Doppler cooling has proven to be a powerful technique to increase the phase-space density of most alkali atoms and other atoms with multiple-level structure [1–3]. However, in the case of lithium and potassium, the narrow excited-state structure of the D_2 transition compromises the efficiency of this cooling scheme [4,5]. Both species possess stable fermionic and bosonic isotopes, and they play an important role in recent experimental studies of strongly correlated quantum gases. Thus, important efforts have been devoted to searching for alternative laser cooling schemes.

For instance, it has recently been shown that three-dimensional (3D) Sisyphus cooling for ^{7}Li, some gigahertz red detuned from the D_2 line, can lead to temperatures as low as 100 μK, with up to 45% of the atoms in the cooled fraction [6]. A second option is to operate the magneto-optical trap (MOT) on a transition with a smaller linewidth to reduce the Doppler temperature [7–9]. Such transitions exist for ^{6}Li and ^{40}K in the near-UV and blue regions of the spectrum, respectively, leading to temperatures of 33 μK for ^{6}Li and 63 μK for ^{40}K. Yet, special optics and a coherent source at 323 nm for ^{6}Li and at 405 nm for ^{40}K are needed for this approach. Additionally, at these wavelengthes the available power is still a limiting factor.

More recently a simpler sub-Doppler cooling scheme using blue-detuned molasses operating on the D_1 line was proposed and demonstrated on ^{40}K [10] and has been extended to other atomic species such as ^{7}Li [11], ^{39}K [12,13], and ^{6}Li [14]. Using this technique, temperatures as low as 20 μK (^{40}K), 50 μK (^{7}Li), 6 μK (^{39}K), and 40 μK (^{6}Li) were reached.

Even though the main ingredients of the D_1 cooling scheme are now understood at a qualitative level, in particular, the role of the coherences between hyperfine ground-state levels [11], a complete picture, taking into account the full level structure of the atoms, is still missing. In this paper, we present a 3D semiclassical solution of the optical Bloch equations that takes into account the full set of relevant energy levels of alkali atoms and we apply it to the case of ^{6}Li and ^{40}K. The model fully confirms the experimentally observed cooling behavior and its robustness with respect to changes in experimental parameters. The model is validated by a good match between the simulation and the experimentally measured temperature and fluorescence rate. We recover the important role of the Raman detuning between the main cooling laser and the repumping laser on the achievable temperature. We show here, for both ^{6}Li and ^{40}K, that the gain in temperature of a factor of $\sim$3 at the exact Raman resonance is well reproduced by the theoretical model and that the amount of coherence between both hyperfine states shows a pronounced resonance behavior. Beyond individual studies of the two species, we also show experimentally that simultaneous cooling of ^{6}Li and ^{40}K does not lead to any severe trade-off and is technically easy to implement. We are able to capture more than 1×10^9 atoms of each species, with a capture efficiency exceeding 60% from a compressed magneto-optical trap (CMOT), and reach temperatures as low as 44 μK for ^{6}Li and 11 μK for ^{40}K within 5 ms.

II. D_1 COOLING MECHANISM

In a typical D_1 cooling setup (Fig. 1), all the D_1 hyperfine levels are involved in the interaction. The sub-Doppler cooling effects include a mix of Sisyphus cooling, motion-induced and off-resonant light coupling from gray to bright levels, and

*franz.sievers@lkb.ens.fr
†saijunwu@fudan.edu.cn

 ©2015 American Physical Society

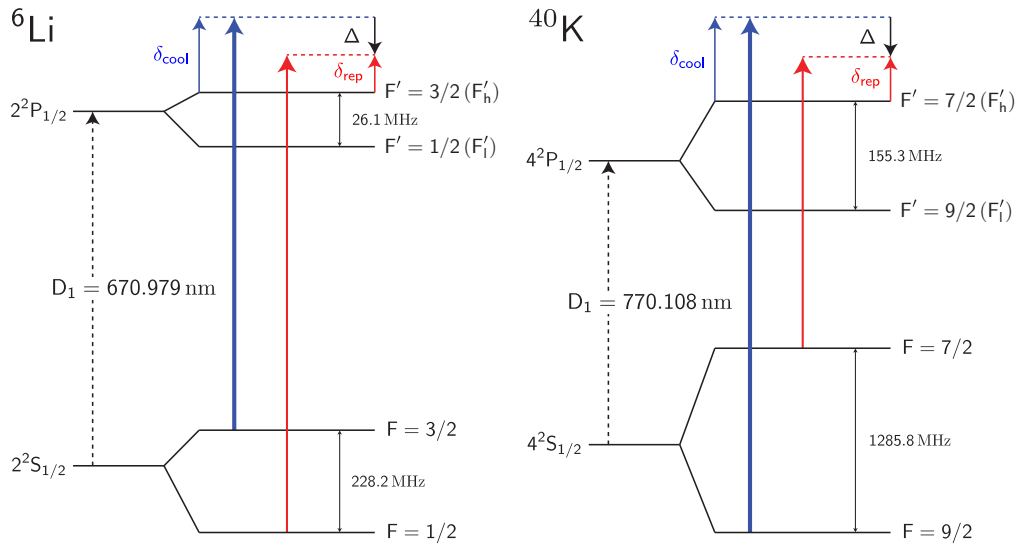

FIG. 1. (Color online) Cooling scheme on the ^{6}Li and ^{40}K D_1 lines. The cooling beam (blue) is blue detuned by $\delta_{\rm cool}$ from the $|F = 3/2\rangle \to |F'_h = 3/2\rangle$ ($|F = 9/2\rangle \to |F'_h = 7/2\rangle$) transition, where F'_h (F'_l) is the upper (lower) excited-state level. The repumping beam (red) is blue detuned by $\delta_{\rm rep}$ from the $|F = 1/2\rangle \to |F'_h = 3/2\rangle$ ($|F = 7/2\rangle \to |F'_h = 7/2\rangle$) transition. Detuning from the Raman condition is denoted $\Delta = \delta_{\rm rep} - \delta_{\rm cool}$.

coherent population trapping of slow atoms in nearly decoupled states. In this section we first introduce our semiclassical laser cooling model. We then present and compare the results from experimental observations and numerical simulations and, finally, discuss the physical mechanism of D_1 cooling.

A. Semiclassical Monte Carlo simulation

The level diagrams of our bichromatic cooling scheme for both ^{6}Li and ^{40}K are depicted in Fig. 1. The D_1 molasses is composed of a 3D lattice whose polarization configuration is the same as that of a six-beam standard MOT, but with two sidebands to address the $|F = 3/2\rangle$ and $|F = 1/2\rangle$ hyperfine ground states of ^{6}Li (respectively, $|F = 9/2\rangle$ and $|F = 7/2\rangle$ for ^{40}K) in the D_1 Λ system at positive detunings.

Here, by convention, we refer to the $|F = 3/2\rangle \to |F'_h\rangle$ and $|F = 1/2\rangle \to |F'_h\rangle$ transitions as cooling and repumping transitions. It is, however, important to note that neither the cooling nor the repumping D_1 transitions are actually closed.

Our numerical simulation of the cooling process is based on a semiclassical Monte Carlo wave-function method. The simulation takes into account the 3D optical molasses setup and the dipole interaction between the single atoms and the polarized light driving the transitions of the D_1 manifold, which is spanned by the $4(2I + 1)$ hyperfine Zeeman sublevels ($I > 0$ is the nuclear spin). We treat the external states of the atom classically and update its position $\mathbf{r}(t)$ and velocity $\mathbf{v}(t)$ according to the calculated expectation value of the light force:

$$\mathbf{f}(t) = \frac{\langle\psi(t)| - \nabla H_{\rm eff}(\mathbf{r}(t))|\psi(t)\rangle}{\langle\psi(t)|\psi(t)\rangle}. \tag{1}$$

The atomic internal states $|\psi(t)\rangle$ evolve in a dressed basis with respect to the cooling laser (Fig. 1), according to the Monte Carlo wave-function method [15,16] with the effective rotating-wave Hamiltonian

$$H_{\rm eff} = H_0 + H_{F=I-1/2} + H_{F=I+1/2} - i\hat{\Gamma}/2, \tag{2}$$

where

$$H_0 = \sum_m |F = I - 1/2,m\rangle\hbar\Delta\langle F = I - 1/2,m| - \sum_{F'm'} |F',m'\rangle\hbar(\delta_{\rm cool} + \delta_{{\rm hfs},F'})\langle F',m'|. \tag{3}$$

Here H_0 operates over the whole D_1 manifold and $\delta_{\rm cool}$ is the detuning of the cooling laser with respect to the $F = I + 1/2 \to F'_h$ transition, where F'_h (Fig. 1) corresponds to the excited hyperfine level that is higher in energy, e.g., $F'_h = 3/2$ for ^{6}Li and $F'_h = 7/2$ for ^{40}K. $\Delta = \delta_{\rm rep} - \delta_{\rm cool}$ is the two-photon detuning for the $F = I - 1/2 \to F = I + 1/2$ Raman transition, $\delta_{{\rm hfs},F'}$ the hyperfine splitting of the excited state for F'_l, and 0 for F'_h. The 0 of energy is chosen as that of the bare $F = I + 1/2$ ground state.

The light-atom coupling Hamiltonian

$$H_{F=I\pm1/2} = \hbar \sum_{m,\sigma,F',m'} \Omega_{F,\sigma} c_{F,m,\sigma,F',m'} \times |F,m\rangle\langle F',m'| + {\rm H.c.} \tag{4}$$

describes the cooling ($F = I + 1/2$) and repumping ($F = I - 1/2$) interactions [17]. Here $\Omega_{F,\sigma}$ are the Rabi frequencies of the repumping and cooling laser beams for $F = I - 1/2$ $F = I + 1/2$, respectively. $c_{F,m,\sigma,F'm'}$ represent the Clebsch-Gordan coefficients associated with the transitions coupled by σ polarized light. To take into account the radiation damping we include the spontaneous emission rate $\hat{\Gamma} = \Gamma\hat{P}_{ee}$ where Γ is the excited-state linewidth and $\hat{P}_{ee} = \sum_{F',m'} |F'm'\rangle\langle F'm'|$. This leads to a decay of the internal-state wave-function norm $\langle\psi(t)|\psi(t)\rangle$. The speed of this decay probabilistically dictates the collapse of the internal quantum states in the numerical simulation, which corresponds to spontaneous emission. We take into account the polarization of the spontaneous scattering photon and follow the standard quantum jump procedure to project the atomic states to ground states, with the norm

reset to unity [15]. To effectively account for heating due to both absorption and spontaneous emission, we assign a recoil momentum shift to $\mathbf{v}(t)$ twice before continuing to evolve $|\psi(t)\rangle$ via $H_{\text{eff}}(\mathbf{r}(t))$.

The simulations are performed with parameters matching the experimental setup by properly introducing the spatially dependent $\Omega_{F,\sigma}(\mathbf{r})$, the detunings Δ, δ_{cool}, and atomic initial conditions. To reproduce experimental conditions, we fix the relative phases for all 12 cooling and repumping laser beams at values randomized for each simulation trial. We record the evolution of the 3D atomic velocity, the time-stamped fluorescence events corresponding to quantum jumps, and internal-state properties such as state population and coherence. The observables are averaged over multiple simulation trials for comparison with the experiment.

B. Raman-detuning dependence for ^{6}Li

A critical parameter in the D_1 molasses scheme is the Raman detuning Δ (Fig. 1). In the following we investigate the Raman-detuning dependence of the ^{6}Li molasses temperature and fluorescence rate both theoretically and experimentally, for various cooling and repumping laser intensities.

Our ^{6}Li-^{40}K machine is described in [18]. We first load a lithium MOT using a laser-slowed atomic beam (Zeeman slower). After a compressed MOT phase the magnetic field and the D_2 light are switched off and the D_1 molasses is applied (a more detailed description of the sequence is presented in the Appendix). To probe the Raman-detuning dependence we apply a 100-μs D_1 molasses pulse with variable Δ to an atomic cloud precooled to 100 μK. Figures 2(a) and 2(b) show the fluorescence rate and the temperature after the pulse as functions of the Raman detuning Δ for the intensities used in the simulations. We observe a temperature dip at zero Raman detuning and a heating and fluorescence peak at positive Δ whose position and amplitude are correlated with the molasses intensity.

In the simulations we set the initial velocity of lithium to 0.2 m/s ($T \sim 30\ \mu$K). The simulation time is set to 200 μs. In the first 100 μs we allow the cooling dynamics to equilibrate, and during the second 100 μs we record the velocity $\mathbf{v}(t)$ as well as the time-stamped quantum jump events to calculate the equilibrium temperature and fluorescence rate. At each Raman detuning we average over 25 trajectories. The simulation results for two intensities, $I_{\text{cool}} = 2.7\ I_{\text{sat}}$, $I_{\text{rep}} = 0.13\ I_{\text{sat}}$ and $I_{\text{cool}} = 9\ I_{\text{sat}}$, $I_{\text{rep}} = 0.46\ I_{\text{sat}}$, are shown in Figs. 2(c) and 2(d), respectively (here I_{sat} refers to the saturation intensity of the D_2 line).

The simulated heating and fluorescence peak positions for low and high intensities (Fig. 2) agree well with the experimental findings. Also, the shift between the heating and the fluorescence peak, which increases with the molasses intensity, is numerically reproduced without any freely adjustable parameters.

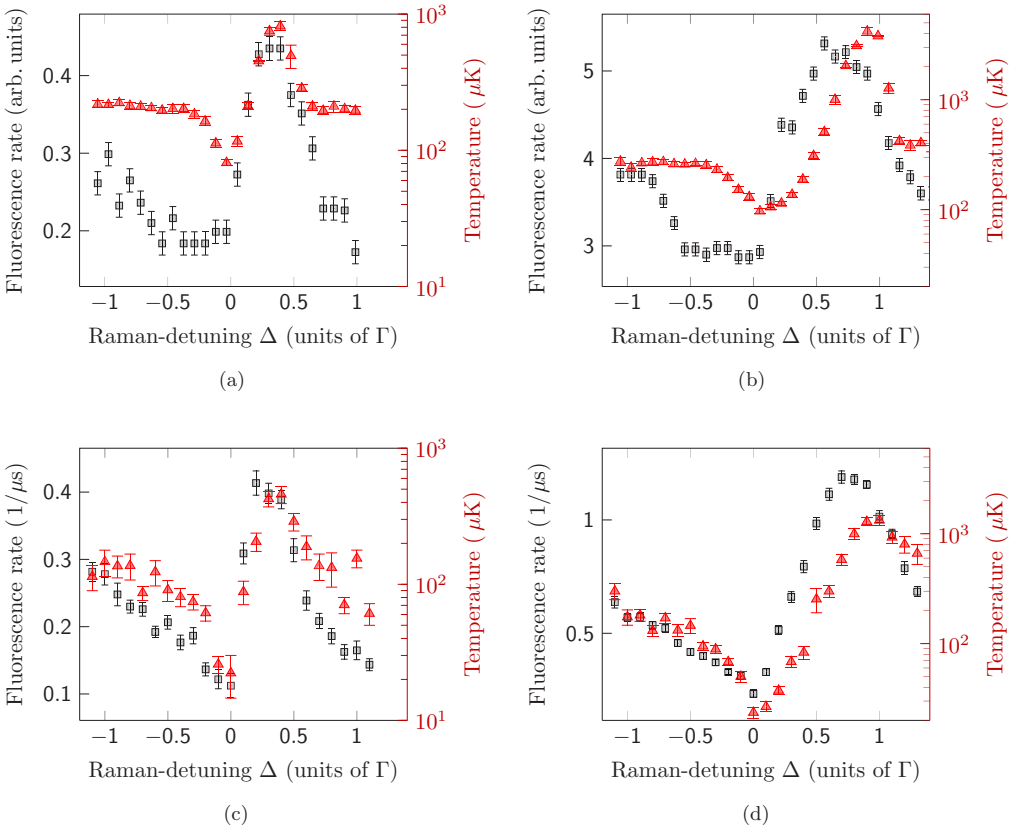

FIG. 2. (Color online) Fluorescence (squares) and temperature (triangles; logarithmic scale) of the ^{6}Li atomic cloud after a 100-μs pulse of D_1 light with variable Raman detuning Δ. Experiment: (a) low intensity; (b) high intensity. Simulation: (c) low intensity; (d) high intensity. Experimental and simulation results (a, c) for $I_{\text{cool}} = 2.7 I_{\text{sat}}$, $I_{\text{rep}} = 0.13 I_{\text{sat}}$ and (b, d) for $I_{\text{cool}} = 9\ I_{\text{sat}}$, $I_{\text{rep}} = 0.46\ I_{\text{sat}}$ per beam.

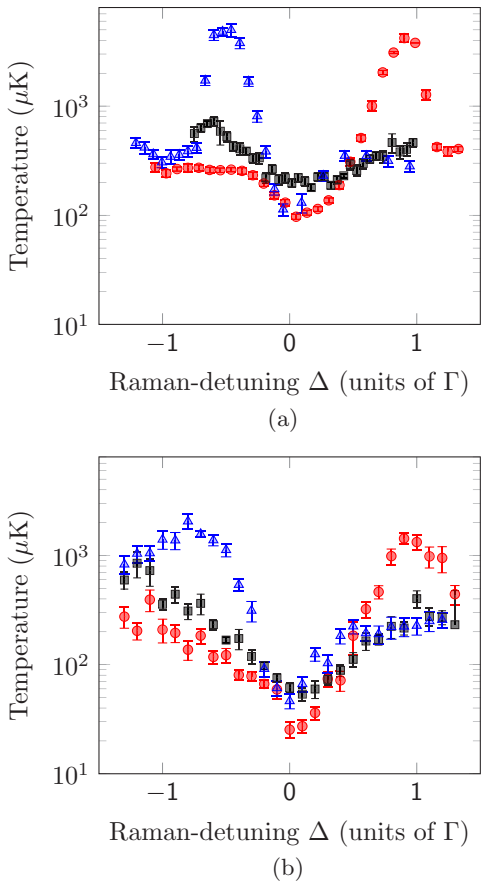

FIG. 3. (Color online) Temperature of the ^{6}Li D_1 molasses after a 100-μs pulse with variable Raman detuning Δ for different cooling and repumping intensities. (a) Experiment; (b) simulation. Standard intensities [(red) circles]: $I_{\rm cool} = 9\,I_{\rm sat}$, $I_{\rm rep} = 0.46\,I_{\rm sat}$. Equal cooling/repumping ratio (black squares): $I_{\rm cool} = I_{\rm rep} = 9\,I_{\rm sat}$. Inverted cooling/repumping ratio [(blue) triangles]: $I_{\rm cool} = 0.6\,I_{\rm sat}$, $I_{\rm rep} = 4.6\,I_{\rm sat}$.

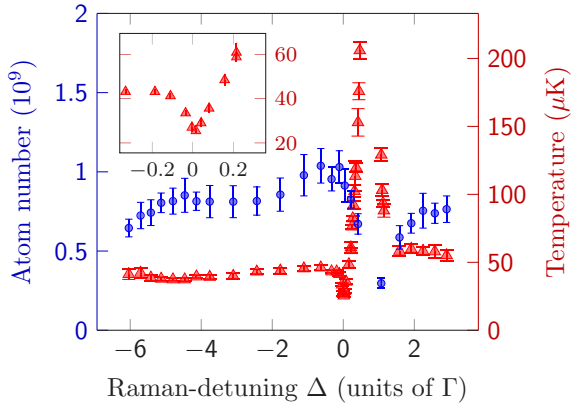

FIG. 4. (Color online) Experiment: Atom number and equilibrium temperature of the ^{40}K D_1 molasses as functions of the Raman detuning Δ. $\delta_{\rm cool} = 3\,\Gamma$, $I_{\rm cool} = 6\,I_{\rm sat}$, $I_{\rm rep}/I_{\rm cool} = 7.6\%$, $t_{\rm m} = 5$ ms. In the constant-temperature regions below $-0.1\,\Gamma$ and above $2\,\Gamma$ gray molasses cooling involves coherences between Zeeman states in a given hyperfine state but not between hyperfine states. At the exact Raman condition $\Delta = 0$, long-lived coherences between hyperfine states are established, as shown in the simulation in Fig. 5. In a narrow detuning range, the temperature [(red) triangles] drops to 20 μK. Inset: Expanded scale.

Despite the nice match between simulations and experiments in Figs. 2 and 3, we observe that the semiclassical simulations provide temperatures that are systematically lower by a factor of 2 to 4 than the measured ones, particularly near the Raman-resonance condition $\Delta = 0$. Here the simulation predicts a temperature of 20 μK, whereas the lowest measured temperature is 50 μK. The reason for this is not fully understood and may come from both theory and experimental limitations. First, the simulation is semiclassical and neglects the wave-function extent of the cold atoms. The predicted temperature of 20 μK corresponds to only six times the recoil energy $E_R = \frac{1}{2}mv_{\rm recoil}^2 = k_B \times 3.5\ \mu$K. Therefore, only a quantum treatment of the atoms' external motion can be expected to give a quantitative equilibrium temperature prediction in the low-intensity limit. In the simulation we observe that slow atoms are likely trapped within subwavelength regions, where the light shift is minimal and the atom is nearly decoupled from light over a long time without quantum jump. This coherent population trapping effect enhances the cooling at both large and small Δ, although it is most pronounced at the Raman resonance ($\Delta = 0$) since more choices of decoupled states emerge. The semiclassical picture clearly exaggerates the cooling effect since the wave nature of the atoms' external motion is not included in the model. In fact, the wave function of the slow atoms will sample a larger volume of the subwavelength traps and will shorten the lifetime of the dark periods.

On the experimental side the residual magnetic field cancellation has only been coarsely tuned for the data set presented in Fig. 2 (as well as in Figs. 3 and 4). With careful tuning of the magnetic field zeroing we were able to lower the ^{40}K temperature to 11 μK (Sec. II C, on ^{40}K) for lower-density samples. Interestingly, other groups have indeed found on ^{39}K lower temperatures (6 μK) than ours under the Raman condition [12]. Note also that in Fig. 2 for positive Raman detunings ($\Delta \sim 0.5\Gamma$ at low intensity and $\Delta \sim \Gamma$ at high intensity) the "temperature" corresponds to out-of-equilibrium situations as the atoms are quickly heated away and lost from the molasses. The notion of temperature should thus be taken with care in this region, unlike for negative Raman detunings, where a steady-state temperature is reached.

Another reason for shortening the lifetime of dark periods of the slow atoms is reabsorption of photons emitted by other atoms. We have indeed seen a density-dependent excess temperature, which we measured to be 4.6 μK $\times\ 10^{11}$ at/cm^3 for ^{40}K. A careful simulation of cooling including photon reabsorption processes is far more complex and is beyond the scope of this work.

We also study the same Raman-detuning-dependent effects, but for different cooling/repumping ratios. Typical experimental and simulation results are presented in Fig. 3. Here again, the simulation parameters are chosen according to the experimental values. The simulation and experiments match fairly well. In particular, for the usual configuration with $I_{\rm cool}/I_{\rm rep} > 1$ ($I_{\rm cool} = 9I_{\rm sat}$ and $I_{\rm rep} = 0.45I_{\rm sat}$), we observe a

heating peak at $\Delta > 0$. When inverting the roles of the cooling and repumping light, i.e., $I_{\rm cool}/I_{\rm rep} < 1$ ($I_{\rm cool} = 0.6 I_{\rm sat}$ and $I_{\rm rep} = 4.6 I_{\rm sat}$), the heating peak appears for $\Delta < 0$ instead. In all cases, cooling is most efficient at the Raman resonance ($\Delta = 0$). Finally, for $I_{\rm cool}$ equal to $I_{\rm rep}$, both as large as $9 I_{\rm sat}$, we observe less efficient cooling at $\Delta = 0$, with moderate heating at blue and red detunings.

C. Raman-detuning dependence for ^{40}K

Typical simulation results for ^{40}K are shown in Fig. 5(a). Compared to ^{6}Li, simulations for ^{40}K require a significantly higher computational power due to the larger internal-state dimensions as well as the larger atomic mass and therefore slower cooling dynamics. To save computation time, we start at a velocity of 0.2 m/s ($T \sim 50\ \mu$K) and set the simulation time to 2 ms. We record the velocity $\mathbf{v}(t)$ as well as the time-stamped quantum jump events for $t > 1$ ms to calculate the fluorescence rate. For each Raman detuning Δ, 13 trajectories are simulated.

Experimental results for ^{40}K are presented in Fig. 4, which shows the temperature and atom number of the D_1 molasses as functions of the Raman detuning Δ. The total molasses duration $t_{\rm m} = 5$ ms. In the last 2 ms a linear intensity ramp to $I_{\rm cool} = 6 I_{\rm sat}$ is performed. Just like ^{6}Li, we observe a sharp temperature drop under the Raman condition, a heating resonance at $\sim$0.7 Γ, and constant-temperature regions below $-0.1\ \Gamma$ and above $2\ \Gamma$. For the constant-temperature regions the temperature $T \sim 45\ \mu$K is low compared to the Doppler temperature $T_{\rm Doppler,K} = 145\ \mu$K. Under the Raman condition the temperature decreases to 23 μK. Under carefully optimized conditions we measured temperatures as low as 11 μK.

As for ^{6}Li, the comparison between Fig. 4 and Fig. 5(a) again demonstrates the qualitative agreement between simulations and experimental results and that the heating peak position is reproduced by the simulation without adjustable parameters. Interestingly, the inverted hyperfine structure in the ground and excited states of ^{40}K and the different $F \to F' = F - 1$ transition for the cooling laser and $F \to F' = F$ repumping transition does not significantly modify the D_1 cooling scheme compared to ^{6}Li.

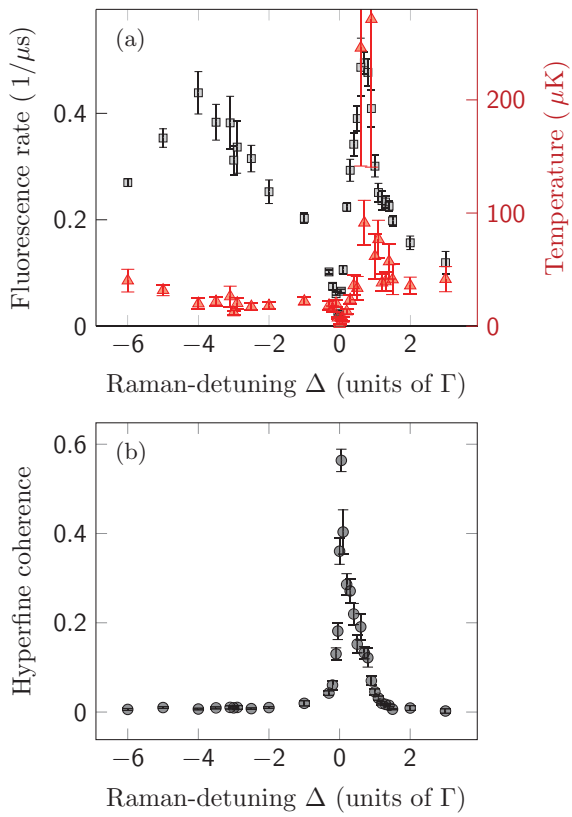

FIG. 5. (Color online) Simulation: Hyperfine coherence and Λ-enhanced cooling for the ^{40}K D_1 molasses. Simulation time, 2 ms; $\delta_{\rm cool} = 3\ \Gamma$; $I_{\rm cool} = 6 I_{\rm sat}$; $I_{\rm rep}/I_{\rm cool} = 7.6\%$. (a) Fluorescence (squares) and temperature (triangles) as functions of the Raman detuning Δ. (b) Coherence $4 \cdot \langle \rho^2_{F=7/2,F=9/2} \rangle$ between the two hyperfine ground states, $F = 7/2$ and $F = 9/2$ (see Sec. II E). The coherence is peaked under the Raman-resonance condition, with a width matching the temperature dip.

D. The D_1 cooling mechanism

The agreement between simulation and experiment suggests that the semiclassical picture is able to catch the essential physics behind the D_1 molasses cooling. In particular, the mechanisms behind the cooling dips and heating peaks in Figs. 2 to 4, previously interpreted using the dressed atom picture with a simplified three-level model [11], survive in the full level scheme of the D_1 transition.

It is well known that efficient D_2 sub-Doppler cooling requires isolated excited hyperfine levels for alkaline atoms [4,5]. In contrast, D_1 gray molasses operates well even when all D_1 levels are excited (as in the case of ^{6}Li) and even at zero excited-state hyperfine splitting as confirmed numerically. The robustness of D_1 molasses is also seen in its insensitivity to the relative phase between the "cooling" and the "repumping" lattices, a critical parameter for D_2 bichromatic cooling where no polarization gradient was introduced [19].

In the following we discuss the physics behind the robustness of the D_1 sub-Doppler cooling. We then revisit the cooling dips and heating peaks in Figs. 2 to 4.

We note that all the dipole-allowed D_1 transitions (Fig. 1) are "open": when addressed with weak off-resonant light, the probability of inelastic (m_F- or F-changing) photon scattering is comparable to or higher than that of elastic scattering. When blue detuned from the D_1 transitions, an off-resonant bichromatic lattice can establish a correlation between the spatially varying light shift (due to virtual elastic scattering) and decay (due to real inelastic scattering) for the dressed ground states, since a larger light shift is accompanied by a stronger light-atom coupling and typically a larger inelastic scattering cross section.

We verify this idea with the full D_1 model for ^{6}Li atoms subjected to a 1D lattice with orthogonal linear polarizations (lin $\perp$ lin configuration) with typical cooling parameters. The spatially varying light shifts ϵ of the six dressed ground states of ^{6}Li are plotted in Fig. 6(a). The decay of the dressed states, due to inelastic light scattering, is characterized by the decay rate γ, which is plotted versus ϵ in Fig. 6(d). We see a correlation between ϵ and γ for $\epsilon < 1.5$ MHz. This correlation is robustly established for the D_1 transitions, as

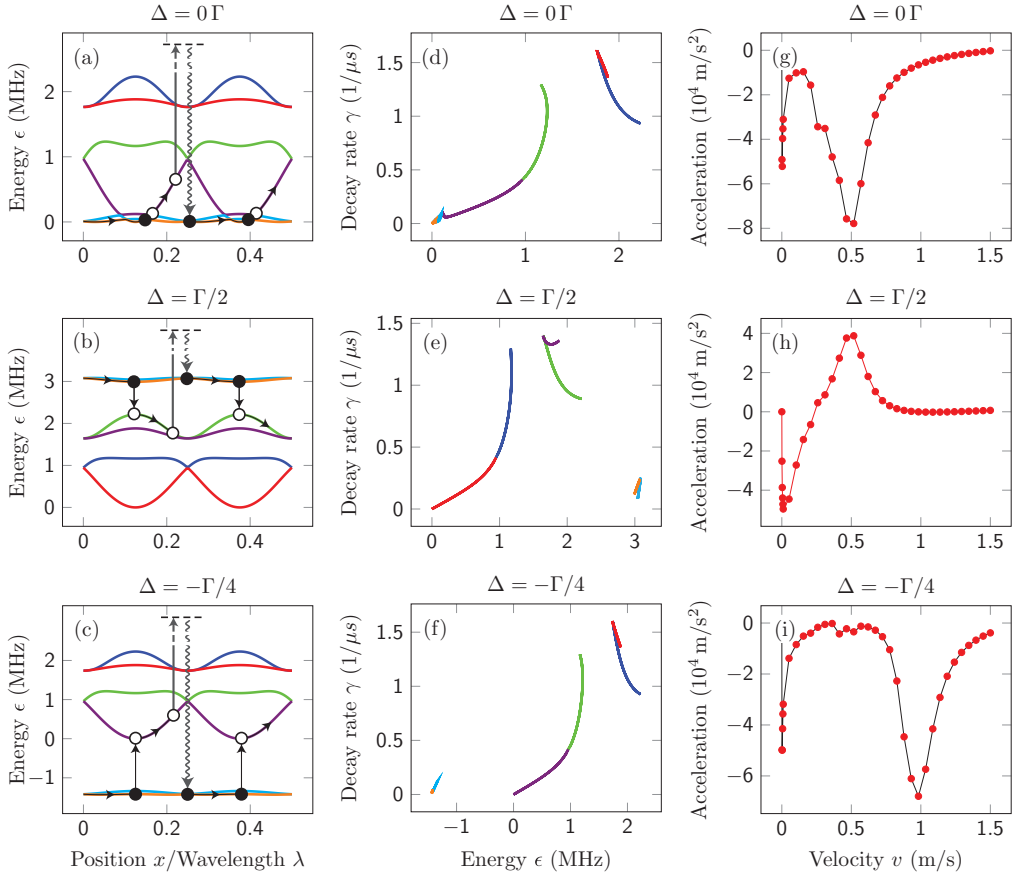

FIG. 6. (Color online) Cooling mechanism around the Raman condition in a simplified model. Optical Bloch equation simulation for ^{6}Li subjected to a 1D bichromatic lattice with linear orthogonal polarizations near D_1 resonance. The cooling lattice and repumping lattice are displaced by π ($\lambda/4$). $I_{\rm cool} = 15 I_{\rm sat}$, $I_{\rm rep} = 0.75 I_{\rm sat}$, $\delta_{\rm cool} = 4\,\Gamma$. (a–c) Dressed states as functions of the position, in units of the D_1 optical wavelength. The two dressed $F = 1/2$ levels (light blue and orange) are nearly flat in all the graphs due to the small $I_{\rm rep}$. (d–f) Decay rate of dressed states as a function of their energy shifts. Here the two dressed $F = 1/2$ levels span a very small energy range and have a low decay rate. (g–i) Velocity-dependent optical force for an atom dragged at velocity v. (a, d, g) $\Delta = 0$; (b, e, h) $\Delta = \Gamma/2$; (c, f, i) $\Delta = -\Gamma/4$. Note the negative sign of the force in (g) and (i), implying cooling, and the anticooling force for velocities near 0.5 m/s in (h).

verified numerically in the more complicated 3D lattices and for other atomic species. The correlation even persists for a fictitious atom with vanishing D_1 hyperfine splitting and reduced m_F-changing light scattering [20].

Such a correlation between the spatially dependent light shift ϵ and decay rate γ has two consequences: First, atoms with $kv < \gamma$ tend to accumulate in dressed states with low light shifts, which facilitates cooling through motion-induced coupling to higher energy dressed states [21]. This coupling is nonadiabatic as in the famous σ^+–σ^- 1D velocity selective coherent population trapping subrecoil cooling mechanism (VSCPT), where the spatial gradient of the atomic wave function induces a coupling to a bright state. Second, for a slowly moving atom that adiabatically follows a particular dressed state, the atom tends to leave the dressed state when the light shift is high, leading to Sisyphus cooling. In addition, at locations where $\epsilon, \gamma \sim 0$, slow atoms can be confined near the local dark states such as those in Fig. 6(a) near $x = 0, \lambda/8, \lambda/4, 3\lambda/8$ [22]. The resulting optical cooling force is plotted in Fig. 6(g) and is negative (cooling effect) over a broad range. We emphasize that this simplified 1D analysis remains valid in the more complex 3D beam geometry and is not restricted to ^{6}Li atoms. The D_1 laser cooling mechanism applies to all alkalis, even those amenable to efficient D_2 sub-Doppler cooling such as cesium and rubidium. As D_1 laser cooling involves dark states, it is less affected by density-dependent photon multiple scattering and heating than D_2 sub-Doppler cooling. Therefore it would be interesting to quantify the gain in phase-space density by applying D_1 sub-Doppler cooling for these atoms.

In comparison, sub-Doppler cooling on the D_2 lines is significantly different. While the $F = I \pm 1/2 \rightarrow F' = I \pm 1/2$ transitions are as "open" as in D_1, the $F = I + 1/2 \rightarrow F' = I + 3/2$ and $F = I - 1/2 \rightarrow F' = I - 3/2$ transitions have both "closed" and open transitions. Here the closed transitions are characterized by a greater-than-unity elastic-to-inelastic scattering ratio. If the $F = I + 1/2 \rightarrow F' = I + 3/2$ transitions can be isolated, then by taking advantage of the nearly closed $m_F - m_{F'}$ transitions, a correlation between the light shift and the decay rate can be established with (instead) a red-detuned lattice, as in standard sub-Doppler cooling [1–3]. However, in the case of small hyperfine splitting the open hyperfine transitions are as well addressed at red detuning, leading to short-lived potential minima and

degraded correlations, contributing to the inefficiency of the sub-Doppler cooling [23].

E. Physical picture of the Raman-detuning effect

We now extend the three-level picture in Ref. [11] to understand the details of the experiment. The cooling dips observed both experimentally and numerically under the Raman-resonance condition are also fairly easy to understand in the full model: At $\Delta = 0$ the resonant Raman-coupling splits the $F = I \pm 1/2$ hyperfine ground states into a bright and a dark manifold. The dark manifold is weakly coupled to the molasses. More precisely, the coupling strength of the Raman dark manifold is even weaker than those due to individual cooling-repumping couplings. Therefore the emergence of the Raman dark manifold enhances all sub-Doppler cooling effects.

Since the dark manifold is a coherent superposition of the two hyperfine states $F_1 = I - 1/2$ and $F_2 = I + 1/2$, we expect that laser-cooled atoms mostly occupy the dark manifold and therefore display a hyperfine coherence ρ_{F_1,F_2} with significant amplitude. To test this picture, we record the time-dependent off-diagonal density matrix quantity $4 \cdot \langle \rho^2_{F_1,F_2}(t)\rangle$ for all the quantum trajectories of the numerical simulations. The factor 4 ensures the normalization to one for the maximally coherent situation. To compute the two-photon detuning Δ-dependent quantity $4 \cdot \langle \rho^2_{F_1,F_2}\rangle$, we average over both the equilibrium time and many quantum trajectories at fixed Δ. Typical results for ^{40}K are given in Fig. 5, with the cooling parameters corresponding to Fig. 4. We see that the coherence $4 \cdot \langle \rho^2_{F_1=7/2,F_2=9/2}\rangle$ is peaked under the Raman-resonance condition and becomes significant, with a width matching the temperature dip.

As in Figs. 2 to 4 and [11] we now explain the heating peaks with the full D_1 model. We first focus on the case of $I_{\rm cool} \gg I_{\rm rep}$ so that at large $|\Delta|$ the dressed $F = I - 1/2$ hyperfine level is relatively long-lived and populated. As shown in Figs. 6(b) and 6(c), the Raman detuning Δ determines the energy level of the dressed $F = I - 1/2$ hyperfine level, and it is clear that when $\Delta < 0$, the motion-induced coupling to the dressed $F = I + 1/2$ level should still contribute to cooling [as in Figs. 6(c), 6(f), and 6(i)] [21], apart from Sisyphus cooling. On the contrary, for $\Delta > \max[\epsilon_{F=I+1/2}]$, e.g., a Raman detuning beyond the maximum light shift of the dressed $F = I + 1/2$ manifold [as in Figs. 6(b), 6(e), and 6(h)], motion-induced coupling to the lower energy dressed $F = I + 1/2$ manifold would lead to heating. In addition, the Sisyphus effect at the $F = I + 1/2$ manifold also contributes to heating, since atoms coupled from $F = I - 1/2$ are more likely to start at the antitrap positions. The corresponding heating peak is located at $\Delta \sim \max[\epsilon_{F=I+1/2}] > 0$.

When $I_{\rm cool} \ll I_{\rm rep}$, the heating peak is shifted to $\Delta \sim -\max[\epsilon_{F=I-1/2}] < 0$, as in Fig. 3. This is straightforward to understand, as the roles of the two hyperfine ground states are now inverted with respect to the previous case. Finally, for $I_{\rm cool} \sim I_{\rm rep}$, the two hyperfine ground states have similar lifetimes and therefore similar steady-state populations. As the heating effects are balanced by cooling effects, the corresponding heating peaks in Fig. 3 (black squares) at $\Delta \sim \max[\epsilon_{F=I+1/2}]$, $\Delta \sim -\max[\epsilon_{F=I-1/2}]$ are substantially suppressed.

TABLE I. Parameters of the simultaneous ^{6}Li and ^{40}K D_1 cooling phase.

Parameter	Potassium	Lithium
P (mW)	230	300
$\delta_{\rm cool}$ (Γ)	2.3	4
$\delta_{\rm rep}$ (Γ)	2.3	4
$I_{\rm cool}$ per beam ($I_{\rm sat}$)	14	14
$I_{\rm cool}/I_{\rm rep}$	8	20
D-line property	^{40}K	^{6}Li
$\Gamma/(2\pi)$ (MHz)	6.04	5.87
$I_{\rm sat}$ (mW/cm^2)	1.75	2.54

III. SIMULTANEOUS ^{6}Li AND ^{40}K D_1 COOLING

Finally, we discuss the simultaneous operation of the ^{6}Li and ^{40}K D_1 molasses. We found that this simultaneous operation is required for subsequent efficient thermalization between both species in a quadrupole magnetic trap. The timing sequence and parameters are the same as for single-species operation. Experimental details are given in the Appendix and in [10]. The D_1 molasses phase is composed of a 3-ms capture phase and a 2-ms cooling phase. Table I summarizes the optimal parameters of the dual-species molasses. The presence of the other species reduces the atom numbers in the MOTs by 4% for ^{6}Li and by 10% for ^{40}K. However, we observe no mutual influence during the CMOT and the D_1 molasses phase. The temperatures and relative atom numbers in dual-species operation do not differ from those in single-species operation. There are several reasons for this. First, the D_1 resonances and lasers are ~100 nm apart in wavelength. Second, the CMOT and molasses phases are short in duration (5 ms) and the light-induced interspecies collision losses or heating are minimized as atoms are accumulated in dark states. Table II summarizes the performance of the different experimental

TABLE II. Performance of the different experimental phases for ^{6}Li and ^{40}K, in dual-species operation. We list the optimum temperature T, the atom number N, the density n, and the phase-space density ϕ.

	T (μK)	N (10^9)	n (10^{10} cm^{-3})	ϕ[a] (10^{-5})
		Lithium		
MOT	1000	2	2.6	0.03
CMOT	800	2	18	0.29
Molasses	48	1.2	7.6	8.2
		Potassium		
MOT	240	3.2	7	0.02
CMOT	2000	3.2	37	0.06
Molasses	11	3.2	30	10.7

[a]The given phase-density does not take into account the different internal states and is calculated as $\phi = n\lambda_{\rm B}^3$, where $\lambda_{\rm B}$ is the thermal de Broglie wavelength.

phases in dual-species operation. For both ^{6}Li and ^{40}K the D_1 molasses phase largely reduces the temperature, while the cloud size after the CMOT phase is conserved. For both species this leads to a phase-space density close to 10^{-4}.

IV. CONCLUSION

In this study we have investigated the properties of D_1 laser cooling both experimentally and with numerical simulations. The simulations take into account all relevant Zeeman and hyperfine levels as well as the 3D bichromatic lattice geometry. Simulations and experimental results match fairly well for both lithium and potassium. Various sub-Doppler cooling effects [10] are recovered in the full model. We have outlined the importance of coherences between the ground-state hyperfine levels [11] and interpreted the cooling mechanisms as resulting from a combination of VSCPT-like nonadiabatic transitions between dark and coupled states and Sisyphus-type cooling. The discrepancy (factor of 2 to 4) between the temperature predicted by the semiclassical model and the experimentally observed ones calls for further investigations and the development of a full quantum treatment of the external atomic motion using a Monte Carlo wave-function approach [15,29].

We have discussed the physics behind the robustness of the D_1 cooling scheme, in particular, its insensitivity to the excited-state hyperfine splitting and to the relative phase between the cooling and the repumping lattices, which is in sharp contrast to its D_2 counterpart [4,5,19]. We first suggest and numerically verify that, due to the predominance of the "open transitions" at D_1, the bichromatically dressed ground states exhibit a robust correlation between light shift and decay. We clarify that such a correlation leads to the accumulation of an atomic population in the lowest energy dressed states at Raman resonance for both nonadiabatic and Sisyphus cooling. The picture also helps to explain the enhanced cooling at Raman resonance, as well as the reduced cooling or even heating at large Raman detunings. Because of the smaller absorption cross section for atoms cooled in weakly coupled states, D_1 gray molasses should also be less affected by the density-dependent heating than its D_2 counterpart [24].

Experimentally, using commercial semiconductor laser sources delivering $\sim$200 mW of CW power, we achieve efficient, simultaneous cooling of ^{6}Li and ^{40}K, resulting in a phase-space density close to 10^{-4} for both species. This D_1 cooling scheme enables efficient direct loading of a dipole or magnetic trap because of the large gain in temperature. As recently shown in [12] and [14], these conditions are well suited to direct loading of an optical dipole trap and to the performance of all-optical evaporation to quantum degeneracy. In our own experiments, we load a magnetic trap, transport the atoms to a separate science cell, and perform evaporative cooling of ^{40}K in two Zeeman states with a combined magnetic-optical trap scheme introduced in [25]. Deep quantum degeneracy ($T/T_F = 0.14$) in the dipole trap has been achieved and will be the subject of a future publication.

Finally, we have also used the D_1 gray molasses scheme to cool the bosonic ^{41}K isotope. All of 5×10^9 ^{41}K atoms from a CMOT were cooled to a final temperature of 20 μK, leading to a phase-space density of 1.1×10^{-4}. This confirms the generality of this D_1 sub-Doppler cooling method.

ACKNOWLEDGMENTS

We acknowledge useful discussions with A. T. Grier, I. Ferrier-Barbut, B. S. Rem, M. Delehaye, S. Laurent, and J. V. Porto and support from Région Ile de France (DIM Nano-K and IFRAF), the European Union (ERC grants Ferlodim and Thermodynamix), Institut de France (Louis D. Award), and Institut Universitaire de France. D.R.F. acknowledges the support of Fundação para a Ciência e Tecnologia (FCT-Portugal) through Grant No. SFRH/BD/68488/2010. S.W. acknowledges the support of the Physics Department at Swansea University, where part of this research was carried out.

APPENDIX: EXPERIMENTAL DETAILS

In this section we describe the experimental details, as well as the results of additional measurements on the D_1 molasses scheme, in particular, the single-species operation of ^{6}Li. Our experimental setup has been described previously [18]. A Zeeman slower for ^{6}Li and a 2D$^+$ MOT for ^{40}K load the 3D dual-species MOT in the MOT chamber. The D_2 laser systems for ^{6}Li and ^{40}K comprise master oscillator power amplifiers (MOPAs) to produce light at 671 and 767 nm, respectively. Beamsplitters and acousto-optic modulators generate the cooling and repumping beams, which are combined before injecting tapered amplifiers for the Zeeman slower and 3D MOT for ^{6}Li and, accordingly, the 2D$^+$ MOT and 3D MOT for ^{40}K.

The D_1 laser system for ^{40}K operates at 770 nm and is composed of a MOPA and an electro-optic modulator to produce the repumping frequency. The total power used for the ^{40}K cooling is 240 mW, with an intensity per molasses beam of $14 I_{\text{sat}}$.

The source for the ^{6}Li D_1 light at 671 nm used in this work is a homemade solid-state laser, the next generation of [26] and [27], with up to 5 W output power. Acousto-optic modulators allow us to independently tune the frequencies and powers of the cooling and repumping beams, before recombination and injection into an optical fiber. We typically use 300 mW total power for the ^{6}Li D_1 cooling. The waist of the ^{6}Li D_1 beam after the telescope (Fig. 7) is 8.6 mm. We have also used a commercial 671-nm tapered amplifier system (MOPA) with 130 mW available power impinging on the atoms and obtained similar performances for the capture efficiency and sub-Doppler temperatures.

Our optical scheme superimposes the D_1 and D_2 light for both ^{6}Li and ^{40}K and produces the molasses and 3D MOT beams (Fig. 7). D-shaped mirrors (M_{D}) superimpose the D_1 cooling light and the 3D MOT light of each species before a dichroic mirror (M_{dichroic}) combines the lithium and potassium light. The beam containing all eight frequencies is expanded and distributed to the three pairs of σ^+-σ^- counter-propagating beams of the 3D MOT and the D_1 molasses. The two horizontal axes are retroreflected, and the vertical axis consists of two independent beams. The $\lambda/2$ plates of order 4 for lithium ($\lambda/2^*_{\text{Li}}$) and potassium ($\lambda/2^*_{\text{K}}$)

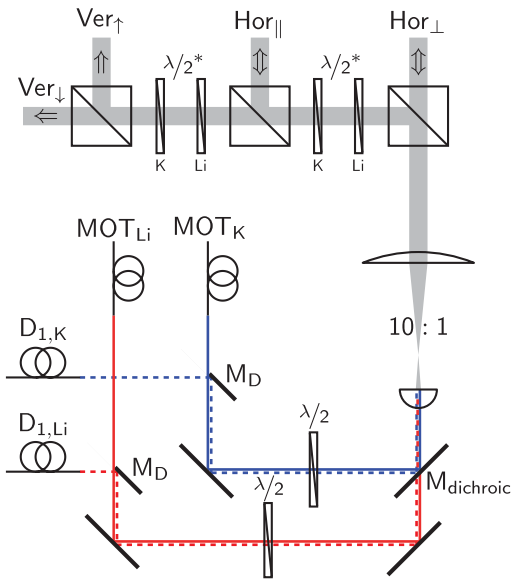

FIG. 7. (Color online) Optical scheme of the D_1 molasses. The 3D MOT light and the D_1 cooling light are superposed using a D-shaped mirror (M_D). Afterwards a dichroic mirror (M_{dichroic}) combines the lithium and potassium light, which is subsequently expanded and distributed to the three perpendicular axes of the 3D MOT.

allow for independent control of the ^{6}Li and ^{40}K MOT power distribution.

The experiment starts with the loading of the dual-species MOT. In 10 s we typically load 8×10^8 ^{6}Li atoms with an initial temperature of 1 mK and 3×10^9 ^{40}K atoms at 200 μK. Then a CMOT phase [28] increases the density of the atom cloud. The magnetic gradient is linearly ramped from 9 to 60 G/cm in 5 ms. Meanwhile the frequencies of the cooling and the repumping beams are tuned closer to resonance and their intensities are linearly decreased. The CMOT phase results in an increase in the peak density by a factor of 7 (5.3) and a temperature of 800 μK (2 mK) for ^{6}Li (^{40}K). At the end of the CMOT phase the current of the MOT coils is switched off within ~100 μs. We start the D_1 molasses phase for ^{6}Li with a delay of 200 μs in order to wait for transient magnetic fields to decay. We found that this delay is not needed for ^{40}K.

1. ^{6}Li D_1 molasses

Here we study the cooling dynamics of ^{6}Li alone. We set the peak intensity of the molasses to $14.6 I_{\text{sat}}$ per beam, set the cooling/repumping ratio to $I_{\text{cool}}/I_{\text{rep}} = 20$, and fix the global detuning to $\delta = \delta_{\text{cool}} = \delta_{\text{rep}} = 4\ \Gamma$. Here $I_{\text{sat}} = 2.54$ mW/cm^2 is the saturation intensity of the D_2 cycling transition, and $\Gamma = 2\pi \times 5.87$ MHz the D_1 line natural linewidth for ^{6}Li. Figure 8 shows the atom number and temperature of the D_1 molasses as functions of the molasses duration t_m. The temperature is determined through time-of-flight measurements. We capture 60% of the 8×10^8 CMOT atoms. Within 3 ms the atoms are cooled from 800 μK to the asymptotic temperature of 120 μK with a $1/e$ cooling time constant $\tau_{\text{cool}} = 0.6$ ms. The direct

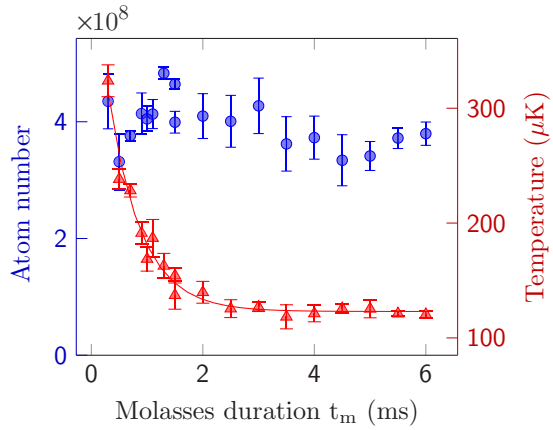

FIG. 8. (Color online) Number of atoms captured in the ^{6}Li D_1 molasses (circles) and their temperature (triangles) as functions of the molasses duration, with a $1/e$ cooling time constant $\tau_{\text{cool}} = 0.6$ ms. The number of atoms in the compressed MOT is 8×10^8.

measurement of the fluorescence shows a very fast decay at the beginning ($\tau_{\text{fast}} < 1\ \mu$s), followed by a further decrease by another factor of 2 within 2 ms. This indicates that the atoms are accumulated in dark states during the cooling process. We find the $1/e$ lifetime of the D_1 molasses atom number for these parameters to be $\tau_{\text{D1}} = 90$ ms.

The molasses atom number and temperature as functions of the global detuning δ are shown in Fig. 9. We observe a decrease in the temperature from 188 to 100 μK for $\delta_{\text{cool}} = 2 \ldots 7$. The capture efficiency increases sharply until 4 Γ and stays constant until 7 Γ.

We now study the influence of the D_1 light intensity. When increasing the cooling intensity, while keeping the molasses time fixed to 3 ms, we observe an increase in both the capture efficiency and the temperature (Fig. 10). To take advantage of the intensity-dependent temperature, we use two successive phases in the cooling sequence. During the first

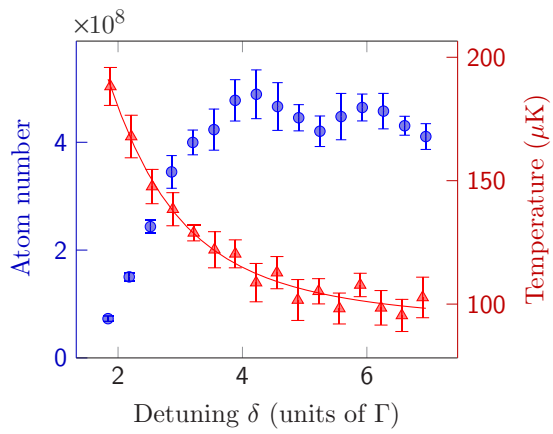

FIG. 9. (Color online) Number of atoms captured in the ^{6}Li D_1 molasses (circles) and their temperature (triangles) after a 3-ms capture phase at a high intensity, $I_{\text{cool}} = 14.6 I_{\text{sat}}$, as functions of the global detuning $\delta = \delta_{\text{cool}} = \delta_{\text{rep}}$. The number of atoms in the compressed MOT is 8×10^8.

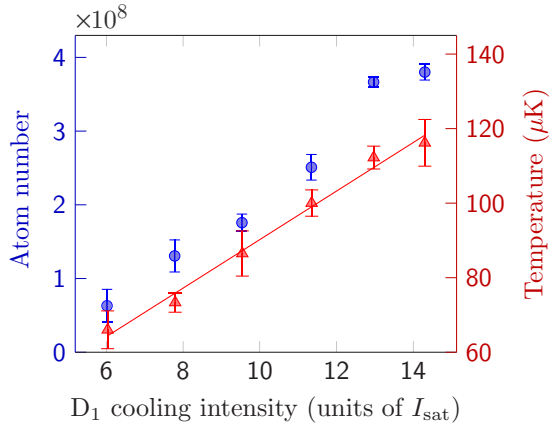

FIG. 10. (Color online) Number of atoms captured in the ^{6}Li D_1 molasses (circles) and their temperature (triangles) as functions of the D_1 cooling beam intensity for $\delta_{\rm cool} = 4\,\Gamma$ and $I_{\rm rep} = I_{\rm cool}/20$. The number of atoms in the compressed MOT is 8×10^8. The atom number (temperature) increases linearly with a slope of 4×10^7 atoms/$I_{\rm sat}$ (6.5 μK/$I_{\rm sat}$).

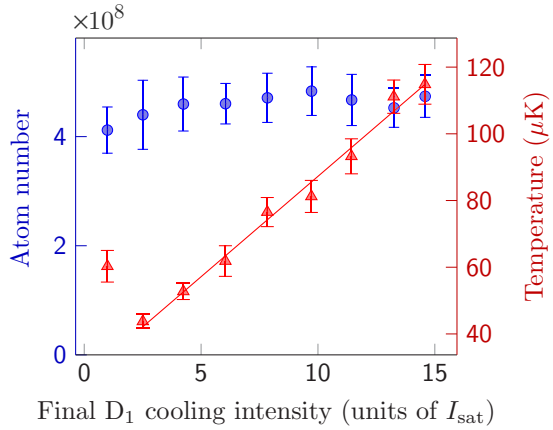

FIG. 11. (Color online) Number of atoms captured in the ^{6}Li D_1 molasses (circles) and their temperature (triangles) after a 3-ms capture phase at a high intensity, $I_{\rm cool} = 14.6 I_{\rm sat}$, followed by a 2-ms linear intensity ramp to an adjustable value. The temperature increases linearly for a higher intensity, with a slope of $\sim$6 μK/$I_{\rm sat}$. The detuning is fixed to $\delta_{\rm cool} = 4\,\Gamma$. The number of atoms in the compressed MOT is 8×10^8.

3 ms we capture the atoms at a high intensity, yielding the highest capture efficiency. Then the intensity is linearly ramped within 2 ms to an adjustable final intensity to further lower the temperature. Figure 11 shows that the intensity ramp reduces the final temperature from 115 to 44 μK without a significant atom loss, for a final intensity $I_{\rm cool,final} = 2.5 I_{\rm sat}$. For lower intensities we observe heating and atom loss. The cooling/repumping intensity ratio influences the atom number and the temperature. We find an optimal temperature for $I_{\rm cool}/I_{\rm rep} = 20$. For a lower ratio the temperature increases slightly and the atom number starts to drop at around $I_{\rm cool}/I_{\rm rep} = 7$. For $I_{\rm cool}/I_{\rm rep} > 33$ the cooling mechanism becomes inefficient, leading to atom loss and heating.

Measuring the atom cloud size at the end of the CMOT and molasses phases, we see no significant change, proving that diffusion during the molasses phase is small. In terms of the phase-space density the atom loss is largely overcompensated by the 14 times reduction in temperature.

[1] J. Dalibard and C. Cohen-Tannoudji, J. Opt. Soc. Am. B **6**, 2023 (1989).
[2] P. D. Lett, W. D. Phillips, S. L. Rolston, C. E. Tanner, R. N. Watts, and C. I. Westbrook, J. Opt. Soc. Am. B **6**, 2084 (1989).
[3] D. S. Weiss, E. Riis, Y. Shevy, P. J. Ungar, and S. Chu, J. Opt. Soc. Am. B **6**, 2072 (1989).
[4] A. Bambini and A. Agresti, Phys. Rev. A **56**, 3040 (1997).
[5] X. Xu, T. H. Loftus, J. W. Dunn, C. H. Greene, J. L. Hall, A. Gallagher, and J. Ye, Phys. Rev. Lett. **90**, 193002 (2003).
[6] P. Hamilton, G. Kim, T. Joshi, B. Mukherjee, D. Tiarks, and H. Müller, Phys. Rev. A **89**, 023409 (2014).
[7] P. M. Duarte, R. A. Hart, J. M. Hitchcock, T. A. Corcovilos, T.-L. Yang, A. Reed, and R. G. Hulet, Phys. Rev. A **84**, 061406 (2011).
[8] D. C. McKay, D. Jervis, D. J. Fine, J. W. Simpson-Porco, G. J. A. Edge, and J. H. Thywissen, Phys. Rev. A **84**, 063420 (2011).
[9] J. Sebastian, C. Gross, K. Li, H. C. J. Gan, W. Li, and K. Dieckmann, Phys. Rev. A **90**, 033417 (2014).
[10] D. R. Fernandes, F. Sievers, N. Kretzschmar, S. Wu, C. Salomon, and F. Chevy, EPL (Europhys. Lett.) **100**, 63001 (2012).
[11] A. T. Grier, I. Ferrier-Barbut, B. S. Rem, M. Delehaye, L. Khaykovich, F. Chevy, and C. Salomon, Phys. Rev. A **87**, 063411 (2013).
[12] G. Salomon, L. Fouché, P. Wang, A. Aspect, P. Bouyer, and T. Bourdel, EPL (Europhys. Lett.) **104**, 63002 (2013).
[13] D. Nath, R. K. Easwaran, G. Rajalakshmi, and C. S. Unnikrishnan, Phys. Rev. A **88**, 053407 (2013).
[14] A. Burchianti, G. Valtolina, J. A. Seman, E. Pace, M. De Pas, M. Inguscio, M. Zaccanti, and G. Roati, Phys. Rev. A **90**, 043408 (2014).
[15] J. Dalibard, Y. Castin, and K. Mølmer, Phys. Rev. Lett. **68**, 580 (1992).
[16] H. Carmichael, *An Open Systems Approach to Quantum Optics*, *Lecture Notes in Physics Monographs*, Vol. 18 (Springer-Verlag, Berlin, 1993).
[17] By assuming the ground-state hyperfine splitting to be large enough, the $F = I + 1/2$ ($F = I - 1/2$) is dark to the repumping (cooling) laser and the associated couplings are ignored in the Hamiltonian. This approximation allows us to write down the Hamiltonian in the time-independent form.
[18] A. Ridinger, S. Chaudhuri, T. Salez, U. Eismann, D. R. Fernandes, K. Magalhães, D. Wilkowski, C. Salomon, and F. Chevy, Eur. Phys. J. D **65**, 223 (2011).
[19] R. Gupta, C. Xie, S. Padua, H. Batelaan, and H. Metcalf, Phys. Rev. Lett. **71**, 3087 (1993).
[20] W. Happer, Rev. Modern Phys. **44**, 169 (1972).

[21] C. Cohen-Tannoudji, *Atomic Motion in Laser Light*, edited by J. Dalibard, J. Raimond, and J. Zinn Justin (Les Houches, Session LIII, 1990), pp. 1–164.

[22] Exact locations of the dark states depend on the relative phase between the cooling and the repumping lattices.

[23] For D_2 transitions the complication is also Δ dependent. A complete comparison of D_1 and D_2 cooling will be the subject of a future publication.

[24] M. Drewsen, P. Laurent, A. Nadir, G. Santarelli, A. Clairon, Y. Castin, D. Grison, and C. Salomon, Appl. Phys. B **59**, 283 (1994).

[25] Y.-J. Lin, A. R. Perry, R. L. Compton, I. B.Spielman, and J. V. Porto, Phys. Rev. A **79**, 063631 (2009).

[26] U. Eismann, F. Gerbier, C. Canalias, A. Zukauskas, G. Trénec, J. Vigué, F. Chevy, and C. Salomon, Appl. Phys. B **106**, 25 (2011).

[27] U. Eismann, A. Bergschneider, F. Sievers, N. Kretzschmar, C. Salomon, and F. Chevy, Opt. Express **21**, 9091 (2013).

[28] M.-O. Mewes, G. Ferrari, F. Schreck, A. Sinatra, and C. Salomon, Phys. Rev. A **61**, 011403 (1999).

[29] Y. Castin and K. Mølmer, Phys. Rev. Lett. **74**, 3772, (1995).

Analog Simulation of Weyl Particles with Cold Atoms

Daniel Suchet, Mihail Rabinovic, Thomas Reimann, Norman Kretschmar, Franz Sievers, Christophe Salomon, Johnathan Lau, Olga Goulko, Carlos Lobo and Frédéric Chevy, 'Analog Simulation of Weyl Particles with Cold Atoms', *Europhysics Letters*, **vol. 114**, page 26005 (2016)

A Letters Journal Exploring the Frontiers of Physics

April 2016

EPL, **114** (2016) 26005
doi: 10.1209/0295-5075/114/26005

www.epljournal.org

Analog simulation of Weyl particles with cold atoms

Daniel Suchet[1], Mihail Rabinovic[1], Thomas Reimann[1], Norman Kretschmar[1], Franz Sievers[1], Christophe Salomon[1], Johnathan Lau[2], Olga Goulko[3], Carlos Lobo[2] and Frédéric Chevy[1]

[1] *Laboratoire Kastler Brossel, ENS-PSL Research University, CNRS, UPMC, Collège de France 24, rue Lhomond, 75005 Paris, France*
[2] *Mathematical Sciences, University of Southampton - Highfield Southampton, SO17 1BJ, UK*
[3] *Department of Physics, University of Massachusetts - Amherst, MA 01003, USA*

received on 25 April 2016; accepted by G. Shlyapnikov on 1 May 2016
published online 18 May 2016

PACS 67.85.-d – Ultracold gases, trapped gases
PACS 05.20.Dd – Kinetic theory
PACS 05.70.Ln – Nonequilibrium and irreversible thermodynamics

Abstract – In this letter we report on a novel approach to study the dynamics of harmonically confined Weyl particles using magnetically trapped fermionic atoms. We find that after a kick of its center of mass, the system relaxes towards a steady state even in the absence of interactions, in stark contrast with massive particles which would oscillate without damping. Remarkably, the equilibrium distribution is non-Boltzmann, exhibiting a strong anisotropy which we study both numerically and experimentally.

editor's choice Copyright © EPLA, 2016

Introduction. – Weyl fermions were introduced for the first time in 1929 as massless solutions of the Dirac equation [1]. Despite constituting one of the paradigms of contemporary high-energy physics, their existence in Nature has remained unconfirmed until very recently. While at first suggested to describe neutrinos, the observation of flavor oscillations implying a non-zero rest mass ruled out this hypothesis [2]. It had been pointed out that they could be observed in the form of low-energy excitations of crystalline structures with a linear dispersion relation around a so-called Weyl point. The non-trivial topology of such Weyl semimetals is responsible for the Adler-Bell-Jackiw chiral anomaly [3,4] which leads to remarkable properties such as negative magnetoresistance, anomalous Hall effect and non-local transport [5]. Moreover, the confinement of quasiparticles obeying a linear dispersion relation was suggested as a way to engineer individual quantum dots [6], notably for the improvement of multiple exciton generation in solar cells [7].

The mere existence of Weyl points in reciprocal space requires a broken time-reversal or inversion symmetry, which are challenging to implement experimentally. As a consequence, observations of Weyl particles were reported only recently in 3D compounds such as HgCdTe, HgMnTe [8], TaAs [9,10] as well as in photonic crystals [11]. Owing to their high degree of control and versatility, cold atoms offer a promising and complementary route for the experimental study of Weyl fermions. Early proposals in this context were based on the band structure of cold atoms in 3D optical lattices extending the 2D Harper Hamiltonian [12]. Yet another approach is analog simulation where one takes advantage of the mathematical equivalence between two seemingly different physical systems. Such mapping were successfully used in the past to relate, for instance, Anderson localization to the δ-kicked rotor [13–15], quantum magnetism to the filling factor of an optical lattice [16,17], the solutions of the Dirac equation to the dynamics of ion chains [18,19], or quantum Hall edge states to the eigenmodes of classical coupled pendula [20].

In this letter, we report on the analog simulation of Weyl particles in a harmonic potential using a dilute gas of cold magnetically trapped atoms. Using a canonical mapping exchanging position and momentum in the system's Hamiltonian, we address the dynamics of an ensemble of non-interacting Weyl particles after excitation of their center of mass (CoM). The system's ensuing relaxation towards a steady state exhibits intriguing dynamics, resulting in a strongly anisotropic and non-thermal momentum distribution of the cold gas. Our observations are interpreted using a kinetic model based on virial theorem and energy conservation.

Mapping. – The magnetic quadrupole trap is a common technique for confining neutral atoms [21]. It is made up of a pair of coils carrying anti-parallel currents, creating

close to their symmetry center a linear magnetic field $\boldsymbol{B}_0(\boldsymbol{r}) = b(\alpha_x x,\, \alpha_y y,\, \alpha_z z)$, where z is the symmetry axis of the coils. Here b denotes the magnetic-field gradient and Maxwell's equations imply that $\alpha_x = \alpha_y = 1$, $\alpha_z = -2$. For a spin-(1/2) atom of mass m carrying a magnetic moment μ, the coupling to this field leads to the single-particle Hamiltonian

$$h\,(\boldsymbol{r}, \boldsymbol{p}) = \frac{p^2}{2m} - \mu\, \boldsymbol{\sigma} \cdot \boldsymbol{B}_0(\boldsymbol{r}), \tag{1}$$

where $\boldsymbol{\sigma}$ are the Pauli matrices. By means of the canonical mapping $X_i = cp_i/\mu b\alpha_i$ and $P_i = -\mu b\alpha_i x_i/c$ with c being an arbitrary velocity scale, the Hamiltonian (1) becomes

$$H = c\,\boldsymbol{\sigma} \cdot \boldsymbol{P} + \frac{1}{2}\sum_i k_i X_i^2. \tag{2}$$

The first term corresponds to the kinetic energy $c\boldsymbol{\sigma} \cdot \boldsymbol{P}$ of a massless Weyl particle moving at velocity c while the second one is readily identified as an anisotropic harmonic potential, characterized by spring constants $k_i = \alpha_i^2 \mu^2 b^2/mc^2 = \alpha_i^2 k$ along each direction i. This mapping is at the core of our work and it shows that neutral atoms confined by a linear potential can be used to simulate experimentally the dynamics of Weyl particles.

The single-particle trajectories of the Weyl particles can be obtained using Ehrenfest's theorem applied to the Hamiltonian (2). Using uppercase (lowercase) symbols for the phase-space coordinates of the Weyl particles (spin-(1/2) atoms), we obtain respectively in the Heisenberg representation:

$$\dot{X}_i = c\sigma_i, \qquad \dot{p}_i = \mu b\alpha_i\sigma_i, \tag{3}$$

$$\dot{P}_i = -k_i X_i, \qquad \dot{x}_i = p_i/m, \tag{4}$$

$$\dot{\boldsymbol{\sigma}} = \frac{2c}{\hbar}\boldsymbol{\sigma} \times \boldsymbol{P}, \qquad \dot{\boldsymbol{\sigma}} = \frac{2\mu}{\hbar}\boldsymbol{\sigma} \times \boldsymbol{B}(\boldsymbol{r}). \tag{5}$$

Equations (3) to (5) are fully quantum, but in the following we will focus on the classical regime, and consider the operator mean values. Noting that $\langle\boldsymbol{\sigma}\rangle^2 = 1$, The first of eqs. (3) immediately shows that even in a harmonic trap Weyl particles move at a constant velocity c. Equations (5) describe respectively the particle's spin precession around the momentum $\boldsymbol{P}$ and magnetic field $\boldsymbol{B}$. The adiabatic following results in the conservation of helicity and of the Zeeman populations, giving rise to topological properties. The analogy existing between these two equations allows to draw a parallel between a peculiar feature of Weyl particles, the Klein paradox [22], and the well-known Majorana losses [23–26] for magnetic traps. The Klein paradox states if the rate of change of the particle's energy is too high (*i.e.* much larger than $2Pc/\hbar$ for Weyl particles), the spin will not follow the momentum adiabatically and the helicity of the particle is not conserved. The resulting transfer of the particle to negative energy states leads to dramatic effects, such as the suppression of back-scattering for electrons in 1D carbon nanotubes [27]. For the equivalent picture of magnetically trapped atoms, in regions where the Larmor frequency $2\mu B/\hbar$ is smaller than the rate of change of the Zeeman energy, the atomic spin will not follow adiabatically the direction of the local magnetic field. This results in Majorana losses. The absence of backscattering in carbon nanotubes then appears as equivalent to the impossibility to trap atoms in a 1D magnetic quadrupole. Furthermore, for an ensemble of particles at temperature T, we can define a Klein loss rate Γ_{Klein} equivalent to the Majorana rate $\Gamma_{\text{Maj.}}$:

$$\Gamma_{\text{Maj.}} \simeq \frac{\hbar}{m}\left(\frac{\mu_B b}{k_B T}\right)^2, \qquad \Gamma_{\text{Klein}} \simeq \hbar k\left(\frac{c}{k_B T}\right)^2. \tag{6}$$

Just like Majorana losses prevent the existence of a true thermodynamic equilibrium in a quadrupole trap, the Klein paradox prevents stable trapping of Weyl particles in external potentials [6]. Nevertheless, at high enough temperature such as that considered in our experiments below, particles spend little time close to 0 and we can neglect Majorana-Klein losses. Particles of positive and negative helicities can therefore be described by the effective Hamiltonians

$$H_\pm = \pm c|P| + \sum_i \frac{k_i X_i^2}{2}. \tag{7}$$

The negative-helicity Hamiltonian H_- is not bounded from below, which implies diverging trajectories. This directly corresponds to the anti-trapped high-field seeking states of the atomic problem. In the following we shall therefore restrict our study to the case of metastable, positive-helicity particles.

Results. – Using the mapping derived above, we explore the dynamics of Weyl particles using a sample of spin-polarized ^{6}Li atoms confined in a quadrupole magnetic trap.

The experimental preparation of the sample starts with a dual species magneto-optical trap which is loaded with fermionic ^{6}Li and ^{40}K [28]. In a second step the clouds are subjected to blue detuned D1 molasses [29,30], cooling both species down to the $50\,\mu$K regime. Subsequently the atoms are optically pumped into their low-field seeking stretched Zeeman states $|F = 3/2, m_F = 3/2\rangle$ and $|9/2, 9/2\rangle$, respectively. Finally, we ramp a magnetic quadrupole field up to $b = 80\,\text{G/cm}$ within 500 ms, capturing 10^7 ^{6}Li and 10^9 ^{40}K atoms. Inter-species- as well as p-wave collisions among ^{40}K atoms [31] allow for the complete thermalization of the two clouds at approximately $T_0 = 300\ \mu$K. This value is high enough to preclude Majorana losses during the experiment's duration and is well below the p-wave collision threshold. After thermalization the ^{40}K atoms are removed from the trap by shining in resonant light, which leaves ^{6}Li unaffected.

We deliver a momentum kick to the cloud by quickly turning on a magnetic bias field $\boldsymbol{B}$ which shifts the center of the trapping potential by a distance $\boldsymbol{\delta}$ for a short

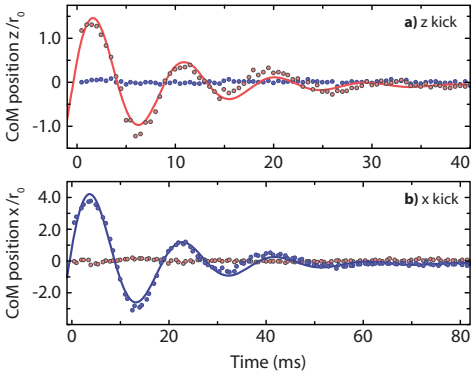

Fig. 1: (Colour online) Center-of-mass oscillations of the lithium cloud after a kick along the symmetry axis of the coils $\boldsymbol{z}$ (a) and along $\boldsymbol{x}$, within the symmetry plane (b). Blue squares (respectively, red circles) are experimental data along $\boldsymbol{x}$ (respectively, $\boldsymbol{z}$). Solid lines are exponentially damped sinusoidal oscillations. Damping results solely from dephasing of single-particle trajectories. Equivalently, this corresponds to momentum oscillations of Weyl particles in a harmonic trap. Here, $r_0 = k_B T/\mu_B b \sim 0.6\,\mathrm{mm}$ and $t_0 = \sqrt{mk_B T}/\mu_B b \sim 1\,\mathrm{ms}$.

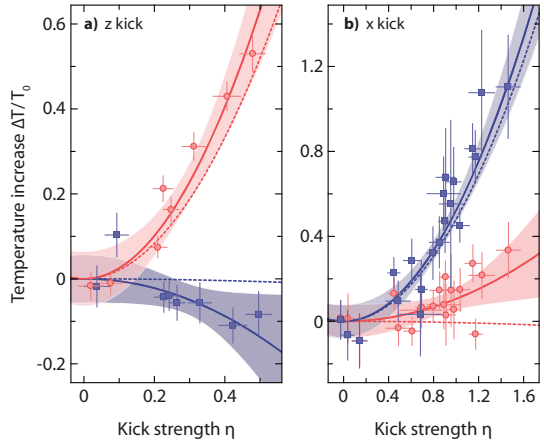

Fig. 2: (Colour online) Temperature increase $\Delta T/T_0 = (T - T_0)T_0$ along $\boldsymbol{x}$ (blue squares) and $\boldsymbol{z}$ (red circles) as a function of the normalized CoM momentum η acquired during the kick. (a) $\boldsymbol{z}$ momentum kick at $b = 70\,\mathrm{G/cm}$. (b) $\boldsymbol{x}$ momentum kick at $b = 55\,\mathrm{G/cm}$. Solid lines are quadratic fits to the experimental data with coefficients given in the text. Error bars represent the temperature statistical uncertainty and shaded zones give the 95% confidence level of the fits. Dashed lines are results of numerical simulations presented in fig. 3.

time τ. Maximum trap center displacements are of order $\delta \sim 7\,r_0$ along $\boldsymbol{x}$ and $\delta \sim 5\,r_0$ along $\boldsymbol{z}$, where $r_0 = k_B T/\mu_B b \sim 0.6\,\mathrm{mm}$ is the characteristic thermal size of the cloud. The kick duration τ is typically a few ms, being constrained by the coil inductances and eddy currents in the surrounding vacuum chamber. During the kick, the ensemble acquires an overall momentum of magnitude $q \sim \mu_\mathrm{B} b\tau$, similar to free fall in gravity. The potential is then quickly brought back to its initial position, and the cloud is left to evolve during a variable time t before switching off all fields to perform a time of flight measurement of the momentum distribution. Temperatures and kick velocities are measured with a time-of-flight (TOF) technique: the trapping potential is abruptly switched-off and the atomic cloud expands freely during a few ms, before it gets imaged on a CCD camera by resonant light absorption. The center-of-mass velocity can be extracted by tracking the center of the distribution during the TOF, while the temperature is measured using the standard deviation of the position distribution for sufficiently long TOF expansion times. A limitation for the accurate determination of the kick amplitude originates from transient currents lasting about 3 ms, which appear while abruptly switching off the quadrupole magnetic trap with gradients of the order of 100 G/cm. The transient magnetic field creates a position-dependent Zeeman effect which deforms the atomic-cloud profile at short TOF durations. This results in a potential error in the measurement of the center-of-mass momentum with or without kick. For instance, in the absence of a kick we observe a small parasitic velocity v_0 which is proportional to the magnetic gradient b and reaches 30 cm/s at our highest value $b = 165\,\mathrm{G/cm}$. Therefore, to infer the actual momentum delivered to the cloud solely by the kick, we subtract v_0 measured after the thermalization time of 500 ms from the velocity right after the kick. The fit errors are given by the error bars in fig. 2 and account for our statistical errors of typically $0.05/mk_\mathrm{B}$ on temperature. Performing the experiment with 4 different magnetic-field gradients, we estimate a systematic uncertainty of $0.2/mk_\mathrm{B}$ for the fitted coefficient of the parabolic dependence of the heating on the momentum kick strength in fig. 2.

For Weyl fermions, this excitation corresponds to displacing the Weyl point in momentum space, waiting until the distribution has moved by a distance $\boldsymbol{R}$ and switching the Weyl point back to its initial position. The resulting time evolution of the position (respectively, momentum) distribution of the lithium atoms (respectively, Weyl particles) is shown in fig. 1. Even though collisions are absent, oscillations are damped as a consequence of the dephasing between single-particle trajectories. The initially imparted energy is converted into internal energy of the cloud and the distribution reaches a steady state within a few units of time $t_0 = \sqrt{mk_B T}/\mu_B b \sim 1\,\mathrm{ms}$.

To characterize the steady state, we kicked the cloud along the $\boldsymbol{z}$- and $\boldsymbol{x}$-directions and measured i) the center-of-mass velocity right after the kick and ii) the respective steady-state momentum distribution after a sufficiently long relaxation time, typically 250 t_0. We define the steady state's effective temperature along direction i as the second moment of the momentum (respectively, position) distribution:

$$k_B T_i = \frac{\langle p_i^2 \rangle}{m} = k_i \langle X_i^2 \rangle, \tag{8}$$

where $\langle \cdot \rangle$ denotes the statistical average.

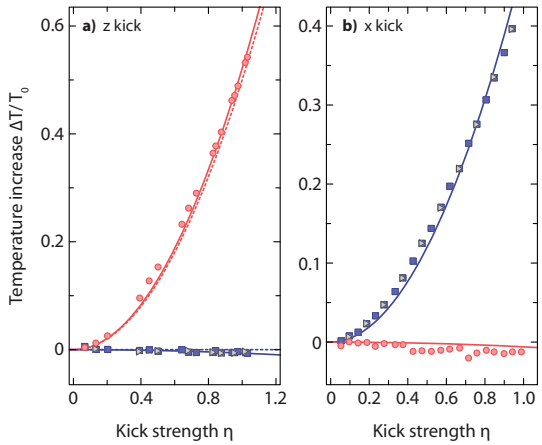

Fig. 3: (Colour online) Numerical simulation of the temperature increase as a function of the normalized CoM momentum kick η. Data points are obtained by solving the classical equations of motion along $\boldsymbol{x}$ (blue squares), $\boldsymbol{y}$ (gray triangles) and $\boldsymbol{z}$ (red circles). In the simulation, kick duration is kept constant at $\tau = 0.6\,t_0$ for $\boldsymbol{z}$ and $\tau = 3\,t_0$ for $\boldsymbol{x}$, with increasing values of displacement δ. The effective temperatures along $\boldsymbol{x}$ and $\boldsymbol{y}$ are equal and almost totally decoupled from $\boldsymbol{z}$. Solid lines are the best quadratic fits to the data: $\Delta T_x/T_0 = \Delta T_y/T_0 = 0.48 \times \eta^2$ and $\Delta T_z/T_0 = -0.006 \times \eta^2$ for a kick along $\boldsymbol{x}$ and $\Delta T_x/T_0 = \Delta T_y/T_0 = -0.006\,\eta^2$, $\Delta T/T_0 = 0.52\,\eta^2$ for a kick along $\boldsymbol{z}$. The dashed line in (a) is given by eq. (16), assuming zero cross-thermalization between $\boldsymbol{z}$ and $\boldsymbol{x}$.

The heating ΔT and the center-of-mass momentum $\boldsymbol{q}$ induced by the momentum kick are extracted from the difference between the corresponding values at quasi-equilibrium and the ones measured right after the kick. While for a fully thermalized system the temperatures in both directions should be equal, our results presented in fig. 2, show a very strong anisotropy, thus demonstrating that the final distribution is non-thermal. The temperature increases much more in the direction of the kick than in the transverse directions. A kick in the $\boldsymbol{z}$-direction produces strong heating along $\boldsymbol{z}$, but a much weaker energy transfer along $\boldsymbol{x}$. Conversely, a kick in the $(\boldsymbol{x}, \boldsymbol{y})$-plane results in smaller heating in the $\boldsymbol{z}$-direction than along $\boldsymbol{x}$. Quantifying the strength of the kick through the dimensionless parameter

$$\eta = \frac{\langle q \rangle}{\sqrt{m k_B T_0}} = \sqrt{\frac{\sum_i k_i \langle R_i \rangle^2}{k_B T_0}}, \tag{9}$$

we find that for kicks along $\boldsymbol{x}$ the best quadratic fits are given by $\Delta T_x/T_0 = 0.52(5)_{\text{stat}}(20)_{\text{syst}} \times \eta^2$ and $\Delta T_z/T_0 = 0.10(4)_{\text{stat}}(5)_{\text{syst}} \times \eta^2$. For kicks along the strong axis $\boldsymbol{z}$, $\Delta T_z/T_0 = 0.63(7)_{\text{stat}}(20)_{\text{syst}} \times \eta^2$ and $\Delta T_x/T_0 = -0.14(5)_{\text{stat}}(8)_{\text{syst}} \times \eta^2$.

Numerics. In order to interpret these results, we performed single-particle dynamics simulations on an ensemble of 10^5 particles. As in the experiment, an excitation is applied to the initial distribution by displacing the trap center (respectively, the Weyl point in momentum space) by an amount δ for a duration τ before bringing it back to its initial position. To simulate the effect of coil response time and eddy currents, we consider excitations of constant duration and increasing displacement. The simulation does not include any collisions, and yet we observe, as in the experiment, a relaxation towards a steady state after $\sim 100\,t_0$ as all calculated moments of the distribution up to 8th order reach a stationnary value. We also reproduce the strong anisotropy between the $\boldsymbol{z}$- and $\boldsymbol{x}$-direction (see fig. 3). Numerical simulations also provide access to the $\boldsymbol{y}$-direction (not measured in the experiment), which also appears to be decoupled from the strong axis $\boldsymbol{z}$, but reaches the same final effective temperature as the other weak axis $\boldsymbol{x}$, regardless of the kick direction. The simulated dynamics thus features a quasi-thermalization within the symmetry plane of the distribution.

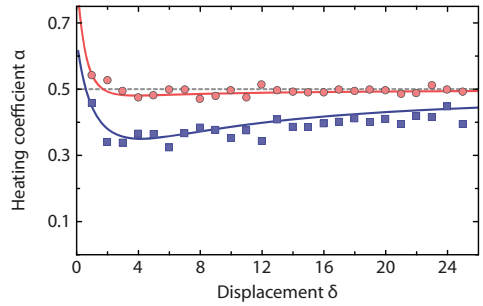

Fig. 4: (Colour online) Heating coefficient α along the kick direction *vs.* Weyl point displacement δ in momentum space (respectively, trap center displacement in position space) for kicks along $\boldsymbol{x}$ (blue) and $\boldsymbol{z}$ (red). α is defined as $\alpha = \Delta T/(T_0 \eta^2)$, relating excess temperature to kick strength η (see text). For kicks along $\boldsymbol{z}$, $\alpha_z \sim 0.5$ and is almost constant. On the contrary, for kicks along $\boldsymbol{x}$, α_x shows a strong dependence on displacement δ. Solid lines are derived from eqs. (13), (14) and (10), (11). Filled symbols are results from numerical simulations.

More quantitatively, the relation between the center-of-mass momentum (respectively, center-of-mass position for Weyl particles) after the kick and the effective temperature in the steady state can be approximated by a quadratic relation $\Delta T_{x,y,z}/T_0 = \alpha_{x,y,z}\eta^2$, where the heating coefficients α_i depend on the kick direction, δ and τ. For short excitation times, α_i are nearly independent of τ. Their explicit dependence on δ is depicted in fig. 4.

For kicks along $\boldsymbol{z}$, α_z does not vary significantly with the trap displacement for the experimentally relevant choice $\delta > 1$, in which case $\alpha_z = \alpha_0 = 0.5$. The value of τ essentially sets the strongest achievable kick η and we take $\tau = 0.6\,t_0$ in the simulation to cover the experimental range of excitations. The heating coefficient $\alpha_0 = 0.5$ is in agreement within error bars with the experimental result $\alpha_z = 0.63(7)_{\text{stat}}(20)_{\text{syst}}$. The decoupling of the $\boldsymbol{x}$-direction appears more pronounced in the simulation than in the experiment with $\Delta T_x/T_0 = -0.006\,\eta^2$, to be compared to the experimental value $\Delta T_x/T_0 = -0.14(5)_{\text{stat}}(8)_{\text{syst}} \times \eta^2$,

a difference we attribute to imperfections of the magnetic excitation procedure.

For kicks along $\boldsymbol{x}$, α_x strongly varies with the kick amplitude δ (blue squares in fig. 4) and, therefore, a quantitative comparison with experiment requires a detailed modeling of the shape of the transient excitation currents, which is difficult. Nevertheless, fitting the duration $\tau = 3\,t_0$ leads to $\Delta T_x/T_0 = 0.48 \times \eta^2$ (to be compared to $\Delta T_x/T_0 = 0.52(5)_{\rm stat}(20)_{\rm syst} \times \eta^2$) and $\Delta T_z/T_0 = -0.006 \times \eta^2$ (to be compared to $\Delta T_z/T_0 = 0.10(4)_{\rm stat}(5)_{\rm syst} \times \eta^2$). The chosen duration $3\,t_0$ is consistent with the decay time of the eddy currents in our chamber ($\sim 3\,$ms).

A simple model. The heating of Weyl particles along the excitation direction can be understood from the constraints imposed on the dynamics by energy conservation and virial theorem $E_{\rm kin} = 2E_{\rm pot}$. Here $E_{\rm kin} = \langle Pc\rangle$ and $E_{\rm pot} = \sum_i k_i\langle X_i^2\rangle/2$ are respectively the kinetic and potential energy of the Weyl particles, and the relation can be derived from its equivalent for massive particles in a linear trap. However, these two conditions are not sufficient to predict the final thermodynamic properties of the system. We therefore make two additional assumptions motivated by the results of the experiment and the simulations. i) Heating occurs predominantly along the kick direction and ii) whatever the kick's orientation may be, the final temperatures along the x- and y-directions are equal by symmetry. Under these conditions one finds for the final temperatures,

$$z\text{-kick: } \Delta T_x = \Delta T_y \ll \Delta T_z, \qquad \Delta T_z \simeq \frac{2\Delta E}{3k_B}, \tag{10}$$

$$x\text{-kick: } \Delta T_x = \Delta T_y \simeq \frac{\Delta E}{3k_B}, \qquad \Delta T_z \ll \Delta T_{x,y}, \tag{11}$$

where ΔE is the energy transferred to the cloud through the excitation. Our numerical simulations satisfy (10), (11) for the redistribution of the imparted energy.

In order to relate ΔE to the experimental kick strength η, we describe the dynamics of the cloud during the excitation through Liouville's equation for the phase-space density $f(\boldsymbol{R},\boldsymbol{P},t)$,

$$\partial_t f\left(\boldsymbol{R},\boldsymbol{P};t\right) = -\mathcal{L} f\left(\boldsymbol{R},\boldsymbol{P};t\right). \tag{12}$$

The Liouville operator is defined as $\mathcal{L} = \partial_{\boldsymbol{P}} H_+^{\rm exc}\cdot\partial_{\boldsymbol{R}} - \partial_{\boldsymbol{R}} H_+^{\rm exc}\cdot\partial_{\boldsymbol{P}}$ with $H_+^{\rm exc} = H_+(\boldsymbol{R},\boldsymbol{P}-\boldsymbol{\delta})$ being the shifted Weyl-point Hamiltonian. The formal solution to this equation is $f(\boldsymbol{R},\boldsymbol{P},\tau) = \exp(-\tau\mathcal{L})[f_0]$; for small excitation times τ, we can Taylor-expand this expression and obtain

$$\langle\boldsymbol{R}\rangle = \tau\int {\rm d}^3\boldsymbol{r}{\rm d}^3\boldsymbol{p}\, f_0\left(\boldsymbol{V}_{\rm exc}-\boldsymbol{V}\right), \tag{13}$$

$$\Delta E = \frac{\tau^2}{2}\int {\rm d}^3\boldsymbol{r}{\rm d}^3\boldsymbol{p}\, f_0 \sum_i k_i\left(\boldsymbol{V}_{\rm exc}-\boldsymbol{V}\right)_i^2, \tag{14}$$

where $\boldsymbol{V} = \partial_{\boldsymbol{P}} H_+$ is the velocity and $\boldsymbol{V}_{\rm exc} = \partial_{\boldsymbol{P}} H_+^{\rm exc}$. The relative scalings of ΔE and $\langle\boldsymbol{R}\rangle$ with τ confirm that $\alpha \propto \Delta E/\langle\boldsymbol{R}\rangle^2$ does not depend on the excitation duration in the short-time limit. The values of α corresponding to eqs. (13), (14) and (10), (11) are presented as solid lines in fig. 4 and confirm the validity of the simulations.

For kicks along the $\boldsymbol{z}$-direction, we estimate the value of α_z by considering large displacements δ, leading to

$$\Delta E = \frac{3}{4}E_0\eta^2. \tag{15}$$

Interestingly, the energy gain is in fact larger than the value $E_0\eta^2/2$ associated with the center-of-mass shift, because the cloud also expands in momentum space during the excitation whereby it gains additional kinetic energy. Inserting these asymptotic developments in eqs. (10) and (11), we finally obtain for $\boldsymbol{z}$ kicks the relative temperature increase along the excitation direction

$$\frac{\Delta T}{T_0} = \frac{\eta^2}{2}, \tag{16}$$

corresponding to $\alpha_z = 0.5$, as discussed above and found in fair agreement with the experimental value.

Conclusion. – Contrary to massive particles, Weyl fermions do not obey Kohn's theorem [32] stating that the center of mass of an ensemble of non-relativistic massive particles oscillates in a 3D harmonic potential without dephasing at frequencies $\sqrt{k_i/m}$. Instead, after an excitation, Weyl fermions move at constant speed even in a quadratic potential. Dephasing of the single-particle trajectories gives rise to damping of the center-of-mass motion and to an anisotropic spread of the position distribution, corresponding to an effective heating. In the symmetry plane, the steady-state distribution is almost decoupled from the strong axis but reach the same effective temperature along both directions regardless of the kick orientation, displaying a quasi-thermalization.

It should also be pointed out the anisotropic heating is not specific to our choice of spring constants for harmonic trap (2), which are in turn constrained by the mapping from the quadrupole potential. Additional simulations have shown that the same behavior is observed for arbitrary anisotropic potentials $V(\boldsymbol{r}) = (k_0x^2+k_0y^2+k_zz^2)/2$. Even in a fully isotropic situation $k_z = k_0$, the two unexcited directions are partially decoupled from the excited one and reach the same final temperatures, as the kick orientation breaks the overall symmetry.

It is crucial to note that in our experiments the energy transfer from the center of mass to the internal energy of the distribution does not depend on interactions between particles. It is solely due to the complexity of the single-particle trajectories in phase-space [33], which originates from the non-harmonicity and non-separability of the underlying Hamiltonian (7). This absence of collisions is responsible for the non-thermal nature of the final distribution. Indeed, according to thermodynamics' second law, Boltzmann's distribution maximizes the entropy of the system for a given energy. In our experiment, we start

with a thermal cloud characterized by a total energy E and equilibrium entropy $S(E)$. A perfect momentum kick delivers an additional energy ΔE per particle, but does so without increasing the system's entropy. The latter is then conserved throughout the ensuing evolution because the ensemble remains collisionless. The quasi-equilibrium state thus exhibits a larger energy $E + \Delta E$ for the same entropy S, in contradiction to the usual entropy growth expected for a collisional system. The absence of real thermalization is then revealed by the anisotropic temperatures measured in the long-time limit. Weyl particles in a harmonic trap therefore provide an intriguing case of quasi-thermalization, midway between massive particles that do not equilibrate and collisional systems that reach a real Boltzmann thermal equilibrium (like in [34]). As shown in [35], this situation can nevertheless be described within the framework of generalized Gibbs ensembles as integrable systems in which a large number of constants of motion —here, the single-particle Hamiltonian of individual atoms— prevents true thermalization [36].

Finally, the canonical mapping presented here is not limited to the simulation of Weyl particles, but can address a broader range of problems. For instance, in a Ioffe-Pritchard trap a bias field gives rise to a non-zero magnetic field at the trap center and the overall field is of the form $B = \sqrt{B_0^2 + b^2 \sum_i \alpha_i^2 x_i^2}$. In this case, the analog system would be described by the relativistic kinetic energy $E = \sqrt{m^2c^4 + p^2c^2}$ where the mass can be tuned through B_0. Another interesting situation arises in a hybrid trap consisting of the superposition of an optical dipole trap and a 2D magnetic quadrupole trap, where the Hamiltonian takes the form $h = \frac{p^2}{2m} + \frac{m\omega^2}{2}(x^2 + y^2) + \frac{m\omega_z^2 z^2}{2} - \mu_{\mathrm{B}} b(\sigma_x x - \sigma_y y)$. Applying our mapping to the variables (x, y, p_x, p_y) leads to the equivalent Hamiltonian $H = \frac{P^2}{2m} + \frac{m\omega^2}{2}(X^2 + Y^2) + \frac{m\omega_z^2 Z^2}{2} - \frac{\mu_{\mathrm{B}} b}{m\omega}(\sigma_x P_x + \sigma_y P_y)$, which turns out to describe a 2D spin-orbit coupled particle [37]. Finally, in the same trap, it is also possible to engineer a Rashba coupling by taking $X = p_y/m\omega$, $P_x = -m\omega y$, $Y = p_x/m\omega$, $P_y = -m\omega_x$.

* * *

The authors would like to thank J. Dalibard and F. Gerbier for stimulating discussions. We are grateful to E. Demler for pointing out to us the analogy to massless relativistic particles. OG acknowledges support from the NSF under the Grant No. PHY-1314735. CS expresses his gratitude to the A. von Humboldt foundation and to Prof. I. Bloch and T. W. Hänsch for their kind hospitality at LMU and MPQ. This work was supported by Région Île de France (Dim nanoK/IFRAF), Institut de France (Louis D. Prize) and the European Union (ERC grant ThermoDynaMix).

Note added in proofs: The authors are grateful to M. Weitz for indicating ref. [38], in which an insightful experimental simulation of the 1D Klein paradox with cold atoms in a bichromatic optical lattice is presented.

REFERENCES

[1] Weyl H., *I. Z. Phys.*, **56** (1929) 330.
[2] Barger V., Marfatia D. and Whisnant K., *Physics of Neutrinos* (Princeton University Press) 2012.
[3] Adler S. L., *Phys. Rev.*, **177** (1969) 2426.
[4] Bell J. S. and Jackiw R., *Nuovo Cimento A*, **60** (1969) 47.
[5] Hosur P. and Qi X., *C. R. Phys.*, **14** (2013) 857.
[6] Silvestrov P. and Efetov K., *Phys. Rev. Lett.*, **98** (2007) 016802.
[7] Delerue C. and Allan G., *Frontiers in Optics 2011/Laser Science XXVII, LWH* (APS) 2011.
[8] Zholudev M. S. *et al.*, *Nat. Phys.*, **10** (2014) 233.
[9] Xu S. *et al.*, *Science*, **349** (2015) 613.
[10] Huang S. *et al.*, *Nat. Commun.*, **6** (2015) 7373.
[11] Lu L. *et al.*, *Science*, **349** (2015) 622.
[12] Lu L. *et al.*, *Phys. Rev. Lett.*, **114** (2015) 25301.
[13] Gremapel D. R. *et al.*, *Phys. Rev. A*, **29** (1984) 1639.
[14] Casati G. *et al.*, *Phys. Rev. Lett.*, **62** (1989) 345.
[15] Chabé J. *et al.*, *Phys. Rev. Lett.*, **101** (2008) 255702.
[16] Sachdev S. *et al.*, *Phys. Rev. B*, **66** (2002) 075128.
[17] Simon J. *et al.*, *Nature*, **472** (2011) 307.
[18] Gerritsma R. *et al.*, *Nature*, **463** (2010) 68.
[19] Gerritsma R. *et al.*, *Phys. Rev. Lett.*, **106** (2011) 060503.
[20] Süsstrunk R. and Huber S. D., *Science*, **349** (2015) 47.
[21] Metcalf H. J. *et al.*, *Phys. Rev. Lett.*, **54** (1985) 2596.
[22] Klein O., *Z. Phys.*, **53** (1929) 157.
[23] Majorana E., *Nuovo Cimento*, **9** (1932) 43.
[24] Bergeman T. H. *et al.*, *J. Opt. Soc. Am. B*, **6** (1989) 2249.
[25] Sukumar C. V. and Brink D. M., *Phys. Rev. A*, **56** (1997) 2451.
[26] Petrich W. *et al.*, *Phys. Rev. Lett.*, **74** (1995) 3352.
[27] Ando T. *et al.*, *J. Phys. Soc. Jpn.*, **67** (1998) 2857.
[28] Ridinger A. *et al.*, *Eur. Phys. J. D*, **65** (2011) 223.
[29] Sievers F. *et al.*, *Phys. Rev. A*, **91** (2015) 023426.
[30] Fernandes D. *et al.*, *EPL*, **100** (2012) 63001.
[31] DeMarco B. *et al.*, *Phys. Rev. Lett.*, **82** (1999) 4208.
[32] Kohn W., *Phys. Rev.*, **123** (1961) 1242.
[33] Surkov E. L. *et al.*, *Phys. Rev. A*, **49** (1994) 4778.
[34] Davis K. *et al.*, *Phys. Rev. Lett.*, **75** (1995) 5205.
[35] Chomaz P. *et al.*, *Ann. Phys.*, **320** (2005) 135.
[36] Rigol M. *et al.*, *Phys. Rev. Lett.*, **98** (2007) 050405.
[37] Koller A. P. *et al.*, *Phys. Rev. A*, **92** (2015) 033608.
[38] Salger T. *et al.*, *Phys. Rev. Lett.*, **107** (2011) 240401.

La quête des températures ultrabasses

Daniel Suchet, 'La quête des températures ultrabasses', in *Le Froid*, Les Presses de l'Université du Québec, coll. « Droit au pôle », to be published in 2016.

This text in the proceeding of a talk given at the colloquium "Le froid : adaptation, production, représentations, effets", organized by the CEARC laboratory (Versailles Saint-Quentin University, France) and the International Laboratory for the Comparative Multidisciplinary Study of Representations of the North (Université du Québec à Montréal, Canada).

La quête des températures ultrabasses

Daniel Suchet, Laboratoire Kastler-Brossel

Résumé – Des vendeurs de glace à l'industrie cryogénique, le froid est souvent perçu comme un produit. Pour le physicien, le froid, réduction de l'agitation aléatoire des particules, apparaît plutôt comme une force productrice, capable de faire émerger des structures complexes et de métamorphoser les propriétés des objets. Les basses températures ont été l'enjeu d'une course effrénée dont la première phase a pris fin en 1908 avec la liquéfaction de l'ensemble des gaz connus. Loin de clore l'aventure, cette étape a fait surgir des nouveaux états de la matière qui ne peuvent être interprétés que par la mécanique quantique. Pour étudier la supraconductivité, la superfluidité ou la condensation de Bose-Einstein, les expériences actuelles visent des températures dites *ultrabasses*, à quelques milliardièmes de degré au-dessus du zéro absolu. Cette présentation propose une mise en perspective historique de la recherche des très basses températures et une introduction aux expériences actuelles d'atomes froids.

Le froid change le monde autour de nous. Il transforme l'eau en glace, la pluie en neige et notre souffle en brouillard. Mais ces observations quotidiennes ne rendent compte que d'une infime partie des modifications engendrées par le froid. A très basses températures, des phénomènes nouveaux apparaissent et le monde change du tout au tout. Dès le XVIIIe siècle, les scientifiques tentent d'imaginer les conséquences d'une chute brutale de la température. Ainsi, en 1789, Antoine Laurent de Lavoisier imagine que, tout comme la vapeur d'eau peut se condenser en gouttelettes, l'air pourrait devenir liquide s'il était soumis à un froid suffisamment intense :

> *Si la terre se trouvait tout à coup placée dans des régions très froides, l'eau qui forme aujourd'hui nos fleuves et nos mers, et probablement le plus grand nombre des fluides que nous connaissons, se transformerait en montagnes solides. […]*
>
> *L'air, dans cette supposition, ou au moins une partie des substances aériformes qui ie composent, cesseraient sars doute d'exister dans l'état de vapeurs […], faute d'un degré de chaleur suffisant; elles reviendraient donc à l'état de liquidité, et il en résulterait de nouveaux liquides dont nous n'avons aucune idée.* [1]

Initiée par Lavoisier et ses contemporains, la quête du froid cherche à atteindre des températures de plus en plus basses et à étudier les propriétés de la matière soumise à ces conditions extrêmes. Si le domaine de recherche a connu de nombreuses révolutions, il reste particulièrement actif à l'heure

[1] Antoine Laurent de Lavoisier, *Traité élémentaire de Chimie*, Paris, Cuchet, 1789, p33

actuelle et met en évidence l'importance de la mécanique quantique.

En plongeant vers des températures de plus en plus basses, on pourra retracer les grandes étapes historiques de la quête du froid et mettre en avant les propriétés surprenantes qui surgissent lorsque le froid devient prédominant. Comme toute plongée, cette exploration se fera par paliers successifs : nous allons d'abord descendre jusqu'à -269°C, en regardant comment les éléments peuvent passer d'un état gazeux à un état liquide, puis solide. Un palier intermédiaire jusqu'à -273°C permettra de faire apparaitre de nouveaux changements d'états, moins familiers, tels que la transition vers la supraconductivité. Enfin, on pourra s'aventurer au plus près du zéro absolu en abordant le thème des atomes ultrafroids.

Tout au long de cette exploration des basses températures, on verra comment le froid, en réduisant l'agitation chaotique des particules, permet l'apparition de structures de plus en plus complexes.

De 20°C à -269°C. Solide, liquide ou gaz ?

En 1789, la proposition de Lavoisier est extrêmement spéculative : ce n'est que par analogie avec les quelques gaz connus à l'époque, et en particulier la vapeur d'eau, que Lavoisier formule son idée. Pour comprendre les mécanismes à l'œuvre derrière la liquéfaction de l'eau et estimer leur capacité à liquéfier d'autres gaz il nous faut nous entendre sur ce qu'est la température.

Depuis l'antiquité, la question a longtemps été débattue et on trouve les prémisses du consensus actuel chez Descartes :

> *Dans un corps échauffé, sont des particules animées d'un mouvement peu ample, mais très rapide ; de ce mouvement, un corps donné, porté à un degré de chaleur déterminé, contient une certaine quantité ; cette quantité de mouvement calorifique dans un corps chaud, c'est la quantité de chaleur qu'il renferme* [2]

A l'échelle microscopique, la matière est composée d'atomes, éventuellement assemblés en molécules. Ces particules s'agitent dans tous les sens, se heurtent les unes les autres, rebondissent, repartent dans d'autres directions, en un mouvement chaotique, désordonné : on parle de mouvement Brownien, du nom du botaniste Robert Brown qui en observa les conséquences pour la

[2] Cité par Pierre Duhem, *L'évolution de la mécanique et autres textes*, Vrin, Mathesis, 1992, p 7

première fois[3]. Pour le physicien, la température est une mesure de l'agitation moyenne de ces particules. Plus les particules bougent vite, plus on dit que la température est élevée. Quand on dit que l'air de la pièce est à 20°C, cela veut dire que les molécules qui le composent bougent dans tous les sens à environ 300m/s. De la même manière, les molécules qui composent un solide ou un liquide bougent en permanence plus ou moins librement, vibrant parfois simplement sur place ; la force de leur agitation est mesurée par la température.

Cette image de la température est extrêmement riche et fait apparaitre deux idées importantes. Tout d'abord, elle implique qu'il existe une température minimale. Un corps est d'autant plus froid que ses particules bougent peu ; la température la plus basse est donc obtenue lorsque toutes les particules sont immobiles. En effet, comment imaginer ralentir d'avantage des particules immobiles ? La température qui correspond à l'immobilité de toutes les particules s'appelle le zéro absolu ; elle a été estimée pour la première fois vers 1702 par Guillaume Amontons[4] et on sait aujourd'hui qu'elle vaut -273.15°C. C'est une limite absolue et on a coutume de s'en servir comme référence : on compte les températures à partir du 0 absolu et, au lieu d'employer les degrés Celsius (°C) on parle de kelvin (K) (les kelvins ne sont pas des degrés car ils constituent une mesure absolue de la température du corps et non une mesure relative.) Comptée en Kelvin, une température quatre fois plus élevée correspond à des particules bougeant deux fois plus vite.

Cette image de la température permet également de comprendre comment le froid permet l'émergence de structures. A courte distance, deux particules peuvent interagir et avoir tendance à s'accrocher l'un à l'autre. Cependant, si les particules bougent trop vite et dans tous les sens, leur agitation risque de les empêcher de s'associer et donc de former des édifices complexes. Cette compétition entre l'agitation désordonnée de la température et les interactions entre particules est un élément central pour comprendre les effets du froid.

On peut illustrer cette idée sur un exemple bien connu : les états de la matière, et en particulier de l'eau. L'eau liquide est composée de molécules d'eau, H_2O, elles-mêmes constituées en deux atomes d'hydrogène et d'un atome d'oxygène. Sous forme de vapeur, de liquide ou de solide, la formule de l'eau est toujours la même : H_2O. Pourtant, les comportements des trois forment sont radicalement différents. La différence tient à la présence de liaisons entre les molécules d'eau (voir figure 1). A

---

[3] Robert Brown ; *A brief account of microscopical observations made in the months of June, July and August, 1827, on the particles contained in the pollen of plants; and on the general existence of active molecules in organic and inorganic bodies.*, Philosophical Magazine 4 (1828), 161-173

[4] Cité par Kurt Mendelssohn, *La recherche du Zéro absolu,* Hachette, L'Univers des connaissances, 1966, p11

l'état solide, les molécules sont fermement attachées les unes aux autres par des liaisons solides, qui assurent la cohésion et la rigidité de la glace. Si les molécules bougent trop vite, une partie de ces liaisons est brisée : l'eau perd en rigidité et devient liquide. Si toutes les liaisons entre les molécules sont brisées (ou presque), les molécules peuvent s'éparpiller dans tous les sens et on parle de vapeur. On voit ici comment la compétition entre la température, c'est-à-dire l'agitation des molécules, et l'ordre issu des liaisons permet d'interpréter les états de la matière.

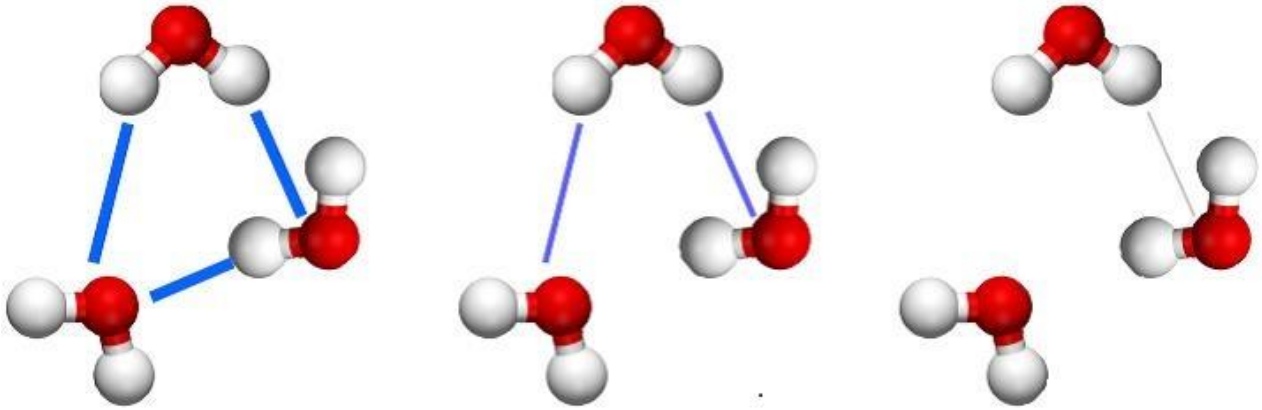

Figure 1 : les états de l'eau. Qu'elle soit solide (à gauche), liquide (au centre) ou gazeuse (à droite), l'eau est toujours composée des mêmes molécules. La différence entre les états de la matière vient des liaisons qui rassemblent ces molécules.

Ce raisonnement peut-il s'appliquer à tous les corps ? Tous les gaz peuvent-ils devenir liquides, si leur température, ou leur agitation, est suffisamment faible pour que les molécules s'accrochent un peu les unes aux autres ? Ou existe-t-il des gaz permanents, incapables de devenir liquides ? Cette question a motivé des générations de physiciens qui ont ouvert la marche vers les températures les plus basses[5].

En 1784, Gaspard Monge devient le premier physicien à liquéfier artificiellement un gaz, en refroidissant du dioxyde du soufre à -8°C. Pendant un siècle, les physiciens s'attaquent aux éléments de la classification périodique les uns après les autres, descendant toujours plus bas dans les températures. En 1877, Pictet et Cailletet liquéfient tous deux l'oxygène à -182°C, soit 77K. Quelques années plus tard, Olszewski et Wroblewski parviennent à attendre -196°C et à liquéfier l'azote. Ces résultats répondent à la question soulevée un siècle plus tôt par Lavoisier. En effet, l'air que nous respirons est composé à 20 % d'oxygène et à 80 % d'azote. Si la Terre se trouvait porter dans des régions très froides, l'air deviendrait bel et bien liquide et ressemblerait à un mélange d'oxygène et d'azote liquide.

On peut facilement trouver de nombreuses vidéos sur internet mettant en avant les propriétés

[5] Locqueneux, Robert, *Histoire de la thermodynamique classique : de Sadi Carnot à Gibbs*, Belin Science, 2009

surprenantes de l'air liquide. Ce liquide est incolore et bout au contact de l'air. Proche de -200°C, il gèle immédiatement n'importe quel objet immergé et transforme l'humidité ambiante en cristaux de glace. Versé sur une surface plane, il forme des gouttelettes qui flottent sans frottement et glissent rapidement.

A la fin du XIXe siècle, tous les gaz sont liquéfiés. Tous ? Non, car l'hélium, particulièrement récalcitrant, résiste encore et toujours à la communauté scientifique. Pendant quelques années, on envisage même que l'hélium soit le seul gaz permanent de l'Univers, condamnée à rester gazeux même aux températures les plus basses. Coup de tonnerre en 1908 : dans son laboratoire de Leide, Kammerlingh Onnes mène un dernier assaut et, en atteignant la température de 4K, parvient liquéfier l'hélium et à clore ainsi la première partie de la course vers les basses températures.

De -269°C à -273°C. La supraconductivité

La quête des basses températures n'en est pas restée là. Si le froid peut changer tous les gaz en liquides, il génère de nombreux autres changements que les physiciens, curieux et armés d'hélium liquide à -269°C, voulaient explorer.

Après son succès dans la liquéfaction de l'hélium, Kammerlingh Onnes s'est donc tourné vers un second problème : comment les métaux conduisent-ils le courant électrique lorsqu'ils sont refroidis ? Des expériences précédentes avaient montré que la résistance électrique diminuait avec la température : un métal plus froid conduit mieux l'électricité qu'un métal plus chaud. Mais au début du XXème siècle, plusieurs théories s'affrontaient pour extrapoler ce comportement jusqu'au plus près du zéro absolu. Certains (dont Lord Dewar[6]) pensaient que la résistance continuerait à tendre vers zéro et qu'un métal totalement refroidi pourrait conduire le courant sans aucune perte (voir figure 2, courbe bleue). D'autres (dont Lord Kelvin[7]) remarquaient que le courant électrique correspond au mouvement des électrons, qui *courent* dans le métal. Si le zéro absolu signifie l'immobilité parfaite, alors les électrons eux-mêmes doivent être figés et donc incapables de porter le courant : la résistance doit donc augmenter brutalement à très basse température (voir figure 2, courbe rouge). D'autres enfin (dont Matthissen[8]) envisageaient une solution intermédiaire qui verrait la résistance électrique tendre vers une valeur finie et non nulle (voir figure 2, courbe verte).

---

[6] Stephen Blundell, *La supraconductivité, 100 ans après,* Belin, Pour la science, 2011, p32
[7] Ibid., p32
[8] Ibid., p32

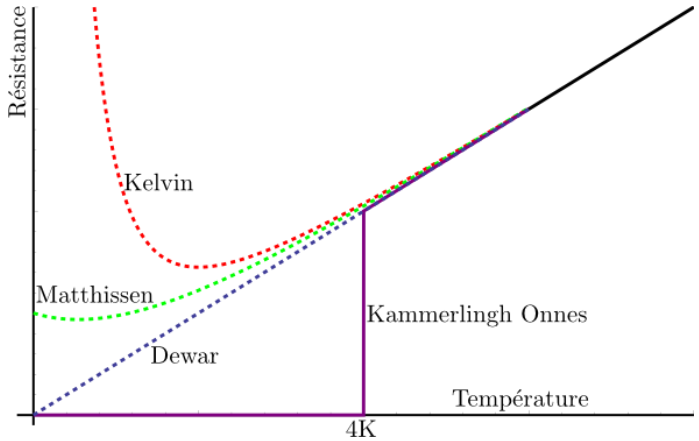

Figure 2 : Résistance du mercure en fonction de la température. Les trois courbes en pointillé sont des modèles théoriques, la courbe pleine décrit le résultat expérimental obtenu par Kammerlingh Onnes en 1911.

Kammerlingh Onnes mène l'expérience en refroidissant du mercure par de l'hélium liquide. Son résultat est complètement inattendu : la résistance du mercure tombe brutalement à zéro quand la température atteint 4.2K (voir figure 2, courbe violette) ! Tout à coup, le mercure conduit le courant sans aucune perte : on dit qu'il est devenu supraconducteur. A l'heure actuelle, on estime qu'un courant électrique peut tourner en boucle dans un anneau supraconducteur pendant plus de 100 000 ans sans que la moindre perte puisse être mesurée. Il faut également noter que cette transition vers la supraconductivité est brutale : tout comme l'eau est liquide juste au-dessus de 0°C et solide juste en dessous, avec des propriétés radicalement différentes, le mercure présente une résistance électrique juste au-dessus de 4.2K et absolument aucune résistance juste en dessous. Cette discontinuité des propriétés physiques est caractéristique des changements d'états. On voit ici que le froid a des effets autre que le passage solide / liquide / gaz : il peut aussi induire une transition supra / normale.

Un domaine de recherche particulièrement actif vise à produire un matériau supraconducteur à « haute température critique », c'est-à-dire qui deviendrait supraconducteur en dessous d'une température relativement élevée (et en tout cas plus facilement atteignable que quelques Kelvin). A l'heure actuelle, les matériaux les plus performants deviennent supraconducteurs dès qu'ils atteignent -135°C. Cependant, ces matériaux sont le plus souvent des céramiques, friables et cassantes, dont les propriétés mécaniques limitent considérablement l'usage industriel.

Une autre conséquence surprenante de la supraconductivité a été découverte par Walther Meissner et Robert Ochsenfeld en 1933 : un supraconducteur repousse les champs magnétiques. Cet effet Meissner est à l'origine de la lévitation magnétique, l'une des manifestations les plus spectaculaires de la supraconductivité. A température ambiante, une pastilla supraconductrice n'a aucune propriété magnétique remarquable et on peut en approcher un aimant sans effort. Mais si la

pastille est refroidie en dessous de sa température critique, elle devient supraconductrice et repousse les aimants qui s'en approchent. On peut alors faire voler un aimant au-dessus de la pastille (voir figure 3) ; cet effet est suffisamment fort pour qu'une équipe du laboratoire Matériaux et Phénomènes Quantiques construise un *MagSurf*[9], un skate supraconducteur digne de retour vers le futur qui flotte à quelques centimètres sur un rail d'aimants !

Figure 3 : la lévitation magnétique. La pastille noire posée dans la coupole est un supraconducteur refroidi par de l'azote liquide. Un aimant est approché : il est repoussé par la pastille et flotte à quelques millimètres au-dessus du support.

Entre la découverte de ces phénomènes et leur modélisation théorique, il se passe plus de quarante ans. Le premier modèle complet de la supraconductivité nait en 1957 de la collaboration de trois physiciens : John Bardeen, Léon Cooper et John Robert Schrieffer. Dans la théorie BCS, les propriétés des supraconducteurs viennent de la capacité des électrons dans le métal à former des paires qui présentent un comportement collectif. Une analogie classique compare les électrons à des poissons dans l'eau. A température ambiante, les électrons se déplacent sans tenir compte les uns des autres, comme un nuage de poissons désordonné. En dessous de la température critique, les électrons s'apparient et se comportent comme un banc de poissons, dans lequel chaque individu ajuste se trajectoire en fonction des autres. Impossible de venir déranger un poisson sans déranger tout le banc ! De la même manière, dans un métal devenu supraconducteur, il est impossible d'empêcher la propagation d'un électron sans perturber tous les autres. Il devient alors énergétiquement couteux de s'opposer au courant électrique et les électrons-poissons peuvent donc se déplacer sans encombres, ce qui se traduit par la disparition de toute dissipation.

Il peut sembler surprenant que deux électrons puissent former une paire : tous les électrons sont chargés négativement et par conséquent se repoussent les uns les autres ; comment pourraient-ils s'attirer au point de s'apparier ? L'explication tient à la présence du réseau atomique dans lequel évoluent les électrons (voir figure 4) : lors de son déplacement dans le réseau, un électron attire (très légèrement) vers lui les atomes environnants. Par conséquent, un deuxième électron verra dans le sillage du premier des atomes légèrement plus rapprochés et sera donc attiré dans cette direction préférentiellement. Tout se passe comme si le premier électron avait attiré le second à sa suite !

[9] http://www.univ-paris-diderot.fr/sc/site.php?bc=accueil&np=pageActu&ref=3658

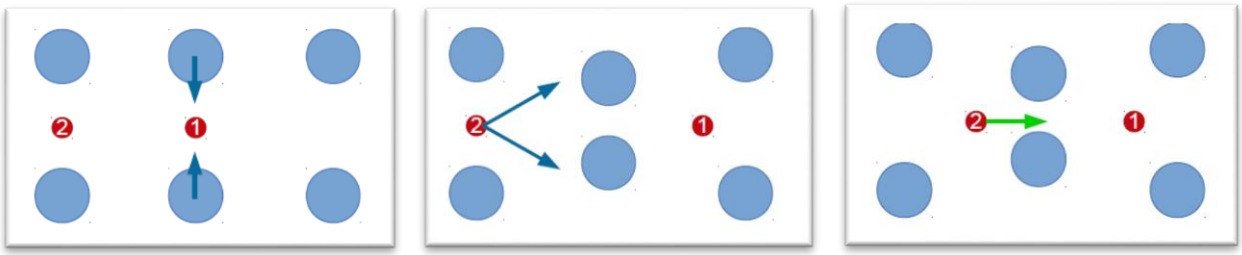

Figure 4 : théorie BCS : comment deux électrons peuvent-ils s'attirer ?

Cette image permet de comprendre pourquoi un supraconducteur ne peut exister qu'à basse température. A température ambiante, les atomes vibrent dans tous les sens et le déplacement dû au passage d'un électron est noyé dans l'agitation moyenne. Il faut diminuer considérablement la température (et donc l'agitation) pour que le faible effet des électrons sur les atomes ne soit pas complètement négligeable.

Cependant, comme toutes les images, sa description du phénomène reste limitée : elle n'explique ni pourquoi l'attraction entre électrons engendrent l'apparition de paires (et pas de triplets etc.), ni pourquoi les paires d'électrons présentent un comportement collectif si particulier. Pour décrire correctement le phénomène, il faudrait utiliser une théorie physique plus subtile : la mécanique quantique, qui s'avère indispensable comprendre ce qui se passe lorsqu'on descend encore plus proche du zéro absolu.

Vers le zéro absolu. Les atomes ultrafroids.

Les techniques de cryogénie ont considérablement progressé depuis l'époque de Kammerlingh Onnes. A l'heure actuelle, les meilleurs cryostats sont capables de descendre jusqu'à quelques miliKelvins, c'est-à-dire quelques millièmes de degrés au-dessus du zéro absolu. Ces températures sont remarquables : les températures dont nous parlons ici sont cent mille fois plus basses que les 300 kelvins de la température ambiante ! Par comparaison, rappelons que la surface du Soleil, portée à quelques 5000K, n'est qu'environ dix fois plus chaude que la température ambiante.

C'est à des températures encore bien inférieures que nous allons descendre pour achever notre plongée. Particulièrement actif depuis une vingtaine d'années, le domaine des atomes froids s'intéresse à des températures dites « ultrabasses », où la nature quantique des particules, déjà mentionnée dans la supraconductivité, devient omniprésente.

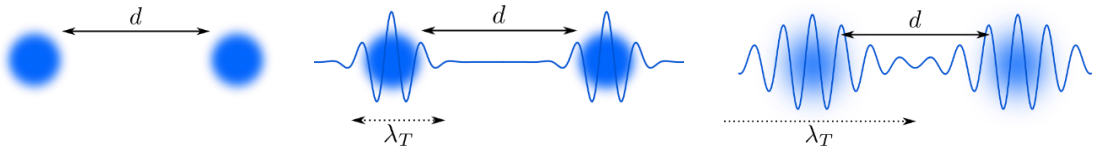

Figure 5 : les températures ultrabasses. Considérons deux particules, distantes de d. Chacune de ces

particules est décrite par une onde, qui présente une taille λ_T. Si λ_T est plus grand que d, les ondes se superposent le unes aux autres et la nature quantique du système devient prédominante.

A quel point doit-on être froid pour être ultrafroid et d'où viennent ces effets quantiques ? Les ordres de grandeur apparaissent à l'échelle microscopique (voir figure 5). Pour décrire un nuage de gaz, une première longueur caractéristique semble évidente : la distance moyenne entre les particules, qu'on peut noter d. Mais cette longueur ne suffit pas : d'après la mécanique quantique, les particules ne sont pas ponctuelles mais sont décrites par une onde qui s'étend dans un certain volume. L'extension de ce paquet d'onde est donnée par la longueur d'onde de de Broglie, notée λ_T , qui dépend de la masse des particules et de la température.

Pour un gaz d'atomes à température ambiante (l'air par exemple), la distance entre particules d est beaucoup plus grande que la longueur d'onde de de Broglie ; et chaque petit paquet d'onde est bien isolé des autres. Mais si la température baisse, longueur d'onde de de Broglie augmente ; elle peut devenir plus grande que la distance qui sépare les particules si la température est assez basse. Les paquets finissent alors par se superposer et les particules interfèrent les unes avec les autres. On parle dans ce cas de températures ultrabasses. Pour un gaz d'atomes, il faut atteindre des températures de l'ordre de 100 nanoKelvins (cent milliardièmes de degrés au-dessus du zéro absolu) pour rentrer dans ce régime.

Lorsque les paquets d'onde se superposent, les particules ne peuvent plus être isolées les uns des autres mais présentent au contraire un comportement collectif. On observe alors deux types de comportements : certaines particules, appelées *bosons*, ont tendance à toutes s'accumuler dans la même configuration et forment un nouvel état de la matière appelé *condensat de Bose Einstein.* A l'inverse, d'autres particules, les *fermions*, refusent catégoriquement d'être deux dans la même configuration et chaque nouvelle particule doit trouver une configuration non occupée. C'est dans cette seconde catégorie que se rangent entre autres les électrons. La première réalisation expérimentale d'un condensat de Bose-Einstein en 1995 par l'équipe d'Eric Cornell et Carl Wieman (voir figure 6) montre la vivacité du domaine.

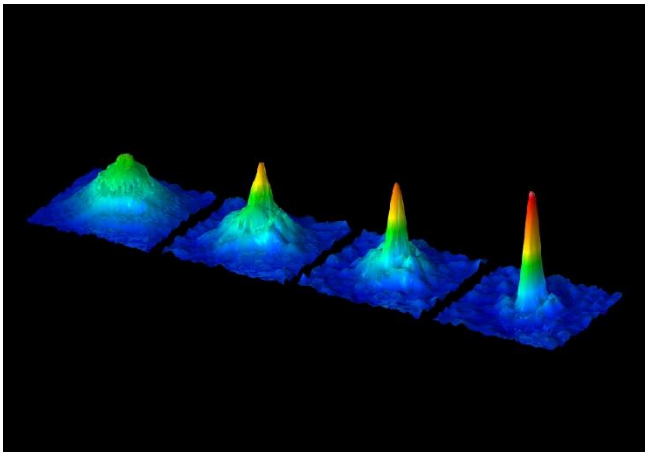

Figure 6 : formation d'un condensat de Bose Einstein[10]. Chacune des images présente un nuage d'environ six milliards d'atomes de Rubidium 87, qui se comporte comme un boson. La seule différence entre les nuages est leur température (de gauche à droite : 800 nK, 400nK, 200nK et 100nK). Au fur et à mesure que la température diminue, on voit les atomes s'accumuler dans une seule distribution, qui devient de plus en plus piquée.

L'un des enjeux majeurs de ce domaine de recherche a été imaginé par l'idole des physiciens, Richard Feynman, qui évoque en 1982 un *simulateur quantique universel*[11], une machine susceptible d'être ajustée pour simuler de n'importe quel système physique qu'on souhaite étudier.

Le monde réel est horriblement compliqué et le nombre de facteurs intervenant dans un problème est quasiment infini. Pour élaborer une théorie, le physicien ne retient que quelques-uns de ces paramètres et néglige les autres ; il établit ainsi un modèle simplifié qu'il espère néanmoins fidèle à la réalité. Pour tester sa théorie, le physicien doit s'assurer que le système décrit par son modèle simplifié se comporte effectivement comme le système réel qu'il veut décrire. Pour ce faire, il peut calculer certaines propriétés à partir de sa théorie puis comparer ces prédictions aux réactions réelles du système : réagit-il comme prévu à tels ou tels stimuli ? Se déforme-t-il comme l'affirment les calculs ? Malheureusement, dans la plupart des cas, les calculs sont complexes au point d'en être irréalisables, même par ordinateur. C'est là que l'idée de Feynman prend toute sa force : au lieu de mener ces calculs, on peut *simuler* les propriétés du modèle en réglant la machine pour qu'elle suive exactement la théorie. Si le comportement du simulateur ressemble au comportement du système réel, c'est que la théorie décrit correctement son objet d'étude ; à l'inverse, si le simulateur ne se comporte pas du tout comme le système réel, c'est qu'il manque dans la théorie des éléments cruciaux.

Les atomes ultrafroids se prêtent particulièrement bien à ce projet. En effet, ces atomes forment un système particulièrement ajustable : on peut non seulement dessiner le paysage dans lequel ils évoluent avec des faisceaux laser mais également ajuster leurs interactions avec un champ magnétique et les forcer ainsi à s'attirer ou à se repousser les uns les autres, plus ou moins fortement.

On peut ainsi reproduire des comportements analogues à ceux des supraconducteurs (voir figure 7) : un nuage d'atomes fermioniques joue le rôle des électrons dans le métal et un réseau optique reproduit le potentiel périodique que les électrons ressentent habituellement. Les interactions entre

[10] Equipe BEC, Max Planck Institute, 2003

[11] Feynman, Richard, *Simulating Physics with Computers*, International Journal of Theoretical Physics 21, 1982

atomes sont réglées de façon à ce que deux atomes s'attirent légèrement – comme les électrons de la théorie BCS. On observe alors un comportement identique à celui des supraconducteurs, mais dans un système parfaitement manipulable où on peut varier chacun des paramètres pour étudier son influence sur l'ensemble du système.

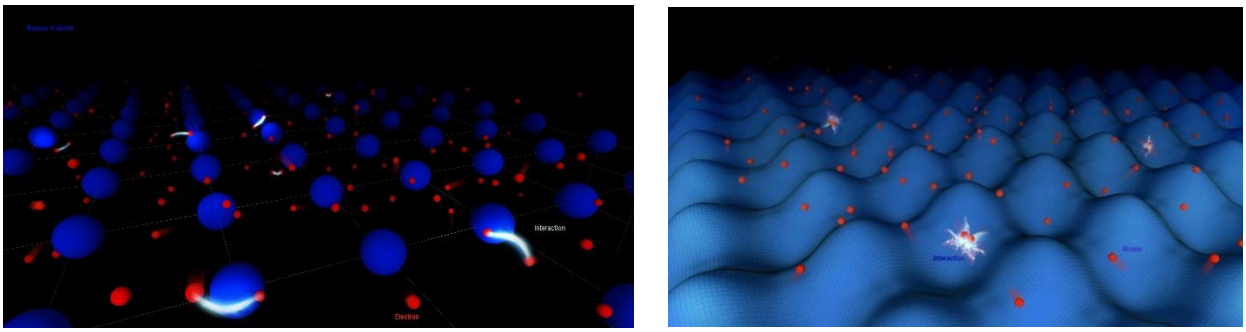

Figure 7 : *(à gauche) Dans un métal, les électrons (en rouge) évoluent dans un réseau périodique d'ions (en bleu) et interagissent entre eux. (à droite) De manière analogue, on peut placer des atomes (en rouge) dans un réseau optique (en bleu) et ajuster leurs interactions pour qu'elles soient identiques à celles des électrons.*

Vues d'artiste par Germain Morisseau.

Pour le physicien, le froid n'est pas tant un produit qu'une force de production. De la cristallisation de la glace à la formation des condensats de Bose Einstein en passant par l'appariement des électrons supraconducteurs, la diminution progressive de l'agitation thermique permet l'émergence de structures de plus en plus subtiles. L'exploration des basses températures constitue donc une aventure à la fois technique (comment parvenir à atteindre des températures de plus en plus basses ?) et fondamentale (que se passe-t-il quand on atteint effectivement ces températures). Si les questions soulevées et les méthodes employées ont beaucoup évolué depuis le XVIIIème siècle, ce domaine de recherche reste à l'heure actuelle particulièrement actif et les expériences d'atomes ultrafroids montrent que, à l'extrême limite du zéro absolu, c'est l'universalité même de la physique que le froid fait émerger.

Bibliography

[Abbott 1884] E. Abbott. *Flatland, A Romance of Many Dimensions*. SEELEY and Co (1884). ISBN 2264022507 (cited page 139)

[Abo-Shaeer *et al.* 2001] J. R. Abo-Shaeer, C. Raman, J. M. Vogels and W. Ketterle. 'Observation of vortex lattices in Bose-Einstein condensates.' *Science*, **vol. 292**, no. 5516, pp. 476–479 (2001) (cited page 6)

[Adler 1969] S. L. Adler. 'Axial-vector vertex in spinor electrodynamics'. *Physical Review*, **vol. 177**, no. 5, p. 2426 (1969) (cited page 95)

[Aharonov and Stern 1992] Y. Aharonov and A. Stern. 'Origin of the geometric forces accompanying Berrys geometric potentials'. *Physical Review Letters*, **vol. 69**, no. 25, p. 3593 (1992) (cited page 104)

[Aidelsburger *et al.* 2011] M. Aidelsburger, M. Atala, S. Nascimbène, S. Trotzky, Y.-A. Chen and I. Bloch. 'Experimental Realization of Strong Effective Magnetic Fields in an Optical Lattice'. *Physical Review Letters*, **vol. 107**, p. 255301 (2011) (cited page 12)

[Aidelsburger *et al.* 2013] M. Aidelsburger, M. Atala, M. Lohse, J. T. Barreiro, B. Paredes and I. Bloch. 'Realization of the hofstadter hamiltonian with ultracold atoms in optical lattices'. *Physical Review Letters*, **vol. 111**, no. 18, pp. 1–5 (2013) (cited page 12)

[Allen and Misener 1938] J. F. Allen and A. D. Misener. 'Flow of Liquid Helium II'. *Nature*, **vol. 141**, pp. 75–75 (1938) (cited page 5)

[Amo *et al.* 2009] A. Amo, J. Lefrère, S. Pigeon, C. Adrados, C. Ciuti, I. Carusotto, R. Houdré, E. Giacobino and A. Bramati. 'Superfluidity of polaritons in semiconductor microcavities'. *Nature Physics*, **vol. 5**, pp. 805 – 810 (2009) (cited page 6)

[Anderson 1958] P. Anderson. 'Absence of Diffusion in Certain Random Lattices'. *Physical Review*, **vol. 109**, no. 5, pp. 1492—-1505 (1958) (cites pages 11, 140)

[Anderson *et al.* 1995] M. H. Anderson, J. R. Ensher, M. R. Matthews, C. E. Wieman and E. A. Cornell. 'Observation of Bose-Einstein Condensation in a Dilute Atomic Vapor'. *Science*, **vol. 269**, no. 5221, pp. 198–201 (1995) (cites pages 5, 56)

[Ando *et al.* 1998] T. Ando, T. Nakanishi and R. Saito. 'Berry's Phase and Absence of Back Scattering in Carbon Nanotubes'. *Journal of the Physical Society of Japan*, **vol. 67**, no. 8, pp. 2857–2862 (1998) (cited page 99)

[Arimondo *et al.* 1977] E. Arimondo, M. Inguscio and P. Violino. 'Experimental determinations of the hyperfine structure in the alkali atoms'. *Reviews of Modern Physics*, **vol. 49**, no. 1, p. 31 (1977) (cited page 165)

[Armijo *et al.* 2011] J. Armijo, T. Jacqmin, K. Kheruntsyan and I. Bouchoule. 'Mapping out the quasicondensate transition through the dimensional crossover from one to three dimensions'. *Phys. Rev. A*, **vol. 83**, no. 2, pp. 1–4 (2011) (cited page 11)

[Arnold *et al.* 1997] V. I. Arnold, A. Weinstein and K. Vogtmann. *Mathematical Methods of Classical Mechanics*. Springer, 2nd editio ed. (1997). ISBN 0387968903, 520 pp. (cited page 178)

[Ashery 2012] D. Ashery. 'Physics beyond the standard model with trapped cold atoms'. *Journal of Low Temperature Physics*, **vol. 168**, no. 1-2, pp. 1–17 (2012) (cited page 13)

[Aspect *et al.* 1988] A. Aspect, E. Arimondo, R. Kaiser, N. Vansteenkiste and C. Cohen-Tannoudji. 'Laser cooling below the one-photon recoil energy by velocity-selective coherent population trapping'. *Physical Review Letters*, **vol. 61**, pp. 826–829 (1988) (cited page 33)

[Bach 1977] R. Bach. *Illusions: The Adventures of a Reluctant Messiah*. Delacorte Press (1977). ISBN 0385285019, 128 pp. (cited page iii)

[Baker 1999] G. A. Baker. 'Neutron matter model'. *Phys. Rev. C*, **vol. 60**, no. 5, p. 054311 (1999) (cited page 7)

[Bakr *et al.* 2009] W. S. Bakr, J. I. Gillen, A. Peng, S. Folling and M. Greiner. 'A quantum gas microscope for detecting single atoms in a Hubbard-regime optical lattice'. *Nature*, **vol. 462**, no. 7269, pp. 74–77 (2009) (cited page 10)

[Balibar 2015] S. Balibar. *Climat : Y Voir Clair pour Agir*. Le pommier, manifeste ed. (2015). ISBN 274650927X, 200 pp. (cited page viii)

[Balili *et al.* 2007] R. Balili, V. Hartwel, D. Snoke, L. Pfeiffer and K. West. 'Bose-Einstein Condensation of Microcavity Polaritons in a Trap'. *Science*, **vol. 316**, no. 5827, pp. 1007–1010 (2007) (cited page 6)

[Bardeen *et al.* 1957] J. Bardeen, L. N. Cooper and J. R. Schrieffer. 'Theory of superconductivity'. *Phys. Rev.*, **vol. 108**, pp. 1175–1204 (1957) (cited page 7)

[Bartenstein *et al.* 2005] M. Bartenstein, A. Altmeyer, S. Riedl, R. Geursen, S. Jochim, C. Chin, J. H. Denschlag, R. Grimm, A. Simoni, E. Tiesinga, C. J. Williams and P. S. Julienne. 'Precise determination of ^{6}Li cold collision parameters by radio-frequency spectroscopy on weakly bound molecules'. *Phys. Rev. Lett.*, **vol. 94**, p. 103201 (2005) (cited page 190)

[Bauer *et al.* 2013] J. Bauer, C. Salomon and E. Demler. 'Realizing a Kondo-correlated state with ultracold atoms'. *Physical Review Letters*, **vol. 111**, no. 21, pp. 1–5 (2013) (cited page 12)

[Bausmerth *et al.* 2009] I. Bausmerth, A. Recati and S. Stringari. 'Chandrasekhar-Clogston limit and phase separation in Fermi mixtures at unitarity'. *Phys. Rev. A*, **vol. 79**, no. 4, pp. 1–7 (2009) (cited page 11)

[Behrends *et al.* 2015] J. Behrends, A. G. Grushin, T. Ojanen and J. H. Bardarson. 'Visualizing the chiral anomaly in Dirac and Weyl semimetals with photoemission spectroscopy'. *arXiv:1503.04329*, pp. 1–10 (2015) (cited page 95)

[Bell and Jackiw 1969] J. S. Bell and J. Jackiw. 'A PCAC Puzzle $\pi^0 \to \gamma\gamma$ in the σ-Model .' *Il Nuovo Cimento A*, **vol. 60**, no. 1, p. 47 (1969) (cited page 95)

[Berezinskiĭ 1972] V. L. Berezinskiĭ. 'Destruction of Long-range Order in One-dimensional and Two-dimensional Systems Possessing a Continuous Symmetry Group. II. Quantum Systems'. *Soviet Journal of Experimental and Theoretical Physics*, **vol. 34**, p. 610 (1972) (cited page 139)

[Bergeman *et al.* 1989] T. H. Bergeman, P. McNicholl, J. Kycia, H. Metcalf and N. L. Balazs. 'Quantized motion of atoms in a quadrupole magnetostatic trap'. *Journal of the Optical Society of America B*, **vol. 6**, no. 11, p. 2249 (1989) (cites pages 58, 73)

[Bernevig 2015] B. A. Bernevig. 'It's been a Weyl coming'. *Nature Physics*, **vol. 11**, no. 9, p. 698 (2015) (cited page 92)

[Berry 1984] M. V. Berry. 'Quantal Phase Factors Accompanying Adiabatic Changes'. *Proceedings of the Royal Society of London A: Mathematical, Physical and Engineering Sciences*, **vol. 392**, no. 1802, pp. 45–57 (1984) (cites pages 94, 104)

[Bertrand 1873] J. Bertrand. 'Théorême relatif au mouvement d'un point attire vers un centre fixe'. *Comptes Rendus des Séances de l'Académie des Sciences*, **vol. 77**, p. 849 (1873) (cited page 177)

[Billy *et al.* 2008] J. Billy, V. Josse, Z. Zuo, A. Bernard, B. Hambrecht, P. Lugan, D. Clement, L. Sanchez-Palencia, P. Bouyer and A. Aspect. 'Direct observation of Anderson localization of matter waves in a controlled disorder'. *Nature*, **vol. 453**, no. 7197, pp. 891–894 (2008) (cited page 11)

[Bloch *et al.* 2012] I. Bloch, J. Dalibard and S. Nascimbène. 'Quantum simulations with ultracold quantum gases'. *Nature Physics*, **vol. 8**, no. 4, pp. 267–276 (2012) (cited page 9)

[Bloom *et al.* 2014] B. Bloom, T. Nicholson, J. Williams, S. Campbell, M. Bishof, X. Zhang, W. Zhang, S. Bromley and J. Ye. 'A new generation of atomic clocks: Total uncertainty and instability at the 10^{-18} level.' *Nature*, **vol. 506**, pp. 71–75 (2014) (cited page 13)

[Boada *et al.* 2012] O. Boada, A. Celi, J. I. Latorre and M. Lewenstein. 'Quantum Simulation of an Extra Dimension'. *Physical Review Letters*, **vol. 108**, p. 133001 (2012) (cited page 11)

[Boettcher *et al.* 2016] I. Boettcher, L. Bayha, D. Kedar, P. A. Murthy, M. Neidig, M. G. Ries, A. N. Wenz, G. Zürn, S. Jochim and T. Enss. 'Equation of state of ultracold fermions in the 2D BEC-BCS crossover'. *Physical Review Letters*, **vol. 116**, no. 4, p. 045303 (2016) (cited page 11)

[Boiron *et al.* 1995] D. Boiron, C. Triché, D. R. Meacher, P. Verkerk and G. Grynberg. 'Three-dimensional cooling of cesium atoms in four-beam gray optical molasses'. *Phys. Rev. A*, **vol. 52**, pp. R3425–R3428 (1995) (cited page 33)

[Bose 1924] S. Bose. 'Plancks Gesetz und Lichtquantenhypothese'. *Zeitschrift für Physik*, **vol. 26**, no. 1, pp. 178–181 (1924) (cited page 5)

[Bouchendira *et al.* 2011] R. Bouchendira, P. Cladé, S. Guellati-Khélifa, F. Nez and F. Biraben. 'New determination of the fine structure constant and test of the quantum electrodynamics'. *Physical Review Letters*, **vol. 106**, p. 080801 (2011) (cited page 13)

[Breit and Rabi 1931] G. Breit and I. I. Rabi. 'Measurement of Nuclear Spin'. *Physical Review*, **vol. 38**, no. 11, pp. 2082–2083 (1931) (cited page 168)

[Brey *et al.* 1989] L. Brey, N. Johnson and B. Halperin. 'Optical and magneto-optical absorption in parabolic quantum wells'. *Phys. Rev. B*, **vol. 40**, no. 15, pp. 10647–10649 (1989) (cited page 175)

[Bulgac and Forbes 2007] A. Bulgac and M. M. Forbes. 'Zero-temperature thermodynamics of asymmetric Fermi gases at unitarity'. *Phys. Rev. A*, **vol. 75**, no. 3, pp. 1–4 (2007) (cited page 11)

[Burchianti *et al.* 2014] A. Burchianti, G. Valtolina, J. A. Seman, E. Pace, M. De Pas, M. Inguscio, M. Zaccanti and G. Roati. 'Efficient all-optical production of large Li6 quantum gases using D1 gray-molasses cooling'. *Phys. Rev. A*, **vol. 90**, no. 4, p. 043408 (2014) (cited page 35)

[Burkhardt and Leventhal 2010] C. E. Burkhardt and J. J. Leventhal. *Topics in atomic physics*. Springer-Verlag New York Inc (2010). ISBN 1441920684, 288 pp. (cited page 165)

[Burkov 2014] A. A. Burkov. 'Anomalous hall effect in weyl metals'. *Physical Review Letters*, **vol. 113**, p. 187202 (2014) (cited page 97)

[Burkov 2015] A. A. Burkov. 'Chiral anomaly and transport in Weyl metals.' *Journal of physics. Condensed matter : an Institute of Physics journal*, **vol. 27**, no. 11, p. 113201 (2015) (cited page 95)

[Casati *et al.* 1989] G. Casati, I. Guarneri and D. L. Shepelyansky. 'Anderson Transition in a One-Dimensional System with Three Incommensurate Frequencies'. *Physical Review Letters*, **vol. 62**, no. 4, pp. 345–348 (1989) (cited page 11)

[Castro Neto *et al.* 2009] a. H. Castro Neto, N. M. R. Peres, K. S. Novoselov, a. K. Geim, F. Guinea and A. Neto. 'The electronic properties of graphene'. *Reviews of Modern Physics*, **vol. 81**, no. 1, pp. 109–162 (2009) (cited page 98)

[Cataliotti *et al.* 1998] F. Cataliotti, E. Cornell, C. Fort, M. Inguscio, F. Marin, M. Prevedelli, L. Ricci and G. Tino. 'Magneto-optical trapping of Fermionic potassium atoms'. *Phys. Rev. A*, **vol. 57**, no. 2, pp. 1136–1138 (1998) (cited page 6)

[Celi *et al.* 2014] A. Celi, P. Massignan, J. Ruseckas, N. Goldman, I. B. Spielman, G. Juzeliūnas and M. Lewenstein. 'Synthetic Gauge Fields in Synthetic Dimensions'. *Physical Review Letters*, **vol. 112**, p. 043001 (2014) (cited page 11)

[Chabé *et al.* 2008] J. Chabé, G. Lemarié, B. Grémaud, D. Delande, P. Szriftgiser and J. C. Garreau. 'Experimental Observation of the Anderson Metal-Insulator Transition with Atomic Matter Waves'. *Physical Review Letters*, **vol. 101**, no. 25, p. 255702 (2008) (cited page 11)

[Chandrasekhar 1962] B. S. Chandrasekhar. 'A note on the maximum critical field of high-field superconductors'. *Applied Physics Letters*, **vol. 1**, no. 1, pp. 7–8 (1962) (cited page 10)

[Cheuk *et al.* 2012] L. W. Cheuk, A. T. Sommer, Z. Hadzibabic, T. Yefsah, W. S. Bakr and M. W. Zwierlein. 'Spin-Injection Spectroscopy of a Spin-Orbit Coupled Fermi Gas'. *Physical Review Letters*, **vol. 109**, p. 095302 (2012) (cited page 13)

[Cheuk *et al.* 2015] L. W. Cheuk, M. A. Nichols, M. Okan, T. Gersdorf, V. V. Ramasesh, W. S. Bakr, T. Lompe and M. W. Zwierlein. 'Quantum-gas microscope for fermionic atoms'. *Physical Review Letters*, **vol. 114**, no. 19, pp. 1–5 (2015) (cited page 10)

[Chevy 2006] F. Chevy. 'Universal phase diagram of a strongly interacting Fermi gas with unbalanced spin populations'. *Phys. Rev. A*, **vol. 74**, no. 6, pp. 29–32 (2006) (cited page 11)

[Chevy and Salomon 2012] F. Chevy and C. Salomon. 'Thermodynamics of Fermi gases'. In W Zwerger, editor, 'The BCS-BEC crossover and the unitarity Fermi gas', p. 532. Springer (2012). ISBN 978-3-642-21977-1 (cited page 7)

[Chicireanu *et al.* 2007] R. Chicireanu, Q. Beaufils, A. Pouderous, B. Laburthe-Tolra, E. Marechal, J. V. Porto, L. Vernac, J. C. Keller and O. Gorceix. 'Accumulation and thermalization of cold atoms in a finite-depth magnetic trap'. *Phys. Rev. A*, **vol. 76**, no. 2, p. 23406 (2007) (cited page 59)

[Chin *et al.* 2004] C. Chin, M. Bartenstein, A. Altmeyer, S. Riedl, S. Jochim, J. H. Denschlag and R. Grimm. 'Observation of the pairing gap in a strongly interacting fermi gas'. *Science*, **vol. 305**, no. 5687, pp. 1128–1130 (2004) (cited page 190)

[Chin *et al.* 2010] C. Chin, R. Grimm, P. Julienne and E. Tiesinga. 'Feshbach resonances in ultracold gases'. *Reviews of Modern Physics*, **vol. 82**, no. 2, pp. 1225–1286 (2010) (cited page 188)

[Chomaz *et al.* 2005] P. Chomaz, F. Gulminelli and O. Juillet. 'Generalized Gibbs ensembles for time-dependent processes'. *Annals of Physics*, **vol. 320**, pp. 135–163 (2005) (cited page 54)

[Clausius 1870] R. Clausius. 'On a mechanical theorem applicable to heat'. *Philosophical Magazine Series 4*, **vol. 40**, no. 265, p. 122 (1870) (cited page 176)

[Clogston 1962] a. M. Clogston. 'Upper limit for the critical field in hard superconductors'. *Physical Review Letters*, **vol. 9**, no. 6, pp. 266–267 (1962) (cited page 10)

[Cohen-Tannoudji 1996] C. Cohen-Tannoudji. 'Atomes ultrafroids - Piégeage non dissipatif et refroidissement évaporatif'. *Cours au College de France* (1996) (cited page 124)

[Cohen-Tannoudji and Guery Odelin 2011] C. Cohen-Tannoudji and D. Guery Odelin. *Advances In Atomic Physics: An Overview* (2011). ISBN 9812774971, 796 pp. (cited page 181)

[Cohen-Tannoudji *et al.* 1997] C. Cohen-Tannoudji, B. Diu and F. Laloe. *Mécanique quantique I*. Editions Hermann (1997). ISBN 2705660747, 889 pp. (cited page 165)

[Cohen-Tannoudji *et al.* 2001] C. Cohen-Tannoudji, J. Dupont-Roc and G. Grynberg. *Processus d'interaction entre photons et atomes*. EDP Sciences, CNRS édition (2001). ISBN 2868833586, 628 pp. (cited page 46)

[Colzi *et al.* 2016] G. Colzi, G. Durastante, E. Fava, S. Serafini, G. Lamporesi and G. Ferrari. 'Sub-doppler cooling of sodium atoms in gray molasses'. *Phys. Rev. A*, **vol. 93**, p. 023421 (2016) (cited page 35)

[Costa *et al.* 2010] L. Costa, J. Brachmann, A.-C. Voigt, C. Hahn, M. Taglieber, T. W. Hänsch and K. Dieckmann. '*s*-wave interaction in a two-species fermi-fermi mixture at a narrow feshbach resonance'. *Physical Review Letters*, **vol. 105**, p. 123201 (2010) (cited page 14)

[Courteille *et al.* 1998] P. Courteille, R. S. Freeland, D. J. Heinzen, F. A. van Abeelen and B. J. Verhaar. 'Observation of a Feshbach resonance in cold atom scattering'. *Physical Review Letters*, **vol. 81**, no. 1, pp. 69–72 (1998) (cited page 189)

[Dalibard 2013] J. Dalibard. 'Des cages de lumière pour les atomes : la physique des pièges et des réseaux optiques'. *Cours au College de France* (2013) (cited page 152)

[Dalibard 2015] J. Dalibard. 'A Brief History of Cold Atoms'. *Cours au College de France* (2015) (cites pages 28, 29)

[Dalibard and Cohen-Tannoudji 1989] J. Dalibard and C. Cohen-Tannoudji. 'Laser cooling below the Doppler limit by polarization gradients: simple theoretical models'. *Journal of the Optical Society of America B*, **vol. 6**, no. 11, p. 2023 (1989) (cited page 32)

[Dalibard *et al.* 2011] J. Dalibard, F. Gerbier, G. Juzeliunas and P. Öhberg. 'Colloquium: Artificial gauge potentials for neutral atoms'. *Reviews of Modern Physics*, **vol. 83**, no. 4, pp. 1523–1543 (2011) (cited page 12)

[Davis *et al.* 1995a] K. Davis, M.-O. Mewes, M. Joffe, M. Andrews and W. Ketterle. 'Evaporative Cooling of Sodium Atoms'. *Physical Review Letters*, **vol. 75**, no. 26, p. 5205 (1995) (cites pages 5, 54, 128)

[Davis *et al.* 1995b] K. B. Davis, M. O. Mewes and W. Ketterle. 'An analytical model for evaporative cooling of atoms'. *Applied Physics B Laser and Optics*, **vol. 60**, no. 2-3, pp. 155–159 (1995) (cited page 124)

[de Lavoisier 1789] A. L. de Lavoisier. *Traité élémentaire de Chimie*. Paris (1789) (cited page 1)

[Delehaye *et al.* 2015] M. Delehaye, S. Laurent, I. Ferrier-Barbut, S. Jin, F. Chevy and C. Salomon. 'Critical Velocity and Dissipation of an Ultracold Bose-Fermi Counterflow'. *Physical Review Letters*, **vol. 115**, no. 26, pp. 1–5 (2015) (cites pages 7, 154, 158)

[Delerue and Allan 2011] C. Delerue and G. Allan. 'Optimization of carrier multiplication in quantum dots for more efficient solar cells: Theoretical aspects'. In 'Frontiers in Optics 2011/Laser Science XXVII', p. LWH2. Optical Society of America (2011) (cited page 98)

[DeMarco 2001] B. DeMarco. *Quantum Behavior of an Atomic Fermi Gas*. Ph.D. thesis, JILA (2001) (cites pages 41, 60)

[Demarco and Jin 1998] B. Demarco and D. S. Jin. 'Exploring a quantum degenerate gas of fermionic atoms'. *Phys. Rev. A*, **vol. 58**, no. 6, pp. 4267–4270 (1998) (cited page 6)

[DeMarco and Jin 1999] B. DeMarco and D. S. Jin. 'Onset of Fermi degeneracy in a trapped atomic gas'. *Science*, **vol. 285**, no. 5434, pp. 1703–1706 (1999) (cites pages 6, 127)

[DeMarco *et al.* 1999] B. DeMarco, J. Bohn, J. Burke, M. Holland and D. Jin. 'Measurement of p-Wave Threshold Law Using Evaporatively Cooled Fermionic Atoms'. *Physical Review Letters*, **vol. 82**, no. 21, pp. 4208–4211 (1999) (cites pages 66, 127, 128, 187)

[Demokritov *et al.* 2006] S. O. Demokritov, V. E. Demidov, O. Dzyapko, G. A. Melkov, A. A. Serga, B. Hillebrands and A. N. Slavin. 'Bose-Einstein condensation of quasi-equilibrium magnons at room temperature under pumping.' *Nature*, **vol. 443**, no. 7110, pp. 430–433 (2006) (cited page 6)

[Dobson 1994] J. F. Dobson. 'Harmonic-Potential Theorem: Implications for Approximate Many-Body Theories John'. *Physical Review Letters*, **vol. 73**, no. 16, p. 2244 (1994) (cited page 175)

[Drewsen *et al.* 1994] M. Drewsen, P. Laurent, A. Nadir, G. Santarelli, A. Clairon, Y. Castin, D. Grison and C. Salomon. 'Investigation of sub-Doppler cooling effects in a cesium magneto-optical trap'. *Applied Physics B*, **vol. 59**, no. 3, pp. 283–298 (1994) (cited page 29)

[Duarte *et al.* 2011] P. M. Duarte, R. A. Hart, J. M. Hitchcock, T. A. Corcovilos, T.-L. Yang, A. Reed and R. G. Hulet. 'All-optical production of a lithium quantum gas using narrow-line laser cooling'. *Phys. Rev. A*, **vol. 84**, no. 6, p. 061406 (2011) (cited page 31)

[Dubček *et al.* 2015] T. Dubček, C. J. Kennedy, L. Lu, W. Ketterle, M. Soljačić and H. Buljan. 'Weyl Points in Three-Dimensional Optical Lattices: Synthetic Magnetic Monopoles in Momentum Space'. *Physical Review Letters*, **vol. 114**, no. 22, p. 225301 (2015) (cited page 99)

[Dubessy *et al.* 2012] R. Dubessy, K. Merloti, L. Longchambon, P.-E. Pottie, T. Liennard, A. Perrin, V. Lorent and H. Perrin. 'Rubidium-87 Bose-Einstein condensate in an optically plugged quadrupole trap'. *Phys. Rev. A*, **vol. 85**, no. 1, p. 013643 (2012) (cites pages 59, 128)

[Editorial 2015] Editorial. 'After a Weyl'. *Nature Physics*, **vol. 11**, no. 9, p. 697 (2015) (cited page 92)

[Efimov 1970] V. Efimov. 'Energy levels arising from resonant two-body forces in a three-body problem'. *Physics Letters B*, **vol. 33**, no. 8, pp. 563–564 (1970) (cited page 160)

[Efimov 1973] V. Efimov. 'Energy levels of three resonantly interacting particles'. *Nuclear Physics A*, **vol. 210**, no. 1, pp. 157–188 (1973) (cited page 160)

[Einstein 1917] A. Einstein. 'Zur Quantentheorie der Strahlung'. *Physikaliche Zeitschrift*, **vol. 18**, p. 121 (1917) (cited page 5)

[Einstein 1924] A. Einstein. 'Quantentheorie des einatomigen idealen Gases'. *Sitzungs- berichte der Preussischen Akademie der Wissenschaften*, **vol. 6**, pp. 261–267 (1924) (cited page 5)

[Endres *et al.* 2012] M. Endres, T. Fukuhara, D. Pekker, M. Cheneau, P. Schauβ, C. Gross, E. Demler, S. Kuhr and I. Bloch. 'The 'Higgs' amplitude mode at the two-dimensional superfluid/Mott insulator transition'. *Nature*, **vol. 487**, no. 7408, pp. 454–458 (2012) (cited page 10)

[Enesa 2015] C. Enesa. 'Towards quantum degenerate Fermimixtures'. *Master thesis* (2015) (cited page 136)

[Ensher *et al.* 1996] J. Ensher, D. Jin, M. Matthews, C. Wieman and E. Cornell. 'Bose-Einstein Condensation in a Dilute Gas: Measurement of Energy and Ground-State Occupation'. *Physical Review Letters*, **vol. 77**, no. 25, pp. 4984–4987 (1996) (cited page 11)

[Falke *et al.* 2008] S. Falke, H. Knöckel, J. Friebe, M. Riedmann, E. Tiemann and C. Lisdat. 'Potassium ground-state scattering parameters and Born-Oppenheimer potentials from molecular spectroscopy'. *Phys. Rev. A*, **vol. 78**, no. 1, pp. 1–13 (2008) (cited page 187)

[Fallani *et al.* 2008] L. Fallani, C. Fort and M. Inguscio. 'Bose–Einstein Condensates in Disordered Potentials'. *Advances In Atomic, Molecular, and Optical Physics*, **vol. 56**, pp. 119–160 (2008) (cited page 11)

[Fedichev and Shlyapnikov 2001] P. O. Fedichev and G. V. Shlyapnikov. 'Critical velocity in cylindrical Bose-Einstein condensates'. *Phys. Rev. A*, **vol. 63**, no. 4, pp. 1–3 (2001) (cited page 6)

[Fenech *et al.* 2016] K. Fenech, P. Dyke, T. Peppler, M. G. Lingham, S. Hoinka, H. Hu and C. J. Vale. 'Thermodynamics of an Attractive 2D Fermi Gas'. *Physical Review Letters*, **vol. 116**, no. 4, p. 045302 (2016) (cited page 11)

[Fernandes 2014] D. R. Fernandes. *Trapping and cooling of fermionic alkali atoms to quantum degeneracy . Sub-Doppler cooling of Potassium-40 and Lithium-6 in gray molasses Diogo Rio Fernandes Trapping and cooling of fermionic alkali atoms to quantum degeneracy . Sub-Doppler cooling of Pot*. Ph.D. thesis, Université Pierre et Marie Curie (2014) (cites pages 24, 39, 127, 134)

[Fernandes *et al.* 2012] D. R. Fernandes, F. Sievers, N. Kretzschmar, S. Wu, C. Salomon and F. Chevy. 'Sub-Doppler laser cooling of fermionic 40 K atoms in three-dimensional gray optical molasses'. *Europhysics Letters*, **vol. 100**, p. 63001 (2012) (cites pages 15, 32)

[Ferrier-Barbut *et al.* 2014] I. Ferrier-Barbut, M. Delehaye, S. Laurent, A. T. Grier, M. Pierce, B. S. Rem, F. Chevy and C. Salomon. 'A mixture of Bose and Fermi superfluids'. *Science*, **vol. 345**, no. 6200, p. 1035 (2014) (cited page 155)

[Feshbach 1962] H. Feshbach. 'A unified theory of nuclear reactions. II'. *Annals of Physics*, **vol. 19**, no. 2, pp. 287–313 (1962) (cited page 187)

[Feynman 1982] R. P. Feynman. 'Simulating Physics with Computers'. *International Journal of Theoretical Physics*, **vol. 21**, pp. 467–488 (1982) (cited page 9)

[Franzosi *et al.* 2004] R. Franzosi, B. Zambon and E. Arimondo. 'Nonadiabatic effects in the dynamics of atoms confined in a cylindric time-orbiting-potential magnetic trap'. *Phys. Rev. A*, **vol. 70**, p. 053603 (2004) (cited page 104)

[Fried *et al.* 1998] D. G. Fried, T. C. Killian, L. Willmann, D. Landhuis, S. C. Moss, D. Kleppner and T. J. Greytak. 'Bose-Einstein Condensation of Atomic Hydrogen'. *Physical Review Letters*, **vol. 81**, p. 3811 (1998) (cited page 5)

[Friedrich and Herschbach 2003] B. Friedrich and D. Herschbach. 'Stern and Gerlach: How a Bad Cigar Helped Reorient Atomic Physics'. *Physics Today*, **vol. 56**, no. 12, p. 53 (2003) (cited page 115)

[Fuchs *et al.* 2007] J. N. Fuchs, A. Recati and W. Zwerger. 'Oscillating Casimir force between impurities in one-dimensional Fermi liquids'. *Phys. Rev. A*, **vol. 75**, no. 4, pp. 1–6 (2007) (cited page 140)

[Fulde and Ferrell 1964] P. Fulde and R. A. Ferrell. 'Superconductivity in a Strong Spin-Exchange Field'. *Physical Review*, **vol. 135**, no. 3A, p. A550 (1964) (cited page 10)

[Gaebler *et al.* 2007] J. P. Gaebler, J. T. Stewart, J. L. Bohn and D. S. Jin. 'p-wave feshbach molecules'. *Phys. Rev. Lett.*, **vol. 98**, p. 200403 (2007) (cited page 131)

[Garay *et al.* 2000] L. J. Garay, J. R. Anglin, J. I. Cirac and P. Zoller. 'Sonic analog of gravitational black holes in Bose-Einstein condensates'. *Physical Review Letters*, **vol. 85**, no. 22, pp. 4643–4647 (2000) (cited page 9)

[Gehm 2003] M. Gehm. 'Properties of 6 Li'. *unpublished*, pp. 1–33 (2003) (cites pages 20, 23)

[Geim and Novoselov 2007] a. K. Geim and K. Novoselov. 'The rise of graphene'. *Nature Mater.*, **vol. 6**, pp. 183–191 (2007) (cited page 94)

[Gerbier *et al.* 2003] F. Gerbier, J. H. Thywissen, S. Richard, M. Hugbart, P. Bouyer and A. Aspect. 'Critical temperature of a trapped, weakly interacting Bose gas.' *Physical Review Letters*, **vol. 92**, no. 3, p. 030405 (2003) (cited page 11)

[Gerbier *et al.* 2004] F. Gerbier, J. H. Thywissen, S. Richard, M. Hugbart, P. Bouyer and A. Aspect. 'Experimental study of the thermodynamics of an interacting trapped Bose-Einstein condensed gas'. *Phys. Rev. A*, **vol. 70**, no. 1, pp. 1–10 (2004) (cited page 11)

[Gerritsma *et al.* 2010] R. Gerritsma, G. Kirchmair, F. Zähringer, E. Solano, R. Blatt and C. F. Roos. 'Quantum simulation of the Dirac equation.' *Nature*, **vol. 463**, no. 7277, pp. 68–71 (2010) (cited page 99)

[Gerritsma *et al.* 2011] R. Gerritsma, B. P. Lanyon, G. Kirchmair, F. Zähringer, C. Hempel, J. Casanova, J. J. García-Ripoll, E. Solano, R. Blatt and C. F. Roos. 'Quantum Simulation of the Klein Paradox with Trapped Ions'. *Physical Review Letters*, **vol. 106**, no. 6, p. 060503 (2011) (cited page 99)

[Gezerlis and Carlson 2008] A. Gezerlis and J. Carlson. 'Strongly paired fermions: Cold atoms and neutron matter'. *Phys. Rev. C*, **vol. 77**, no. 3, pp. 1–4 (2008) (cited page 10)

[Giamarchi 2004] T. Giamarchi. *Quantum Physics in One Dimension*. Oxford University Press (2004). ISBN 0198525001, 440 pp. (cited page 139)

[Girardeau 1960] M. Girardeau. 'Relationship between Systems of Impenetrable Bosons and Fermions in One Dimension'. *Journal of Mathematical Physics*, **vol. 1**, no. 6, p. 516 (1960) (cited page 139)

[Giuliani and Vignale 2005] G. Giuliani and G. Vignale. *Quantum Theory of the Electron Liquid*. Cambridge University Press (2005). ISBN 9780521821124, 777 pp. (cited page 149)

[Gokhroo *et al.* 2011] V. Gokhroo, G. Rajalakshmi, R. K. Easwaran and C. S. Unnikrishnan. 'Sub-Doppler deep-cooled bosonic and fermionic isotopes of potassium in a compact 2D +–3D MOT set-up'. *Journal of Physics B: Atomic, Molecular and Optical Physics*, **vol. 44**, no. 11, p. 115307 (2011) (cited page 32)

[Goldstein *et al.* 2001] H. Goldstein, J. Pool, Charles P and J. L. Safko. *Classical Mechanics*. Addison-Wesley, 3rd editio ed. (2001). ISBN 0201657023, 680 pp. (cited page 177)

[Gordon and Ashkin 1980] J. P. Gordon and A. Ashkin. 'Motion of atoms in a radiation trap'. *Phys. Rev. A*, **vol. 21**, no. 5, pp. 1606–1617 (1980) (cited page 29)

[Görlitz *et al.* 2001] A. Görlitz, A. P. Chikkatur and W. Ketterle. 'Enhancement and suppression of spontaneous emission and light scattering by quantum degeneracy'. *Phys. Rev. A*, **vol. 63**, pp. 1–4 (2001) (cited page 159)

[Grandati *et al.* 2008] Y. Grandati, A. Bérard and F. Menas. 'Inverse problem and Bertrand's theorem'. *American Journal of Physics*, **vol. 76**, no. 8, p. 782 (2008) (cited page 178)

[Greiner *et al.* 2002] M. Greiner, O. Mandel, T. Esslinger, T. Hänsch and I. Bloch. 'Quantum phase transition from a superfluid to a Mott insulator in a gas of ultracold atoms'. *Nature*, **vol. 415**, no. 6867, pp. 39–44 (2002) (cited page 10)

[Greiner *et al.* 2003] M. Greiner, C. Regal and D. Jin. 'Emergence of a molecular Bose-Einstein condensate from a Fermi gas'. *Nature*, **vol. 426**, no. 6966, pp. 537–540 (2003) (cited page 9)

[Grempel *et al.* 1984] D. R. Grempel, R. E. Prange and S. Fishman. 'Quantum dynamics of a nonintegrable system'. *Phys. Rev. A*, **vol. 29**, no. 4, p. 1639 (1984) (cited page 11)

[Grier *et al.* 2013] A. T. Grier, I. Ferrier-Barbut, B. S. Rem, M. Delehaye, L. Khaykovich, F. Chevy and C. Salomon. 'Λ-enhanced sub-Doppler cooling of lithium atoms in D1 gray molasses'. *Phys. Rev. A*, **vol. 87**, no. 6, p. 63411 (2013) (cites pages 34, 35)

[Griesmaier 2007] A. Griesmaier. 'Generation of a dipolar bose–einstein condensate'. *Journal of Physics B: Atomic, Molecular and Optical Physics*, **vol. 40**, no. 14, p. R91 (2007) (cited page 12)

[Grimm *et al.* 2000] R. Grimm, M. Weidemüller and Y. B. Ovchinnikov. 'Optical dipole traps for neutral atoms'. *Advances In Atomic, Molecular, and Optical Physics*, **vol. 42**, p. 95 (2000) (cites pages 41, 129)

[Guery Odelin 1998] D. Guery Odelin. *Dynamique collisionnelle des gaz d'alcalins lourds : du refroidissement évaporatif à la condensation de Bose Einstein*. Ph.D. thesis, Université Pierre et Marie Curie (1998) (cited page 125)

[Guery-Odelin *et al.* 1999] D. Guery-Odelin, F. Zambelli, J. Dalibard and S. Stringari. 'Collective oscillations of a classical gas confined in harmonic traps'. *Phys. Rev. A*, **vol. 60**, no. 6, p. 6 (1999) (cited page 119)

[Gunter *et al.* 2006] K. Gunter, T. Stoferle, H. Moritz, M. Kohl and T. Esslinger. 'Bose-Fermi Mixtures in a Three-Dimensional Optical Lattice'. *Physical Review Letters*, **vol. 96**, no. 18, p. 180402 (2006) (cited page 10)

[Gurarie *et al.* 2009] V. Gurarie, L. Pollet, N. V. Prokof'ev, B. V. Svistunov and M. Troyer. 'Phase diagram of the disordered Bose-Hubbard model'. *Phys. Rev. B*, **vol. 80**, p. 214519 (2009) (cited page 11)

[Gustavson *et al.* 2002] T. L. Gustavson, A. P. Chikkatur, A. E. Leanhardt, A. Görlitz, S. Gupta, D. E. Pritchard and W. Ketterle. 'Transport of Bose-Einstein Condensates with Optical Tweezers'. *Physical Review Letters*, **vol. 88**, no. 2, pp. 3–6 (2002) (cited page 37)

[Hadzibabic and Dalibard 2011] Z. Hadzibabic and J. Dalibard. 'Two-dimensional Bose fluids: An atomic physics perspective'. *Rivista del Nuovo Cimento*, **vol. 34**, no. 6, pp. 389–434 (2011) (cited page 139)

[Hadzibabic *et al.* 2006] Z. Hadzibabic, P. Krüger, M. Cheneau, B. Battelier and J. Dalibard. 'Berezinskii-Kosterlitz-Thouless crossover in a trapped atomic gas.' *Nature*, **vol. 441**, no. 7097, pp. 1118–1121 (2006) (cited page 140)

[Haller *et al.* 2010] E. Haller, M. J. Mark, R. Hart, J. G. Danzl, V. Melezhik and P. Schmelcher. 'Confinement-Induced Resonances in Low-Dimensional Quantum Systems'. *Physical Review Letters*, **vol. 104**, no. 15, p. 153203 (2010) (cited page 140)

[Haller *et al.* 2015] E. Haller, J. Hudson, A. Kelly, D. A. Cotta, B. Peaudecerf, G. D. Bruce and S. Kuhr. 'Single-atom imaging of fermions in a quantum-gas microscope'. *Nature Physics*, **vol. 11**, pp. 738–742 (2015) (cited page 10)

[Hanle 1984] W. Hanle. *Progress in Atomic Spectroscopy: Part C*. Springer-Verlag New York Inc. (1984). ISBN 146129651X (cited page 166)

[Hänsch and Schawlow 1975] T. W. Hänsch and A. L. Schawlow. 'Cooling of gases by laser radiation'. *Optics Communications*, **vol. 13**, no. 1, pp. 68–69 (1975) (cited page 5)

[Heer 1963] C. V. Heer. 'Feasibility of Containment of Quantum Magnetic Dipoles'. *Review of Scientific Instruments*, **vol. 34**, no. 5, p. 532 (1963) (cited page 55)

[Heo *et al.* 2010] M.-S. Heo, J.-y. Choi and Y.-i. Shin. 'Fast production of large 23Na Bose-Einstein condensates in an optically plugged magnetic quadrupole trap'. *Phys. Rev. A*, **vol. 83**, no. 1, p. 6 (2010) (cited page 59)

[Hess 1986] H. F. Hess. 'Evaporative cooling of magnetically trapped and compressed spin-polarized hydrogen'. *Phys. Rev. B*, **vol. 34**, no. 5, pp. 3476–3479 (1986) (cited page 111)

[Hess *et al.* 1987] H. F. Hess, G. P. Kochanski, J. M. Doyle, N. Masuhara, D. Kleppner and T. J. Greytak. 'Magnetic trapping of spin-polarized atomic hydrogen'. *Physical Review Letters*, **vol. 59**, no. 6, pp. 672–675 (1987) (cited page 111)

[Hofstadter 1976] D. R. Hofstadter. 'Energy levels and wave functions of bloch electrons in rational and irrational magnetic fields'. *Phys. Rev. B*, **vol. 14**, pp. 2239–2249 (1976) (cited page 12)

[Horikoshi *et al.* 2010] M. Horikoshi, S. Nakajima, M. Ueda and T. Mukaiyama. 'Measurement of Universal Thermodynamic Functions for a Unitary Fermi Gas'. *Science*, **vol. 327**, no. 5964, pp. 442–445 (2010) (cited page 11)

[Hosur and Qi 2013] P. Hosur and X. Qi. 'Recent developments in transport phenomena in Weyl semimetals'. *Comptes Rendus Physique*, **vol. 14**, no. 9-10, p. 857 (2013) (cites pages 94, 96)

[Houbiers *et al.* 1998] M. Houbiers, H. T. C. Stoof, W. I. McAlexander and R. G. Hulet. 'Elastic and inelastic collisions of ^{6}Li atoms in magnetic and optical traps'. *Phys. Rev. A*, **vol. 57**, pp. R1497–R1500 (1998) (cited page 60)

[Huang *et al.* 2015] X. Huang, L. Zhao, Y. Long, P. Wang, D. Chen, Z. Yang, H. Liang, M. Xue, H. Weng, Z. Fang, X. Dai and G. Chen. 'Observation of the chiral anomaly induced negative magneto-resistance in 3D Weyl semi-metal TaAs'. *Phys. Rev. X*, **vol. 5**, no. 3, p. 031023 (2015) (cites pages 92, 96)

[Hung *et al.* 2011] C. Hung, X. Zhang, N. Gemelke and C. Chin. 'Observation of scale invariance and universality in two-dimensional Bose gases'. *Nature*, **vol. 470**, no. 7333, pp. 236–9 (2011) (cited page 11)

[Inouye *et al.* 1998] S. Inouye, M. R. Andrews, J. Stenger, H.-J. Miesner, D. M. Stamper-Kurn and W. Ketterle. 'Observation of Feshbach resonances in a Bose-Einstein condensate'. *Nature*, **vol. 392**, no. 6672, pp. 151–154 (1998) (cites pages 7, 188)

[Jacob *et al.* 2007] A. Jacob, P. Öhberg, G. Juzeliunas and L. Santos. 'Cold atom dynamics in non-Abelian gauge fields'. *Applied Physics B*, **vol. 89**, no. 4, pp. 439–445 (2007) (cited page 13)

[Jag *et al.* 2014] M. Jag, M. Zaccanti, M. Cetina, R. S. Lous, F. Schreck, R. Grimm, D. S. Petrov and J. Levinsen. 'Observation of a strong atom-dimer attraction in a mass-imbalanced fermi-fermi mixture'. *Physical Review Letters*, **vol. 112**, p. 075302 (2014) (cited page 14)

[Jaksch and Zoller 2005] D. Jaksch and P. Zoller. 'The cold atom Hubbard toolbox'. *Annals of Physics*, **vol. 315**, no. 1, pp. 52 – 79 (2005). Special Issue (cited page 9)

[Jordens *et al.* 2008] R. Jordens, N. Strohmaier, K. Gunter, H. Moritz and T. Esslinger. 'A Mott insulator of fermionic atoms in an optical lattice'. *Nature*, **vol. 455**, no. 7210, pp. 204–207 (2008) (cited page 10)

[Kadau *et al.* 2016] H. Kadau, M. Schmitt, M. Wenzel, C. Wink, T. Maier, I. Ferrier-Barbut and T. Pfau. 'Observing the Rosensweig instability of a quantum ferrofluid'. *Nature*, **vol. 530**, pp. 194–197 (2016) (cited page 12)

[Kapitza 1938] P. Kapitza. 'Viscosity of liquid helium below the l-point'. *Nature*, **vol. 141**, p. 74 (1938) (cited page 5)

[Kastler 1950] A. Kastler. 'Quelques suggestions concernant la production optique et la détection optique d'une inégalité de population des niveaux de quantifigation spatiale des atomes. Application à l'expérience de Stern et Gerlach et à la résonance magnétique'. *Journal de Physique et le Radium*, **vol. 11**, no. 1, pp. 255–265 (1950) (cited page 5)

[Katsnelson *et al.* 2006] M. I. Katsnelson, K. S. Novoselov and A. K. Geim. 'Chiral tunneling and the Klein paradox in graphene'. *Nature Physics*, **vol. 2**, no. 620, pp. 1–15 (2006) (cited page 99)

[Ketterle 2002] W. Ketterle. 'When Atoms Behave As Waves : Bose-Einstein condensation and the atom laser'. In 'Les Prix Nobel 2001', pp. 77–108. The Nobel Foundation (2002). ISBN 978-981-4485-34-0 (cited page 6)

[Ketterle and Druten 1996] W. Ketterle and N. V. Druten. 'Evaporative Cooling of Trapped Atoms' (1996) (cites pages 111, 127)

[Ketterle and Zwierlein 2008] W. Ketterle and M. Zwierlein. 'Making, probing and understanding ultracold Fermi gases'. In M Inguscio, W Ketterle and C Salomon, editors, 'Ultracold Fermi Gases, Proceedings of the International School of Physics "Enrico Fermi", Course CLXIV', June 2006, pp. 20–30. IOS Press, Amsterdam (2008). ISBN 158603846X (cites pages 66, 189)

[Ketterle *et al.* 1999] W. Ketterle, S. Durfee and M. Stamper-Kurn. 'Making, probing and understanding Bose-Einstein condensates'. In M Inguscio, S Stringari and C Wieman, editors, 'Bose-Einstein condensation in atomic gases, Proceedings of the International School of Physics "Enrico Fermi", Course CXL', pp. 67–176. IOS Press, Amsterdam, (1999) (cited page 6)

[Kim *et al.* 2013] H.-J. Kim, K.-S. Kim, J.-F. Wang, M. Sasaki, N. Satoh, A. Ohnishi, M. Kitaura, M. Yang and L. Li. 'Dirac versus Weyl Fermions in Topological Insulators: Adler-Bell-Jackiw Anomaly in Transport Phenomena'. *Physical Review Letters*, **vol. 111**, no. 24, p. 246603 (2013) (cited page 96)

[Kinnunen and Bruun 2015] J. J. Kinnunen and G. M. Bruun. 'Induced interactions in a superfluid Bose-Fermi mixture'. *Phys. Rev. A*, **vol. 91**, no. 4, pp. 1–6 (2015) (cited page 151)

[Kinoshita *et al.* 2006] T. Kinoshita, T. Wenger and D. S. Weiss. 'A quantum Newton's cradle'. *Nature*, **vol. 440**, no. April, pp. 900–903 (2006) (cited page 54)

[Klein 1929] O. Klein. 'Die Reflexion von Elektronen an einem Potentialsprung nach der relativistischen Dynamik von Dirac'. *Zeitschrift für Physik*, **vol. 53**, no. 3-4, p. 157 (1929) (cited page 98)

[Köhl *et al.* 2005] M. Köhl, H. Moritz, T. Stöferle, K. Günter and T. Esslinger. 'Fermionic atoms in a three dimensional optical lattice: Observing Fermi surfaces, dynamics, and interactions'. *Physical Review Letters*, **vol. 94**, no. 8, pp. 1–4 (2005) (cited page 10)

[Kohn 1961] W. Kohn. 'Cyclotron resonance and de haas-van alphen oscillations of an interacting electron gas'. *Physical Review*, **vol. 123**, no. 4, p. 1242 (1961) (cites pages 54, 175)

[Kohstall *et al.* 2012] C. Kohstall, M. Zaccanti, M. Jag, A. Trenkwalder, P. Massignan, G. M. Bruun, F. Schreck and R. Grimm. 'Metastability and coherence of repulsive polarons in a strongly interacting Fermi mixture'. *Nature*, **vol. 485**, pp. 615–618 (2012) (cited page 14)

[Koller *et al.* 2015] A. P. Koller, J. Mundinger, M. L. Wall and A. M. Rey. 'Demagnetization dynamics of noninteracting trapped fermions'. *Physical Review A*, **vol. 92**, no. 3, pp. 1–8 (2015) (cited page 110)

[Kondo 1964] J. Kondo. 'Resistance Minimum in Dilute Magnetic Alloys'. *Progress of Theoretical Physics*, **vol. 32**, no. 1, pp. 37–49 (1964) (cited page 12)

[Kondov *et al.* 2011] S. S. Kondov, W. R. McGehee, J. J. Zirbel and B. DeMarco. 'Three-Dimensional Anderson Localization of Ultracold Matter'. *Science*, **vol. 334**, no. 6052, pp. 66–68 (2011) (cited page 11)

[Kosterlitz and Thouless 1973] J. M. Kosterlitz and D. J. Thouless. 'Ordering, metastability and phase transitions in two-dimensional systems'. *Journal of Physics C: Solid State Physics*, **vol. 6**, no. 7, p. 1181 (1973) (cited page 139)

[Ku *et al.* 2012] M. J. H. Ku, A. T. Sommer, L. W. Cheuk and M. W. Zwierlein. 'Revealing the Superfluid Lambda Transition in the Universal Thermodynamics of a Unitary Fermi Gas'. *Science*, **vol. 335**, no. February, pp. 563–568 (2012) (cited page 7)

[Lahav *et al.* 2010] O. Lahav, A. Itah, A. Blumkin, C. Gordon, S. Rinott, A. Zayats and J. Steinhauer. 'Realization of a sonic black hole analog in a Bose-Einstein condensate'. *Physical Review Letters*, **vol. 105**, no. 24, pp. 1–4 (2010) (cited page 9)

[Lahaye *et al.* 2009] T. Lahaye, C. Menotti, L. Santos, M. Lewenstein and T. Pfau. 'The physics of dipolar bosonic quantum gases'. *Reports on Progress in Physics*, **vol. 72**, no. 12, p. 126401 (2009) (cited page 12)

[Lamporesi *et al.* 2010] G. Lamporesi, J. Catani, G. Barontini, Y. Nishida, M. Inguscio and F. Minardi. 'Scattering in Mixed Dimensions with Ultracold Gases'. *Physical Review Letters*, **vol. 104**, no. 15, pp. 1–4 (2010) (cited page 145)

[Landau 1932] L. Landau. 'On the theory of transfer of energy at collisions II''. *Phys. Z. Sowjetunion*, **vol. 2**, no. 46 (1932) (cited page 118)

[Landau 1946] L. D. Landau. 'On the vibrations of the electronic plasma'. *J. Phys.(USSR)*, **vol. 10**, pp. 25–34 (1946). [Zh. Eksp. Teor. Fiz.16,574(1946)] (cited page 54)

[Langen *et al.* 2015] T. Langen, S. Erne, R. Geiger, B. Rauer, T. Schweigler, M. Kuhnert, W. Rohringer, I. E. Mazets, T. Gasenzer and J. Schmiedmayer. 'Experimental Observation of a Generalized Gibbs Ensemble'. *Science*, **vol. 348**, no. 6231, p. 207 (2015) (cited page 54)

[Larkin and Ovchinnikov 1965] A. Larkin and Y. Ovchinnikov. 'Nonuniform state of superconductors'. *Sov. Phys. JETP*, **vol. 20**, p. 762 (1965) (cited page 10)

[Laurent *et al.* 2015] P. Laurent, D. Massonnet, L. Cacciapuoti and C. Salomon. 'The ACES/PHARAO space mission'. *Comptes Rendus Physique*, **vol. 16**, no. 5, pp. 540–552 (2015) (cited page 13)

[Léonard *et al.* 2014] J. Léonard, M. Lee, A. Morales, T. M. Karg, T. Esslinger and T. Donner. 'Optical transport and manipulation of an ultracold atomic cloud using focus-tunable lenses'. *New Journal of Physics*, **vol. 16**, no. 093028 (2014) (cited page 37)

[Lepori *et al.* 2015] L. Lepori, I. C. Fulga, A. Trombettoni and M. Burrello. 'PT invariant Weyl semimetals in gauge symmetric systems'. *arXiv:1506.04761*, pp. 1–6 (2015) (cited page 99)

[Lett *et al.* 1989] P. D. Lett, W. D. Phillips, S. L. Rolston, C. E. Tanner, R. N. Watts and C. I. Westbrook. 'Optical molasses'. *Journal of the Optical Society of America B*, **vol. 6**, no. 11, p. 2084 (1989) (cited page 31)

[Levinsen and Parish 2015] J. Levinsen and M. M. Parish. 'Strongly interacting two-dimensional Fermi gases'. *Annual Review of Cold Atoms and Molecules*, **vol. 3**, no. 1, p. 71 (2015) (cited page 140)

[Levinsen and Petrov 2011] J. Levinsen and D. S. Petrov. 'Atom-dimer and dimer-dimer scattering in fermionic mixtures near a narrow Feshbach resonance'. *European Physical Journal D*, **vol. 65**, no. 1-2, pp. 67–82 (2011) (cited page 14)

[Levitov *et al.* 1996] L. S. Levitov, H. Lee and G. B. Lesovik. 'Electron counting statistics and coherent states of electric current'. *Journal of Mathematical Physics*, **vol. 37**, no. 10, pp. 4845–4866 (1996) (cited page 10)

[Lewandowski 2002] H. Lewandowski. *Coherences and correlations in an ultracold Bose gas*. Ph.D. thesis, JILA (2002) (cited page 37)

[Lin *et al.* 2009a] Y.-J. Lin, R. L. Compton, K. Jimenez-Garcia, J. V. Porto and I. B. Spielman. 'Synthetic magnetic fields for ultracold neutral atoms'. *Nature*, **vol. 462**, no. 7273, pp. 628–632 (2009) (cited page 12)

[Lin *et al.* 2009b] Y. J. Lin, A. R. Perry, R. L. Compton, I. B. Spielman and J. V. Porto. 'Rapid production of R 87 b Bose-Einstein condensates in a combined magnetic and optical potential'. *Phys. Rev. A*, **vol. 79**, no. 6, pp. 1–8 (2009) (cited page 128)

[Lobo *et al.* 2006] C. Lobo, a. Recati, S. Giorgini and S. Stringari. 'Normal state of a polarized fermi gas at unitarity'. *Physical Review Letters*, **vol. 97**, no. 20, pp. 4–7 (2006) (cited page 11)

[Lobser *et al.* 2015] D. S. Lobser, A. E. S. Barentine, E. A. Cornell and H. J. Lewandowski. 'Observation of a persistent non-equilibrium state in cold atoms'. *Nature Physics*, **vol. 11**, pp. 1009–1012 (2015) (cited page 172)

[Loftus *et al.* 2002] T. Loftus, C. a. Regal, C. Ticknor, J. L. Bohn and D. S. Jin. 'Resonant Control of Elastic Collisions in an Optically Trapped Fermi Gas of Atoms'. *Physical Review Letters*, **vol. 88**, no. 17, p. 173201 (2002) (cited page 7)

[London 1938] F. London. 'The λ-Phenomenon of Liquid Helium and the Bose-Einstein Degeneracy'. *Nature*, **vol. 141**, pp. 643–644 (1938) (cited page 5)

[Loschmidt 1876] J. Loschmidt. 'Uber den Zustand des Warmegleichgewichtes eines Systems von Körpern mit Rückshicht auf die Scwherkraft'. *Wien. Ber.*, **vol. 73**, no. 128 (1876) (cited page 173)

[Lounis and Cohen-Tannoudji 1992] B. Lounis and C. Cohen-Tannoudji. 'Coherent population trapping and Fano profiles'. *J. Phys. II France*, **vol. 2**, no. 4, pp. 579–592 (1992) (cited page 34)

[Lu *et al.* 2015] L. Lu, Z. Wang, D. Ye, L. Ran, L. Fu, J. D. Joannopoulos and M. Solja i. 'Experimental observation of Weyl points'. *Science*, **vol. 349**, no. 6248, p. 9273 (2015) (cites pages 92, 95)

[Luo *et al.* 2007] L. Luo, B. Clancy, J. Joseph, J. Kinast and J. E. Thomas. 'Measurement of the entropy and critical temperature of a strongly interacting fermi gas'. *Physical Review Letters*, **vol. 98**, no. 8, pp. 1–4 (2007) (cited page 11)

[Maartens 2004] R. Maartens. 'Brane-World Gravity'. *Living Reviews in Relativity*, pp. 1–99 (2004) (cited page 140)

[MacKay 2009] D. MacKay. *Sustainable Energy - Without the Hot Air*. UIT Cambridge Ltd (2009). ISBN 0954452933, 384 pp. (cited page viii)

[Madison *et al.* 2000] K. Madison, F. Chevy and W. Wohlleben. 'Vortex formation in a stirred Bose-Einstein condensate'. *Physical Review letters*, **vol. 84**, no. 5, pp. 806–809 (2000) (cites pages 6, 12)

[Majorana 1932] E. Majorana. 'Atomi orientati in campo magnetico variabile'. *Il Nuovo Cimento*, **vol. 9**, no. 2, pp. 43–50 (1932) (cited page 58)

[Manai *et al.* 2015] I. Manai, J. F. Clément, R. Chicireanu, C. Hainaut, J. C. Garreau, P. Szriftgiser and D. Delande. 'Experimental Observation of Two-Dimensional Anderson Localization with the Atomic Kicked Rotor'. *Physical Review Letters*, **vol. 115**, no. 24, pp. 1–5 (2015) (cited page 11)

[Mancini *et al.* 2015] M. Mancini, G. Pagano, G. Cappellini, L. Livi, M. Rider, J. Catani, C. Sias, P. Zoller, M. Inguscio, M. Dalmonte and L. Fallani. 'Observation of chiral edge states with neutral fermions in synthetic hall ribbons'. *Science*, **vol. 349**, no. 6255, pp. 1510–1513 (2015) (cited page 12)

[Martinez-y Romero *et al.* 1992] R. P. Martinez-y Romero, H. N. Nunez-Yepez and A. L. Salas-Brito. 'Closed orbits and constants of motion in classical mechanics'. *European Journal of Physics*, **vol. 13**, no. 1, p. 26 (1992) (cited page 177)

[Massignan and Castin 2006] P. Massignan and Y. Castin. 'Three-dimensional strong localization of matter waves by scattering from atoms in a lattice with a confinement-induced resonance'. *Phys. Rev. A*, **vol. 74**, pp. 1–20 (2006) (cited page 144)

[Matthews *et al.* 1999] M. R. Matthews, B. P. Anderson, P. C. Haljan, D. S. Hall, C. E. Wieman and E. A. Cornell. 'Vortices in a Bose-Einstein Condensate'. *Physical Review Letters*, **vol. 83**, no. 13, pp. 2498–2501 (1999) (cited page 6)

[Matveeva *et al.* 2011] N. Matveeva, A. Recati and S. Stringari. 'Dipolar drag in bilayer harmonically trapped gases'. *European Physical Journal D*, **vol. 65**, no. 1-2, pp. 219–222 (2011) (cited page 154)

[McKay *et al.* 2011] D. C. McKay, D. Jervis, D. J. Fine, J. W. Simpson-Porco, G. J. A. Edge and J. H. Thywissen. 'Low-temperature high-density magneto-optical trapping of potassium using the open $4S \rightarrow 5P$ transition at 405 nm'. *Phys. Rev. A*, **vol. 84**, no. 6, p. 063420 (2011) (cited page 31)

[Mermin and Wagner 1966] N. D. Mermin and H. Wagner. 'Absence of ferromagnetism or antiferromagnetism in one- or two-dimensional isotropic heisenberg models'. *Phys. Rev. Lett.*, **vol. 17**, pp. 1133–1136 (1966) (cited page 139)

[Metcalf and van der Straten 1999] H. J. Metcalf and P. van der Straten. *Laser Cooling and Trapping*. Springer (1999). ISBN 0387987282, 324 pp. (cites pages 26, 31)

[Meyrath 2004] T. P. Meyrath. 'Electromagnet Design Basics for Cold Atom Experiments'. Tech. rep. (2004) (cited page 37)

[Migdall *et al.* 1985] A. L. Migdall, J. V. Prodan and W. D. Phillips. 'First Observation of Magnetically Trapped Neutral Atoms'. *Physical Review Letters*, **vol. 54**, no. 24, pp. 2596–2599 (1985) (cited page 56)

[Miller *et al.* 2007] D. E. Miller, J. K. Chin, C. a. Stan, Y. Liu, W. Setiawan, C. Sanner and W. Ketterle. 'Critical velocity for superfluid flow across the BEC-BCS crossover'. *Physical Review Letters*, **vol. 99**, no. 7, pp. 1–4 (2007) (cited page 7)

[Minnhagen 1987] P. Minnhagen. 'The two-dimensional Coulomb gas, vortex unbinding, and superfluid-superconducting films'. *Reviews of Modern Physics*, **vol. 59**, no. 4, p. 1001 (1987) (cited page 139)

[Miyake *et al.* 2013] H. Miyake, G. A. Siviloglou, C. J. Kennedy, W. C. Burton and W. Ketterle. 'Realizing the harper hamiltonian with laser-assisted tunneling in optical lattices'. *Physical Review Letters*, **vol. 111**, no. 18, pp. 1–5 (2013) (cited page 12)

[Modugno *et al.* 1999] G. Modugno, C. Benkő, P. Hannaford, G. Roati and M. Inguscio. 'Sub-Doppler laser cooling of fermionic ^{40}K atoms'. *Phys. Rev. A*, **vol. 60**, no. 5, pp. R3373–R3376 (1999) (cited page 32)

[Modugno *et al.* 2001] G. Modugno, G. Ferrari, G. Roati, R. J. Brecha, a. Simoni and M. Inguscio. 'Bose-Einstein condensation of potassium atoms by sympathetic cooling.' *Science (New York, N.Y.)*, **vol. 294**, no. 5545, pp. 1320–1322 (2001) (cited page 133)

[Moerdijk *et al.* 1995] A. J. Moerdijk, B. J. Verhaar and A. Axelsson. 'Resonances in ultracold collisions of ^{6}Li, ^{7}Li, and ^{23}Na'. *Phys. Rev. A*, **vol. 51**, pp. 4852–4861 (1995) (cited page 188)

[Moerdijk *et al.* 1996] A. Moerdijk, B. Verhaar and T. Nagtegaal. 'Collisions of dressed ground-state atoms'. *Phys. Rev. A*, **vol. 53**, no. 6, pp. 4343–4351 (1996) (cited page 189)

[Moritz *et al.* 2005] H. Moritz, T. Stöferle, K. Günter, M. Köhl and T. Esslinger. 'Confinement induced molecules in a 1D fermi gas'. *Physical Review Letters*, **vol. 94**, no. 21, pp. 1–4 (2005) (cited page 140)

[Müller *et al.* 2000] J. H. Müller, O. Morsch, D. Ciampini, M. Anderlini, R. Mannella and E. Arimondo. 'Atomic micromotion and geometric forces in a triaxial magnetic trap'. *Phys. Rev. Lett.*, **vol. 85**, pp. 4454–4457 (2000) (cited page 104)

[Nagaosa *et al.* 2010] N. Nagaosa, J. Sinova, S. Onoda, A. H. MacDonald and N. P. Ong. 'Anomalous Hall effect'. *Reviews of Modern Physics*, **vol. 82**, no. 2, pp. 1539–1592 (2010) (cited page 97)

[Naik *et al.* 2011] D. Naik, A. Trenkwalder, C. Kohstall, F. M. Spiegelhalder, M. Zaccanti, G. Hendl, F. Schreck, R. Grimm, T. M. Hanna and P. S. Julienne. 'Feshbach resonances in the 6Li- 40K Fermi-Fermi mixture: Elastic versus inelastic interactions'. *European Physical Journal D*, **vol. 65**, no. 1-2, pp. 55–65 (2011) (cited page 133)

[Nascimbene *et al.* 2010] S. Nascimbene, N. Navon, K. J. Jiang, F. Chevy and C. Salomon. 'Exploring the thermodynamics of a universal Fermi gas'. *Nature*, **vol. 463**, no. 7284, pp. 1057–U73 (2010) (cited page 11)

[Nath *et al.* 2013] D. Nath, R. K. Easwaran, G. Rajalakshmi and C. S. Unnikrishnan. 'Quantum-interference-enhanced deep sub-Doppler cooling of ^{39}K atoms in gray molasses'. *Phys. Rev. A*, **vol. 88**, no. 5, p. 053407 (2013) (cited page 35)

[Navon *et al.* 2010] N. Navon, S. Nascimbène, F. Chevy and C. Salomon. 'The equation of state of a low-temperature Fermi gas with tunable interactions.' *Science*, **vol. 328**, no. 5979, pp. 729–732 (2010) (cited page 11)

[Nesmeyanov and Margrave 1964] A. N. Nesmeyanov and J. L. Margrave. 'Vapour Pressure of the Elements'. *J. Chem. Educ.*, **vol. 41**, no. 8, p. A590 (1964) (cited page 26)

[Ni *et al.* 2008] K.-K. Ni, S. Ospelkaus, M. H. G. de Miranda, A. Pe'er, B. Neyenhuis, J. J. Zirbel, S. Kotochigova, P. S. Julienne, D. S. Jin and J. Ye. 'A high phase-space-density gas of polar molecules'. *Science* (2008) (cited page 12)

[Nicholson *et al.* 2015] T. Nicholson, S. Campbell, R. Hutson, G. Marti, B. Bloom, R. McNally, W. Zhang, M. Barrett, M. Safronova, G. Strouse, W. Tew and J. Ye. 'Systematic evaluation of an atomic clock at 2 10^{-18} total uncertainty'. *Nature Communications*, **vol. 6**, p. 6896 (2015) (cited page 13)

[Nielsen and Ninomiya 1981] H. Nielsen and M. Ninomiya. 'Absence of neutrinos on a lattice'. *Nuclear Physics B*, **vol. 193**, no. 1, pp. 173–194 (1981) (cited page 95)

[Nielsen and Ninomiya 1983] H. Nielsen and M. Ninomiya. 'The Adler-Bell-Jackiw anomaly and Weyl fermions in a crystal'. *Physics Letters B*, **vol. 130**, no. 6, p. 389 (1983) (cites pages 93, 95)

[Nikuni *et al.* 2000] T. Nikuni, M. Oshikawa, A. Oosawa and H. Tanaka. 'Bose-Einstein Condensation of Dilute Magnons in $TlCuCl_3$'. *Physical Review Letters*, **vol. 84**, no. 25, pp. 5868—-5871 (2000) (cited page 6)

[Nishida 2010] Y. Nishida. 'Phases of a bilayer fermi gas'. *Phys. Rev. A*, **vol. 82**, p. 011605 (2010) (cites pages 140, 150, 156)

[Nishida and Tan 2008] Y. Nishida and S. Tan. 'Universal Fermi Gases in Mixed Dimensions'. *Physical Review Letters*, **vol. 101**, no. 17, pp. 1–4 (2008) (cites pages 140, 142, 144)

[Nishida and Tan 2011] Y. Nishida and S. Tan. 'Liberating Efimov Physics from Three Dimensions'. *Few-Body Systems*, **vol. 51**, no. 2-4, pp. 191–206 (2011) (cited page 160)

[Novoselov *et al.* 2005] K. S. Novoselov, D. Jiang, F. Schedin, T. J. Booth, V. V. Khotkevich, S. V. Morozov and A. K. Geim. 'Two-dimensional atomic crystals.' *Proceedings of the National Academy of Sciences of the United States of America*, **vol. 102**, no. 30, pp. 10451–3 (2005) (cited page 140)

[O'Hara *et al.* 2001] K. O'Hara, M. Gehm, S. Granade and J. Thomas. 'Scaling laws for evaporative cooling in time-dependent optical traps'. *Phys. Rev. A*, **vol. 64**, no. 5, pp. 1–4 (2001) (cited page 131)

[Olshanii 1998] M. Olshanii. 'Atomic Scattering in Presence of an External Confinement and a Gas of Impenetrable Bosons'. *Physical review letters*, **vol. 81**, no. 5, p. 5 (1998) (cited page 140)

[Ol'shaniî and Minogin 1992] M. Ol'shaniî and V. Minogin. 'Three-dimensional velocity-selective coherent population trapping of a (3+3)-level atom'. *Optics Communications*, **vol. 89**, no. 5-6, p. 393 (1992) (cited page 32)

[Onofrio and Presilla 2004] R. Onofrio and C. Presilla. 'Ultracold Atomic Fermi–Bose Mixtures in Bichromatic Optical Dipole Traps: A Novel Route to Study Fermion Superfluidity'. *Journal of Statistical Physics*, **vol. 115**, no. 1, pp. 57–89 (2004) (cited page 13)

[Onofrio *et al.* 2000] R. Onofrio, C. Raman, J. M. Vogels, J. R. Abo-Shaeer, A. P. Chikkatur and W. Ketterle. 'Observation of superfluid flow in a Bose-Einstein condensed gas'. *Physical Review Letters*, **vol. 85**, no. 11, pp. 2228–2231 (2000) (cited page 6)

[Orlita *et al.* 2014] M. Orlita, D. M. Basko, M. S. Zholudev, F. Teppe, W. Knap, V. I. Gavrilenko, N. N. Mikhailov, S. a. Dvoretskii, P. Neugebauer, C. Faugeras, A.-L. Barra, G. Martinez and M. Potemski. 'Observation of three-dimensional massless Kane fermions in a zinc-blende crystal'. *Nature Physics*, **vol. 10**, no. 2, p. 233 (2014) (cited page 96)

[Ospelkaus *et al.* 2006] S. Ospelkaus, C. Ospelkaus, O. Wille, M. Succo, P. Ernst, K. Sengstock and K. Bongs. 'Localization of Bosonic Atoms by Fermionic Impurities in a Three-Dimensional Optical Lattice'. *Physical Review Letters*, **vol. 96**, p. 180403 (2006) (cited page 10)

[Osterloh *et al.* 2005] K. Osterloh, M. Baig, L. Santos, P. Zoller and M. Lewenstein. 'Cold atoms in non-abelian gauge potentials: From the hofstadter "moth" to lattice gauge theory'. *Physical Review Letters*, **vol. 95**, no. 1, pp. 1–4 (2005) (cited page 13)

[Ottenstein *et al.* 2008] T. B. Ottenstein, T. Lompe, M. Kohnen, a. N. Wenz and S. Jochim. 'Collisional stability of a three-component degenerate fermi gas'. *Physical Review Letters*, **vol. 101**, no. November, pp. 1–4 (2008) (cited page 187)

[Ozawa *et al.* 2014] T. Ozawa, A. Recati, M. Delehaye, F. Chevy and S. Stringari. 'Chandrasekhar-Clogston limit and critical polarization in a Fermi-Bose superfluid mixture'. *Phys. Rev. A*, **vol. 90**, no. 4, pp. 1–5 (2014) (cited page 10)

[Pais 2005] A. Pais. *Subtle Is the Lord: The Science and the Life of Albert Einstein*. Oxford University Press (2005). ISBN 9780192806727, 576 pp. (cited page 5)

[Pal 2010] P. B. Pal. 'Dirac, Majorana and Weyl fermions'. *American Journal of Physics*, **vol. 79**, no. 5, p. 32 (2010) (cited page 92)

[Papoular *et al.* 2010] D. J. Papoular, G. V. Shlyapnikov and J. Dalibard. 'Microwave-induced Fano-Feshbach resonances'. *Phys. Rev. A*, **vol. 81**, no. 4, p. 041603 (2010) (cited page 189)

[Parameswaran *et al.* 2014] S. Parameswaran, T. Grover, D. Abanin, D. A. Pesin and A. Vishwanath. 'Probing the Chiral Anomaly with Nonlocal Transport in Three-Dimensional Topological Semimetals'. *Phys. Rev. X*, **vol. 4**, no. 3, p. 031035 (2014) (cites pages 97, 98)

[Paredes *et al.* 2004] B. Paredes, a. Widera, V. Murg, O. Mandel, S. Folling, I. Cirac, G. V. Shlyapnikov, T. W. Hansch and I. Bloch. 'Tonks – Girardeau gas of ultracold atoms in an optical lattice'. *Nature*, **vol. 429**, p. 277 (2004) (cited page 140)

[Park *et al.* 2012] J. W. Park, C.-H. Wu, I. Santiago, T. G. Tiecke, S. Will, P. Ahmadi and M. W. Zwierlein. 'Quantum degenerate bose-fermi mixture of chemically different atomic species with widely tunable interactions'. *Phys. Rev. A*, **vol. 85**, p. 051602 (2012) (cited page 14)

[Park *et al.* 2015] J. W. Park, S. A. Will and M. W. Zwierlein. 'Ultracold dipolar gas of fermionic ^{23}Na^{40}K molecules in their absolute ground state'. *Physical Review Letters*, **vol. 114**, p. 205302 (2015) (cited page 14)

[Parsons *et al.* 2015] M. F. Parsons, F. Huber, A. Mazurenko, C. S. Chiu, W. Setiawan, K. Wooley-Brown, S. Blatt and M. Greiner. 'Site-Resolved Imaging of Fermionic ^{6}Li in an Optical Lattice'. *Physical Review Letters*, **vol. 114**, no. 21, p. 213002 (2015) (cited page 10)

[Pethick and Smith 2008] C. Pethick and H. Smith. *Bose-Einstein condensation in dilute gases*. Cambridge University Press (2008). ISBN 052184651X, 584 pp. (cited page 151)

[Petrich *et al.* 1995] W. Petrich, M. Anderson, J. Ensher and E. Cornell. 'Stable, Tightly Confining Magnetic Trap for Evaporative Cooling of Neutral Atoms'. *Physical Review Letters*, **vol. 74**, no. 17, pp. 3352–3355 (1995) (cites pages 58, 104, 111)

[Petrov and Shlyapnikov 2001] D. S. Petrov and G. V. Shlyapnikov. 'Interatomic collisions in a tightly confined Bose gas'. *Phys. Rev. A*, **vol. 64**, no. 1, p. 12706 (2001) (cited page 140)

[Petrov *et al.* 2004] D. S. Petrov, C. Salomon and G. V. Shlyapnikov. 'Weakly bound molecules of fermionic atoms'. *Physical Review Letters*, **vol. 93**, no. August, p. 90404 (2004) (cited page 7)

[Petrov *et al.* 2005] D. S. Petrov, C. Salomon and G. V. Shlyapnikov. 'Scattering properties of weakly bound dimers of fermionic atoms'. *Phys. Rev. A*, **vol. 71**, no. 1, pp. 1–15 (2005) (cited page 151)

[Pohl *et al.* 2010a] R. Pohl, A. Antognini, F. Nez, F. D. Amaro, F. Biraben, J. a. M. R. Cardoso, D. S. Covita, A. Dax, S. Dhawan, L. M. P. Fernandes, A. Giesen, T. Graf, T. W. Hänsch, P. Indelicato, L. Julien, C.-Y. Kao, P. Knowles, E.-O. L. Bigot, Y.-W. Liu, J. A. M. Lopes, L. Ludhova, C. M. B. Monteiro, F. Mulhauser, T. Nebel, P. Rabinowitz, J. M. F. dos Santos, L. A. Schaller, K. Schuhmann, C. Schwob, D. Taqqu, J. a. F. C. A. Veloso and F. Kottmann. 'The size of the proton'. *Nature*, **vol. 466**, pp. 213–216 (2010) (cited page 13)

[Pohl *et al.* 2010b] T. Pohl, E. Demler and M. D. Lukin. 'Dynamical Crystallization in the Dipole Blockade of Ultracold Atoms'. *Physical Review Letters*, **vol. 104**, p. 043002 (2010) (cited page 12)

[Poincaré 1890] H. Poincaré. 'Sur le problème des trois corps et les équations de la dynamique'. *Acta mathematica*, **vol. 13**, pp. 1–270 (1890) (cited page 173)

[Pottier 2007] N. Pottier. *Physique statistique hors d'équilibre : Processus irréversibles linéaires*. EDP Sciences, savoirs actuels ed. (2007). ISBN 2868839347, 524 pp. (cited page 170)

[Press *et al.* 2007] W. H. Press, S. A. Teukolsky, W. T. Vetterling and B. P. Flannery. *Numerical Recipes: The Art of Scientific Computing*. 0521880688, third edit ed. (2007). ISBN 0521880688, 1256 pp. (cited page 67)

[Price *et al.* 2015] H. M. Price, O. Zilberberg, T. Ozawa, I. Carusotto and N. Goldman. 'Four-Dimensional Quantum Hall Effect with Ultracold Atoms'. *Physical Review Letters*, **vol. 115**, p. 195303 (2015) (cited page 11)

[Purcell 1946] E. M. Purcell. 'Spontaneous Emission Probabilities at Radio Frequencies'. *Physical Review*, **vol. 69**, pp. 674–674 (1946) (cited page 159)

[QuantumManifesto 2016] QuantumManifesto. 'http://qurope.eu/manifesto' (2016) (cited page 13)

[Raab *et al.* 1987] E. L. Raab, M. Prentiss, A. Cable, S. Chu and D. E. Pritchard. 'Trapping of Neutral Sodium Atoms with Radiation Pressure'. *Physical Review Letters*, **vol. 59**, no. 23, pp. 2631–2634 (1987) (cited page 5)

[Raman *et al.* 1999] C. Raman, M. Kohl, R. Onofrio, D. S. Durfee, C. E. Kuklewicz, Z. Hadzibabic and W. Ketterle. 'Evidence for a critical velocity in a Bose-Einstein condensed gas'. *Physical Review letters*, **vol. 83**, no. 13, p. 4 (1999) (cited page 6)

[Rath *et al.* 2010] S. P. Rath, T. Yefsah, K. J. Günter, M. Cheneau, R. Desbuquois, M. Holzmann, W. Krauth and J. Dalibard. 'Equilibrium state of a trapped two-dimensional Bose gas'. *Phys. Rev. A*, **vol. 82**, no. 1, pp. 2–6 (2010) (cited page 11)

[Ray *et al.* 2014] M. W. Ray, E. Ruokokoski, S. Kandel, M. Möttönen and D. S. Hall. 'Observation of Dirac monopoles in a synthetic magnetic field'. *Nature*, **vol. 505**, pp. 657–660 (2014) (cited page 104)

[Recati *et al.* 2005] A. Recati, J. N. Fuchs, C. S. Peça and W. Zwerger. 'Casimir forces between defects in one-dimensional quantum liquids'. *Phys. Rev. A*, **vol. 72**, p. 023616 (2005) (cited page 140)

[Regal *et al.* 2003] C. a. Regal, C. Ticknor, J. L. Bohn and D. S. Jin. 'Creation of ultracold molecules from a Fermi gas of atoms.' *Nature*, **vol. 424**, no. 6944, pp. 47–50 (2003) (cites pages 9, 189)

[Ridinger 2011] A. Ridinger. *Towards quantum degenerate Fermi mixtures : Photoassociation of weakly bound 6 Li 40 K molecules*. Ph.D. thesis (2011) (cites pages 18, 29)

[Ridinger *et al.* 2011a] A. Ridinger, S. Chaudhuri, T. Salez, U. Eismann, D. R. Fernandes, K. Magalhães, D. Wilkowski, C. Salomon and F. Chevy. 'Large atom number dual-species magneto-optical trap for fermionic 6Li and 40K atoms'. *European Physical Journal D*, **vol. 65**, pp. 223–242 (2011) (cited page 15)

[Ridinger *et al.* 2011b] A. Ridinger, S. Chaudhuri, T. Salez, D. R. Fernandes, N. Bouloufa, O. Dulieu, C. Salomon and F. Chevy. 'Photoassociative creation of ultracold heteronuclear 6 li 40 k * molecules'. *EPL (Europhysics Letters)*, **vol. 96**, no. 3, p. 33001 (2011) (cited page 15)

[Riehle 2015] F. Riehle. 'Towards a redefinition of the second based on optical atomic clocks'. *Comptes Rendus Physique*, **vol. 16**, no. 5, pp. 506–515 (2015) (cited page 13)

[Rigol *et al.* 2007] M. Rigol, V. Dunjko, V. Yurovsky and M. Olshanii. 'Relaxation in a Completely Integrable Many-Body Quantum System: An Ab Initio Study of the Dynamics of the Highly Excited States of 1D Lattice Hard-Core Bosons'. *Physical Review Letters*, **vol. 98**, no. 5, p. 050405 (2007) (cited page 54)

[Ritt *et al.* 2004] G. Ritt, G. Cennini, C. Geckeler and M. Weitz. 'Laser frequency offset locking using a side of filter technique'. *Applied Physics B*, **vol. 79**, no. 2004, pp. 363–365 (2004) (cited page 25)

[Roati *et al.* 2008] G. Roati, C. D/'Errico, L. Fallani, M. Fattori, C. Fort, M. Zaccanti, G. Modugno, M. Modugno and M. Inguscio. 'Anderson localization of a non-interacting Bose-Einstein condensate'. *Nature*, **vol. 453**, no. 7197, pp. 895–898 (2008) (cited page 11)

[Rosi *et al.* 2014] G. Rosi, F. Sorrentino, L. Cacciapuoti, M. Prevedelli and G. M. Tino. 'Precision measurement of the Newtonian gravitational constant using cold atoms'. *Nature*, **vol. 510**, pp. 518–521 (2014) (cited page 13)

[Rubbmark *et al.* 1981] J. R. Rubbmark, M. M. Kash, M. G. Littman and D. Kleppner. 'Dynamical effects at avoided level crossings: A study of the landau-zener effect using rydberg atoms'. *Phys. Rev. A*, **vol. 23**, pp. 3107–3117 (1981) (cited page 118)

[Ryutov 1999] D. D. Ryutov. 'Landau damping: half a century with the great discovery'. *Plasma Physics and Controlled Fusion*, **vol. 41**, no. 3A, p. A1 (1999) (cited page 54)

[Saito *et al.* 2009] H. Saito, Y. Kawaguchi and M. Ueda. 'Ferrofluidity in a two-component dipolar bose-einstein condensate'. *Phys. Rev. Lett.*, **vol. 102**, p. 230403 (2009) (cited page 12)

[Salez 2011] T. Salez. *Towards quantum degenerate atomic Fermi mixtures*. Ph.D. thesis (2011) (cites pages 18, 26)

[Salomon *et al.* 2013] G. Salomon, L. Fouché, P. Wang, A. Aspect, P. Bouyer and T. Bourdel. 'Gray-molasses cooling of 39 K to a high phase-space density'. *EPL (Europhysics Letters)*, **vol. 104**, no. 6, p. 63002 (2013) (cited page 35)

[Santos 2010] L. Santos. 'Theory of dipolar gases'. In C Salomon, GV Shlyapnikov and LF Cugliandolo, editors, 'Many-Body Physics with Ultracold Gases', Oxford University Press (2010). ISBN 9780199661886 (cited page 12)

[Santos *et al.* 2009] F. C. Santos, V. Soares, A. C. Tort and R. D. Janeiro. 'The determination of the apsidal angles and Bertrand's theorem'. *Physical Review E*, **vol. 79**, no. 3, p. 036605 (2009) (cited page 178)

[Santos *et al.* 2011] F. C. Santos, V. Soares and A. C. Tort. 'An English translation of Bertrand ' s theorem'. *Lat. Am. J. Phys. Educ.*, **vol. 5**, no. 4, p. 694 (2011) (cited page 177)

[Schauß *et al.* 2012] P. Schauß, M. Cheneau, M. Endres, T. Fukuhara, S. Hild, A. Omran, T. Pohl, C. Gross, S. Kuhr and I. Bloch. 'Observation of spatially ordered structures in a two-dimensional Rydberg gas'. *Nature*, **vol. 491**, no. 7422, pp. 87–91 (2012) (cited page 12)

[Schecter and Kamenev 2014] M. Schecter and A. Kamenev. 'Phonon-Mediated Casimir Interaction between Mobile Impurities in One-Dimensional Quantum Liquids'. *Physical Review Letters*, **vol. 112**, no. 2, p. 155301 (2014) (cited page 140)

[Schneider *et al.* 2008] U. Schneider, L. Hackermüller, S. Will, T. Best, I. Bloch, T. A. Costi, R. W. Helmes, D. Rasch and A. Rosch. 'Metallic and Insulating Phases of Repulsively Interacting Fermions in a 3D Optical Lattice'. *Science*, **vol. 322**, no. 5907, pp. 1520–1525 (2008) (cited page 10)

[Schreck 2002] F. Schreck. *Mélanges de gaz ultrafroids : mer de Fermi et condensats de Bose Einstein du Lithium*. Ph.D. thesis (2002) (cited page 26)

[Schreck *et al.* 2001] F. Schreck, G. Ferrari, K. L. Corwin, J. Cubizolles, L. Khaykovich, M. Mewes and C. Salomon. 'Sympathetic cooling of bosonic and fermionic lithium gases towards quantum degeneracy'. *Phys. Rev. A*, **vol. 64**, pp. 5–8 (2001) (cited page 6)

[Schreiber *et al.* 2015] M. Schreiber, S. S. Hodgman, P. Bordia, H. P. Lüschen, M. H. Fischer, R. Vosk, E. Altman, U. Schneider and I. Bloch. 'Observation of many-body localization of interacting fermions in a quasirandom optical lattice'. *Science*, **vol. 349**, no. 6250, pp. 842–845 (2015) (cited page 11)

[Shahriar *et al.* 1993] M. S. Shahriar, P. R. Hemmer, M. G. Prentiss, P. Marte, J. Mervis, D. P. Katz, N. P. Bigelow and T. Cai. 'Continuous polarization-gradient precooling-assisted velocity-selective coherent population trapping'. *Phys. Rev. A*, **vol. 48**, no. 6, pp. R4035—-R4038 (1993) (cited page 33)

[Sherson *et al.* 2010] J. F. Sherson, C. Weitenberg, M. Endres, M. Cheneau, I. Bloch and S. Kuhr. 'Single-atom-resolved fluorescence imaging of an atomic Mott insulator.' *Nature*, **vol. 467**, no. 7311, pp. 68–72 (2010) (cited page 10)

[Shin *et al.* 2008] Y.-I. Shin, C. H. Schunck, A. Schirotzek and W. Ketterle. 'Phase diagram of a two-component Fermi gas with resonant interactions.' *Nature*, **vol. 451**, no. 7179, pp. 689–693 (2008) (cited page 11)

[Shuve and Thywissen 2009] B. Shuve and J. H. Thywissen. 'Enhanced Pauli blocking of light scattering in a trapped Fermi gas'. p. 12 (2009) (cited page 159)

[Sievers 2014] F. Sievers. *Ultracold Fermi mixtures and simultaneous sub-Doppler laser cooling of fermionic* ^{6}*Li and* ^{40}*K*. Ph.D. thesis (2014) (cites pages 39, 61)

[Sievers *et al.* 2015] F. Sievers, N. Kretzschmar, D. R. Fernandes, D. Suchet, M. Rabinovic, S. Wu, C. V. Parker, L. Khaykovich, C. Salomon and F. Chevy. 'Simultaneous sub-Doppler laser cooling of fermionic ^{6}Li and ^{40}K on the D_1 line: Thoery and experiment'. *Phys. Rev. A*, **vol. 91**, no. 2, p. 023426 (2015) (cites pages 15, 32, 33, 34)

[Silvestrov and Efetov 2007] P. G. Silvestrov and K. B. Efetov. 'Quantum dots in graphene'. *Physical Review Letters*, **vol. 98**, no. 1, pp. 1–4 (2007) (cited page 99)

[Simoni *et al.* 2003] A. Simoni, F. Ferlaino, G. Roati, G. Modugno and M. Inguscio. 'Magnetic Control of the Interaction in Ultracold K-Rb Mixtures'. *Physical Review Letters*, **vol. 90**, no. 16, p. 163202 (2003) (cited page 133)

[Snoke and Wolfe 1989] D. W. Snoke and J. P. Wolfe. 'Population dynamics of a Bose gas near saturation'. *Phys. Rev. B*, **vol. 39**, no. 7, pp. 4030–4037 (1989) (cited page 66)

[Son and Spivak 2013] D. T. Son and B. Z. Spivak. 'Chiral anomaly and classical negative magnetoresistance of Weyl metals'. *Phys. Rev. B*, **vol. 88**, no. 10, p. 104412 (2013) (cited page 96)

[Spiegelhalder *et al.* 2009] F. M. Spiegelhalder, A. Trenkwalder, D. Naik, G. Hendl, F. Schreck and R. Grimm. 'Collisional Stability of K40 Immersed in a Strongly Interacting Fermi Gas of Li6'. *Physical Review Letters*, **vol. 103**, no. 22, pp. 1–4 (2009) (cites pages 14, 133)

[Spiegelhalder *et al.* 2010] F. M. Spiegelhalder, A. Trenkwalder, D. Naik, G. Kerner, E. Wille, G. Hendl, F. Schreck and R. Grimm. 'All-optical production of a degenerate mixture of Li6 and K40 and creation of heteronuclear molecules'. *Phys. Rev. A*, **vol. 81**, no. 4, pp. 1–11 (2010) (cites pages 14, 134)

[Stamper-Kurn and Ueda 2013] D. M. Stamper-Kurn and M. Ueda. 'Spinor bose gases: Symmetries, magnetism, and quantum dynamics'. *Rev. Mod. Phys.*, **vol. 85**, pp. 1191–1244 (2013) (cited page 12)

[Stanescu *et al.* 2007] T. D. Stanescu, C. Zhang and V. Galitski. 'Nonequilibrium spin dynamics in a trapped fermi gas with effective spin-orbit interactions'. *Physical Review Letters*, **vol. 99**, no. 11, pp. 1–4 (2007) (cited page 13)

[Steck 2012] D. Steck. 'Quantum and Atom Optics'. *http://steck.us/teaching* (2012) (cited page 117)

[Stewart *et al.* 2006] J. T. Stewart, J. P. Gaebler, C. a. Regal and D. S. Jin. 'Potential Energy of a ^{40}K Fermi Gas in the BCS-BEC Crossover'. *Physical Review Letters*, **vol. 97**, no. 22, p. 220406 (2006) (cited page 11)

[Strohmaier *et al.* 2007] N. Strohmaier, Y. Takasu, K. Günter, R. Jördens, M. Köhl, H. Moritz and T. Esslinger. 'Interaction-Controlled Transport of an Ultracold Fermi Gas'. *Physical Review Letters*, **vol. 99**, p. 220601 (2007) (cited page 10)

[Struck *et al.* 2013] J. Struck, M. Weinberg, C. Olschlager, P. Windpassinger, J. Simonet, K. Sengstock, R. Hoppner, P. Hauke, A. Eckardt, M. Lewenstein and L. Mathey. 'Engineering Ising-XY spin-models in a triangular lattice using tunable artificial gauge fields'. *Nature Physics*, **vol. 9**, no. 11, pp. 738–743 (2013) (cited page 12)

[Suchet *et al.* 2016] D. Suchet, M. Rabinovic, T. Reimann, Norman, Kretzschmar, F. Sievers, C. Salomon, J. Lau, O. Goulko, C. Lobo and F. Chevy. 'Analog simulation of Weyl particles with cold atoms'. *Europhysics Letters*, **vol. 114**, p. 26005 (2016) (cited page 15)

[Sukumar and Brink 1997] C. V. Sukumar and D. M. Brink. 'Spin-flip transitions in a magnetic trap'. *Phys. Rev. A*, **vol. 56**, pp. 2451–2454 (1997) (cites pages 104, 109)

[Surkov *et al.* 1994] E. L. Surkov, J. T. M. Walraven and G. V. Shlyapnikov. 'Collisionless motion of neutral particles in magnetostatic traps'. *Phys. Rev. A*, **vol. 49**, pp. 4778–4786 (1994) (cited page 73)

[Taglieber *et al.* 2006] M. Taglieber, A.-C. Voigt, F. Henkel, S. Fray, T. W. Hänsch and K. Dieckmann. 'Simultaneous magneto-optical trapping of three atomic species'. *Phys. Rev. A*, **vol. 73**, p. 011402 (2006) (cited page 14)

[Taglieber *et al.* 2008] M. Taglieber, A. C. Voigt, T. Aoki, T. W. Hänsch and K. Dieckmann. 'Quantum degenerate two-species fermi-fermi mixture coexisting with a Bose-Einstein condensate'. *Physical Review Letters*, **vol. 100**, no. 1, pp. 1–4 (2008) (cited page 14)

[Theis *et al.* 2004] M. Theis, G. Thalhammer, K. Winkler, M. Hellwig, G. Ruff, R. Grimm and J. H. Denschlag. 'Tuning the scattering length with an optically induced feshbach resonance'. *Physical Review Letters*, **vol. 93**, no. 12, pp. 10–13 (2004) (cited page 189)

[Thomas *et al.* 2005] J. E. Thomas, J. Kinast and a. Turlapov. 'Virial theorem and universality in a unitary fermi gas'. *Physical Review Letters*, **vol. 95**, no. 12, pp. 1–4 (2005) (cited page 11)

[Tiecke 2009] T. Tiecke. *Feshbach resonances in ultracold mixtures of the fermionic quantum gases*. Ph.D. thesis (2009) (cited page 133)

[Tiecke 2010] T. G. Tiecke. 'Properties of Potassium'. *unpublised*, pp. 1–14 (2010) (cites pages 20, 23)

[Tiecke *et al.* 2009] T. G. Tiecke, S. D. Gensemer, A. Ludewig and J. T. M. Walraven. 'High-flux two-dimensional magneto-optical-trap source for cold lithium atoms'. *Phys. Rev. A*, **vol. 80**, no. 1, pp. 1–12 (2009) (cited page 14)

[Tiecke *et al.* 2010a] T. G. Tiecke, M. R. Goosen, A. Ludewig, S. D. Gensemer, S. Kraft, S. J. J. M. F. Kokkelmans and J. T. M. Walraven. 'Broad feshbach resonance in the Li6-K40 mixture'. *Physical Review Letters*, **vol. 104**, no. 5, pp. 1–4 (2010) (cites pages 14, 133)

[Tiecke *et al.* 2010b] T. G. Tiecke, M. R. Goosen, J. T. M. Walraven and S. J. J. M. F. Kokkelmans. 'Asymptotic-bound-state model for feshbach resonances'. *Phys. Rev. A*, **vol. 82**, no. 4, pp. 1–11 (2010) (cites pages 14, 133)

[Tiesinga *et al.* 1993] E. Tiesinga, B. J. Verhaar and H. T. C. Stoof. 'Threshold and resonance phenomena in ultracold ground-state collisions'. *Phys. Rev. A*, **vol. 47**, no. 5, p. 4114 (1993) (cited page 188)

[Tisza 1938] L. Tisza. 'Transport Phenomena in Helium II'. *Nature*, **vol. 141**, pp. 913–913 (1938) (cited page 5)

[Tisza 1947] L. Tisza. 'The Theory of Liquid Helium'. *Phys. Rev.*, **vol. 72**, pp. 838–854 (1947) (cited page 5)

[Trenkwalder *et al.* 2011] A. Trenkwalder, C. Kohstall, M. Zaccanti, D. Naik, A. I. Sidorov, F. Schreck and R. Grimm. 'Hydrodynamic expansion of a strongly interacting fermi-fermi mixture'. *Physical Review Letters*, **vol. 106**, p. 115304 (2011) (cited page 14)

[Turner and Vishwanath 2013] A. M. Turner and A. Vishwanath. 'Beyond band insulators: Topology of semimetals and interacting phases'. *Contemporary Concepts of Condensed Matter Science*, **vol. 6**, pp. 293–324 (2013) (cited page 94)

[Valentin *et al.* 1992] C. Valentin, M.-C. Gagné, J. Yu and P. Pillet. 'One-Dimension Sub-Doppler Molasses in the Presence of Static Magnetic Field'. *EPL (Europhysics Letters)*, **vol. 17**, no. 2, p. 133 (1992) (cited page 33)

[Van Amerongen *et al.* 2008] A. H. Van Amerongen, J. J. P. Van Es, P. Wicke, K. V. Kheruntsyan and N. J. Van Druten. 'Yang-Yang thermodynamics on an atom chip'. *Physical Review Letters*, **vol. 100**, no. 9, pp. 13–15 (2008) (cited page 11)

[Van Dongen *et al.* 2011] J. Van Dongen, C. Zhu, D. Clement, G. Dufour, J. L. Booth and K. W. Madison. 'Trap-depth determination from residual gas collisions'. *Phys. Rev. A*, **vol. 84**, no. 2, pp. 1–11 (2011) (cited page 19)

[Vilani 2010] C. Vilani. '(Ir)reversibilit et entropie'. *Seminaire Poincare XV : Le Temps*, pp. 17–75 (2010) (cites pages 53, 172)

[Vishwanath 2015] A. Vishwanath. 'Where the Weyl Things Are'. *Physics*, **vol. 8**, no. 84 (2015) (cited page 92)

[Voigt *et al.* 2009] A.-C. Voigt, M. Taglieber, L. Costa, T. Aoki, W. Wieser, T. W. Hänsch and K. Dieckmann. 'Ultracold heteronuclear fermi-fermi molecules'. *Physical Review Letters*, **vol. 102**, p. 020405 (2009) (cited page 14)

[Walraven 2010] J. Walraven. 'Elements of Quantum Gases : Thermodynamic and Collisional Properties of Trapped Atomic Gases'. *Cold-Atoms PreDoc School* (2010) (cites pages 56, 124, 181)

[Wang *et al.* 2012] P. Wang, Z.-Q. Yu, Z. Fu, J. Miao, L. Huang, S. Chai, H. Zhai and J. Zhang. 'Spin-Orbit Coupled Degenerate Fermi Gases'. *Physical Review Letters*, **vol. 109**, p. 095301 (2012) (cited page 13)

[Weber *et al.* 2003] T. Weber, J. Herbig, M. Mark, H.-C. Nägerl and R. Grimm. 'Bose-Einstein condensation of cesium.' *Science (New York, N.Y.)*, **vol. 299**, no. 5604, pp. 232–5 (2003) (cited page 129)

[Weidemuller *et al.* 1994] M. Weidemuller, T. Esslinger, M. A. Ol'Shanii, A. Hemmerich and T. W. Hansch. 'A Novel Scheme for Efficient Cooling below the Photon Recoil Limit .' *Europhyscs letters*, **vol. 27**, no. 2, p. 109 (1994) (cited page 33)

[Weimer *et al.* 2008] H. Weimer, R. Löw, T. Pfau and H. P. Büchler. 'Quantum Critical Behavior in Strongly Interacting Rydberg Gases'. *Physical Review Letters*, **vol. 101**, p. 250601 (2008) (cited page 12)

[Weyl 1929] H. Weyl. 'Elektron und Gravitation. I'. *Zeitschrift für Physik*, **vol. 56**, no. 5, p. 330 (1929) (cited page 92)

[Wille *et al.* 2008] E. Wille, F. Spiegelhalder, G. Kerner, D. Naik, a. Trenkwalder, G. Hendl, F. Schreck, R. Grimm, T. Tiecke, J. Walraven, S. Kokkelmans, E. Tiesinga and P. Julienne. 'Exploring an Ultracold Fermi-Fermi Mixture: Interspecies Feshbach Resonances and Scattering Properties of Li6 and K40'. *Physical Review Letters*, **vol. 100**, no. 5, p. 053201 (2008) (cites pages 133, 187)

[Wineland and Dehmelt 1975] D. J. Wineland and H. Dehmelt. 'Proposed $10^{14}\Delta\nu < \nu$ laser fluorescence spectroscopy on Tl+ mono-ion oscillator'. *Bulletin of the American Physical Society*, **vol. 20**, p. 637 (1975) (cited page 5)

[Wing 1984] W. Wing. 'On Neutral Particle Trapping in Quasistatic Electromagnetic Fields.' *Prog. Quant. Elect*, **vol. 8**, no. 181 (1984) (cited page 55)

[Wu *et al.* 2011] C. H. Wu, I. Santiago, J. W. Park, P. Ahmadi and M. W. Zwierlein. 'Strongly interacting isotopic Bose-Fermi mixture immersed in a Fermi sea'. *Phys. Rev. A*, **vol. 84**, no. 1, pp. 1–4 (2011) (cited page 14)

[Xu *et al.* 2015a] S.-y. Xu, I. Belopolski, N. Alidoust, M. Neupane, G. Bian, C. Zhang, R. Sankar, G. Chang, Z. Yuan, C.-c. Lee, S.-m. Huang, H. Zheng, D. S. Sanchez, B. Wang, A. Bansil, F. Chou, P. P. Shibayev, H. Lin, S. Jia and M. Z. Hasan. 'Discovery of a Weyl fermion semimetal and topological Fermi arcs'. *Science*, **vol. 349**, no. 6248, p. 613 (2015) (cited page 95)

[Xu *et al.* 2015b] S.-Y. Xu, C. Liu, S. K. Kushwaha, R. Sankar, J. W. Krizan, I. Belopolski, M. Neupane, G. Bian, N. Alidoust, T.-R. Chang, H.-T. Jeng, C.-Y. Huang, W.-F. Tsai, H. Lin, P. P. Shibayev, F.-C. Chou, R. J. Cava and M. Z. Hasan. 'Observation of Fermi arc surface states in a topological metal'. *Science*, **vol. 347**, no. 6219, pp. 294–298 (2015) (cites pages 92, 95)

[Yakimovich and Mozgovoi 2000] K. A. Yakimovich and A. G. Mozgovoi. 'Experimental investigation of the density and surface tension of molten lithium at temperatures up to 1300 K'. *High Temperature*, **vol. 38**, no. 4, p. 657 (2000) (cited page 27)

[Yefsah *et al.* 2011] T. Yefsah, R. Desbuquois, L. Chomaz, K. J. Günter and J. Dalibard. 'Exploring the thermodynamics of a two-dimensional bose gas'. *Physical Review Letters*, **vol. 107**, no. 13, pp. 1–5 (2011) (cited page 11)

[Young *et al.* 2012] S. M. Young, S. Zaheer, J. C. Y. Teo, C. L. Kane, E. J. Mele and a. M. Rappe. 'Dirac Semimetal in Three Dimensions'. *Physical Review Letters*, **vol. 108**, no. 14, p. 140405 (2012) (cited page 93)

[Zener 1932] C. Zener. 'Non-adiabatic crossing of energy levels'. *Proceedings of the Royal Society of London A: Mathematical, Physical and Engineering Sciences*, **vol. 137**, no. 833, pp. 696–702 (1932) (cited page 118)

[Zeng *et al.* 2015] T.-S. Zeng, C. Wang and H. Zhai. 'Charge Pumping of Interacting Fermion Atoms in the Synthetic Dimension'. *Physical Review Letters*, **vol. 115**, p. 095302 (2015) (cited page 11)

[Zermelo 1896] E. Zermelo. 'Uber einen Satz der Dynamik und die mechanische Warmetheorie'. *Annalen der Physik*, **vol. 293**, no. 3, p. 485 (1896) (cited page 173)

[Zhang *et al.* 2009] P. Zhang, P. Naidon and M. Ueda. 'Independent Control of Scattering Lengths in Multicomponent Quantum Gases'. *Physical Review Letters*, **vol. 103**, no. 13, pp. 1–4 (2009) (cited page 189)

[Zhang *et al.* 2014] R. Zhang, W. Zhang, H. Zhai and P. Zhang. 'Calibration of the interaction energy between Bose and Fermi superfluids'. *Phys. Rev. A*, **vol. 90**, no. 6, pp. 1–9 (2014) (cited page 150)

[Zwerger 2012] W. Zwerger, editor. *The BCS-BEC Crossover and the Unitary Fermi Gas*. Springer-Verlag (2012). ISBN 978-3-642-21977-1, 532 pp. (cited page 7)

[Zwierlein *et al.* 2003] M. Zwierlein, C. Stan, C. Schunck, S. Raupach, S. Gupta, Z. Hadzibabic and W. Ketterle. 'Observation of Bose-Einstein Condensation of Molecules'. *Physical Review Letters*, **vol. 91**, no. 25, p. 250401 (2003) (cited page 9)

[Zwierlein *et al.* 2004] M. W. Zwierlein, C. A. Stan, C. H. Schunck, S. M. F. Raupach, A. J. Kerman and W. Ketterle. 'Condensation of Pairs of Fermionic Atoms near a Feshbach Resonance'. *Physical Review Letters*, **vol. 92**, no. 12, p. 120403 (2004) (cited page 7)

[Zwierlein *et al.* 2005a] M. W. Zwierlein, A. Schirotzek, C. H. Schunck and W. Ketterle. 'Vortices and superfluidity in a strongly interacting Fermi gas'. *Nature*, **vol. 435**, no. June, pp. 1047–1051 (2005) (cited page 7)

[Zwierlein *et al.* 2005b] M. W. Zwierlein, C. H. Schunck, C. A. Stan, S. M. F. Raupach and W. Ketterle. 'Formation Dynamics of a Fermion Pair Condensate'. *Physical Review Letters*, **vol. 94**, no. 18, p. 180401 (2005) (cites pages 7, 190)

[Zwierlein *et al.* 2006] M. W. Zwierlein, A. Schirotzek, C. H. Schunck and W. Ketterle. 'Fermionic Superfluidity with Imbalanced Spin Populations'. *Science*, **vol. 311**, no. January, pp. 492–496 (2006) (cites pages 7, 11)

Simulating the dynamics of harmonically trapped Weyl particles with cold atoms

Résumé : Au cours de ma thèse, j'ai travaillé à la construction de l'expérience FERMIX, consacrée à l'étude d'un mélange de fermions (^{6}Li-^{40}K) à très basses températures où les effets quantiques sont prédominants. Nous présentons ici deux résultats principaux. Premièrement, nous avons développé une nouvelle méthode de refroidissement sub-Doppler qui tire parti de l'existence d'états noirs dans la raie optique D_1. Cette *mélasse grise* permet d'atteindre une densité de l'espace des phases de 10^{-4}, la valeur la plus élevée rapportée dans la littérature pour le refroidissement laser simultané des deux espèces. Grâce à cette étape, nous avons pu réaliser un gaz fortement dégénéré de 3×10^5 atomes de ^{40}K répartis dans deux états de spins, à une température de 62 nK, soit 17% de la température de Fermi. D'autre part, nous introduisons une transformation canonique pour montrer l'équivalence formelle entre le comportement de particules ultra-relativistes sans interactions (particules de Weyl) dans un potentiel harmonique et celui de fermions froids confinés dans un piège quadrupolaire. Nous étudions expérimentalement, numériquement et théoriquement la relaxation de tels systèmes vers un état stationnaire, non-Botlzmanien, caractérisé par des températures effectives fortement anisotropes. Cette analogie permet également d'interpréter des propriétés caractéristiques des particules relativistes. Ainsi, nous montrons que le paradoxe de Klein est analogue aux pertes Majorana. Pour finir, nous proposons une étude théorique des interactions médiées à longue distance par un système en dimensions mixtes. Ce système permettra l'étude directe des interactions médiées en mesurant la fréquence de battement entre deux nuages confinés dans les plans voisins d'un réseau optique.

Mots clés : Atomes froids, gaz de fermions dégénéré, mélasses grises, particules de Weyl

Abstract : During my PhD, I contributed to the design and construction of the FERMIX experiment, dedicated to the study of a ^{6}Li-^{40}K fermionic mixture at ultra low temperatures. Our main results are twofold. First, we developed a new sub-Doppler laser cooling scheme, taking advantage of the existence of dark states in the D_1 line of alkali atoms. This so-called *grey molasses* allows for a phase space density up to 10^{-4}, the highest value reported for the simultaneous laser cooling of those two species. The improvement due to this cooling step enabled the production of a quantum degenerate ^{40}K gas in a dipole trap, with 3×10^5 atoms in two spin states at 62 nK, corresponding to 17% of the Fermi temperature. Second, introducing a canonical mapping, we showed that non-interacting ultra-relativistic particles (Weyl fermions) in a harmonic trap can be simulated by cold fermions confined in a quadrupole potential. We study experimentally, numerically and theoretically the relaxation of these systems towards a steady state which can not be described by a Boltzman distribution, but rather presents strongly anisotropic effective temperatures. This analogy also allows us to translate fundamental properties of relativistic particles in the language of cold atoms. In particular, we demonstrate that the Klein paradox is equivalent to Majorana losses. Finally, we present a theoretical study of the long range interactions between particles confined in two 2D layers immersed in a 3D atomic cloud. We show that mediated interactions can be studied experimentally by measuring the beat-note of two clouds confined in neighboring planes of an optical lattice.

Keywords : ultracold atoms, degenerate Fermi gas, grey optical molasses, Weyl particles